Biodiesel production from low quality feedstocks using novel core-shell heterogeneous acid nanocatalysts

Brandon Glen Connor Lowe

Submitted in accordance with the requirements for the degree of

Doctor of Philosophy

The University of Leeds

School of Chemical and Process Engineering

March 2025

Declaration

I confirm that the work submitted is my own, except where work which has formed part of jointly authored publications has been included. My contribution and the other authors to this work has been explicitly indicated below. I confirm that appropriate credit has been given within the thesis where reference has been made to the work of others.

- The work in Chapter Two of the thesis has appeared in publication as follows:

  Lowe, B., Ahmad, A.M., Gardy, J. and Hassanpour, A. Nanomaterials used in biorefineries: Types, properties, and synthesis methods. In: Ingle, A.P. ed. Nanotechnology for Biorefinery. Amsterdam, The Netherlands: Elsevier, 2021.

  Lowe, B., Gardy, J., Wu, K. and Hassanpour, A. Mixed Metal Oxide Catalysts in Biodiesel Production. In: Rokhum, L. ed. Biodiesel Production: Feedstocks, Catalysts and Technologies. Hoboken, NJ, USA: John Wiley and Sons, 2022, pp.143-166.

  Lowe, B., Gardy, J. and Hassanpour, A. The Role of Sulfated Materials for Biodiesel Production from Cheap Raw Materials. Catalysts. [Online]. 2022, 12(2). Available from: https://doi.org/10.3390/catal12020223

I confirm that this work has been completed fully by myself including writing of the thesis, except from supervision roles and accessing some of the analytical equipment as noted in the upcoming acknowledgements section.

Acknowledgements

I wish to thank my entire supervision team for all of their help, guidance and support throughout my PhD journey. This includes my primary supervisor Dr. Ali Hassanpour alongside Dr. Jabbar Gardy, Dr. Kejun Wu and Dr Hu Li as secondary supervisors. I also wish to thank them for their kind assistance in proposing, reviewing and editing conference material and published works. I express gratitude to my transfer panel Dr. Xiaoan Mao and Dr. Xiaojun Lai for their thorough review and guidance during the upgrade process. Thanks are given to Dr. Xiaoan Mao, Dr. David Harbottle, Dr. Girish Kale and Dr. Frans Muller for their guidance during progress reviews. Much appreciation is given to Dr. Xiaoan Mao and Dr. Mohammed Rehan as my viva examiners, and Dr. David Harbottle is thanked as viva chair. SCAPE faculty, administration and support staff at the University of Leeds are thanked for the help, assistance and pleasant interactions I had. I lack the words to express my gratitude for the incredible support and guidance I received performing various analytical techniques throughout the University of Leeds. Significant appreciation is given to Dr. Adrian Cunliffe and Dr. Karine Alves Thorne at the Energy labs building for support with FTIR, GC-MS, CHONS, TGA and Flashpoint analysis methods, as well as generously providing so much of their time and guidance with my queries. Gratitude is expressed to Dr. Ben Douglas for support with BET, DLS-Zetapotential, rheology and lab access. Dr. Xiaojun Lai, Dr. Ali Hassanpour and Dr. Jabbar Gardy are thanked for providing lab access and Dr. Jabbar Gardy is also thanked for providing initial support and training with catalyst synthesis. Dr. Laksha Parameswaran and Prof. Kevin Roberts are thanked for training and access to ATR-FTIR facilities. Thanks are given to Dr. Faye Esat, Mohammed Javed and Dr. Thomas Brown for their running of XRD analysis and guidance. Stuart Micklethwaite, Dr. Zabeada Aslam and LEMAS facilities are thanked for their support with performing STEM-EDX and SAED analysis. Dr. Andrew Britton and Bragg centre are thanked for assistance in XPS. School of Chemistry staff including Dr. Alex Heyam and Dr. Mary Bayana are thanked for graciously providing access to their labs and providing training on NMR and GC-MS facilities respectively. I also wish to thank financial support given by EPSRC Doctoral Training Partnership (EP/T517860/1) and SCAPE department at the University of Leeds in support of equipment, training and analysis costs. Finally, I wish to thank my research group community: fellow PhD students, postgraduates, academic staff and all others I forgot to include for their support, assistance and camaraderie during the research journey.

Dedication

This research work is dedicated to my wonderful, loving and ever patient family and friends who have been just as much a part of this research journey as I have. From every dark moment that you were there to commiserate with me, to every joyous breakthrough in which we celebrated together. While I may lack to words to fully express my gratitude and heartful appreciation for your continued support, I hope that this completed thesis stands testament to our combined spirit of perseverance, determination and resilience. To never giving up. Thank you.

Conference Attendances

- ***B. Lowe***, A. Hassanpour, "*Synthesis and Functionalisation of (Ti/Zn)-Fe-Si Solid Acid Metal Oxide Nanocatalysts for Conversion of Low-Grade Waste Cooking Oil to Biodiesel*" ***poster presentation*** on **15-16th January 2024** to Royal Society of Chemistry (RSC) Chemical Nanoscience & Nanotechnology Group Annual Symposium: Nanotechnology for Energy, Environment and Biomedicine at Burlington House, W1J 0BA London, UK.

- ***B. Lowe***, A. Hassanpour, H. Li "*Application of (Ti/Zn)-Fe-Si Solid Acid Metal Oxide Nanocatalysts for Conversion of Low-Grade Waste Cooking Oil to Biodiesel*" ***poster presentation*** on **25-26th April 2024** to ChemEngDayUK 2024 at Imperial College London, SW7 2AZ London, UK.

- ***B. Lowe***, A. Hassanpour, H. Li "*Application of (Ti/Zn)-Fe-Si Solid Acid Metal Oxide Nanocatalysts for Conversion of Low-Grade Waste Cooking Oil to Biodiesel*" ***oral presentation*** on **18th June 2024** to Bragg PhD Colloquium at Bragg Centre for Materials Research, University of Leeds, LS2 9JT, Leeds, Uk.

Abstract

Biodiesel production must increase to meet demand. Use of cheap waste feedstocks such as used cooking oils (UCO) can avoid "food vs. fuel" competition. In this work, six novel nanocatalysts were developed based on unreported TiFeSi and ZnFeSi core-shell design. Functionalisation conditions were explored via three chlorosulfonic acid concentrations (0.1 M, 0.55 M, 1.0 M). TiFeSi series achieved more desirable thermal, chemical, morphological and structural properties compared to ZnFeSi series.

STEM revealed core shell morphology, with 100-450 nm dense aggregates decorated with <100 nm nanoparticles. Porosity was mesoporous with 3-4 nm ink bottle pores. BET specific surface areas of 72-82 m^2/g for Ti series were achieved independent of acid concentration. Very low 6-13 m^2/g surface area for Zn series indicated ZnFeSi synthesis requires improvement. Crystalline phases of anatase TiO_2 and hexagonal wurtzite ZnO was observed pre-functionalisation via XRD and SAED. Post acidification, Ti series crystallinity remained similar however new crystalline phases of $Zn(OH)_2$ or sulfated ZnO were seen. Surface S-O and S=O species were confirmed via ATR-FTIR and XPS with bridged bidentate sulfate structure. Pyridine TPD indicated high Brønsted acidity with no notable Lewis acidity. Batch trials confirmed nanocatalysts were only esterification active under reasonable reaction conditions.

Oleic acid as model FFA was explored using Design of Experiments modelling, with 0.1M-TiFeSi and 0.55M-TiFeSi showing highest activity. Optimal ~100% methyl oleate yield was obtained with 0.55M-TiFeSi after 6.75 hours, 60 °C, 3.19 wt% catalyst and 16:1 methanol to oleic acid. In a two-step pathway with 0.55M-TiFeSi and KOH, 15.8% and 30.6% increase in biodiesel yield was achieved with fresh/degraded UCO. Although sulfate leaching prevented reusability, TiFeSi nanocatalysts were demonstrated to successfully reduce FFA content and improve base catalyst performance. While inclusion of new chemical species may improve activity, TiFeSi results appear promising. Future studies should optimise synthesis route and two-step pathway.

Keywords:

UCO, Biodiesel, Nanocatalyst, Esterification, Sulfated Metal Oxide, Chlorosulfonic Acid, Characterisation, Design of Experiments, Optimisation, Two-Step

Table of Contents

List of Tables

List of Figures

Nomenclature

List of abbreviations

Abbreviation	Description
ABF/ADF	Annular Brightfield/Darkfield
AES	Auger Electron Spectroscopy
ANOVA	Analysis of variance
ASTM	American Society for Testing and Materials
ATR	Attenuated Total Reflectance
AV	Acid Value
BET	Brunauer, Emmett and Teller
BF	Brightfield
BJH	Barrett-Joyner-Halenda
BS	British Standard
CHONS	Carbon, Hydrogen, Oxygen, Nitrogen and Sulfur
CNF	Carbon Nanofibers
CNT	Carbon Nanotubes
COK	Centrum voor Oppervlaktechemie en Katalyse (Centre for Research Chemistry and Catalysis)
CY	Cheng-Yang
DES	Deep eutectic solvent
DG	Diglycerides
DLS	Dynamic Light Scattering
DOE	Design of Experiment
DR	Dubinin-Radushkevich
DSC	Differential Scanning Calorimetry
DSD	Definitive Screening Designs
DTG	Derivative Thermogram
EDX/EDS	Energy Dispersive X-ray Spectrometry
EN	Europäische Norm (European Standards)
EV	Electric vehicles
FAME	Fatty acid methyl esters
FFA	Free fatty acids
FSM	Folded Sheets Mesoporous Material
FTIR	Fourier Transform Infrared Spectroscopy
FWHM	Full Width Half Maximum
GC-FID	Gas Chromatography Flame Ionisation Detection
GC-MS	Gas Chromatography Mass Spectrometry
GHG	Greenhouse gases
GO	Graphene Oxide
GPC	Gel Permeation Chromatography
HAADF	High Angular Annular Darkfield
HK	Horvath-Kawazoe
HMM	Hiroshima Mesoporous Material
HO	Hückel-Onsager
HPA	Heteropoly acids
HS	Helmholtz-Smoluchowski
HZSM	H+ Zeolite Socony Mobil
IEA	International Energy Agency
IL	Ionic Liquid
IR	Infrared (Near, Mid, Far)

Abbreviation	Description
ISO	International Organization for Standardization
IUPAC	International Union of Pure and Applied Chemistry
KCC	KAUST Catalyst Centre
KIT	Korea advanced Institute of science and Technology
LDH	Layered double hydroxide
LogitPct	Logistical Percentage Fit on Response (denoted Logistic model)
MCM	Mobil Composition of Matter
ME	Main Effect
MeOH	Methanol
MG	Monoglycerides
MMO	Mixed Metal Oxide
MRI	Magnetic resonance imaging
MSNP	Mesoporous Silica NanoParticles
MW	Microwave / Molecular Weight
MWCNT	Multiwalled Carbon Nanotubes
NDC	Nationally determined contributions
NMR	Nuclear magnetic resonance
OFAT	One variable (factor) at a time
PDI	Polydispersity index
PFAD	Palm Fatty Acid Distillate
RQ	Research Question
RSF	Relative Sensitivity Factors
SAED	Selected Area Electron Diffraction
SBA	Santa Barbara Amorphous
SEC	Size Exclusion Chromatography
SF	Saito-Foley
SG	Specific Gravity
SHER	Sulphonated hyper crosslinked exchange resin
STEM	Scanning Transmission Electron Microscopy
SV	Saponification Value
TG	Triglycerides
TGA	Thermogravimetric Analysis
THF	Tetrahydrofuran
TMS	Tetramethylsilane
TOF	Turnover frequency
TON	Turnover number
TPA	Tungstophosphoric acid
TPD	Temperature-Programmed Desorption
TUD	Technische Universiteit Delft (Delft Technical University)
TWI	Two Way Interaction
UCO	Used Cooking Oil
UV	Ultraviolet
VO	Vegetable Oil
XPS	X-ray Photoelectron Spectroscopy
XRD	X-Ray Diffraction
XRF	X-ray Fluorescence Spectroscopy

List of Roman letters

Roman letter	Description
A	Absorbance
A, B, C, D, E	Coefficients
Ak	Peak Area
AME/TG	Peak area ME/TG
B	External magnetic field
C	BET Constant, Concentration
C_0	Initial Concentration
c	Speed of light (299792458 ms^{-1})
D	Crystallite size
D	Diffusion constant
d	Average Pore Diameter
d	Plane lattice spacing
E	Energy
E	Electric Field Strength
E_1, E_L	Heats of adsorption in first layer, heat of vaporisation
E_a	Activation Energy
E_K	Kinetic Energy
e	Electron charge ($1.602x10^{-19}$ C)
f	Frequency
$G^{\ddagger}$	Activation Gibbs free energy
g_1	Electric field correlation function
g_2	Intensity correlation function
$H^{\ddagger}$	Activation Enthalpy
h	Planck Constant ($6.626x10^{-34}$ Js)
I	Intensity
K	Scherrer shape factor (0.9)
k	Rate constant
k_B	Boltzmann constant ($1.38x10^{-23}$ $m^2kgs^{-1}K^{-1}$)
l	Path Length
M, I	Gradient, Intercept
M_V	Molar volume of adsorbate (22414 cm^3/mol for N_2).
m	Magnetic quantum number
N	Normality
N_A	Avogadro's constant ($6.022x10^{23}$ mol^{-1}),
NA	Numerical Aperture
n	Rate order
n, N, k, i, j	Integers
P	Probability
P, P0	Equilibrium/Saturation pressure
p	Momentum
q	Bragg wave vector
R	Gas Constant (8.314 $Jmol^{-1}K^{-1}$)
R^2	Regression Fit Coefficient
R_H	Hydrodynamic radius
S	Surface Area
$S^{\ddagger}$	Activation entropy
$\mathbf{S_e}$	Micropore surface area
s	Adsorbate cross sectional area (0.162 nm^2 for N_2)
T	Temperature
t	Film thickness

Roman letter	Description
t,f	Student t / f test
V	Acceleration Voltage
V	Volume
V, V_m	Adsorbed gas volume overall sample / monolayer
V_L	Liquid molar volume (34.68 cm^3/mol for Liquid N_2)
W	Worth
w	Weight, peak width
$\bar{x}$	Factor mean
xc, xi	Peak centre, factor i setpoint
y	Yield
y,y0	Peak height, offset
Z	Atomic Number
Z_{avg}	Intensity averaged diameter

List of Greek characters

Greek character	Description
Å	Angstrom (0.1 nm)
f(κa)	Henry's Function
α, γ, ε	Crystal Phase
β	FWHM
β	Calibrated coherence factor
γ	Surface tension $8.88x10^{-3}$ N/m for Liquid N_2
γ	Gyromagnetic ratio
δ	Chemical Shift
ε	Molar absorption coefficient
ζ	Zetapotential
η	Dynamic viscosity
θ_r	Incidence Angle
μ	Mean, Micron
ρ	Density
σ	Shear stress
σ^2, σ	Variance/Standard Deviation
τ	Time Delay
ϕ	Work Function
χ^2	Chi-squared Test
ν	Frequency
λ	Wavelength
θ	Bragg Angle, Scattering Angle
Θ	Total Scattering Angle (Θ = 2θ for Bragg Angle θ)

List of Symbols

Symbol	Description
B10	10% Biodiesel Fuel
B20	20% Biodiesel Fuel
B100	100% Biodiesel Fuel
C14:0	Methyl Tetradecanoate
C16:0	Methyl Palmitate
C16:1	Methyl Palmitoleate
C18:0	Methyl Stearate
C18:1	Methyl Oleate
C18:2	Methyl Linoleate
C18:3	Methyl Linolenate
C19	Methyl Nonadecanoate
C20:0	Methyl Arachidate
C22:0	Methyl Behenate

Chapter 1.

Chapter 1. Introduction

1.1 Motivation for Biodiesel Technologies

Society is increasingly becoming aware of the environmental harms caused from historical use of fossil fuels. Increasing concentrations of atmospheric greenhouse gases (GHG) such as CO_2 has been consistently upheld in the scientific literature as a primary cause of anthropogenic (human-driven) climate change [1-6]. Continuing with the current trajectory of CO_2 release is predicted to pose grave risks to societal health and wellbeing [7-9]. Global efforts will be required to change course. Recent international treaties such as the Paris Agreement made good first steps to limit "*global average temperature to well below 2 °C above pre-industrial levels*" with further commitments attempting to "*limit the temperature increase to 1.5 °C above pre-industrial levels*" [10]. However, it remains ultimately up to each signatory country as to how their nationally determined contributions (NDC) are to be reduced [11]. Figure 1.1 provides most recent data for UK GHG emissions by sector.

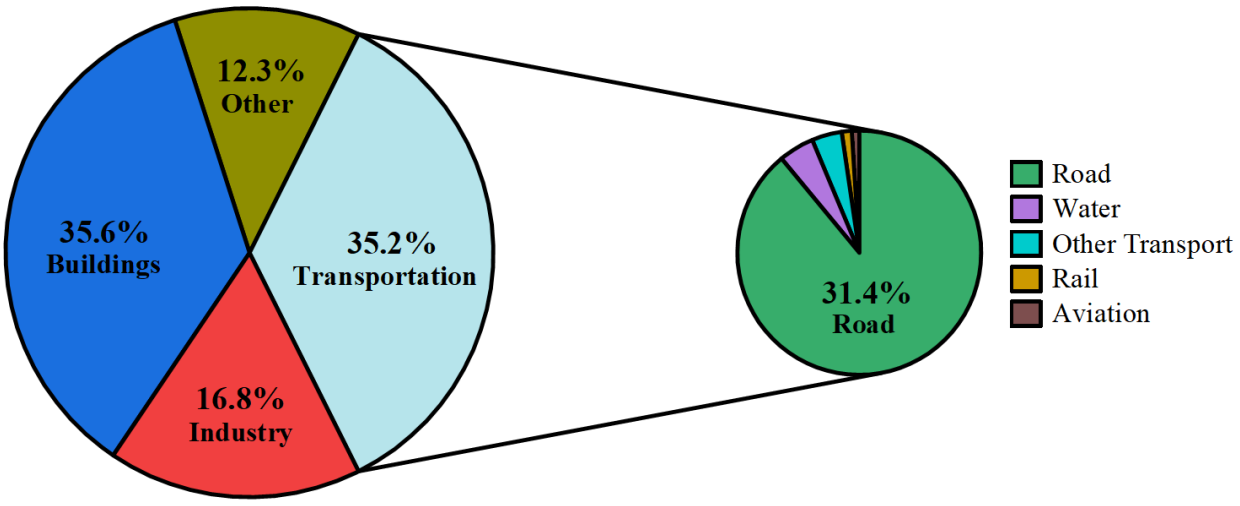

Figure 1.1 - UK GHG Emissions by Sector from 1990-2022 [12]

Transportation accounted for 35.2% of UK GHG emissions from the period of 1990 until 2022. Approximately 31.4% of this could be attributed directly to road vehicles such as cars, vans, buses and heavy goods vehicles. It is clear therefore that decarbonisation of road transport should be a key priority for achieving UK nationally determined contribution to GHG emission. Globally, combustion of fuels within the transportation sector accounted for ~24% of global emissions from the period of 1971 to 2022, therefore road transportation is highly desirable to decarbonise [13]. Until recently however road transportation has been seen as a difficult sector to effectively decarbonise due to high energy demands and limited availability of low or zero emission technologies [14]. Despite global sales of electric vehicles (EV) increasing exponentially since 2009 as illustrated in Figure 1.2a, issues such as infrastructure costs, availability of charging stations, battery performance and safety concerns still remain to be addressed [15-17]. Furthermore, electrical supply networks must be upgraded to meet charging demand and obtain sufficient electrical energy without further GHG emissions [18]. This may prove especially challenging in developing countries where electrical generation already struggles to satisfy demand, and where fuel combustion is the primary method of generating electricity [19-21]. International Energy Agency (IEA) predictions for how road transportation energy share may develop from 2022 to 2050 is presented in Figure 1.2b. While long-term energy share may become dominated by road vehicle electrification, in the short to medium term there remains a high dependency on fossil fuel internal combustion technologies. Fuel cell technologies involving green hydrogen production continue to develop, but may not be ready at the scale required until closer to 2050 [22]. It is here that biofuels hold most promise.

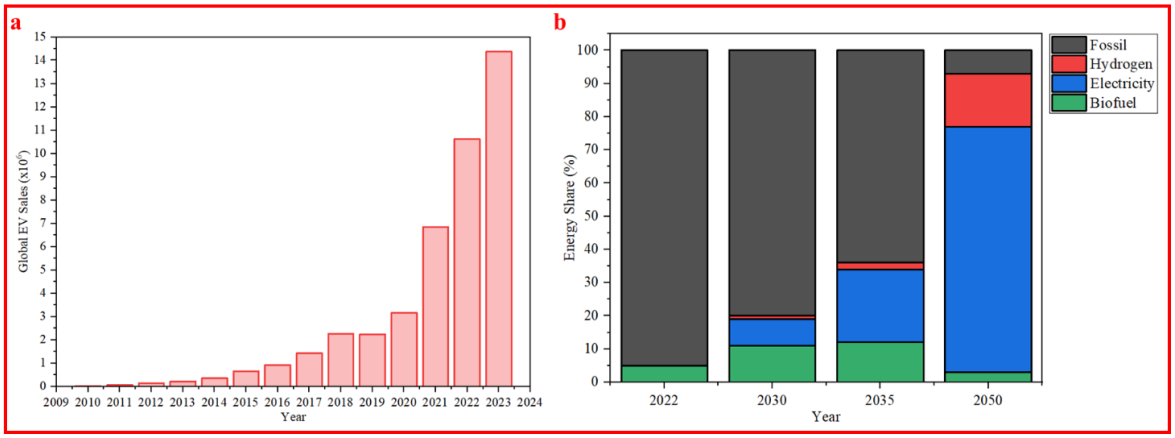

Figure 1.2 - Global EV Sales (a) [23, 24], Predicted Road Transportation Energy Share (b) [25]

Biofuels can be defined as the combustion of plant or animal biomass for use as a fuel source. Biofuels have existed across the entirety of human existence, from the use of firewood for heating homes to the burning of lamp oils derived from plant and animal fats [26]. In theory, the amount of CO_2 released during combustion of a biofuel is taken in during the growth of biological material and could hence be considered "carbon neutral". In reality, a complete lifecycle assessment considering GHG emissions due to agriculture, transportation and processing indicates biofuels may reduce GHG emissions compared to fossil fuel depending on feedstock and production route [27]. Modern liquid biofuels suitable for road vehicle usage include bioethanol and biodiesel. Bioethanol utilises the fermentation of biological starches and lignocellulosic biomass to produce fuel grade alcohol [28]. Biodiesel is the main focus of this research work, and a simplified diagram of the production route is given in Figure 1.3. Naturally occurring triglycerides (TG), diglycerides (DG) and monoglycerides (MG) undergo transesterification reactions whilst free fatty acids (FFA) undergo esterification reaction to produce a mixture of fatty acid alkyl esters, glycerol and water byproducts [29, 30]. Use of methanol (MeOH) as preferred primary alcohol due to increased reactivity leads to formation of fatty acid methyl esters (FAME) [31, 32]. Biodiesel can be utilised as either a direct drop-in replacement of conventional diesel, denoted as B100 fuel, or as a percentage blend such as B10 or B20 depending on the engine capabilities [33]. Requirements of biodiesel properties for commercial sale in the UK and EU is covered under BS EN 14214 standard [34] as summarised in Table 1.1. While biodiesel may prove essential to the decarbonisation of road transportation, there remains many challenges that have yet to be suitably addressed to produce sufficient quantity at scale required.

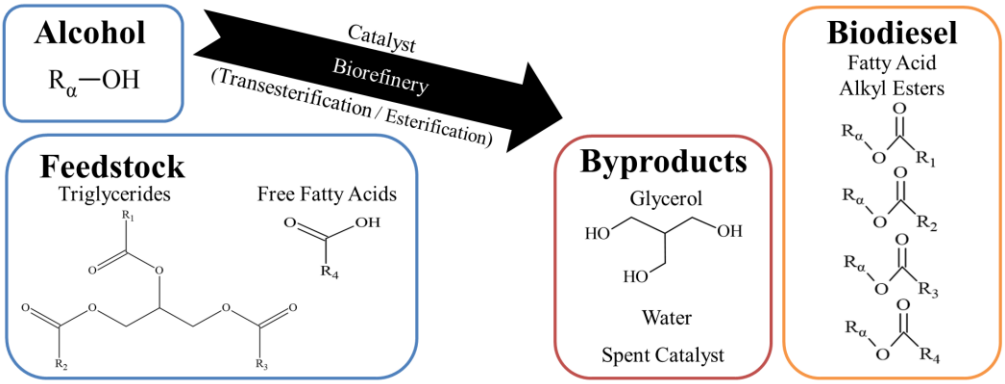

Figure 1.3 - Production Route for Biodiesel Synthesis [35]

Table 1.1 - Biodiesel Properties Specified in BS EN 14214 Standard [34]

Property	Units	Range	Test Method
FAME Content	wt%	96.5	EN 14103
Density at 15 °C	kg/m^3	860-900	EN ISO 3675/12185, EN 12185
Viscosity at 40 °C	mm^2/s	3.5-5.0	EN ISO 3104 / EN 14105
Flashpoint	°C	>120	EN ISO 3679
Cetane Number	-	>51	EN ISO 5165
Water Content	mg/kg	<500	EN ISO 12937
Sulfated Ash Content	wt%	<0.02	BS ISO 3987
Sulfur Content	mg/kg	<10	EN ISO 20846/20884
Phosphorus Content	mg/kg	<4	EN 14107
Group I Metal Content	mg/kg	<12	EN 14108/14109/14538
Group II Metal Content	mg/kg	<12	EN 14538
Acid Value	mgKOH/g	0.5	EN 14104
Iodine Value	$gI_2/100g$	<120	EN 14111
Oxidation stability at 110 °C	hr	>8	EN 14112
Methanol Content	wt%	<0.2	EN 14110
Monoglyceride Content	wt%	<0.7	EN 14105
Diglyceride Content	wt%	<0.2	EN 14105
Triglyceride Content	wt%	<0.2	EN 14105
Free Glycerine	wt%	<0.02	EN 14105/14106
Total Glycerine	wt%	<0.25	EN 14105
Linolenic Acid Methyl Ester	wt%	<12	EN 14103
Polyunsaturated Methyl Ester	wt%	<1	EN 14103
Total Contamination	mg/kg	<24	EN 12662

1.2 Challenges in Biodiesel Production

One of the key issues currently limiting the commercial viability of biodiesel remains the sourcing of sufficient economically, environmentally and socially sustainable feedstocks in quantities required to meet market demands. As illustrated in Figure 1.4a, the IEA predicts a doubling in biodiesel energy demand from 2022 levels by 2030 [36]. Biomass has an inherent lag time from initial planting of agricultural crops or rearing of animals until eventual biodiesel production, so it is paramount that investment begins rapidly to mitigate feedstock scarcity. Unfortunately, as shown in Figure 1.4b the majority of biodiesel sources within the near future are predicted to be sourced from food crops such as sugars, maize, soybean, rapeseed and palm. These "first generation" biodiesel feedstocks create a harmful "food versus fuel" competitive market that may lead to food scarcity and rising food prices [37]. To continue producing socially sustainable biodiesel, new feedstock sources must therefore be developed. An estimated 70% of biodiesel production costs can arise from feedstock acquisition so finding a feedstock that is economically viable remains a challenge [38, 39]. One example of a "second generation" biodiesel feedstock that meets all three pillars of sustainability is waste products such as used cooking oil (UCO). Disposal of UCO via waste collection, sewage systems or direct dumping to local land is environmentally harmful and inefficient when recycling into biodiesel could create an advantageous circular economy [40-42]. Third and fourth generation biodiesels from algae and advanced genetic engineering processes are also currently under active development [43]. However, the urgent and pressing need to dramatically reduce GHG emissions has made UCO a highly desirable feedstock for current needs.

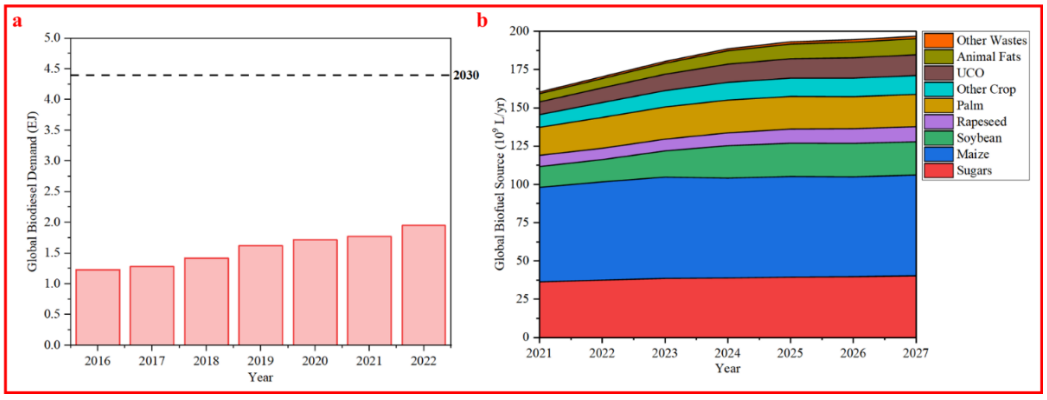

Figure 1.4 - Predicted Global Biodiesel Demand (a) [36],
Current Global Biodiesel Sources (b) [44]

Used cooking oil however is an impure feedstock that contains a high quantity of FFA impurities and moisture. Base catalysed transesterification has regularly been reported as more desirable than acid catalysed route due to improved reaction kinetics [45, 46], however FFA content is often recommended to be kept below < 2% in literature to avoid unwanted saponification reactions that lead to soap formation, loss of FAME yield and increased difficulties in biodiesel layer separation [47]. A two-step reaction scheme is therefore often utilised for impure feedstocks in modern biorefineries where acidic esterification reduces FFA loading followed by base catalysed transesterification of the cleaned up feedstock [48]. Catalysts are required to achieve high FAME yields at reasonable reaction pressures and temperatures by reducing the activation energy barrier, thereby enhancing reaction kinetics [49]. Since catalysts are not consumed during reaction, provided no deactivation occurs, it is possible to recover and reuse catalysts multiple times [50]. Homogeneous catalysts have high catalytic activity but often suffer from challenges to recyclability, while heterogeneous catalysts are more easily recycled at the cost of reduced activity [51]. Nanoscale materials could offer benefits of both catalyst types due to high specific surface area, pore structures and improved active site accessibility leading to desirable reactivity while remaining easily separable [52]. Challenges remain in nanocatalyst synthesis and design to ensure advantageous properties can be engineered at the nanoscale. Noncatalytic routes are also under development however these may be unsuitable to implement into existing biorefineries. Recent advances in the field of catalytic and non-catalytic biodiesel production are explored in Chapter 2.

While biodiesel synthesis faces challenges from feedstock selection to effective design of suitable catalytic materials, the urgent need for biofuel is clear. Rapid scaleup of biodiesel production to meet predicted demand is set to play a key role in the societal shift away from fossil fuels and towards a lower carbon future. Biodiesel combustion has also been reported as cleaner burning than conventional fuels due to combustion producing lower levels of soot, sulfur oxides (SO_x) and carbon monoxide as compared to fossil fuels [53, 54], although increased levels of nitrogen oxides (NO_x) remains to be mitigated [55]. Ultimately, combustion of biodiesel blends or pure biodiesel in current road vehicles will lower GHG emissions and ensure global average temperature increase can remain below the 1.5 °C limit. In this research, a new design of nanocatalyst will be explored to test effectiveness of producing biodiesel from impure UCO in a two-step pathway.

1.3 Research Aims

The title of this thesis clearly sets out the major themes of this research work: "*Biodiesel production from low quality feedstock using novel core-shell heterogeneous acid nanocatalysts*". A new range of novel nanocatalysts are to be developed in a production route inspired by a core-shell design philosophy. Different catalytically active materials, oxides of titanium and zinc, will be functionalised with chlorosulfonic acid at varying concentration levels to create surface acidic sulfate sites. Structural, morphological, chemical, thermal and crystalline properties of each nanocatalyst will be investigated in detail post synthesis. The influence of both catalytically active metal oxide used and chlorosulfonic acid concentration upon these physical properties can then be explored to observe how the synthesis process may lead to varying catalytic desirability. Each novel nanocatalyst will then need be tested to investigate suitability for biodiesel production in esterification and transesterification pathways. After optimisation of the most influential reaction process conditions to maximise methyl oleate and FAME yields, the superior nanocatalyst can be identified and further explored to determine commercial applicability with UCO feedstocks over repeated reuses. Suggestions for how to improve the optimal nanocatalyst design further or proposed changes to the initial synthesis pathway will then hopefully provide opportunities for future research work. The overall research aims as discussed are summarised in Table 1.2 as six individual Research Questions (RQ) that need to be answered by the end of this work.

Table 1.2 - Proposed Research Questions Under Investigation

Number	Topic of Investigation
RQ1	Can novel core-shell nanocatalyst designs be successfully synthesised based on the proposed synthesis route outlined in Chapter 3.2?
RQ2	What structural, morphological and chemical properties do the novel nanocatalysts possess when Ti or Zn oxide is used for catalytically active layer?
RQ3	How does chlorosulfonic acid concentration during functionalisation step influence the properties of the novel nanocatalysts?
RQ4	Can the novel nanocatalysts successfully convert high FFA% waste feedstocks such as UCO into biodiesel through transesterification and/or esterification pathways?
RQ5	Which novel nanocatalyst is most optimal for biodiesel production from impure feedstocks within the range of explored reaction conditions?
RQ6	Can the optimal novel nanocatalyst lead to an enhancement in FAME yield in a two-step pathway as compared to one step base transesterification over multiple reaction cycles?

1.4 Thesis Layout

Summarised in Figure 1.5 is a flowchart of how the thesis is structured and where each research question is addressed. A brief description of each chapter will now follow.

Chapter 1 focuses on the cultural significance of biodiesel production, particularly with regards to the use of impure feedstocks such as UCO, and the current challenges in developing suitable catalysts to handle the high levels of FFA and moisture present in such impure feedstocks.

Chapter 2 presents a review of the recent literature in biodiesel production through catalytic and non-catalytic technologies. Particular attention is paid to the area of sulfated metal oxides, mixed metal oxides and the application of nanotechnology in catalyst development.

Chapter 3 introduces the experimental and analytical methodologies applied during this research work. The chapter includes discussion of underlying theory, a detailed synthesis pathway of the novel nanocatalysts, creation of the design of experiment models and a list of key chemicals used.

Chapter 4 explores the characterisation of each novel nanocatalyst produced to determine structural, morphological, thermal, chemical and crystalline nature. Results are used to determine if novel core-shell nanocatalysts have been successfully synthesised (RQ1), differences in properties between the Ti series and Zn series of nanocatalysts (RQ2) and how varying the chlorosulfonic acid concentration influences these properties (RQ3).

Chapter 5 tests the esterification performance of each novel nanocatalyst in trial batch reactions using oleic acid as a model FFA impurity present in UCO. A design of experiments approach is used to determine how changing metal oxide and chlorosulfonic acid concentration impacted the esterification activity (RQ2, RQ3). Initial transesterification attempts and oleic acid reactions are used to determine if novel nanocatalysts exhibit an ability to convert FFA and UCO into biodiesel (RQ4). Finally, a comparison of batch trial results identifies the likely optimal nanocatalyst (RQ5).

Chapter 6 further develops the obtained design of experiments models to predict and experimentally confirm which novel nanocatalyst is most optimal for FFA esterification (RQ5). This is followed by kinetic and thermodynamic modelling of optimal nanocatalyst in oleic acid esterification. A study of UCO feedstock prior to reaction explores the extent of FFA formation over long term storage. Homogeneous base transesterification is optimised then tested in one step pathway to validate impact of FFA loading on reaction performance. Finally, two-step reactions are performed with UCO feedstocks to determine if optimal novel nanocatalyst improves biodiesel yield over the one step base route, including a study into recyclability and loss of activity (RQ6).

Chapter 7 provides an overall summary of the results obtained throughout Chapters 4-6, linking back to the six research questions with a discussion of the final answers as indicated by this research. Demonstration of originality, how this research contributes new knowledge to the field and what the results indicate in the context of current literature is emphasised. The chapter closes with a critical review of the research project to highlight future research opportunities and provide recommendations for where new research is best focused.

Chapter 8 provides a complete list of all literature cited throughout the thesis.

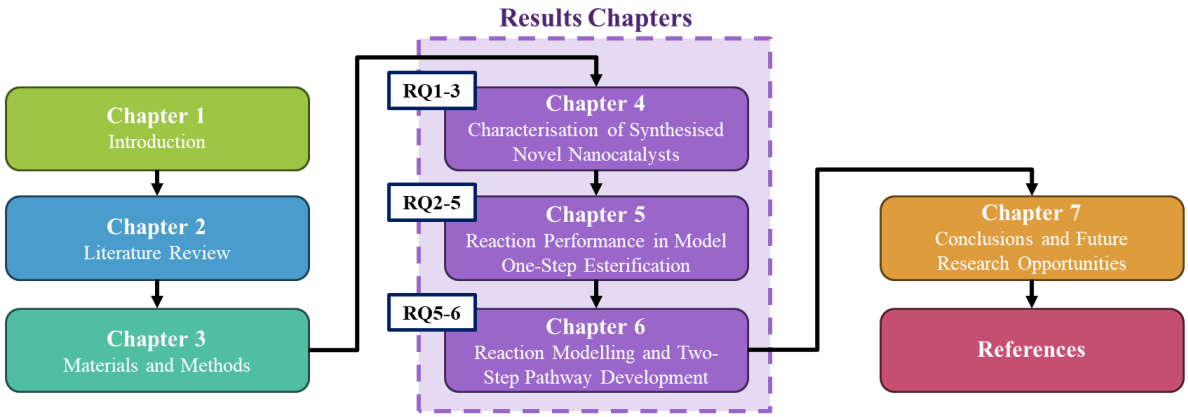

Figure 1.5 - Overall Thesis Layout by Chapter and Research Questions

Chapter 2.

Chapter 2. Literature Review

2.1 Biodiesel Production

The two major reactions that occur during biodiesel production are transesterification and esterification. Used cooking oil is a complex mixture of many different fatty acid molecules of predominantly even numbered carbon chain lengths, typically reported to be between 12-22 carbons long [56, 57]. Triglycerides, diglycerides and monoglycerides undergo transesterification pathway with an alcohol such as methanol to produce a mixture of Fatty Acid Methyl Esters (FAME) of which biodiesel is composed. Through storage or cooking processes glycerides will break down into Free Fatty Acids (FFA) which can be converted into FAME via esterification. Figure 2.1 summarises these reactions. Glycerol and water are also produced as byproducts.

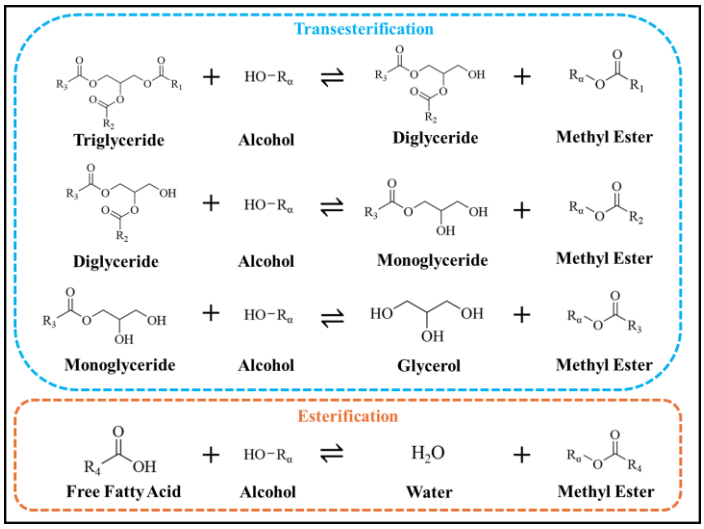

Figure 2.1 - Key Reactions for Biodiesel Production

2.1.1 Acid Catalysed Route

The simplified mechanism pathway of Brønsted and Lewis acidic transesterification is shown in Figure 2.2, where replacing R_2 glyceride/glycerol terminal group with H will give the esterification pathway [58, 59]. Acidic route begins in steps I and II with formation of carbonyl intermediate via protonation or accepting electron density, facilitating nucleophilic attack via alcohol group. Proton rearrangement occurs in steps III and IV facilitated by Brønsted acid site or protonated alcohol leading to elimination of R_2 group in step V. Catalyst is reformed in final step VI achieving a new ester structure where group R_2 has been exchanged for group R_3 from the alcohol. Here R_A indicates either a Brønsted or Lewis acidic catalyst species.

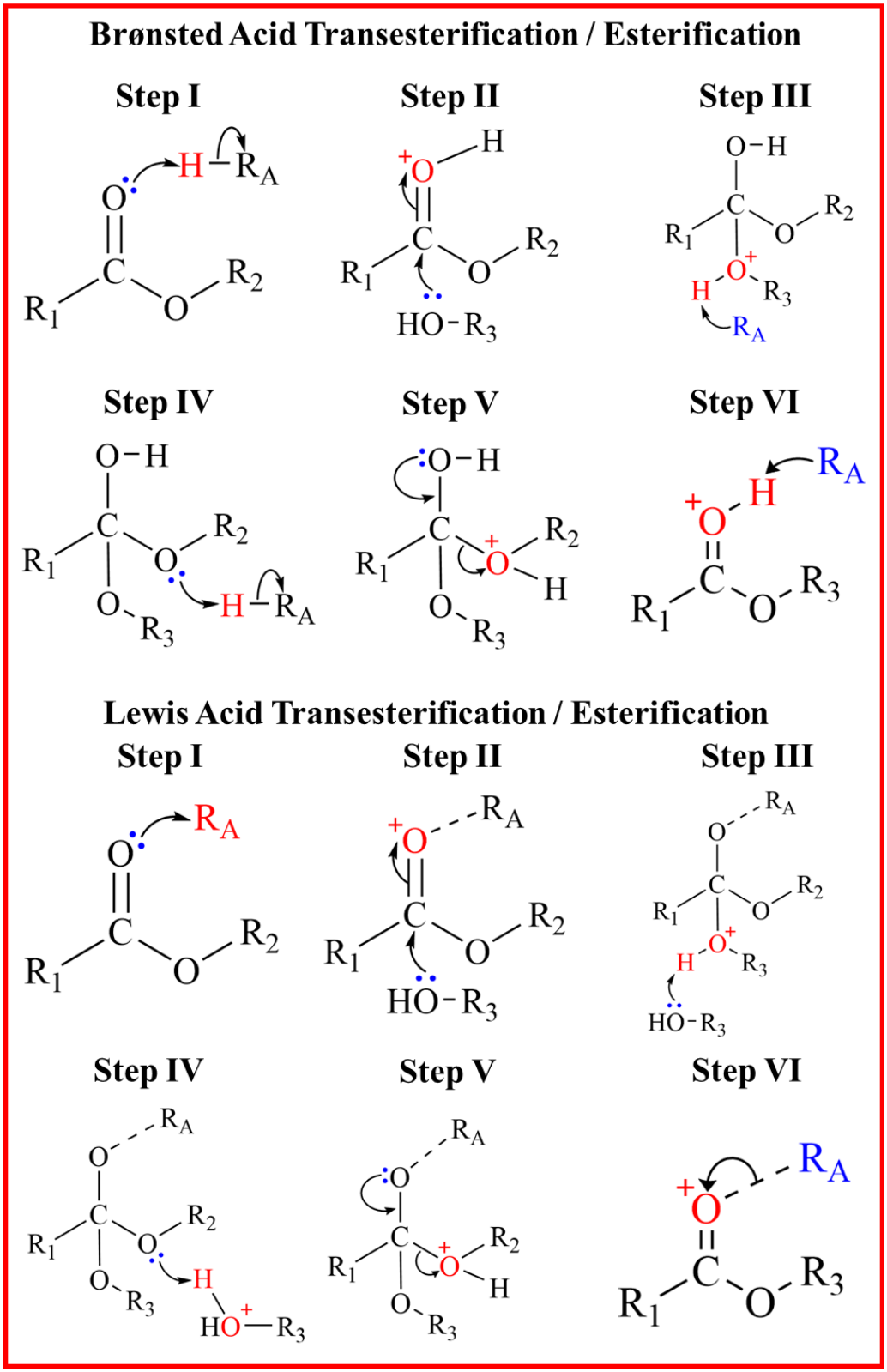

Figure 2.2 - Acid Catalysed Transesterification and Esterification Mechanism

2.1.2 Base Catalysed Route

A simplified mechanism pathway of Brønsted and Lewis base transesterification is provided in Figure 2.3 where again replacing R_2 glyceride/glycerol terminal group with H gives the esterification pathway [60, 61]. Reaction initiates in step I by formation of alkoxide intermediate via deprotonation or electron pair donation by basic catalyst, facilitating nucleophilic attack from the alkoxide in step II. Reformation of the carbonyl group via electron density redistribution in step III leads to elimination of R_2 group and formation of a new ester that has exchanged group R_2 with group R_3 from alcohol reactant. In step IV the basic catalyst site is reformed by deprotonation.

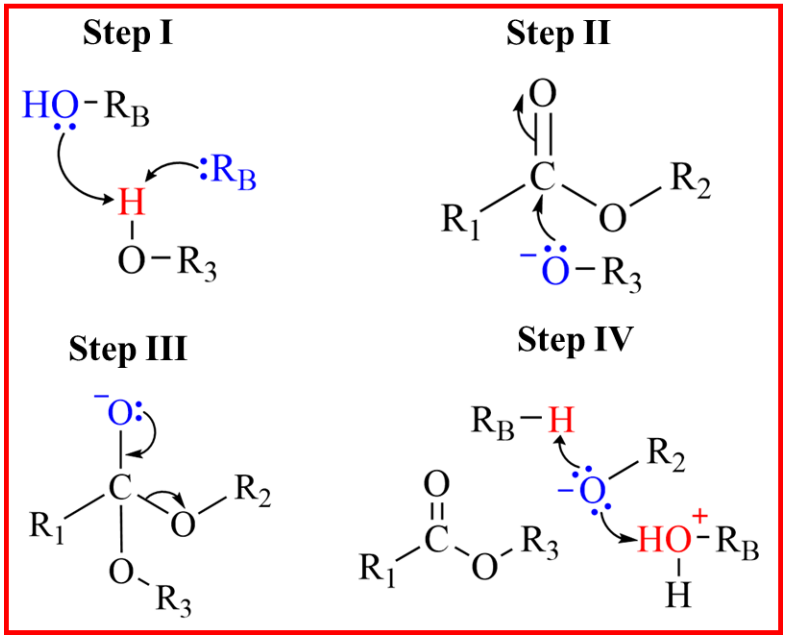

Figure 2.3 - Base Catalysed Transesterification and Esterification Mechanism

2.1.3 Saponification Reaction

Presence of water in base catalyst route can instead allow for nucleophilic attack via hydroxide as shown in step I of Figure 2.4 in a saponification reaction pathway [62]. Elimination of R_2 group and deprotonation occurs in steps II and III similar to base route, however due to addition of hydroxide instead of alkoxide the end product cannot lead to ester reformation. Instead, a cationic carboxylic group is obtained which can react with Na^+ or K^+ ions to form a mixture of carboxylic salts, commonly referred to as soap. This undesirable side reaction is enhanced if FFA groups or large quantities of water are present and can both reduce FAME yield as well as deactivate a basic catalyst [63]. Pre-drying feedstock and acidic esterification can both help mitigate saponification.

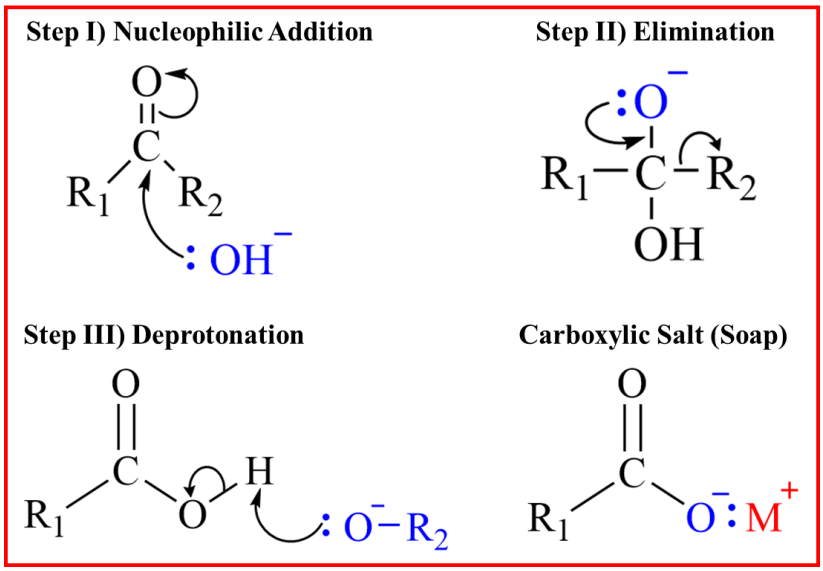

Figure 2.4 - Saponification Mechanism via Base Route

2.1.4 One Step and Two Step Approaches

Biodiesel production typically occurs at industrial scale as illustrated in Figure 2.5 via one-step base transesterification for pure feedstocks, or via two step acidic esterification followed by base transesterification for impure feedstocks. It is desirable to transition away from homogeneous acid and bases to facilitate recycling of catalytic material multiple times. Although high reactivities are often reported in solid base catalysed transesterification throughout literature, when UCO feedstock is used, it is often pre-refined or pre-esterified with acid such as H_2SO_4 first to reduce moisture and FFA levels. The obtained optimised FAME yield and recyclability found in such studies should therefore be considered within the context of a wider two step synthesis procedure. Conversely, when high reactivities are reported in acid catalysed transesterification using realistic UCO feedstocks, the reaction time and temperature is typically beyond reasonable conditions suitable for industrial application. It would seem therefore more beneficial to work with the strengths of each catalyst design and allow the acidic esterification step to complement a base transesterification step. The technology readiness level of sulfated solid acid nanoscale catalysts is currently estimated to be between 3–4. It is hoped that with renewed efforts to provide evidence that commercial viability is attainable, larger pilot scale studies may commence within the near future. Upcoming studies must focus on optimising both the esterification step to achieve maximum reduction in FFA content, as well as optimising the subsequent transesterification step. Catalyst synthesis routes must be scalable, reproducible and controllable to meet the challenge.

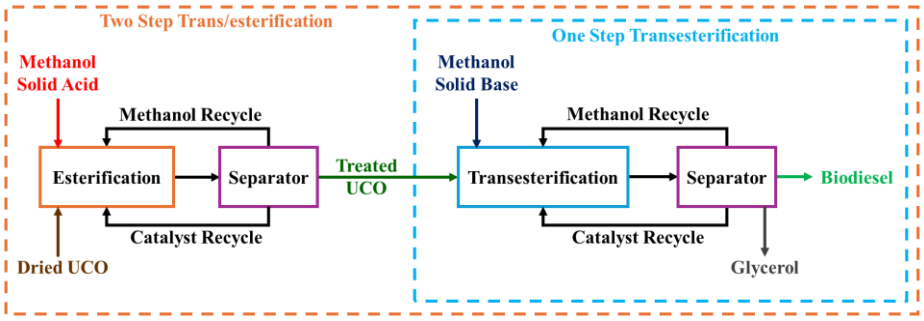

Figure 2.5 - Simplified Process Flow Diagram of Biodiesel Production

Several studies have considered the overall two-step approach when developing new catalysts for biodiesel production. In 2009 Omar et al. [64] optimised the pretreatment step of UCO with ferric sulphate using Design of Experiment (DoE) method, to find optimum treatment condition of 60 °C, 3 hours reaction, and 7:1 alcohol to oil ratio gave approximately 96.9% pretreatment yield. Application of the pretreated UCO in CaO transesterification step led to overall 81.3% FAME yield in two step process. Transesterification step was not modelled for further optimisation. In 2012 Srilatha et al. [48] explored 12-tungstophosphoric acid (TPA) on Nb_2O_5 under previously optimised reaction conditions [65] of 14:1 methanol to UCO ratio, 65 °C temperature, 1.65 wt% acid catalyst loading and 5 hours esterification time that achieved ~90% FFA conversion. Second step transesterification was then studied using ZnO/Na-Y zeolite solid base catalyst. Maximum 94.7% FAME yield was obtained using 24:1 methanol to treated UCO ratio, 20 wt% base catalyst, 65 °C temperature and 12 hours reaction time, however ~80% yield could be achieved after 6 hours. Recycling of both catalysts was verified for 6 runs with only slight loss of activity. Microwave assisted two-step route with beef tallow was modelled by Suwannapa and Tippayawong in 2017 [66] using 340 W power at 60 °C. Experimental validation of ~99% FAME yield was obtained with 12:1 methanol to oil ratio, 1.35% H_2SO_4 and 30 minute esterification followed by 9:1 methanol to oil ratio, 0.62% NaOH and 25 minute transesterification. More recently, Ogunsola et al. [67] converted shea butter oil via H_2SO_4 esterification followed by a solid base CaO catalyst derived from snail shell. Around 60.4% FFA reduction in first step was achieved under 6:1 alcohol to oil ratio, 78 °C temperature, 2 hours of reaction and 6.5 mL H_2SO_4 using 600 rpm agitation. Overall process FAME yield of 97.4% was obtained after second step with 9:1 alcohol to oil ratio, 78 °C temperature, 15 minutes of reaction, 3 wt% CaO loading and 600 rpm. Obtained biodiesel met EN 4214 standards. More studies focused on optimising the overall two-step route is encouraged.

2.2 Catalyst Synthesis

A wide variety of synthesis routes have been explored in the literature to produce nanocatalytic materials, broadly these can be split into two groups of "Top-Down" and "Bottom-Up" techniques. A Top-Down method starts with solid materials significantly larger than nanoscale and through physical or chemical techniques reduces the size to obtain solid with at least one dimension <100nm. Bottom-Up approaches instead produce nanosized materials directly from individual atoms or molecules, with growth facilitated until desired size has been achieved.

2.2.1 Top-Down Methods

Shown in Figure 2.6 are common Top-Down synthesis approaches that have been explored in literature. Physical methods such as mechanical grinding apply external forces to reduce material size [68, 69]. Amongst these mechanical methods, ball milling [70-73] has been widely explored and can produce nanomaterials of various morphology by adjusting milling speed, mill time, ball material, ball size and use of dry or wet material. Due to the energy imparted during the ball milling process, some researchers have even used the technique as part of a biodiesel production step [74-76]. Chemical techniques include etching [77-79] in which material is selectively removed via chemical reaction and can be enhanced through high energy electron beam [80] or laser ablation techniques [81, 82]. Alternatively thermal decomposition reactions can be used to create nanostructured catalytically active materials from bulk precursor [83-85]. Thermal decomposition can achieve desirable crystallinity, as the technique is essentially calcination, with no risk of extra impurities being included [86]. Finally, chemisorption techniques combine bottom-up routes such as sol-gel deposition and top-down lithographic methods to achieve thin surface nanofilms [87].

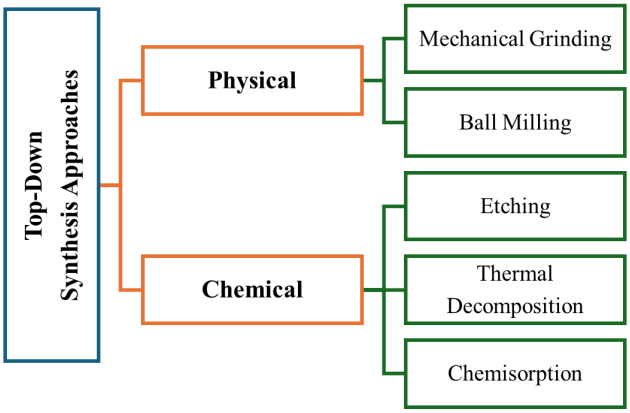

Figure 2.6 - Top-Down Nanocatalyst Synthesis Approaches

2.2.2 Bottom-Up Methods

A selection of Bottom-Up synthesis approaches is given in Figure 2.7 where initial molecules are combined into nanostructured materials. Biological synthesis utilises bacterial, fungal and algal methods of producing nanocatalysts at environmentally friendly low temperatures [88, 89]. To overcome the slow nanoparticle formation rate of microbial synthesis and challenges of ensuring culture survival, use of plants to form nanomaterials may help increase production rates [90].

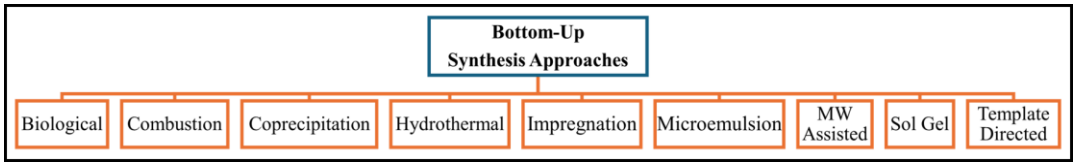

Figure 2.7 - Bottom-Up Nanocatalyst Synthesis Approaches

Combustion synthesis route is similar to top-down thermal decomposition however utilises material in solution instead of bulk solids. While solution combustion is a simple, rapid and affordable method of producing nanomaterial, challenges remain in ensuring desired phase and morphology can be achieved [91]. There are also environmental concerns of NO_x emissions and other harmful gases released during combustion synthesis if performed at industrial scales [92].

Coprecipitation route has been widely studied in the context of biodiesel production [93-98]. Metallic ions are dissolved into solution from precursor salts prior to addition of base such as NaOH or NH_4OH solution. Rapid change in pH promotes precipitation of nanoparticles out of solution, which over time grow and reform into larger structures via Ostwald Ripening [99]. Coprecipitation method is simple, rapid and low cost [100] and various studies have reported coprecipitation as a superior synthesis route due to formation of more favourable surface area and pore structures [101-103]. However, issues such as contamination and mass losses during treatment of precipitate have been raised [104]. Obtained morphology is highly sensitive to final pH level, temperature, agitation rate and precipitation agent used [105-107]. For instance, NH_4OH can lead to more homogeneous shape with no risk of Na impurities [108]. Controlling the temperature and amount of time to allow solution to develop can influence size range obtained [109, 110], as well as use of surfactants to mitigate aggregation [111]. In order to fully optimise the coprecipitation route, selection of optimal precursors, precipitating agent, temperature, time, pH endpoint and calcination temperature may be explored. Justifications for selecting a multi-step coprecipitation route as most suitable for this research work are discussed later in Chapter 2.2.3.

Hydrothermal synthesis route [112, 113] is similar to coprecipitation however utilises the change in solubility of metal ions with temperature instead of pH. While hydrothermal route can facilitate formation of nanomaterials of more desirable crystalline phases [114] including those not typically stable under ambient conditions [115], high temperatures and pressures are required to achieve synthesis which demands specialised equipment, increasing process cost and complexity [116].

Impregnation route allows for coating of a starting support nanomaterial by dispersed or dissolved precursor material that gradually deposits onto surface or within pore structure [117]. While some studies highlight that impregnation can lead to inhomogeneity and high aggregation effects as compared to other approaches [118, 119], or use of large quantities of reducing agent to facilitate deposition [120], other studies have achieved greater catalytic activity to biodiesel production via impregnation route [121-123].

A microemulsion can be created by mixing two immiscible liquids together with amphiphilic surfactants leading to nanoscale bubbles called micelles. Microemulsion techniques have been explored to allow high degree of controlling nanostructure formation by entrapment of reactive precursors within micelle structure [124, 125]. Each micelle acts as a nanoreactor [126] and constrains the size and shape of produced nanomaterial allowing formation of highly spherical and homogeneous morphologies [127].

Microwave (MW) energy has also been explored in various studies [128-130] to assist formation of nanocatalytic materials by more efficient and directed transfer of energy to initiate chemical synthesis, with MW route also hence utilised as part of biodiesel production step [131-133].

Sol gel route provides an alternative method to coprecipitation in which hydrolysis of precursor solution forms a colloidal suspension (sol) [134, 135]. Further polycondensation reactions then occur to obtain a viscous gel phase that can be calcinated to form a dry nanocatalyst powder. Some studies have reported sol-gel route led to increased surface area and porosity as compared to coprecipitation [136, 137], and it may be easier to obtain more homogeneous size distribution via sol-gel route [103, 138, 139]. Molecular templating can also lead to highly controlled nanocatalyst morphology [140-142], however it may be challenging to remove template material [143].

2.2.3 Selection of Synthesis Route

Considering the many synthesis parameters that can be optimised for and the impact each may have on catalytic performance, it is understandable that disagreement exists within the literature as to which synthesis route leads to superior nanocatalyst. Whatever route is selected, careful reporting of how the method was performed is essential to ensure reproducibility and identify where further optimisation may be possible. The industrial feasibility of scaling up the synthesis route to produce nanocatalyst quantities required to meet biodiesel demand must also be considered. Moreover, the selected nanocatalyst synthesis route must be both economically sustainable as well as minimise lifecycle environmental impacts.

Since a core-shell nanocatalyst was desired, a bottom-up synthesis route was most suitable to ensure material could be engineered starting from core and successively adding shell layers. Due to lack of suitable facilities, biological, hydrothermal and MW assisted routes were ruled out. Additionally, hydrothermal route presented issues with elevated pressures and temperatures required, while biological route was seen to be slow and challenging to ensure continued survival of cultures. Continued impurity accumulation throughout the multistep synthesis was identified as a particular concern, hence ruling out template directed and combustion routes where removal of template or incomplete combustion products may prove challenging to achieve and validate. The desire to use a commercially available, highly spherical nanoparticle as a supportive core material led to the choice between co-precipitation or impregnation route. Use of a dispersed solid core may provide a site for which new layers could be successively deposited without need of micelle formation or production of a colloidal sol phase. While literature appeared divided on which route is superior, coprecipitation has been reported successfully for Zn, Fe and Ti based nanomaterials [100, 105, 107, 108, 144], particularly with magnetically separable iron oxides by controlling Fe^{2+}/Fe^{3+} precursor ratio. Coprecipitation was seen to be simple, rapid, economically viable and readily scalable. Provided that centrifugation and washing steps were thorough and impurity levels tested in washings, issues of low yield and contamination may be avoidable. Precursor materials are easy to source, and synthesis conditions can be readily adjusted for future optimisation studies. Moreover, highly active and recyclable core-shell nanocatalysts have been reported in recent work including Gardy et al. [145, 146] using multistep coprecipitation route. Identified issues of reproducibility, sensitivity and optimisation of synthesis parameters, and overall lifecycle impact at industrial scale are beyond scope of this work but are encouraged for future research.

2.2.4 Key Design Parameters

Synthesis route selected and experimental conditions can both have a dramatic impact on the reactivity of obtained nanocatalyst to effectively produce biodiesel. Key properties that must be considered are summarised in Figure 2.8 that can help increase reactivity. High surface area and extensive pore structure enables efficient mass transfer of glycerides and FFA towards catalyst active sites. While nanocatalysts can achieve much higher specific surface areas as compared to bulk material, mass transfer may still be problematic due to immiscibility of methanol and oil phase. Methods to promote mixing such as mechanical agitation or ultrasonication can help to mitigate mass transfer barriers [147, 148], however use of small particle morphologies can enhance dispersion of catalyst throughout the methanol and glyceride layers. Nanocatalyst morphology is hence important to consider, with degree of aggregation influencing the accessibility to surface active sites [149]. Crystal phase can be influential in reaction performance, for example anatase TiO_2 is typically reported as more catalytically active than rutile [150]. Selection of functional group to load onto surface will naturally determine whether biodiesel production occurs through acidic, basic or simultaneous route. Various functionalisation agents are available which can influence site density, acidic or basic strength, and chemical functional group loaded onto surface. As discussed throughout Chapter 2.1 the presence of Lewis or Brønsted site activity influences how transesterification and esterification proceed, and which feedstocks will be most suitable. Since it is difficult to predict what synthesis route or starting materials will lead to high FAME yield over multiple recycles, the field of catalytic design for biodiesel production continues to see much work and interest. Current developments within the field are presented in next subchapter.

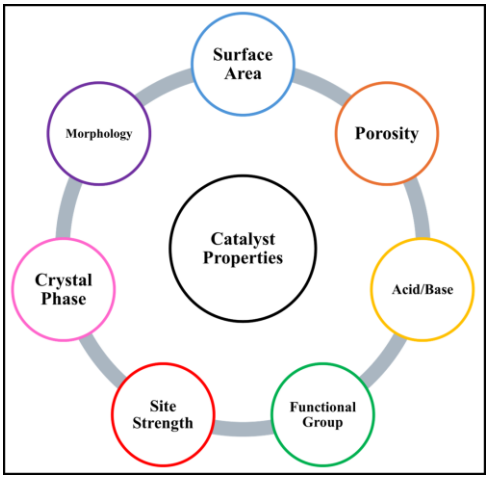

Figure 2.8 - Important Properties of Synthesized Nanocatalyst

2.3 Catalytic Biodiesel Production

2.3.1 Homogeneous Catalysis

2.3.1.1 Homogeneous Acid Catalysts

In general, base catalysts have increased reaction rates compared to acids, however acid catalysts are more tolerant to impurities in feedstocks such as FFA and moisture making acidic route especially desirable for UCO treatment. As discussed in Chapter 2.1.4 a two-step route is hence preferred to reduce impurities with an acid via esterification in the first step prior to more rapid transesterification with base catalyst in second step. Acids explored in the literature to date include sulphuric acid [151-153], phosphoric acid and hydrochloric acid [154, 155], boron trifluoride [156], aluminium trichloride [157], organic sulfonic acids like p-toluenesulfonic acid [158, 159], trifluoroacetic acid [160], and soluble HPA acids such as 12-tungstophosphoric acid [161]. Of these, sulphuric acid is the most commonly used acid catalyst [162]. A selection of homogeneous acid catalysts previously studied in literature is summarised below in Table 2.1.

Table 2.1 - Homogeneous Acid Catalysts for Biodiesel Production

Feedstock	A:O Ratio	Catalyst	Catalyst Loading (wt%)	Reaction Time (min)	T (°C)	Yield Y Conversion C	Ref.
Canola oil	24:1[a]	$AlCl_3$	5	1080	110	98% Y	[157]
Corn oil	6:1[b]	$CH_3C_6H_4SO_3H$	4	120	80	100% Y	[159]
Palm oil	40:1	H_2SO_4	5	540	95	97% Y	[151]
Palm Fatty Acid Distillate (PFAD)	12:1	H_3PO_4 (85% P_2O_5)	9	300	70	95% C	[163]
Soybean	20:1	CF_3COOH	2M	300	120	98.4% Y	[160]
Soybean-Sunflower Blend	6:1	H_2SO_4	2.5	-	60	96.6% Y	[153]
Soybean FFA	7.92:1	HCl	0.54M	104	76.7	98.2% C	[164]
UCO	3:1	H_2SO_4	2	-	80	93% C	[165]
UCO	70:1	$H_3PW_{12}O_{40}$	3.75	960	65	87% Y	[166]

a: THF cosolvent, b: DME cosolvent, A:O Alcohol to Oil Ratio

2.3.1.2 Homogeneous Base Catalysts

Homogeneous bases are considerably more active in the transesterification reaction pathway, with previous literature reporting up to 4000 times faster reaction rate as compared to homogeneous acid catalysts [167]. However, under presence of water and FFA both NaOH and KOH take part in saponification reactions as discussed prior in Chapter 2.1.3. It has been reported that use of ethanol can increase the rate of FAME saponification due to reduced acidity in comparison to methanol as alcohol reactant [168]. Various group 1 metal compounds have been utilised in homogeneous base biodiesel production including KOH and NaOH [156], CH_3OK and CH_3ONa [169-171] and K_2CO_3-glycerol deep eutectic solvent (DES) [162]. While some studies have found alkoxides facilitate increased rates of reaction [172, 173], they are typically more expensive and require higher feedstock purity to perform effectively [174-176]. A selection of homogeneous base catalysts previously studied are summarised below in Table 2.2.

Table 2.2 - Homogeneous Base Catalysts for Biodiesel Production

Feedstock	A:O Ratio	Catalyst	Catalyst Loading (wt%)	Reaction Time (min)	T (°C)	Yield Y Conversion C	Ref.
Beef tallow	10:1	CH_3ONa	1	60	65	95.6% Y	[170]
Castor Oil	9:1	CH_3OK	1	180	65	94.7% Y	[177]
Duck tallow	6:1	KOH	1	180	65	97% Y	[178]
Jatropha oil	5:1	NaOH	0.8	180	65	95.5% Y	[179]
Jatropha oil	32.6:1	K_2CO_3/glycerol DES	8.96	69.6	60	98.9% Y	[180]
Karanja oil	6:1 12:1	KOH	1	15 60	65	~ 85% Y 98% Y	[181]
Refined vegetable oil UCO	6:1	KOH	1.2	60 120	65	97.5% Y 93.2% Y	[182]
S. triostegus fish oil	6:1	KOH	0.5	60	32	96% Y	[183]
Sunflower oil	6:1	KOH	1	-	40	99.5% Y	[184]
UCO	6:1	CH_3OK	1	30	60	99% Y	[185]
UCO	7.5:1	NaOH	0.5	30	50	96% Y	[186]
UCO	4.8:1	NaOH	0.6	60	65	~90% Y	[176]

2.3.2 Heterogeneous Acid Catalysis

2.3.2.1 Sulfated Metal Oxide

Sulfated Iron Oxides

Iron oxides have seen a diverse range of applications, from the production of durable dyes and paints to use in welding through the thermite reaction. Although many different types of iron oxide exist, the three most commonly explored forms for chemical catalysis are those of hematite (α-Fe_2O_3), maghemite (γ-Fe_2O_3) and magnetite (Fe_3O_4). The magnetic properties of these oxides are of particular interest, and Figure 2.9 illustrates the crystal structure of each respective oxide.

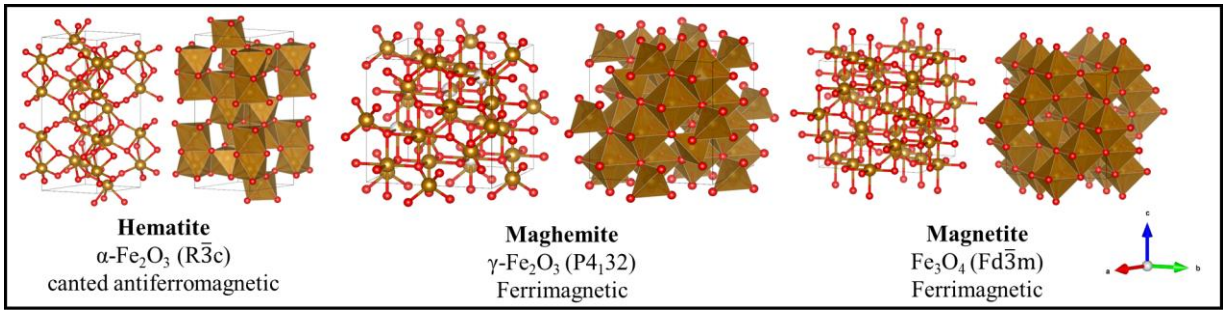

Figure 2.9 - Crystallographic Structure of Iron Oxides [35], Drawn in VESTA [187]

Hematite is only very weakly magnetic, maghemite and magnetite meanwhile are ferrimagnetic in nature and much more magnetically separable [188]. At the nanoscale, it is possible to create catalysts that display superparamagnetism, a desirable state in which external magnetic fields can induce magnetic separation with far greater susceptibility than typically expected for a paramagnetic material [189]. This allows for significantly enhanced manoeuvrability and has been explored in the biomedical field for MRI imaging and targeted drug delivery [190]. The magnetic properties of these oxides have led to significant recent research into nanocatalysts that can be recovered post reaction by application of external magnetic field. The potential opportunity for a rapid separation technique that easily facilitates nanomaterial regeneration and reuse is highly desirable. Although the Lewis acidic nature of iron oxides can be used for catalysing biodiesel production, surface functionalization is often performed to introduce new acidic functional groups, producing a more reactive and highly separable Fe oxide acidic nanocatalyst. A summary of recent sulfated Fe oxide nanocatalysts studied in literature is provided in Table 2.3.

Table 2.3 - Summary of Recent Sulfated Fe Oxide Nanocatalysts

Catalyst	Feedstock	A:O Ratio	Catalyst Loading (wt%)	Time (min)	T (°C)	Yield Y Conversion C	Reusability (runs)	Particle Size (nm)	Pore Size (nm)	Surface Area (m^2/g)	Acidity (mmol/g)	Ref.
FCHC-SO_3H	Oleic acid	15:1	4	180	80	96.7-84.3% Y	5	144	6.4	41.4	1.20	[191]
SO_4/Mg/Al/Fe_3O_4	UCO	9:1	4	300	95	~98.5% Y	5	core: 20–150 shell: 5–15	6.5	123	2.35	[146]
AC-Fe-SO_3Cl	PFAD	16:1	4	180	100	98.6- ~79% C	6	45.21	8.8	20.4	29.5	[192]

Sulfated Titanium Oxides

Titania (TiO_2) also enjoys a wide range of commercial application, such as: water and air purification systems, use as a white pigment, cosmetics and sunscreen, sensors, and self-cleaning films. Alongside being a widely researched photocatalyst, a desirable surface area combined with strong physical and chemical stability makes titania an excellent choice for a reactive catalyst support [193]. Sulfated titania has hence been widely studied as a solid acid heterogeneous catalyst for biodiesel production [194]. Titania exists in three main forms known as anatase, rutile and brookite as displayed in Figure 2.10. Of these three structures, anatase has been most widely explored for solid catalysis due to optimal surface area and strong interaction with other metallic oxide species, with rutile rarely achieving superior catalytic activity [150]. Anatase transforms to the more thermally stable rutile above calcination temperatures of approximately 600 °C, thereby restricting the maximum desirable calcination temperature when synthesizing a solid acid nanocatalyst. Recent developments in sulfated titania nanocatalysis are summarised in Table 2.4.

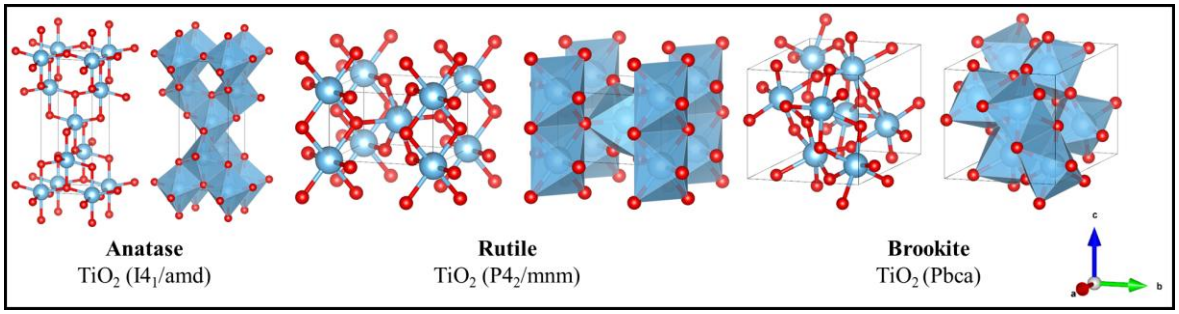

Figure 2.10 - Crystallographic Structure of Titanium Oxides [35], Drawn in VESTA [187]

Table 2.4 - Summary of Recent Sulfated Ti Oxide Nanocatalysts

Catalyst	Feedstock	A:O Ratio	Catalyst Loading (wt%)	Time (min)	T (°C)	Yield Y Conversion C	Reusability (runs)	Particle Size (nm)	Pore Size (nm)	Surface Area (m^2/g)	Acidity (mmol/g)	Ref.
$SO_4^{2-}/ZrO_2–TiO_2/La^{3+}$	Rapeseed oil fatty acids	1ml/g	5	300	60	95->90% C	5	-	-	-	-	[94]
$TiO_2/SO_4^{2-}/(NH_4)_2SO_4$	Oleic acid	10:1	2	180	80	82.2% C	-	-	4.2	178	1.1	[195]
TiO_2/SO_4^{2-}	Acetic acid	1.2 butanol	1.8g	150	120	92.2-52.1% Y	4	8-10	12.9	121	0.79	[196]
Sulfated Fe_2O_3/TiO_2	Soybean oil	20:1	15	120	100	~100-~80% C	4	89-103	-	16	-	[197]
$Ti(SO_4)O$	UCO	9:1	1.5	180	75	97.1 - 94.12% Y	8	25	22.7	44.5	-	[198]
$TiO_2/PrSO_3H$	UCO	15:1	4.5	540	60	98.3 - 94.16% Y	4	23.1	24.6	38.6	-	[199]
$SO_4/Fe-Al-TiO_2$	UCO	10:1	3	150	90	96->90% Y	10	<50	11.1	51	1.18	[145]
ZrO_2-TiO_2-SO_3H	Palmitic acid	20:1	5	240	100	93.1-85.1% Y	5	Length: 4000, Width: 100	-	32.5	1.9	[121]

Sulfated Zinc Oxides

Zinc oxide has many important industrial applications, from rubber manufacturing, textiles, and pharmaceuticals to specialized uses in electronics and photocatalysis [200, 201]. As an amphoteric oxide, zinc oxide has been explored as both an acidic and basic catalytically active species for the production of biodiesel through transesterification and esterification pathways. Alongside direct use of zinc oxide and in combination with other metallic oxides to form mixed metal oxide (MMO) materials, zinc oxide has been successfully sulfated to introduce Brønsted acidity. The crystalline structure of zinc oxide commonly used for biodiesel production is that of hexagonal wurtzite, shown in Figure 2.11, since this form is most thermodynamically stable at ambient pressures. To produce a cubic form, pressures of around 9 GPa would be required, and degradation soon occurs when returned to ambient conditions [202]. Table 2.5 summarizes different sulfated zinc oxide solid acid catalysts that have been used for biodiesel production.

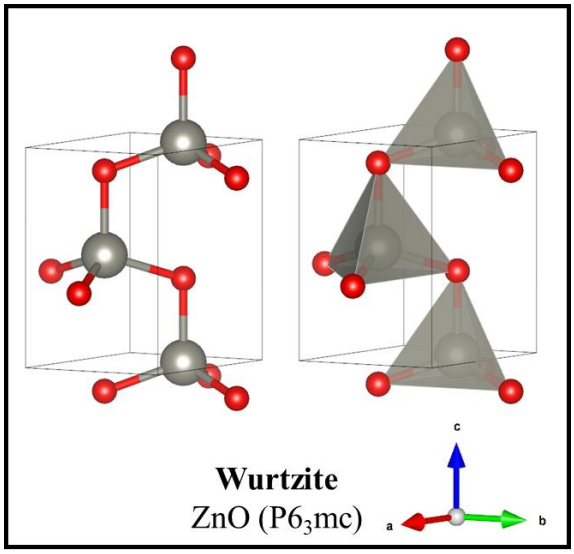

Figure 2.11 - Crystallographic Structure of Zinc Oxide [35], Drawn in VESTA [187]

Table 2.5 - Summary of Previous Sulfated Zn Oxide Nanocatalysts

Catalyst	Feedstock	A:O Ratio	Catalyst Loading (wt%)	Time (min)	T (°C)	Yield Y Conversion C	Reusability (runs)	Particle Size (nm)	Pore Size (nm)	Surface Area (m^2/g)	Acidity (mmol/g)	Ref.
ZnO	Pongamia oil	10:1	11.5	90	60	92% C	-	-	-	-	-	[203]
SO_4^{2-}/ZnO	Soybean oil	6:1	4	240	65	80.2% Y	-	-	-	-	-	[204]
ZnO-SO_3H	PFAD	9:1	2	90	120	95.6 - >80% Y	6	-	3.16	305.62	1.72	[205]

Sulfated Zirconium Oxides

Zirconia (ZrO_2) is an important ceramic material, commonly used in fields such as dentistry, nuclear power, and catalysis due to high mechanical and chemical resilience [206]. Similar to titania, the sulfation of zirconia to introduce Brønsted acidity has been widely explored as a solid acid nanocatalyst for biodiesel production. Unfortunately, while zirconia itself may be resilient, sulfated zirconia often suffers catalytic deactivation after a few runs via leaching of sulfate sites [47, 207]. In order to improve recyclability, recent studies have explored combining zirconia with other metal oxides to promote stronger bonding of acid groups to the solid surface. Such MMO catalysts have successfully achieved much higher numbers of recycles before deactivation occurs. Zirconia is typically utilised in three major crystallographic forms, as shown in Figure 2.12.

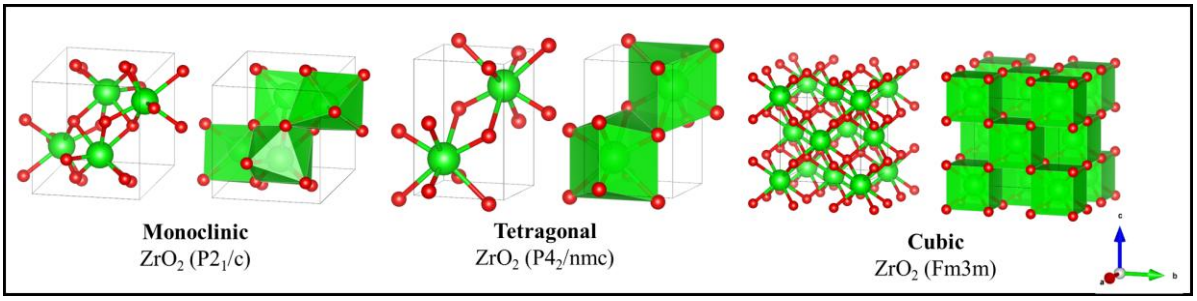

Figure 2.12 - Crystallographic Structure of Zirconium Oxides [35], Drawn in VESTA [187]

The monoclinic phase is the largest crystal structure and most stable under ambient conditions. Through calcination and introduction of other species such as sulfate groups and metal oxides, desirable tetragonal structures can be stabilized. While similar can be achieved with cubic forms, predominantly catalysts explored for biodiesel production only focus on monoclinic and tetragonal structures. Tetragonal zirconia is highly desirable because acidity and therefore catalytic activity are enhanced for sufficiently large tetragonal to monoclinic ratios [208]. This is due to how basic surface hydroxyls interact differently with each crystal structure [209]. A summary of developments over time in solid acid zirconia based catalysts is provided in Table 2.6.

Table 2.6 - Summary of Previous Sulfated Zr Oxide Nanocatalysts

Catalyst	Feedstock	A:O Ratio	Catalyst Loading (wt%)	Time (min)	T (°C)	Yield Y Conversion C	Reusability (runs)	Particle Size (nm)	Pore Size (nm)	Surface Area (m^2/g)	Acidity (mmol/g)	Ref.
SO_4^{2-}/ZrO_2	Palm kernel oil	6:1	1	60	60	90.3% Y	1	-	-	-	-	[47]
Sulphated ZrO_2	Soybean oil	20:1	5	60	120	98.6% Y	1	-	-	126	-	[210]
Sulphated ZrO_2	Neem oil	9:1	1	120	65	94% C	-	2-3 $x10^4$	-	-	-	[211]
SO_4^{2-}/ZrO_2–B_2O_3–Fe_3O_4	Acetic acid	-	-	240	100	98.2 – 96.7% Y	5	-	-	-	-	[212]
SO_4-ZrO_2/Al_2O_3	Jatropha oil	9.88:1	7.61	240	150	90% Y	-	-	-	-	-	[213]
Fe_2O_3-MnO- SO_4^{2-} /ZrO_2	UCO	20:1	3	240	180	~96.5% Y	6	11.5-21	-	1.39 $x10^{-6}$	4.32 A 1.52 B	[214]
Sulphated ZrO_2	Oleic acid	10:1	10	240	150	81.3% Y	-	-	5.9	65.8	0.414	[208]

2.3.2.2 Supported Acids

Porous silica (SiO_2) and other zeolitic aluminosilicate materials have been extensively explored in a wide range of fields, from drug delivery and pharmaceuticals to separation technology and chemical catalysis. A summary of commonly explored support materials is provided in Table 2.7. As an inert catalyst support, silica facilitates the production of materials with impressively large surface areas and highly porous, nanoscale channel networks. The amphoteric nature of Al oxides however can also contribute slightly to biodiesel production, especially if surface acidity is enhanced by functionalisation with sulfate species [215]. The ability to tune pore size distribution and functionalize the surface of support materials with a wide range of metal oxides and sulfated groups has produced many solid acid catalysts for biodiesel production. A summary of some of these recent developments is included in Table 2.8. As per International Union of Pure and Applied Chemistry (IUPAC) definitions, pore sizes can be classed as either microporous (<2 nm diameter), mesoporous (2-50 nm) or macroporous (>50 nm) [216]. Macropores facilitate high mass transfer rates of reactants into the internal nanoscale structure, while meso/micropores provide substantial reaction surface area for catalysis to occur. As illustrated in Figure 2.13, since triglyceride molecules are typically 2-6 nm in molecular diameter [217], only esterification can occur in micropores whereas both transesterification and esterification occur in mesoporous nanochannels.

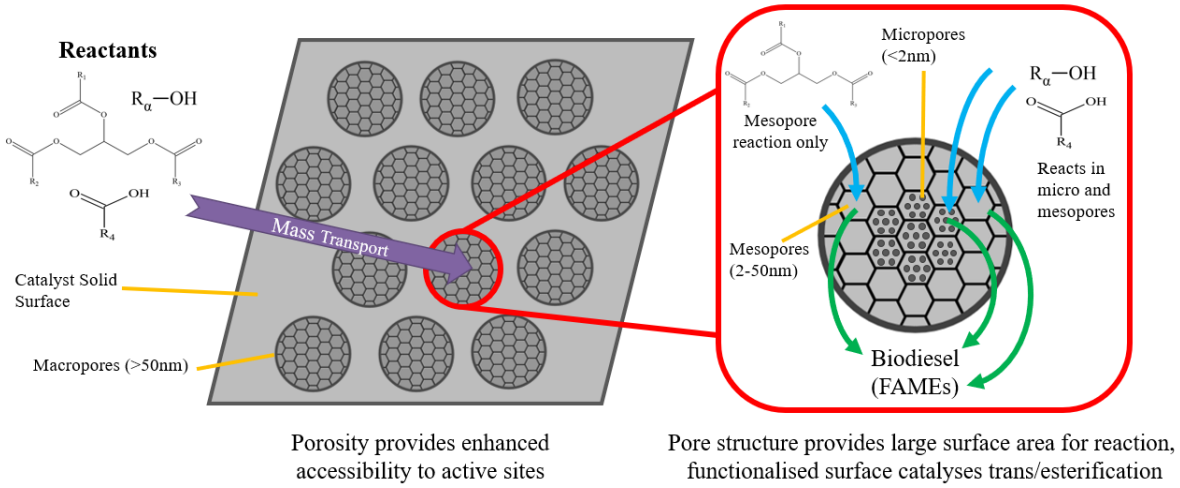

Figure 2.13 - Mass Transport and Chemical Reaction in Porous Supported Solid Acids [35]

Table 2.7 - Commonly Studied Silica and Aluminosilicate Support Materials

Abbreviation	Full Name
COK	Centrum voor Oppervlaktechemie en Katalyse (Centre for Research Chemistry and Catalysis)
FSM	Folded Sheets Mesoporous Material
HMM	Hiroshima Mesoporous Material
HZSM	H+ Zeolite Socony Mobil
KCC	KAUST Catalyst Centre
KIT	Korea advanced Institute of science and Technology
MCM	Mobil Composition of Matter
MSNP	Mesoporous Silica NanoParticles
SBA	Santa Barbara Amorphous
TUD	Technische Universiteit Delft (Delft Technical University)

Table 2.8 - Summary of Previously Studied Sulfated Supported Nanocatalysts

Catalyst	Feedstock	A:O Ratio	Catalyst Loading (wt%)	Time (min)	T (°C)	Yield Y Conversion C	Reusability (runs)	Particle Size (nm)	Pore Size (nm)	Surface Area (m^2/g)	Acidity (mmol/g)	Ref.
$SO_4^{2-}/TiO_2/SiO_2$	Acetic acid	-	-	-	120	91.4% C	-	-	-	550	-	[218]
SBA-15-SO_3H-Pr	Untreated beef tallow	20:1	10	120	120	92 – 84% C	2	-	4.8	920	0.91	[219]
SBA-15-SO_3H	Palmitic acid	30:1	0.05g	360	60	50% Y	-	-	3.9	938	0.22	[220]
TMS Capped/arene-SO_3H/SBA-15	Palm oil	20:1	6	240	140	~95% Y	3	-	8.3	533	1.04	[221]
SBA-15-SO_3H	Palmitic acid	30:1	0.05g	360	60	33.5% C	-	-	13.8	531	0.19	[222]
KIT-6/C-SO_3H	Maleic anhydride	6:1	0.2g	1800	-	~60% Y	4	-	11	590	3.0	[223]
$SO_4^{2-}/TiO_2/SiO_2$	UCO	20:1	10	180	120	77-74.3% C	2	-	2.85	457	-	[224]
SO_4^{2-}/La_2O_3/HZSM-5	Oleic acid	5:1	10	420	100	~100% C	1	17-150 $x10^3$	5.2-120	217	-	[225]
Fe/Fe_3O_4/SiO_2/APTES-$NHSO_2H$	Glyceryl trioleate	8:1	5	1200	100	100 - >90% C	5	60	-	-	0.48	[226]
SO_4^{2-}/Zr-SBA-15	UCO	40:1	3	180	160	98.5 - ~80% C	6	-	3.27-5.47	271	-	[227]
SZ/MgO/SBA-15	Tributyrin	$60cm^3$ meOH, 5mmol TG	34	180	60	40% C	-	-	4-350	350	0.13 A 0.045 B	[228]

2.3.2.3 Heteropoly Acids

Heteropoly acids (HPA) are a class of acids containing multiple different elemental species, that have seen wide usage in acid catalysis [229]. A particularly well studied branch of HPA is those with Keggin structure $[XM_{12}O_{40}]^{n-}$ where X is the central element and M the surrounding element. In a protonated form Keggin HPAs can act as homogeneous catalysts, however by supporting on solid materials, inclusion of new metal ions or adjustment of metal ratios until formation of an insoluble salt, a highly Brønsted acidic heterogeneous catalyst can be synthesised with activity potentially greater than traditional mineral acids [230]. Previous heterogeneous HPA catalysts that have been synthesised include $Cs_xH_{4-x}SiW_{12}O_{40}$ [231], $Cs_xH_{3-x}PW_{12}O_{40}$ [232], $Sn_{1.2}H_{0.6}PW_{12}O_{40}$ [233] and $Ce_{0.7}H_{0.9}PW$ [234]. Bifunctional HPA catalysts can also be produced by addition of basic metallic species such as La included 12-tungstophosphoric acid (La_xTPA) [235], or by use of amphoteric support materials such as HPA/ZIF-8 [236]. Basic sites can be used to promote transesterification activity while acidic sites help protect against saponification reactions. A summary of solid HPA catalysts previously explored is provided in Table 2.9.

Table 2.9 - Summary of Heterogeneous HPA Catalysts Previously Studied

Feedstock	A:O Ratio	Catalyst	Catalyst Loading (wt%)	Reaction Time (min)	Particle Size (nm)	Acidity (A) Basicity (B) (mmol/g)	T (°C)	Yield Y Conversion C	Reusability (runs)	Ref.
Canola oil	9:1	ZrO_2-$H_3PW_{12}O_{40}$	3	-	-	-	200	90% Y	2	[237]
Glyceryl tributyrate	30.36:1	$Cs_xH_{4-x}SiW_{12}O_{40}$	0.05g	1440	23.7-98.6	0.39 A	60	~46% C	3	[231]
Glyceryl tributyrate	12:1	La_xTPA	5	140	~115	0.0281 A, 0.0341 B	70	~90% C	5	[235]
Macauba oil	11.9:1[a]	$Sn_{1.2}H_{0.6}PW_{12}O_{40}$	2mol%	480	-	-	90	80% C	4	[233]
Rapeseed oil	10:1	HPA/ZIF-8	4	120	~200	17.44 A, 15.03 B	200	~98.02% Y	5	[236]
Tributyrin	30.36:1	$Cs_xH_{3-x}PW_{12}O_{40}$	0.05g	360	~20	0.19 A	60	~50.2% C	3	[232]
UCO	21:1	$Ce_{0.7}H_{0.9}PW$	0.175g	720	4×10^4	1.85 A	65	98 - >90% C	5	[234]

a: Ethanol to oil

2.3.2.4 Functionalised Carbon

Instead of the sulfation of metal oxides or porous inert silicas, carbon based solid acid nano catalysts can also be developed through treatment with strong acids. Compared with metals, acidic carbon materials can be produced more economically and with a lower overall environmental impact, since a wide variety of readily available waste biomasses can be converted into catalyst supports [238]. However, issues facing solid carbon acid catalysts such as reduced activity, deactivation and poor thermal stability still need to be addressed in order to improve catalytic performance and recyclability [239]. For the most challenging production of biodiesel from impure feedstocks such as UCO, metal oxide technology will therefore likely remain superior. New studies continue to address such problems however, with recent developments shown in Table 2.10.

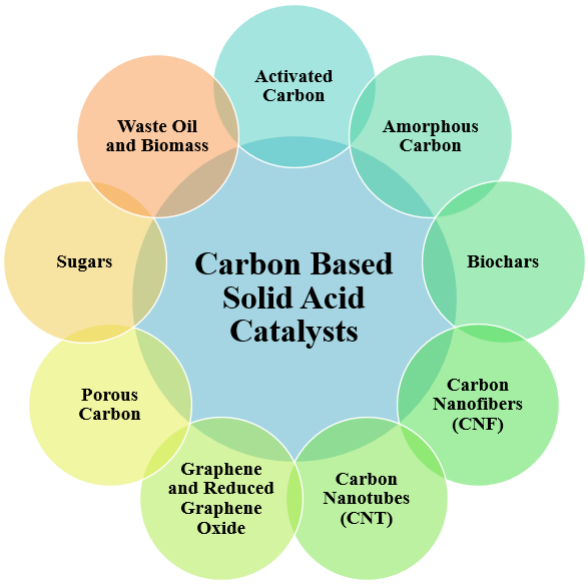

Figure 2.14 - Types of Carbon Based Acidic Catalysts Developed [35]

Nanoscale carbon can be engineered bottom-up through the creation of nanofiber, nanotube, or graphene structures; or developed top-down from converting sugars, algae residues, and biomasses into solid catalysts. A range of carbon support types have been studied, summarized in Figure 2.14. Plant biomasses often contain both carbon and metallic species [240], and mixing metal oxides with carbon has been explored to exploit differences in surface behaviour. The more non-polar carbon advantageously draws in other hydrophobic molecules such as triglycerides towards catalytic sites, whilst impeding polar species such as water that might lead to deactivation [241].

Table 2.10 - Previously Developed Acidic Functionalized Carbon Nanocatalysts

Catalyst	Feedstock	A:O Ratio	Catalyst Loading (wt%)	Time (min)	T (°C)	Yield Y Conversion C	Reusability (runs)	Particle Size (nm)	Pore Size (nm)	Surface Area (m^2/g)	Acidity (mmol/g)	Ref.
CNF-Ar-SO_3H	Triolein	10:1	0.75g	240	120	~72% Y	4	-	-	-	0.62	[242]
SO_3H-Graphene Oxide (GO)	Oleic acid	0.1 mol/g	5	240	100	97.6 – 74% C	3	-	3.8	437	-	[239]
PC-SO_3H	Acetic acid	10:1	10	600	75	94 – 80% C	3	0.2-0.4 $x10^5$	17	140	1.58	[243]
S-Multiwalled CNTs (MWCNT)	Trilaurin	20:1	3.7	60	150	97.8 - ~85% Y	2	Length: 0.5-2 $x10^3$ Width: 20-30	5-35	199	-	[244]
Al^{3+}/ SO_4^{2-}/MWCNT	Oleic acid	12:1	0.9	420	65	95 – 81.1% C	8	Width: ~25	-	-	-	[245]
Graphene-SO_3H	Palm oil	20:1	10	600	100	~98% Y	4	-	-	-	1.75	[246]

2.3.2.5 Discussion of Solid Acid Developments

Heterogeneous solid acid catalysts have been explored in a wide range of impure and high FFA containing feedstocks, demonstrating high FAME yield and good recyclability. While use of model feedstocks such as oleic acid (FFA) and triolein (triglyceride) are useful for initial work in modelling and optimising the esterification and transesterification pathways respectively, it should be encouraged to subsequently use genuine UCO feedstocks within the same research work. UCO is a complex mixture of glycerides, FFA, water and other impurities and strong catalytic activity in a model feedstock does not necessarily indicate similar performance could be achieved upon reaction with UCO, only serving as an indication of which produced catalyst has the best likelihood of high activity. It is vital that society begins to start increasing biodiesel production to match future predicted demand, and so much greater focus needs to be spent now on validating catalytic performance with realistic feedstocks to provide concrete proof these catalysts are industrially useful. Moreover, while high FAME yields have been observed in all solid acid catalyst types, extensive reaction temperatures or reaction duration has frequently been used to compensate for slow kinetics of acidic transesterification. Modern biorefineries using homogeneous base catalysis are currently designed to operate under 1 bar pressure and ~60-70 °C temperatures [62], increasing pressure and temperature would increase both capital and operating costs.

Therefore, if a high yield of FAME is reported in literature but reaction time is significant, or reaction temperature exceeds ~65 °C (Boiling point of MeOH: 64.7 °C), it can reasonably be argued that such a catalyst would not see much use within currently operating biorefineries. Instead of trying to force solid acid catalysts to achieve high FAME yield in transesterification, it would be more industrially relevant to use solid acids to clean up impure feedstocks through esterification and then have a facile transesterification step. Although it may be argued that a multi-step reaction scheme adds process complexity and inherent costs, modern biorefineries already utilise pretreatment steps to reduce FFA, filter out impurities and reduce moisture content [247]. Use of solid acid materials would simplify washing step by allowing for a more easily recoverable catalyst while avoiding the need to neutralise acid prior to transesterification step.

Sulfated metal oxides have been explored both as a singular functionalised metal oxide alongside mixing with other metallic species to achieve synergistic chemical or other physical properties such as enhanced surface area, magnetic separability or bifunctionality. Development of nanoscale catalysts for biodiesel production continues to be a highly studied research area, allowing for enhanced reactivity through improved mass transfer while still remaining separable post reaction. Support materials such as SiO_2 and aluminosilicate zeolites have led to increased surface area of sulfated metal oxides which also improves site accessibility during reaction via more optimal surface area and pore structures. Work by Gardy et al. [145, 248] is especially of interest due to use of core-shell principle to combine stability of nanoscale TiO_2 with Lewis acidity of Al_2O_3 support to increase surface area and porosity while Fe inclusion enabled magnetic separability. Sulfation with chlorosulfonic acid led to high FAME yield in UCO feedstock at reasonable reaction time over 10 uses. Small nanoparticle size and multiple catalytically active species may have enabled both high transesterification and esterification performance, indicating the advantages of mixing multiple metal oxides together into one nanocatalyst. Recyclability of supported HPA and functionalised acidic carbon catalysts has been demonstrated. Work by Zhang et al. [234] confirms that solid HPA can convert UCO multiple times at 65 °C temperature however reaction time of 12 hours highlights the slow acidic transesterification rate. Work by Shu et al. [245] shows that taking advantage of sulfated metal oxides by loading onto solid carbon support can lead to impressive recyclability at reasonably reaction conditions in esterification pathway, however solid acid carbon catalysts still require validation with real UCO.

Opportunities for new research includes combining multiple metal oxides onto support surfaces in core-shell designs, attempting to perform biodiesel synthesis at more industrially applicable reaction conditions and exploring multi step reaction schemes over a one-step approach. Reaction time and temperature should be restricted to force a design of nanocatalyst that is more industrially relevant. Similarly, catalyst loading and excess methanol ratio should also be restricted to simplify unreacted methanol separation post reaction, and to filter out nanocatalysts that require significant mass concentration due to suboptimal reactivity. If poor transesterification performance occurs as a result of these restrictions, then a two-step method should be explored to take advantage of solid acid resilience to moisture and FFA levels in the initial pretreatment step. Use of model feedstocks is still encouraged to initially filter out less active nanocatalyst designs, however once an optimal design has been determined, the focus must be on producing biodiesel from commercial UCO to demonstrate industrial relevance. While sulfated oxides of Ti, Fe and Zn have been explored as single metal oxides or supported onto SiO_2 support materials, no studies have yet considered sulfated SiO_2-Fe-Ti or sulfated SiO_2-Fe-Zn core-shell designs biodiesel production. The synthesis of Fe(III) layer is significantly less complex since no inert N_2 atmosphere or coprecipitation with multiple iron salt precursors would be required, and at nano-micro scales past literature [249, 250] does suggest that hematite can be magnetically separable. However, literature to date that developed magnetically separable acidic nanoparticles such as work by Guan et al. [212] and Gardy et al. [145, 248] tend to focus on inclusion of Fe(II) and Fe(III) salts. It is unclear if hematite can be used at nanoscale to achieve magnetic separability and may be worth further exploration. A range of synthesis conditions have been explored including the use of various functionalisation agents as discussed later in Chapter 2.5.2.2. Use of different functionalisation concentrations and calcination temperatures can influence catalyst performance as indicated in work by Li et al. [94] using H_2SO_4 where an optimal concentration of 0.5 M likely balanced acid strength with dissolution of oxide support, and a calcination temperature of 550 °C that may balance crystal phase formation with loss of sulfate. While it is clear that changing functionalisation concentration impacted esterification performance, exact changes to physical and chemical properties were not characterised and so the underlying cause of activity variation is poorly understood. Recent work using chlorosulfonic acid functionalised hydroxyapatite by Rezki et al. [251] notes that chemical and physical properties vary at increased concentration hindering esterification. Further research to understand how concentration impacts catalyst nature and hence FAME yield is recommended.

2.3.3 Heterogeneous Base Catalysis

2.3.3.1 Basic Metal Oxide

An extensive variety of basic metal oxides have been explored in the literature for biodiesel production as summarised in Table 2.11 and Table 2.12. It is immediately apparent that reaction time and temperatures used are on average significantly less than conditions reported throughout Chapter 2.3.2 as a consequence of superior base transesterification kinetics. While work by Banerjee et al. [252], Sulaiman et al. [253, 254], Malani et al. [255] and Sahani et al. [42] all suggest that solid base catalysts can effectively transesterify UCO it is important to note that in all cases the feedstock was either refined prior to the study or cleaned up via activated carbon or acid esterification step. Consequently, the results of such studies should be considered as part of a wider two-step biodiesel production process where an acid catalyst is still required to enable reduction of UCO acid value.

Table 2.11 - Summary of Basic Metal Oxide Catalysts Previously Explored

Feedstock	A:O Ratio	Catalyst	Catalyst Loading (wt%)	Reaction Time (min)	Particle Size (nm)	Acidity/ Basicity (mmol/g)	T (°C)	Yield Y Conversion C	Reusability (runs)	Ref.
B. aegyptiaca oil	12:1	$BaO\text{-}MoO_2$	4.5	120	-	0.621 B	65	97.8->80% Y	5	[256]
Canola oil	15:1	$15\text{-}Kf/nano\text{-}\gamma\text{-}Al_2O_3$	3	480	-	1.68 B	65	98% Y	3	[257]
Canola oil	6:1	$NdAlO_3$	10	300	~100	1.13 B	200	75-50% Y	6	[258]
Canola oil	12:1	$KOH/Ca_{12}Al_{14}O_{33}$	4	240	24	0.392 B	65	85.9-75.3% Y	4	[259]
Canola oil	6.67:1	MgO	3	120	5.7	0.8207 B	190	98.2 - ~95% Y	5	[260]
Ethyl butyrate	4:1	MgO/CaO	0.062g	60	-	-	60	60% C	-	[261]
Goat fat	12:1	MgO	1	180	5.5	-	70	93.12% Y	-	[262]
J. curcas oil	12:1	1.75-Li/CaO	5	120	500	-	65	>99% C	1	[263]
J. curcas oil	20:1	CaO/B_2O_3	4	120	-	2.68 A, 1.89 B	105	~96% Y	5	[264]
M. ferrea oil	9:1	Co/ZnO	2.5	180	~27.8	-	60	~98% C	2	[144]
Microalgae oi	6:1	CaO/MgO Dolomite	3	180	-	-	65	90-76% Y	5	[265]
Palm kernel oil	30:1	CaO/ZnO	10	180	200-9700	-	60	>90% Y	3	[266]
Palm oil	6:1	Cr/Ca and Cr/Zn	1	60	-	-	60	27.8% and 7.4% Y	-	[267]

Table 2.12 - Continuation of Table 2.11

Feedstock	A:O Ratio	Catalyst	Catalyst Loading (wt%)	Reaction Time (min)	Particle Size (nm)	Acidity/ Basicity (mmol/g)	T (°C)	Yield Y Conversion C	Reusability (runs)	Ref.
Phoenix dactylifera L. Kernel oil	15:1	Mn/MgO-ZrO_2	3	240	18-39	2.12 A, 3.48 B	90	96.4->80% Y	6	[268]
Rapeseed oil	6:1	$CaZrO_3$ and CaO–CeO_2	10	600	-	-	60	92-79% Y	5 and 7	[269]
RBD palm olein	30:1	ZnO/CaO	7.5	120	62-85	25.81 B	56.9	86.99-83.87% Y	2	[270]
S. foetida oil	9:1	CuO-CeO_2	0.25	180	32.3-54.4	-	70	~92% Y	4	[93]
Soybean oil	9:1	Na/NaOH/γ-Al_2O_3	20	120	-	-	60	94% C	-	[271]
Soybean oil	20:1	KI/Mg-Al	5	480	-	-	70	>90% Y	-	[272]
Soybean oil	25:1	CaO/MgO	5	180	24–68	0.453 B	120	90% Y	5	[273]
Soybean oil	6:1	20-nano-MgO/TiO_2	0.1	60	-	-	225	95% C	-	[274]
Soybean oil	25:1	$Sr_3Al_2O_6$	1.3	61	15-25	1.62 B	60	95.7-78% Y	4	[275]
Soybean oil	20:1	Mg/Zn	0.5g	240	200–500	0.15 B	65	90-85% Y	3	[276]
Soybean Oil Castor Oil Soybean Oil Castor Oil	6:1 MeOH 6:1 BuOH	MgO/γ-Al_2O_3 1.5 Zn/Mg 1.5 Zn/Mg 0.5 Zn/Mg	5	120-360	-	-	60 80	57% Y 76% Y 66% Y 99-80% Y	- - - 3	[277]
Spirulina oil	18:1	Ba/Ca/Zn MMO	2.5	120	-	2.65 B	65	98.94-~80% C	5	[278]
Sunflower oil	14:1	Li/CaO	0.2	60	-	-	~60	90% Y	-	[279]
Sunflower oil	12:1	CaO/γ-Al_2O_3	0.5	300	1-3 x 10^6	9.087 B	60	94.3-76.4% Y	2	[280]
Sunflower oil	12:1	MgO/$MgAl_2O_4$	3	180	11	-	110	95% C	6	[281]
Sunflower oil	4:1	MgO	0.3g	120 40 (MW)	50–200	-	70	~80% Y ~98 - 90% Y	- 7	[282]
Vegetable Oil	12:1	Cs–Ca/SiO_2–TiO_2	2	120	45	0.266 B	60	~98% Y	4	[283]
Vegetable Oil	8:1	Li_2ZrO_2	6	120	2-5 x 10^4	-	65	99-90% C	7	[284]
UCO	50:1	MgO/TiO_2	10	360	21.4	-	170	92.3-81.2% Y	5	[285]
UCO	14:1	Sr/Ce	2	120	-	1.35 B	65	99.5-~90% C	4	[252]
UCO	20:1	Cu/Zn/γ-Al_2O_3	10	120	~10	3.74 B	65	89.5-82.64% Y	6	[253]
UCO	11.68:1	KI/ZnO	7	60	300-700	5.00 B	59	92.35-~60%	5	[255]
UCO	11:1	Sr-Ti 4:1	1	80	350	2.89 B	65	98-83% C	8	[42]
Waste fish oil	12:1	CaO-$Ca_3Al_2O_6$	10	120	-	-	65	>95% C	7	[286]

2.3.3.2 Layered Double Hydroxide

Naturally occurring minerals such as hydrotalcite [287] have been the subject of much interest in the field of solid base catalysis [288]. Natural existence of basic sites has enabled use of layered double hydroxide (LDH) materials as catalysts for biodiesel production either directly or as a support onto which other catalytically active species can be loaded [289]. The general structure of a LDH has form $[M_{1-x}^{2+}M_x^{3+}(OH)_2]^{x+}(A^{n-})_{x/n}\cdot yH_2O$ where metal species M exist in varying 2^+ and 3^+ oxidation states and A represents the interlayer anion species [290]. Synthesis can be performed via calcination of natural hydrotalcites or via coprecipitation to obtain precise ratios of M^{2+}/M^{3+} that can be highly influential on FAME yield. Calcination temperatures between 450-600 °C have been found most optimal. Literature largely disagrees on best ratio of Mg/Al with highest biodiesel yields observed at 0.59 [95], 2.3 [291] and 3.0 [292, 293]. For other metal cations, optimum Co/Fe ratio of 4.0 [294] and Mg/Fe ratio of 3.0 [295] has been seen, while Li et al. [296] reported no influence of Mg/La ratio to catalytic activity. Evidently it is challenging to predict optimal synthesis conditions to maximise FAME yield, hence a wide variety of designs should be explored.

Table 2.13 - Summary of LDH Derived Catalysts Previously Studied

Feedstock	A:O Ratio	Catalyst	Catalyst Loading (wt%)	Reaction Time (min)	Particle Size (nm)	Acidity (A) Basicity (B) (mmol/g)	T (°C)	Yield Y Conversion C	Reusability (runs)	Ref.
Canola oil	16:1	Mg-Co-Al	2	300	>1 x 10^5	0.36 B	~200	~96–97%	7	[296]
Cooking oil	6:1	Co-Fe	2	20	-	-	65	96% C	-	[294]
Methyl stearate	6:1[a]	Ce-Mg-Al	4	360	-	0.0046 B	220	83-78% Y	2	[123]
Palm oil	30:1	1.5% K-Mg/Al	7	360	-	0.27 B	100	86.6% Y	-	[297]
Poultry fat	30:1	Mg–Al	10	480	200-600	0.043 A 0.096 B	120	93-90% C	5	[291]
Rapeseed oil	6:1	Mg–Al	1.5	240	3–120 x 10^3	-	65	90.5-88.3% C	3	[292]
Rapeseed Oil	24:1[b]	Mg-Fe	1	240	-	-	120	97.5% Y	-	[295]
Soybean oil	15:1	Li–Al	1	180	~25	0.0814 B	65	78-83% Y	1	[298]
Soybean oil	6:1	10% Fe-Mg/Al	1	60	-	-	80	100% C	-	[96]
Soybean oil	9:1	Ca-Al & Mg-Al	1	240	-	0.12 B & 0.11 B	65	95.1% & 5.5% Y	-	[299]
Soybean oil methyl-acetate	6:1	Ba–Mg-Al	4	480 30	66	4.499 B	70 50	71.5% Y ~80% Y	- 3	[300]
Sunflower oil	23:1	Mg-Al	3.5	60	-	-	65	98.59% C	-	[95]
Sunflower Oil	15:1	Ca–Mg–Al	2.5	360	-	-	60	95% Y	-	[122]
UCO	9:1	Zn/MgAl(O)	3	180	~30	0.62 B	65	78.45-65.74% Y	5	[301]
UCO	30:1	Mg-Al	5	1440	-	-	65	87.23% Y	-	[293]

a: glycerol to methyl stearate, b: equal parts methanol to butanol

2.3.3.3 Supported Bases

Instead of using LDH materials as a basic support, silica and aluminosilicate materials can be used as discussed prior in Chapter 2.3.2.2 for supported acid catalysts. A summary of various supported base catalysts previously explored for biodiesel production is provided in Table 2.14. Recyclability remains a challenge due to leaching of group 1/2 metal ions from support surface. It is hence important to perform multiple reuses to ensure high reactivity is not simply due to homogeneous catalysis of leached base. As noted by Xie and Zhao [302], cleanup of biodiesel fuel via use of exchange resins may be required to avoid exceeding regulatory limits of metal contamination since leached Ca from support exceeded EN 14214 specifications. Doping of 20 wt% Ce on Li-SBA-15 introduced both Lewis basicity and acidity in work by Malhotra and Ali [303] allowing for basic site to be protected against high FFA present in the waste cottonseed oil. Since a support material such as zeolite can constrain acidic and basic sites to avoid neutralisation, provided a suitable synthesis method is developed, it would be highly beneficial to create bifunctional catalysts that protects base site activity by simultaneous removal of FFA impurities. More research into such catalysts is highly encouraged. Alternatively, supported base catalysts can be used in two step approaches to avoid saponification by prior initial esterification. While base catalysts are already highly active in transesterification of purified oils, support material can both increase reactivity through high specific surface area as well as provide improved separability. Efforts to explore reducing alkali metal leaching are encouraged, possibly via exploration of new support materials.

Table 2.14 - Summary of Supported Base Catalysts for Biodiesel Production

Feedstock	A:O Ratio	Catalyst	Catalyst Loading (wt%)	Reaction Time (min)	Particle Size (nm)	Acidity (A) Basicity (B) (mmol/g)	T (°C)	Yield Y Conversion C	Reusability (runs)	Ref.
Cottonseed oil	24:1	5-Na/ZnO/SBA-15	12	240	-	5.19B	65	98-93% Y	4	[304]
Cottonseed oil	40:1	CeO_2/Li/SBA-15	10	240	-	5.66 A+B	65	~98% Y	5	[303]
Soybean oil	12:1	Cinder supported CaO/KF	2.1	20	~0.9–20 x 10^5	-	65	~99.99- 96.6% C	4	[305]
Soybean oil	20:1	Mg/Al/Zn/SBA-15	-	1.2h^{-1}	5-8 x 10^5	0.18B	225	85-90% Y	200hr	[306]
Soybean oil	50:1	CaO–MoO_3–SBA-15	6	3000	-	-	~65	83.2-77.2% C	5	[302]
Soybean oil	12:1	SBA-15-pr-NR_3OH	2.5	30	~1 x 10^3	1.26 B	65	99.4-97.8% Y	5	[307]

a: average conversions across C_4 – C_{18} alcohols in 2.4:1 ratio to fats, b: ethanol to oil

2.3.4 Other Catalytic Approaches

2.3.4.1 Ion Exchange Resins

Ion exchange resins of cationic (acidic) and anionic (basic) type have been explored in past studies, with a selection summarised in Table 2.15. Sulfonic acid cationic resins have successfully been applied to lower FFA levels in UCO within reasonable reaction times and temperatures. Common sources of deactivation include group 1/2 metal ions present in UCO due to cooking processes, however washing with HCl has been demonstrated to restore activity [308]. Alongside use of commercial exchange resins such as Amberlyst, other researchers have improved beyond these products by creation of novel resins with greater porosity and specific surface area. Optimising the quantities of monomer, comonomer, cross-linking agent and acid functionalisation concentration used during synthesis allows for controlled polymerisation to give a more desirable catalyst [309]. Anionic ion exchange resins have demonstrated moderate transesterification performance, however issues of excessive methanol loading [310], use of idealised triolein feedstocks [311] and unsuitability for high FFA% feedstock [312] means more work is required to demonstrate viability of anionic resins for low quality feedstock applications. It is recommended to continue optimising both anionic and cationic resins for transesterification and esterification pathways respectively.

Table 2.15 - Summary of Ion Exchange Resins for Biodiesel Production

Feedstock	A:O Ratio	Catalyst	Catalyst Loading (wt%)	Reaction Time (min)	Particle Size (nm)	Acidity (A) Basicity (B) (mmol/g)	T (°C)	Yield Y Conversion C	Reusability (runs)	Ref.
J. curcas oil	35:1[a]	Amberlyst A26 (OH)	15	540	-	-	55	36.81% Y	-	[312]
Oleic acid	0.5:1	Amberlyst-31	4g	180	5.5-7 x 10^5	7.1 A	60	80.2 - 78.9% C	4	[313]
Oleic acid	0.96:1	Amberlyst-15	5g	-	7.4 x 10^5	-	100	97.5% Y	300 min	[314]
Soybean oil	100:1	Amberlyst-26OH	12.5 mol%	480	-	1.3 B	65	100% C	-	[310]
Triolein	10:1	Diaion PA306s	4g	300	1.5-2.5 x 10^5	1.24 B	50	~80% C	4	[311]
UCO	12.2:1	EBD-100	1	300 1440	<6.3 x 10^4	5.37 A	65	~80% C 97.7 - 85% C	5	[308]
UCO	3:1	NKC-9	18	180	4-12.5 x 10^5	1.5-4.7 A	66	~90% C	10	[315]
UCO	12:1	SHER	1.5	480	3–450 x 10^3	5.1 A	60	90% C	-	[309]
X. sorbifolia oil	8:1	Amberlite IRA-900	3	90 (MW)	4-12.5 x 10^5	1.1-3.6 B	60	96 - 70% C	10	[316]

a: ethanol to oil, SHER: sulphonated hyper crosslinked **exchange resin**

2.3.4.2 Ionic Liquids

Ionic liquids (IL) are defined as low melting point salts comprised completely of ions. The melting temperature is considered low when below 100 °C in most literature [317]. IL catalysts can be formed either by being insoluble within organic oil layer as a biphasic liquid-liquid system or via immobilisation onto support materials as a heterogeneous catalyst [318]. Both approaches have been explored for biodiesel production with some recent studies summarised in Table 2.16. While biphasic liquid-liquid IL catalysts are simpler to synthesise and highly reactive, separation is slightly more challenging compared to immobilised IL, although still more easily recoverable than traditional KOH or H_2SO_4 homogeneous catalysts. Immobilised IL have improved separability but at cost of reactivity and synthesis complexity [319]. Literature has highlighted the challenges of developing supported IL catalysts that are both chemically and thermally resilient over multiple recycles [320]. Other researchers have decided to explore deep eutectic solvents (DES) instead as a lower cost and more readily synthesisable alternative to IL catalysts [321]. In general, acidic IL still face similar problems of kinetic unfavorability towards transesterification and basic IL can promote saponification at increased levels of FFA and moisture similar to all previously discussed catalysts. Work by Sun et al. [322] however demonstrated that while LDH support deactivated under high FFA% of UCO, the high basicity of [Bmim]OH was surprisingly acid resistant and enabled high FAME yield 6 recycles at reasonable reaction conditions. It is recommended that studies continue to explore nanoscale supported IL with high recyclability in UCO treatment.

Table 2.16 - Recent Ionic Liquid Catalysts for Biodiesel Production

Feedstock	A:O Ratio	Catalyst	Catalyst Loading (wt%)	Reaction Time (min)	Particle Size (nm)	Acidity (A) Basicity (B) (mmol/g)	T (°C)	Yield Y Conversion C	Reusability (runs)	Ref.
Oleic acid	10:1	MIL-101(Cr) /MBIAILs	11	240	-	-	67	91.0-82.1% C	6	[323]
Oleic acid	10.39:1	$[(CH_2COOH)_2IM]HSO_4$/H-UiO-66	6.28	300	-	1.13 A	80	93.82-90.95% Y	5	[324]
Oleic acid	11:1	P-APTMS-PS-5 SHIL	6	120	-	1.08 A	70	96.55-95.37% C	7	[325]
Rapeseed oil	0.466:1	$[BMIM]-[CH_3SO_3]$	2 mmol	420	-	-	70	~98.2% Y	10	[326]
Soybean oil	18:1	SO_4^{2-}/ZrO_2-SiO_2(Et)-IL	5	180	-	1.16 A	150	98.99-95.22% Y	5	[327]
Soybean oil	11:1	BNPs-CCH	4.13	264	180	-	60	95.2-83% Y	5	[328]
UCO	12:1	[Bmim]OH/Mg-Al-La	3	360	-	2.48 B	65	98.8-85.4% Y	6	[322]

2.3.4.3 Enzymes

Biologically derived enzymes can be used to convert glycerides into FAME, with a particular category of enzyme called lipase able to facilitate various hydrolysis, acidolysis, glycerolysis, interesterification and the desirable alcoholysis reaction pathways [329]. Immobilisation onto a support material is common to enable repeated reuse and simple recovery post reaction. Commercial lipases include Novozym 435 [330] derived from Candida antarctica fungus and Lipozyme IM-20 [331] derived from Rhizomucor miehei fungus. Loading of Candida rugosa fungal lipase onto commercial sepabeads has been explored by Winayanuwattikun et al. [332] while loading of Pseudomonas fluorescens bacterial lipase onto silica support has been studied by Ferrero et al. [333] as alternative to commercial enzymatic catalysts. A select summary of biodiesel production studies using supported enzyme catalysts is provided in Table 2.17. Common issues with enzymatic catalysis include the requirement of long reaction times and inability to increase kinetics via temperature due to thermal instability of lipases [334]. For a continuous process plant this would require large residence times. Furthermore, it has been reported that short chain alcohols such as methanol can deactivate certain biological lipases [335]. Selection of more resilient enzymes is hence required to maximise yield and recyclability. Alternatively, work by Macías-Alonso et al. [336] has explored conversion of UCO completely into FFA via lipase hydrolysis prior to acidic esterification in a two-step approach, avoiding need of methanol resilience. Future studies should continue to focus on enhancing reaction rates and reporting enzyme reusability.

Table 2.17 - Previous Studies in Enzyme Catalysed Biodiesel Production

Feedstock	A:O Ratio	Catalyst	Catalyst Loading (wt%)	Reaction Time (min)	T (°C)	Yield Y Conversion C	Reusability (runs)	Ref.
C. Colocynthis oil	5:1	Novozym 435	4	222	43	97.8% Y	-	[337]
M. Latifolia fat M. Indica kernel fat S. Robusta kernel fat	2.4:1[a]	Lipozyme IM-20	10	360	60	94.6% C 94.2% C 93.6% C	-	[338]
Palm oil	3:1	C.rugosaon on Sepabeads EC-OD	-	2880	40	64% C	-	[332]
Rapeseed oil	3:1	Novozym 435	5	1440	40	76.1% C	-	[339]
UCO	0.33:1-0.67:1	Novozym 435	4	3000	30	~90% C	50	[340]
UCO	4:1[b]	heterogeneous low ordered biosilicified enzyme	12.5	1440	37	~80% Y	-	[333]

2.4 Non Catalytic Approaches

Various approaches have been developed that remove the need of a catalyst altogether. By eliminating the catalyst requirement, the process complexity may be reduced by minimising the number of separation steps required. Less waste may also be produced by avoiding the need to regenerate or replace spent catalytic material, a potential economic as well as environmental benefit. Figure 2.15 displays some of the alternative routes that have been explored in the synthesis of biodiesel to date within the literature.

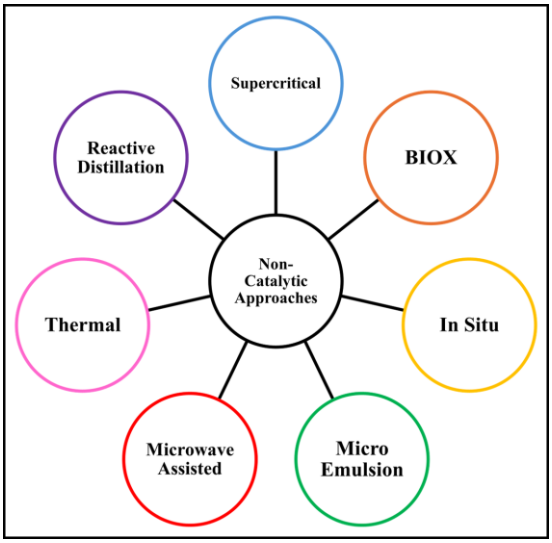

Figure 2.15 - Non-Catalytic Approaches to Biodiesel Production

Oil feedstock and methanol are usually immiscible at traditional operating temperatures, commonly a maximum temperature of 65 °C is chosen as boiling point of methanol and the reaction is performed under reflux. Due to the multiphase system, mass transfer can initially be a limiting condition until sufficient FAME is produced to act as a cosolvent. The supercritical route instead involves heating both feedstock and alcohol to a very high temperatures and pressure (300-400 °C, ~80 atm), until the mixture becomes a single homogeneous phase [341-345]. By removing interphase mass transfer resistance, accelerated reaction kinetics are achievable with high FAME conversion in significantly reduced time. Unlike catalytic routes, water content and FFA content is less of a detrimental effect via supercritical reaction. However, the extreme conditions required presents various engineering challenges. Increased process operating and capital costs are likely, from both greater energy consumption and costly vessels specifically designed for harsh reaction conditions.

Alongside the additional safety concerns of such conditions, the sustainability is also questionable due to increased heat duty requirement. To mitigate extreme reaction conditions, use of other cosolvents such as hexane [346] and toluene [347], or even inclusion of some catalytic material such as CH_3ONa may help to increase yields or lower the operating temperatures and pressures required [348]. Alternatively, the thermal energy required may be supplied via microwave (MW) assisted heating technologies [349-353]. Compared with conventional industrial heating methods, MW irradiation is both highly efficient and rapid since energy can be transferred directly at the molecular level instead of relying on conductive and convective heat transfers [354]. A similar concept has been explored in reactive distillation systems, where supercritical reaction and separation can occur in parallel [355]. Ozonolysis has also been explored in reactive distillation of oleic acid into FAME product [356].

The BIOX process, as pioneered by Boocock et al. [357] and commercialised via the BIOX Corporation, is illustrated below in Figure 2.16. The process in an innovative two step non-catalytic approach to biodiesel production built on the concept of using a cosolvent to improve methanol-oil solubility. The resulting single phase mixture hence benefits from enhanced mass transfer rate and can subsequently facilitate both catalytic and non-catalytic biodiesel production. High FFA content is reduced in the first refinement step followed by subsequent conversion of triglycerides into FAME, with methanol and cosolvent recovered for reuse in both steps. Advantages include short reaction time, ambient reaction conditions, ease of glycerol separation and tolerance of impurities up to 10% FFA [358]. Nevertheless, tetrahydrofuran cosolvent is toxic and difficult to separate from methanol due to similar boiling point, so great care must be taken to ensure residual solvent in biodiesel remains minimal. Alternative cosolvents such as MTBE have also been explored in the literature [359].

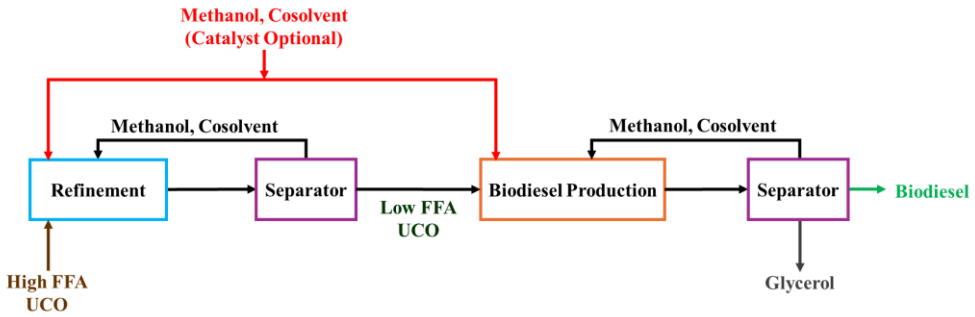

Figure 2.16 - Simplified Process Flow Diagram of BIOX Biodiesel Production Process

In situ transesterification is a reactive extraction process in which the alcohol performs both extraction and transesterification in a combined step. Since extraction step can be avoided the conversion may be more cost effective by process simplification. While acidic or basic catalysts can be utilised, using cosolvents such as water or direct processing of wet feedstocks like algae can create a pseudo-catalytic system [360-362]. Water presence can also hydrolyse cellular membranes and improve lipid extraction [363]. Use of ultrasonication and MW heating can be utilised to enhance reaction rate [364].

Other non-catalytic routes include microemulsion, where raw oil properties are adjusted using dispersants and surfactants to create blends suitable for current engine technology [365], and thermal routes such as thermal cracking [366]and pyrolysis [367]. These routes however are less environmentally sustainable, producing inferior fuel that may increase engine damage or pollution. While membrane and ultrasonic assisted reactor technology has mainly focused on catalytic biodiesel production to date [368, 369], there is potential for future non-catalytic implementations such as separation of FFA from UCO via membrane [370] and ultrasonic enhanced routes [371] as discussed above.

2.5 Challenges and Opportunities

2.5.1 Challenges Facing Industrial Application

2.5.1.1 Scaling Up

There are several pressing challenges that still need addressing before current nanocatalyst technologies can be scaled up for industrial application. Modern biorefineries have been designed with process intensification in mind, reducing complexity, wastage, and energy requirements, thereby improving economic and environmental aspects of biodiesel production. An important side effect of this is the use of continuous reaction technology. In comparison, unfortunately most studies from literature instead focus on batch reaction schemes. While this is acceptable for initial trials of newly developed catalysts, it is not a true demonstration of how these materials would be utilised commercially. Unlike batch reactors, continuous systems can achieve a more consistent biodiesel product, ensuring international fuel standards such as EN 14214 and ASTM D6751 [34, 372] are met with little variation in quality. Higher throughputs are also attainable, producing sufficient biodiesel to meet the forecasted ever growing market demand. By transitioning from lab scale batch trials towards assessing performance in pilot scale continuous reaction and separation schemes, performance could be validated in more industrially relevant scenarios. The design of continuous reactors to test newly developed catalysts would depend on knowing the kinetic parameters for the esterification and transesterification reactions. Regrettably only a few studies tend to perform or simulate kinetic trials to determine such information. Presented in Table 2.18 is kinetic data reported for sulfated solid acid catalysts that have been recently explored. The turnover frequency (TOF) can be understood as a measure of active site efficiency, and ranges from 10^{-2} min^{-1} to 10^{1} min^{-1} for recently developed catalysts, which is within the expected range for industrial usability [373]. Reaction order is found to be unitary, which could be predicted since methanol is almost always added in large excess of the stoichiometric ratio, shifting equilibrium towards biodiesel production as described by Le Chatelier's principle. Therefore, for sufficiently high alcohol to oil ratios, biodiesel production could be reasonably expected to be a pseudo first order reaction. Activation energy lies mainly within the 30-80 kJ/mol range often observed for biodiesel production [374]. It is recommended that more studies report kinetic and thermodynamic parameters to better inform future applications in continuous reaction schemes.

Table 2.18 - Kinetic Data for Recent Sulfated Metal Oxide Nanocatalysts

Catalyst	Temperature (°C)	TOF (min^{-1})	Activation Energy (kJ/mol)	Rate Constant (min^{-1})	Order	Reference
SBA-15/sulfonic acid	60	0.13 - 0.58	-	-	-	[220]
KIT-6/C-SO_3H	-	0.57	-	-	-	[223]
SBA-15/sulfonic acid	60	0.20 - 2.00	-	-	-	[222]
SO_4^{2-}/La_2O_3/HZSM-5	100	-	44	-	1	[225]
CNF-Ar-SO_3H	120	0.32	-	-	-	[242]
SO_3H-GO	100	-	13	0.921	1	[239]
S-MWCNTs	150	-	72	0.0498	1	[244]
Fe_3O_4-Chitosan-Hollow-Chitosan-SO_3H	80	-	38	0.0173	1	[191]

The major advantage of sulfated acidic catalysts compared to solid bases is a superior tolerance to impurities such as FFA and water, reducing deactivation effects and avoiding the issue of soap formation via saponification. While many studies have demonstrated successful esterification and resilience in FFA models such as oleic and palmitic acid, it is important to also demonstrate successful biodiesel production can still be achieved when using realistic, economical, and readily available feedstocks as noted in Chapter 2.3.2.5. Reported catalytic performances of solid acidic nanocatalysts using realistic UCO feedstock is summarised in Table 2.19 and it can be observed that reaction temperature and treatment time is often suboptimal. As recommended in Chapter 2.1.4 it may be more viable to optimise a two-step approach suitable for modern biorefineries.

Table 2.19 - Solid Acid Nanocatalysts with UCO Feedstock

Catalyst	A:O Ratio	Catalyst Loading (wt%)	Time (min)	T (°C)	Yield Y Conversion C	Reusability (runs)	Particle Size (nm)	Pore Size (nm)	Surface Area (m^2/g)	Acidity (mmol/g)	Ref.
SO_4^{2-}/TiO_2-SiO_2	20:1	10	180	120	77% C	1	-	2.85	457	-	[224]
Fe_2O_3-MnO-SO_4^{2-}/ZrO_2	20:1	3	240	180	~96.5% Y	6	11.5-21	-	1.39 x10^{-6}	4.32 A 1.52 B	[214]
SO_4^{2-}/Zr-SBA-15	40:1	3	180	160	98.5 - 80% C	6	-	3.27-5.47	271	-	[227]
Ti(SO_4)O	9:1	1.5	180	75	97.1 - 94.12% Y	8	25	22.7	44.5	-	[198]
$TiO_2/PrSO_3H$	15:1	4.5	540	60	98.3 - 94.16% Y	4	8.2 - 42	24.6	38.6	-	[199]
SO_4^{2-}/Fe-Al-TiO_2	10:1	3	150	90	96->90% Y	10	<50	11.1	51	1.18	[145, 248]
SO_4^{2-}/Mg-Al-Fe_3O_4	9:1	4	300	95	~98.5% Y	5	25-165	6.5	123	2.35	[146]

Synthesis routes of catalytic material will also need to be demonstrated at scale. Recent work by Mahin and Torrente-Murciano [375] demonstrated the continuous production of Fe/Fe_3O_4 core-shell magnetic nanoparticles via thermal decomposition of $Fe(CO)_5$ precursor. Precise control over a narrow size distribution could be achieved and functionalisation via oleic acid was successfully performed. Optimisation of flowrate and reactor length led to high levels of mixing and sufficient residence times above 12 seconds. Balancing the mixing and residence time led to optimum size distribution and a high production rate of 2.6 g/hr in the helical microreactor. Research such as this opens up future exploration into continuous catalyst synthesis, as current batch production techniques face issues of batch variability and often unconfirmed reproducibility. Sensitivity of synthesis routes should also be verified to confirm that consistently active nanocatalysts can be obtained in a controlled manner, even under small deviations in synthesis parameters.

2.5.1.2 Catalyst Recyclability

Recyclability remains a challenge despite new catalysts being regularly developed. Deactivation can occur due to a variety of reasons and different regeneration approaches have been tried to extend activity, as illustrated in Figure 2.17. Although recent work by Gardy et al. [145, 248] using SO_4^{2-}/Fe-Al-TiO_2 achieved high yield over an impressive 10 consecutive runs with impure UCO feed, there continues to be a strong desire to further extend catalyst lifespan without expending significant cost in material regeneration. Work involving sulfated zirconia as part of mixed metal oxide catalysts has led to encouraging improvements in recyclability and retention of sulfate groups. While it may be that sulfated metal oxides are more suitable for conversion of cheap raw feedstocks than sulfated carbon, recent work such as Al^{3+}/SO_4^{2-}/MWCNT catalyst synthesized by Shu et al. [245] could challenge that theory. An impressive 8 consecutive uses could be performed, although it would have been preferable to see UCO used instead of model FFA oleic acid. It is hoped that similar improvements over time may be made with other types of sulfated solid acids. Batch or continuous separation and regeneration tests of catalytic material could also be explored further, for instance by performing reacidification of lost sulfate surface groups and washing as independent continuous steps, aiming towards an eventual completely closed loop. It is often noted how external magnetic fields could simplify nanocatalyst recovery by inclusion of magnetic species like iron oxides into sulfated acids. Thus far however there is a lack of work demonstrating successful continuous magnetic separation within the application of biodiesel production.

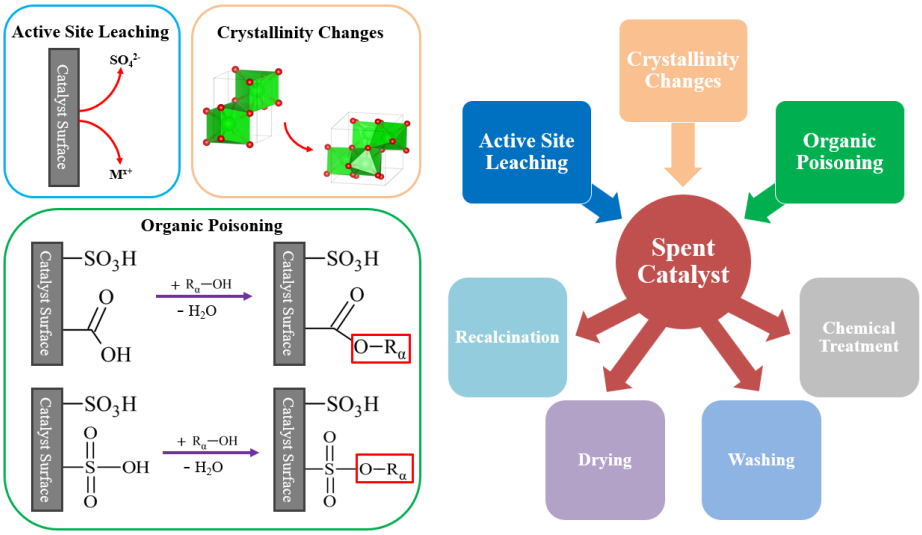

Figure 2.17 - Catalytic Deactivation Routes and Regeneration Approaches [35]

2.5.2 Opportunities for Research

2.5.2.1 New Catalyst Designs

Through a thorough review of current literature, it is clear there are still many new nanocatalyst designs awaiting discovery. In order to reduce FFA in UCO feedstocks via esterification it is clear that a solid acid nanocatalyst should be selected. Areas of particular promise include mixed metal oxides, sulfated metal oxides and supported acid catalysts. Sulfated TiO_2 has demonstrated high reactivity in esterification and is both chemically and thermally resilient enough to facilitate repeated recycling. Combining with another oxide such as Fe_2O_3 may be able to introduce magnetic separability as well as contribute further catalytic activity. While it is unclear if hematite is magnetically active enough to allow magnetic separability post reaction, use of Fe(III) salts only would simplify synthesis process and is worth testing. Use of a SiO_2 support could increase surface area and pore structure by providing a core structure to impregnate or coprecipitate around. Reduced leaching of metallic species, particularly Fe, may also be possible if a layer of FeSi is formed prior to coating with outer catalytically active layer. Comparison with other outer active layers such as ZnO or ZrO_2 that have been sulfated and previously studied would allow for a range of slightly different new catalysts to be developed and compared. There is no prior reporting of a SiO_2-Fe-(Ti/Zn) sulfated core-shell nanocatalyst design in literature so such research would be especially novel. These considerations were used to inform the proposed new nanocatalyst designs.

2.5.2.2 Functionalisation Agents

A variety of acidic functionalisation agents have been explored to improve catalytic activity towards biodiesel formation. A summary of different surface sulfate groups that have been loaded onto solid nanomaterials is provided in Figure 2.18. Inclusion of sulfur based compounds onto the catalyst surface by reacting with concentrated sulfuric acid [196], chlorosulfonic acid [198] or ammonium sulfate [195] have all been utilised to increase FFA resilience. Total acid site density and acidic strength achieved is dependent on both functionalisation conditions and sulfation agent. For instance, it has been noted that chlorosulfonic acid can greatly enhance sulfur loading and acid site density as compared to sulfuric acid [376]. Use of organic alkyl or aromatic groups has also been explored by using propylsulfonic and toluenesulfonic acids [191, 199]. Introduction of nonpolar organic acid sites has been observed to reduce deposition from polar FFA impurities and hence improve reusability, at the potential cost of reduced activity due to weaker acidity achieved.

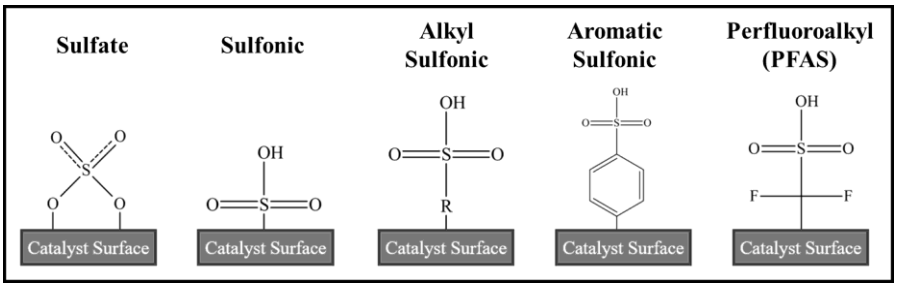

Figure 2.18 - Sulfated Functional Groups Previously Explored [35]

Sulfation not only increases Brønsted acid behaviour that favours esterification but also can enhance the transesterification favouring Lewis acidity of metal based solid catalysts via the inductive effect, drawing electron density away from the metal cation and increasing the ability for electron pair acceptance to occur. The sulfate ion (SO_4^{2-}) can exist in a variety of forms, for sulfated metal oxides this includes monodentate bonding, bidentate chelated and bridged structures, or free ion structure as illustrated in Figure 2.19. The sulfate loading achieved can influence both the Brønsted/Lewis ratio and acidic strength, with high loadings leading to polynuclear sulfate structures with more Brønsted sites present [377]. More stable bidentate or polynuclear structures have improved stability enabling increased recycling without loss of sulfate, however deactivation may still occur via pore blockage and organic deposition. Excess sulfur loading may also block pores and lower surface area, hence acid density and strength must be balanced with morphology.

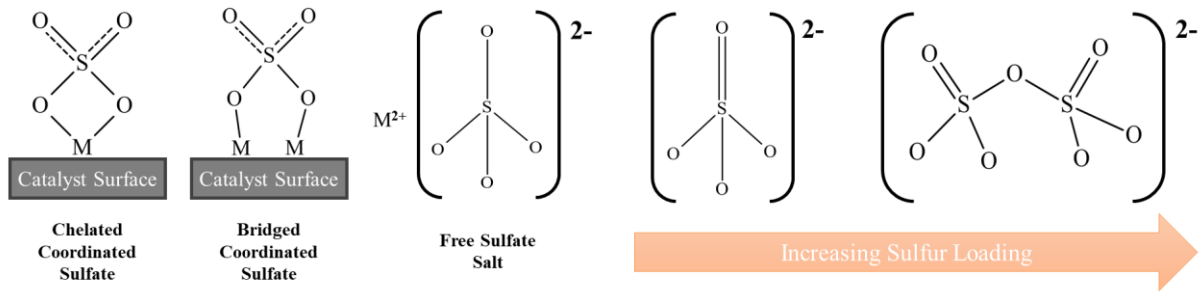

Figure 2.19 - Surface Sulfate Structures and Dependence on Sulfur Content [35]

Limited studies have been performed on varying the concentration of functionalisation agent used. Studies such as Li et al. [94] and Rezki et al. [251] confirm that an optimum concentration of acid treatment exists. Too dilute a solution can cause poor sulfur loading, low acid density, and weak acidic strength. Excess concentration can instead promote solid digestion and conversion of metal oxide into sulfate salt. The nature of how concentration impacts fundamental properties such as surface area, pore size, crystallinity, surface chemistry, dispersion, morphology and esterification performance is often not investigated, poorly understood and requires much more research. Functionalisation conditions are likely just as important to optimise as other synthesis parameters and hence a range of nanocatalysts should be developed at varying treatment conditions.

2.5.2.3 Optimisation of Two Step Route

Design of Experiment (DOE) approaches have been successfully utilised in prior studies [42, 254, 378] to reduce the number of reaction trials required to explore influential factors such as reaction time, temperature, alcohol to oil ratio and catalyst loading. Development of statistical models can reveal important reaction parameters via effect screening and simulate yield responses to determine points of maximum FFA conversion. Such model predictions need to be confirmed experimentally but may assist in identifying promising nanocatalyst designs, especially if multiple designs are synthesised and many hundreds of reaction trials are not feasible. Limiting design space to industrially applicable reasonable reaction conditions may lead to only strong esterification performance with acidic catalysts, in which case a two-step route should be explored to confirm FFA treatment can promote superior base activity in second step. While model feedstocks can unquestionably confirm if esterification and/or transesterification is facilitated, optimum nanocatalyst and reaction conditions should also be applied to various UCO feedstocks to confirm desirable performance can still be achieved.

Chapter 3.

Chapter 3. Materials and Methods

3.1 Introduction

This chapter focuses on the materials and methods that were developed and used throughout the research work. Chapter 3.2 presents and discusses the multistep synthesis pathway that produced six different novel catalytic materials. Chapter 3.3 focuses on the various characterisation techniques that have been used to study the synthesised catalyst as well as providing a brief summary of the background and history of these methods. Chapter 3.4 details the Design of Experiments approach that was taken for measuring, modelling and optimising catalyst performance. Further details of these batch trials and determination methods of computing methyl oleate or FAME yield are provided in Chapter 3.5. Finally, Chapter 3.6 provides a list of all materials used during the research as well as supplier information and specification details.

3.2 Catalyst Synthesis Route

3.2.1 Design Considerations

As discussed in Chapter 2, there are many different types of nanocatalyst design currently being researched for conversion of low grade feedstocks to biodiesel and in this research six novel core-shell nanocatalysts were produced following a multistep synthesis pathway as illustrated in Figure 3.1 below. A core-shell design was proposed in which each successive layer of the nanocatalyst is fulfilling a different design objective. The central ~100 nm SiO_2 nanoparticle support would provide a high specific surface area and ideal pore structure for which subsequent layers could coprecipitate around. Literature review in Chapter 2 had identified coprecipitation method as a facile and economical synthesis route. Early on it was identified that a multistep pathway may lead to potential issues with leaching, pore blockage and reducing of surface area, hence the central support was used in an effort to combat this. The secondary iron oxide layer was included in an attempt to introduce desirable magnetic behaviour that would enable simple separation post reaction. Since iron oxides are less chemically stable in acidic environments and issues with iron species leaching has been reported previously, it was clear that an iron layer should not be the outermost layer. However, iron oxides have been demonstrated to display some catalytic activity for biodiesel conversion. To best take advantage of this activity while still utilising silica as superior support material, the iron oxide layer was selected as intermediate layer.

Typically, magnetically separable catalysts utilise the more strongly magnetic properties of Fe^{2+} materials such as magnetite and maghemite. This requires a synthesis route under N_2 conditions to avoid oxidation into only slightly magnetic hematite. Since some literature reported successful separability using hematite phase and in order to reduce cost and complexity of synthesis it was decided to produce this intermediate phase with Fe^{3+} salt. Concentrated NH_4OH was selected over NaOH as precipitating agent to avoid contamination with metal ions. Chapter 3.2.2 discusses the first step of obtaining FeSi support material.

The outermost layer was identified as needing to be highly catalytically active as well as chemically and thermally stable since this layer would be in contact with low grade reactants for extended periods at high temperature. From work performed in Chapter 2 sulfated metal oxide materials appeared most favourable to higher levels of FFA and moisture content. Two of the most frequently explored were those based on TiO_2 and ZnO. The FeSi support was therefore to be coated with a layer of TiO_2 or ZnO respectively prior to further functionalisation. Step 2A is discussed in Chapter 3.2.3 and resulted in a TiFeSi support material while Step 2B is discussed in Chapter 3.2.4 and resulted in ZnFeSi support. Research from Chapter 2 suggests that anatase phase titania is most catalytically active but converts to less active rutile at higher temperatures. As a result, the calcination temperature of 400 °C was selected to prevent this transition. Since calcination temperature was not part of the research scope, this temperature was also used in other steps to balance sufficient thermal energy for recrystallisation to occur but not too excessive a temperature that might lead to extensive grain growth and loss of surface area or porosity.

The last part of the synthesis pathway (Step 3) is detailed in Chapter 3.2.5 and involves functionalising the TiFeSi and ZnFeSi support surface with three different concentration levels of chlorosulfonic acid to produce a total of six different catalytically active materials for further study. Different functional groups have been explored for biodiesel production as discussed in Chapter 2, chlorosulfonic acid was selected to ensure acid sites of high strength and activity would be produced to enable maximum reactivity of FFA esterification alongside the novelty of exploring how catalyst properties may change with varying concentration of this functionalisation step.

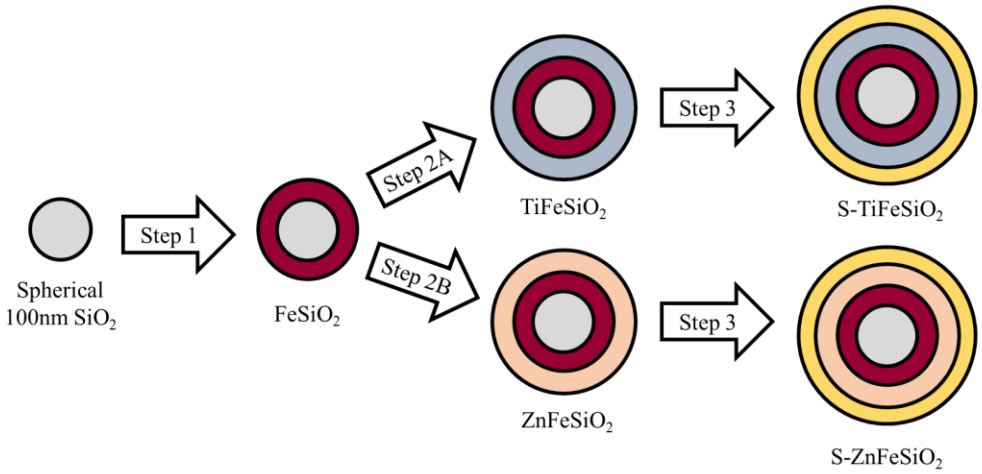

Figure 3.1 - Overview of Catalyst Synthesis Pathway

3.2.2 Synthesis of FeSi Catalyst Support

The synthesis of Fe layer by coprecipitation was adapted and modified from previous methodology reported by Gardy et al. [145, 146], wherein this work only a single iron oxide precursor (Fe^{3+}) was utilised. Approximately 0.125 moles of Iron(III) sulfate hydrate (Sigma-Aldrich) were dissolved into 100 mL equal volume of ethanol-deionised water and ultrasonicated for 5 minutes to produce a rust red solution. Next 2 g of 100 nm SiO_2 (Fiber Optics Center) was suspended in 50 mL ethanol (VWR) and 10mL ethylene glycol (Fisher Scientific) to minimise magnetic aggregation on silica surface. The Fe^{3+} solution was then added dropwise to the suspended SiO_2 solution at room temperature under 250 rpm agitation via magnetic stirring. A Mettler Toledo SevenCompact pH probe was then inserted followed by injection of concentrated NH_4OH solution (Sigma-Aldrich) at room temperature until a desired pH of 9-10 had been achieved. The mixture was observed for dark red/brown precipitate confirming initial coprecipitation had occurred prior to heating under reflux at 75 °C via mineral oil bath and vigorous 500 rpm agitation for 2 hours to facilitate Ostwald ripening around SiO_2 support. The mixture was then allowed to cool and statically age overnight prior to repeated washing of solids in equal volume of ethanol-deionised water via centrifuge at 5 °C, 9000 rpm and 10 minute run cycles. Washing step was repeated until no further SO_4^{2-} could be detected in wash solvent via 0.1 M BaCl (Fisher Scientific) indicator test and no further change in pH reading. Solid was dried overnight in a vacuum oven at 120 °C prior to calcination in a muffle furnace for 4 hours at 400 °C in air. Material after this step is denoted FeSi. Figure 3.2 displays the synthesis setup, pH probe and wet FeSi solid pre-drying.

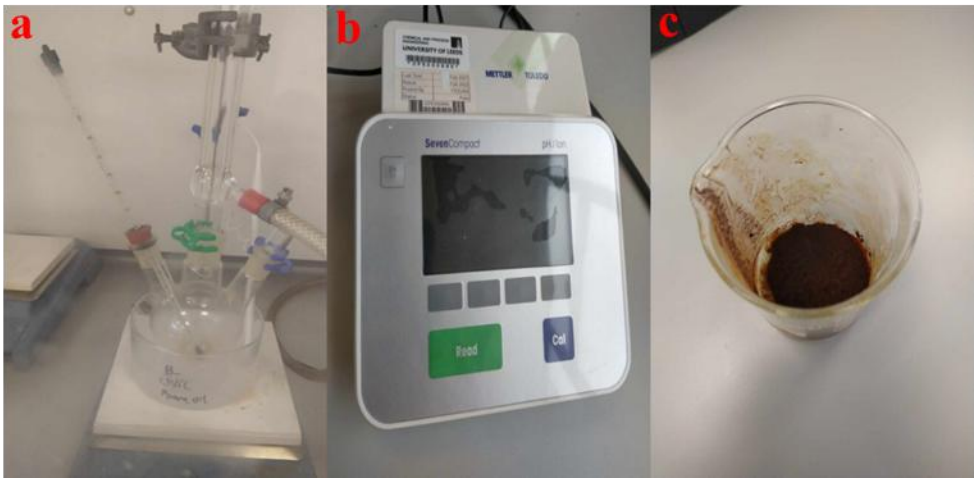

Figure 3.2 - Synthesis setup (a), pH probe (b) and wet FeSi solid (c)

3.2.3 Synthesis of TiFeSi Catalyst Support

Synthesis of Ti containing layer was performed using a modified coprecipitation method adapted from Gardy et al. [145] with selected Ti precursor and organic solvent. Approximately 0.1 moles of Titanium(IV) Butoxide (Sigma-Aldrich) were dispersed into 50 mL of ethanol via ultrasonification for 5 minutes. Into this solution 1 g of FeSi material was subsequently added and dispersed via ultrasonification for 5 minutes until no solid residue was observed at bottom. The mixture was stirred via magnetic stirring at 250 rpm while pH probe was added followed by addition of concentrated NH_4 solution until desired pH of 9-10 was measured. The mixture was observed for production of a white sol prior to vigorous agitation at 500 rpm and heating under reflux for 2 hours at 75 °C to promote Ostwald ripening around FeSi support. This mixture was then left to cool and statically age overnight. On returning it was noted that two different solid phases had developed. A small quantity of bulky red/brown phase at the bottom of the flask which was likely FeSi aggregate that had not been coated, and a fine white solid throughout the rest of the flask that was likely the desired TiFeSi material. The two solid phases were separated by gravity decanting followed by repeated washing of white TiFeSi solids in equal volume ethanol-deionised water via centrifugation at 5 °C, 9000 rpm and 10 minute run cycles. Washing was continued until pH remained constant in washings. Solid was dried overnight at 120 °C in vacuum oven then calcinated in a muffle furnace for 4 hours at 400 °C in air environment. The support material produced after this step is entitled TiFeSi. Figure 3.3 displays bulk and fine TiFeSi solids obtained as well as the ceramic crucibles and muffle furnace used during calcination.

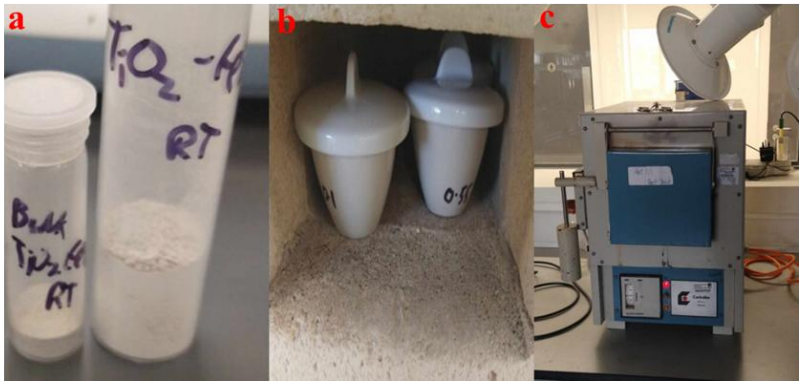

Figure 3.3 - Bulk and Fine TiFeSi (a), Ceramic Crucibles (b) and Muffle Furnace (c)

3.2.4 Synthesis of ZnFeSi Catalyst Support

Synthesis of Zn layer was performed using modified coprecipitation route adapted from work by Gardy et al. [145] with selected Zn precursor. Deionised water was used to ensure sufficient salt solubility. Approximately 0.1 moles of Zinc Sulfate Heptahydrate (Sigma-Aldrich) were dispersed into 50 mL deionised water via ultrasonication for 5 minutes prior to addition of 1 g FeSi and further dispersion for 5 minutes in ultrasonic bath until no solid residue was observed. The mixture was then stirred via magnetic stirrer at 250 rpm and pH probe was inserted followed by addition of concentrated NH_4OH solution until desired pH of 9-10 was obtained. A very thick cream sol was noted confirming initial coprecipitation had occurred. The mixture was then heated at 75 °C under reflux at 500 rpm stirring rate for 2 hours to promote Ostwald ripening around FeSi support. After leaving to cool and statically age overnight, the cream solid was repeatedly washed in deionised water via centrifuge at 5 °C, 9000 rpm and 10 minute run cycles. Washing was repeated until neutral pH was measured in wash water and no SO_4^{2-} content could be detected via 0.1 M BaCl indicator test. The cream solid was then dried overnight at 120 °C in vacuum oven before calcination at 400 °C in muffle furnace for 4 hours in air. Solid material produced after this step is denoted ZnFeSi. Figure 3.4 displays the thick sol and solid aggregate obtained post ageing, the BaCl test for sulfate ions and the vacuum oven used for solid drying. As can be seen in Figure 3.4a, the formation of highly thick and viscous sol obtained was noted to retain excess water and impeded drying process. Future work in Chapter 4 will discuss the excess hydration of ZnO phase likely caused due to synthesis challenges. Future work is recommended to improve this coprecipitation step, either through use of alternate non sulfate precursor, alternate solvents or increased drying time/temperature.

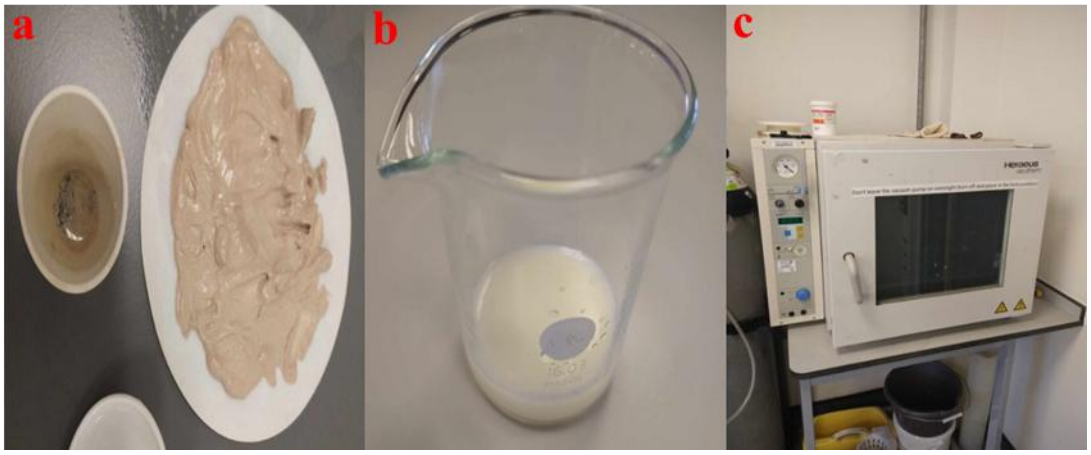

Figure 3.4 - ZnFeSi Sol and Bulk Aggregate (a), BaCl Sulfate Ion Test (b), Vacuum Oven (c)

3.2.5 Synthesis of Functionalised (Ti/Zn)-FeSi Catalyst

Functionalisation method using chlorosulfonic acid was adapted from method previously reported by Gardy et al. [145] with varying acid concentrations. For both TiFeSi and ZnFeSi supports, 1 g of solid material was dispersed into 50 mL of toluene via ultrasonication for 5 minutes until no solid residue was left at bottom of flask. This suspension was then cooled down to -5 °C via NaCl (Fisher Scientific) ice bath under 250 rpm stirring via magnetic stirrer. Sufficient quantity of concentrated Chlorosulfonic acid (Sigma-Aldrich) was then added dropwise at a rate of 0.1 mL/min until final concentration of solution became 0.1 M, 0.55 M or 1.0 M respectively. The resulting mixture was then refluxed a 60 °C for 2 hours under vigorous 500 rpm stirring to facilitate surface functionalisation reaction prior to being left to cool to ambient temperature. Dry toluene was then used to repeatedly wash solid via centrifuge at 5 °C, 9000 rpm and 10 minute run cycles until via analysis of the washings: pH remained unchanged, no SO_4^{2-} was detected via 0.1 M BaCl indicator test and no Cl^- was detected via 0.1 M $AgNO_3$ (Sigma-Aldrich) indicator test. Solid was then dried in vacuum oven overnight at 120 °C prior to calcination for 4 hours in a muffle furnace at 400 °C in air environment. The resultant functionalised catalysts are denoted X-TiFeSi and X-ZnFeSi where X = 0.1 M, 0.55 M or 1.0 M corresponding to the functionalisation conditions respectively. Figure 3.5 shows the NaCl ice bath used during chlorosulfonic acid addition and the FEP centrifuge tubes used during toluene washing steps.

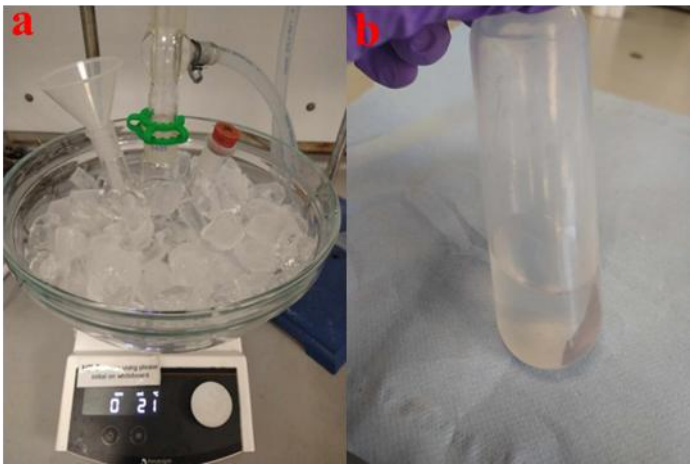

Figure 3.5 - Ice Bath Setup (a), FEP Tubes for Centrifuge Washing (b)

3.3 Catalyst Characterisation Techniques

3.3.1 X-ray Diffraction

The discovery in 1912 that X-rays have the ability to diffract in crystalline materials such as ZnS has been attributed to the work of Walter Friedrich, Paul Knipping and Max Laue [379, 380]. The phenomena of Laue diffraction confirmed that X-rays were behaving in a wave-like manner similar to light, which also displays constructive and destructive interference patterns. Further work by W.L. Bragg and his father Sir W.H. Bragg in 1913 [381] led to the proposed Bragg Law of diffraction. The Nobel Prize in Physics was jointly awarded to W.H. Bragg and W.L. Bragg in 1915 "for their services in the analysis of crystal structure by means of X-rays" [382].

When an X-ray encounters a crystalline or semi-crystalline material, diffraction occurs in a predictable manner as described by Bragg's Law in Equation 3.1. The derivation of this equation can be inferred from Figure 3.6. The path difference between two successive X-rays of wavelength λ and integer multiplier n is equal to 2dsinθ where d is the plane lattice spacing and θ is the Bragg angle for which peak constructive interference occurs.

$$n\lambda = 2d \sin\theta$$

Equation 3.1 - Bragg's Law of Diffraction

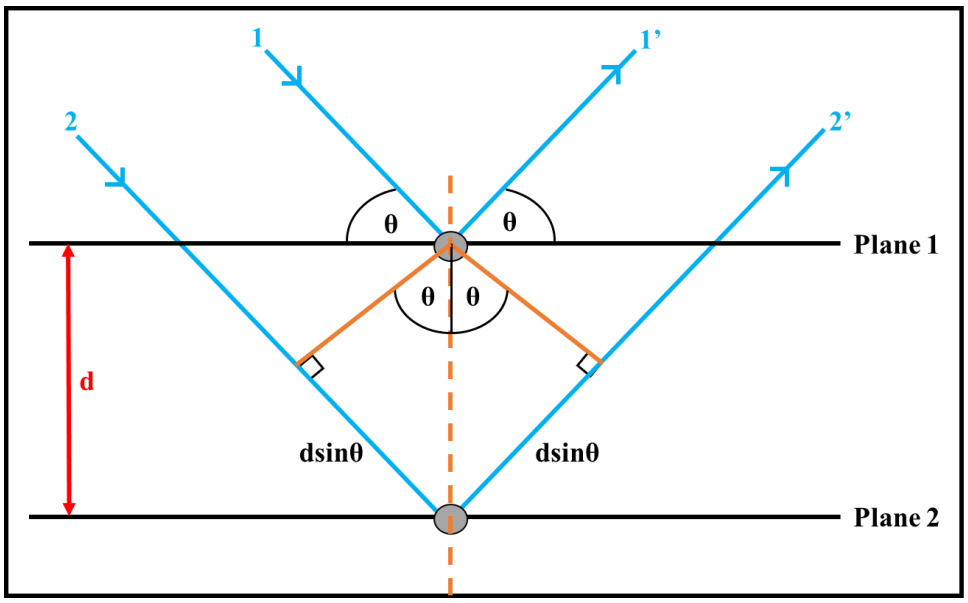

Figure 3.6 - Diagram of Bragg's Law Derivation

Using the Bragg Law, it is possible to identify the plane spacing of a given crystalline material if the wavelength and incident angle for the X-ray beam is known. The observed value of d and resulting X-ray spectrum can therefore be used to determine the bulk chemical composition, crystallinity and crystal phases present for an unknown material. Figure 3.7 shows a comparison between the shape of X-Ray Diffraction (XRD) spectra produced by amorphous, semi-crystalline and crystalline materials. Amorphous materials have no long range order and hence produce broad "amorphous halo" diffraction patterns. As the degree of crystallinity increases, the diffraction pattern becomes sharper with greater peak height and reduced peak width [383].

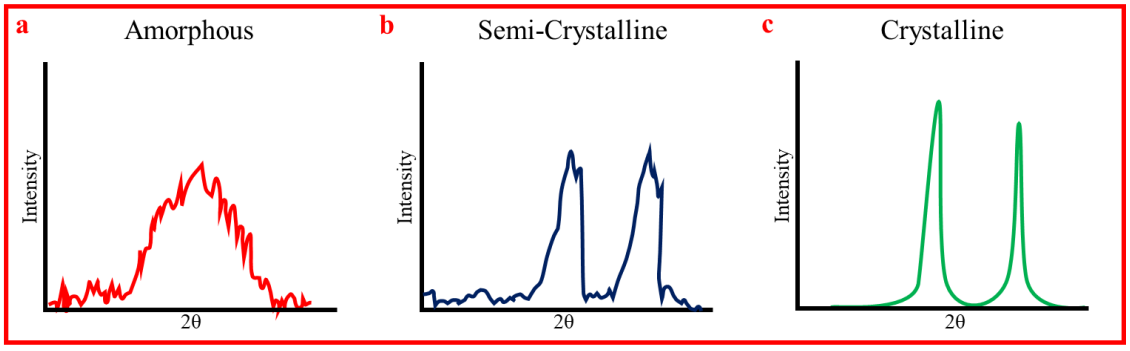

Figure 3.7 - Comparison between amorphous (a), semi-crystalline (b) and crystalline (c) diffraction spectra for silica materials observed via XRD

A diagram of how XRD measurements are taken is displayed in Figure 3.8 while method details used in this work have been included in Table 3.1. Spectral data was compared against literature to determine crystal phases present. Profex software [384] was also used to compare obtained results graphically against reference spectral library for phase identification.

Table 3.1 - Method parameters used for XRD analysis

Property	Value
Model	Bruker D8 ADVANCE
Detector	LYNXEYE
Radiation Source	Cu K-α (Monochromatic,8.04 keV)
Wavelength	0.154 nm
Scan Range (2θ)	10 ° - 70 °
Step Size	0.0169 °
Scan Time	1 hour

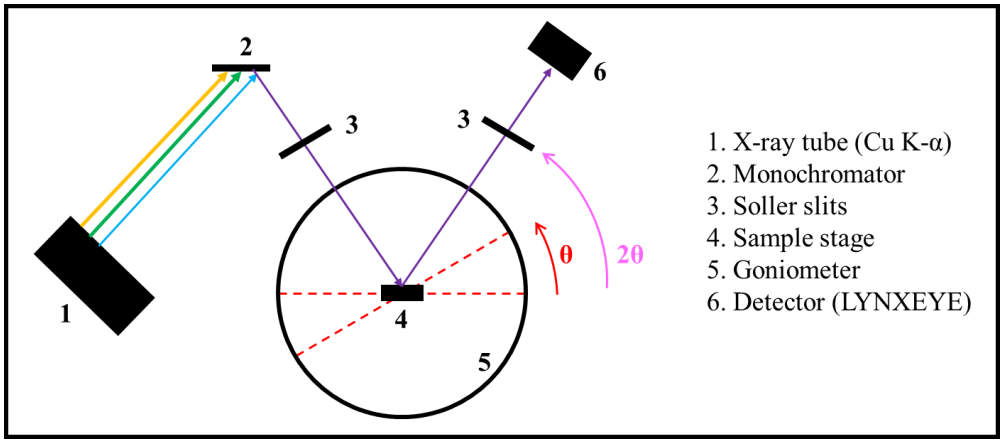

Figure 3.8 – Simplified diagram of Bruker D8 ADVANCE

To determine the crystallite size, the Debye-Scherrer equation was used in a form given by Equation 3.2. Here D is the crystallite size in nm, K is the Scherrer shape factor constant [385] (assumed to be approximately 0.9 for this work [386, 387]), λ is the beam wavelength (0.154 nm), β is the full width at half maximum (FWHM, rad) and θ_r is the incident angle (rad).

$$D = \frac{K\lambda}{\beta \cos \theta_r}$$

Equation 3.2 - Debye-Scherrer Equation

3.3.2 Thermal Analysis

3.3.2.1 Thermogravimetric Analysis

The mass changes that are observed upon heating a sample can be used to determine thermal stability and provide insight into chemical nature. The percentage mass change indicates the quantity of each species that was originally present. Bond breakage is an endothermic process that requires thermal energy. Physisorption effects such as Van der Waals, dipole attraction and hydrogen bonding are typically weaker than chemisorption in which chemical bonds must be cleaved. The decomposition temperature therefore can indicate how strongly bound a given species was to the starting material and what type of bond may have been responsible. Solid materials often have physically adsorbed gases and water from the environment which become desorbed under mild heating. Presence of residual solvent and impurities can be vaporised under increased temperatures. At greater temperatures functional groups may then decompose into evolved gases.

Shown in Figure 3.9 is an example Thermogravimetric Analysis (TGA) and Derivative Thermogram (DTG) profile for 0.1M-TiFeSi catalyst. Derivative thermograms were calculated as the rate of change of wt% with increasing temperature to better identify thermal range of maximum mass change. All TGA and DTG measurements were performed on a Mettler Toledo TGA-DSC system and analysis was performed using STAR^e software [388]. Method parameters for solid sample analysis are included in Table 3.2.

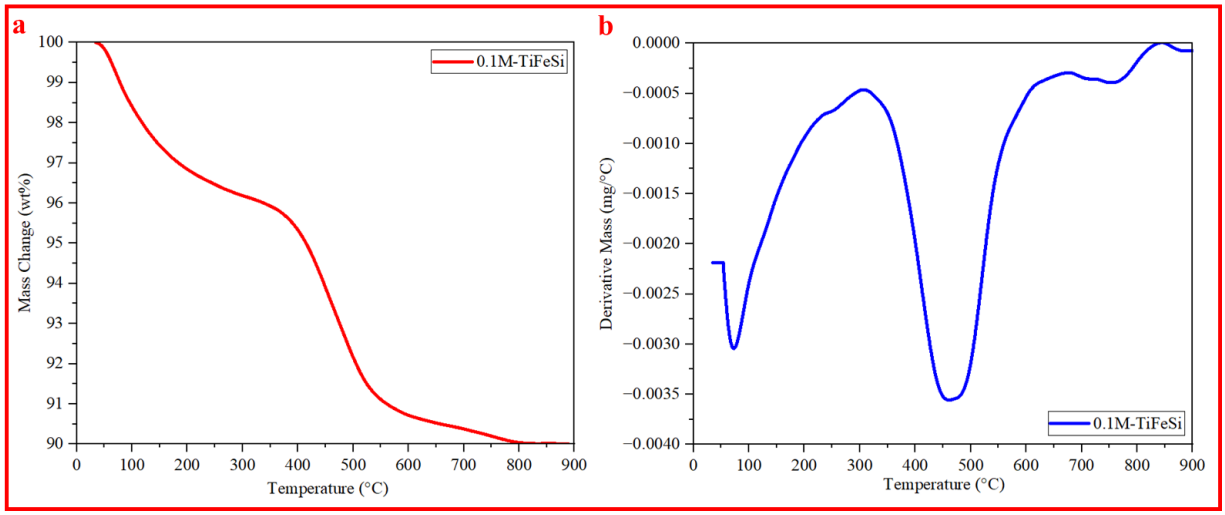

Figure 3.9 - Example TGA (a) and DTG (b) Plot for 0.1M-TiFeSi

Table 3.2 - Method Parameters for TGA, DTG and DSC Analysis of Nanocatalysts

Property	Value
Model	Mettler Toledo TGA-DSC
Temperature Range	30 - 900 °C
Ramp Rate	10 °C / min
Purge Gas	N_2
Purge Flowrate	50 mL / min

3.3.2.2 Differential Scanning Calorimetry

Typically evolved gases are analysed via combined techniques such as TGA with Infrared or Mass Spectroscopy (TGA-IR/TGA-MS) to determine the chemical species that were thermally decomposed. Unfortunately, such facilities were unable during this work so instead the species responsible for specific mass losses were identified based on degradation temperature and inspection of the Differential Scanning Calorimetry (DSC) curve. It was expected that exothermic heat flows would be principally due to recrystallisation effects as solid relaxes into a more energetically favourable structure. Trace solvent and impurity vaporisation would appear as endothermic heat flow at lower temperatures meanwhile phase changes would give a characteristic endothermic peak at very high temperatures. Acid site decomposition is endothermic in nature and would occur at intermediate temperatures within the analysis range, exhibiting a strong mass loss signal. Therefore, by comparing TGA/DTG data with endothermic peaks from DSC the mass losses resulting from acidic functional groups could be indirectly determined. Shown in Figure 3.10 below is the TGA-DSC equipment used and example DSC curve for 0.1M-TiFeSi.

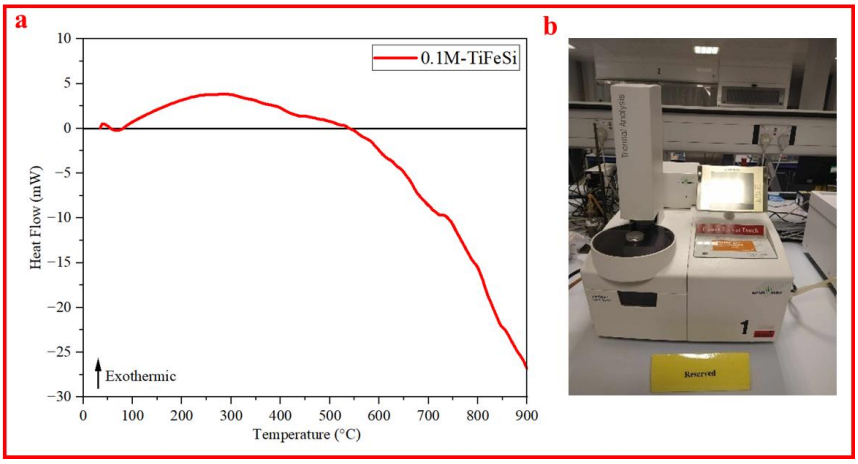

Figure 3.10 - Example DSC curve for 0.1M-TiFeSi (a) on Mettler Toledo TGA-DSC (b)

3.3.3 Infrared Spectroscopy

Infrared (IR) light was first discovered by Sir William Herschel in 1800 [389] and is a class of invisible electromagnetic radiation of wavelength between visible light and microwaves (780-1000 μm) [390]. Infrared is typically subdivided into near infrared (NIR, 0.78-3 μm), mid infrared (MIR, 3-50 μm) and far infrared (FIR, 50-1000 μm) regions and wavenumbers between 400-4000 cm^{-1} are most utilised for IR spectroscopy since this matches the vibrational frequency of chemical bonds [391]. The mechanism for how infrared radiation interacts with matter is shown in Figure 3.11 below. For a chemical bond to be IR active there must be a change in magnetic dipole moment during the vibration. If this is not the case, then other infrared based techniques such as Raman Scattering may be utilised instead that depend on changes in polarizability [392].

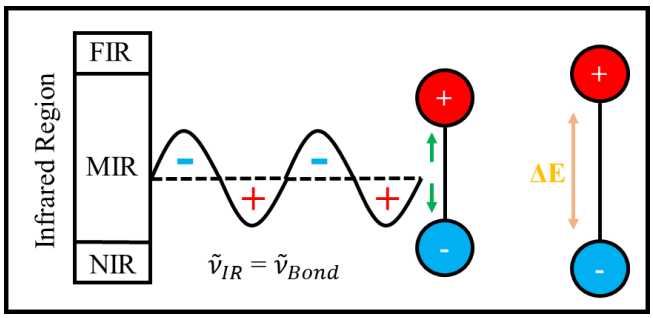

Figure 3.11 – Mechanism for IR being absorbed by a functional group

When infrared radiation of equal vibrational frequency encounters a chemical bond, the energy can be absorbed and increase the amplitude of the vibration. By measuring the specific wavenumbers absorbed the presence of various functional groups can be determined. Furthermore, through the Beer-Lambert Law given in Equation 3.3, the amount of absorbance A observed is proportional to concentration C (M) of a given species and can be calculated if molar absorption coefficient ε ($M^{-1}cm^{-1}$) and path length l (cm) are known.

$$A = \varepsilon c l$$

Equation 3.3 - Beer-Lambert Law

The region 400-1500cm^{-1} is denoted as the fingerprint region of an IR spectrum due to the complex and often overlapping peaks which makes individual functional group determination difficult but can be used to uniquely identify many chemical species. The region 1500-4000 cm^{-1} is known as the functional group region since peaks are more easily determinable, separated and less complex.

Initial dispersive IR spectrometer designs used in early 1900s by pioneers such as William Weber Coblentz [393] operated by varying narrow frequency bands of IR light and measuring the percentage absorbance or transmittance for each individual band. This process was laborious, time consuming and measurements suffered a low signal-to-noise ratio. Work by Cooley and Tukey in 1965 [394] developing rapidly solvable Fast Fourier Transform algorithms revolutionised how IR spectra could be collected. Figure 3.12 demonstrates how a typical Fourier Transform IR (FTIR) spectrometer operates. A Michelson interferometer is used to produce IR interference patterns and through adjusting the mirror position a plot of intensity against mirror position (cm) can be obtained. Conversion into inverse space (cm^{-1}) is then computed by performing a Discrete Fourier Transform operation which is included in Equation 3.4 below. Hence the absorbance or transmittance for each wavenumber of IR can be obtained all at once. The major advantage of FTIR is the speed of data collection and higher signal-to-noise ratio.

$$X(k) = \sum_{n=0}^{N-1} x(n) e^{\frac{-2\pi i}{N} kn} = \sum_{n=0}^{N-1} x(n) \left[\cos\left(\frac{-2\pi}{N} kn\right) - i \sin\left(\frac{-2\pi}{N} kn\right) \right]$$

Equation 3.4 - Discrete Fourier Transform

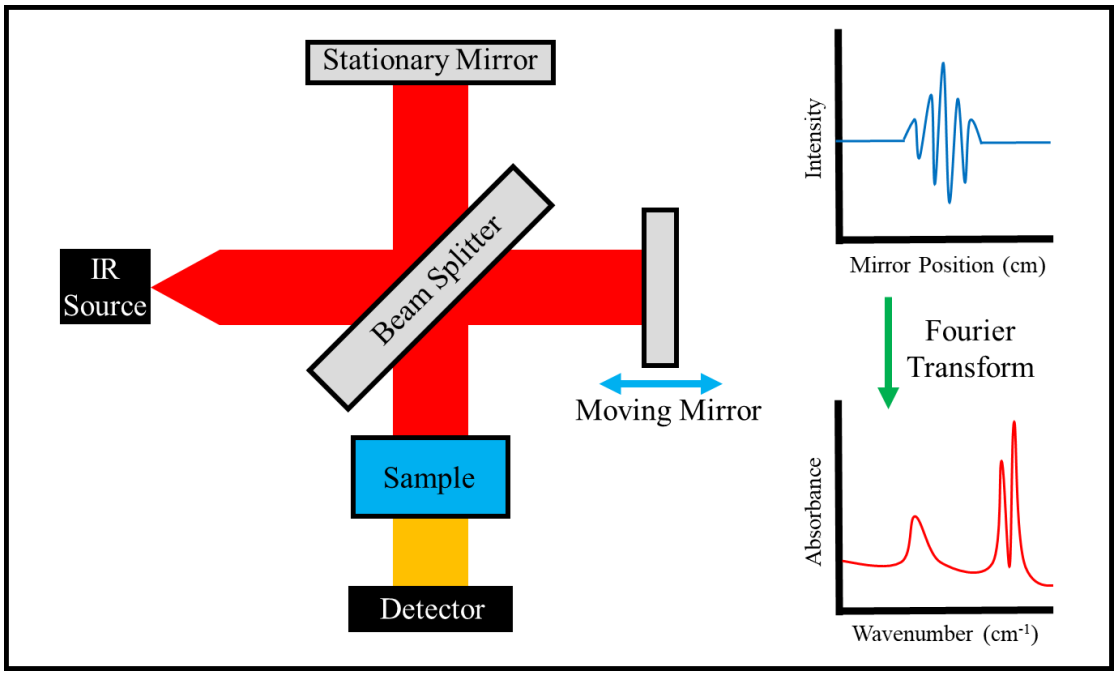

Figure 3.12 - Diagram Showing the Operation of FTIR Spectrometer

3.3.3.1 Attenuated Total Reflectance

There are different measuring approaches to performing FTIR depending on the type of sample in use as shown in Figure 3.13. In order to investigate chemical species present on the solid surface of support and catalyst material, Attenuated Total Reflectance (ATR) approach was utilised due to low penetration depth ensuring only the near surface was imaged. Method parameters used for ATR-FTIR analysis are included in Table 3.3 and an example ATR-FTIR spectrum of 0.1M-TiFeSi is displayed in Figure 3.14. Background corrections were performed in OMNIC and Origin.

Table 3.3 - Method parameters used for ATR-FTIR Spectroscopy

Property	Value
Model	Nicolet iS10
Crystal	Specac Zn-Se
Total Scans	64
Resolution	4 cm^{-1}
Scan Range	650 - 4000 cm^{-1}

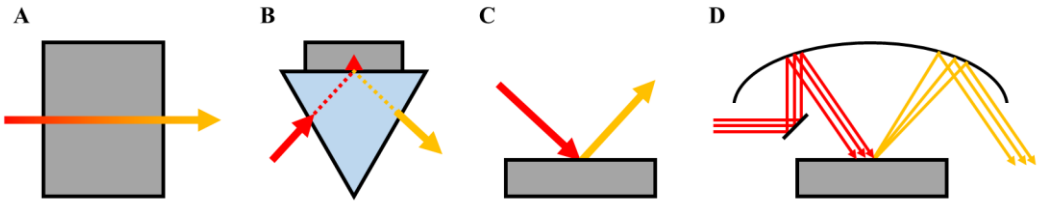

Figure 3.13 - Different types of FTIR apparatus: Transmission (A), ATR (B), Specular Reflectance (C) and Diffuse Reflectance (D)

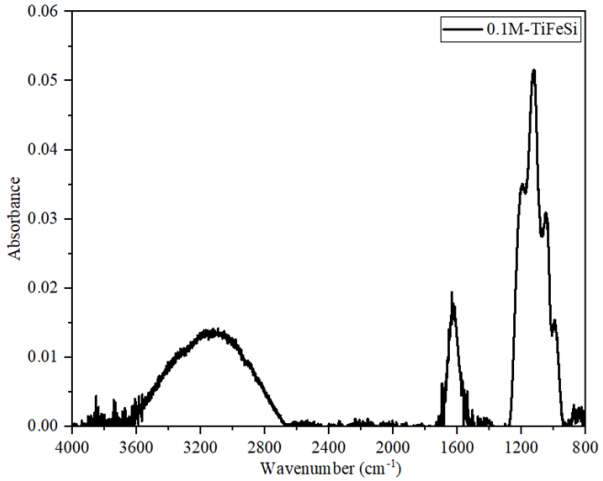

Figure 3.14 - Example ATR-FTIR Spectrum of 0.1M-TiFeSi

3.3.3.2 Pyridine Temperature Programmed Desorption

In order to confirm acidic site species are present on the surface, a basic probe molecule is often used that will chemically bond to surface sites. Some commonly used basic probe molecules include gaseous ammonia (pK_a of 9.25), pyridine (pK_a of 5.23), n-propylamine (pK_a of 10.71) and isopropylamine (pK_a of 10.63) [395-398]. The high basic strength of ammonia can lead to overestimation of weaker acidic sites [399], leading to pyridine being favoured for detecting medium and strong acid site activity. The temperature at which decomposition of probe molecule from acidic site occurs is dependent on the acidic strength, with common classifications in the literature [400] summarised in Table 3.4. Upon heating in a TGA apparatus, propylamines undergo thermal degradation similar to Hofmann Elimination to produce propene that can be detected via evolved gas analysis [401]. Alternatively, the concentration of pyridine remaining chemisorbed on a treated surface as temperature is varied can be detected via FTIR technique.

Table 3.4 - Desorption Temperature and Acid Site Strength

Temperature (°C)	Acid Strength
<150	Physisorbed Only
150-250	Weak
250-350	Medium
350-500	Strong
>500	Very Strong

Since evolved gas analysis TGA was unavailable, pyridine was instead used as probe molecule. ATR-FTIR was used to detect presence of pyridine on nanocatalyst surface post temperature programmed desorption (TPD) at 150 °C or 300 °C calcination temperature to determine the type and concentration of weak, medium and strong acidic sites. Displayed in Figure 3.15 is an illustration of how pyridine can be chemisorbed to both Brønsted acidic sites as well as Lewis acidic sites. Brønsted sites were attributed to surface hydroxyl groups, for which sulfate groups can enhance the acid strength, while Lewis sites were attributed to metal cation species. Since some degree of metal cation and metal hydroxide species was expected to be present in all samples, lack of detection of acidic sites at 150 °C heat treatment indicated that any Brønsted or Lewis sites present were chemically too weak to interact with the basicity of pyridine and would therefore be unlikely to contribute any catalytic activity towards biodiesel production.

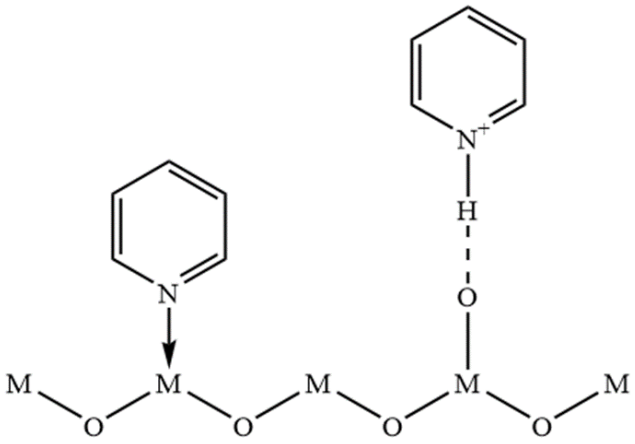

Figure 3.15 - Pyridine Bonding to Surface Acid Sites

Approximately 100mg of each solid sample was heated overnight at 200 °C under vacuum to remove physically adsorbed gases and weakly bound water before being submerged in excess pyridine (~1mL), ultrasonicated for 10 minutes and left on a stirring plate at 200 rpm and ambient temperature for 4 hours. Samples were then dried in muffle furnace at 120 °C for 4 hours to remove bulk liquid prior to calcination overnight at 150 °C or 350 °C to remove chemisorbed pyridine. Dried sample was analysed via ATR-FTIR by application of Beer-Lambert Law as discussed in Equation 3.3. Peaks at ~1540 cm^{-1} and ~1450 cm^{-1} were attributed to Brønsted and Lewis acid groups respectively [402], with molar absorption coefficients reported to be 0.078 cm/µmol and 0.165 cm/µmol from literature [403]. Effective pathlength of ATR ZnSe cell at measured peak centres was determined based on manufacturer recommendations [404]. Brønsted to Lewis (B:L) acid ratio at calcination temperature T was calculated as the ratio of peak heights as given in Equation 3.5 while the acid strength A was determined by Equation 3.6 where the ratio of a given acid site peak intensity at 350 °C calcination temperature was compared to 150 °C sample.

$$\left(\frac{B}{L}\right)_T = \left(\frac{I_B}{I_L}\right)_T$$

Equation 3.5 - Brønsted to Lewis Ratio

$$A = \frac{I_{350}}{I_{150}}$$

Equation 3.6 - Acid Strength by Pyridine Temperature Programmed Desorption

3.3.4 Nitrogen Porosimetry

Pore structure and surface area are both vitally important metrics for solid catalyst design. A high surface area and sufficiently large pore size improves reactant mass transfer to catalytically active sites and therefore enhances reactivity. Alternatively, pore size can be used to restrict non-desirable reaction pathways from occurring by sterically hindering the formation of unwanted products or access into catalytic regions. Pore structures can be closed holes, blind holes, cross-linked channels or through pores and common pore shape categories include cylinder, slit, cone and ink-bottle like morphologies [405, 406]. Pore size is defined by IUPAC to be either macroporous (>50 nm), mesoporous (2-50 nm) or microporous (<2 nm) [407, 408]. Common pore morphologies are illustrated in Figure 3.16.

In order to determine the porosity, pore size distribution and surface area of complex solid surfaces, an inert probe material such as Hg, N_2 or He can be utilised dependant on the specific material and size range of interest for study. He is typically preferred for highly microporous materials due to very small atomic diameter, while care must be taken with Hg intrusion methods due to toxicity and potential destruction of pore structure during testing [409, 410]. It is important to first degas a solid sample at elevated temperature prior to porosity analysis to remove bound gases and water vapour present in the environment and suitable degas conditions may be determined via TGA stability analysis. For N_2 porosimetry, a known quantity of solid material is loaded into a fixed volume cell and kept at constant temperature (boiling point of N_2 = 77 K), with liquid N_2 used to enhance detectability of adsorption effect. By measuring the relative cell pressure and volume of N_2 adsorbed and desorbed, an adsorption-desorption isotherm can be plotted. Various isotherm adsorption models have been developed such as early work by Langmuir in 1916 [411] and Freundlich in 1909. However, these models have issues such as only considering monolayer formation (Langmuir) or failure to predict maximum adsorption at high pressure (Freundlich) [412]. Updated isotherm models based on work by Brunauer, Emmett and Teller (BET model) in 1938 [413] have become a standard method for determining specific surface area. The BET model is given in Equation 3.7 where: P and P_0 are the equilibrium and saturation pressure, V and V_m are the adsorbed gas volumes for overall sample and monolayer and C is the BET constant. The value of C as shown in Equation 3.8 is proportional to the energy of adsorbent-surface interactions, where E_1 and E_L are the heats of adsorption in first layer and heat of vaporisation respectively ($Jmol^{-1}$) for gas constant R (8.314 $Jmol^{-1}K^{-1}$) and temperature T (K).

A linear plot of Equation 3.7 can be used to determine monolayer volume of gas adsorbed V_m and hence the BET specific surface area can be found via Equation 3.9, where w is the degassed sample weight (g), N_A is Avogadro's constant (6.022×10^{23} mol^{-1}), s is the adsorbate cross sectional area (assumed 0.162 nm^2 or 1.62×10^{-15} cm^2 for N_2) and M_V is the molar volume of adsorbate (taken as 22414 cm^3/mol for N_2).

$$\frac{P}{V(P_0 - P)} = \frac{1}{V_m C} + \left(\frac{C-1}{V_m C}\right)\frac{P}{P_0}$$

Equation 3.7 - BET Model

$$C = e^{\frac{E_1 - E_L}{RT}}$$

Equation 3.8 - BET Constant

$$S_{BET} = \frac{S_{Tot}}{w} = \frac{1}{w}\left(\frac{V_m N_A s}{M_V}\right)$$

Equation 3.9 - BET Specific Surface Area

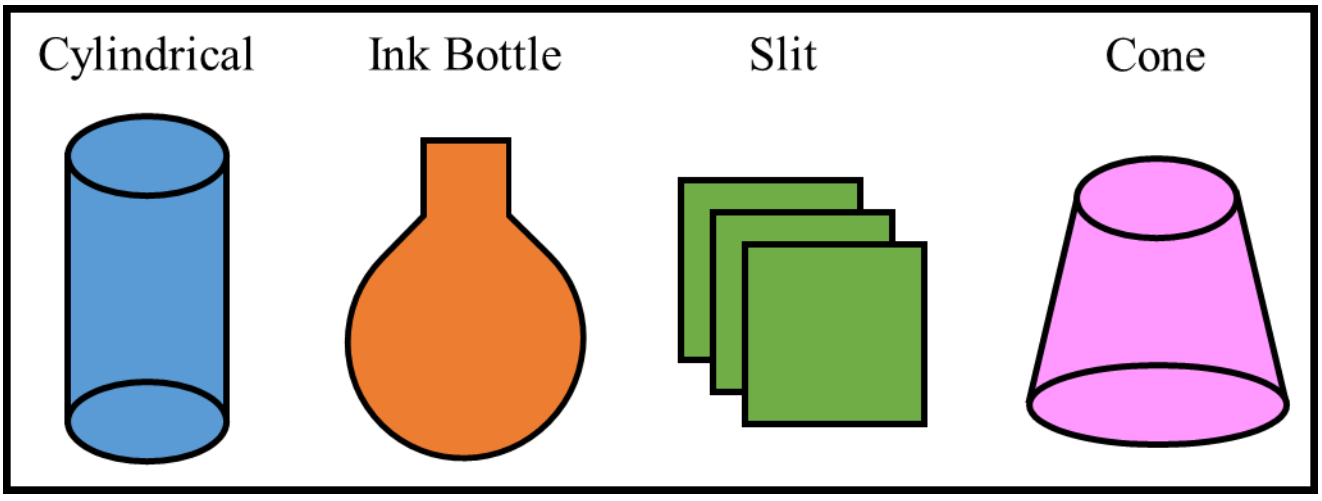

Figure 3.16 - Common Pore Morphologies

A wide range of isotherm shapes has been observed that IUPAC have categorised [414] as shown in Figure 3.17. Type I isotherms are reversible and indicate narrow I(a) or broad I(b) microporous materials. Type II reversible isotherms are observed in nonporous or highly macroporous materials with detectable monolayer formation, whereas Type III display no notable monolayer. Type IV isotherms indicate mesoporous materials with hysteresis behaviour IV(a) indicating pores are above critical size facilitating capillary condensation, below this critical size reversible adsorption-desorption occurs IV(b). Type V isotherms are similar to Type III and are observed in hydrophobic meso/microporous systems. Type VI isotherms are characteristic of multi-layered uniform nonporous surfaces, with each adsorbed layer capacity adding a step height increase to the isotherm. The hysteresis loop indicates the type of pore morphology observed: cylindrical (H1), ink-bottle with varying neck width (H2a/b), plates (H3), slits (H4) or combinations of open and partially blocked pore structures (H5).

While the BET method is a straightforward approach to determining specific surface area, there are several limitations to the model [415, 416]. Firstly, the underlying assumptions of the model are problematic and potentially unrealistic [417, 418]. Assuming that gas adsorption occurs on a uniform surface, no interactions occur between each adsorbed layer and a theoretically infinite number of such layers can be constructed has been questioned. Inability to accurately model highly porous materials or samples with significant microporosity can also lead to large margins of error in calculated surface area. Care must therefore be taken to report specific surface area as S_{BET} as it may differ from other techniques such as NMR spin relaxation or geometric analysis.

In an attempt to address these shortcomings, the linear range of relative pressure is recommended to be taken between 0.05 - 0.3 since values that are too low will only feature monolayer adsorption and too high values initiate capillary condensation effects and notable hysteresis can occur [419]. Checking for linear behaviour alone within this region has been found as insufficient for reliable BET modelling and recommendations by Rouquerol et al. [417] include rejecting upper values of P/P_0 that are beyond the maximum value in a plot of $V(P_0-P)$ against P/P_0 and then confirming that the calculated value of C remains non-negative. These adjustments help to adjust the BET model to a wide range of isotherm behaviours beyond just Type II isotherms. BET analysis was performed on Anton Paar NOVA 800 and method parameters are included in Table 3.5. Figure 3.18 shows the degassing and analysis chamber, including liquid N_2 dewar and glass test cells.

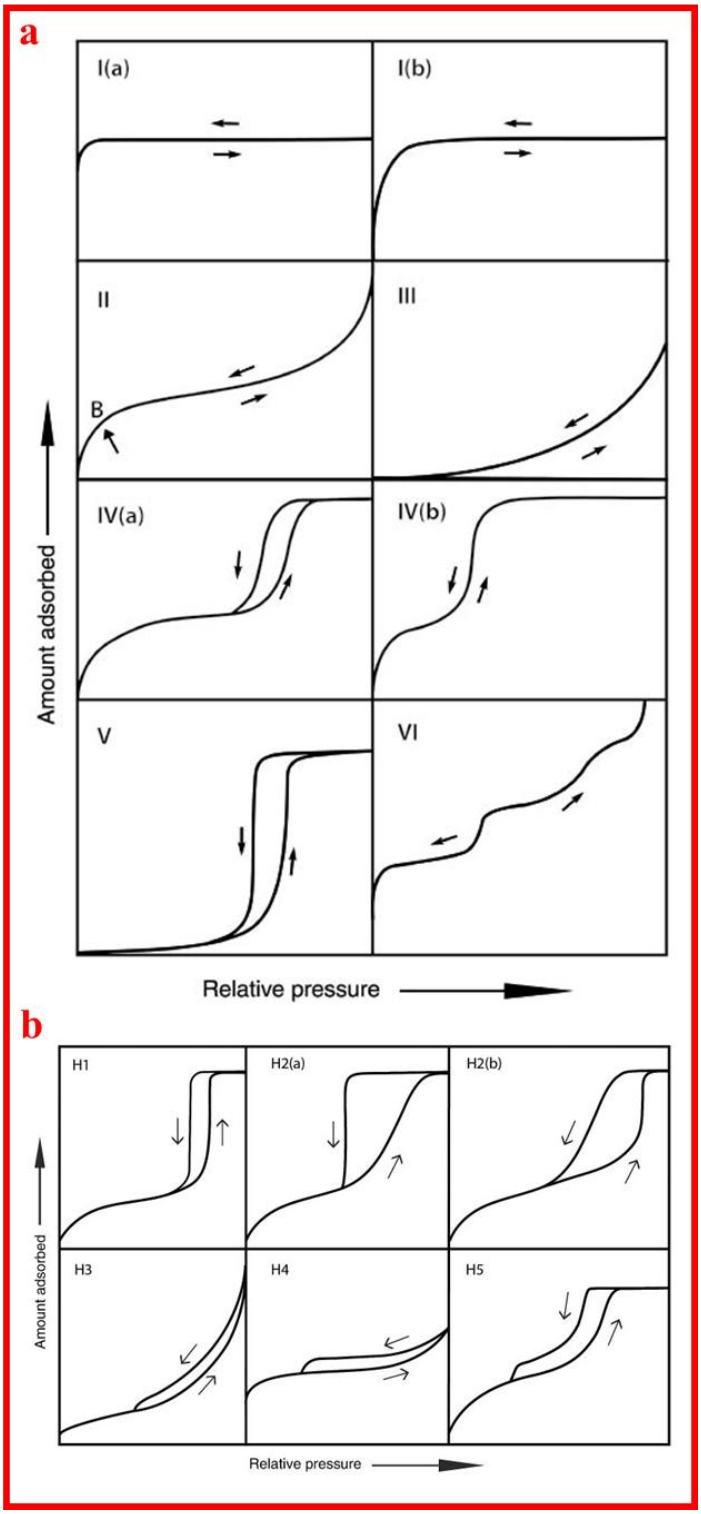

Figure 3.17 - Isotherms (a) and Hysteresis Loop (b) Classifications

Reproduced with Permission © 2015 IUPAC and De Gruyter [414]

Table 3.5 - Method parameters for N_2 Porosimetry

Property	Value
Model	Anton Paar NOVA 800
Analysis Software	Kaomi for Nova
Degas Ramp 1	20 °C to 80 °C at 5 °C/min
Degas Hold Time 1	30 min
Degas Ramp 2	80 °C to 200 °C at 5 °C/min
Degas Hold Time 2	960 min
Degas Ramp 3	200 °C to 20 °C at 30 °C/min
Degas Type	Vacuum Degas
Cell Type	6mm with Filler Rod
Void Measurement	He
Adsorbate Gas	N_2 (28.0134 g/mol, 16.2 $Å^2$/molecule)
Bath Temperature	77.35 K
Relative Pressure Range	0.025 - 0.988

Figure 3.18 - Nova 800 Degas Chamber (a) and Analysis Chamber (b)

Since presence of microporosity can lead to large errors, the quantity of microporosity was evaluated via t-plot method, in which the statistical thickness of condensed adsorbed gas is computed as a function of relative pressure and compared to a reference plot of nonporous material with similar chemistry. The presence of curvature indicates microporosity and via subtracting the determined t-plot surface area from S_{BET} an estimate of micropore surface area and hence degree of microporosity can be obtained. Various models to compute the t-plot surface area have been developed depending on the type of material under investigation, including work by de Boer, Harkins-Jura and Halsey [420]. This work utilised a method first proposed by Harkins and Jura [421, 422] and was calculated via Anton Paar Kaomi for Nova software. The de Boer linear model [423] is given in Equation 3.10 and relates adsorbed volume V to micropore volume V_m for known relative pressure ratios. A negative value of intercept, or intercept at origin, indicates no microporosity. A positive intercept indicates the presence of microporosity, and the gradient can be used to determine micropore surface area S_e for a known film thickness t and fitting constant k determined by models such as Harkins and Jura (Equation 3.11) or Halsey (Equation 3.12) [424, 425]. For this work Harkins and Jura was selected since superior fit was observed in all samples.

$$V\left(\frac{P}{P_0}\right) = V_m + kS_e t\left(\frac{P}{P_0}\right)$$

Equation 3.10 - de Boer Linearised Model

$$t = \left(\frac{13.99}{0.34 - \log_{10}\left(\frac{P}{P_0}\right)}\right)^{\frac{1}{2}}$$

Equation 3.11 - Harkins and Jura Thickness Model

$$t = 3.54\left(\frac{-5}{\ln\left(\frac{P}{P_0}\right)}\right)^{\frac{1}{3}}$$

Equation 3.12 - Halsey Thickness Model

Pore size distribution within the mesoporous range can be calculated based on a method first proposed by Barrett-Joyner-Halenda [422] and now referred to as the BJH method. The method is valid under the assumption of cylindrical pores of sizes >2 nm, with other methods such as Dubinin-Radushkevich (DR) [426], Horvath-Kawazoe (HK) [427], Cheng-Yang (CY) [428] and Saito-Foley (SF) methods [429] more applicable to micropores of varying geometries. Since all synthesised materials in this work were identified by BET to be mesoporous, application of BJH was used and significant deviations from BET results investigated via t-plot analysis as discussed prior. Capillary condensation that occurs within mesopores as seen through hysteresis loop can be modelled through the Kelvin Equation [423, 424] as provided in Equation 3.13 where pore radius r is a function of thickness t at each value of relative pressure measurement. For N_2 values of surface tension γ and liquid molar volume V_L were taken as 8.88×10^{-3} N/m and 34.68 cm^3/mol at ~77 K temperature and molar gas constant R as 8.314 J/mol·K respectively. Harkins and Jura thickness model was again used to produce pore size estimates at all measured P/P_0 values. Calculation of the BJH method was performed using Kaomi for Nova software and plots of dV(r) and dS(r) on desorption branch obtained alongside cumulative values of pore volume V and total surface area S denoted as S_{BJH} to distinguish from S_{BET} result. Deviation in surface area results between BET and BJH method may be expected for highly non-cylindrical pore shapes leading to overestimation or microporosity leading to underestimation [430, 431]. For very small mesopores between 2-5 nm up to 20% error may be expected [432] and so significantly lower S_{BJH} values were interpreted as pores being close to meso-microporous boundary. Much larger values were interpreted as large deviation from cylindrical shape. Average pore diameter d was calculated using Equation 3.14 from BJH results assuming a cylinder shape.

$$r\left(\frac{P}{P_0}\right) = \frac{2\gamma V_L}{RT \ln\left(\frac{P}{P_0}\right)} + t\left(\frac{P}{P_0}\right)$$

Equation 3.13 - Kelvin Equation

$$\bar{d} = \frac{4V_{BJH}}{S_{BJH}}$$

Equation 3.14 - Average Pore Diameter from BJH Method

3.3.5 Electron Microscopy

Although the original inventor of the optical microscope remains disputed [433], the field of optical microscopy can be dated back to the end of the 16th century with pioneering work by Hans and Zacharias Janssen [434]. Later work produced by Galileo Galilei in 1609 led to the first recorded use of the term "microscope" by Giovanni Faber in 1625 [435]. Due to optical distortion and resolution loss via diffraction it is not possible to resolve objects smaller than around half the wavelength of incident light [436]. This is illustrated by the Abbe limit [437, 438] in Equation 3.15, where a microscope using light wavelength λ has a minimum resolvable distance d dependant on the numerical aperture NA dependant on sample refractive index n and lens half angle θ.

$$d = \frac{\lambda}{2NA} = \frac{\lambda}{2n\sin\theta} \approx \frac{\lambda}{2}$$

Equation 3.15 - Abbe Limit

For visible light (λ = 380-700 nm) this makes objects below ~200 nm challenging to resolve and presents a major issue for observing nanomaterials. One potential solution is to utilise ultraviolet (UV) or X-ray photons of shorter wavelengths. Alternatively, high speed electrons can be used to explore nanoscale structures. The idea that objects of matter can display wave-particle duality was first discussed by Louis de Broglie in 1924 [439] and experimentally confirmed from electron diffraction studies on Ni metal by Clinton Davisson and Lester H. Germer in 1927 [440]. Later work by Hans Busch [441] discovered that electron waves can be directed via electromagnetic fields similar to optical microscopes, leading to the first constructed electron microscope in 1932 by Knoll and Ruska [442]. The de Broglie wavelength condition is displayed in Equation below, where an electron of momentum p will have wavelength λ. Substituting momentum with electron rest mass m_0 (9.109×10^{-31} kg) and determining velocity via conservation of electrical potential into kinetic energy, the effect of microscope acceleration voltage V on electron wavelength is seen to be inversely proportional. In this equation, h is Planck Constant (6.626×10^{-34} Js), e is electron charge (1.602×10^{-19} C) and c is speed of light (299792458 ms^{-1}). For high accelerating voltage electron microscopes, relativistic effects become especially important to consider.

$$\lambda = \frac{h}{p} = \frac{h}{\sqrt{2m_0eV\left(1+\frac{eV}{2m_0c^2}\right)}} \approx \frac{h}{\sqrt{2m_0eV}} \; at\ low\ accelerating\ voltages$$

Equation 3.16 - de Broglie Wavelength and Effect of Acceleration Voltage

3.3.5.1 Scanning Electron Microscopy

A simplified diagram of a Scanning Electron Microscope (SEM) is shown in Figure 3.19a. Electrons are accelerated by the positively charged anode to a set acceleration voltage to achieve an electron beam of desired wavelength. Electromagnet condenser lenses converge the beam prior to further convergence by objective lenses before electrons encounter the sample housed on a stage. Scanning coils modulate the electron beam to scan across the sample surface analogous to raster scanning in cathode ray televisions. Both electron gun and analysis chamber are housed under high vacuum during analysis to prevent interference or contamination to the electron beam. The imaging signal can be created from both elastically backscattered electrons as well as secondary inelastic scattered electrons. Secondary inelastic electrons are typically preferred for high resolution surface imaging since their emission is limited to atoms close to sample surface, while elastic backscattered electrons can be produced from atoms deeper within the sample [443].

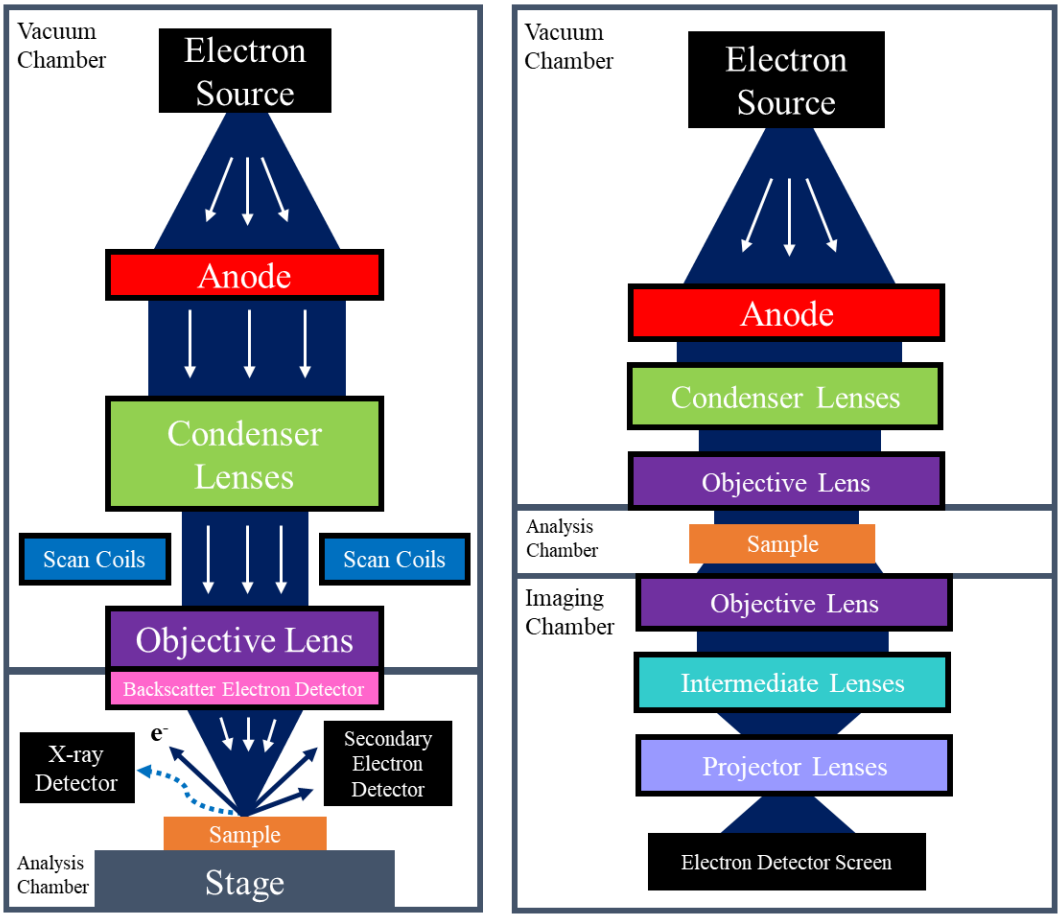

Figure 3.19 - Simplified Diagrams of SEM (a) and TEM (b) Imaging

SEM imaging was performed using a Hitachi SU8230 FESEM setup and experiment parameters are included in Table 3.6. Acceleration voltage was kept relatively low at 2 kV to improve sensitivity to surface morphologies from inelastic scattering [444]. Catalyst samples were prepared by using anti-static gun to reduce surface charge prior to loading small quantities of mass onto double sided adhesive tape. Large aggregates were removed with dry compressed air. A Safematic CCU-010 sputter coater as shown in Figure 3.20a was then used to deposit a thin carbon layer onto surface to minimise surface charge buildup during analysis. After coating, the prepared tape was affixed to an aluminium sample stud and transferred into SEM analysis chamber. Entire chamber was then steadily evacuated to high vacuum and liquid nitrogen circulated to maintain a cold field effect cathode before imaging. Initial images were taken at 1 k magnification and zoom was gradually increased until maximum magnification of 100 k, with working distance manually adjusted for each step. Example SEM images of 0.1M-TiFeSi are shown in Figure 3.20b, c.

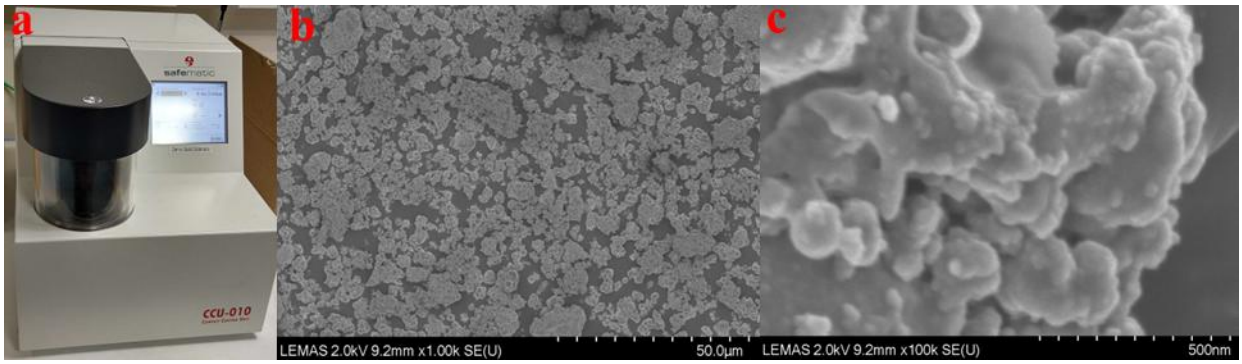

Figure 3.20 - Sputter Coater (a), 0.1M-TiFeSi at 1k and 100k Magnification (b, c)

Table 3.6 - Experiment Parameters for SEM Imaging

Property	Value
Microscope Model	Hitachi SU8230 FESEM
Coating Material	Carbon
Sputter Coater	Safematic CCU-010
Acceleration Voltage	2 kV (λ = 27.4 pm)
Working Distance	4415.83 µm - 9177.08 µm
Zoom Level	1 k - 100 k
Emission Current	15200 nA
Image Resolution	1280x960

3.3.5.2 Transmission Electron Microscopy

Unlike a Scanning Electron Microscope that can analyse samples of any thickness by using scattering to build images of surface morphology; a Transmission Electron Microscope (TEM) requires sample to be very thin to ensure electrons are able to pass through. The main difference between the previously discussed SEM setup and TEM apparatus is illustrated in Figure 3.19. Electrons are accelerated to a significantly higher acceleration voltage in a TEM apparatus to ensure successful transmission through the sample. Intermediate and Projector lenses are then used to focus a high-resolution signal onto the detector screen. As a consequence of the higher acceleration voltage required, electron wavelength can be substantially reduced allowing for even greater image resolution at single nanometre scale. Additionally, because electrons pass directly through the sample, information on internal structure can be obtained from the detected electrons.

3.3.5.3 Scanning Transmission Electron Microscopy

A scanning Transmission Electron Microscope combines the features of both SEM and TEM to reveal both surface and internal properties of the sample. The major difference between TEM and STEM setup is demonstrated below in Figure 3.21.

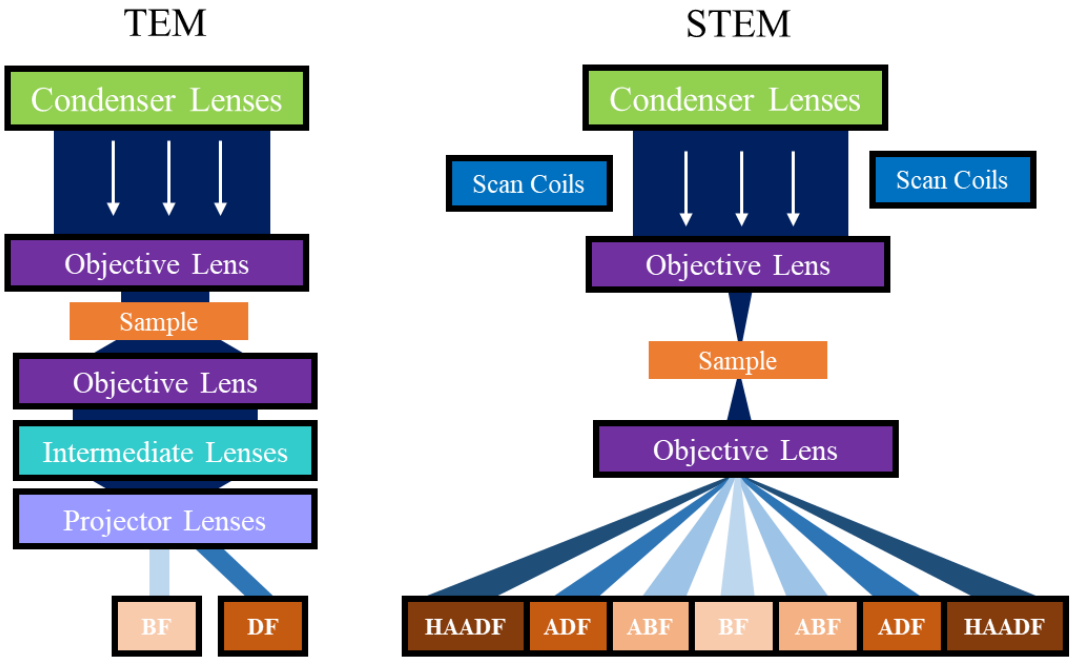

Figure 3.21 – Simplified Diagram of TEM and STEM Imaging Differences

Unlike TEM where broad parallel electron beams are directed through the sample, in STEM imaging electrons converge into a narrow spot that can be scanned over the sample via scanning coils whilst still transmitting through the thin sample. Depending on the size of atom the electron encounters when traversing through the sample, the degree of scattering will vary. Corelating the scattering angle to atomic number Z is a technique known as Z-contrast [445]. Brightfield (BF) and Annular Brightfield (ABF) detectors detect electrons with low scattering angles produced from light atomic elements, whereas Annular Darkfield (ADF) and High Angular Annular Darkfield (HAADF) detectors measure electrons that interacted with heavier atomic elements leading to higher scattering angles. An example STEM image is shown below in Figure 3.22 using both Brightfield and Annular Darkfield detectors.

STEM imaging was performed using a Tescan Tensor system under operating conditions given in Table 3.7. Approximately 1mg of sample to be analysed was dispersed into methanol via ultrasonication for 5 minutes before being drop casted onto a copper-carbon film grid (agar scientific). The grid provided a support for thin nanocatalyst with holes to facilitate electrons to pass through more easily. Images of sample preparation and STEM setup are shown in Figure 3.23.

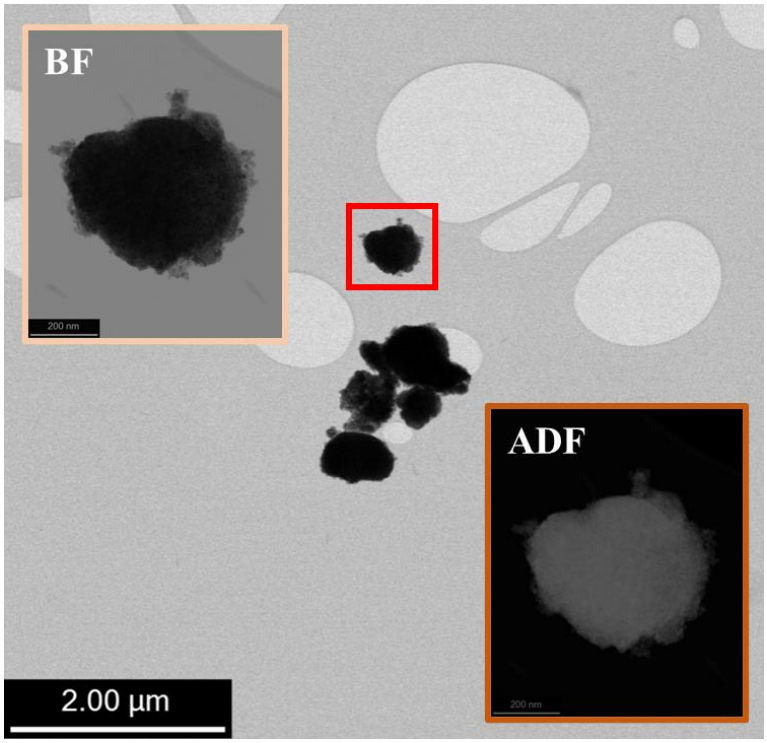

Figure 3.22 - STEM Image of 0.1M-TiFeSi via BF and ADF

Table 3.7 - Experiment Parameters for STEM Imaging

Property	Value
Microscope Model	Tescan Tensor
Grid Material	Cu-C (AGS147-4)
Manufacturer	Agar scientific
Acceleration Voltage	100 kV (λ = 3.7 pm)
Probe Current	100 pA
Scanning Probe Size	0.4 nm
Pixel Dwell Time	10 µs

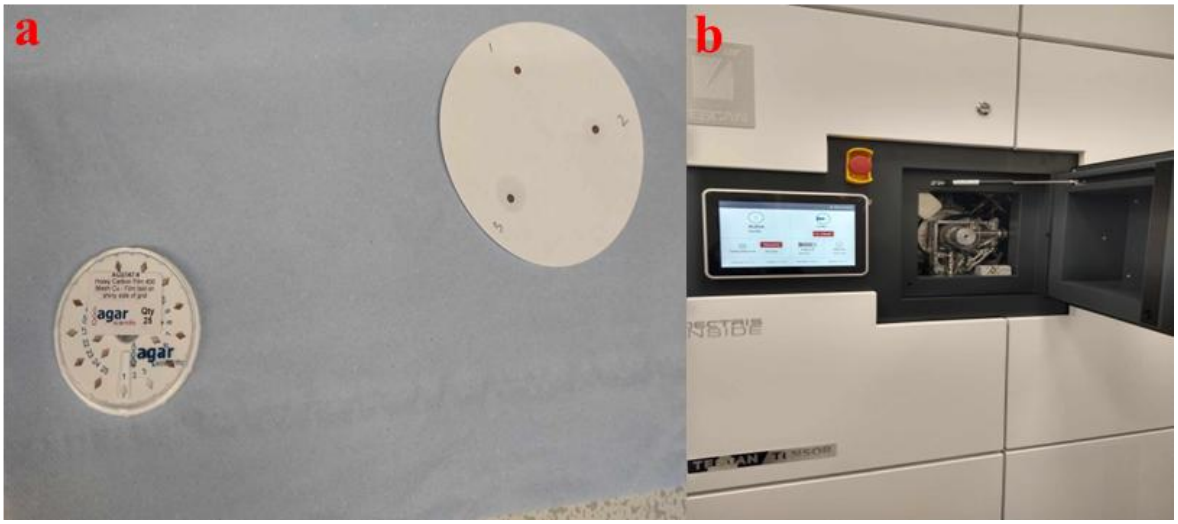

Figure 3.23 - Sample Preparation (a) and Tescan Tensor STEM System (b)

3.3.5.4 Selected Area Electron Diffraction

As previously illustrated in Equation 3.16 electrons can display wavelike properties which includes the ability to produce diffraction patterns. Unlike diffraction patterns produced by x-rays, discussed earlier in Chapter 3.3.1, electron diffraction from a microscope can be directed to a highly specific region of sample instead of bulk sample analysis. Shown in Figure 3.24 is a schematic diagram of an electron diffraction pattern. Due to the 2D nature of STEM imaging, a grid of bright spots representing maximum constructive interference can often be observed. These 2D patterns are a rotationally symmetrical analogue to 1D line spectra as illustrated. Figure 3.24 also demonstrates the different types of Selected Area Electron Diffraction (SAED) patterns that may be observed, taken for the TiFeSi series of catalysts in this example. Pattern A corresponds to a diffuse halo characteristic of amorphous materials, pattern B is a typical result for single crystal diffraction and pattern C indicates polycrystallinity as many individual crystal diffraction patterns overlap to form rotationally symmetric rings. SAED patterns were obtained via Tescan Tensor STEM system whilst performing morphological analysis using identical analysis conditions in Table 3.7, and analysed using ImageJ software for comparison to bulk XRD analysis.

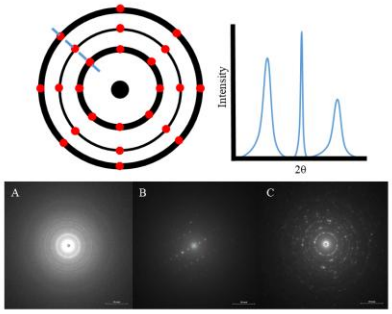

Figure 3.24 - Schematic Diagram of SAED Patterns and Obtained Results for TiFeSi Series

Obtained SAED patterns were used to determine the nature of crystallinity present in tested samples. By measuring each diffraction ring radius in ImageJ, small angle Bragg Law as given in Equation 3.17 was used to convert total scattering angle Θ (rad) as given in SAED pattern scalebar into d-spacings (nm) for known beam wavelength (λ = 3.7 pm at 100 kV). Values of d were compared with XRD method from Chapter 3.3.1 to confirm agreement of identified crystal phases.

$$d \approx \frac{\lambda}{\Theta}$$

Equation 3.17 – Small Angle Bragg Law for SAED Pattern Ring Spacings

3.3.6 X-ray Spectroscopy

Work first pioneered by Charles G. Barkla and C.A. Sadler in 1909 [446] demonstrated that upon bombarding matter with electrons, characteristic X-rays could be observed. This discovery led to Barkla being awarded the Nobel Prize in 1917 "for his discovery of the characteristic Röntgen radiation of the elements" [447]. Later work by Henry Moseley in 1913-1914 [448] determined that the square root of x-ray frequency ν is approximately equal to the atomic number Z as illustrated in Equation 3.18 for given fitting constants a and b for spectral line of interest.

$$\sqrt{\upsilon} = \ a\,(Z - b)$$

Equation 3.18 - Moseley's Law of Characteristic X-ray Emission

The cause for these x-rays to be emitted is illustrated below in Figure 3.25. When high energy electrons such as those from SEM or TEM microscopes collide with atoms, a core hole can be produced from the emission of the previously bound atomic electron. Electrons from higher energy levels can then transition down to fill in this lower energy level gap after releasing excess energy. Energy release is hence observed as a photon of characteristic X-ray frequency. Alternatively, this energy can also be released via emission of another electron from an even higher orbital, denoted as the Auger Effect as discovered by Pierre Auger and Lise Meitner in the early 1920s [449]. Such electrons are known as Auger electrons and their detection can be utilised in Auger Electron Spectroscopy (AES) to determine elemental composition similar to X-ray techniques.

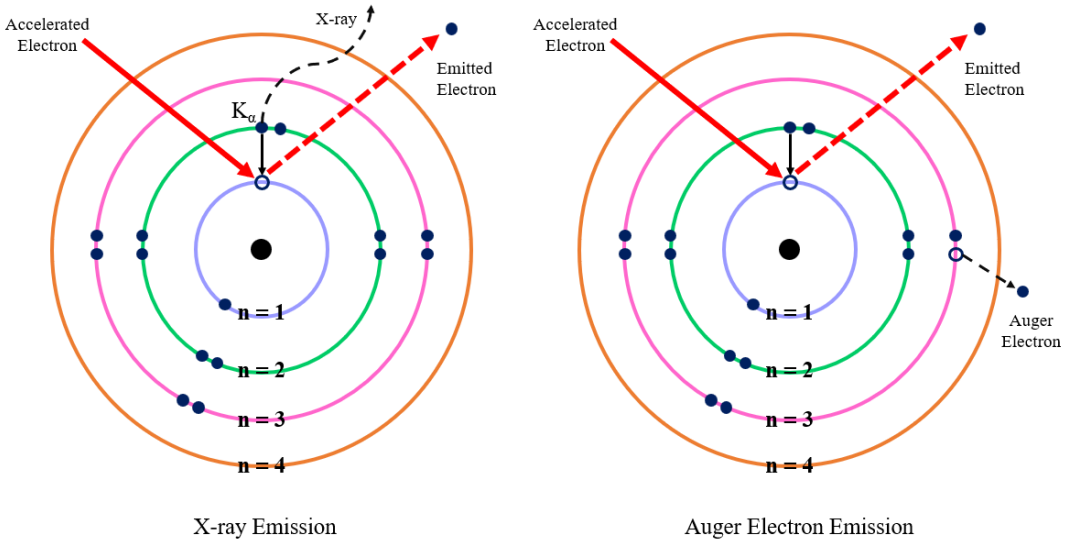

Figure 3.25 – Atomic Energy Transitions due to Accelerated Electron Beam

Characteristic x-ray emission lines are typically denoted in older literature by Siegbahn notation. Figure 3.26 shows the Bohr atomic model with some of the major spectral line groups. K series transitions result from electrons filling core holes produced in the K (n = 1) shell, whereas L series transitions result from filling holes in the L (n = 2) shell. Work by Ivar Malmer and Manne Siegbahn in 1916 [450] indicated that these transitions can be further split into subshell energy levels. This subshell splitting is called spin-orbit coupling and can be expressed as total angular momentum quantum number j being the sum of angular momentum quantum number l and spin angular momentum number s such that j = l + s. Figure 3.26 also depicts an energy level diagram for the K series of characteristic x-rays illustrating some of these energy transitions, for example K_α transition from L to K shell can occur via $2p_{3/2}$ or $2p_{1/2}$ subshells.

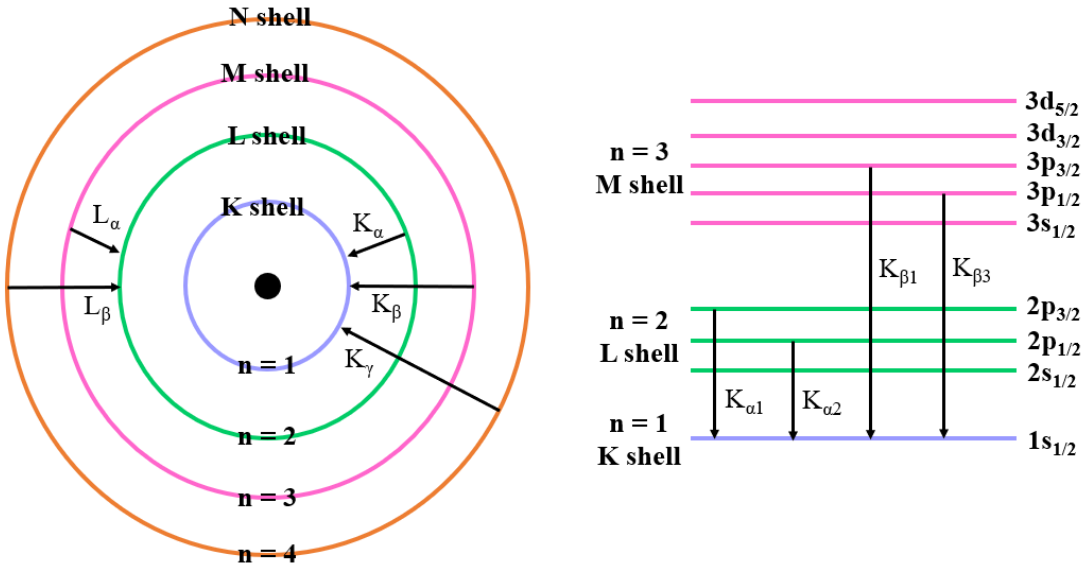

Figure 3.26 - Diagram of Select Characteristic X-ray Emission Lines

The technique of using accelerated electrons to produce characteristic x-rays for determination of elemental composition is denoted Energy Dispersive X-ray Spectrometry (EDX/EDS) and is discussed further in Chapter 3.3.6.1. It should not be surprising to note that this process can also occur in reverse, i.e. high energy X-rays can instead be used to produce electrons and secondary X-rays of characteristic energy for elemental determination. Examples of two such techniques are X-ray Fluorescence Spectroscopy (XRF) and X-ray Photoelectron Spectroscopy (XPS) and are the focus of Chapter 3.3.6.2.

3.3.6.1 Energy Dispersive X-ray Spectroscopy

As discussed earlier, EDX analysis is the process of using high energy accelerated electrons to produce characteristic x-rays. Key X-ray regions of interest are included in Table 3.8, with Kα emission peaks used to construct both 2D elemental maps and averaged area spectral plots. EDX results were collected as part of SEM/STEM analysis as previously discussed in Chapter 3.3.5. X-rays were detected using 80mm X-Max SDD detectors and processing was performed using Oxford Instruments Aztec Software. Unexpected elements were filtered out to avoid misidentification due to peak overlap. An example EDX result of TiFeSi support analysed via SEM is included in Figure 3.27.

Table 3.8 - Peak Regions of Interest for EDX Analysis

Element	X-ray Energy (keV)
C	Kα 0.277
O	Kα 0.525
Si	Kα 1.739
S	Kα 2.307
Ti	Kα 4.508, Lα 0.452
Fe	Kα 6.398, Lα 0.705
Zn	Kα 8.630, Lα 1.012

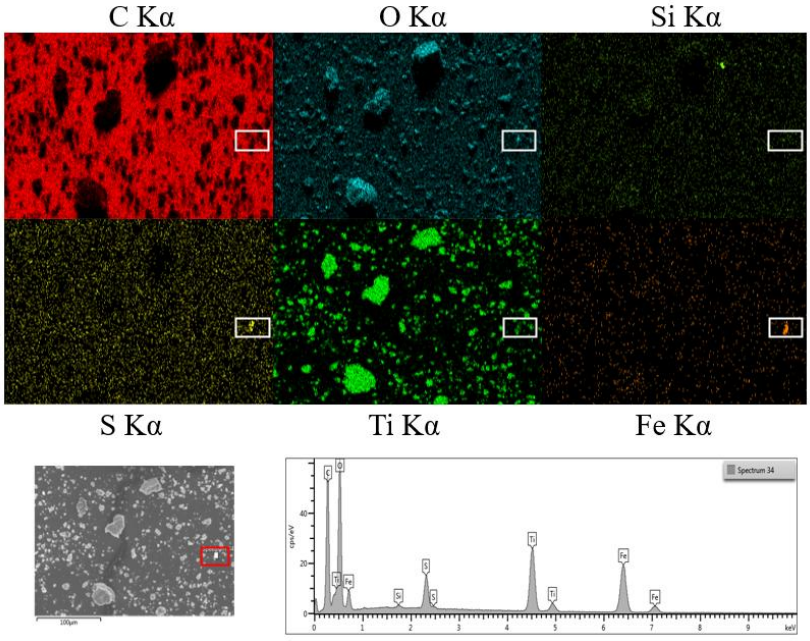

Figure 3.27 - Example EDX 2D element map and spectrum plot of TiFeSi Support (SEM)

3.3.6.2 X-ray Photoelectron Spectroscopy

Instead of using accelerated electrons to produce characteristic X-rays, a high energy X-ray source can be used to produce electron and secondary X-ray emission at characteristic energies. Two common techniques often reported in literature include X-ray Fluorescence Spectroscopy and X-ray Photoelectron Spectroscopy. The major difference between these techniques is illustrated in Figure 3.28. Upon irradiation of high energy X-rays of frequency ν, electrons gain energy equal to hν where h is the Planck Constant (6.626x10-34 Js). If this energy is released as secondary X-rays, element detections can be made throughout the entire sample and therefore XRF is a bulk analysis method. If the energy is instead released as an electron, either via Photoelectric effect (discussed below) or Auger effect, only those electrons released close to the sample surface will be able to reach the detector. Emitted electrons deeper than a few nanometres will lose energy via inelastic scattering with adjacent atoms and hence become undetectable. Therefore, XPS and AES are highly surface sensitive techniques. In this work, XPS results have been used to compare with EDX data to highlight the difference between surface and bulk elemental composition.

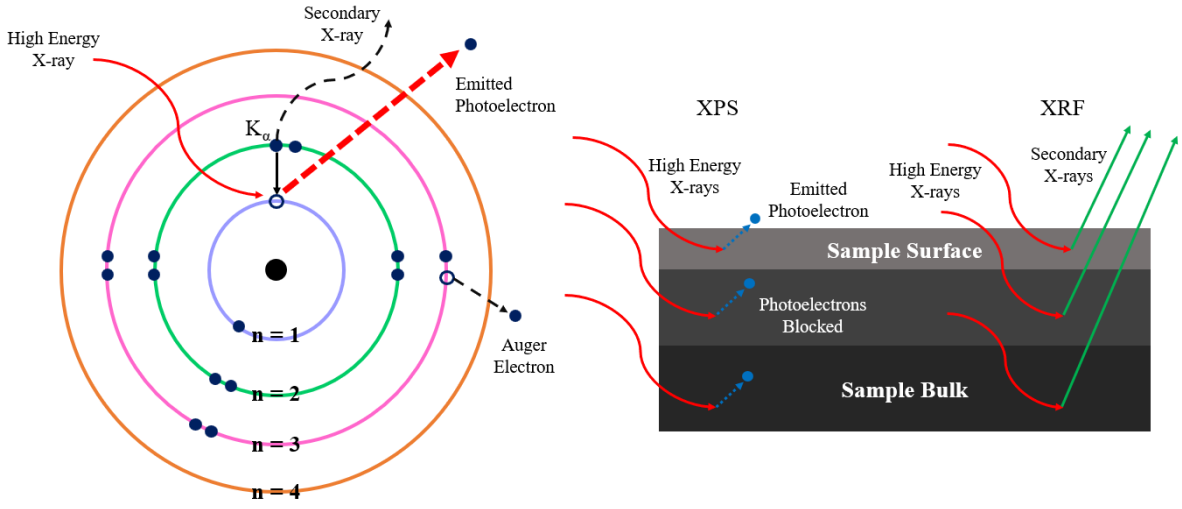

Figure 3.28 - Comparison of XPS and XRF Analysis Techniques

The photoelectric effect was first observed in 1887 by Heinrich Rudolf Hertz [451] noting that UV light affected the voltage required to produce electrical sparks. Later work by Philipp Lenard in 1902 [452] demonstrated that negatively charged particles (electrons) were emitted when a metal is illuminated with UV and that electron energy was independent of intensity, conflicting with the wave model of light. In 1905 as part of Albert Einstein's "Annus Mirabilis" [453], a breakthrough paper was published on the photoelectric effect suggesting that photoelectron emission occurred only above a specific threshold frequency due to quantisation, where quantised packets (photons) interacted with electrons in one-on-one particle like interactions. The Law of Photoelectric Effect won Einstein the Nobel prize in 1921 [454].

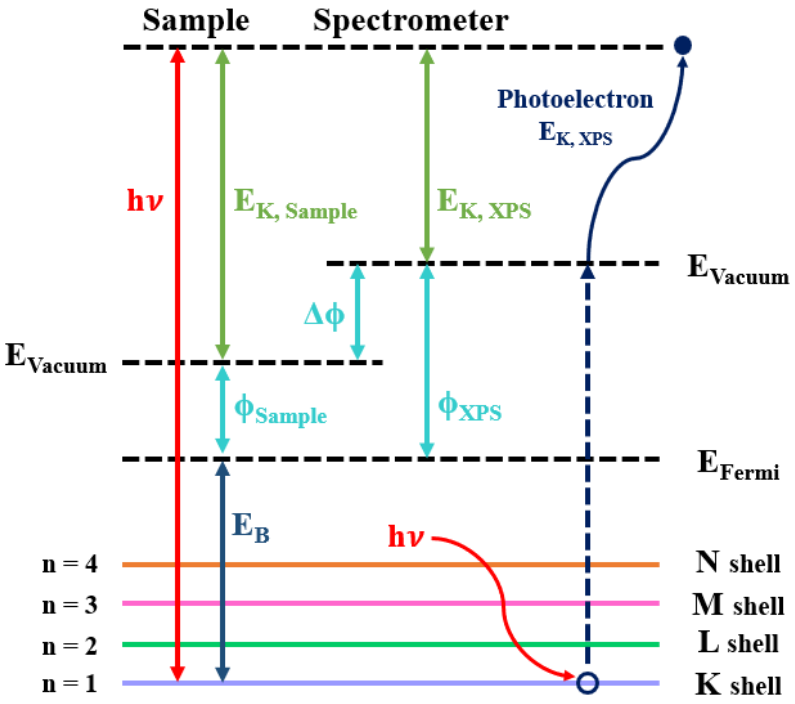

Figure 3.29 - Energy level diagram for XPS analysis

Using an energy level diagram as shown in Figure 3.29, the energy transitions that occur during photoelectron emission can be better understood. If sufficient incoming energy hν is transferred from high frequency photons such as UV or X-ray to an atomic electron, the binding energy E_B keeping the electron bound to the nucleus can be overcome. Extra energy must be expended to facilitate the electron's travel towards the sample surface and is described via the work function ϕ. Leftover energy is then converted into the kinetic energy E_K of the escaping photoelectron which can be measured by XPS apparatus.

Although the theoretical kinetic energy and work function is likely different when analysed in an environment such as a spectrometer, by using a standard value of energy transition (typically C 1s peak), the quantity of photoelectrons detected at each kinetic energy interval can be calibrated and converted into binding energy to plot a spectrum. This is summarised below in Equation 3.19.

$$E_B = h\upsilon - E_{K,sample} - \phi_{sample} = h\upsilon - E_{K,XPS} - \phi_{XPS}$$

Equation 3.19 - Binding Energy of Detected Photoelectron

A simplified diagram of how XPS apparatus works is shown in Figure 3.30 alongside the SPECS FlexMod UHV-XPS system used in this work. An electron gun fired at Aluminium anode produces X-rays which are then monochromated and directed towards sample via rotatable stage. X-rays lead to photoelectron emission as previously discussed and those photoelectrons near sample surface escape and are focused by electromagnetic lenses into a hemispherical analyser. An electric field gradient causes photoelectrons to curve with path radius proportional to kinetic energy, hence E_k can be determined once reaching the detector plate. A thin layer of sample was attached to carbon tape and attached to Omicron sample plate. Prior to analysis an electron flood gun was used to reduce surface charging. Spectra were energy calibrated to C-C C 1s peak at ~285 eV. Table 3.9 provides more detailed experimental parameters used during the analysis.

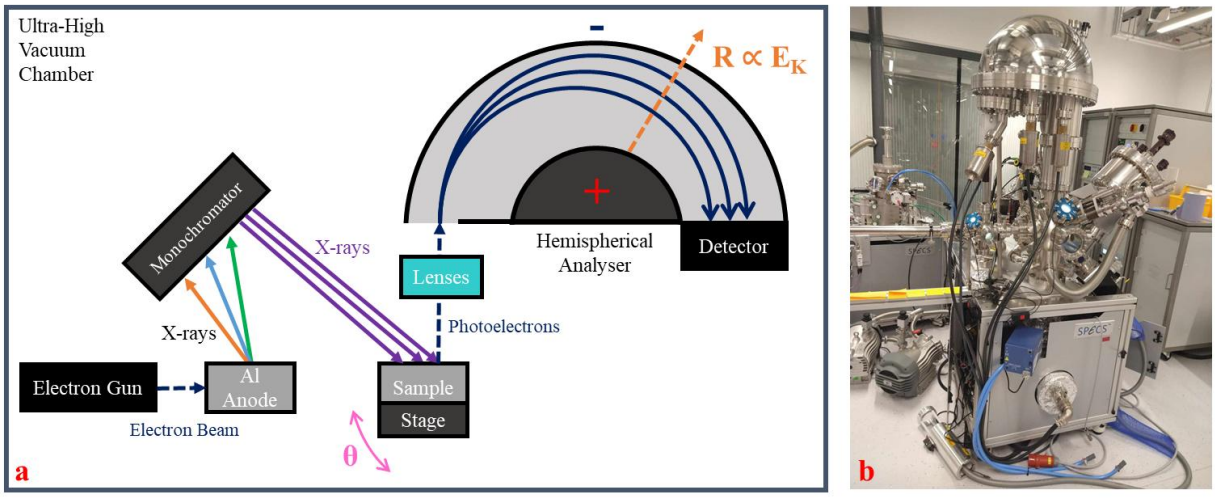

Figure 3.30 - Simplified Diagram of XPS (a), SPECS FlexMod UHV-XPS System (b)

Table 3.9 - Experiment Parameters for XPS Analysis

Property	Value
XPS System	SPECS FlexMod UHV-XPS
Hemispherical Analyser	Phoibos 150
Sample Preparation	Carbon tape + Omicron plate
Electron Detection	1D-DLD Detector
X-ray Source	Monochromated Al (1486.7 eV)
Accelerating Voltage	15 kV
Electron Gun Power	400 W
Analysis Spot Size	1x3.5 mm
Flood Gun Energy / Current	1.5 eV / 25 µA
Survey Scan Pass Energy / Step Size	50 eV / 1 eV
High Resolution Pass Energy / Step Size	30 eV / 0.1 eV

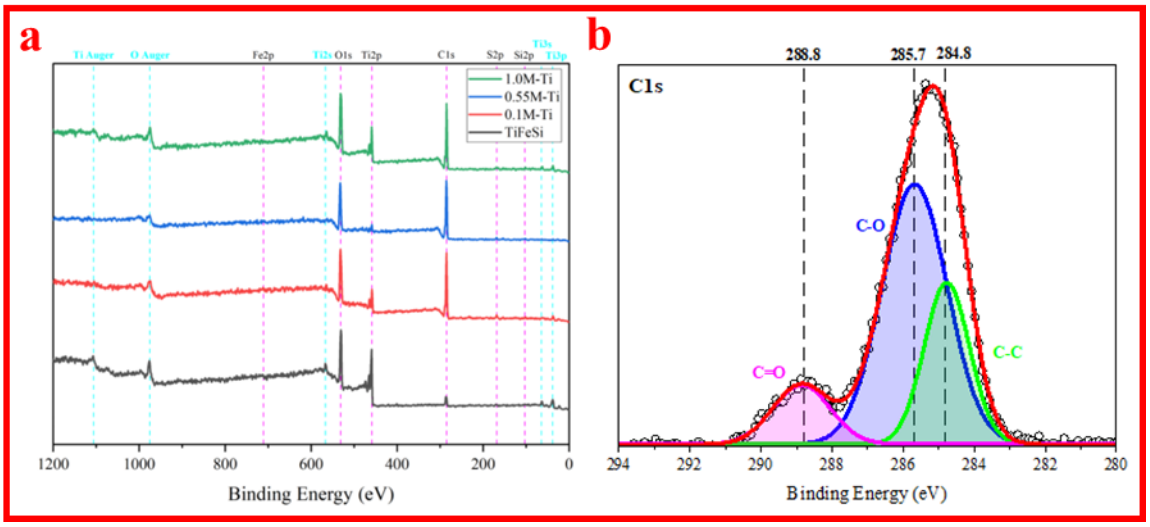

Figure 3.31 - Example XPS Survey Spectrum for Ti Series (a), High Resolution C1s Peak for FeSi Support with Gaussian Deconvolution (b)

Initial survey spectra were collected to calibrate based on C-C Carbon 1s peak and determine major and minor components. Figure 3.31a shows example survey spectra for Ti series of catalysts with major peaks and regions of interest labelled. High resolution spectra were then performed around identified peak regions of interest and these scan parameters are included in Table 3.10.

Table 3.10 - High Resolution XPS Scanning Regions and Relative Sensitivity Factors (RSF)

Peak Region	Bounds (eV)	RSF (CasaXPS)
Survey	0 - 1300	-
C1s	275 - 305	1
O1s	520 - 550	2.93
Fe2p	700 - 740	16.42
S2p	155 - 185	1.677
Si2p	90 - 120	0.817
Ti2p	445 - 480	7.81
Zn2p	1000 - 1060	28.72

Peak fitting was performed using CasaXPS software initially to compute baseline corrections and perform peak smoothing prior to deconvolution using Gaussian curves in Origin. Figure 3.31b shows an example high resolution spectrum of C1s peak for FeSi support material and the result of deconvolution. Levenberg Marquardt algorithm [455, 456] was applied until $\chi^2 < 1x10^{-6}$ to ensure high degree goodness of fit. Total number of peaks to fit was determined based on notable peak curvature, restricted to number of expected species present and selected to ensure individual peaks had area >1% of total. Peak constraints of equal FWHM and theoretical split peak area ratios were initially applied to ensure correct fitting, with constraint relaxation only used on noisy signals where desirable level of convergence failed. Equation 3.20 illustrates the Gauss curve fitting model used with fitting parameters y offset y_0, centre point x_c, area A and width W equal to twice the standard deviation σ. In order to covert peak area A_k of element k into atomic composition $x_{Atomic,k}$% for n total elements being considered, relative sensitivity factors RSF_k were used as given in Table 3.10 and as described in Equation 3.21. Surface composition was compared to bulk values determined via EDX discussed in Chapter 3.3.6.1 and key surface atomic ratios were calculated.

$$y = y_0 + \frac{A}{w\sqrt{\frac{\pi}{2}}} e^{-2\frac{(x-x_c)^2}{w^2}}$$

Equation 3.20 - Gaussian Fit Model for Peak Deconvolution

$$x_{Atomic,k}\% = \frac{A_k/RSF_k}{\sum_{k=1}^{n} A_k/RSF_k} \times 100\%$$

Equation 3.21 - Atomic Composition from XPS Spectra

3.3.7 CH(O)NS Elemental Analysis

In order to quantify carbon, hydrogen, oxygen, nitrogen and sulfur (CHONS) content present in bulk solid nanocatalyst samples, CHONS analysis was performed using Thermo Scientific Flash EA2000 unit shown in Figure 3.32a. Approximately 2 mg of sample was weighed into soft metallic foil capsules, tin for CHNS and silver for O analysis, as shown in Figure 3.32b. Capsules were then tightly pressed and folded to minimise excess atmospheric air. Two capsules were prepared for each analysis run to monitor correct sample preparation had been achieved and values were within uncertainty. Alongside blank runs, calibrated standards of known composition were used to monitor analysis performance. For CHNS analysis the standards used were oatmeal, barley flour and 2,5-Bis(5-tert-butyl-2-benzo-oxazol-2-yl) thiophene [BBOT] (Elemental Microanalysis). For O analysis the standards used were Nicotinamide, Sulphanilamide and Cystine (Elemental Microanalysis). Simplified analysis reaction pathways that occur within the analysis unit are detailed in Equation 3.22 and detection was based on thermal conductivity analysis of evolved gas.

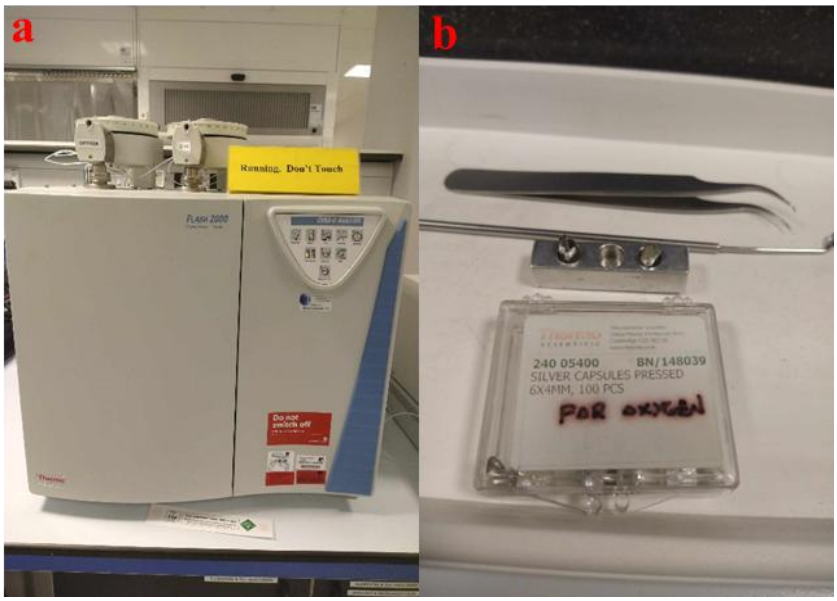

Figure 3.32 – Thermo Scientific Flash EA2000 (a), Sample Encapsulation (b)

$$\text{(I)} \quad Sample \xrightarrow[900°C]{Pure\ O_2} CO_2 + H_2O + N_2 + SO_2 + Solid\ Residue$$

$$\text{(II)} \quad Sample \xrightarrow[1060°C]{Pure\ He} O_2 + Solid\ Residue \xrightarrow[1060°C]{Carbon,He} CO$$

Equation 3.22 - Reaction Pathways for CHNS (I) and O (II) Analysis

3.3.8 Nuclear Magnetic Resonance Spectroscopy

The principle of nuclear magnetic resonance (NMR) and magnetic resonance imaging (MRI) relies on the fact that certain atomic nuclei will absorb and emit specific characteristic frequencies of radio waves when placed in a high strength magnetic field. Pioneering work by Isidor Rabi in 1938 demonstrated that nuclear magnetic moments can be measured experimentally in molecular beams [457]. For this work Rabi was awarded the Nobel Prize in 1944 for developing the "resonance method for recording the magnetic properties of atomic nuclei" [458]. Later experimental work in 1946 by E. M. Purcell et al. [459] and F. Bloch et al. [460] continued to develop the method of using radio frequency absorption and emission at specific frequencies for solid samples exposed to external magnetic fields. Figure 3.33 demonstrates energy transitions during nuclear resonance.

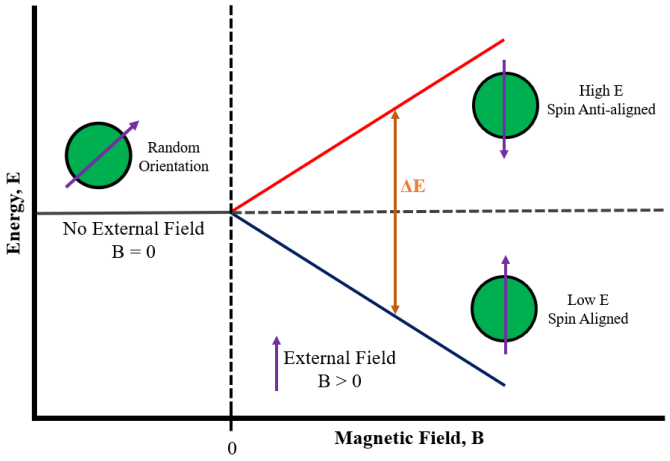

Figure 3.33 - Nuclear Energy Level Splitting in Magnetic Field

For atomic nuclei with odd number of neutrons (spin ½) and protons (spin ½) such as ^{1}H and ^{13}C, the overall spin of the nucleus will be nonzero and therefore possess a magnetic moment μ. When no external magnetic field B is present, magnetic moments will be under random orientation. However, once an external magnetic field is present, nuclei become aligned either with or against the external field. The energy state E becomes split as detailed in Equation 3.23 where m is magnetic quantum number, h is the Planck Constant (6.626x10-34 Js) and γ is the ratio of magnetic moment to angular momentum known as the gyromagnetic ratio.

$$E = -\frac{mh\gamma B}{2\pi} \; where \; \Delta E = \frac{h\gamma B}{2\pi}$$

Equation 3.23 – Nuclear Energy Level Splitting in Magnetic Field

Once the energy state has been split, it is possible for a radio wave photon of energy hν to become absorbed and cause a spin flip from low energy to high energy level. This excited nucleus will then later relax over a gradual relaxation time and produce characteristic radio wave photons unique to that nucleus. The frequency required for a spin flip to occur is provided by Equation 3.24. Since the frequency range for radio waves is typically MHz to GHz range, a very strong external magnetic field is required when performing NMR analysis. Additionally, increasing the energy gap between low and high energy state by using a stronger electromagnet improves detection sensitivity and hence desirable for low concentration samples.

$$\Delta E = h\nu = \frac{h\gamma B}{2\pi} \qquad \therefore \nu = \frac{\gamma B}{2\pi}$$

Equation 3.24 - Spin Flip Frequency

For this work only ^{1}H nuclei were analysed due to ^{13}C being significantly less sensitive for low concentration species as a result of low natural abundance of the ^{13}C isotope [461]. Each chemical bond involving a ^{1}H nucleus will have a slightly different electron environment and as such a varying degree of magnetic shielding, with greater shielding reducing ΔE. Therefore, each functional group has a corresponding relaxation frequency and by performing Fourier Transform as detailed earlier in Equation 3.4 on the relaxation time spectrum, individual frequency peaks can be determined with peak area corresponding to abundance. An example of an NMR spectrum before and after Fourier Transform for a sucrose calibration standard is provided in Figure 3.34.

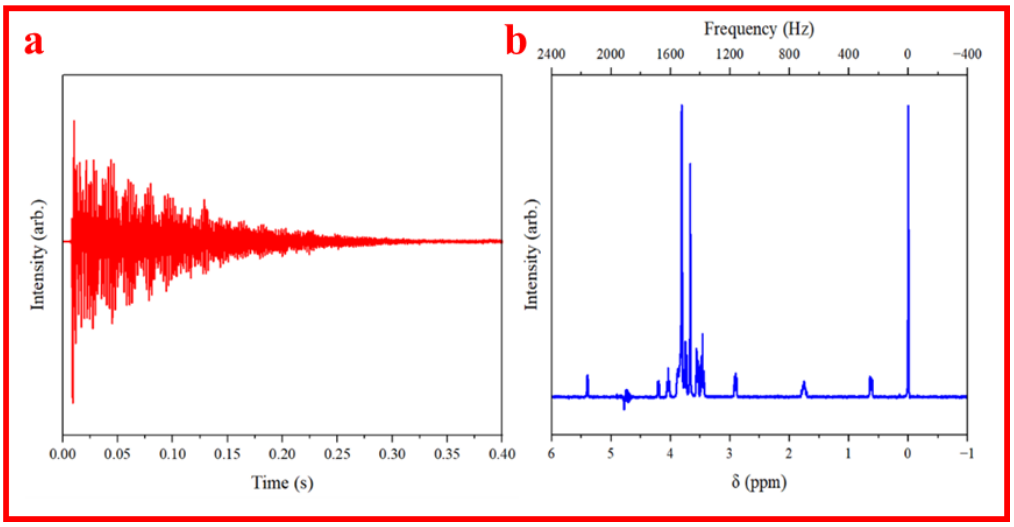

Figure 3.34 - Free Induction Decay (a), Frequency Spectrum (b) for ^{1}H NMR of Sucrose

Frequency axis is typically calibrated to tetramethylsilane (TMS) standard as a chemical shift δ as given in Equation 3.25, where frequency of functional group ν_i is adjusted to chemical shift δ_i by subtracting TMS frequency (ν_{TMS} = 100MHz) and dividing by spectrometer frequency $\nu_{Spectrometer}$.

$$\delta_i = \frac{\nu_i - \nu_{TMS}}{\nu_{Spectrometer}} \times 10^6$$

Equation 3.25 - Chemical Shift

Proton NMR was measured using a Bruker Ascend 400 spectrometer as shown in Figure 3.35a. Scan conditions are provided in Table 3.11. For solid nanocatalyst analysis, approximately 10 mg of sample was dispersed into 2 mL of deuterated $CDCl_3$ (99.8% D, VWR) and ultrasonicated for 5 minutes. Immediately after approximately 500 µL of this solution was transferred to Norell tube to a fill level of around 4.5 cm, before spinner was affixed as shown in Figure 3.35b. Analysis was performed immediately to avoid solid aggregating out of dispersion. NMR control used TopSpin 3.6.3 software and calculations were performed using OpenChrom. Use of NMR spectra for determination of molar/mass ratios of OH/H_2O via peak integration is discussed later in Chapter 3.5.2 and was computed in similar manner to Equation 3.33, with division by 2 of H_2O area.

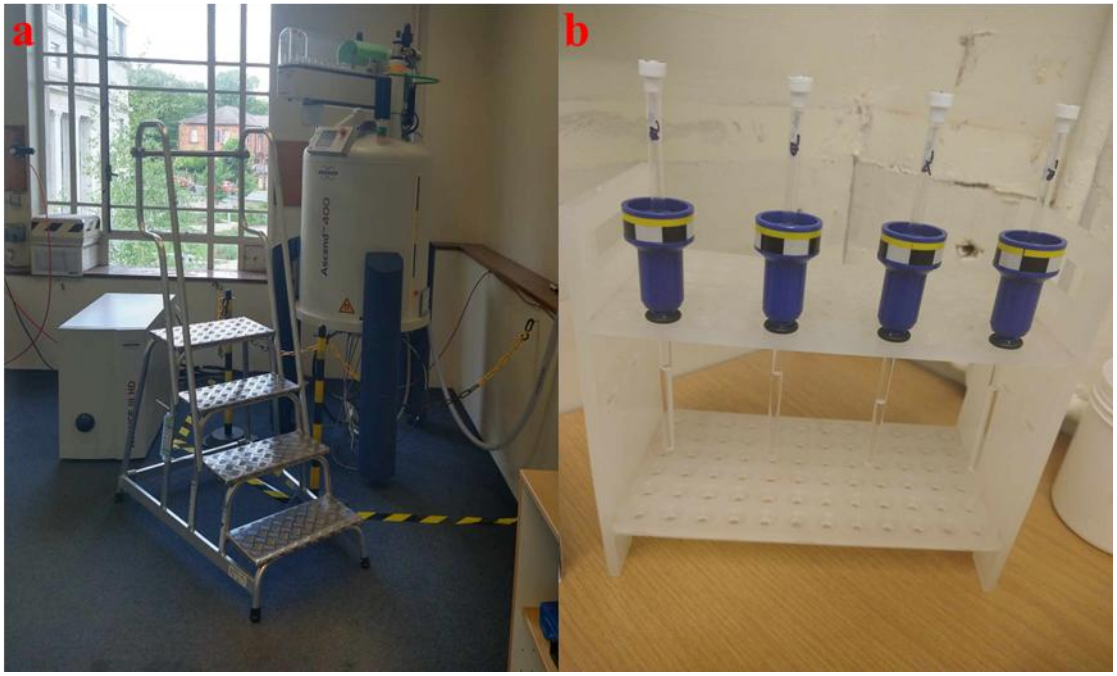

Figure 3.35 - Bruker Ascend 400 Spectrometer (a), Prepared Sample Tubes (b)

Table 3.11 - Method Parameters used for ^{1}H NMR Analysis

Property	Value
Carrier Frequency	400 MHz
Temperature	298 K
Number of Scans	32
Spectral Width	8013 Hz
Resolution	0.245 Hz
Data Points	32768
Acquisition Time	4.09 s
Dwell Time	62.4 µs
Relaxation Delay	0.5 s
Zero/First-Order Phase	3.17 µs / 9.50 µs
Receiver Gain	25.7
Pulse Power	17 W
Line Broadening	-0.1 Hz

3.3.9 Dispersion Analysis

A common definition of sol type colloids is a liquid with insoluble solid particles of size < 1 µm. Solid insoluble nanocatalyst suspended in liquid phase during batch biodiesel production fits this colloid definition. Unfortunately, colloids tend to undergo aggregation leading to reduced active site accessibility and hence loss of catalytic activity whilst in suspension. Even worse, bulk catalyst aggregates may settle out completely and deposit onto the reactor walls instead of catalysing reaction. Therefore, it is important to understand the amount of aggregation that is occurring and the stability of the colloidal dispersion. Such measurements are typically performed in aqueous solutions however for biodiesel production the nanocatalyst is suspended preferentially in the less viscous methanol phase and agitated via mechanical or ultrasonic methods. To explore the dispersibility of synthesised nanocatalyst in methanol environment, two techniques were explored: Dynamic Light Scattering (DLS) and Zetapotential analysis.

3.3.9.1 Dynamic Light Scattering

Initial work by George Stokes in 1845 [462] demonstrated that the friction a particle experiences when moving through a fluid is proportional to viscosity and particle size. Later work by Albert Einstein in 1905-1906 [463, 464] extended the concepts of Brownian motion first reported by Robert Brown in 1828 [465] to expand on Stoke's Law by incorporating the diffusion coefficient. Around the same time, William Sunderland [466] also reported a similar form of what is now known as the Stokes-Einstein equation as depicted in Equation 3.26. Particle hydrodynamic radius R_H (m) can be determined if translational diffusion constant D ($m \cdot ms^{-1}$) is known, where k_B is Boltzmann constant ($1.38x10^{-23}$ $m^2kgs^{-1}K^{-1}$), T is absolute temperature (K) and η is dynamic viscosity ($kgm^{-1}s^{-1}$). Note that hydrodynamic radius is slightly larger than true particle radius due to surface solvent effects but is a good approximation to size magnitude of suspended particles.

$$R_H = \frac{k_B T}{6\pi\eta D}$$

Equation 3.26 - Stokes-Einstein Equation

In order to determine the value of D in a liquid of known viscosity and temperature, it can be noted that the units are equivalent to a particle moving a distance (m) at a linear speed (ms^{-1}) thus by observing particle motion the quantity can be obtained. Work by John Tyndall in 1869 [467] showed that light of wavelength smaller than particle size scatters in colloidal solutions, and in 1871 Lord Rayleigh observed scattering for wavelengths greater than particle size and of the importance of refractive index in this scattering [468, 469]. Gustav Mie [470] developed a theory in 1908 to link scattering behaviour to particle shape and differences in refractive index between sample and liquid. Since then, many papers [471-473] have been published that attempt to link the scattering behaviour of light to determine the diffusion constant and consequently hydrodynamic radius, with further historical summary of the development of modern DLS technique provided in literature [474]. Figure 3.36 provides a simplified diagram for the basic principles of DLS. Monochromatic light is passed through a sample and the scattered light measured at a scattering angle θ. Scatter intensity will vary in amplitude due to constructive and destructive interference (Doppler Broadening) and fluctuate over time, with larger particle size correlated to greater intensity change over a slower period of time. From applying a correlation function to this data, a particle size distribution may be obtained. The correlation function is reproduced in Equation 3.27.

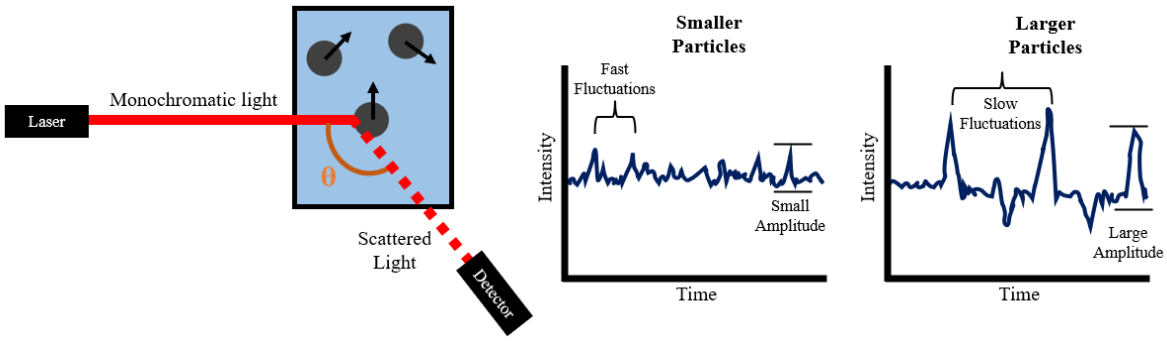

Figure 3.36 - Principles of DLS Measurement

The intensity correlation function g_2 is calculated based on averaged intensity measurements I at time value t and after a delay τ. Via the Siegert relation [473] this correlation can then be expressed through the electric field correlation function g_1. B is the baseline value and can be approximated to unity and β is the calibrated coherence factor of the DLS apparatus. By linking g_2 exponential decay rate due to Brownian motion a value of D may be calculated. The value of q represents the propagation of Bragg wave vector for monochromatic light of known wavelength λ and detected scattering angle θ. More detailed derivations of these equations are given in literature [474-476].

(I) $$g_2(\tau) = \frac{\langle I(t)I(t+\tau)\rangle}{\langle I(t)\rangle^2}$$

(II) $$g_2(\tau) = B + \beta[g_1(\tau)]^2 \approx 1 + \beta e^{-2Dq^2\tau}$$

(III) $$q = \frac{4\pi n}{\lambda}\sin\left(\frac{\theta}{2}\right)$$

Equation 3.27 - Intensity Correlation Functions

By plotting a logarithmic form of the correlation function with a second order polynomial, the intensity averaged diameter Z_{avg} and polydispersity index (PDI) may be obtained alongside the diffusion constant and hence hydrodynamic radius, as given in Equation 3.28.

(I) $$y(\tau) = a_0 - a_1\tau + a_2\tau^2$$

(II) $$Z_{avg} = \frac{1}{a_1}\frac{kT}{3\pi\eta}q^2$$

(III) $$PDI = \frac{2a_2}{{a_1}^2}$$

Equation 3.28 - DLS Correlation Fitting Parameters

For values of PDI < 0.05 the sample is said to be highly monodisperse and typically observed in DLS calibration standards. For values of PDI > 0.7 a sample is said to be highly polydisperse and as such presents a challenge for DLS cumulant analysis due to broad particle size distribution [477]. In this work, degree of aggregation under typical sample preparation for biodiesel production was of interest and hence values of PDI were often very high. Therefore, Z_{avg} was unsuitable to report due to averaging over a wide size range producing fictitious results. Cumulant analysis assumption of a monomodal particle distribution also becomes invalid. Hence DLS results were reported based on distribution analysis, which takes the cumulant correlation plot and attempts to optimise a better fit to observed data by splitting analysis range into a series of size bands. Default "General Purpose" regularizer built into Malvern Zetasizer software was utilised and further details of the algorithm may be found in literature [478]. Additionally, techniques more illustrative of true particle sizes such as SEM and TEM were used as comparison to DLS results. Measurements were carried out using Malvern Panalytical Zetasizer Nano using a quartz cuvette and dip cell. Approximately 1 mg of solid sample was dispersed into 1 mL prefiltered methanol and ultrasonicated for 5 minutes. The 1 $mgml^{-1}$ solutions were notably translucent and unsuitable for DLS analysis hence 10x dilution with extra methanol was performed to produce colourless 0.1 $mgml^{-1}$ colloidal dispersions ready for analysis. No further filtering was performed in order to assess degree of aggregation that would be present in methanol-nanocatalyst mixture utilised in biodiesel production. Right before analysis was to begin, a final 5minute ultrasonication was performed to negate settling that occurred during storage. Cuvette and dip cell were rinsed with acetone and allowed to dry prior and after each analysis to ensure no dust or residue remained. DLS measurement was performed using parameters given in Table 3.12.

Figure 3.37 - Zetasizer for DLS and Zetapotential Measurements (a), Dip cell and Quartz Cuvette (b), TiFeSi Support in Methanol at 1 $mgml^{-1}$ and 0.1 $mgml^{-1}$ Concentration (c)

Table 3.12 - Method Parameters for DLS Analysis

Property	Value
Temperature	30 °C
Scattering Angle	173 °
Wavelength of Light	632.8 nm
Dispersion Method	Ultrasonicate (5 min)
Number of Measurements	7
Solvent	Methanol
Solvent Viscosity	0.5123 cP
Solvent Refractive Index	1.326
Regularization Method	General Purpose
Size Classes	70
Size Limit	0.4 – 10^4 nm
Size Lower / Upper Threshold	0.05 / 0.01

An example DLS result obtained for TiFeSi support at 0.1 $mgml^{-1}$ using distribution analysis method is given in Figure 3.38, Gaussian curve fitting of histogram data was performed in Origin as previously discussed in Chapter 3.3.6.2 by taking average of 7 concordant results (within ±5%). Distributions were kept in intensity basis rather than volume or number basis to avoid extra errors during transformation and uncertainties from estimating unknown sample refractive indexes and extinction coefficients.

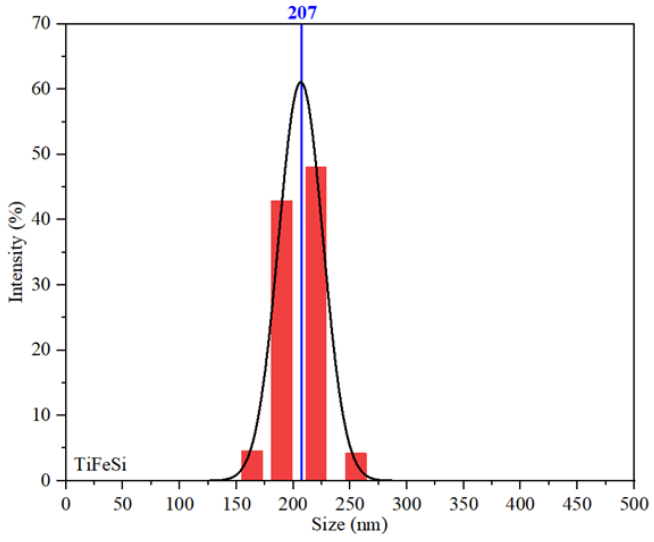

Figure 3.38 - Example DLS Size Distribution for TiFeSi Support in Methanol

3.3.9.2 Zetapotential

The electrical charges present on a solid surface strongly influences the overall stability of the colloidal dispersion. These charges can be due to surface functional groups such as acids and bases or for inert surfaces due to localised charged species accumulating around the solid. A diagram of a solid particle suspended in a liquid is shown in Figure 3.39 and known as the electrical double layer. Surrounding a solid surface is a Stern layer of oppositely charged ions and further out exists a diffuse layer of positive and negatively charged ions with a bias towards similar charge as present on surface. The theoretical boundary between bulk liquid solution and the second outer layer is known as the slipping or shear plane and has a measured potential ζ referred to as the Zetapotential. The sign of zetapotential indicates whether the surface is positively or negatively charged.

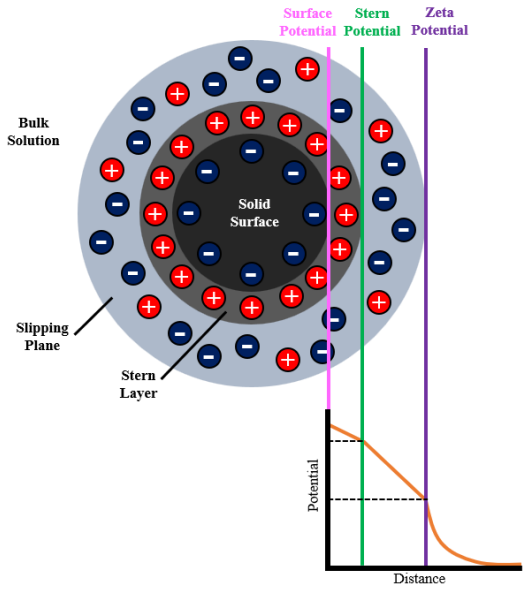

Figure 3.39 - Electrical Double Layer Structure

The absolute value of zetapotential can be used to predict the stability of a colloidal dispersion and various classes of stability range are reported in the literature [479, 480] as reproduced in Table 3.13. For high values of absolute zetapotential, this indicates mutual repulsion between solid particles and hence a monodisperse colloid with aggregation unfavourable. As absolute zetapotential decreases the degree of repulsion between particles decreases also, hence aggregation becomes more likely and particle distribution more polydisperse. One technique to measure zetapotential is similar to DLS measurements and in this work the same Malvern Panalytical Zetasizer Nano was used.

Table 3.13 - Stability Classes for Zetapotential

Zetapotential Range	Stability Class
$0 \leq \|\zeta\| < 5$	Rapid Aggregation
$5 \leq \|\zeta\| < 10$	Highly Unstable
$10 \leq \|\zeta\| < 30$	Incipient Instability
$30 \leq \|\zeta\| < 40$	Moderate Stability
$40 \leq \|\zeta\| < 60$	Good Stability
$\|\zeta\| \geq 60$	Excellent Stability

Electrophoretic Light Scattering measures zetapotential by determination of how fast individual particles move in an applied external electric field. A simplified diagram of the experimental setup is depicted in Figure 3.40. As discussed previously in Chapter 3.3.9.1, scattered light will experience a frequency shift (Doppler Broadening) after scattering off a suspended particle. The measured frequency shift Δf can be used to determine particle velocity v in the electric field via Equation 3.29 for known scattering angle θ and wavelength of light λ.

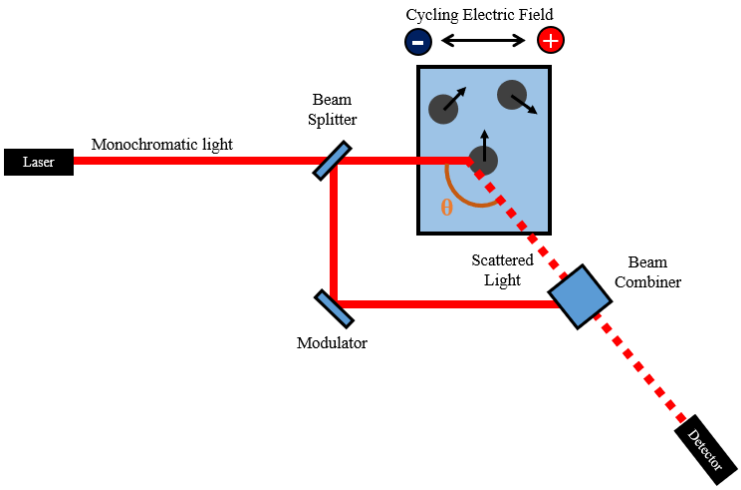

Figure 3.40 - Phase Analysis Electrophoretic Light Scattering Setup

$$\Delta f = \frac{2v \sin\left(\frac{\theta}{2}\right)}{\lambda}$$

Equation 3.29 - Frequency Shift of Scattered Light

For DLS the time behaviour of intensity signal as a consequence of frequency shift was sufficient to correlate to a diffusive speed. For zetapotential determination however, both the speed and direction are important in order to quantify the sign of electric charge as well as the magnitude. Unfortunately, frequency difference may be quite small due to slow movement velocity, especially in solvents with greater viscosities or larger particles of less mobility. To increase sensitivity, a modulated coherent wave of light is used as a reference signal and combined with the scattered light to produce a significantly lower "beat frequency" equal to the frequency difference between reference and scattered light [481-483]. From this an accurate value of particle velocity v can be determined, and with a known externally applied electric field strength E, the electrophoretic mobility u_E can be calculated as shown in Equation 3.30. Also shown is how the value of u_E can be converted into zetapotential for any solvent of known dielectric constant ε and viscosity η using Henry's equation [484].

$$u_E = \frac{v}{E} = \frac{2\varepsilon\zeta}{3\eta} f(\kappa a)$$

Equation 3.30 - Electrophoretic Mobility to Zetapotential Relationship

The conversion from electrophoretic mobility to zetapotential requires knowledge of Henry's function f(κa) which depends on particle radius a and the reciprocal Debye length which can be understood as the point where potential has decreased to a fraction e^{-1} (~37%) of surface value [485]. Two common evaluations of Henry's function in literature are the Helmholtz-Smoluchowski (HS) model where f(κa) = 1.5 and Hückel-Onsager (HO) model where f(κa) = 1 and both can be seen as limiting cases [486, 487]. The HS model is typically utilised with polar (aqueous) systems or for large particle sizes much greater than the double layer thickness [488]. For non-polar dispersants or smaller particle sizes the HO model is typically more suitable [488, 489]. The trend of f(κa) is illustrated in Figure 3.41. In this work, zetapotential was measured using same solutions as prepared for DLS analysis discussed earlier in Chapter 3.3.9.1 with methanol as dispersant. Since methanol is regarded as fairly polar (relative polarity of ~0.77 where water is 1.0 by definition [490-492]) and particle sizes were predicted to be at least >100 nm, HS was predicted to be most accurate and so f(κa) = 1.5 was taken for zetapotential analysis.

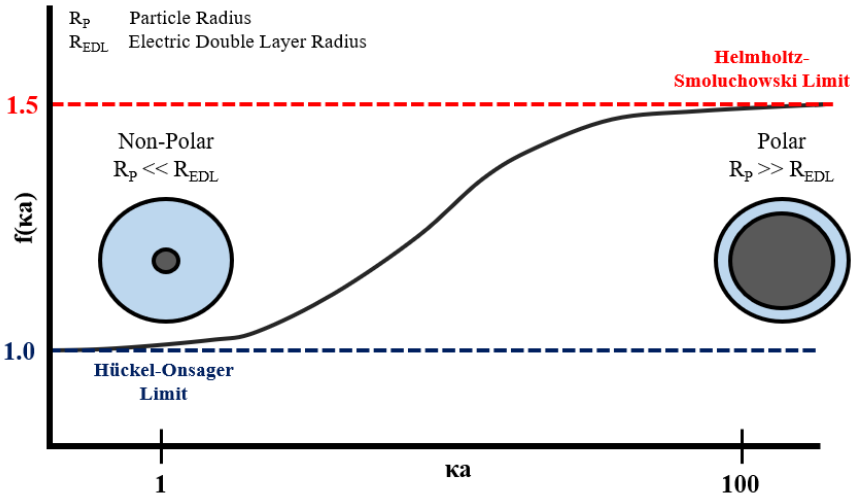

Figure 3.41 – Simplified Plot of Henry Function

Since zetapotential changes with pH and temperature [493] measurements were performed in pure methanol such that any variation was due to catalyst sample only. Temperature was kept within range the biodiesel reaction would be studied (30 °C – 60 °C) and the thermal effects on dispersant viscosity and dielectric constant were modelled using built in Malvern model for methanol in Zetasizer software. Analysis conditions and preparation is similar to DLS analysis previously given in Table 3.12. Example result for 0.1M-TiFeSi at 30 °C of electrophoretic mobility and the computed zetapotential using Helmholtz-Smoluchowski model is shown in Figure 3.42.

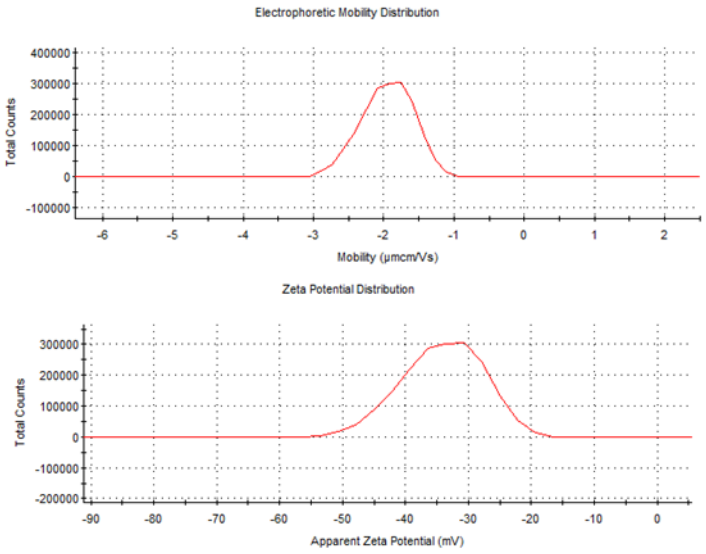

Figure 3.42 - Electrophoretic Mobility and Zetapotential for 0.1M-TiFeSi at 30 °C

3.4 Design of Experiments

3.4.1 Motivation for Design of Experiments Approach

The traditional method of performing experiments by changing one variable (factor) at a time (OFAT) while keeping the remaining variables constant may be a simple technique for studying the effect that individual variable has on a desired response, however it is not without several major downsides. Firstly, many more experimental runs are typically carried out than is necessary for similar amount of information, especially when only a relatively small number of studied factors were statically significant [494]. In the case of multiple factors this can add substantial extra research cost in terms of materials used or experiment runtime [495]. Secondly, since only one factor is changed at a time, the potential interaction effects that may be occurring are unable to be modelled and may be significant [496]. And finally, even if an optimum point was identified in an OFAT design it is unlikely to be a truly optimal setting of factors. This is both due to inherent bias towards the starting point conditions and design space selected, as well as unaccounted for lurking variables that may contribute variability between each experiment [497]. In order to address these issues with OFAT designs, the field of statistical experimental design was born starting with landmark work by Ronald Fisher in 1926 and 1935 introducing the concepts of factorial design of experiments (DOE) and analysis of variance (ANOVA) approach [498-500]. Fisher's principles consolidated and emphasised the importance of concepts such as randomisation, replication and blocking in order to reduce the influence of undesirable lurking variables and random noise. Later work by R. L. Plackett and J. P. Burman in 1946 [501] introduced new reduced factorial designs that traded less information for smaller number of runs, ideal for screening experiments where many factors are present but only a few are likely to be significant. Later work by George Box and Donald Behnken in 1960 [502] introduced response surface designs (RSM) ideal for studying nonlinear models where curvature was expected to be significant. Genichi Taguchi adapted DOE models in 1980 with a key emphasis on "robustness" in the manufacturing industries, where insensitivity to noise was of great importance [503]. The field of DOE continues to see improvements, with recent work by Bradley Jones and Christopher Nachtsheim in 2011 leading to the development of Definitive Screening Designs (DSD) as a technique to extract even more information out of a screening design in as few runs as possible [504]. There is a wide variety of software available for producing experimental designs, in this work JMP-18 was utilised [505].

3.4.2 Development of a Custom Design

Due to limited quantities of catalyst available to be synthesised and restrictions on how many experiments could be performed within the research timeframe, it was clear early on that a design of experiments approach would be ideal. In order to assess catalyst reaction performance in batch esterification/transesterification trials, a list of potentially influential factors to be explored, controlled and deemed uncontrollable was produced as given in Table 3.14.

Table 3.14 - Factors Considered in DOE Model

Design Factors	Controlled Factors	Uncontrollable Factors
Reaction Time	Reaction Pressure	Laboratory Temperature
Reaction Temperature	Agitation Method	Feedstock Purity
Mass of Reactants	Stirring Rate	Methyl Oleate / FAME Yield Detection Error
Mass of Catalyst	Calcination Temperature	Mass Balance Error
Acid Concentration	Calcination Time	
Active Metal Oxide		

Main factors that were desired to be studied included reaction time (°C), reaction temperature (hr), mass of reactants and mass of catalyst loaded into the reactor. Masses were expressed as the molar ratio of methanol to oil (A:O) and catalyst weight percentage (wt%) to oil mass. While acid concentration (0.1 M, 0.55 M and 1.0 M) and active metal oxide (TiO_2 and ZnO) were explored by producing six different catalyst designs, these factors were not included in the DOE model due to not being able to continuously vary these factors post synthesis and desire to avoid introducing discrete factors into the design. While literature has indicated calcination time and temperature to be influential on catalytic activity, as discussed previously in Chapter 2, these factors were selected based on previously reported constraints and optimal settings hence beyond the scope of this research work. Due to difficulties in reliably and safely operating under ultrasonic conditions, in this work agitation was restricted to magnetic stirring bar of one singular geometry. Reaction pressure was kept at ambient similarly due to safety concerns and lack of pressure reactor. The influence of stirring rate has been highlighted in aiding the mass transfer between immiscible methanol and oil layers, however with experimental setup used there was insufficient visible catalyst suspension below 400 rpm and excess catalyst leaving liquid phase and remaining on side of reactor above 600 rpm hence agitation rate was fixed to 500 rpm for all runs.

Lurking variables that could lead to experimental noise was identified and controlled to as best extent possible. To mitigate fluctuating laboratory temperatures over the course of a day, trials were performed in randomised order and no influence was observed. Feedstock purity was maintained as constant as possible by prefiltering reactants and heating UCO for 4 hours at 100 °C then stored under airtight conditions prior to analysis, alongside using same batch of methanol, oleic acid and UCO for all experiments. Errors in weighing were minimised by using same set of pre calibrated scales and measuring three times, whereas methyl ester detection was performed using internal standards as detailed in Chapter 3.5.2.3. Finally, each trial run was replicated to increase statistical power, tighten confidence interval and check reproducibility within ± 5% error.

$$y(x_1 \dots x_n) = A + \sum_{i=1}^{n} B_i x_i + \sum_{i=1}^{n} C_i {x_i}^2 + \sum_{\substack{i=1,j=2 \\ i<j}}^{i=n-1,j=n} D_{ij} x_i x_j + E$$

Equation 3.31 - DOE Second Order Design Equation for n Factors

Expressed in Equation 3.31 is the second order design equation for a DOE model with n factors x_1 to x_n, where A is the intercept for all zero x, B represents the main (first order) term coefficients, C represents the quadratic (second order) term coefficients, D represents the 2-way interaction term coefficients between factors x_i and x_j, and E is the statistical error inherent in the model. After finalising the number of design factors down to four and considering the potential need to explore nonlinear (quadratic) and interaction effects, a range of DOE designs was created using JMP software. Some of the main designs that were considered are included in Table 3.15. Accounting for mass of catalyst available and project timeline, it was determined that a maximum of 20 runs were feasible. In order to confirm reproducibility and ensure confidence in model (within ± 5% error), each run would be replicated hence 10 unique runs could be performed. JMP custom designer predicted 10 runs could model all main effects and curvature analysis (quadratic terms) with an extra run at model centre point. Centre points can be used to improve model fit where curvature is expected and lower prediction variance in the centre of design space by providing extra degrees of freedom [506, 507]. Quadratic effects were deemed a higher priority compared to two-way interaction effects since studies explored throughout Chapter 2 repeatedly demonstrated nonlinear response of yield against reaction time, temperature, catalyst loading and alcohol to oil ratio. Experimental runs at predicted optima would hence be used to ensure fit was within error.

Table 3.15 - Comparison of Different DOE Models Explored

Design	Minimum Runs	Modelled Terms
Full Factorial 3 Level	81	All ME, All TWI, All Q
Box-Behnken Design	25	All ME, All TWI, All Q, C
Central Composite Design	24	All ME, All TWI, All Q
Definitive Screening, Quadratics	17	All ME, All Q, 4 TWI
Definitive Screening, 2-way Interactions	17	All ME, All TWI, 2 Q
Full Factorial 2 Level	16	All ME, All TWI
Custom Design, 2-way Interactions	12	All ME, All TWI, C
Custom Design, Quadratics	10	All ME, All Q, C
Fractional Factorial 2-level Screen	8	All ME, 3 TWI
Fractional Factorial 2-level Screen	5	All ME

ME: Main Effects, TWI: Two-Way Interactions, Q: Quadratic Effects, C: Centrepoint

Once a custom design was created, constraints for each design factor was selected such that the design space was symmetrical to ensure good fit throughout. Reaction temperature was limited to boiling point of methanol (64.7 °C) and desired to be sufficiently above ambient (25 °C) to avoid influence of laboratory temperature hence was set from 30-60 °C. Maximum reaction runtime that could be performed in batch mode safely during the day was 9 hours after including setup and shutdown time, hence time was restricted between 1-9 hours. Catalyst loading typically ranged between 1 – 5 wt% in the literature to ensure sufficient catalyst was present without impeding liquid-liquid reaction due to increased viscosity from excess catalyst. Minimum methanol to oil stoichiometry is 3:1 for triglyceride transesterification however excess is required to favour product formation at equilibrium while too much dilution impedes reaction kinetics. Hence ratio was limited between 4:1 and 16:1 in line with literature. Table 3.16 summarises these encodings.

Table 3.16 - Encoding Table for Custom Design

Design Factor	-1	0	+1
Time (hr)	1	5	9
Temperature (°C)	30	45	60
Catalyst Loading (wt%)	1	3	5
Methanol : Oil Ratio	4	10	16

Table 3.17 - 10 Run Custom Design

Run	Time	Temperature	Catalyst Loading	Methanol : Oil Ratio	Run Order
A1, A2	-1	-1	0	-1	2, 12
B1, B2	0	1	-1	-1	1, 16
C1, C2	-1	1	1	1	10, 13
D1, D2	-1	0	-1	0	6, 18
E1, E2	0	0	0	1	4, 17
F1, F2	0	-1	1	0	9, 19
G1, G2	1	1	0	0	7, 14
H1, H2	1	0	1	-1	3, 20
I1, I2	1	-1	-1	1	8, 15
J1, J2	0	0	0	0	5, 11

The custom design utilised for testing catalyst performance in batch esterification and transesterification reactions is shown in Table 3.17. Each treatment condition A-J was run twice as denoted by run number (A1, A2) to give 20 total runs where 10 were replicates. While ideally 3 runs should be performed per treatment, lack of material restricted the number of replications achievable. Through replication, random error was measured to determine potential outlier results, as well as ensuring no significant deviation indicative of erroneous data was present. Runs were performed in non-sequential, randomised order as given in Table 3.17 to detect influence of lurking variables, such as daily lab temperature variations. Analysis was performed in JMP with quadratic and logistic modelling as discussed in Chapter 3.5.4.2. Example results for TiFeSi support oleic acid reactions with logistic model are shown in Figure 3.43 including studentised residual plot used for outlier and lurking variable analysis (A), Pareto plot used for identifying most influential effects (B), and prediction profiler used to determine factor settings for maximum yield (C).

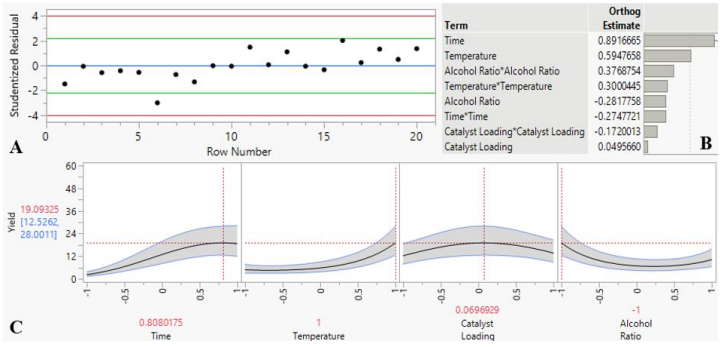

Figure 3.43 - Example Analysis Results for Oleic Acid Esterification with TiFeSi Support

3.5 Batch Trials and Biodiesel Characterisation

3.5.1 Experiment Setup

Batch reactions to explore catalytic activity were performed using the setup shown in Figure 3.44. Initially 2 mg of catalyst was weighed into a 5 mL borosilicate glass vial via mass balance (± 0.01 mg). To this, appropriate amounts of pre-dried (4 hours at 100 °C) and filtered UCO, Vegetable or Oleic Acid feedstock ("oil") was gradually weighed into the vial using adjustable 20-200 µl Eppendorf syringes with disposable pipette tips, depending on the desired catalyst loading percentage. Methanol was weighed last in similar manner until desired methanol to oil molar ratio was achieved before 15 mm magnetic stirring bar added and inner PTFE stopper tightly affixed. Screw cap was bound tightly with PTFE tape to ensure airtight reaction vessel and prevent loss of volatile methanol. Vial was ultrasonicated for 5 minutes prior to being added onto hotplate to ensure desirable catalyst suspension, before temperature and rpm gradually ramped up to desired setpoints. External temperature was monitored via both IR thermometer and thermal probe submerged in mineral oil to confirm temperature equilibration at setpoint prior to starting reaction timer. In each run, a control sample made with identical quantity oil and methanol was ran to confirm reaction was due to catalyst activity and not thermal effects. Post reaction, stopper and cap was removed before sample rapidly flashed at 75 °C to remove all methanol and halt further reaction or potential back-reaction during storage. Sample was left to stand overnight at ambient conditions to gravitationally separate catalyst and glycerol layers at bottom and methyl ester layer at the top. The top layer was isolated into new 5 mL vial for yield determination or further reaction.

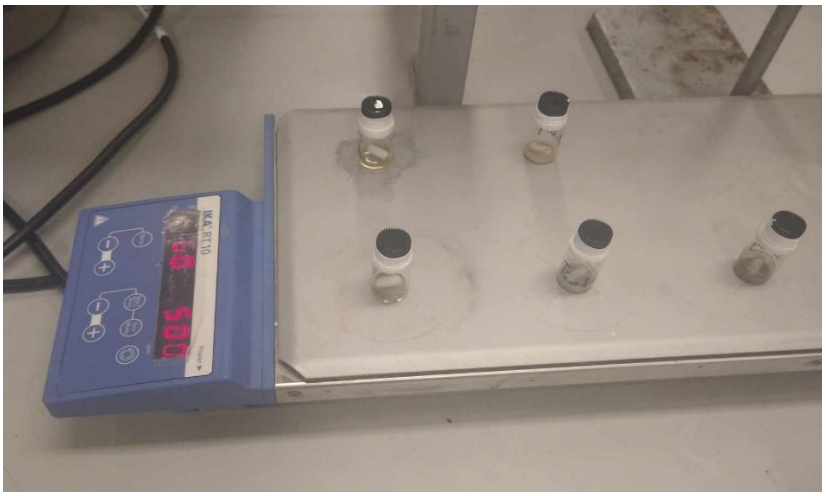

Figure 3.44 - Batch Esterification and Transesterification Reaction Setup

3.5.2 Determination of Reaction Yield

3.5.2.1 Fourier Transform Infrared Spectroscopy

A simple method of determining yield of methyl esters previously reported in literature [508] is to analyse the biodiesel via FTIR spectroscopy and integrate peak areas unique to FAME that are not present in unreacted oil feedstock. Use of C=O ester stretch (1700-1800 cm^{-1}) could not be used since peak was present in both raw oil and FAME, whereas asymmetric C-H_3 bend (1400-1500 cm^{-1}) was present in n-heptane solvent [509]. Unique peaks of slightly different wavenumber were observed for O-C-H_3 methyl stretch (1130-1230 cm^{-1}) between C19 standard and raw oil feedstock as illustrated in Figure 3.45a hence peak area across entire region (1135-1225 cm^{-1}) and higher energy peak (1185-1225 cm^{-1}) were used to calculate FAME yield.

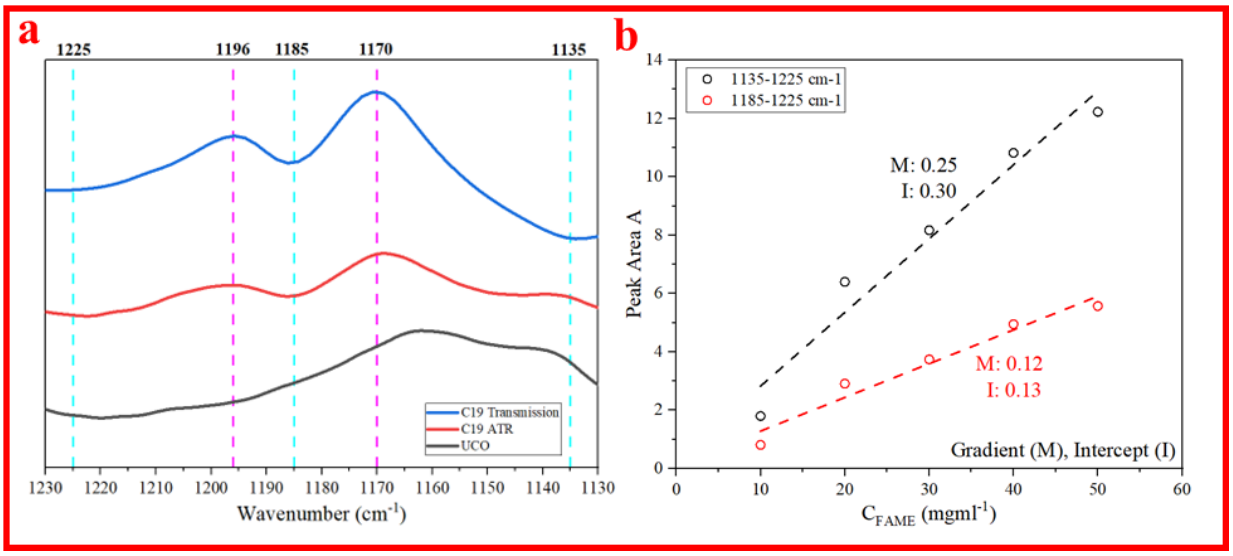

Figure 3.45 - C19 and UCO FTIR Spectra (a), Transmission Calibration Curves (b)

Calibration curves were constructed from dissolving methyl nonadecanoate in n-heptane at intervals of 10-50 $mgml^{-1}$ concentration and correlating with baseline corrected peak area A as shown in Figure 3.45b, where M and I are gradient and intercept of calibration curve respectively. Biodiesel FAME yield was calculated using Equation 3.32 where 50 mg of biodiesel sample were dissolved per 1 mL n-heptane and thoroughly shaken prior to FTIR analysis.

$$FAME\ Yield = \frac{C_{FAME}}{C_{Sample}} \times 100\% = \frac{MA + I}{50\ mgml^{-1}} \times 100\%$$

Equation 3.32 - FAME Yield from FTIR

Both a simple ATR approach as previously discussed in Chapter 3.3.3 was utilised as well as a transmission flowcell shown in Figure 3.46. Method parameters were identical to those in Table 3.3. While ATR is less sensitive to bulk liquid phase concentration as compared to transmission setup, the technique requires significantly less sample volume per analysis run which made it ideal for small batch reaction tests explored in this research work, particularly at high catalyst loading runs where low amounts of raw feedstock were used. Therefore, both ATR and transmission flowcell approach were explored as methods to quantify FAME yield. Comparisons between each approach and degree of success at determining FAME yield is discussed further in Chapter 5.2.

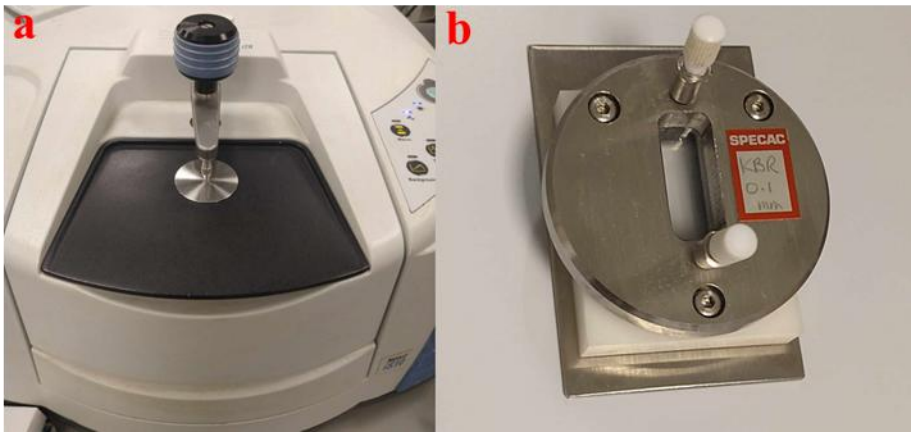

Figure 3.46 - ATR FTIR (a) and Flowcell Transmission FTIR (b) Setups

3.5.2.2 Nuclear Magnetic Resonance Spectroscopy

Similar NMR analysis as detailed in Chapter 3.3.8 was explored to determine FAME yield of biodiesel layer post reaction. Run conditions were identical to those described in Table 3.11. Approximately 10 mg of biodiesel sample was dispersed into 2 mL of deuterated $CDCl_3$ (99.8% D, VWR) and shaken to ensure complete dissolution. Immediately after approximately 500 µL of this solution was transferred to Norell tube to a fill level of around 4.5 cm, before spinner was affixed as shown prior in Figure 3.33b. NMR control used TopSpin 3.6.3 software and calculations were performed using OpenChrom. Example NMR spectrum of methyl nonadecanoate internal standard is displayed in Figure 3.47a. Previous studies [510, 511] have reported that use of methyl ester peak at ~3.7 ppm (A_{ME}) can be compared with triglyceride peak at ~2.3 ppm (A_{TG}) in order to determine FAME yield achieved. The ratio of peak areas to be compared is illustrated in Figure 3.47b and method of calculation provided in Equation 3.33.

$$FAME\ (\%) = \frac{(A_{ME}/3)}{(A_{TG}/2)} \times 100\%$$

Equation 3.33 - FAME Yield from ^{1}H NMR

Values of 3 and 2 account for differences in protons present in each functional group. Evidence of strong singlet peak between 3.6-3.8 ppm was used to qualitatively confirm trial reactions had successfully led to FAME production by appearance of this new peak. While quantitative determination of yield was therefore possible to determine, use of NMR facilities was restricted to low frequency 400 MHz setup only, limiting the data resolution and sensitivity achievable. While run times were rapid, only a limited number of samples were able to be analysed per day at available facilities. Moreover, use of deuterated solvent was required for each analysis. Considerations of NMR for application to FAME detection is discussed further in Chapter 5.2 with NMR ultimately selected to rapidly confirm qualitatively if reaction had been successful. Gas Chromatography Mass Spectrometry (GC-MS) technique, as discussed in next subsection, was then applied for high resolution quantitative FAME / methyl oleate yield determination.

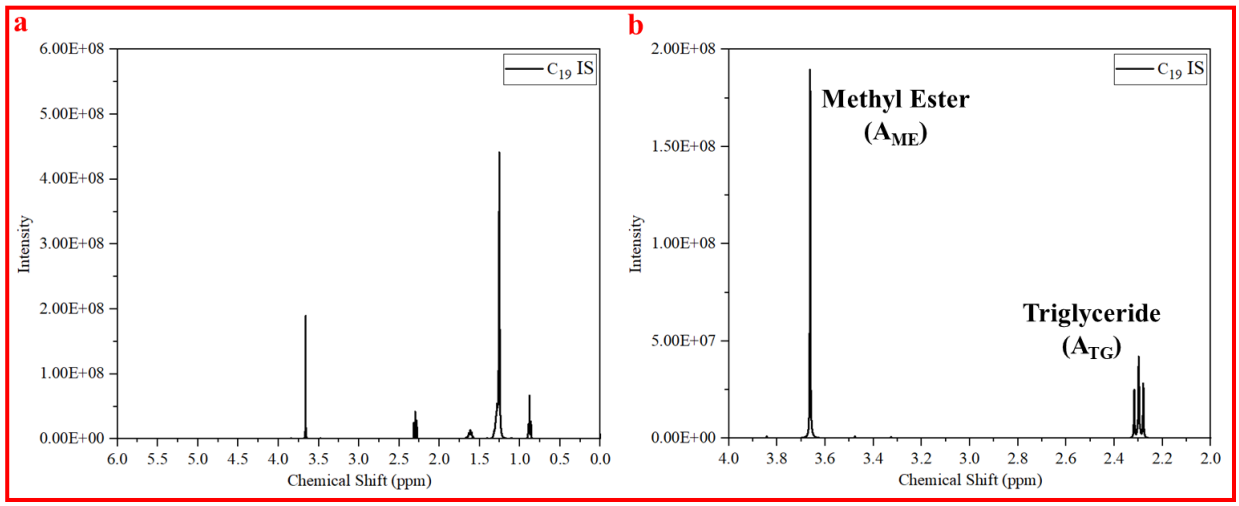

Figure 3.47 - NMR spectrum for Methyl Nonadecanoate (a), FAME Yield Peak Ratio (b)

3.5.2.3 Gas Chromatography Mass Spectrometry

GS-MS analysis to determine FAME yield is a widely performed technique [512, 513] due to high sensitivity with small sample volumes and widespread availability. A simplified diagram illustrating the technique is provided in Figure 3.48. Liquid phase sample is injected via autosampler syringe and mixed with an inert carrier gas such as H_2 that acts as mobile phase. Splitting and removal of purge stream is performed to reduce sample concentration and avoid column overloading, prior to transfer into a chromatography column acting as the stationary phase. Separation inside the column occurs based on affinity to stationary phase, with components more preferentially adsorbed being retained for longer. Additionally, use of an oven to thermally ramp up the column temperature over time allows for separation based on volatility. Bulky components of low volatility are therefore retained for longer until boiling point temperature is achieved. After passing through the column, sample components are passed through an ioniser and become charged species. A quadrupole then deflects and filters out all ions except those of a given mass to charge ratio (m/z) to collide with detector. Signal intensity as a function of time allows for plotting of a chromatogram. For each chromatogram peak, a mass spectrum can be obtained by correlating relative abundance of component fragments based on m/z ratio. Peak furthest to the right of spectrum is denoted the molecular ion peak (M^+) and can determine relative molecular weight. Together these two plots form the GC-MS analysis method used to determine individual FAME components. Figure 3.49a shows the Agilent 7000E GC/TQ - 8890 GC system used during this work and included in Figure 3.49b is an example chromatogram of biodiesel produced by reacting UCO with KOH. A list of main analysis parameters is also provided in Table 3.18.

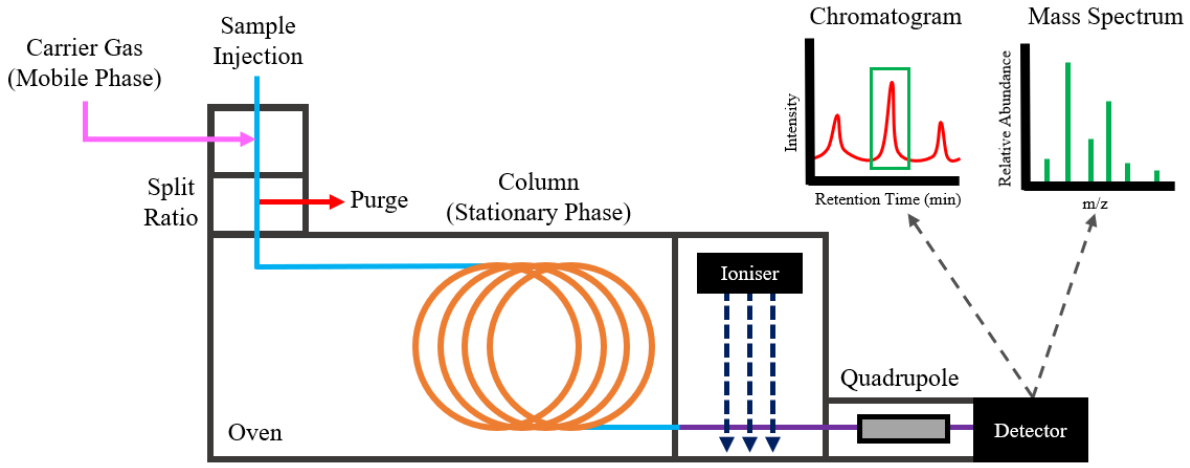

Figure 3.48 - Diagram of GC-MS Technique

Approximately 10 mg of biodiesel sample was weighed into a 2 mL vial. To this was added 1 mL of internal standard (IS) solution. IS was prepared by dissolving 1 mg/mL methyl nonadecanoate (C_{19} methyl ester) concentration into n-heptane. Methyl nonadecanoate was selected as internal standard due to similar chemical properties to expected FAME components, as well as being easily differentiated from biological FAME peaks than are strictly even numbered chain lengths and therefore would not overlap standard peak in chromatogram. Sample was shaken to ensure complete dissolution of biodiesel before loading into GC-MS autosampler. IS peak was identified to elute at ~18.5 min retention time as can be seen in Figure 3.49b, where other peaks are attributed to FAME components. Since IS peak had known concentration and known quantity of biodiesel concentration was loaded into vial, FAME yield [145] could be calculated by Equation 3.34.

$$FAME\ Yield\ \% = \frac{\sum A - A_{IS}}{A_{IS}} \times \frac{C_{IS}V_{IS}}{W} \times 100\%$$

Equation 3.34 - FAME Yield Determination of Biodiesel via GC-MS

Here A and A_{IS} represent peak area of all methyl ester species and methyl nonadecanoate IS respectively. C_{IS} and V_{IS} are the concentration and volume of IS solution used. W is the sample mass of biodiesel layer weighed out and was recorded each time prior to analysis. In the case of oleic acid esterification trials where feedstock was known to have only ~75 wt% purity of oleic acid, Equation 3.34 was adapted to 0.75W in denominator since at 100% methyl oleate yield only 75% of total sample mass would have contributed to methyl oleate peak. The reported yields for esterification reactions are hence based solely on detected methyl oleate content. Comparison of GC-MS technique with FTIR and NMR for use in this project is discussed further in Chapter 5.2.

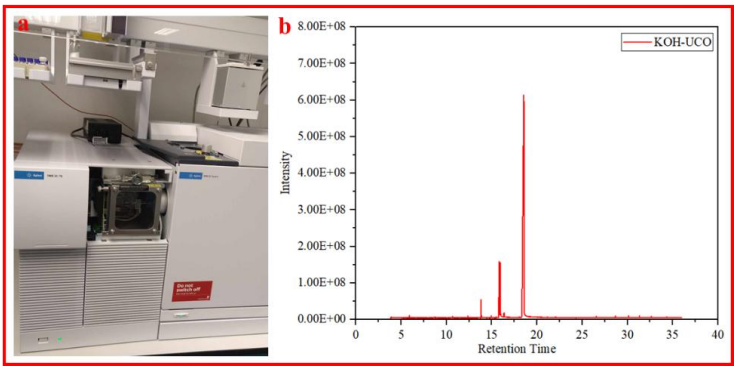

Figure 3.49 - Agilent 7000E GC/TQ with Agilent 8890 GC System (a), Chromatogram of Biodiesel Obtained via KOH-UCO Transesterification (b)

Table 3.18 - Method Parameters for GC-MS Analysis of Biodiesel

Property	Value
Initial Oven Temperature (Hold Time)	60 °C (0 min)
First Ramp Rate	10 °C / min
First Temperature Ramp (Hold Time)	200 °C (10 min)
Second Ramp Rate	10 °C / min
Second Temperature Ramp (Hold Time)	270 °C (5 min)
Equilibration Time	5 min
Total Runtime	36 min
Sample Cycling Time	41 min
Inlet Mode	Pulsed Split
Split Ratio	10:1
Injection Pulse Pressure	25 psi (until 0.5 min)
Injection Volume	1 µL
Wash Solvents	Methanol, Heptane
Liner	Agilent 5190-2293: 900 µL
Total Flow	12.9 mL / min
Split Flow	9 mL / min
Septum Purge Flow	3 mL / min
Column Inlet Pressure	8.38 psi
Column Outlet Pressure	Vacuum
Column Flow	0.9 mL / min
Average Flow Velocity	63.2 cm / s
Holdup Time	0.53 min
Transfer Line Temperature	250 °C
Column Type	Agilent 121-5522UI, DB-5ms Ultra Inert
Thermal Range	-60 °C - 325 °C (Max: 350 °C)
Dimensions	20 m x 180 µm x 0.18 µm
Control Mode	Constant Flow
Carrier Gas (Mobile Phase)	H_2

3.5.3 Feedstock Characterisation and Degradation Study

3.5.3.1 Titrations

In order to determine molecular weight and free fatty acid content of UCO feedstock, titrations to measure the Saponification Value (SV) and Acid Value (AV) were performed as detailed in ASTM D5558 and D974 [514, 515] respectively and calculated using Equation 3.35 and Equation 3.36. SV and AV are both measured in units of mgKOH/g of oil. SV represents how much KOH is required to fully saponify 1 g of oil and higher values indicate shorter fatty acid chain lengths hence lower average molecular weight. AV represents the amount of KOH required to neutralise all acidic components of the oil sample such as FFA, where higher AV indicates increasing acidity. Ethanolic KOH and HCl solutions were prepared with normality N taken as 0.1 Eq/L while mass of oil W was carefully measured out to 1.00 g in each test. Titration volume at equivalence of blank and oil sample are denoted as V_0 and V_1 respectively, measured in mL of standard solution required to initiate phenolphthalein indicator colour change. Constant 56.1 g/mol represents KOH molecular weight. Use of SV and AV allowed calculation of FFA% and molecular weight as demonstrated in Equation 3.37 and Equation 3.38. Factor of 3 in average MW formula is to account for triglyceride, and molecular weight of FFA assuming Oleic Acid is dominant impurity was taken as 282.5 g/mol.

$$SV = \frac{56.1 \times N \times (V_0 - V_1)}{W}$$

Equation 3.35 - Saponification Value via Titration

$$AV = \frac{56.1 \times N \times (V_1 - V_0)}{W}$$

Equation 3.36 - Acid Value via Titration

$$\overline{MW_{UCO}} = \frac{3 \times 1000 \times 56.1}{SV - AV}$$

Equation 3.37 - Average Molecular Weight of UCO via Titration

$$FFA_{Oleic}\ \% = \frac{AV}{56.1} \times \frac{282.5}{10} \approx \frac{AV}{2}$$

Equation 3.38 - FFA Content of UCO

Later GC-MS analysis confirmed C18 species as dominant fatty acid as seen in Figure 3.49b with major FAME peak at 15.8 min retention time having a molecular ion peak at 296 m/z corresponding to methyl oleate formation. Therefore, assumption used in Equation 3.38 is validated and restricts expected average molecular weight to be around the value of triolein (~885 g/mol) with slightly higher values indicating polymerisation during cooking process or contributions of larger triglycerides.

Alongside the use of AV to determine relative acidity of each UCO feedstock, a pH probe was used to monitor the change in deionised water acidity after suspension of a small quantity of oil. Increased UCO acidity would enhance formation of H_3O^+ ions in deionised water phase and hence produce a lower detected measurement of pH in the aqueous phase. Since oil-water is immiscible in larger quantities, approximately 100 µL of UCO sample was pipetted into an excess of 5 mL deionised water. Vial was shaken vigorously followed by 5 minutes of ultrasonication to ensure complete dispersion of oil droplet into bulk water phase. After pH probe was inserted, repeated readings were taken every minute until at least 3 concordant results were obtained.

Determination of feedstock specific gravity was also performed to verify average molecular weight titration results, since UCO and biodiesel density is dependent on the composition of glyceride species present and the level of FFA impurity [516]. Calculation of UCO specific gravity (SG) was performed using Equation 3.39 where ρ_1 and ρ_0 correspond to density of UCO sample and reference deionised water. By using a pipette of equal volume, the values of V_1 and V_0 cancel, and so SG is simply a ratio of measured masses m_1 and m_0. Identical 20 mL glass pipettes with rubber bulb were used to transfer sample of UCO and deionised water into a pre-weighed vial prior to repeated measurements on mass balance. After measurement, a mixture of UCO and deionised water was prepared and left to settle to confirm SG < 1 by appearance of an oil rich upper layer.

$$SG = \frac{\rho_1}{\rho_0} = \frac{m_1}{m_0} \times \frac{V_0}{V_1}$$

Equation 3.39 - Specific Gravity of UCO Feedstock Against Deionised Water

3.5.3.2 Thermal and Chromatographic Analysis

TGA analysis was performed on UCO feedstocks as discussed in Chapter 3.3.2.1 up to a maximum temperature of 200 °C to observe mass losses due to volatiles, absorbed gases and moisture content. Flashpoint was also measured using Stanhope-Seta Flashpoint tester with three repeat measurements taken for fresh and degraded UCO. Thermal analysis results were compared to molecular weight determinations to confirm if increased average molecular weight of fresh UCO led to an expected decrease in volatility and increase in flashpoint.

Gel Permeation Chromatography (GPC), also known as Size Exclusion Chromatography (SEC), was also used to qualitatively compare molecular weight distribution of fresh and degraded UCO. Similar to GC-MS technique, sample components can be separated based on an affinity to stationary phase to produce a chromatogram. Figure 3.50 provides a simplified diagram of how the gel preferentially retains less bulky, low molecular weight components for longer as compared to bulky species with high molecular weights. Use of a calibration standard such as polystyrene at known reference molecular weights can be used to correlate retention time to average size and weight of each component detected in chromatogram. Method parameters and sample preparation conditions are provided in Table 3.19. Since polystyrene calibrations did not behave chemically similar to UCO, obtained chromatograms were used for qualitative analysis of molecular size only.

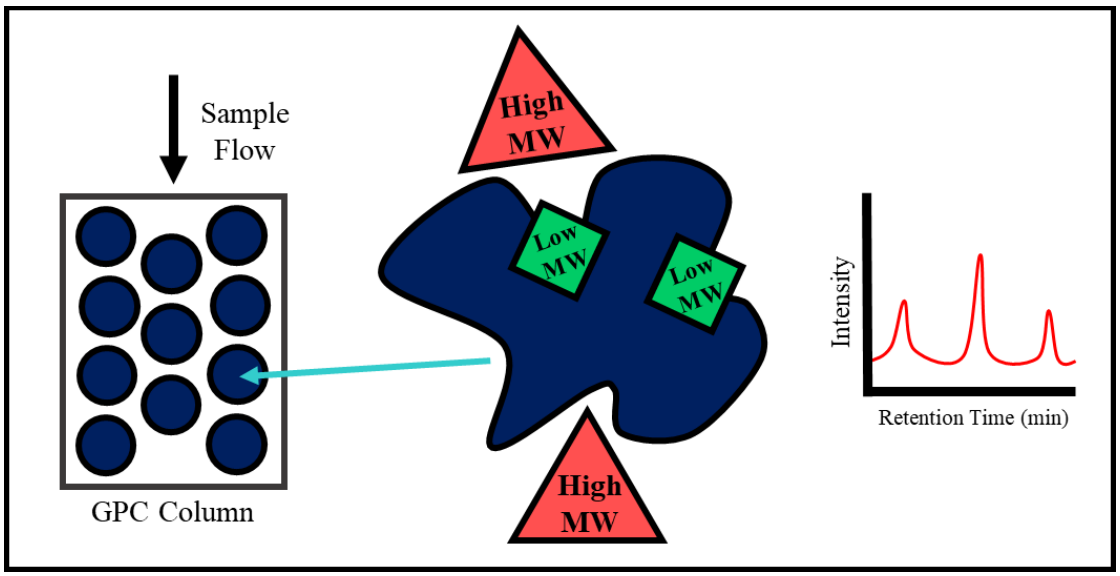

Figure 3.50 - Simplified Diagram of Gel Permeation Chromatography

Table 3.19 - Method Parameters for GPC-SEC Analysis of UCO Feedstocks

Property	Value
Instrument	Perkin Elmer Series 200
Solvent Mobile Phase	Tetrahydrofuran (THF)
Column Size	0.1 - 30 kDa
Detector	Refractive Index
Sample Preparation	~10 mg UCO in 2 mL THF

GC-MS analysis of UCO feedstocks prior to reaction were performed as discussed in Chapter 3.5.2.3 to detect if thermal esterification into FAME had occurred during storage. Typically, highly sensitive Flame Ionisation Detection (GC-FID) is preferred to GC-MS for quantifying the composition of triglycerides, diglycerides, monoglycerides and free fatty acids present in a cooking oil feedstock since only methyl esters may be detected using GC-MS method [517, 518]. However, without access to suitable calibration kit of reference oil mixture to interpret FID results, it was necessary to derivatise glycerides and FFA into FAME prior to GC-MS analysis. Unfortunately, this limited analysis strictly to determining the most common fatty chain lengths. After 1 hour of reaction at 60 °C, 1 wt% KOH and 10:1 ratio of methanol to UCO, obtained biodiesel sample was analysed as discussed prior. Knowledge of methyl ester molecular weights enabled identification of each major retention peak from M^+ signal in MS spectrum. Integrating each chromatogram peak, the relative percentage composition of main glyceride species could then be calculated.

Previous studies have shown that NMR analysis can be utilised to determine AV, SV, glyceride components and FFA% for both unreacted feedstock and synthesised biodiesel [519-521]. An example NMR spectrum of fresh UCO is provided in Figure 3.51a using previously described run conditions and sample preparation steps. As can be seen in Figure 3.51b for the region of interest to determine FFA% via NMR, relatively low resolution of 400 MHz setup for individual peak area calculations meant that accurate quantitative analysis proved challenging. Therefore, as discussed prior in Chapter 3.5.2.2, NMR was only used qualitatively to detect presence of methyl ester peak at ~3.7 ppm and verify if esterification had occurred during frying or storage.

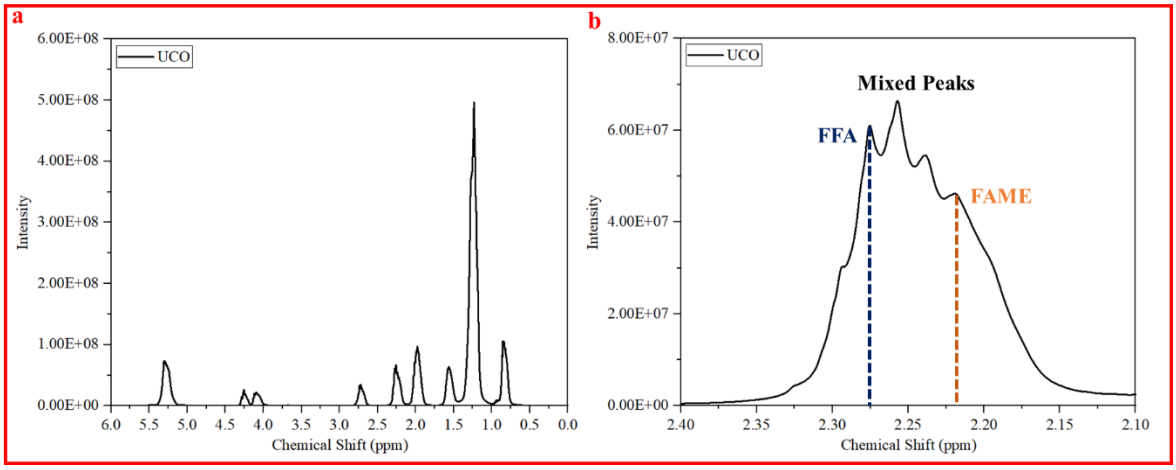

Figure 3.51 - NMR Spectrum of Fresh UCO (a), Peak Area Region for FFA% Calculation (b)

3.5.3.3 Rheology

The viscosity difference between vegetable oil, fresh and degraded UCO was immediately noticeable upon initial handling and pipetting of each feedstock. Degraded UCO was noticeably thinner and poured similarly to water, while fresh UCO was rather viscous and flowed much slower out of a container. Vegetable oil had an intermediate thickness. Since oil-methanol liquid phases are poorly miscible, high degree of agitation is required during reaction to ensure mass transportation issues do not hinder FAME formation. Viscosity also influences separability post reaction, with a thicker unreacted oil layer requiring increased centrifugation time or gravitational settling to recover spent nanocatalyst. Therefore, it was decided to experimentally determine this viscosity difference between feedstocks and what influence reaction temperature may have. Newton's Law of viscosity is provided in Equation 3.40 where dynamic viscosity η (mPa·s) is defined as the ratio of shear stress σ (mPa) to the rate of shear (s^{-1}). For a Newtonian fluid this ratio is constant at a given temperature, however for more complex non-Newtonian fluids a power law model is observed instead as given in Equation 3.41 with constants k and n to be determined.

$$\eta = \frac{\sigma}{\dot{\gamma}}$$

Equation 3.40 - Newton's Law of Viscosity

$$\sigma = k\dot{\gamma}^{n}$$

Equation 3.41 - Power Law Model of Fluid Flow

Rheological studies were performed using an Anton Paar MCR 301 with cone and plate test geometry. Table 3.20 provides experimental parameters used and Figure 3.52a, b shows the rheometer used and a simplified diagram of how measurements were performed. Quantities of oil were pipetted onto a test plate and cone height adjusted to ensure sufficient liquid flow region. Heating plate controller was then set to temperature intervals of 30 °C, 45 °C and 60 °C and left to thermally equilibrate prior to testing. Constant intervals of shear rate were applied via motor and resistive shear stress measured to obtain flow curves as provided in Figure 3.52c for vegetable oil. Gradient of flow curve plot gave value of dynamic viscosity at each temperature interval, with straight line plots indicating Newtonian fluid behaviour. Differences in viscosity between UCO samples was also used to provide additional insight into the structure of glyceride molecules [522].

Table 3.20 - Method Parameters for Rheology Measurements

Property	Value
Instrument	Anton Paar MCR 301
Measuring Geometry	75mm Cone and Plate
Shear Stress Range	0.01 - 5 Pa
Shear Rate	0 - 100 s^{-1}
Temperature Intervals	30 °C, 45 °C, 60 °C

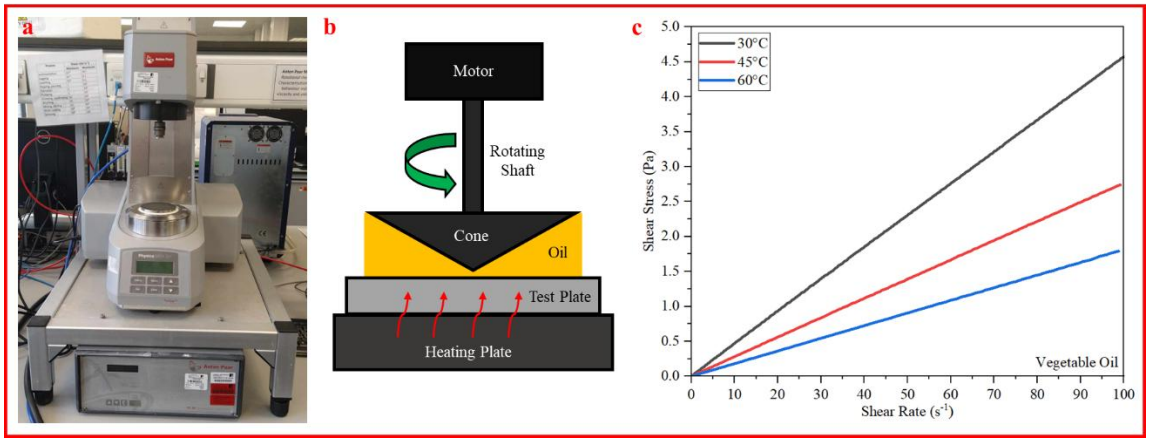

Figure 3.52 - Rheometer (a), Cone and Plate Geometry (b), Flow Curve for Vegetable Oil (c)

3.5.4 Reaction Modelling

3.5.4.1 Effect Screening

Development of the custom screening design has been detailed previously in Chapter 3.4.2, once batch trials had been completed and methyl oleate / FAME yield was determined via GC-MS, JMP software was used to analyse data and screen out most important factors. Figure 3.53 illustrates three different screening methodologies used to identify factor effects most influential on yield.

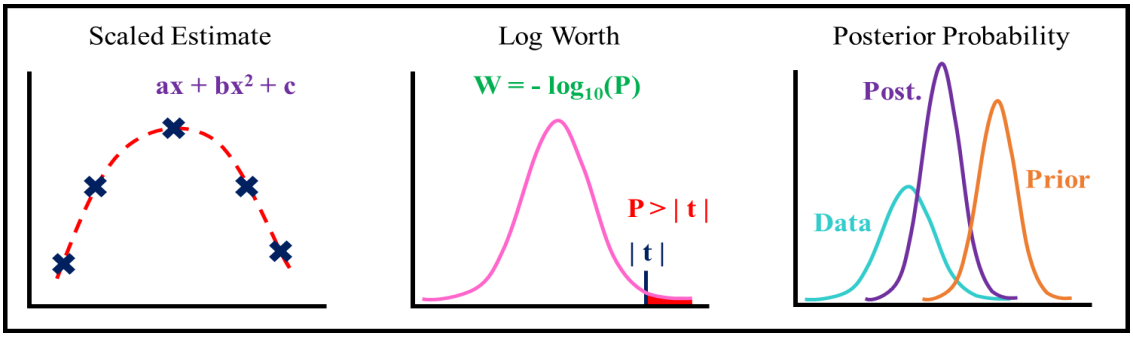

Figure 3.53 - Effect Screening Methodologies

A regression model similar to the form described prior in Equation 3.31 was fitted using intercept, main effects and quadratic (non-linear) terms. The magnitude of each factor term coefficient provides insight into the relationship strength towards yield, with the sign indicating either beneficial or detrimental effect. For non-linear terms, value of sign indicates the presence of a maxima or minima within design space as factor value is increased. Hence a large coefficient in regression model indicates significant influence of that factor term. To check for statistical significance of each factor term, a one tailed t-test was performed as given in Equation 3.42 and calculated in JMP. Values of $\bar{x}$, μ, σ and n correspond to factor mean, theoretical mean, standard deviation and number of datapoints. The p-score (P>|t|) was converted into Log Worth W through Equation 3.43 where large values of W indicate statistically significant effect on yield response.

$$|t| = \left|\frac{\bar{x} - \mu}{\sigma/\sqrt{n}}\right|$$

Equation 3.42 - Student's t Test Statistic

$$W = -\log_{10}(P > |t|)$$

Equation 3.43 - Log Worth Screening Statistic

Bayesian posterior probability test was also used to screen for significant factors as previously reported in literature [523]. Bayes' Law is provided in Equation 3.44. The posterior probability P(A|B) can be understood as the probability of an effect being part of a contaminating distribution with variance $K\sigma^2$ instead of a random noise prior distribution P(A) of variance σ^2 instead. The likelihood of the model P(B|A) is the probability of observing the obtained result under different parameter settings, while P(B) is the marginal likelihood of obtaining the given result considering all parameter settings possible. Default parameters used in JMP were kept, setting K=10 and using a prior probability of 0.2 for P(A). The higher the posterior probability, the more statistically significant the factor term since it becomes more likely that observed yield response cannot be due to a random prior noise distribution.

$$P(A|B) = \frac{P(B|A)P(A)}{P(B)}$$

Equation 3.44 - Bayes' Law of Conditional Probability

Reported t-tests were determined using JMP software. Reported f ratios were calculated using Analysis of Variance (ANOVA) method available in JMP. Results of these statistical tests were used to further indicate if effect mean deviation and variance were statistically significant from random noise of model. Since different effect screening tests may give slightly different results as to the order of most influential factors, results from all three methods were compared to determine if reaction time, temperature, catalyst loading and alcohol to oil ratio linear and non-linear effects significantly influenced yield response.

3.5.4.2 Model Optimisation

Ideally after using the screening model to identify the most promising nanocatalysts in esterification trials, a new custom optimisation design would be created to accurately model all main linear effects, non-linear effects and interaction terms. Due to time and material constraints, it was not possible to perform another Box-Behnken, Central Composite, Definitive Screening or custom optimisation design, especially if replication would also be required. Hence the obtained results of custom screening design were used to predict factor settings of optimality and then checked experimentally to confirm prediction was within ± 5% maximum error. Nonlinear optimisation was performed using JMP software by maximising model desirability function.

During some esterification studies, overprediction of methyl oleate yield beyond 100% was seen likely due to nature of a quadratic curve being unable to model plateaus, alongside the lack of interaction term modelling that may hinder yield at increased factor settings. To account for this, a logistic curve transformation was performed on yield response, denoted as "LogitPct" in JMP software but henceforth referred to as the logistic model. This transformation was used to attempt to model plateau at 100% methyl oleate yields and restrict model output between values of 0-100%, however at increased cost of error around centre point due to unrealistic inflection point, alongside contribution of additional modelling errors. Optimisation point of both quadratic and logistic models were considered for nanocatalysts displaying high esterification activity nearing 100%, with experimental validation of determined optimum point selected to confirm model output within error tolerance. Response surface plots were created to visually explore design space and understand the nature of determined optimum points. Additional checks of model suitability included plotting studentised residuals to check for outlier results and confirm all runs existed within 95% confidence window. Similar to Chapter 3.5.4.1, Student t tests and f ratios determined by ANOVA via JMP software were included as part of screening model results to further indicate if factors were statistically significant compared to the mean and variance of error distribution. ANOVA was used to determine if results were statistically significant as well as identify the main source of error within the fitted quadratic or logistic models. Actual by predicted plots were plotted to observe how closely the obtained data aligned with the model, with close alignment indicated by points lying close to 45 ° line. Example response surface plot, actual by predicted plot and studentised residuals of 0.55M-TiFeSi quadratic and logistic model is provided in Figure 3.54.

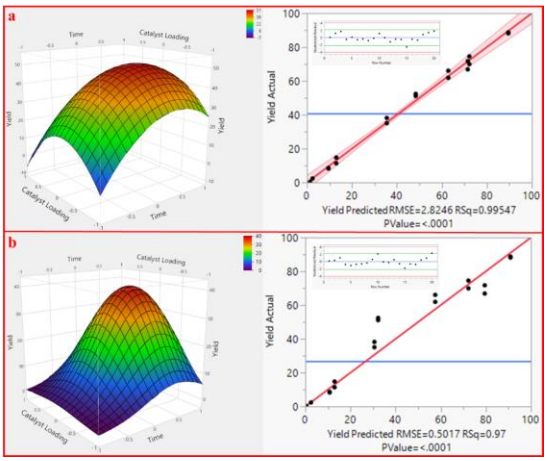

Figure 3.54 - Example Response Surface Plots, Actual by Predicted Plots and Studentised Residuals for 0.55M-TiFeSi Quadratic (a) and Logistic (b) Models

3.5.4.3 Kinetic and Thermodynamic Analysis

A full kinetic and thermodynamic study of optimal nanocatalyst esterification performance would require regular sampling from reactor over 9 hours period which was challenging considering the limited sample masses used per reaction and restricted amount of nanocatalyst available for tests. Previous literature has explored using DoE models to determine parameters [524-526], provided that the developed model could be experimentally determined as accurate within a reasonable level of tolerance at selected reaction conditions. Since reaction time was used as a key factor in the developed models, it was possible to predict the change in methyl oleate yield over time at optimum setting of catalyst loading and alcohol to oil ratio. Predicted yield for 0.55M-TiFeSi optimum catalyst agreed closely with experimental validation tests therefore the model was deemed suitable for determining kinetic and thermodynamic parameters. Three temperature values were selected for simulating yield time curves since model had already been fitted around 30 °C, 45 °C and 60 °C setpoints therefore minimising prediction errors. Example plot of yield with reaction time at 60 °C for 0.55M-TiFeSi nanocatalyst is provided in Figure 3.55a. Regions of extrapolated data points below 1 hour reaction time and the 100% plateau modelled by logistic fit are illustrated. To convert yield into kinetic parameters, a rate equation suggested in past studies [524] was used as given in Equation 3.45 where change in yield x over time t hours is modelled by a log-linear relationship. Value of C_0 was calculated to be ~2.38 M for 75% oleic acid at start of reaction, k is the reaction rate constant in hr^{-1} at given reaction temperature and n is the rate order. Since methanol is added in significant excess, esterification was expected to be pseudo first order hence value of n should lie close to unity. Gradient and intercept of linearised rate plot were hence used to determine reaction order and rate constant at the three selected temperatures. Only data points above 1 hour reaction time were used in fitting the linear rate equation to avoid extrapolation errors. Fit was performed around region of maximum reaction rate given by maximum gradient in yield time plot to obtain a best case scenario of nanocatalyst activity. A linear fit plot at 60 °C for 0.55M-TiFeSi nanocatalyst is included in Figure 3.55b. An instantaneous reaction rate constant was also calculated at maximum gradient to compare result with value obtained via linear fitting.

$$\ln\left(\frac{dx}{dt}\right) = n\ln[C_0(1-x)] + \ln(k)$$

Equation 3.45 - Linearised Rate Equation

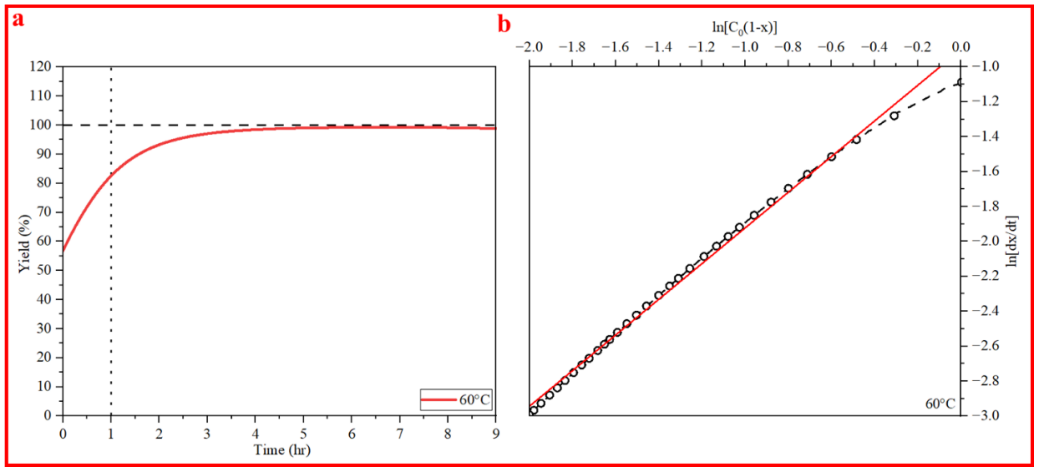

Figure 3.55 - Simulated Yield Time Plot at 60 °C for 0.55M-TiFeSi (a), Linear Kinetic Fit (b)

Once the average rate constant k in s^{-1} had been determined, application of the linearised Arrhenius Law provided in Equation 3.46 was used to determine esterification activation energy and molecular collision rate with 0.55M-TiFeSi nanocatalyst. A is pre-exponential factor and can be understood as the rate of molecular collisions measured in s^{-1} while E_a is the activation energy in J/mol and gives the minimum energy barrier required to initiate esterification via catalytic pathway. Temperature T is measured in K and gas constant R was taken as 8.3145 J/mol·K.

$$\ln(k) = \ln(A) - \frac{E_a}{R}\left(\frac{1}{T}\right)$$

Equation 3.46 - Linearised Arrhenius Law

Thermodynamic parameters were determined from using linearised Eyring-Polanyi Equation [527] as given in Equation 3.47. Values of k_B and h are the Boltzmann and Planck constants, taken to be 1.38×10^{11} J/K and 6.626×10^{-23} Js. Activation enthalpy change $\Delta H^{\ddagger}$ in J/mol and activation entropy change $\Delta S^{\ddagger}$ in J/mol·K were used to calculate the activation Gibbs free energy $\Delta G^{\ddagger}$ via Equation 3.48, where ‡ indicates formation of the intermediate transition state. Positive values of $\Delta H^{\ddagger}$ are endothermic and require thermal energy from surroundings while negative values of $\Delta S^{\ddagger}$ are thermodynamically unfavourable as overall total entropy must increase or at least remain constant ($\Delta S \geq 0$). The value of $\Delta G^{\ddagger}$ determines the initial spontaneity of a chemical reaction and positive values indicate energy must be supplied to initiate reaction hence it is non-spontaneous. Since catalytically active acid site concentration was known via pyridine TPD, values of Turnover Number (TON) and Turnover Frequency (TOF) in hr^{-1} were also calculated using Equation 3.49.

$$\ln\left(\frac{k}{T}\right) = -\frac{\Delta H^{\ddagger}}{RT} + \ln\left(\frac{k_B}{h}\right) + \frac{\Delta S^{\ddagger}}{R}$$

Equation 3.47 - Linearised Eyring-Polanyi Equation

$$\Delta G^{\ddagger} = \Delta H^{\ddagger} - T\Delta S^{\ddagger}$$

Equation 3.48 - Gibbs Free Energy Definition

$$TOF = \frac{TON}{Reaction\ Time} = \frac{moles\ Reactant\ \times Yield}{moles\ Catalyst \times Reaction\ Time}$$

Equation 3.49 - Turnover Frequency and Turnover Number

3.6 Materials

A full list of chemicals utilised throughout this work is provided in Table 3.21 with supplier and product specifications where known. Fresh and Degraded UCO were filtered and dried at 100 °C for 4 hours in drying oven prior to use. Deionised water and liquid N_2 were sourced from facilities at University of Leeds SCAPE department. Test reagents BaCl and $AgNO_3$ were prepared in deionised water to 0.1 M concentration. Phenolphthalein indicator and HCl were prepared in ethanol to 0.1 M concentration. Internal standard (IS C19) used in FTIR, GC-MS and NMR analysis was prepared by addition of 1 mg methyl nonadecanoate per 1 mL of n-heptane solvent. Ice bath was prepared by excess addition of NaCl to commercial ice until temperature of -5 °C was reached. All other chemicals were used without further treatment steps unless specified and stored at recommended temperatures in ambient chemical cupboards, refrigerators or freezers.

Table 3.21 - List of Materials

Material	Supplier	Specification
100nm SiO_2	Fiber Optic Center	Angstrom Sphere 0.10 µm
Acetone	Sigma-Aldrich	99.5%
Ammonium Hydroxide Solution	Sigma-Aldrich	28.0-30.0% NH_3
Barium Chloride, Dihydrate	Fisher Scientific	99%
Barley Flour	Elemental Microanalysis	Reference Standard
BBOT	Elemental Microanalysis	Reference Standard
Chlorosulfonic Acid	Sigma-Aldrich	99%
Cystine	Elemental Microanalysis	Reference Standard
Degraded UCO	Local Restaurant	Collected May 2018
Deuterated Chloroform	VWR	99.8%
Ethanol	VWR	99.8%
Ethylene Glycol	Fisher Scientific	95%
Fresh UCO	Local Restaurant	Collected November 2022
Hydrochloric Acid	APC Pure	35.0-36.6%
Ice	Commercial Grade	-
Iron(III) Sulfate Hydrate	Sigma-Aldrich	97%
Methanol	Fisher Scientific	99.8%
Methyl Nonadecanoate	Sigma-Aldrich	98%
Mineral Oil	Commercial Grade	-
n-heptane	Fisher Scientific	99%
Nicotinamide	Elemental Microanalysis	Reference Standard
Oatmeal	Elemental Microanalysis	Reference Standard
Oleic Acid	APC Pure	75%
Phenolphthalein	Sigma-Aldrich	Solid Powder
Potassium Hydroxide	Fisher Scientific	Anhydrous Pellets
Pyridine	Sigma-Aldrich	99.8%
Silver Nitrate	Sigma-Aldrich	99%
Sodium Chloride	Fisher Scientific	99.5%
Sulphanilamide	Elemental Microanalysis	Reference Standard
Tetrahydrofuran	ACROS Organics	99.9%
Titanium(IV) Butoxide	Sigma-Aldrich	97%
Toluene	Fisher Scientific	99.8%
Vegetable Oil	Commercial Grade	-
Zinc Sulfate Heptahydrate	Sigma-Aldrich	99%

Chapter 4.

Chapter 4. Characterisation of Synthesised Novel Nanocatalysts

4.1 Introduction

Following production of six novel nanocatalysts based on the synthesis pathway presented in Chapter 3.2, an extensive range of characterisation methods were employed to investigate each material's chemical nature, structure, morphology, thermal stability and dispersive properties. Throughout Chapter 2, the literature clearly demonstrates how influential these properties can be to achieving desirable catalytic performance. Results from this chapter will therefore begin to indicate which novel nanocatalysts could be superior for production of biodiesel from impure feedstocks. Later results from Chapter 5 and Chapter 6 then serve to experimentally confirm these predictions in batch reaction trials. Chapter 4.2 begins with visual observations made after completion of each synthesis step. Included are pictures of non-functionalised 100nm SiO_2, FeSi, TiFeSi and ZnFeSi supports and the post chlorosulfonic acid treated TiFeSi and ZnFeSi series of nanocatalysts. In Chapter 4.3 the crystallinity of each nanomaterial is investigated through XRD and SAED analysis, with results used to determine nature of crystal phases present and predict crystallite size. Thermal stability is explored in Chapter 4.4 through the application of TGA-DSC technique, with results providing insight into chemical nature and validating suitability for repeated reactions at elevated temperatures. Chapter 4.5 focuses on the surface chemistry responsible for catalytic activity and changes that occur upon functionalisation with chlorosulfonic acid at varying concentrations. FTIR is used to determine sulfate active site structures and hydroxyl groups responsible for catalysing biodiesel formation. Use of pyridine as probe molecule is also investigated to differentiate and quantify Brønsted / Lewis acid site density. NMR is used to detect nature of surface ^1H protons, while XPS explores the bonding of surface elements and quantifies surface composition. In Chapter 4.6 surface area, porosity and pore shape are investigated via N_2 porosimetry through application of BET, BJH and t-plot methodology. SEM / TEM micrographs provide further insight into the morphology of individual nanocatalyst particles and aggregates to confirm core-shell nature and numerically determine size distributions. Bulk elemental composition is measured in Chapter 4.7 through thermal method of CHONS analysis and via EDX spectra obtained during SEM and TEM imaging. Finally, Chapter 4.8 utilises DLS-Zetapotential to explore aggregation behaviour and stability of nanocatalysts in methanol solvent prior to addition of used cooking oil. A summary of key findings is presented at the end of the chapter.

4.2 Visual Observations

Physical appearance of each synthesised support and catalyst material is displayed in Figure 4.1 for SiO_2 (a), FeSi (b), TiFeSi (c), 0.1M-TiFeSi (d), 0.55M-TiFeSi (e), 1.0M-TiFeSi (f), ZnFeSi (g), 0.1M-ZnFeSi (h), 0.55M-ZnFeSi (i) and 1.0M-ZnFeSi (j). Pure SiO_2 is a pure white very fine solid barely visible at the end of the spatula. Upon loading with Fe oxide, the solid appears more aggregated and rusty red hue that does not respond to external magnet, indicating only α-Fe_2O_3 hematite phase was obtained, in absence of Fe(II) precursor or reducing environment [528, 529].

TiFeSi support is a dull off-white colour unlike pure TiO_2 anatase powder which is typically pure white, confirming presence of other elemental species. Upon treatment with chlorosulfonic acid and further calcination a notable colour change occurs. For 0.1M-TiFeSi a dull orange-brown powder is produced, whereas for 0.55M-TiFeSi and 1.0M-TiFeSi the colour becomes darker brown and grey respectively. ZnFeSi support is a light beige-cream colour and similarly not white like pure ZnO confirming presence of other elemental species. For 0.1M-ZnFeSi a dull grey colour is obtained whereas for 0.55M-ZnFeSi and 1.0M-ZnFeSi colour becomes increasingly darker from dark grey to black respectively. This could be due to significant retention of carbon impurities as Zn series of catalyst was much harder to dry due to a thick viscous sol. Alternatively, a darkening in colour with increased chlorosulfonic acid concentration may be due to increased oxygen vacancies created by addition of sulfur species onto metal oxide surface [530, 531].

Overall, each synthesised catalyst has a slightly different colour confirming a variable chemical environment due to individual synthesis conditions. Bulk vials of all Ti and Zn powders are shown in Figure 4.2. No response to strong external magnetic field was detected, likely due to α-Fe_2O_3 hematite phase being too weakly magnetic for obtained particle size in FeSi [532] and low Fe composition in TiFeSi and ZnFeSi discussed later in Chapter 4.7. Future work should focus on including Fe^{2+} salts under N_2 atmosphere or performing reduction steps to achieve maghemite (γ-Fe_2O_3) or magnetite (Fe_3O_4) crystalline forms. High degree of aggregation was observed for all produced powders when left in storage and hence prior to reaction or analysis, sample was reagitated or dispersed via ultrasonic bath as required. Unfortunately, only a small amount of 1.0M-ZnFeSi catalyst was able to be recovered, with higher chlorosulfonic acid concentration leading to reduced solid recovery likely due to acidic digestion. Therefore, throughout this chapter not all characterisation methods were suitable to perform for 1.0M-ZnFeSi material.

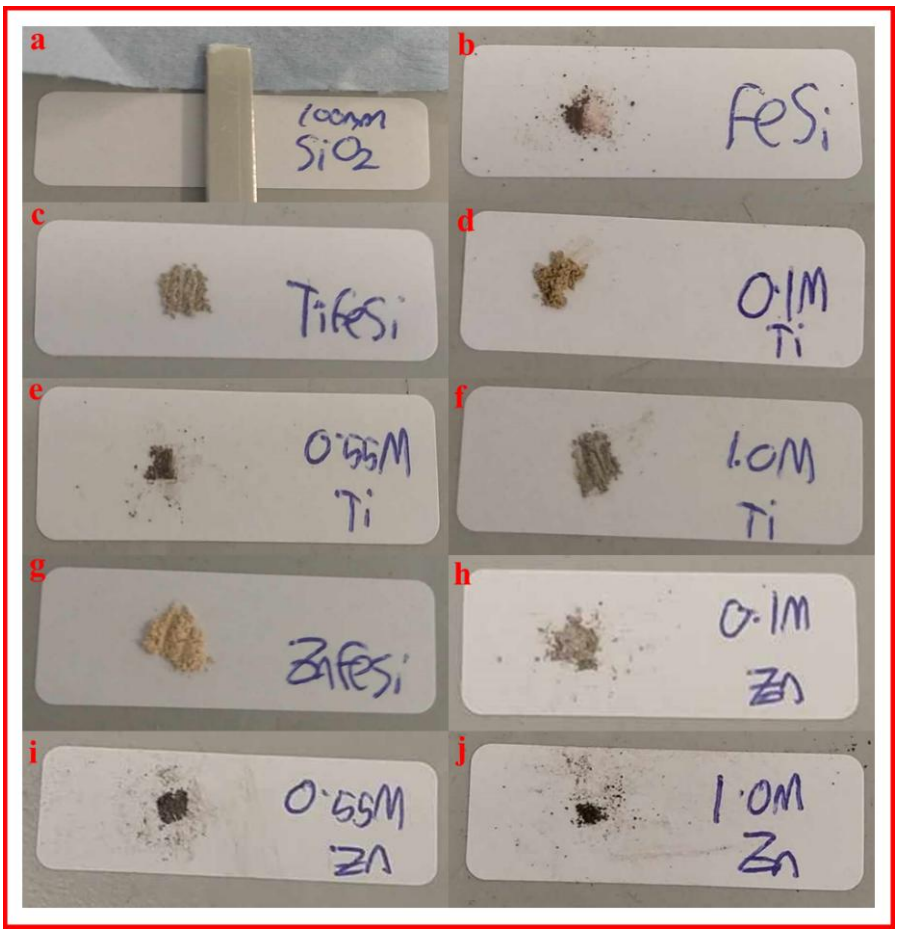

Figure 4.1 - Physical Appearance of Synthesised Support and Catalyst Material

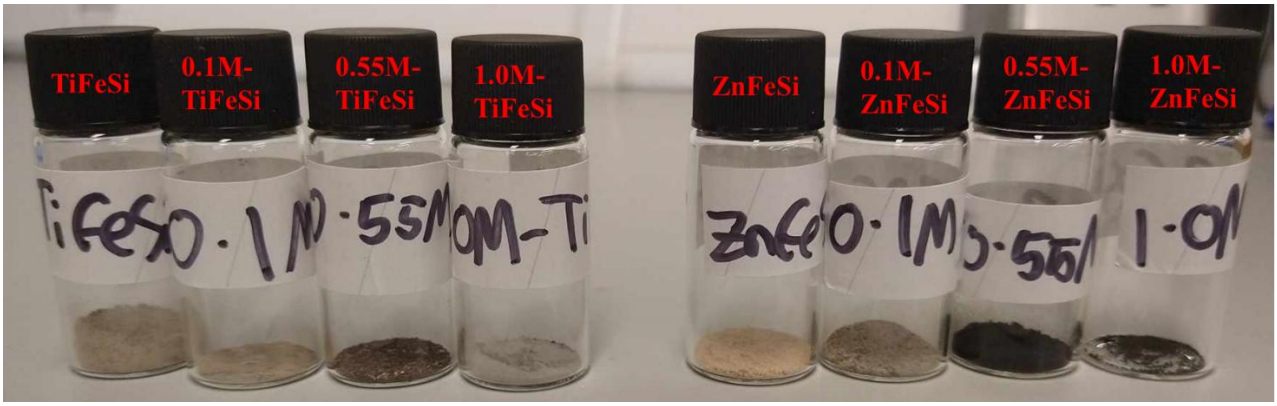

Figure 4.2 - Bulk Samples of Ti Series (Left) and Zn Series (right)

4.3 Crystallinity

4.3.1 X-ray Diffraction

To determine the degree of crystallinity and types of crystal phases present, XRD was performed using Bruker D8. Figure 4.3a-d shows obtained spectra for SiO_2 (a), FeSi (b), TiFeSi (c) and ZnFeSi (d) respectively. The results for SiO_2 and FeSi suggest predominantly amorphous nature due to the typical broad peak shapes caused by lack of long-range order, whereas for TiFeSi and ZnFeSi sharp peaks of high intensity confirm crystalline nature. For SiO_2 the peak at 23.8 ° has been reported as characteristic of amorphous SiO_2 [533-537] with the secondary minor peak at 38.0 ° potentially due to $SiO_2 \cdot nH_2O$ (Opal-CT) hydrated structure [538, 539]. Broad peak shapes in FeSi plot suggests that instead of forming fully crystalline phase, Fe species have been distributed into the surface SiO_2 pore structure with only short-range order. Prior work has reported similar observations of amorphous Fe-Si and Fe hydrate formation [540, 541]. Significant reduction of the broad peak at 23.8 ° validates possible integration of Fe into SiO_2 structure. Semi-crystallinity at 33.5 °, 36.0 ° and 54.1 ° may be attributed to 104, 110 and 116 planes of α-Fe_2O_3 (hematite) [542, 543]. Although peak overlap with Fe_3O_4 (magnetite) and γ-Fe_2O_3 (maghemite) may occur at 36.0 ° and 54.1 °, overall lack of magnetic response and 33.5 ° peak makes α-Fe_2O_3 most likely. Successful loading of Fe onto SiO_2 support is confirmed, as an incorporated Fe-SiO_2 hydrated semicrystalline material with underlying α-Fe_2O_3 planes indicative of Fe(III) oxide.

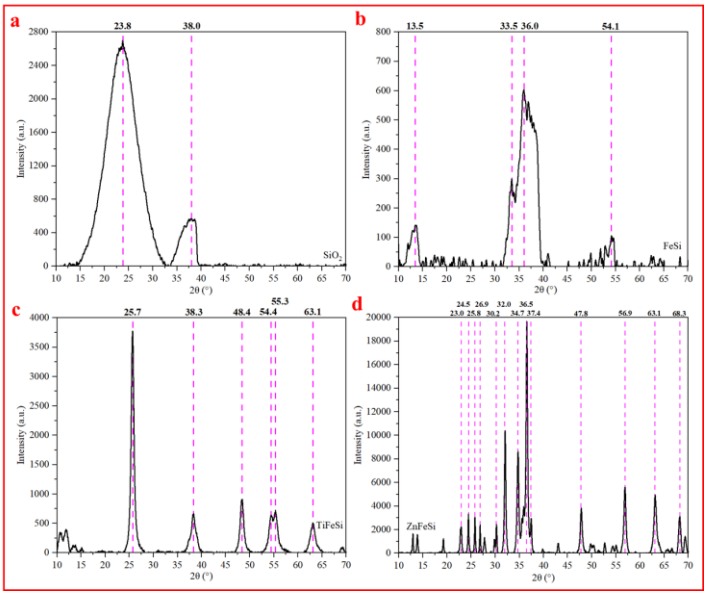

Figure 4.3 - XRD Spectra for SiO_2 (a), FeSi (b), TiFeSi (c) and ZnFeSi (d) Supports

TiFeSi support exhibits strong crystallinity with peaks at 25.7 °, 38.3 °, 48.4 °, 54.4 °, 55.3 ° and 63.1 ° corresponding to 101, 004, 200, 105, 211 and 204 planes for anatase TiO_2 crystals. Presence of these peaks confirms that a calcination temperature of 400 °C was successful in preventing thermal rearrangement to less desirable rutile phase. Plane 004 was excluded from crystallite size calculation due to being an outlier, likely from interference of peak at similar position in SiO_2 and FeSi material. ZnFeSi support also exhibited strong crystallinity with major peaks at 32.0 °, 34.7 °, 36.5 °, 47.8 °, 56.9 °, 63.1 ° attributed to 100, 002, 101, 102, 110 and 103 planes for hexagonal Wurtzite ZnO. Presence of other minor peaks at 23.0 °, 24.5 °, 25.8 °, 26.9 °, 30.2 ° and 37.4 ° are likely detections from hydrated $Zn(OH)_2$ phases [544-546] or residual $ZnSO_4$ precursor [547] alongside SiO_2 and FeSi support material present in ZnFeSi, while peak at 68.3 ° could be attributed to 112 plane in ZnO but was not included in average crystallite size calculations due to small peak area increasing error. A summary of major peaks, interplanar spacings and crystallite size calculated via Debye-Scherrer equation for TiFeSi and ZnFeSi is given in Table 4.1. Experimental values for interplanar spacings agree closely with literature values [548-550]. Average crystallite sizes are 9.95 nm and 20.1 nm for TiFeSi and ZnFeSi respectively. These values are below STEM results in Chapter 4.6 suggesting multiple crystallites form each particle.

Table 4.1 - Interplanar Spacings and Crystallite Sizes for TiFeSi and ZnFeSi

Sample	Plane	2θ (°)	Intensity (a.u.)	FWHM (°)	d_{hkl} Exp. and Lit. (Å)		D (nm)
TiFeSi	101	25.7	3772	0.68	3.46	3.52	12.0
TiFeSi	200	48.4	909	0.83	1.88	1.89	10.5
TiFeSi	105	54.4	640	0.83	1.68	1.70	10.8
TiFeSi	211	55.3	722	1.06	1.66	1.67	8.44
TiFeSi	204	63.1	508	1.17	1.47	1.48	7.97
ZnFeSi	100	32.0	10378	0.32	2.79	2.82	25.4
ZnFeSi	002	34.7	8631	0.42	2.58	2.61	20.0
ZnFeSi	101	36.5	19667	0.37	2.46	2.48	22.5
ZnFeSi	102	47.8	3823	0.45	1.90	1.91	19.1
ZnFeSi	110	56.9	5594	0.49	1.62	1.63	18.4
ZnFeSi	103	63.1	4931	0.62	1.47	1.48	15.1

Post acid functionalisation more XRD spectra were taken to monitor changes in crystallinity, these results are shown in Figure 4.4a and Figure 4.4b for Ti and Zn series respectively. Plots have been rescaled to account for varying maximum intensity based on available sample mass analysed. High degree of anatase crystallinity was maintained for Ti series even under harsh 1.0 M chlorosulfonic acid treatment and an additional calcination step, confirming that crystal structure had not been destroyed or modified during acid site loading. Calculated interplanar spacings and crystallite diameters are included in Table 4.2 and values of d_{hkl} remained consistent within experimental error. Average crystallite size increased slightly from 9.95 nm for TiFeSi support to 11.2 nm, 10.4 nm and 11.0 nm for 0.1M-TiFeSi, 0.55M-TiFeSi and 1.0M-TiFeSi respectively. In all cases, treatment with chlorosulfonic acid led to slight increase in crystallite size. Since interplanar spacings remained consistent this result is not due to unit cell modification. Instead, average size increase likely occurred due to growth effects from acid treatment and further calcination.

A very different result was observed for the Zn series of catalyst. Large reduction of hexagonal Wurtzite ZnO peaks can be observed as well as the formation of new peaks at lower values of 2θ corresponding to increased interplanar spacings. These new peaks are indicated in cyan and are also present in ZnFeSi support material as minor crystalline phase. Later work in Chapter 4.5 confirms enhancement of -OH acidic hydroxyl groups on metal oxide surface post functionalisation, hence these new peaks are likely a hydrated form of ZnO which also explains the reduction of sharp peaks for hexagonal Wurtzite dry ZnO phase. Comparison with literature [544, 546, 547] confirms that peaks at similar 2θ values have been reported for $Zn(OH)_2$ species, with values at 16.6 °, 17.7 °, 19.2 °, 23.0 °, 25.8 ° and 26.9 ° potentially a result of γ-$Zn(OH)_2$, ε-$Zn(OH)_2$, $Zn(OH)_2.0.5H_2O$ or $ZnSO_4$ crystal planes. Calculated interplanar spacings and crystallite diameters for the new peaks observed in functionalised ZnFeSi catalyst are given in Table 4.3. Interplanar spacings increased due to larger unit cell configuration of a hydrated $Zn(OH)_2$ structure as compared to ZnO. Interestingly, average crystallite size varied from 20.1 nm for ZnFeSi support to 16.7 nm and 24.7 nm for 0.1M-ZnFeSi and 0.55M-ZnFeSi respectively, excluding outlier broad peaks with very small and large crystallite size values. Variation in crystallite sizes is likely due to averaged effects of phase transitions and reorientation from ZnO to hydrated $Zn(OH)_2$ structures alongside crystallite growth from acid functionalisation and further calcination steps. Overall, it can be seen that crystal structure is maintained for both Ti and Zn series post acid treatment, however Zn series sees more dramatic change in crystal phase transitions compared to Ti series.

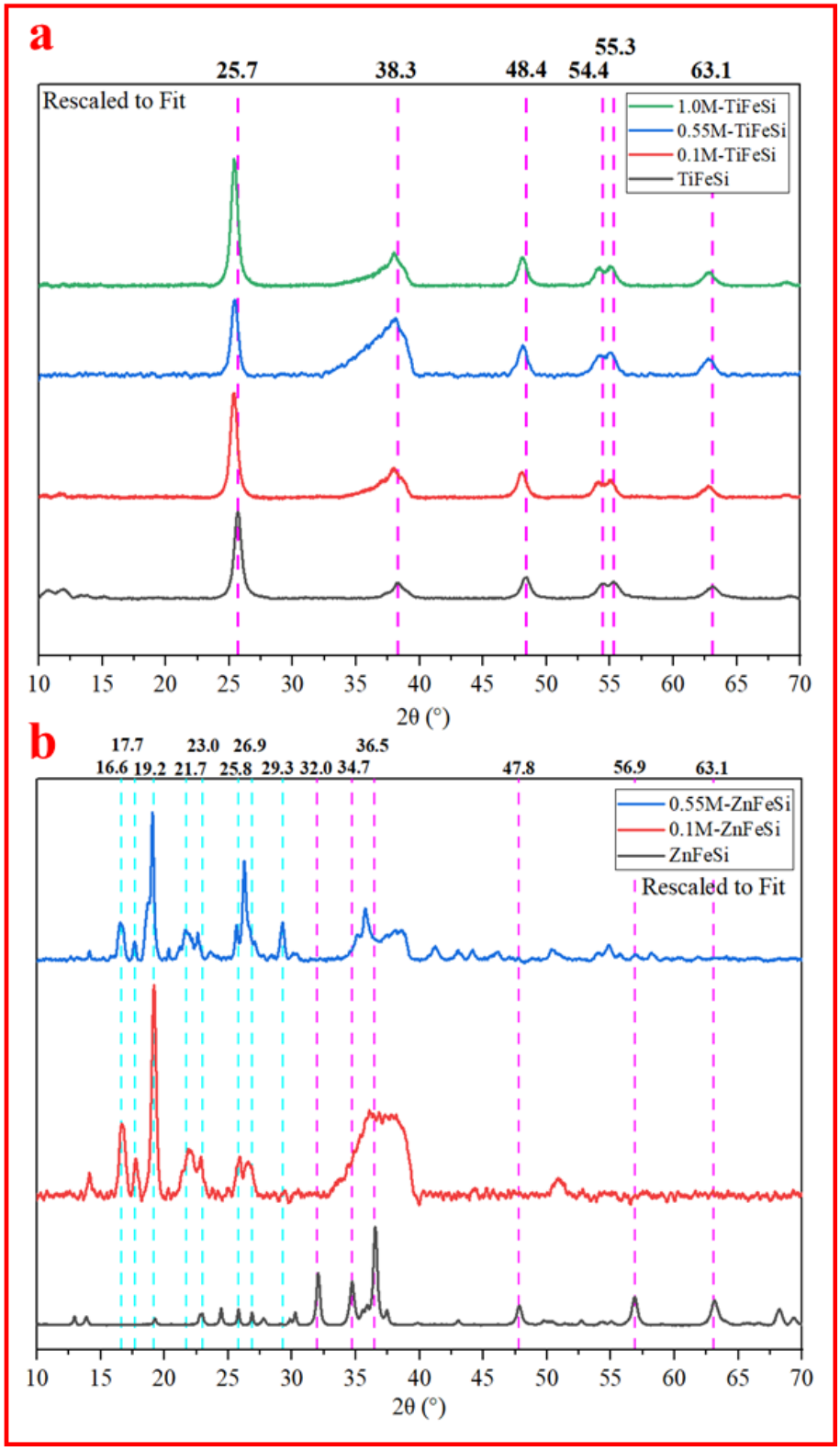

Figure 4.4 - XRD Spectra for Ti Series (a) and Zn Series (b)

Table 4.2 - Comparison of Interplanar Spacings and Crystallite Sizes for TiFeSi Series

Plane	d_{hkl} (Å)				D (nm)			
	TiFeSi	0.1M-TiFeSi	0.55M-TiFeSi	1.0M-TiFeSi	TiFeSi	0.1M-TiFeSi	0.55M-TiFeSi	1.0M-TiFeSi
101	3.46	3.50	3.50	3.51	12.0	12.7	12.6	12.9
200	1.88	1.89	1.89	1.89	10.5	10.7	10.9	10.8
105	1.68	1.69	1.69	1.69	10.8	13.6	8.54	12.5
211	1.66	1.67	1.67	1.67	8.44	8.6	10.6	8.89
204	1.47	1.48	1.48	1.48	7.97	10.4	9.39	9.75
Average	-	-	-	-	9.95	11.2	10.4	11.0

Table 4.3 - New Crystal Phases for 0.1M-ZnFeSi and 0.55M-ZnFeSi Catalysts

2θ (°)	d_{hkl} (Å)		D (nm)	
	0.1M-ZnFeSi	0.55M-ZnFeSi	0.1M-ZnFeSi	0.55M-ZnFeSi
16.6	5.32	5.36	14.2	15.1
17.7	4.99	5.02	23.0	30.1
19.2	4.62	4.65	19.9	29.5
23.0	3.88	3.93	16.8	22.6
25.8	3.44	3.47	16.2	27.9
26.9	3.35	3.39	9.92	22.8
Average	-	-	16.7	24.7

4.3.2 Selected Area Electron Diffraction

Selected area electron diffraction patterns were taken for Ti series of nanocatalysts using Tensor Tescan system to further validate XRD results. Diffraction patterns are illustrated for 0.1M-TiFeSi (Figure 4.5a-d), 0.55M-TiFeSi (Figure 4.5e-h) and 1.0M-TiFeSi (Figure 4.5i-l) respectively. All nanocatalysts exhibited strong degree of polycrystallinity as indicated by ring diffraction patterns. Evidence of amorphous structure and singular crystals near nanocatalyst surface was also noted by diffuse halos and repeating grid of diffraction spots as observed especially in Figure 4.5h and Figure 4.5l. ImageJ software was used to measure diffraction ring radius and calculate approximate d-spacings as discussed in Chapter 3.3.1 to identify predominant crystalline phase that was present.

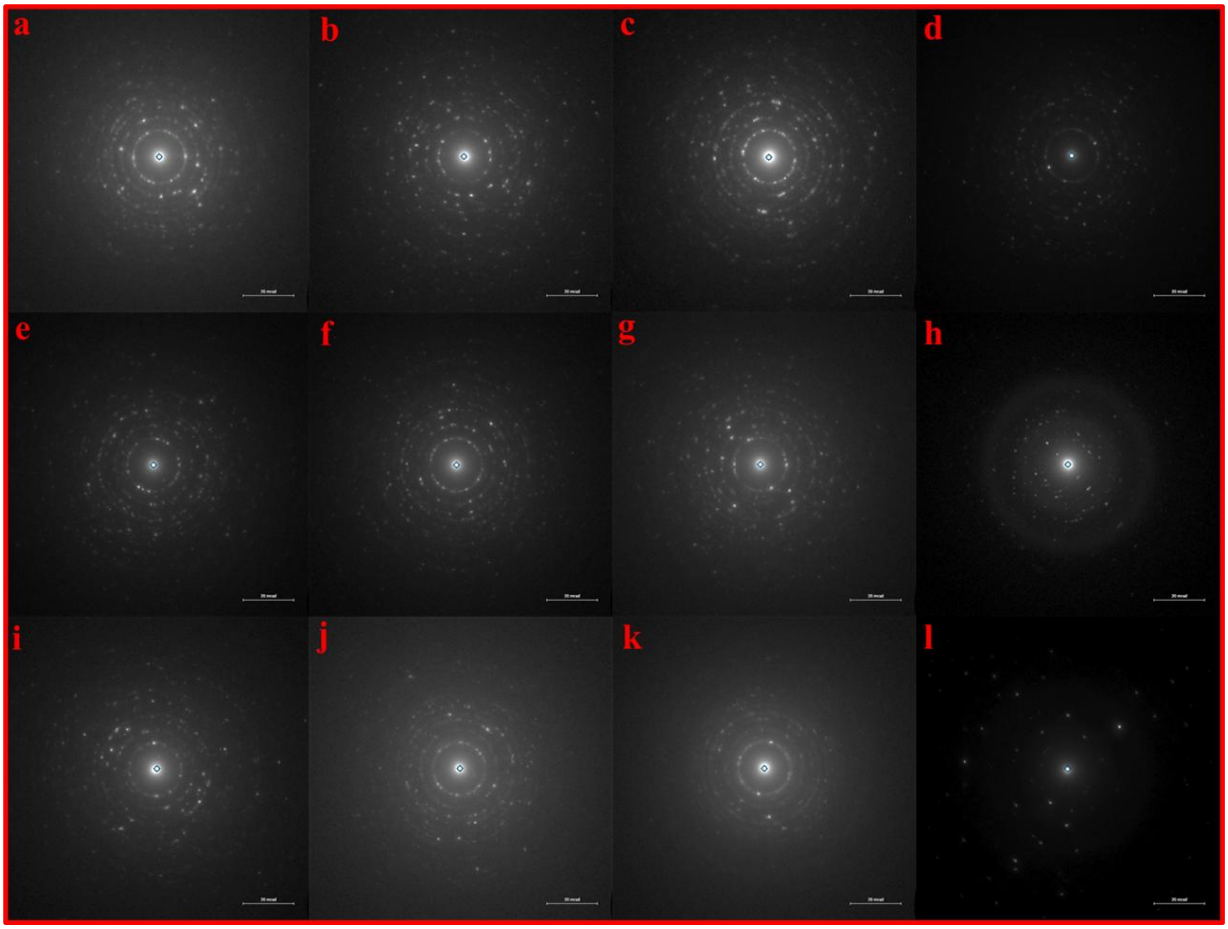

Figure 4.5 - SAED Patterns for 0.1M-TiFeSi (a-d), 0.55M-TiFeSi (e-h), 1.0M-TiFeSi (i-l)

ImageJ analysis results are summarised in Figure 4.6 for SAED patterns shown in Figure 4.5c,f,i. Innermost ring had d-spacing of approximately 3.5 Å corresponding to 101 plane of anatase form of titania. Outer rings had measured d-spacings of approximately 2.4 Å, 1.9 Å and 1.7 Å likely corresponding to 004, 200 and 105 planes of anatase titania. Lack of rutile diffraction rings was noted. Additional minor diffraction spots were observed, possibly due to presence of Fe species, however resolution was too low to determine with confidence. Results from SAED analysis strongly agrees with prior XRD spectra as should be expected.

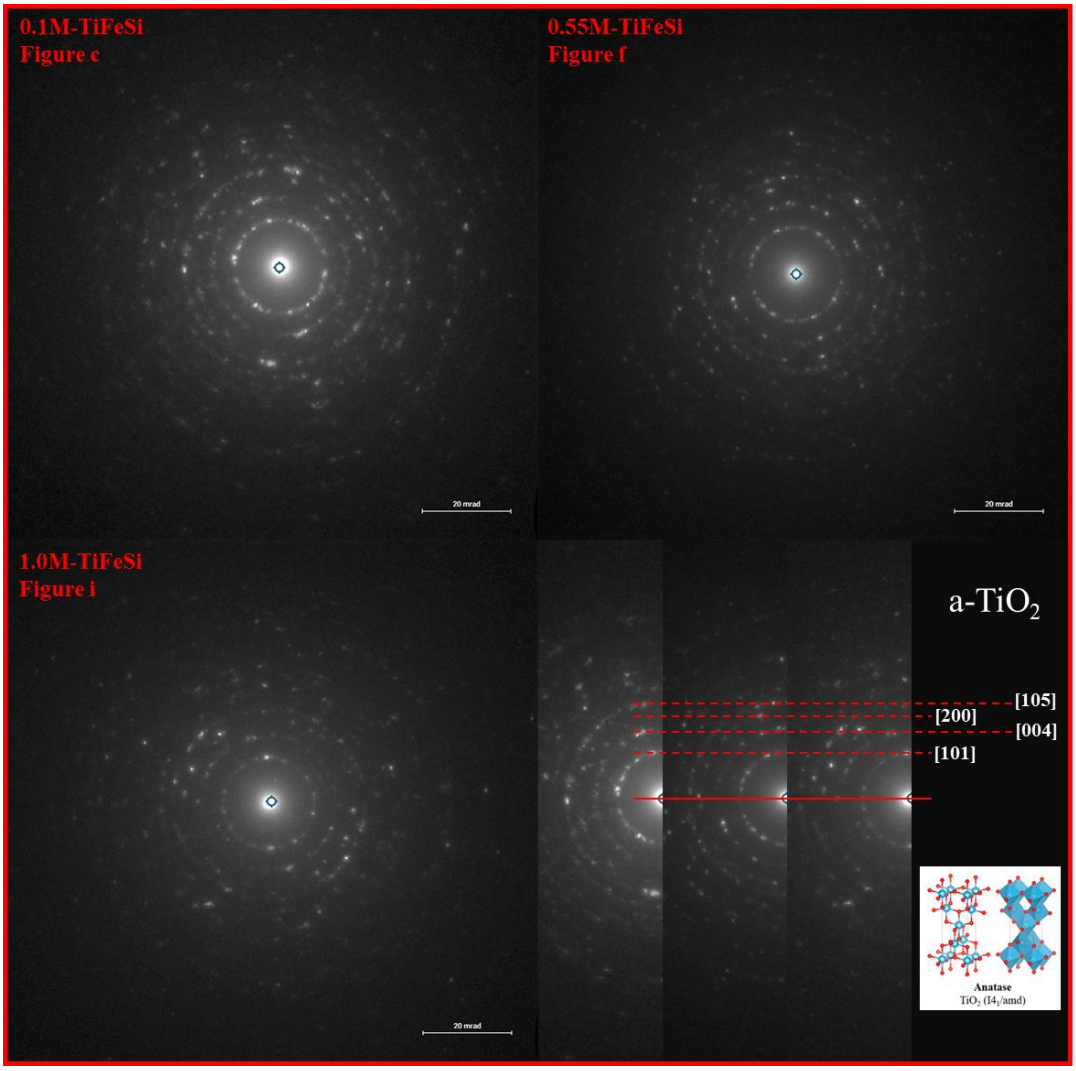

Figure 4.6 - SAED Patterns Indicating Anatase Titania as Primary Crystalline Phase

4.4 Thermal Stability

TGA-DSC analysis was performed to assess thermal stability of catalysts pre and post acid functionalisation via Mettler Toledo instrument. Results for non-functionalised support are plotted in Figure 4.7 and major mass changes are summarised in Table 4.4 where T_1, T_2 and T_{max} represent initial, final and peak temperatures. Total mass loss from ambient to 900 °C for SiO_2, FeSi, TiFeSi and ZnFeSi were 9.37 wt%, 23.8 wt%, 3.14 wt% and 18.9 wt%, respectively, indicating that TiFeSi support was significantly more thermally stable. Initial mass losses <200 °C are attributed to bound water, residual solvent and physically adsorbed gases removed on heating, explaining endothermic nature of DSC curve due to bond breakage. Mass losses between 200-500 °C may be attributed to exothermic recrystallisation transition of amorphous Fe-SiO_2 hydrate into α-Fe_2O_3 hematite phase as well as endothermic removal of weakly bound hydroxyls or sulfate precursor groups not removed during calcination. Above 500 °C highly endothermic behaviour is evidence of decomposition of more strongly bound sulfate functional groups and reduction of metal oxides. For FeSi, sharp endothermic peak at 612 °C could be due to Curie phase transition of FeSi (~680 °C for pure α-Fe_2O_3 hematite phase) [551, 552] leading to loss of magnetic order. For ZnFeSi, sharp endothermic peak at 804 °C may be due to thermal decomposition of $ZnSO_4$ precursor or sulfated ZnO material [553, 554].

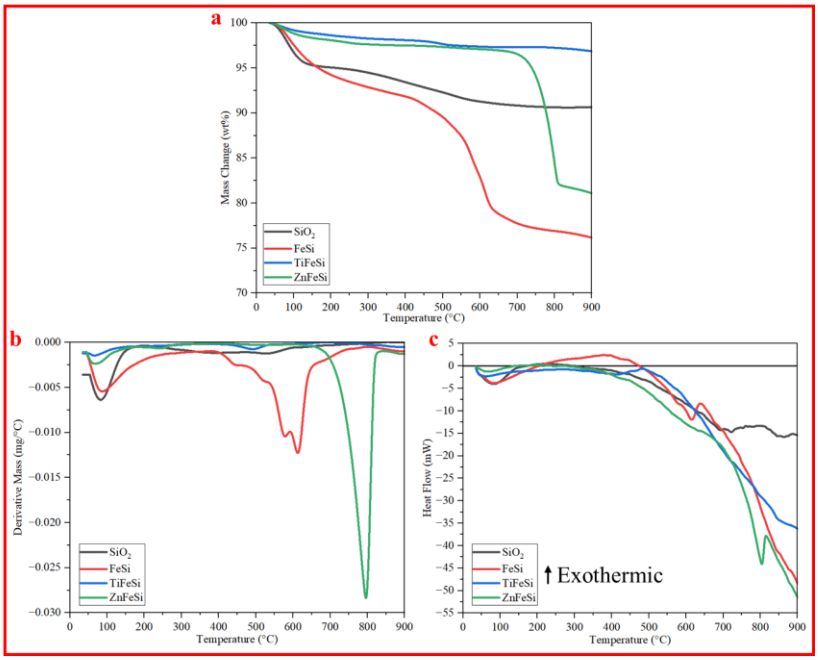

Figure 4.7 - TGA (a), DTG (b) and DSC (c) plots for Support Materials

Table 4.4 - Summary of Mass Losses for Support Materials

Sample	T_1 (°C)	T_2 (°C)	T_{max} (°C)	ΔM (wt%)
SiO_2	35	199	83	4.93
	199	471	394	2.44
	471	854	527	2.00
FeSi	35	380	87	7.96
	380	591	579	8.29
	591	795	612	6.83
	795	889	888	0.66
TiFeSi	35	163	66	1.19
	163	370	183	0.66
	370	688	492	0.83
	688	880	880	0.35
ZnFeSi	35	390	68	2.48
	390	843	796	15.8
	843	888	888	0.46

Post acid functionalisation results for Ti and Zn series are displayed in Figure 4.8 and Figure 4.9 respectively with major mass changes summarised in Table 4.5 and Table 4.6. Total mass loss from ambient to 900 °C for Ti series were 10.0 wt%, 13.8 wt% and 10.4 wt% for 0.1 M, 0.55 M and 1.0 M chlorosulfonic acid concentration, whereas for Zn series total mass losses were 68.7 wt%, 58.3 wt% and 53.9 wt% for 0.1 M, 0.55 M and 1.0 M concentration. The Ti series of catalysts were significantly more thermally stable compared to the Zn series. This is likely a result of both residual zinc sulfate precursor contamination increasing sulfur content and increased hydration of ZnO phase from challenges of drying a thicker sol post acid treatment. Presence of new mass loss peaks in DTG plot indicates sulfate groups were successfully introduced post functionalisation and thermally decompose to release SO_x gases on heating. In Ti series, 0.55M-TiFeSi catalyst had greatest overall mass loss likely indicating highest loading of sulfate groups which agrees with other composition analyses performed in Chapter 4.7. For Zn series however, 0.1M-ZnFeSi catalyst had greatest mass loss despite lowest loading of sulfate as confirmed in later composition analysis. Cause of this is likely due to reduced thermal stability produced at lower concentrations of chlorosulfonic acid treatment. Strength of acid site binding to the surface can be correlated to decomposition temperature and hence more mass loss could be observed for weaker bound sulfate.

Observing the DTG results for both Ti and Zn series it can be seen that decomposition temperature of likely acidic sulfate groups shifts to higher values with increasing chlorosulfonic acid concentration. For Ti series, mass losses above 500 °C were 2.17 wt%, 3.89 wt% and 5.62 wt% for 0.1M-TiFeSi, 0.55M-TiFeSi and 1.0M-TiFeSi confirming that with higher chlorosulfonic acid concentration mass losses are shifted to occur at higher temperatures. Similar trend is seen for Zn series with mass losses above 500 °C of 26.1 wt%, 27.6 wt% and 31.0 wt% for 0.1M-ZnFeSi, 0.55M-ZnFeSi and 1.0M-ZnFeSi, respectively. Furthermore, in Table 4.5 peak mass loss for sulfate group occurs at 461 °C and 470 °C for 0.1M-TiFeSi and 0.55M-TiFeSi indicating enhancement in medium strength acid site stability. For 1.0M-TiFeSi however, peaks at both 461 °C and 633 °C can be observed suggesting existence of medium and strongly bound sulfate groups. Treatment with higher concentration of chlorosulfonic acid may not have increased quantity of sulfate sites loaded onto 1.0M-TiFeSi as indicated in later composition analysis, however thermal stability does appear improved. Similar trend is observed in Table 4.6 with likely sulfate peak decomposition temperatures of 469 °C and 561 °C for 0.1M-ZnFeSi compared to 464 °C, 515 °C and 569 °C for 0.55M-ZnFeSi showing development of new sulfate sites with varying binding strength to surface. Then for 1.0M-ZnFeSi the decomposition temperature increases to 470 °C, 549 °C and 584 °C confirming that higher concentration of chlorosulfonic acid treatment leads to sulfate groups more strongly bonded to the surface. This could be due to reorientation of surface sulfate groups into more stable bidentate structures of increasing acid strength as a higher concentration of chlorosulfonic acid is used during synthesis, as noted in previous work [555] and discussed further in Chapter 4.5.1 via ATR-FTIR analysis. Finally, results from DSC indicate significant exothermic recrystallisation in Zn series [556-559]. Beyond 500 °C only endothermic processes were observed in Ti series corresponding to sulfate bond breakage. Interestingly large exothermic processes continued in Zn series even up to 800 °C indicating the significant hydration that may have been present. This has also been indicated by XRD analysis in Chapter 4.3.1 where dramatic change in crystal structure from ZnO hexagonal wurtzite to hydrated $Zn(OH)_2$ phases post acid treatment was noted. Therefore, large exothermic peak observed from 500-900 °C might be the result of competing effects of energy taken in to break sulfate groups and melt precursor material versus energy released during recrystallization back to ZnO wurtzite structure. Similar to ZnFeSi however, DSC curve eventually becomes endothermic beyond 800 °C as $ZnSO_4$ or sulfated ZnO species are completely thermally decomposed.

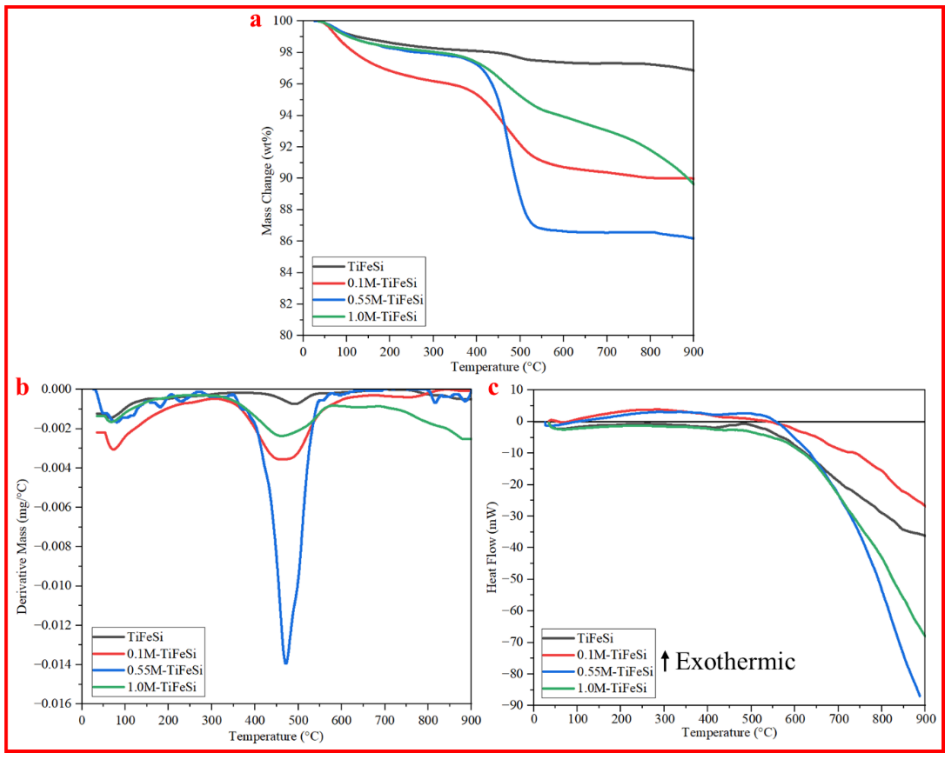

Figure 4.8 - TGA (a), DTG (b) and DSC (c) plots for Ti Series

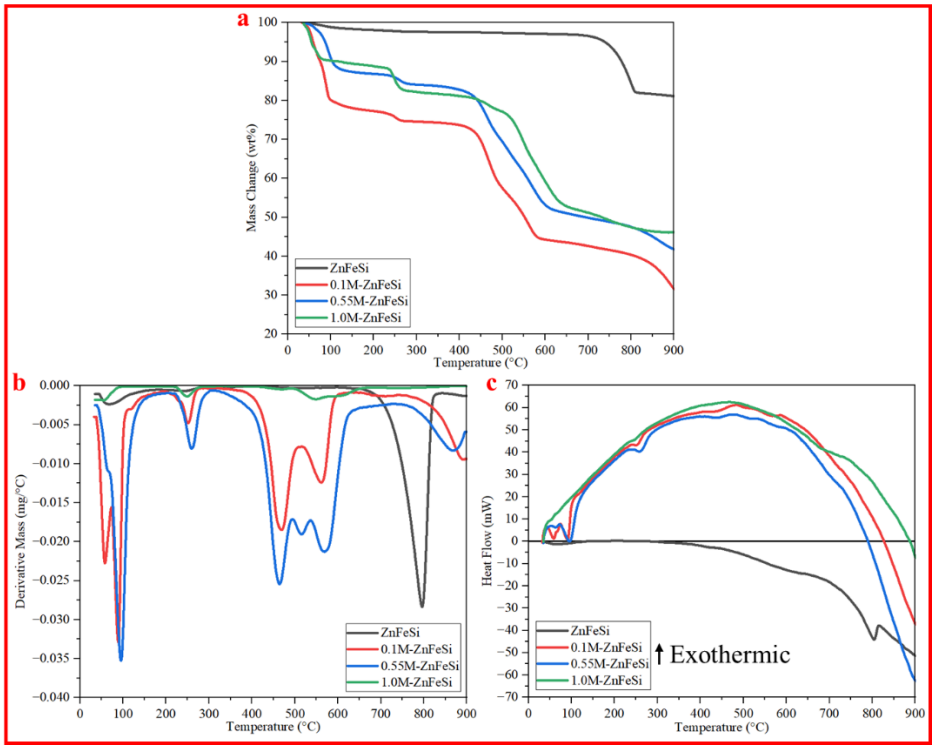

Figure 4.9 - TGA (a), DTG (b) and DSC (c) plots for Zn Series

Table 4.5 - Summary of Mass Losses for TiFeSi Functionalised Catalysts

Sample	T_1 (°C)	T_2 (°C)	T_{max} (°C)	ΔM (wt%)
0.1M-TiFeSi	35	307	73	3.84
	307	677	461	5.71
	677	880	753	0.44
0.55M-TiFeSi	28	264	80	1.98
	264	703	470	11.5
	703	900	814	0.36
1.0M-TiFeSi	35	266	68	1.85
	266	582	461	4.07
	582	685	633	0.91
	685	879	879	2.98

Table 4.6 - Summary of Mass Losses for ZnFeSi Functionalised Catalysts

Sample	T_1 (°C)	T_2 (°C)	T_{max} (°C)	ΔM (wt%)
0.1M-ZnFeSi	33	73	58	9.34
	73	193	89	13.3
	193	307	252	2.82
	307	517	469	19.2
	517	630	561	11.6
	630	896	893	11.7
0.55M-ZnFeSi	35	209	95	13.3
	209	304	260	2.71
	304	494	464	13.7
	494	536	515	6.65
	536	728	569	14.4
	728	896	868	7.31
1.0M-ZnFeSi	35	178	55	10.9
	178	370	249	7.61
	370	492	470	4.00
	492	581	549	14.7
	581	688	584	11.2
	688	886	741	5.40

4.5 Surface Chemistry

4.5.1 Attenuated Total Reflection Fourier Transform Infrared Spectroscopy

ATR-FTIR was performed instead of transmission method to determine functional groups present near to catalyst surface. Figure 4.10a shows obtained spectra for the non-functionalised supports. Presence of hydroxyl -OH groups were clearly observed between ~2800-3600 cm^{-1} for SiO_2, FeSi and ZnFeSi with slight absorption at ~1630 cm^{-1} attributed to bound water hydrate. For TiFeSi only very slight absorption of -OH and bound water was detected, likely due to more effective drying of TiFeSi material during calcination and vacuum oven steps. For SiO_2, peaks at 940 cm^{-1} and 1100 cm^{-1} were attributed to Si-OH and Si-O-Si respectively [560, 561]. In FeSi a broad peak from 850-1300 cm^{-1} could be deconvoluted into three minor peaks of 940 cm^{-1}, 1060 cm^{-1} and 1200 cm^{-1} suggesting presence of Si-O-Si, S-O and S=O peaks respectively [562-565] and confirming not all sulfate had been removed from precursor. Similarly, peaks at 1040 cm^{-1}, 1080 cm^{-1}, 1170 cm^{-1} and 1210 cm^{-1} for ZnFeSi indicate unremoved zinc sulfate S-O and S=O peaks [204]. Figure 4.10b shows the spectra for TiFeSi series of functionalised catalysts. New peaks appearing at 990 cm^{-1} and 1040 cm^{-1} for S-O stretch and 1120 cm^{-1} and 1200 cm^{-1} for S=O stretch confirms treatment with chlorosulfonic acid successfully loaded surface with sulfate groups. Broad peak between ~2800-3600 cm^{-1} and absorption at ~1630 cm^{-1} confirms presence of -OH and bound H_2O respectively. The lack of surface hydroxyls for 1.0M-TiFeSi could be due to excess chlorosulfonic acid protonating these sites into bound hydrate. Similar results to Ti series were observed in functionalised Zn series as shown in Figure 4.10c and extra peak at ~865 cm^{-1} may be due to toluene impurity. Clearer splitting of S-O peaks between 1010-1040 cm^{-1} and addition of H_2O and further -OH groups indicates surface chemistry changes in Zn series post acid treatment.

For both TiFeSi and ZnFeSi series, observed triplet splitting of asymmetric sulfate stretch suggests bidentate C_{2v} surface structure [377, 566-568]. Bridging (binuclear) bidentate structures are reported at slightly lower wavenumbers than chelating (mononuclear) structure, hence considering the slightly lower energy peaks observed in Figure 4.10 sulfate likely possesses a predominantly bridged bidentate surface chemistry. It is noted in literature [569] that increasing sulfur loading favours formation of polynuclear sulfates detectable between 1300-1400 cm^{-1} but no evidence of this is seen for either TiFeSi or ZnFeSi series. Sulfur surface loading was hence sufficient to produce bidentate bridged structures but low enough to prevent $S_2O_7^{2-}$ and $S_3O_{10}^{2-}$ site formation.

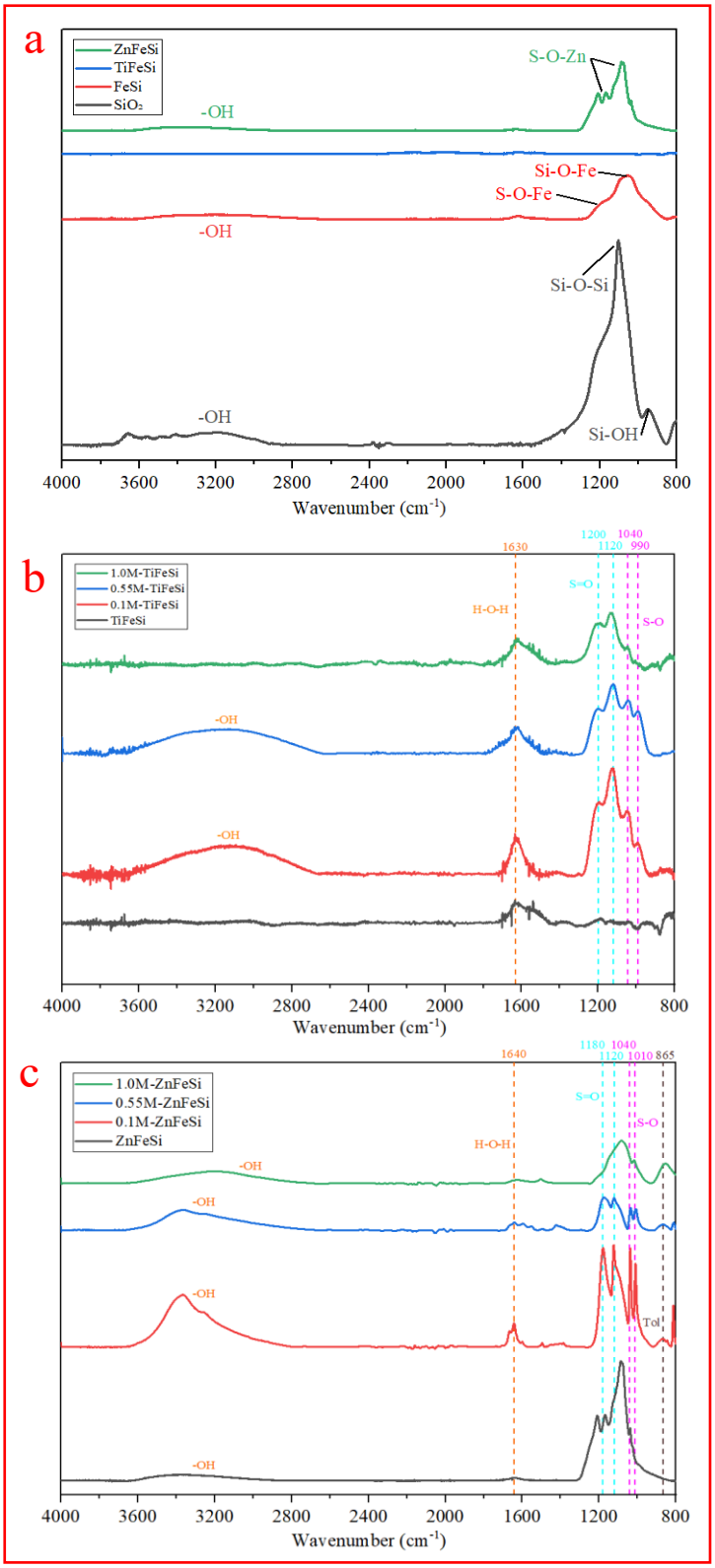

Figure 4.10 – ATR-FTIR Spectra of Catalyst Supports (a), TiFeSi Series (b), ZnFeSi Series (c)

4.5.2 Pyridine Temperature Programmed Desorption

To understand the type of acidity present in support and catalyst materials, pyridine temperature programmed desorption was performed using ATR-FTIR to quantify remaining pyridine loading post calcination. At 150 °C calcination temperature presence of weak, medium and strong acidic sites could be observed whereas at 350 °C remaining pyridine would only be bound to strong acidic sites. Obtained plots are shown in Figure 4.11 for support materials (a, b), Ti series (c, d) and Zn series (e, f) for 150 °C and 350 °C respectively. Peaks between 1420-1450 cm^{-1} are attributed to Lewis acid bound pyridine while peaks between 1530-1560 cm^{-1} are attributed to Brønsted acid bound pyridine. These major peaks of interest were used to calculate Lewis and Brønsted site density as summarised in Table 4.7. Intermediate peaks between 1480-1490 cm^{-1} can be observed and are due to a combination of Lewis-Brønsted site binding. While literature has also confirmed pyridine binding to Lewis and Brønsted acid sites within 1600-1640 cm^{-1} region [402, 570], it is known that bound water can also be observed here as discussed in Chapter 4.5.1 and so these peaks were unable to be uniquely attributed to pyridine chemisorption. For similar reasons, quantitative results were not fully determinable for Zn series of catalyst due to likely misattribution of pyridine detection with toluene impurity suspected of remaining from functionalisation step.

For SiO_2 no additional peaks within 1420-1560 cm^{-1} could be observed suggesting lack of acidic sites strong enough to interact with pyridine. Slight Brønsted acidity of 0.64 mmol/g was noted for FeSi of which 0.45 mmol/g was strongly acidic, this is likely due to sulfate left over from precursor. Lewis acidity of FeSi dominates at weak-medium strength but similar amounts of Brønsted and Lewis acidity is observed at high strength. TiFeSi support was seen to be purely Lewis acidic in nature, potentially due to reduced level of sulfur impurities as compared to FeSi hence no Brønsted activity. Strong acidity ratio of 0.99 for TiFeSi indicates that all Lewis sites are strongly acidic in nature. ZnFeSi was also observed to contain only Lewis acidic sites, however a quarter were weak to medium strength. This result is expected due to amphoteric nature of ZnO leading to weaker acidity as compared to TiO_2 support. In Figure 4.11c-d appearance of new peaks between 1488-1540 cm^{-1} confirms that acidification with chlorosulfonic acid led to development of Brønsted site activity. Disappearance of peak at 1446 cm^{-1} for Ti series catalysts confirms that main interacting sites on surface are Brønsted acidic in nature. It is likely that not all Lewis sites were converted, for instance within pore structures or regions of lower sulfur loading, however predominant surface chemistry for Ti series interacting with pyridine is notably via Brønsted acid route.

Increasing chlorosulfonic acid concentration from 0.1 M to 0.55 M increases the Brønsted site density from 2.08 mmol/g to 2.70 mmol/g however on further increase to 1.0 M the Brønsted site density then falls down to 0.67 mmol/g which is in agreement with CHONS and EDX results of sulfur loading trend achieved in Chapter 4.7. Strong acidity ratio increases from 0.39 for 0.1M-TiFeSi to 0.48 for 0.55M-TiFesi and finally to 0.98 for 1.0M-TiFeSi. While highest chlorosulfonic acid concentration did not lead to enhanced sulfur loading, a notable shift in acidic site strength can be observed. This agrees with Chapter 4.4 where most thermally stable bound sulfate was observed for 1.0M-TiFeSi and could be due to formation of more stabilised bidentate sulfate [555]. While quantitative analysis of Zn series is not possible within Lewis acid region due to potential influence of toluene impurity at values of 1449 cm^{-1}, 1490 cm^{-1} and 1609 cm^{-1}, it was noted in Figure 4.11e-f that enhancement of Brønsted acid peak at 1551 cm^{-1} was obtained upon treatment at 350 °C that could be uniquely attributed to pyridine binding. Site density increased from 0.89 mmol/g to 1.71 mmol/g for 0.1M-ZnFeSi and from 2.26 mmol/g to 4.93 mmol/g for 0.55M-ZnFeSi which would suggest considerable site density and more concerningly, very high strong acid ratio of 1.92 and 2.18 respectively. This is unlikely to be the case since at 350 °C only strong sites are measured compared to weak-strong sites at 150 °C, so this ratio must be strictly ≤ 1. Evidence from XRD analysis in Chapter 4.3.1 suggests that ZnFeSi post acid functionalisation took on a hydrated $Zn(OH)_2$ structure, therefore at recalcination at 350 °C it is possible that bound water species on $Zn(OH)_2$ convert into stronger Brønsted acidic hydroxyls on ZnO, reducing the water peak at 1644-1665 cm^{-1} and causing pyridine to chemisorb at 1551 cm^{-1} to new Brønsted acid sites.

Table 4.7 - Pyridine Temperature Programmed Desorption Calculated Site Densities

Sample	Weak-Strong Acid Sites (T = 150 °C)			Strong Acid Sites (T = 350 °C)			Strong Acidity Ratio
	Brønsted (mmol/g)	Lewis (mmol/g)	Total (mmol/g)	Brønsted (mmol/g)	Lewis (mmol/g)	Total (mmol/g)	
SiO_2	0.00	0.00	0.00	0.00	0.00	0.00	0.00
FeSi	0.64	2.00	2.63	0.45	0.51	0.95	0.36
TiFeSi	0.00	0.33	0.33	0.00	0.33	0.33	0.99
ZnFeSi	0.00	1.03	1.03	0.00	0.77	0.77	0.75
0.1M-TiFeSi	2.08	0.00	2.08	0.81	0.00	0.81	0.39
0.55M-TiFeSi	2.70	0.00	2.70	1.29	0.00	1.29	0.48
1.0M-TiFeSi	0.67	0.00	0.67	0.66	0.00	0.66	0.98

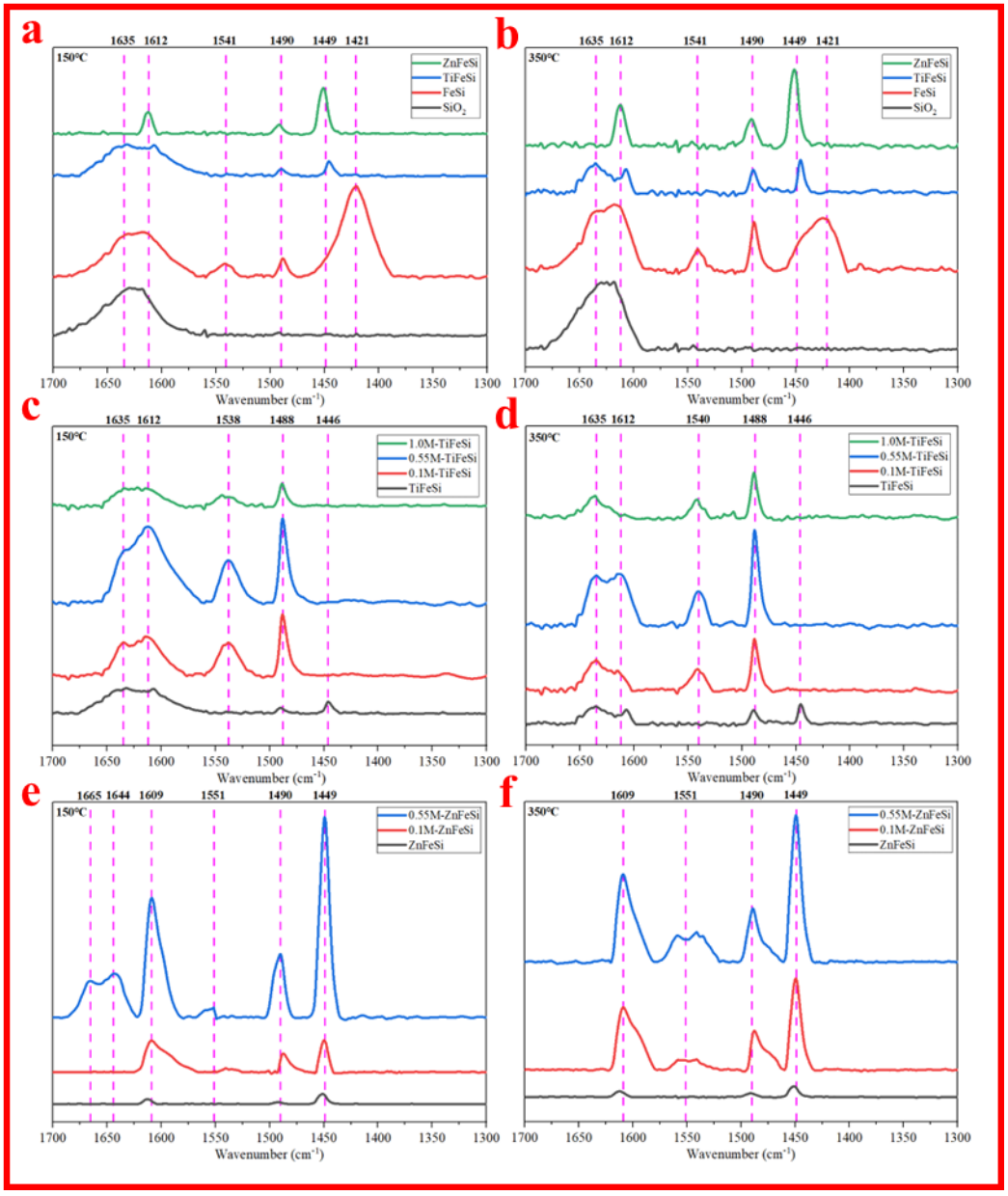

Figure 4.11 - Pyridine TPD for Supports (a, b), Ti Series (c, d) and Zn Series (e, f)

4.5.3 Nuclear Magnetic Resonance Spectroscopy

Colloidal suspensions of TiFeSi and ZnFeSi nanocatalysts in $CDCl_3$ solvent were analysed via ^1H NMR to determine proton containing surface functional groups. Results for Ti series are displayed in Figure 4.12a. Two major peaks at chemical shifts of 1.28 ppm and 1.57 ppm corresponding to -OH hydroxyl group and bound H_2O were observed [571, 572], alongside a peak at 7.28 ppm corresponding to proton exchange with $CDCl_3$ solvent (not shown) [573]. Results for Zn series are displayed in Figure 4.12b and show similar results as Ti series, except there is a small extra peak detected at 1.70 ppm that may be due to alkyl -CH leftover from organic solvents post calcination. Integration results for OH and H_2O peaks are given in Table 4.8.

Table 4.8 - Atomic Ratio of OH to H_2O via ^1H NMR

Sample	Relative Area OH / H_2O		OH / H_2O Atomic Ratio
TiFeSi	38.8	61.2	1.27
0.1M-TiFeSi	18.6	81.4	0.46
0.55M-TiFeSi	5.3	94.7	0.11
1.0M-TiFeSi	5.8	94.2	0.12
ZnFeSi	50.0	50.1	2.00
0.1M-ZnFeSi	57.4	42.6	2.70
0.55M-ZnFeSi	42.9	57.1	1.50

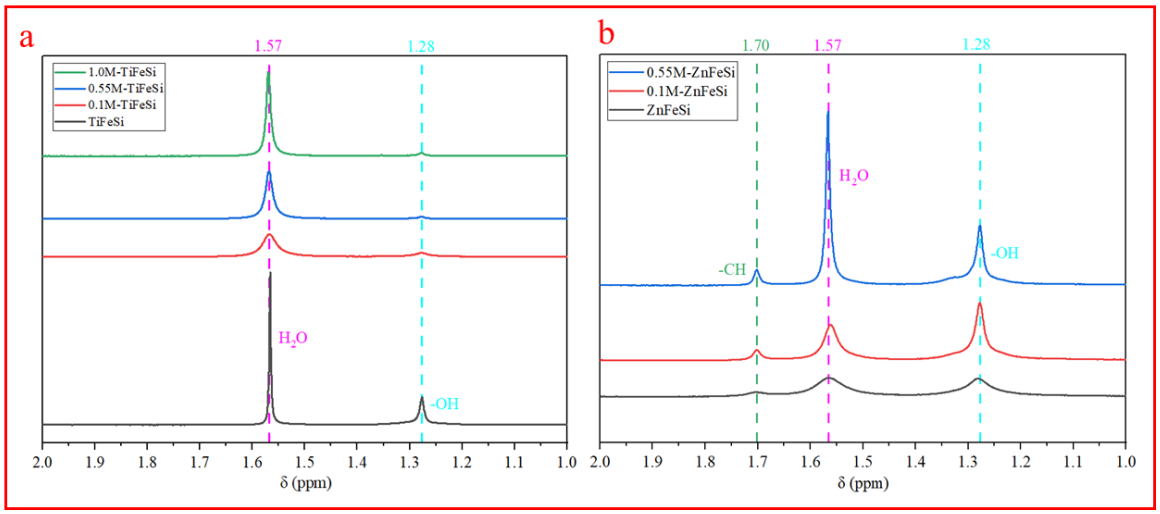

Figure 4.12 - ^1H NMR Major Peaks of TiFeSi Series (a) and ZnFeSi Series (b)

It has been reported previously that hydroxyl groups in upfield position are more shielded and hence basic in nature [574]. Therefore, the peak at 1.28 ppm is likely attributed to Si-OH or metal oxide terminal hydroxyl groups present prior to acid functionalisation. Changes in OH/H_2O ratio in each catalyst sample analysed could therefore be due to protonation of basic OH^- sites during treatment with chlorosulfonic acid or the effects of drying and calcination step. Alternatively, increased reactivity of hydroxyl groups may lead to faster proton exchange with deuterated $CDCl_3$ solvent and signal suppression, since exchange kinetics can be influenced by concentration of acidic and basic species [575, 576]. Brønsted Acidic hydroxyls are reported to be less shielded with higher chemical shifts of around 3-6 ppm [577, 578]. Several minor peaks were detected within this region as shown in Figure 4.13. Largest peak at 5.37 ppm is potentially adsorbed H_2O interacting with acidic metal oxide via hydrogen bonding [579, 580]. Peaks at 4.88 ppm and 3.94 likely indicate stronger and weaker acidic OH groups respectively. It has however been reported that chemical shift increases for more constrained pore structures [581] hence difference in chemical shift could also be due to different pore morphologies. Again, the lack of peaks for Ti series does not necessarily infer lack of such functional groups as presence has been confirmed via FTIR in Chapter 4.5.1 therefore this may indicate greater strength leading to more rapid deuterium exchange with $CDCl_3$ solvent.

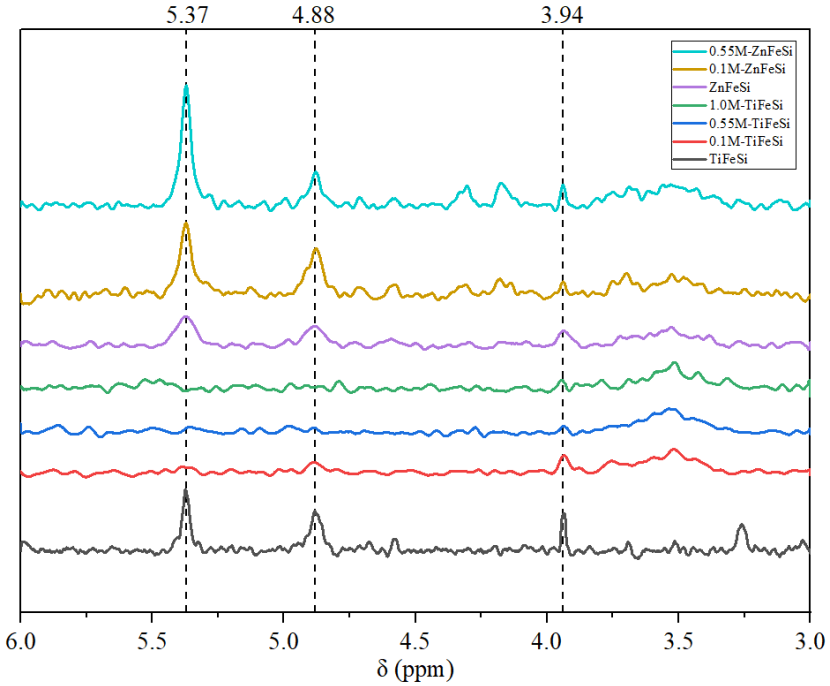

Figure 4.13 - Bronsted Acidic Hydroxyl Group Detection via ^1H NMR

4.5.4 X-ray Photoelectron Spectroscopy

Initial low-resolution survey XPS spectra were taken to check if all expected elements were present on surface and confirm peak regions of interest. Results are given in Figure 4.14 for support materials (a), Ti series (b) and Zn series (c). Peaks at approximately 103 eV, 170 eV, 285 eV, 459 eV, 532 eV, 712 eV, 1024 eV and 1047 eV were identified as Si2p, S2p, C1s, Ti2p, O1s, Fe2p, $Zn2p_{3/2}$ and $Zn2p_{1/2}$ respectively, confirming presence of all expected elements within typical range given by CasaXPS library. Other minor detected peaks were attributed to signals from other electronic orbitals and auger electrons, however only principal major peaks were selected for further high-resolution analysis.

Initial survey results also confirmed expected chemical nature upon consulting CasaXPS reference library. Si2p takes values close to 103 eV when present as SiO_2 compared to values nearer 99 eV for elemental Si. Metal sulfates show values of S2p close to 170 eV whereas metal sulfides shift towards 162 eV. Therefore, presence of both O-Si silica and O-S sulfate bound to metal surface are confirmed to be present. Carbon peak is typically taken as energy calibration and likely due to organic contaminants as well as ambient CO_2 adsorbed on surface. Ti2p values move from 454 eV to 459 eV as Ti becomes bound to oxygen hence Ti species is confirmed TiO_2 as expected. Oxygen was a particular element of interest due to expected presence of metal oxide, sulfate and hydroxyl groups and thus is explored more in high resolution analysis. Similarly to Ti, Fe2p peak shifts from 707 eV to 711 eV upon oxidation confirming oxidised form of Fe species was present on surface. Zn2p peaks showed characteristic splitting as well as being shifted to slightly increased binding energy confirming oxidised form of ZnO species. Hence initial survey results confirm characteristic peaks of metal oxide and sulfate species on material surface. Peaks for Si2p and Fe2p were not observed in every survey spectrum. This is likely due to low bulk wt% composition of Si and Fe from mass losses during synthesis and inhomogeneous elemental distribution both confirmed by EDX analysis in Chapter 4.7.2, as well as XPS being a highly surface sensitive technique. Since core-shell morphology is identified from SEM-TEM analysis in Chapter 4.6 with nanoparticle surface layers between ~20-50 nm, inner layers of SiO_2 and Fe are partially/fully coated in TiO_2, ZnO and sulfate groups throughout the sample region and hence undetectable beyond ~10 nm depth often denoted as XPS analysis depth [582]. Further high-resolution spectra were subsequently taken to understand the chemical environments present for each element of interest with peak deconvolution performed using Origin software.

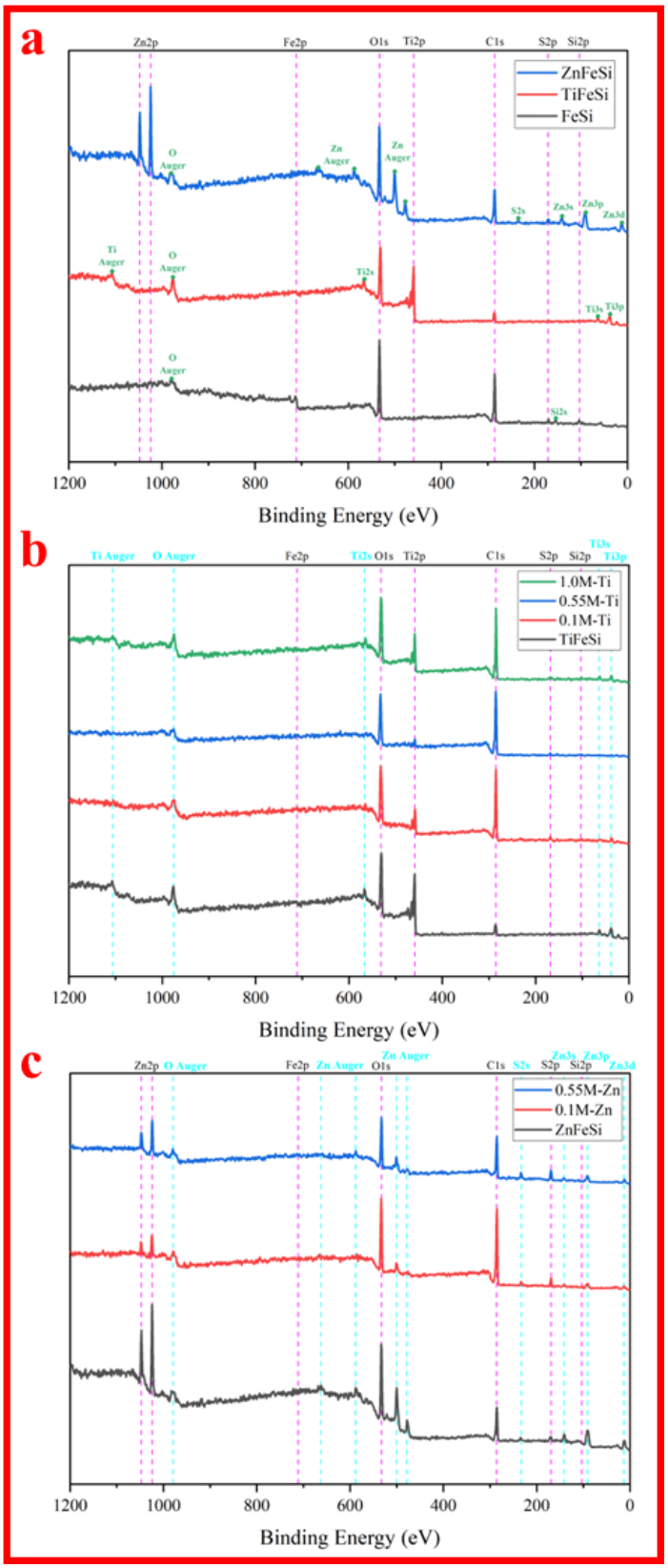

Figure 4.14 - Survey XPS Spectra for Supports (a), Ti Series (b) and Zn Series (c)

High resolution XPS for FeSi, TiFeSi and ZnFeSi non-functionalised support materials are shown in Figure 4.15, Figure 4.16 and Figure 4.17 respectively. For all support materials 3 distinct peaks could be observed within the C1s region which are attributed to C-C, C-O and C=O groups [583, 584] from surface adsorbed CO_2 and organic residues. For FeSi support, three O1s peaks were observed. The lowest energy peak at 530.5 eV could be due to lattice Fe-O or S-O groups [585-587], with next energy peak at 532.2 eV then indicating evidence of Fe-OH surface hydroxyls or a mixed Fe-O-Si lattice oxygen [585, 587]. Highest energy peak at 533.5 eV is likely due to Si-O lattice oxygen or from bound water groups [588-590]. Three O1s peaks were similarly observed for TiFeSi, again lowest energy peak at 530.2 eV is likely to be from Ti-O lattice oxygen [591, 592] while peak at 532.0 eV more likely corresponds to Ti-OH hydroxyls [592, 593] than trace S-O due to lack of S2p signal in TiFeSi. A minor peak at 534.4 eV may be due to bound water or adsorbed CO_2 at surface [594, 595]. In ZnFeSi only two O1s peaks were noted likely from Zn-O lattice oxygen at 532.0 eV and hydrated Zn-OH or S-O groups at 533.0 eV [596]. It is notable that almost all oxygen species at ZnFeSi surface are attributed to hydrated or sulfated ZnO material. This agrees with other observations throughout Chapter 4.7 that ZnFeSi was contaminated with sulfate precursor not fully removed post synthesis.

Only FeSi support had detectable Fe2p signal, suggesting that small quantities of Fe observed in TiFeSi and ZnFeSi via EDX were part of the FeSi core layer. Peaks at 711.8 eV, 713.8 eV and 726.2 eV suggest presence of a Fe(III) species [597] typical of Fe_2O_3 and hence agrees with XRD and SAED results. S2p peak was detected in both FeSi and ZnFeSi support confirming that washing step was unable to completely remove surface precursor sulfate, whereas for TiFeSi support no S2p signal was observed. Two peaks at 168.7-169.7 eV and 170.3-171.4 eV corresponding to $S2p_{3/2}$ and $S2p_{1/2}$ were identified at energy region typical for metal sulfate group [598, 599]. Similar to Fe observations, only FeSi support had a detectable surface Si2p peak. This suggests that small quantities of Si detected in EDX were part of the core layer only. Peak at 103.8 eV is characteristic of Si-O whereas minor lower energy peak at 95.0 eV may be due to elemental Si at regions of oxygen site vacancy [600, 601].

The Ti2p peak region detected for TiFeSi support shows two characteristic combined peaks of lower energy $Ti2p_{3/2}$ and higher energy $Ti2p_{1/2}$ however interestingly these two peaks can be further deconvoluted. Peaks at 459.0 eV and 464.7 eV could be attributed to Ti^{3+} oxidation state while peaks at 460.9 eV and 466.4 eV correspond to Ti^{4+} oxidation state, with previous studies suggesting that Ti^{3+} confirms presence of oxygen vacancy sites that may be located near to surface hydroxyl groups [602, 603]. A similar observation was found for ZnFeSi support in Zn2p peak region, where two characteristic combined peaks of lower energy $Zn2p_{3/2}$ and higher energy $Zn2p_{1/2}$ were detected and can be further deconvoluted. Here the lower energy peaks at 1023.7 eV and 1046.9 eV may be from Zn-O group while higher energy peaks at 1024.2 eV and 1047.3 eV instead due to Zn-OH hydrated sites with all peaks corresponding to Zn^{2+} oxidation state [604]. Integration of peak areas and use of CasaXPS relative sensitivity factors as detailed in Chapter 3.3.6.2 facilitated calculation of surface elemental weight composition. Results for FeSi, TiFeSi and ZnFeSi support materials are summarised in Table 4.9 including the C1s reference peak. Atomic ratios of O/Si in FeSi, O/Ti in TiFeSi and O/Zn in ZnFeSi were found to be 5.44, 2.93 and 6.63 respectively. More oxygen is present than expected for pure SiO_2, TiO_2 or ZnO materials which indicates sulfate groups or surface CO_2 as detected. The O/S ratio for FeSi and ZnFeSi materials were found to be 11.5 and 8.81 respectively, indicating sufficient oxygen for sulfate formation. Additionally, S/Fe and S/Zn ratios for FeSi and ZnFeSi were found to be 2.01 and 0.64. Multiple sulfate groups are present per Fe for FeSi, while Zn is more abundant to S in ZnFeSi.

Table 4.9 - High Resolution XPS Surface Elemental Analysis of Support Materials

Peak Region	Surface Elemental Composition (wt%)		
	FeSi	TiFeSi	ZnFeSi
C1s	42.6	14.5	31.1
O1s	34.8	42.3	35.2
Fe2p	5.25	0	0
S2p	6.06	0	8.02
Si2p	11.2	0	0
Ti2p	-	43.2	-
Zn2p	-	-	25.6

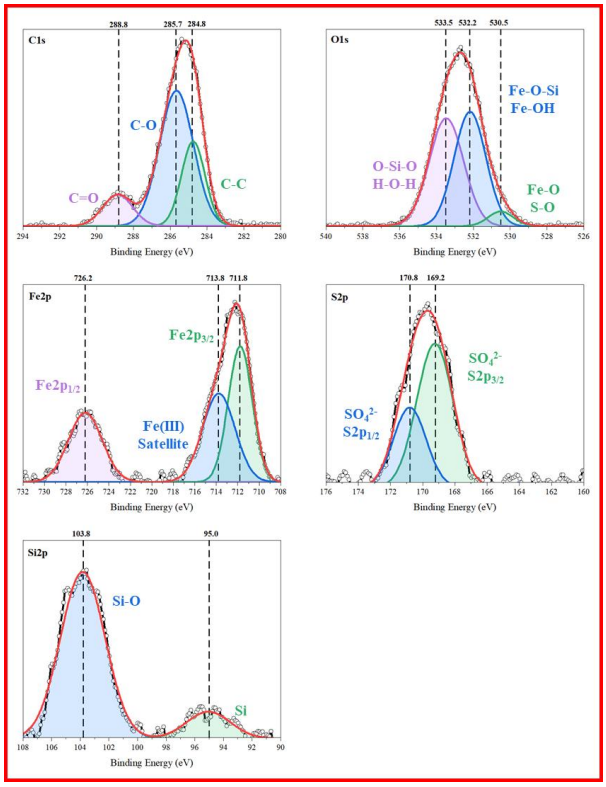

Figure 4.15 - High Resolution XPS of FeSi Support

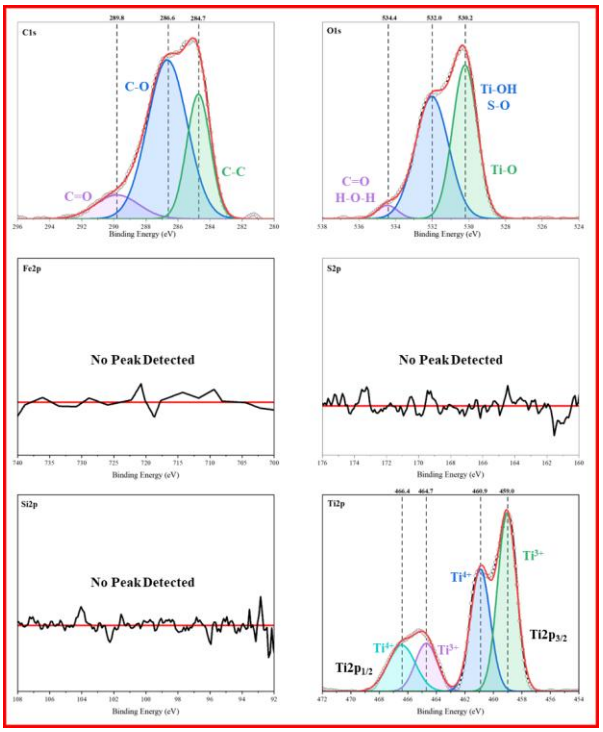

Figure 4.16 - High Resolution XPS of TiFeSi Support

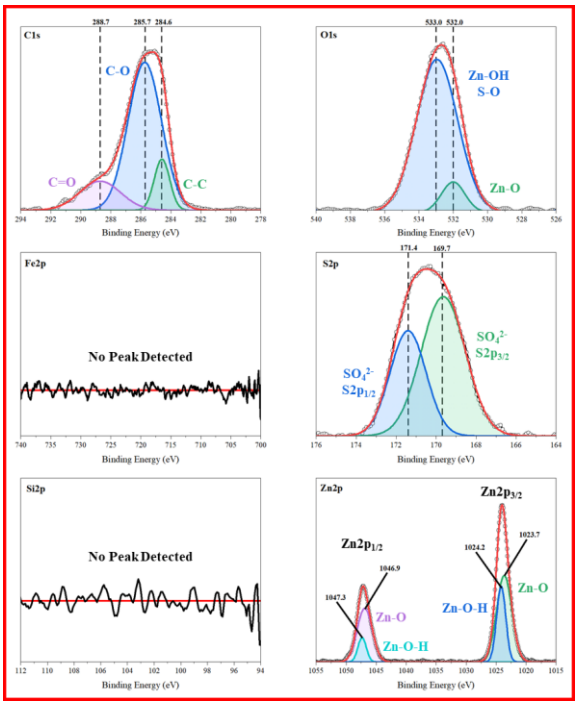

Figure 4.17 - High Resolution XPS of ZnFeSi Support

High resolution XPS analysis of Ti Series nanocatalysts were subsequently taken and results are displayed in Figure 4.18, Figure 4.19 and Figure 4.20 for 0.1M-TiFeSi, 0.55M-TiFeSi and 1.0M-TiFeSi respectively. For all functionalised Ti nanocatalysts, four peaks were observed within C1s region attributed to C=C, C-C, C-O and C=O from environmental CO_2 and organic residues [583, 584]. Deconvolution of O1s region indicated four peaks as compared to only three in TiFeSi spectrum, likely due to increased sulfur loading post functionalisation leading to a more distinguishable sulfate signal. Peak at ~531 eV was attributed to lower energy Ti-OH surface site while peak at 532-533 eV was likely due to sulfate [592, 593]. Lack of Fe2p peak remained consistent with TiFeSi support result and suggested any Fe present in bulk EDX analysis as discussed later in Chapter 4.7.2 formed part of a core layer. Unlike TiFeSi result however, for all functionalised Ti nanocatalysts a weak signal within Si2p region was noted and lowest energy peak between 100-102 eV may be due to Ti-O-Si interface [591]. Middle energy peak at 102-103 eV indicates Si-OH hydroxyl groups while highest energy peak at 103-105 eV range is Si-O-Si lattice silica [605]. Slight metal acidic digestion or rearrangements during acid functionalisation and calcination step may explain the core 100 nm-SiO_2 exposure at nanocatalyst surface, while lack of surface Fe would be expected due to acidic leaching. Lack of surface Si may also be due to non-uniform coating of SiO_2 core.

Appearance of new peaks in S2p region as compared to no peaks for TiFeSi spectra confirms successful loading of sulfur compounds onto surface post acidic functionalisation. Peaks at ~169 eV and ~190 eV confirm sulfur exists in $2p_{3/2}$ and $2p_{1/2}$ orbitals characteristic of surface sulfate sites, while peaks between 167-168 eV and 163-164 eV were not detected prior in FeSi support and may be due to SO_3^{2-} and Ti-S sites respectively [598, 599]. Ti2p region for functionalised Ti nanocatalysts was similar to TiFeSi support with evidence of both Ti^{4+} and Ti^{3+} oxidation states. Results of XPS were used to calculate surface elemental composition as summarised in Table 4.10. Important atomic ratios between O:S, O:Ti and S:Ti for Ti series are reported in Table 4.11. Oxygen loading was significantly higher than sulfur for all nanocatalysts facilitating formation of detected sulfate sites. Ratio of O:Ti was substantially beyond stoichiometry of TiO_2 which also confirms contribution of other oxygen species such as sulfate.

As reported and discussed later in Chapter 4.7 highest bulk sulfur loading was achieved in the order 0.55M-TiFeSi > 0.1M-TiFeSi > 1.0M-TiFeSi via EDX and CHONS analysis. Since sulfur is functionalised onto nanocatalyst surface, it is surprising at first that initial XPS results seem to contradict with bulk findings, with 0.55M-TiFeSi having lowest surface sulfur content of 2.88 wt%. However, it is important to note that Ti content was also significantly decreased at only 3.05 wt% likely due to much higher contribution of adventitious carbon or organic residues at surface during this analysis. Comparing atomic ratios of S:Ti instead, 0.55M-TiFeSi has approximately 1.41 S atoms per Ti atom at the surface on average. This is substantially higher than ratios of 0.54 and 0.31 found in 0.1M-TiFeSi and 1.0M-TiFeSi nanocatalysts accordingly, therefore on average more S atoms are bound to Ti in 0.55M-TiFeSi and identical trend with bulk EDX and CHONS analysis is found. XPS results therefore indicate that greatest loading of sulfate sites that enhance Brønsted acidity was achieved in 0.55M-TiFeSi followed by 0.1M-TiFeSi and 1.0M-TiFeSi nanocatalysts.

Table 4.10 - High Resolution XPS Surface Elemental Analysis of Ti Series

Peak Region	Surface Elemental Composition (wt%)			
	TiFeSi	0.1M-TiFeSi	0.55M-TiFeSi	1.0M-TiFeSi
C1s	14.5	50.9	63.4	44.8
O1s	42.3	31.8	27.5	32.9
Fe2p	0	0	0	0
S2p	0	4.19	2.88	3.45
Si2p	0	1.56	3.14	2.15
Ti2p	43.2	11.5	3.05	16.7

Table 4.11 - Surface Elemental Atomic Ratios of Ti Series

Ratio	TiFeSi	0.1M-TiFeSi	0.55M-TiFeSi	1.0M-TiFeSi
O:S	-	15.2	19.2	19.1
O:Ti	2.93	8.28	27.0	5.92
S:Ti	-	0.54	1.41	0.31

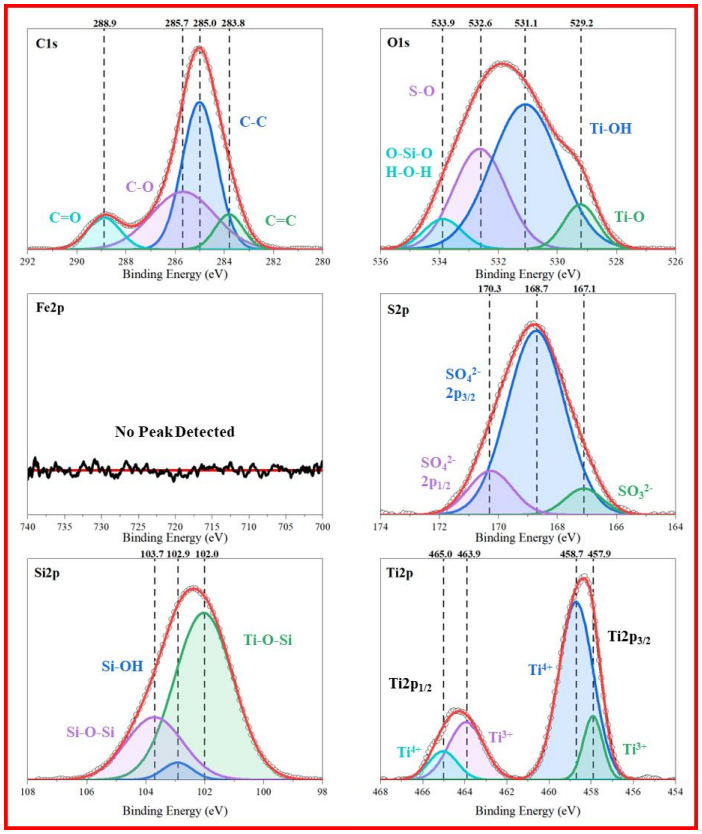

Figure 4.18 - High Resolution XPS of 0.1M-TiFeSi

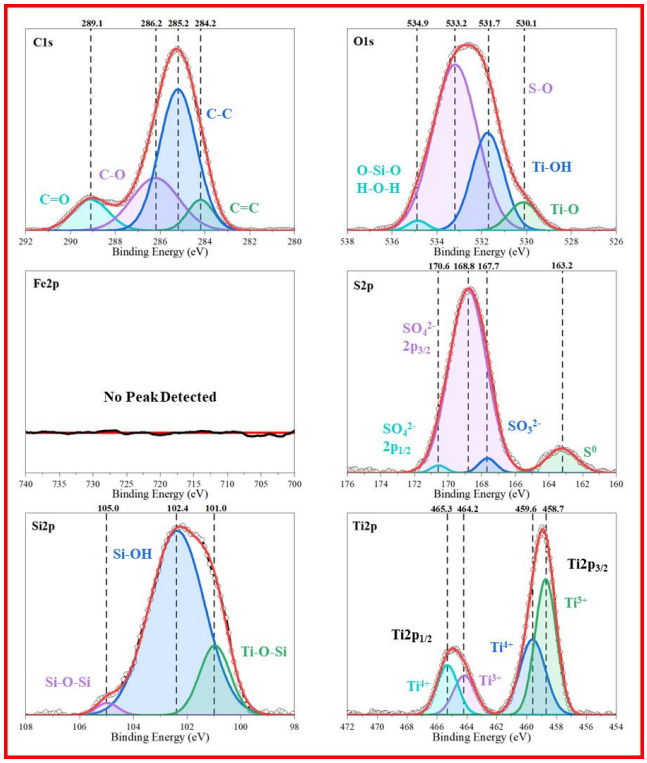

Figure 4.19 - High Resolution XPS of 0.55M-TiFeSi

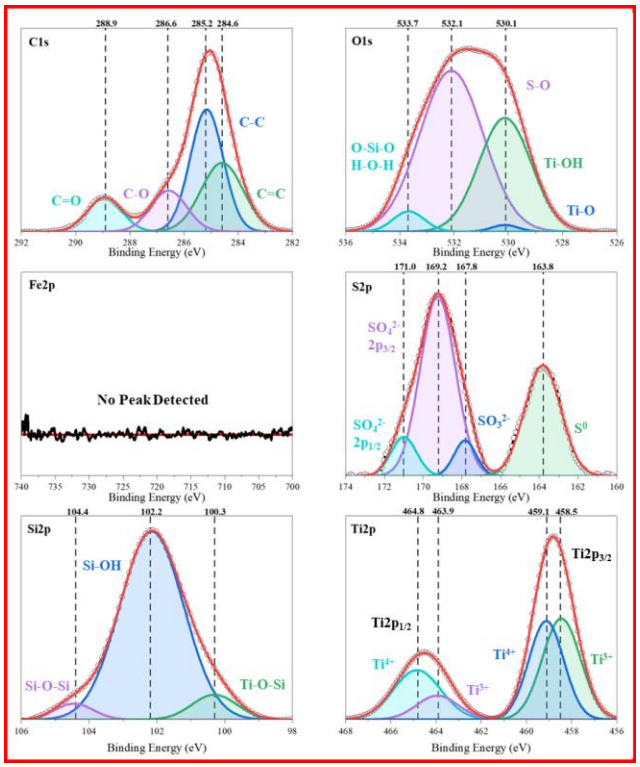

Figure 4.20 - High Resolution XPS of 1.0M-TiFeSi

High resolution XPS of 0.1M-ZnFeSi and 0.55M-ZnFeSi were also taken and are plotted in Figure 4.21 and Figure 4.22 respectively, while insufficient 1.0M-ZnFeSi nanocatalyst was available for analysis. C1s region featured characteristic C-C, C-O and C=O peaks at ~285 eV, ~286 eV and 287-289 eV similar to Ti series. Extra peak at 290.5 eV for 0.1M-ZnFeSi might be attributable to π-π^* aromaticity of surface toluene [606, 607], agreeing with EDX and CHONS analysis that Zn series had more significant level of carbon residues. The O1s region also agreed strongly with Ti series results, with presence of Zn-O, Zn-OH and S-O peaks at ~532 eV, 533 eV and 534 eV. Peak at 535 eV attributed to bound H_2O or Si-O-Si was only present in 0.1M-ZnFeSi sample, likely due to failure to observe Si2p peak in 0.55M-ZnFeSi or increased chlorosulfonic acid treatment converting surface water into acidic hydroxyl sites. Neither Zn nanocatalyst was observed to have Fe present at surface similar to all Ti nanocatalysts. Si2p region detected for 0.1M-ZnFeSi only had similar peak characteristics of Ti series with Zn-O-Si, Si-OH and Si-O-Si peaks determined at 102.6 eV, 103.6 eV and 105.3 eV correspondingly. These results are similar to Ti nanocatalysts where exposed Si can be detected on surface post functionalisation, however surface Fe is likely to have been completely leached during acid treatment and hence only exists in core layer. Lack of Si detection in 0.55M-ZnFeSi sample may be due to lower bulk content of Si compared to 0.1M-ZnFeSi or from inhomogeneity of uncoated SiO_2 in sample as indicated via later TEM-EDX.

Presence of surface sulfate was confirmed for both Zn nanocatalysts with $2p_{3/2}$ and $2p_{1/2}$ orbital peaks within region of 169-172 eV. An extra peak at ~168 eV that was not observed in ZnFeSi support is likely due to formation of SO_3^{2-} sites during functionalisation as well as SO_4^{2-} groups [598, 599]. Results for Zn2p region were similar to ZnFeSi support with peaks at ~1024 eV and ~1047 eV corresponding to Zn-O while peaks at ~1025 eV and ~1048 eV corresponding to Zn-OH. Surface elemental analysis of Zn series is summarised in Table 4.12 and important surface atomic ratios provided in Table 4.13. Ratio of O:S was sufficiently high for sulfate formation on 0.1M-ZnFeSi nanocatalyst surface, however increased sulfur content in 0.55M-ZnFeSi suggests on average some sulfur may need to exist in SO_3^{2-} sulfite form as detected at ~168.5 eV in S2p region. Oxygen loading was beyond stoichiometry of ZnO confirming presence of additional oxygen containing sulfur species. Post chlorosulfonic acid functionalisation led to notable increase in S:Zn ratio similar to Ti series. While 0.55M-ZnFeSi had increased S presence on surface, lower availability of Zn sites meant 0.1M-ZnFeSi had greatest average ratio of S to Zn at 3.34.

Greater sulfur to metal atom ratios were observed in Zn series as compared to Ti series, likely due to residual sulfur species present in non-functionalised ZnFeSi that were unremoved during washing and calcination steps. Zn nanocatalysts hence have a denser surface sulfur structure as compared to Ti nanocatalyst series. High ratio of S to Zn suggests formation of a sulfated surface monolayer rich in SO_4^{2-} as suggested in other work on sulfated metal oxides [608]. Bridging of multiple sulfate groups across Zn-O-Zn lattice is predicted rather than bidentate chelation of one sulfate to each Zn centre from work in Chapter 4.5.1 exploring ATR-FTIR of surface region. Overall, high resolution XPS analysis has confirmed successful synthesis of catalytically active Ti/Zn surface shell layer loaded with sulfur species. Slight evidence of exposed or uncoated Si is observed but no Fe is present near nanocatalyst surface after possible leaching in functionalisation step. Peak deconvolution identified surface hydroxyls and sulfate responsible for catalytic activity.

Table 4.12 - High Resolution XPS Surface Elemental Analysis of Zn Series

Peak Region	Surface Elemental Composition (wt%)		
	ZnFeSi	0.1M-ZnFeSi	0.55M-ZnFeSi
C1s	31.1	56.6	39.4
O1s	35.2	27.5	29.8
Fe2p	0	0	0
S2p	8.02	8.88	18.4
Si2p	0	1.57	0
Zn2p	25.6	5.43	12.5

Table 4.13 - Surface Elemental Atomic Ratios of Zn Series

Ratio	ZnFeSi	0.1M-ZnFeSi	0.55M-ZnFeSi
O:S	8.81	6.21	3.25
O:Zn	5.63	20.7	9.73
S:Zn	0.64	3.34	3.00

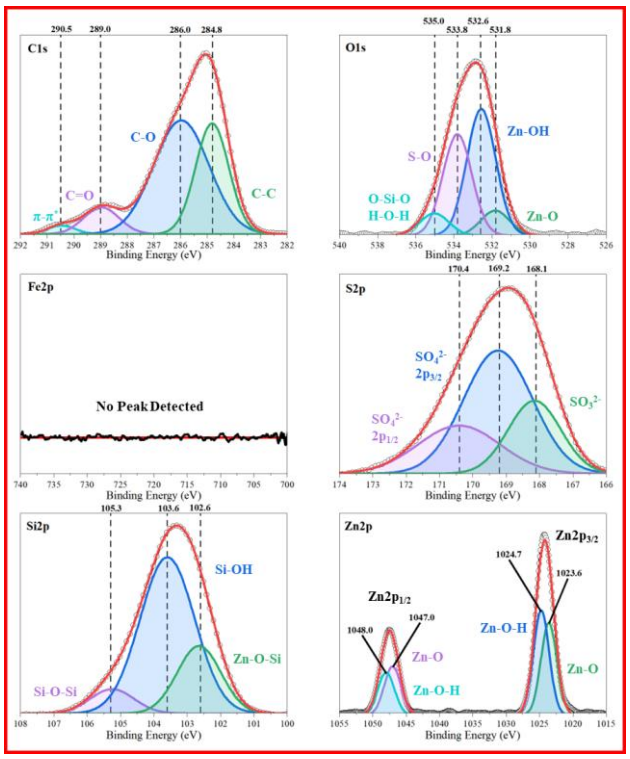

Figure 4.21 - High Resolution XPS of 0.1M-ZnFeSi

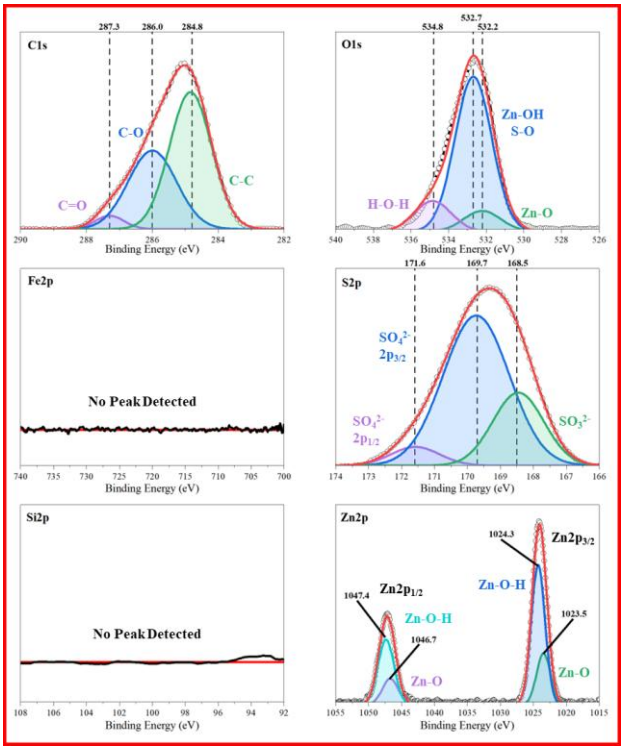

Figure 4.22 - High Resolution XPS of 0.55M-ZnFeSi

4.6 Structure and Morphology

4.6.1 N_2 Porosimetry

Anton Paar Nova 800 apparatus was used to measure N_2 adsorption and desorption isotherms (77 K). Figure 4.23a-d illustrates isotherms obtained for support materials while Figure 4.24a-d and Figure 4.25a-c shows isotherms between TiFeSi and ZnFeSi catalyst series respectively. Starting SiO_2 nanoparticles show type II isotherm with H1 hysteresis loop, suggesting the existence of bulk macroporous interparticle voids and cylindrical mesopores. All other isotherms show type IV behaviour with H2 hysteresis loop, suggesting predominantly mesoporous structure with pores between 2-50 nm due to occurrence of capillary condensation [609]. H2 loop shape suggests ink-bottle pore morphology, which is reasonable to expect since coprecipitated nanomaterials are unlikely to achieve ideal ordered cylindrical or slit-like channels without templating and thus more irregular ink-bottle pore structures form. Differences between volume of N_2 adsorbed on y-axis are due to sample porosity, surface area and quantity of known sample mass loaded into the glass cell. Isotherms in Figure 4.25 are of significantly lower quality as insufficient quantity of N_2 could be adsorbed for ZnFeSi series despite using similar sample mass as compared with TiFeSi series. Experimental errors from insufficient N_2 adsorption explains why measured isotherms were not seen to fully close the hysteresis loop at low pressure. This also indicates that Zn series likely has reduced surface area compared to Ti series. For samples of low surface area, isotherm data in future could be improved by increasing sample mass or equilibrium time between measurements.

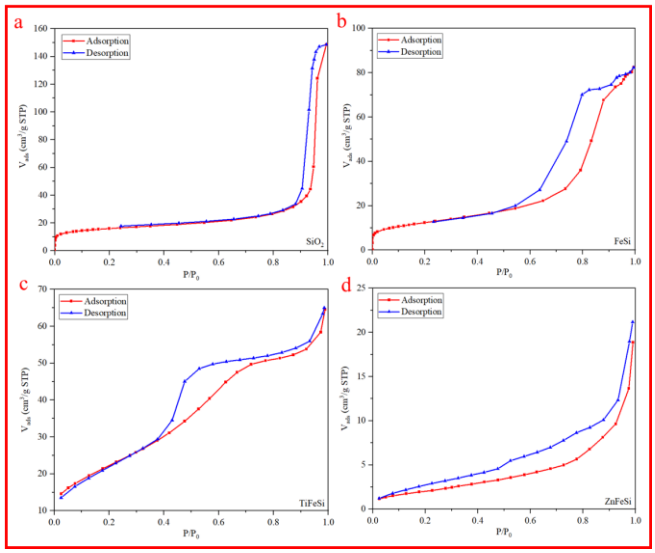

Figure 4.23 - N_2 Isotherm plots for SiO_2 (a), FeSi (b), TiFeSi (c) and ZnFeSi (d) supports

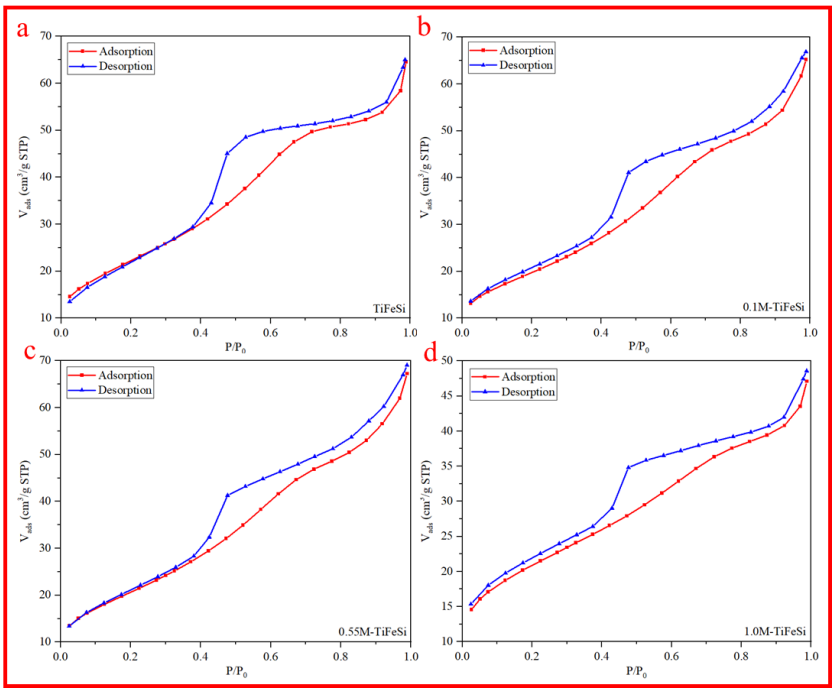

Figure 4.24 - N_2 Isotherm plots for TiFeSi support (a); 0.1M-TiFeSi (b), 0.55M-TiFeSi (c), and 1.0M-TiFeSi (d) chlorosulfonic acid functionalised catalysts

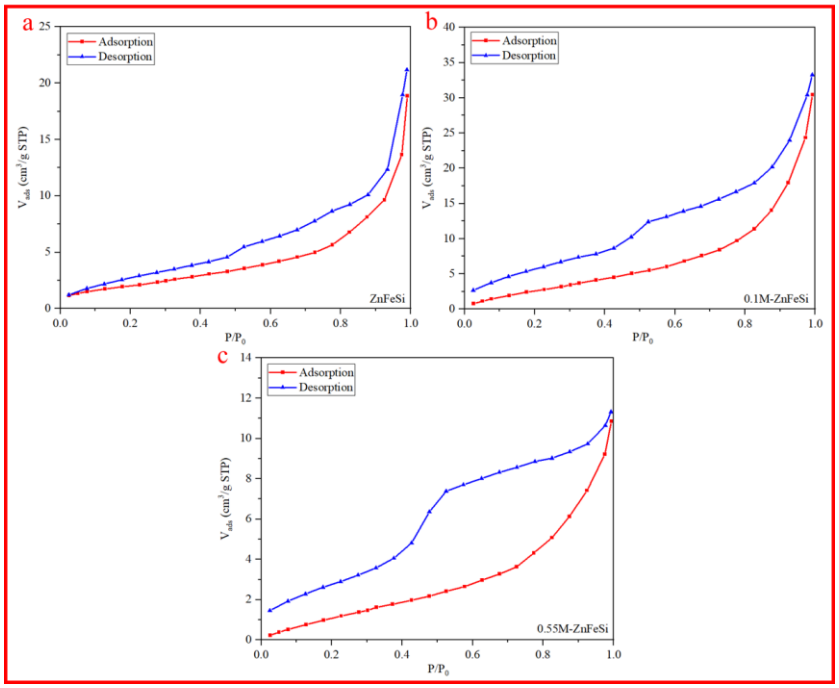

Figure 4.25 - N_2 Isotherm plots for ZnFeSi support (a); 0.1M-ZnFeSi (b) and 0.55M-ZnFeSi (c) chlorosulfonic acid functionalised catalysts

BET analysis was performed as detailed in Chapter 3.3.4 to determine specific surface area. Linearised plots are displayed in Figure 4.26a-d for support materials and Figure 4.27a-d and Figure 4.28a-c for TiFeSi and ZnFeSi series respectively. All plots demonstrate highly linear behaviour within 0.05-0.3 partial pressure region of the adsorption isotherm indicating an excellent degree of fit. Linear fitting results are displayed in Table 4.14 and for all plots a correlation coefficient of unity was achieved. Specific surface area (S_{BET}) initially decreased upon loading SiO_2 with Fe oxide from 56.0 m^2/g to 44.5 m^2/g, suggesting pore blockage, pore filling and aggregation effects occurred during this loading step as Fe coated the SiO_2 nanoparticles. After coating the FeSi support with ZnO, there was further loss of surface area down to only 7.81 m^2/g for the ZnFeSi material. Coating FeSi with TiO_2 instead led to an increase in surface area to 81.3 m^2/g for the TiFeSi support. The order of magnitude difference in surface area between ZnFeSi and TiFeSi is likely due to problems noted during this coprecipitation step. During synthesis it was observed that ZnFeSi formed a thick and viscous sol of highly aggregated material. Decrease in surface area for ZnFeSi is hence likely due to ZnO precipitate clumping and aggregating tightly, leading to pore blockage and failure to achieve new surface pore structure. Whereas the obtained TiFeSi material was a much finer powder that could be successfully dried more readily. Increase in surface area for TiFeSi therefore suggests an increase in surface roughness was achieved with creation of new pore structures. Upon acid functionalisation, TiFeSi series displayed slight decrease in specific surface area likely from slight aggregation or pore blocking via sulfur functional groups. Within 5% experimental error, determined from weighing errors and reported 2% reproducibility of Nova 800 unit [610], no significant trend of surface area change was observed on increasing chlorosulfonic acid concentration strength. This was surprising at first as it was expected that excess chlorosulfonic acid would lead to oversaturation of surface site groups and large reduction in surface area. The fact this was not observed suggests that only relatively small quantities of acidic groups were loaded onto TiFeSi material hence only slight loss of surface area observed. Similar result was observed for ZnFeSi series, however experimental error is likely much higher than 5% due to considerably low quantity of N_2 successfully adsorbed. While all linear correlations exhibited excellent fit, the value of BET constant was notably large for FeSi and 1.0M-TiFeSi while highly negative for SiO_2 indicating potential unsuitability of BET theory due to presence of microporosity [417]. To explore this further, t-plot method was utilised to determine if microporosity was significant as discussed in Chapter 3.3.4.

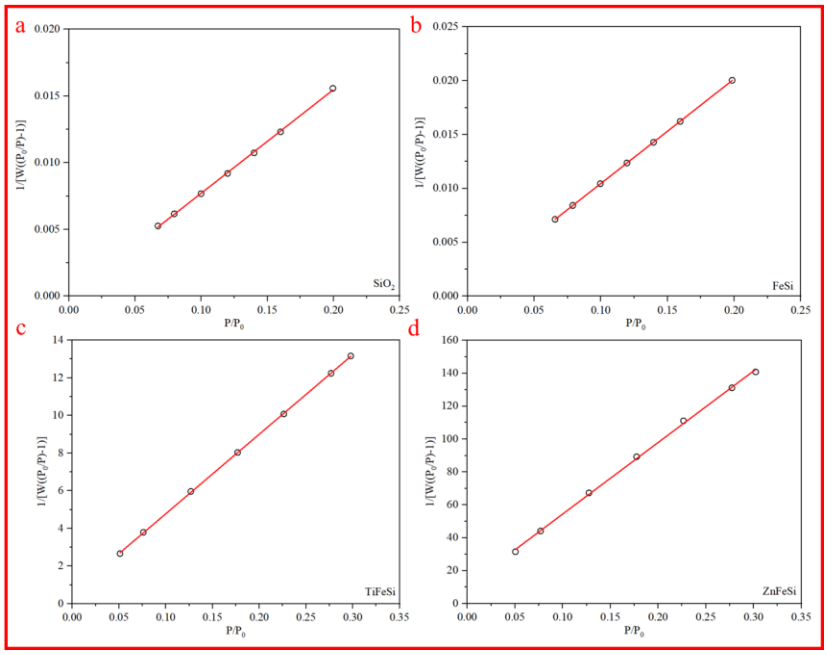

Figure 4.26 - BET Linear Fit for SiO_2 (a), FeSi (b), TiFeSi (c) and ZnFeSi (d) supports

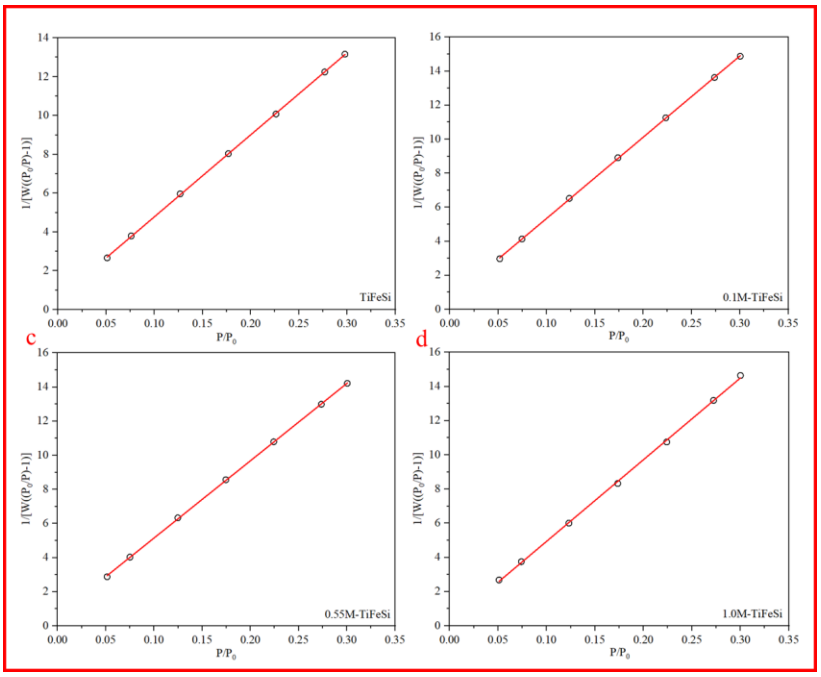

Figure 4.27 - BET Linear Fit for TiFeSi support (a); 0.1M-TiFeSi (b), 0.55M-TiFeSi (c), and 1.0M-TiFeSi (d) chlorosulfonic acid functionalised catalysts

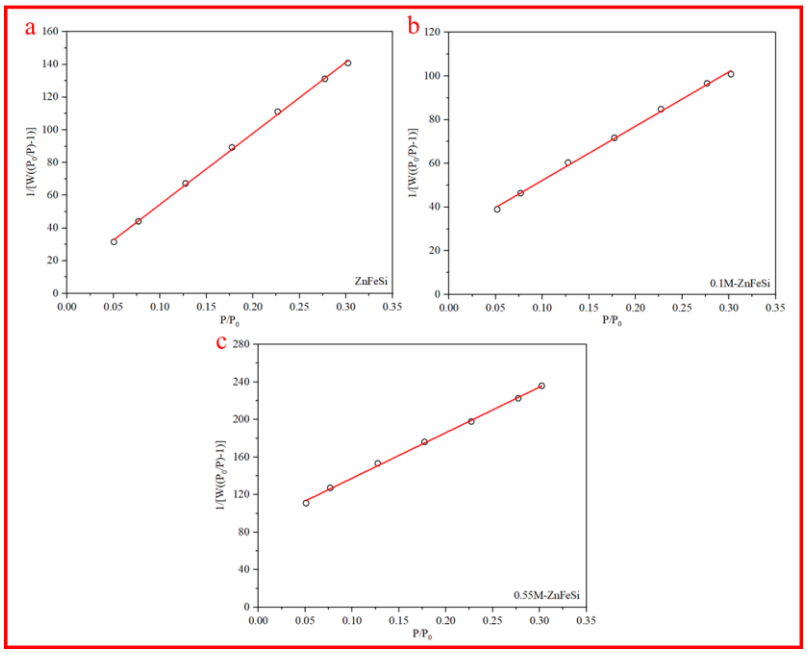

Figure 4.28 - BET Linear Fit for ZnFeSi support (a); 0.1M-ZnFeSi (b) and 0.55M-ZnFeSi (c) chlorosulfonic acid functionalised catalysts

Table 4.14 - Results of N_2 BET Linear Fit

Sample	Gradient	Intercept	Correlation Coefficient R	BET Constant	S_{BET} (m^2/g)
SiO_2	0.0778	-0.0001	1.00	-1232	56.0 ± 2.8
FeSi	0.0971	0.0008	1.00	130	44.5 ± 2.2
TiFeSi	42.3	0.553	1.00	77.4	81.3 ± 4.1
0.1M-TiFeSi	47.7	0.568	1.00	85.1	72.1 ± 3.6
0.55M-TiFeSi	45.3	0.613	1.00	74.9	75.8 ± 3.8
1.0M-TiFeSi	47.8	0.157	1.00	305.3	72.6 ± 3.6
ZnFeSi	435	10.9	1.00	40.8	7.81 ± 0.39
0.1M-ZnFeSi	248	27.4	1.00	10.1	12.6 ± 0.6
0.55M-ZnFeSi	485	88.9	1.00	6.46	6.07 ± 0.30

Results of t-plot analysis are shown in Figure 4.29a-d for support materials and Figure 4.30a-d and Figure 4.31a-c for TiFeSi and ZnFeSi series respectively. Red plot points indicate the partial pressure region on which linear fitting was performed and fitting results are provided in Table 4.15. All results displayed excellent fitting with correlation coefficient of unity. Starting SiO_2 nanoparticles had a relatively high degree of microporosity with 36% of the calculated BET surface area contributed by micropore structures. Post coprecipitation, only 10.7% of the FeSi surface area was due to microporosity and both micropore volume and area noticeably decreased. This indicates Fe oxide species had filled into micropore structure or blocked pore entrances and confirms the successful modification of SiO_2 surface to include Fe oxide species. For all other catalyst support materials and functionalised catalysts except one, a negative intercept was obtained which is interpreted as no micropore area. This suggests that after further coating of FeSi with TiO_2 or ZnO layer all remaining micropores became filled or blocked.

Surprisingly, 1.0M-TiFeSi displayed microporosity with 19.8% of the calculated BET surface area being due to micropore structures. Values of micropore volume and area for 1.0M-TiFeSi are understandably below original SiO_2 nanoparticles due to pore filling or blocking effects, but surprisingly greater than FeSi micropore volume and area, despite the extra coprecipitation steps and acid functionalisation performed to produce 1.0M-TiFeSi material. Other characterisation results presented in this chapter suggests FeSi has greater sulfur content than 1.0M-TiFeSi which may lead to more micropore blockage and pore filling with sulfate groups. However, this does not explain why 1.0M-TiFeSi is the only functionalised catalyst examined with a microporous nature. To explain this result, it is theorised that under 1.0M chlorosulfonic acid functionalisation a considerable degree of acid digestion may occur which would reduce micropore blockages or lead to creation of new micropore structures either by dissolving or aggregating effects. While it should be noted that application of other t-plot fitting models such as generalised Halsey were unable to detect microporosity of 1.0M-TiFeSi like the De Boer model, the subsequent BJH analysis also suggests that 1.0M-TiFeSi surface area may not be sufficiently described by mesopores alone.

Table 4.15 - Results of t-plot Linear Fit

Sample	Gradient	Intercept	Correlation Coefficient R	Micropore Volume (cm^3/g)	Micropore Area (m^2/g)	External Area (m^2/g)	Micropore Area (%)
SiO_2	23.2	5.92	1.00	0.009	20.2	35.9	36.0
FeSi	25.7	1.16	1.00	0.002	4.76	39.7	10.7
TiFeSi	63.9	-6.07	1.00	-	-	81.3	-
0.1M-TiFeSi	60.4	-7.09	1.00	-	-	72.1	-
0.55M-TiFeSi	62.1	-6.88	1.00	-	-	75.8	-
1.0M-TiFeSi	37.6	4.56	1.00	0.007	14.4	58.3	19.8
ZnFeSi	6.91	-1.01	1.00	-	-	7.81	-
0.1M-ZnFeSi	13.2	-3.19	1.00	-	-	12.6	-
0.55M-ZnFeSi	5.70	-1.39	1.00	-	-	6.07	-

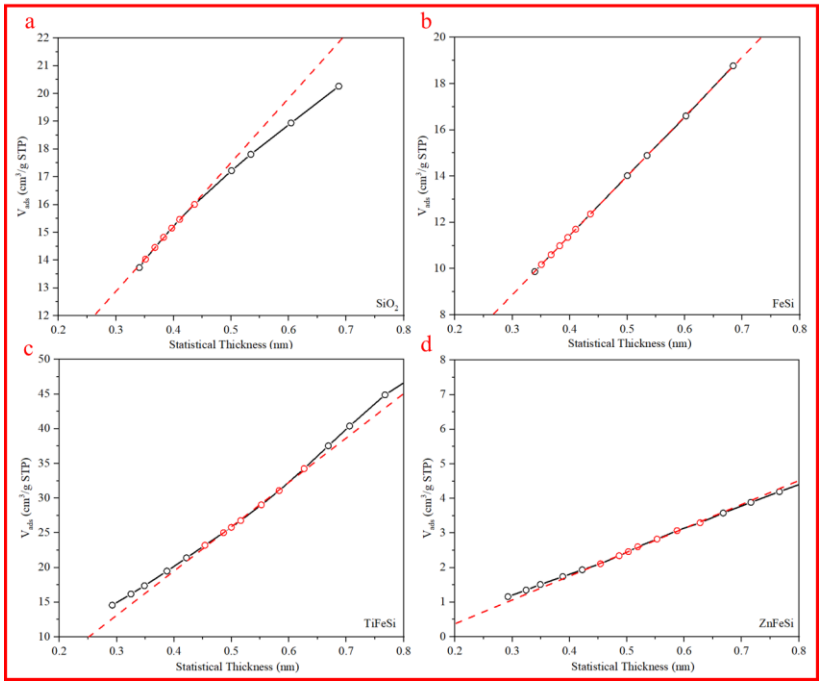

Figure 4.29 - t-plot analysis for SiO_2 (a), FeSi (b), TiFeSi (c) and ZnFeSi (d) supports

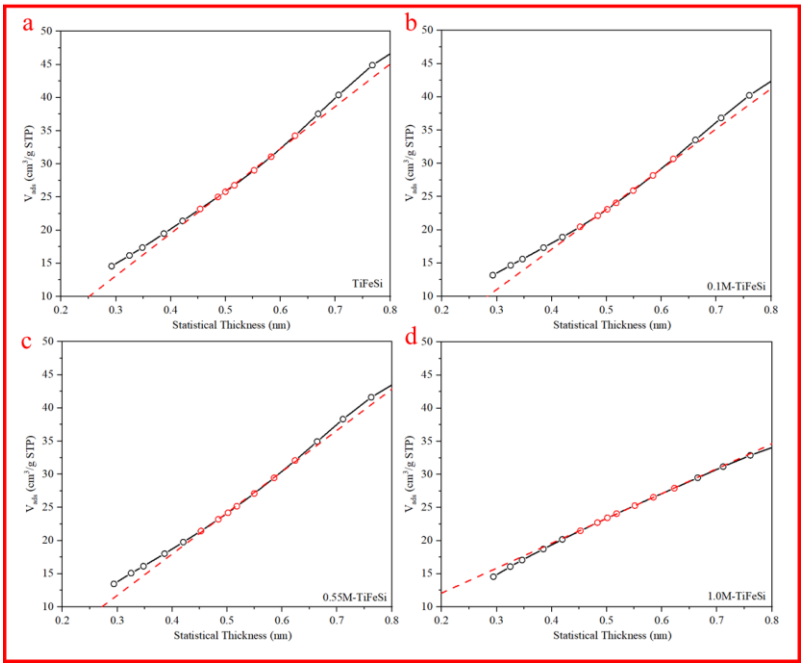

Figure 4.30 - t-plot analysis for TiFeSi support (a); 0.1M-TiFeSi (b), 0.55M-TiFeSi (c), and 1.0M-TiFeSi (d) chlorosulfonic acid functionalised catalysts

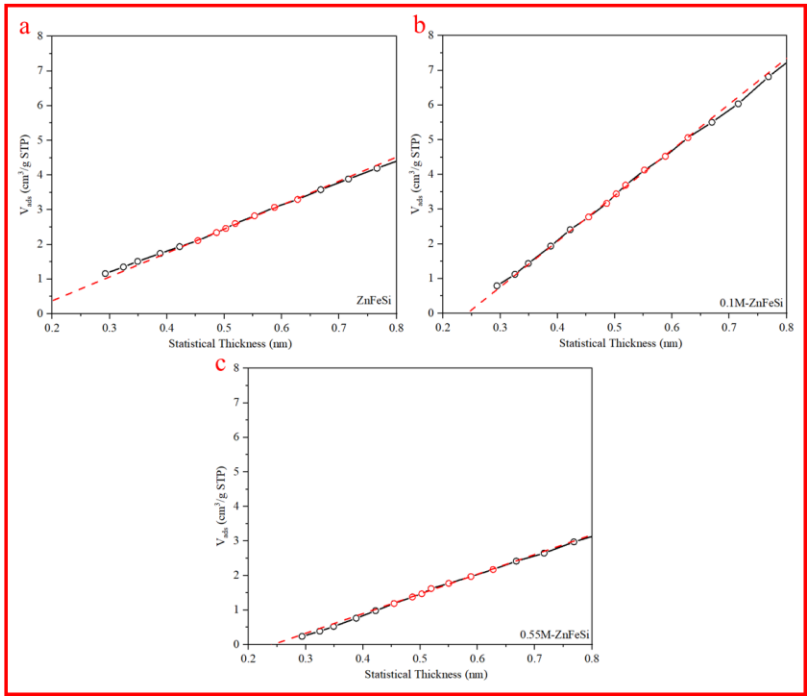

Figure 4.31 - t-plot analysis for ZnFeSi support (a); 0.1M-ZnFeSi (b) and 0.55M-ZnFeSi (c) chlorosulfonic acid functionalised catalysts

BJH pore volume and pore area distribution plots are shown in Figure 4.32a-d for support materials and Figure 4.33a-d and Figure 4.34a-c for TiFeSi and ZnFeSi series respectively, with results summarised in Table 4.16. Large differences between BET surface area (S_{BET}) and BJH surface area (S_{BJH}) is likely due to failure of BJH method to account for microporosity [611] which is present for SiO_2 nanoparticles, FeSi support and 1.0M-TiFeSi functionalised catalyst as determined by t-plot method. While differences in result may also be due to invalid assumption of cylindrical pore shape, especially in case of FeSi where high degree of ink-bottle pores may explain $S_{BJH} > S_{BET}$ result, for all Ti series ink-bottle pore shape was observed yet only 1.0M-TiFeSi had significant discrepancy, suggesting microporosity was main cause of this variation. For all measured materials, average pore diameter is within 2-50 nm mesoporous range which agrees with the type of porosity predicted from N_2 isotherm shape and presence of hysteresis loop. Both average pore diameter and total pore volume decreases from starting SiO_2 nanoparticles to FeSi and then TiFeSi and ZnFeSi supports. This suggests pore filling and blockage occurs with successive layering of material around the inner core structure as would be expected.

With the TiFeSi series it appears that acid functionalisation step did not noticeably influence average pore diameter or total pore volume at low concentrations of chlorosulfonic acid and only led to slight reduction in surface area, agreeing with BET results. At highest concentration the observed “decrease” in pore volume and surface area is likely due to microporosity as previously discussed which is not accounted for in BJH analysis. Interpretation of ZnFeSi series trends is more difficult due to higher experimental errors from low N_2 adsorption capacity. Average pore diameter remained similar between ZnFeSi and 0.1M-ZnFeSi although 0.1M-ZnFeSi had greater total pore volume. This result correlates with increased surface area of 0.1M-ZnFeSi as seen for both BET and BJH analysis. While this result could be insignificant due to higher experimental errors as compared to Ti series due to low N_2 adsorption, it was noted that more ZnFeSi material became lost during acid functionalisation step as compared to TiFeSi. Hence, increased surface area and total pore volume of 0.1M-ZnFeSi may be due to acid digestion leading to creation of more pore structures, similar to explanation for 1.0M-TiFeSi having microporosity. Surface area for 0.55M-ZnFeSi is much closer to ZnFeSi support however both total pore volume and average pore diameter was seen to decrease. CHONS and EDX analysis throughout Chapter 4 identified that carbon contamination was much higher for 0.55M-ZnFeSi compared to all other synthesised catalysts hence pore blockage may be due to retained solvent residues post drying and calcination.

Table 4.16 - Results of BJH Analysis and Comparison to BET Results

Sample	S_{BET} (m^2/g)	S_{BJH} (m^2/g)	Pore Volume (cm^3/g)	Average Pore Diameter (nm)
SiO_2	56.0	33.9	0.218	25.7
FeSi	44.5	70.6	0.125	7.10
TiFeSi	81.3	74.7	0.0905	3.64
0.1M-TiFeSi	72.1	69.6	0.0945	3.64
0.55M-TiFeSi	75.8	68.2	0.0959	3.62
1.0M-TiFeSi	72.6	39.8	0.0532	3.64
ZnFeSi	7.81	10.4	0.0321	4.06
0.1M-ZnFeSi	12.6	22.8	0.0506	4.06
0.55M-ZnFeSi	6.07	13.9	0.0179	3.63

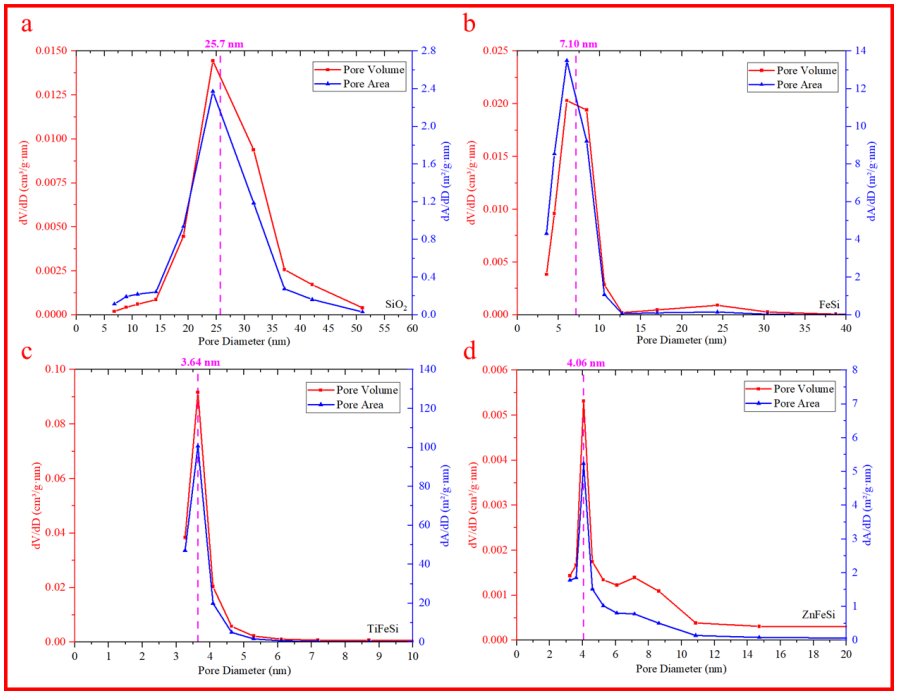

Figure 4.32 - BJH analysis for SiO_2 (a), FeSi (b), TiFeSi (c) and ZnFeSi (d) supports

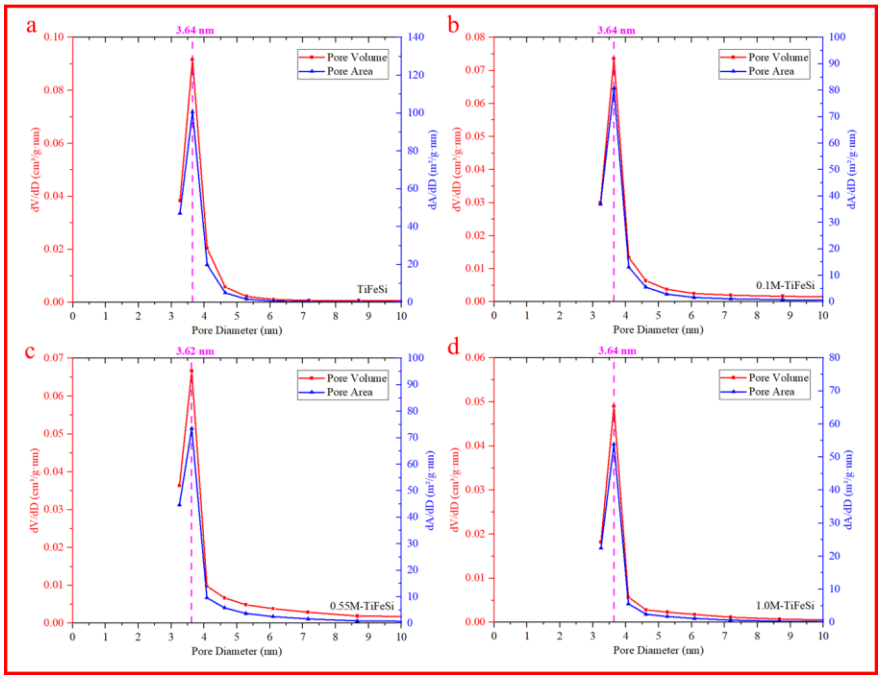

Figure 4.33 - BJH analysis for TiFeSi support (a); 0.1M-TiFeSi (b), 0.55M-TiFeSi (c), and 1.0M-TiFeSi (d) chlorosulfonic acid functionalised catalysts

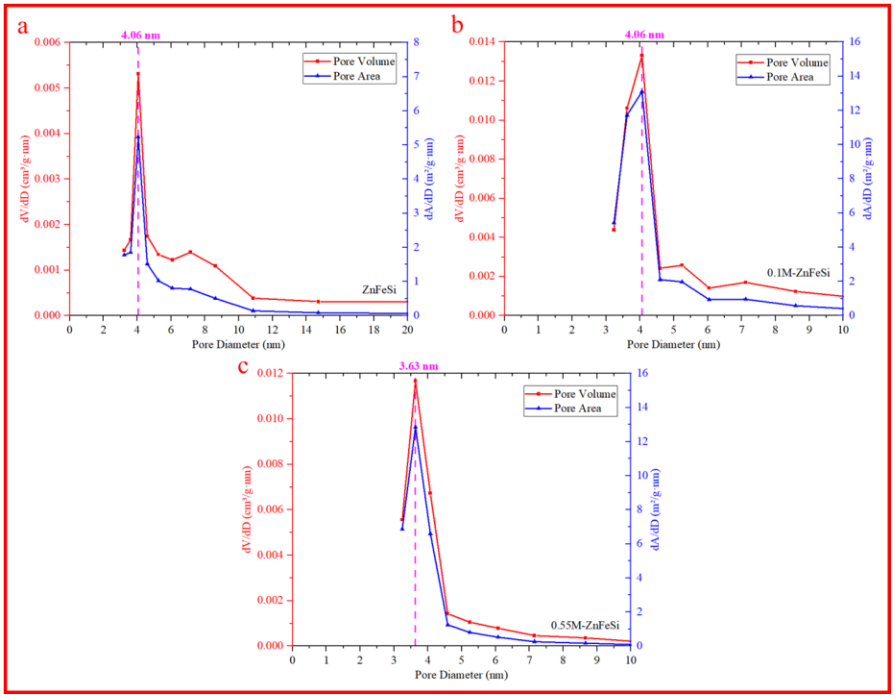

Figure 4.34 - BJH analysis for ZnFeSi support (a); 0.1M-ZnFeSi (b) and 0.55M-ZnFeSi (c) chlorosulfonic acid functionalised catalysts

4.6.2 Scanning Electron Microscopy

SEM micrographs for TiFeSi and ZnFeSi series of functionalised catalysts are shown in Figure 4.36 and Figure 4.37 respectively. All catalyst samples show high degree of aggregation clusters at the microscale with observable nanoscale structures decorating the surface. For TiFeSi series, the presence of spherical microstructure potentially confirms that the coprecipitation synthesis route utilised was successful at forming deposited layers around the starting spherical SiO_2 nanosphere cores. Aggregation of spherical like core-shell nanocatalyst particles into larger spherical microstructures may then occur in dry powder form to produce the observed morphology as shown in Figure 4.35a for 1.0M-TiFeSi. At 100 k magnification nanostructures also appear highly spherical and significantly aggregated.

In ZnFeSi series however, micrographs show that the overall microstructure is substantially less spherical. As can be seen in Figure 4.35b for 0.55M-ZnFeSi the aggregation behaviour leads to more "nugget" like shapes of varying aspect ratios stacked together in irregular morphologies. This pronounced difference in aggregation behaviour might be due to issues with coprecipitation of Zn layer around the FeSi material or previously noted difficulties during the drying and calcination steps during ZnFeSi synthesis and functionalisation. Less spherical, more irregular core-shell ZnFeSi nanocatalyst particles may hence aggregate in more irregular orientations as a dry power hence leading to the observed "nugget" like morphology. At 100 k magnification, the nanostructure is highly aggregated and nanoparticles decorating the surface take on a more expected spherical form. Morphology appears more affected by acid concentration in ZnFeSi series than TiFeSi at the microscale, however structure is still very similar at nanoscale.

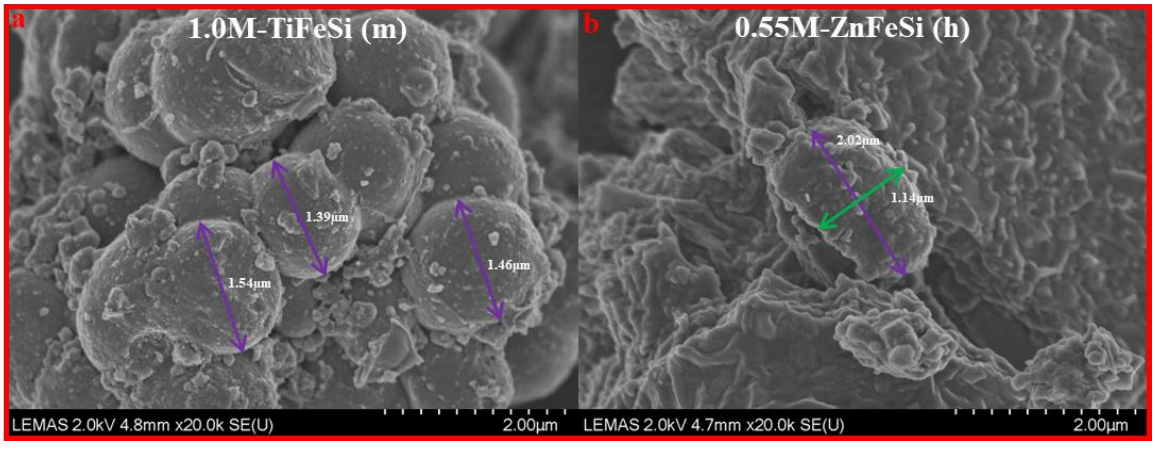

Figure 4.35 - Microscale Morphology of TiFeSi (a) and ZnFeSi (b) Catalysts

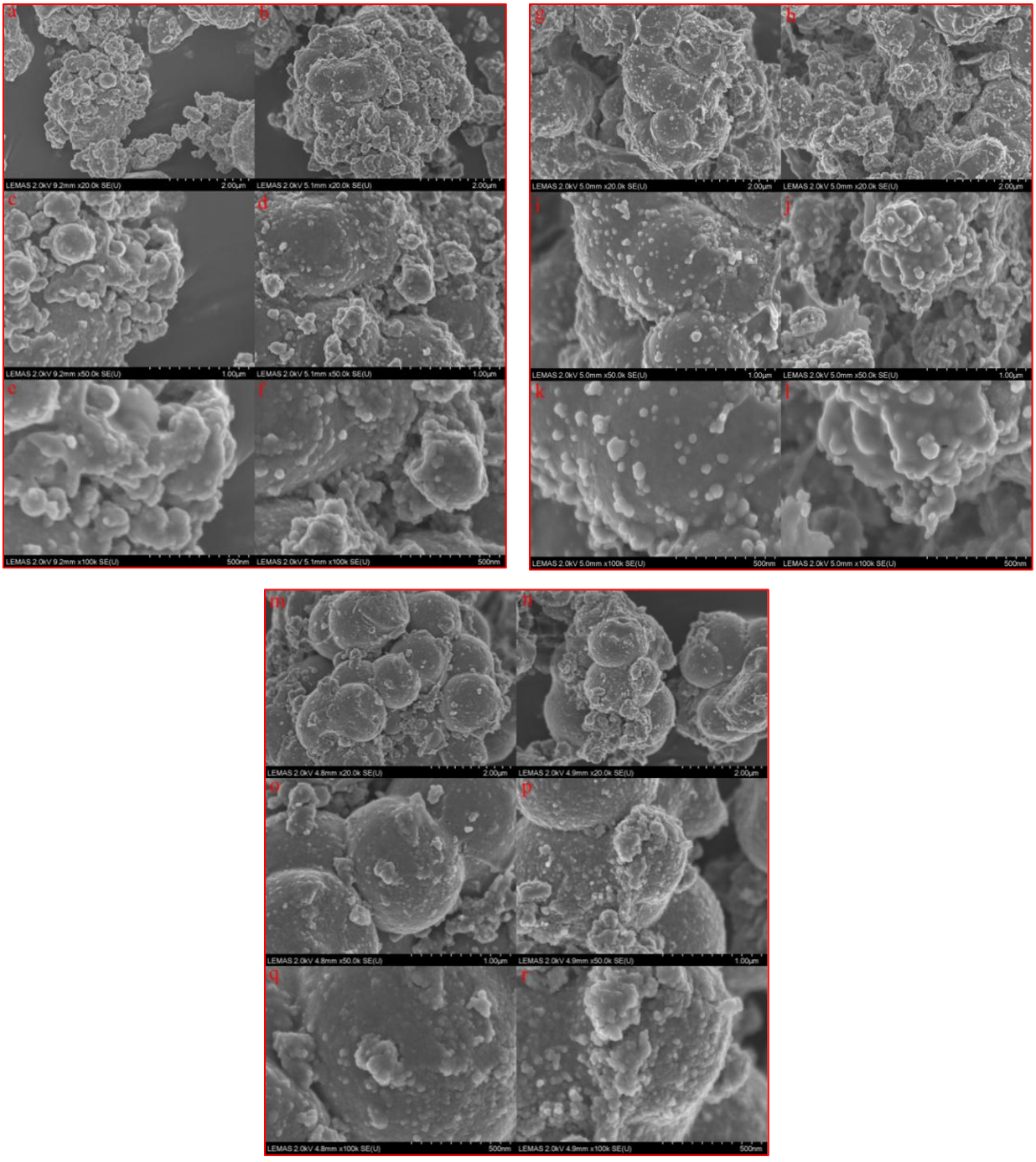

Figure 4.36 - SEM Micrographs of 0.1M-TiFeSi (a-f), 0.55M-TiFeSi (g-l), 1.0M-TiFeSi (m-r)

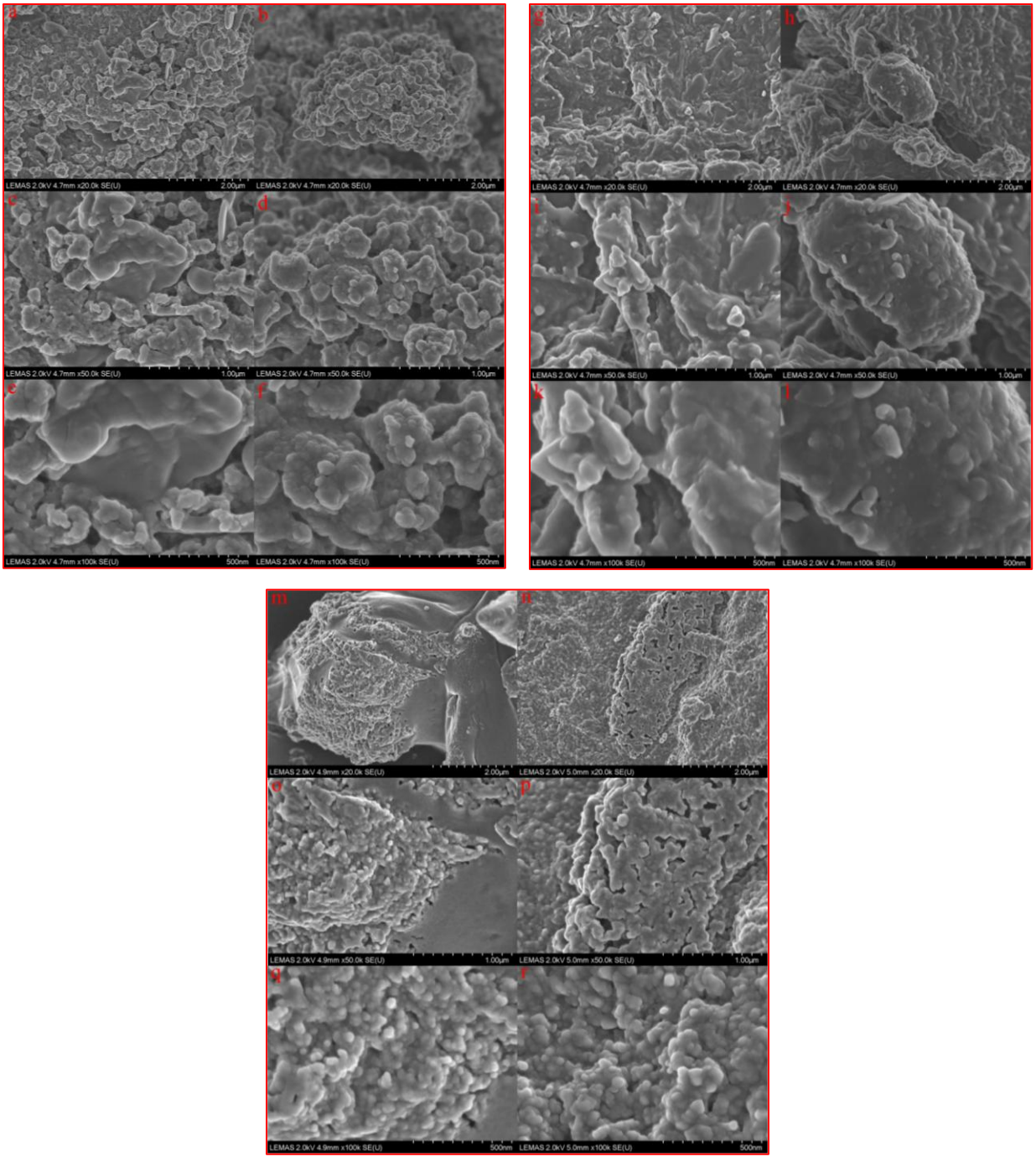

Figure 4.37 - SEM Micrographs of 0.1M-ZnFeSi (a-f), 0.55M-ZnFeSi (g-l), 1.0M-ZnFeSi (m-r)

Using ImageJ software, a nanoparticle size distribution for each catalyst was determined and results illustrated for TiFeSi and ZnFeSi series in Figure 4.38 and Figure 4.39 respectively, with results summarised in Table 4.17. For all catalysts the surface nanoparticles were of similar size, with most nanoparticle structures between approximately 20-50 nm while larger microscale aggregates were also observed between 100-450 nm size. No significant effect on changing acid functionalisation concentration was observed on the surface nanoparticle structures, instead differences between each size distribution can be attributed to random variations in morphology for each SEM micrograph site imaged. N_2 porosimetry analysis in Chapter 4.6.1 indicated a mesoporous surface structure with ink-bottle shaped pores. From the average surface nanoparticle sizes observed in SEM it is reasonable to expect that interparticle voids would be similar in size or smaller, therefore <50 nm required to be considered mesoporous. Additionally, the high degree of aggregation and lack of uniform ordering would suggest ink-bottle pore shape over cylindrical channels, wedges or slits. SEM observations therefore support N_2 porosimetry results.

Table 4.17 - SEM Surface Nanoparticle Size Distribution

Sample	Average Size (nm)	Standard Deviation (nm)
0.1M-TiFeSi	33	10
0.55M-TiFeSi	40	11
1.0M-TiFeSi	28	6.2
0.1M-ZnFeSi	32	8.5
0.55M-ZnFeSi	34	9.0
1.0M-ZnFeSi	38	9.7

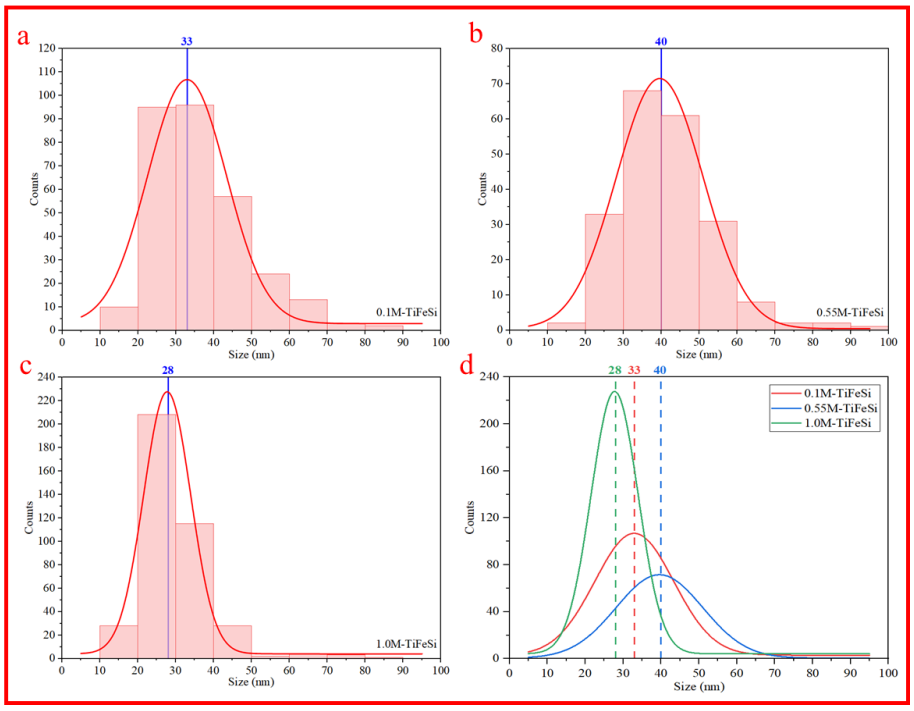

Figure 4.38 - SEM Surface Nanoparticle Size Distributions for 0.1M-TiFeSi (a), 0.55M-TiFeSi (b), 1.0M-TiFeSi (c) and Comparison Plot (d)

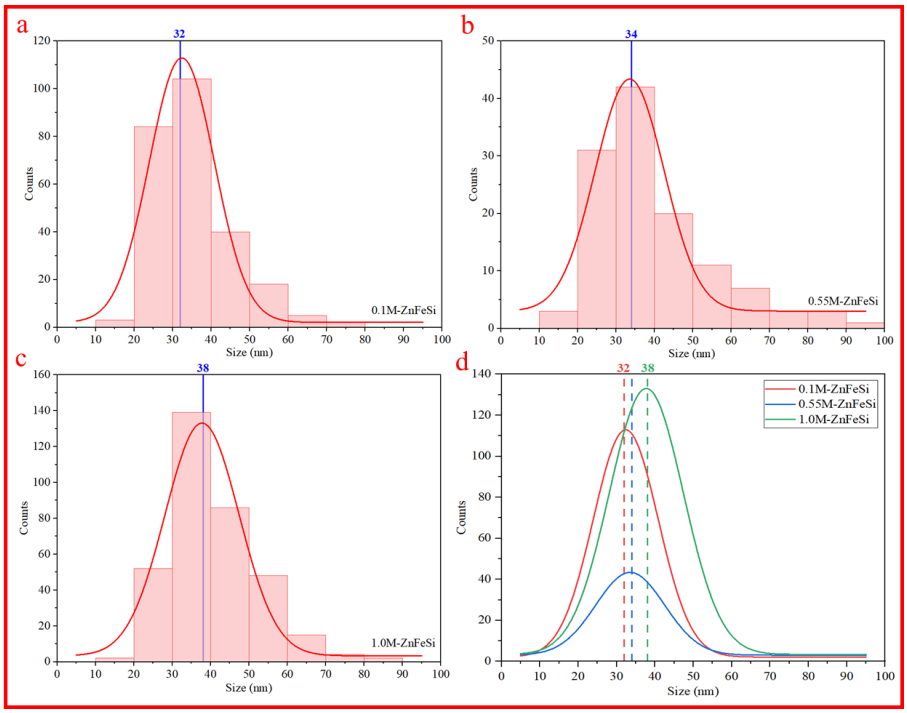

Figure 4.39 - SEM Surface Nanoparticle Size Distributions for 0.1M-ZnFeSi (a), 0.55M-ZnFeSi (b), 1.0M-ZnFeSi (c) and Comparison Plot (d)

4.6.3 Transmission Electron Microscopy

TEM micrographs in brightfield and annular dark field mode are displayed in Figure 4.40a-f, Figure 4.41a-d and Figure 4.42a-d for 0.1M-TiFeSi, 0.55M-TiFeSi and 1.0M-TiFeSi respectively. A high degree of aggregation can be observed with microstructure clusters 100-450 nm in size for all Ti series catalysts. On the surface of the microstructure clusters, evidence of highly aggregated nanoparticles can be seen decorating the surface layer. These results agree with SEM observations made in Chapter 4.6.2 and validate successful synthesis of catalytically active layers present on outer surface in a core-shell nature. Presence of <30 nm unidentified nanofibers were also observed and may be due to minor species of Ti, Fe, and Si oxide crystallites arranging in needle like structures during sample preparation and analysis. Micrographs shown in Figure 4.40b, Figure 4.41a and Figure 4.42a are especially of interest for demonstrating strong evidence of core-shell morphology, where spherical 100nm SiO_2 core is surrounded by thin nanoparticle films. In Figure 4.40b of 0.1M-TiFeSi an uncoated ~120nm SiO_2 sphere can be seen on the right, with a layer of ~20 nm thick sulfated metal oxide coating forming around the left SiO_2 support to produce 113 nm and 144 nm nanoparticles. In Figure 4.41a for 0.55M-TiFeSi coated core-shell nanocatalyst particles of size ~170 nm are observed in bottom left of image. And in Figure 4.42a for 1.0M-TiFeSi multiple highly aggregated core-shell particles of size 100-200 nm can be observed clustering around larger bulk microscale aggregates. Therefore, for all Ti series of nanocatalysts it was observed that nanoscale structures are present in high degree of aggregation. Morphology was found to be inhomogeneous with presence of uncoated SiO_2 support, thin core-shell nanocatalysts comprised of a nanoparticle core and <100 nm shell, and larger bulk microscale aggregate. Future optimisation work may be able to increase homogeneity of nanocatalyst structure by careful control of synthesis conditions. Which might lead to further enhancement in catalytic performance by increased surface area, porosity and active site accessibility. However, without alteration of surface chemistry by addition of surfactants as other studies discuss [612-614] or modifying synthesis route, which may dramatically hinder catalytic activity and physical properties, high degree of aggregation and inhomogeneity may prove challenging to overcome. Combination of multiple wet treatment steps required during synthesis provides sufficient opportunity for aggregation effects to occur, and a way to minimise higher interparticle forces at nanoscale relative to bulk particles [615] without reducing catalytic activity would need to be found. Nevertheless, for all Ti series the results of TEM confirm nanocatalyst morphology was achieved.

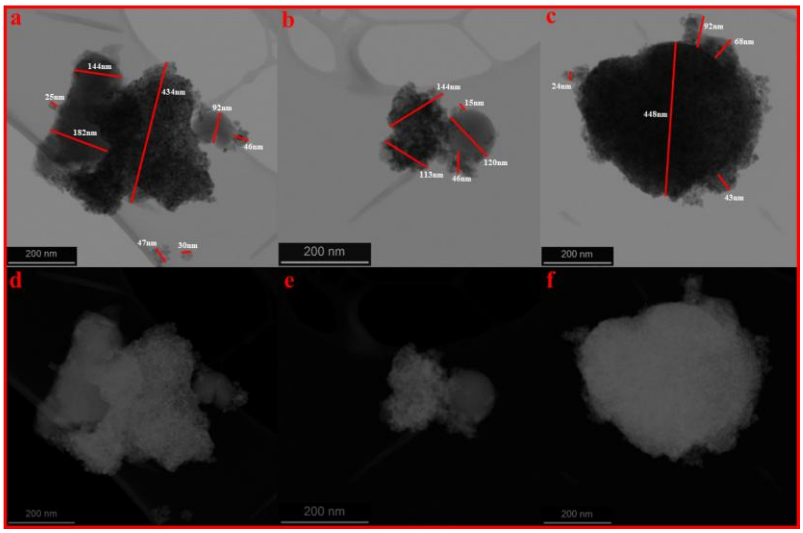

Figure 4.40 - TEM Micrographs of 0.1M-TiFeSi

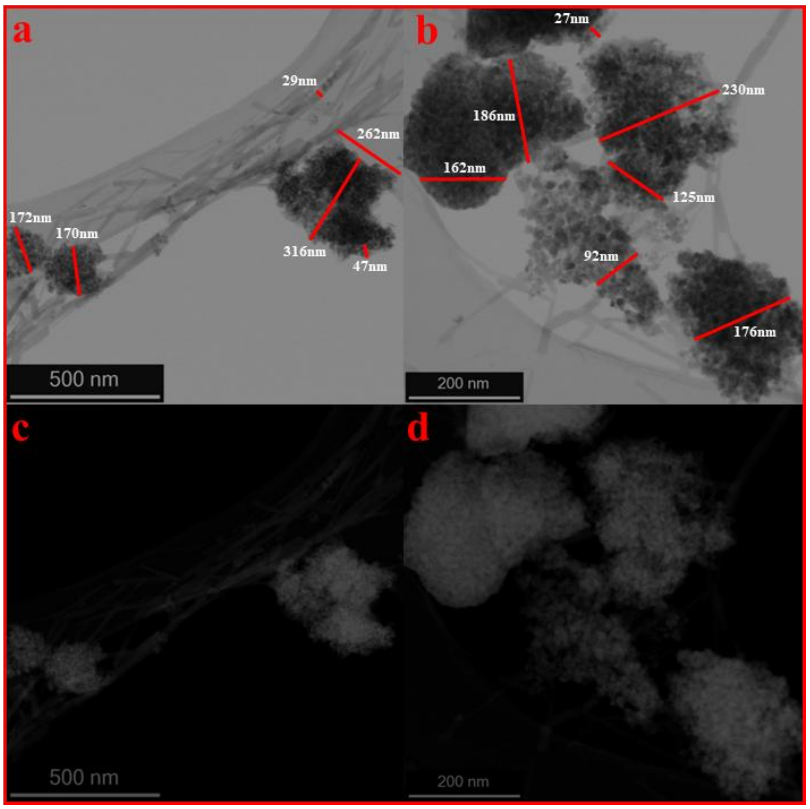

Figure 4.41 - TEM Micrographs of 0.55M-TiFeSi

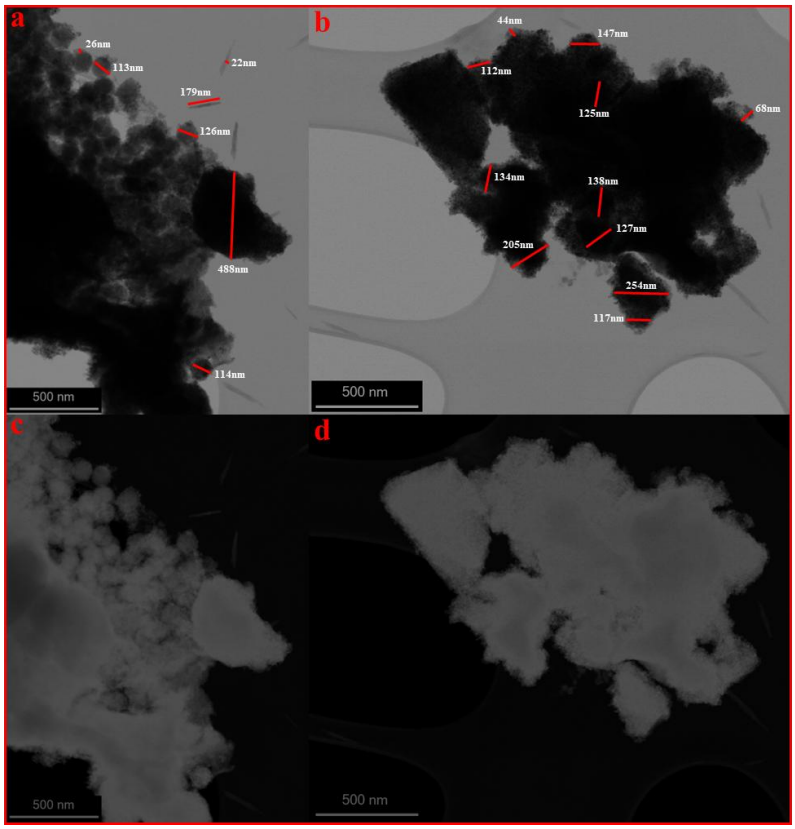

Figure 4.42 - TEM Micrographs of 1.0M-TiFeSi

4.7 Composition

4.7.1 CHONS Analysis

Results of CHONS analyses are summarised in Table 4.18. Figure 4.43a illustrates the composition trends for catalyst support materials. Low oxygen content for SiO_2 and TiO_2 is due to high thermal stability since CHONS relies on thermal decomposition. Trace nitrogen measured in all samples was more likely from physiosorbed air than precipitating agent due to high volatility of ammonium hydroxide. Trace carbon was similarly from atmospheric CO_2 present. Both FeSi and ZnFeSi support had relatively high levels of sulfur content (7.28 wt% and 7.56 wt% respectively) indicating that despite repeated wash steps, testing for sulfate via BaCl and calcination at 400 °C for 4 hours, sulfur contamination of the support material remained. In comparison, TiFeSi support had little carbon contamination from butoxide precursor. Hydrogen content may be from surface hydroxyls, bound water or Brønsted acidic species. Figure 4.43b shows composition trends for TiFeSi series of catalysts. Oxygen content is positively correlated with sulfur content, suggesting presence of sulfur-oxygen groups as expected from sulfated material. Carbon impurities are present in TiFeSi catalysts, presumably from toluene solvent, despite use of vacuum oven and calcination. Other literature has reported on calcination not always effectively removing organic residues [616, 617]. Carbon impurity level increases with acid functionalisation strength likely due to formation of a thicker sol-gel under harsher treatment which hinders drying. Figure 4.43c shows composition trends for ZnFeSi series of catalysts and similarly illustrates the difficulties faced with drying Zn rich material due to formation of even thicker and more viscous sol. Hence a high degree of organic carbon contamination is observed. Carbon impurity increases with acid strength again except for 1.0M-ZnFeSi catalyst where such little solid residue remained drying step was simple. High oxygen content detection is probably due to both high level of sulfate content and low thermal stability of ZnO. Figure 4.43d compares the sulfur content with increasing chlorosulfonic acid concentration for TiFeSi and ZnFeSi series. In both cases functionalisation increased sulfur loading indicating successful treatment. For ZnFeSi catalysts, sulfur content overall increased with acid concentration. Surprisingly, 0.1M-TiFeSi and 1.0M-TiFeSi displayed similar sulfur content. As discussed in Chapter 4.4 and Chapter 4.5.2, higher thermal stability due to increased acid site strength could explain the low sulfur content detected for 1.0M-TiFeSi. Comparison with non-thermal techniques such as EDX and XPS however confirms that 0.1M-TiFeSi and 1.0M-TiFeSi have similar sulfur loading. This detail is explored further in next subsection.

Table 4.18 - Summary of CHONS Results

Sample	Carbon wt% (Error)	Hydrogen wt% (Error)	Oxygen wt% (Error)	Nitrogen wt% (Error)	Sulfur wt% (Error)
SiO_2	0.87 (± 0.02)	0.93 (± 0.12)	2.54 (± 0.03)	0.27 (± 0.03)	0.00 (± 0.00)
FeSi	0.38 (± 0.03)	1.55 (± 0.01)	17.54 (± 1.62)	0.65 (± 0.01)	7.28 (± 0.13)
TiFeSi	0.51 (± 0.01)	0.22 (± 0.02)	1.10 (± 0.02)	0.35 (± 0.02)	0.20 (± 0.05)
ZnFeSi	0.15 (± 0.00)	0.39 (± 0.01)	11.00 (± 0.57)	0.30 (± 0.00)	7.56 (± 0.17)
0.1M-TiFeSi	0.79 (± 0.00)	0.40 (± 0.01)	3.25 (± 0.25)	0.35 (± 0.03)	2.32 (± 0.00)
0.55M- TiFeSi	2.11 (± 0.09)	0.64 (± 0.02)	5.93 (± 0.30)	0.39 (± 0.00)	3.88 (± 0.05)
1.0M-TiFeSi	2.40 (± 0.01)	0.32 (± 0.01)	2.74 (± 0.20)	0.38 (± 0.01)	1.80 (± 0.03)
0.1M-ZnFeSi	21.89 (± 0.41)	3.45 (± 0.23)	28.81 (± 3.26)	0.36 (± 0.02)	13.16 (± 0.26)
0.55M-ZnFeSi	29.07 (± 0.10)	2.93 (± 0.04)	28.37 (± 1.04)	0.39 (± 0.00)	13.21 (± 0.27)
1.0M-ZnFeSi	3.46 (± 0.09)	1.42 (± 0.47)	25.80 (± 3.06)	0.33 (± 0.04)	16.05 (± 0.47)

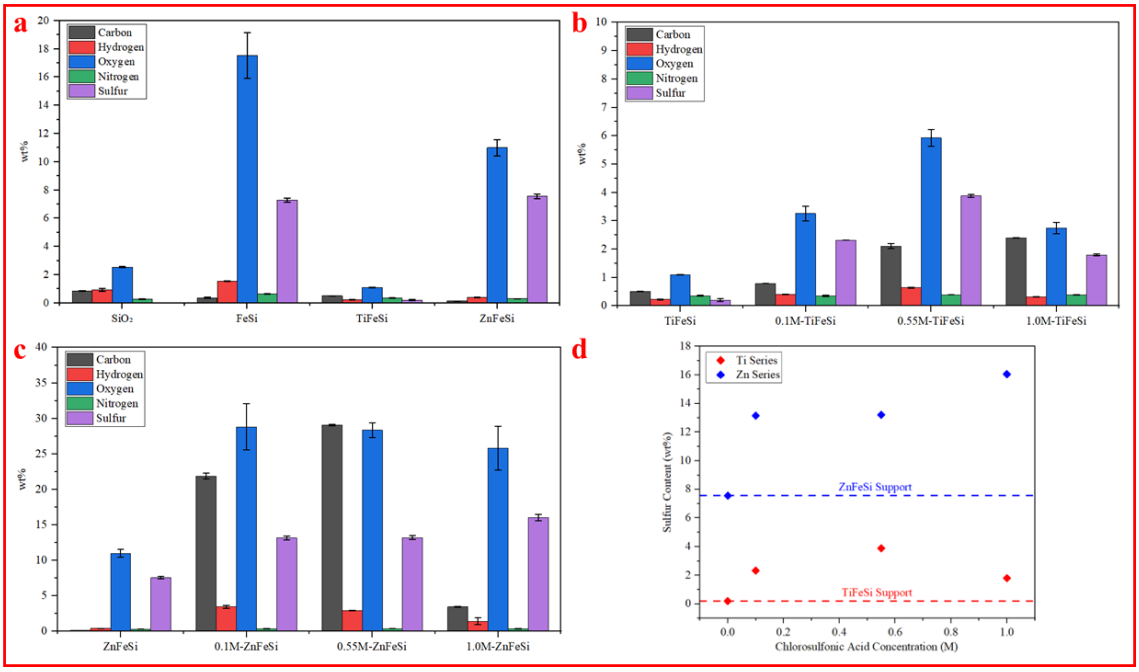

Figure 4.43 - CHONS Results for Catalyst Supports (a), TiFeSi Series (b), ZnFeSi Series (c) and Sulfur Content with Chlorosulfonic Acid Functionalisation Concentration (d)

4.7.2 Energy Dispersive X-ray Spectrometry

SEM-EDX was performed using Hitachi SU8230 FESEM setup to confirm successful synthesis of support materials prior to acid functionalisation. Obtained spectra for SiO_2, FeSi, TiFeSi and ZnFeSi supports are given in Figure 4.44a-d and confirm presence of all expected elements. Presence of S in FeSi, TiFeSi and ZnFeSi material indicates that even after multiple calcination steps and repeated washings until undetectable free sulfate ions in solution, sulfate groups from precursor materials exist on surface prior to chlorosulfonic acid treatment. Use of sulfate precursors was selected to avoid further contamination with other species for this reason. It can also be noted that intensity signal of Si and Fe are low in TiFeSi and ZnFeSi supports, indicative of the material losses that occurred with each subsequent synthesis step. 2D elemental maps were taken for FeSi, TiFeSi and ZnFeSi supports as shown in Figure 4.45, Figure 4.46 and Figure 4.47 respectively. Elemental distribution at the microscale appears inhomogeneous with regions of higher concentrations of Ti, Zn, Fe and Si as well as evidence of strongly aggregated microclusters.

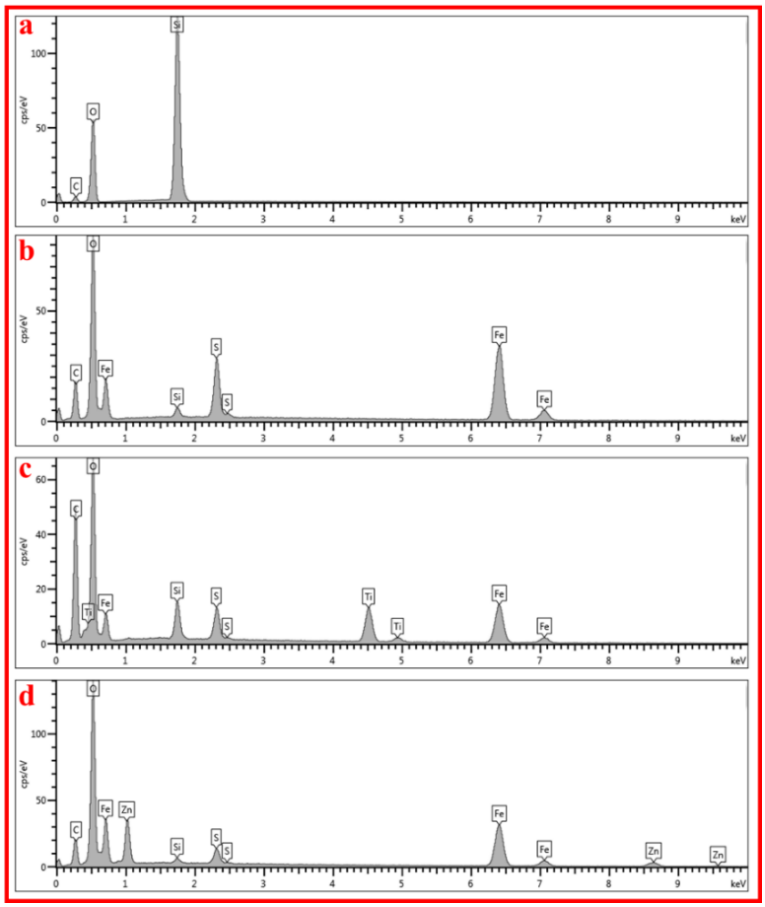

Figure 4.44 - SEM-EDX Spectra for SiO_2 (a), FeSi (b), TiFeSi (c) and ZnFeSi (d)

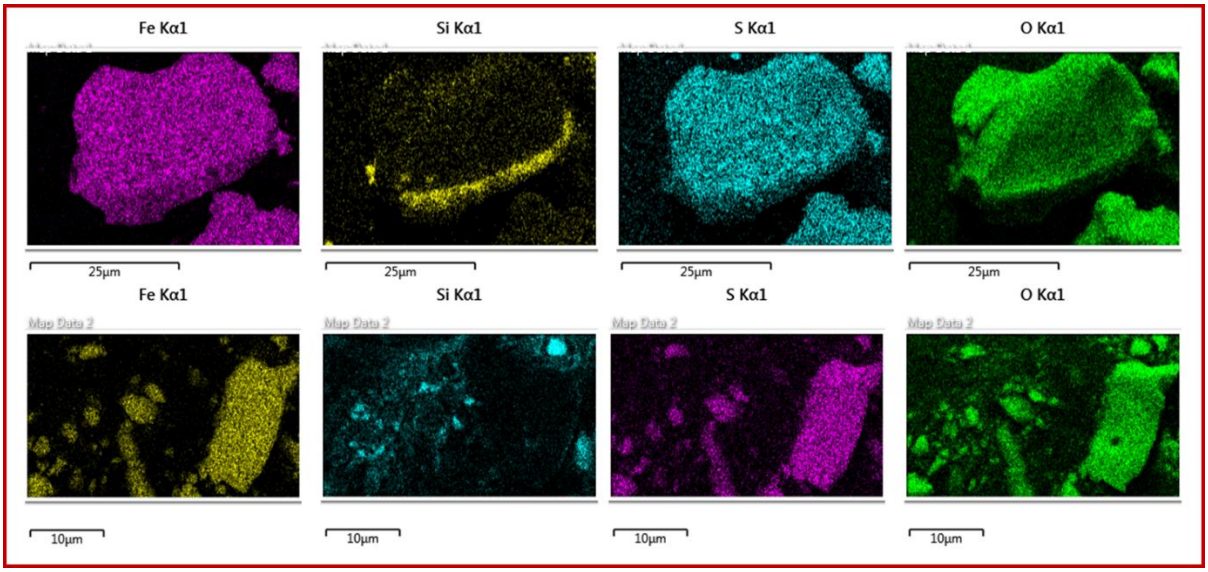

Figure 4.45 - SEM-EDX Element Maps of FeSi Support

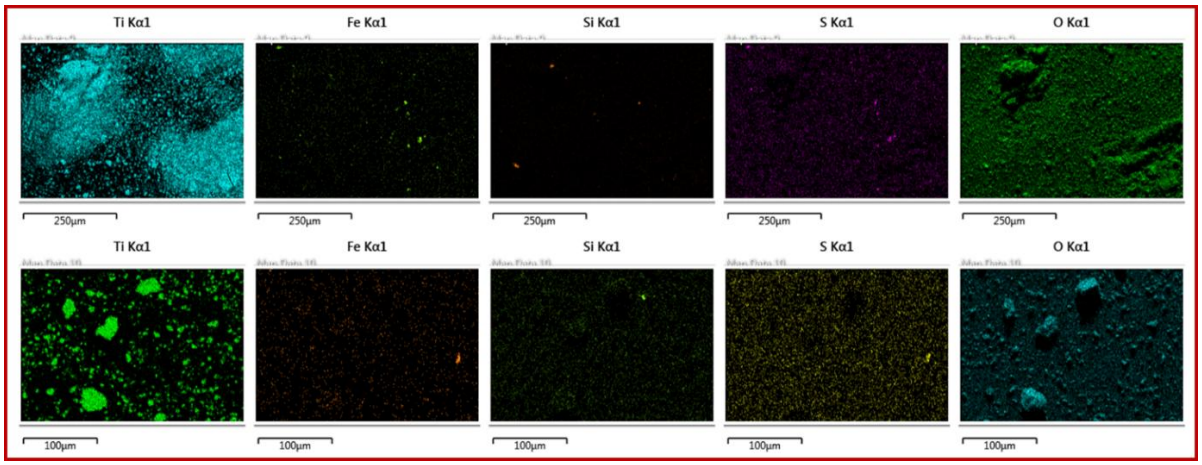

Figure 4.46 - SEM-EDX Element Maps of TiFeSi Support

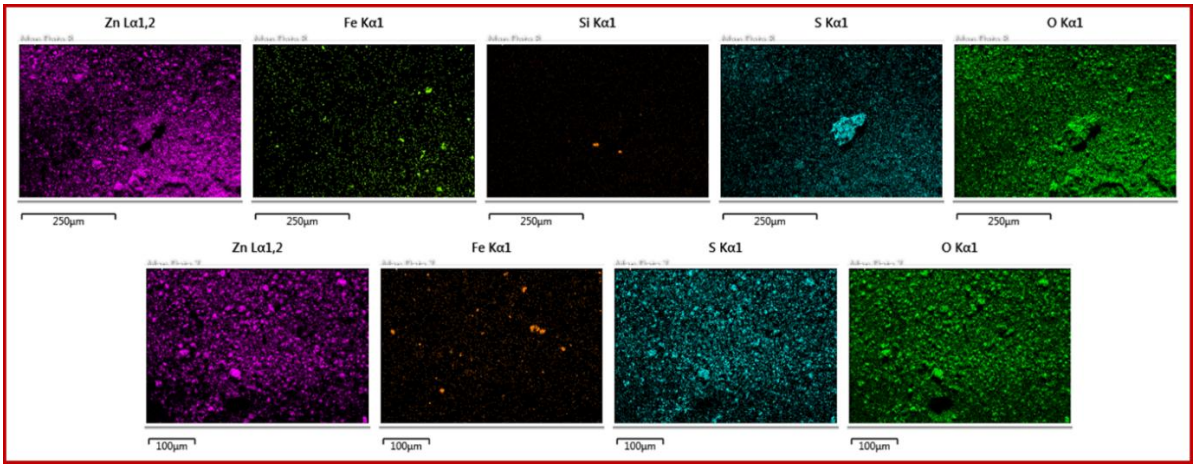

Figure 4.47 - SEM-EDX Element Maps of ZnFeSi Support

More SEM-EDX spectra were taken post acid functionalisation with plots given in Figure 4.48 for both Ti series (a-c) and Zn series (d-f). All expected elements were present with no additional impurities. Some spectra had values of Si below software detection limit hence peak was not automatically identified as indicated in 0.55M-ZnFeSi and 1.0M-ZnFeSi plots (e and f) however visible peak was observed on axis rescaling, likely a result of low sample mass available for these samples and increased detection of S reducing Si overall wt% contribution. Plot f also indicates 1.0M-ZnFeSi containing Ti impurity however this was attributed to background noise from nearby Ti series due to very low count rate and small amount of 1.0M-ZnFeSi material loaded for analysis. Quantitative wt% analysis was performed by peak integration and these results are produced in Table 4.19 and Table 4.20 for Ti and Zn series respectively. Post acid treatment a notable increase in S content was observed indicating successful surface functionalisation. For Zn series, increasing the chlorosulfonic acid concentration increased average S loading from 4.70 wt% for ZnFeSi support up to a maximum of 14.8 wt% for 1.0M-ZnFeSi. However, for Ti series S loading increased from 0.13 wt% for TiFeSi support up to a maximum of 4.86 wt% for 0.55M-TiFeSi. Further increase in chlorosulfonic acid concentration did not add more sulfur content, with 0.1M-TiFeSi having approximately double the S loading than 1.0M-TiFeSi. Lack of S loading in 1.0M-TiFeSi was also observed in CHONS analysis as discussed prior. Possible explanation could be that excess chlorosulfonic acid promotes digestion of support material as observed by increasing mass losses during synthesis, or promotion of dimerization over direct surface functionalisation.

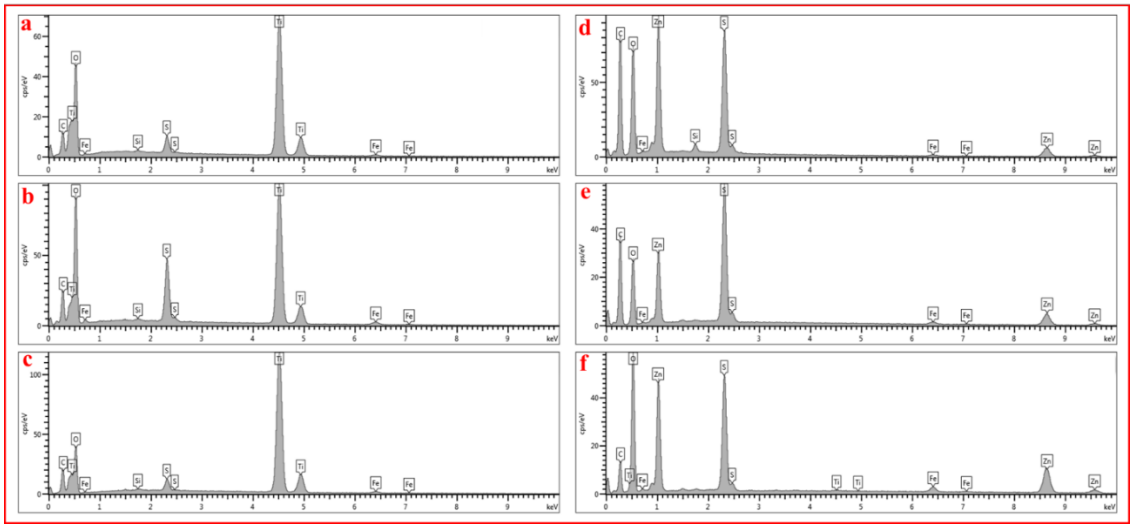

Figure 4.48 - SEM-EDX Spectra for 0.1M-TiFeSi (a), 0.55MTiFeSi (b), 1.0M-TiFeSi (c), 0.1M-ZnFeSi (d), 0.55M-ZnFeSi (e) and 1.0M-ZnFeSi

Table 4.19 - Averaged SEM-EDX Results for Ti Series

Element	Averaged wt%			
	TiFeSi	0.1M-TiFeSi	0.55M-TiFesi	1.0M-TiFeSi
C	11.8 (± 0.18)	7.12 (± 0.18)	11.0 (± 0.20)	9.10 (± 0.18)
O	41.8 (± 0.26)	40.5 (± 0.31)	42.3 (± 0.28)	37.9 (± 0.32)
Si	0.14 (± 0.02)	0.05 (± 0.01)	0.09 (± 0.02)	0.12 (± 0.01)
S	0.13 (± 0.01)	1.92 (± 0.05)	4.86 (± 0.06)	0.95 (± 0.04)
Ti	45.9 (± 0.26)	49.6 (± 0.29)	40.8 (± 0.25)	51.3 (± 0.29)
Fe	0.18 (± 0.03)	0.81 (± 0.09)	0.91 (± 0.09)	0.61 (± 0.09)

Table 4.20 - Averaged SEM-EDX Results for Zn Series

Element	Averaged wt%			
	ZnFeSi	0.1M-ZnFeSi	0.55M-ZnFesi	1.0M-ZnFeSi
C	11.8 (± 0.30)	46.8 (± 0.28)	47.7 (± 0.29)	22.3 (± 0.31)
O	35.6 (± 0.23)	21.2 (± 0.20)	23.1 (± 0.21)	33.8 (± 0.20)
Si	6.44 (± 0.05)	0.10 (± 0.01)	0.03 (± 0.01)	0.15 (± 0.01)
S	4.70 (± 0.07)	12.2 (± 0.10)	13.7 (± 0.11)	14.8 (± 0.10)
Fe	14.4 (± 0.15)	0.70 (± 0.08)	1.05 (± 0.09)	3.75 (± 0.12)
Zn	27.1 (± 0.22)	18.9 (± 0.16)	14.5 (± 0.17)	25.2 (± 0.17)

To explore elemental distribution at the nanoscale, EDX spectra and elemental maps were also taken during TEM analysis of Ti series of nanocatalysts. Figure 4.49, Figure 4.50 and Figure 4.51 corresponding to 0.1M-TiFeSi, 0.55M-TiFeSi and 1.0M-TiFeSi nanocatalysts show elemental maps of Ti, Fe, Si, S and O species along with reference source brightfield image. Averaged results of elemental composition across all sites imaged is summarised in Table 4.21. Results of TEM-EDX agree with SEM-EDX with high levels of O and Ti wt% contribution alongside minor amounts of S, Si and Fe also detected. Again 0.55M-TiFeSi was observed to have highest loading of sulfur species on surface, with 0.1M-TiFeSi and 1.0M-TiFeSi nanocatalysts having similarly lower sulfur loadings after considering the large variation in sulfur detected across all sites imaged.

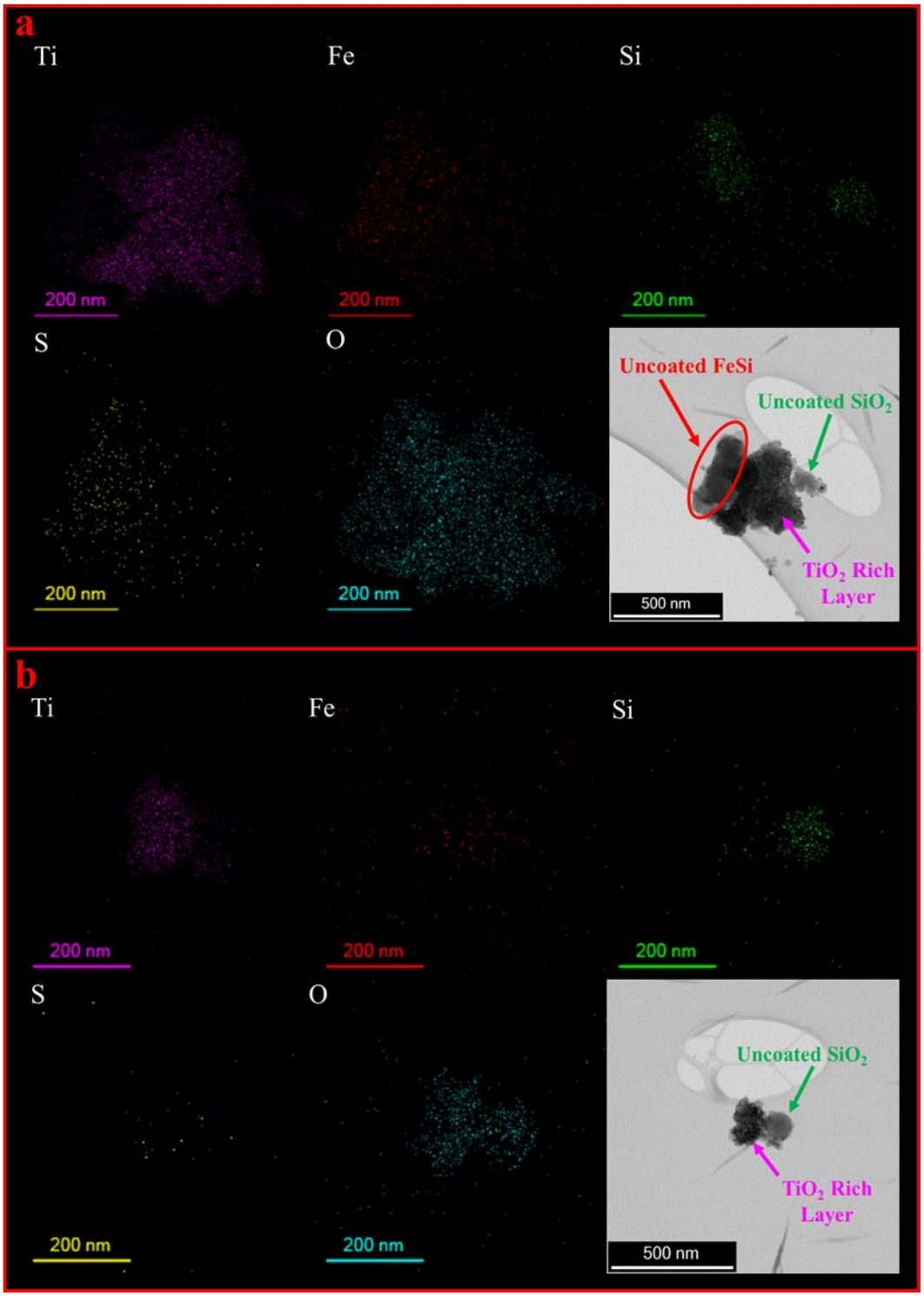

Figure 4.49 - TEM-EDX Elemental Maps of 0.1M-TiFeSi

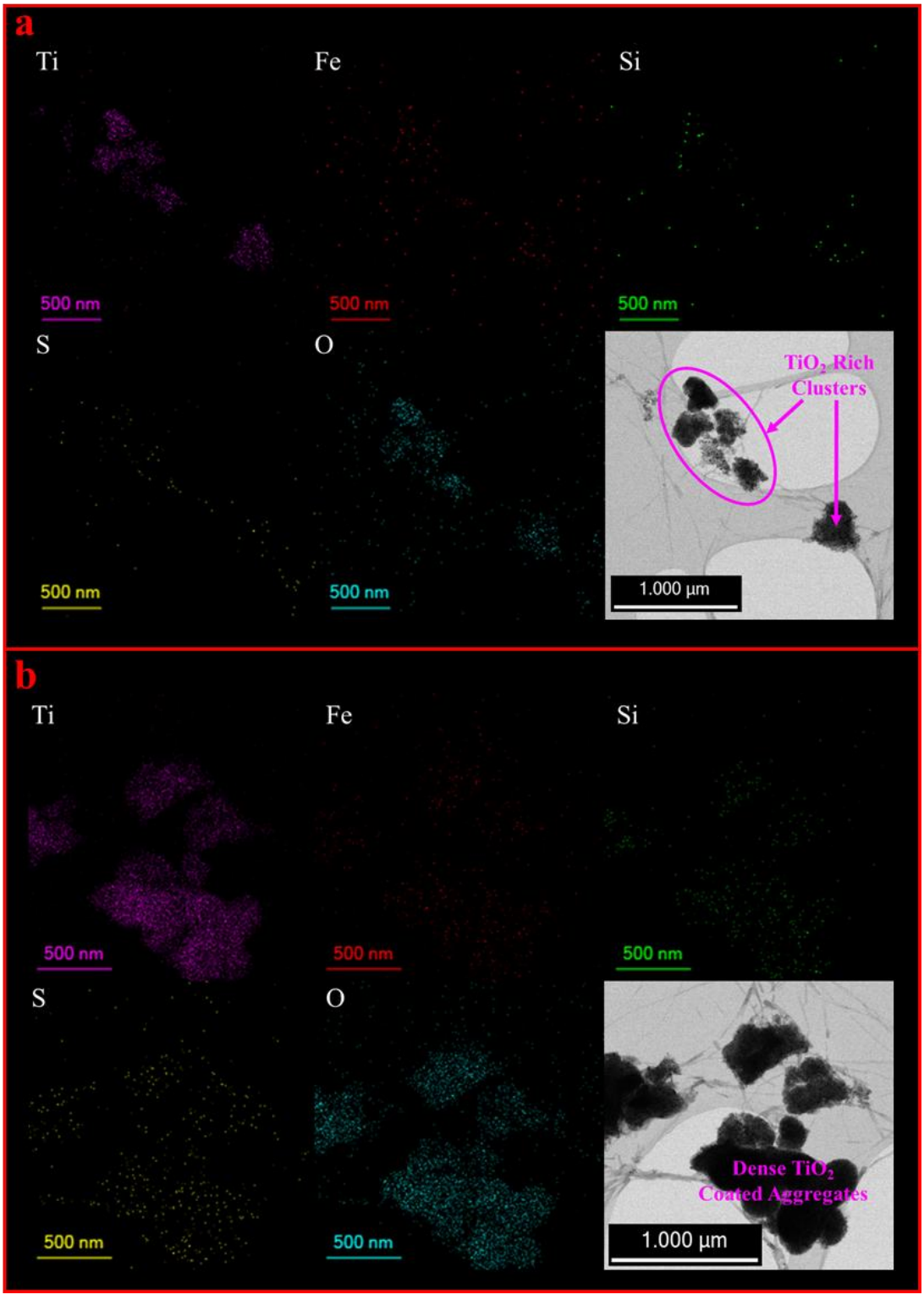

Figure 4.50 - TEM-EDX Elemental Maps of 0.55M-TiFeSi

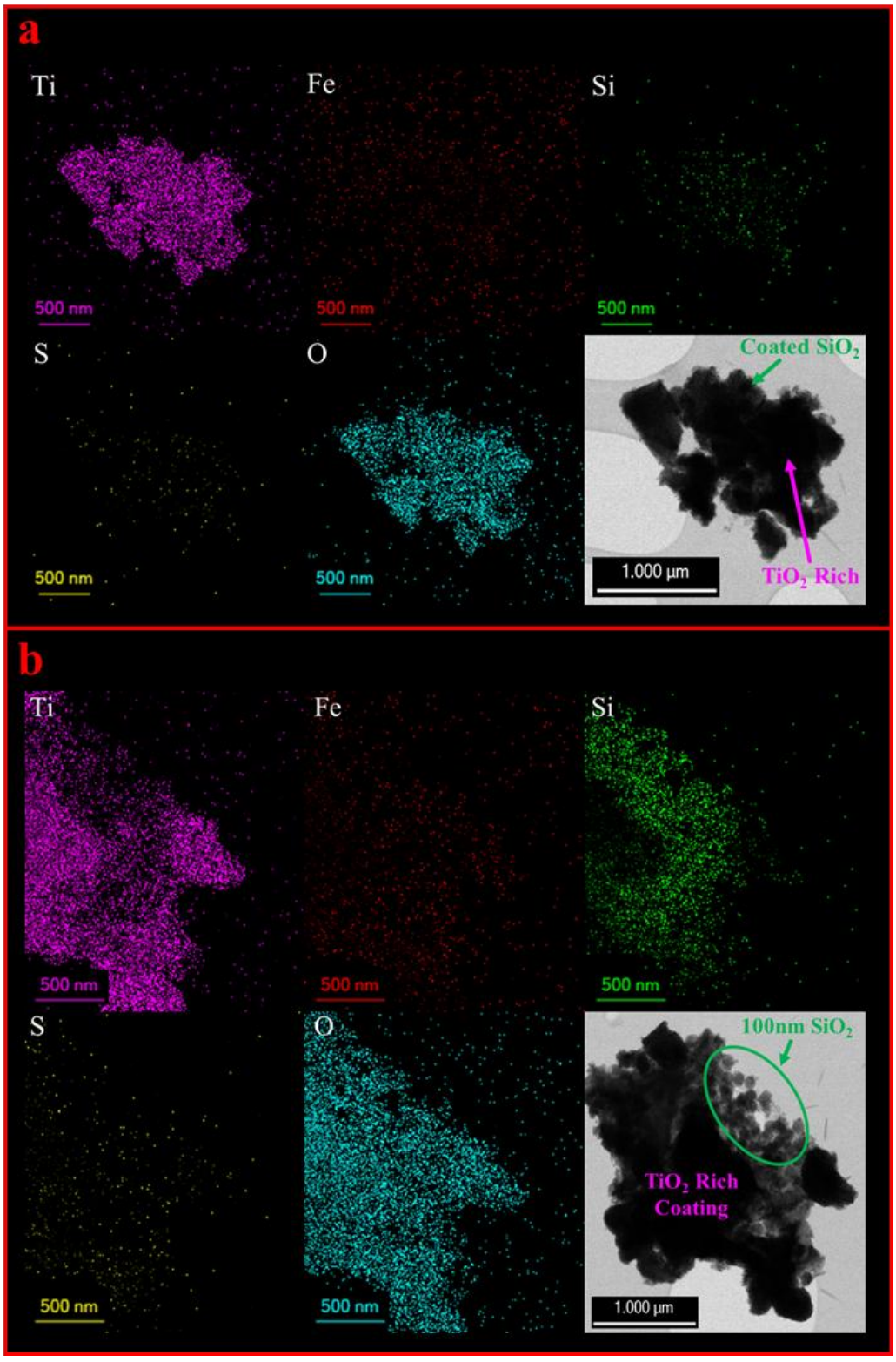

Figure 4.51 - TEM-EDX Elemental Maps of 1.0M-TiFeSi

Figure 4.49a,b of 0.1M-TiFeSi nanocatalyst both provide evidence of regions containing high Si concentration corresponding to uncoated 100 nm SiO_2 support. Figure 4.49a also shows an area of uncoated FeSi where Fe and Si signal is much stronger than Ti. Dense TiO_2 shell coating is confirmed. Sulfur is present throughout and at highest concentration in region associated with uncoated FeSi, indicative of residual sulfate species not removed from iron precursor salt. However, functionalisation with low 0.1 M concentration of chlorosulfonic acid has led to minor quantities of sulfate detected within TiO_2 rich phase as well. Figure 4.49b shows an uncoated SiO_2 support nanoparticle on the right as compared to a coated Ti rich SiO_2 nanostructure on the left confirming a core-shell nature. Trace amounts of Fe and S are detected across both particles. Figure 4.50a,b of 0.55M-TiFeSi shows evidence of low and high density aggregation clusters respectively. Figure 4.50a features regions rich in SiO_2 at centre of TiO_2 rich clusters suggesting coating of SiO_2 support with TiO_2 in a core shell nature similar to 0.1M-TiFeSi. Low levels of Fe and S are present as part of Ti-Si-O rich regions. Figure 4.50b has much denser aggregation phases rich in TiO_2 shell coating and also containing Fe and Si oxides at lower concentration as core species. Presence of S is observed throughout all clusters. Figure 4.51a, b of 1.0M-TiFeSi shows inhomogeneity with high density aggregation and lower density nanostructures. Figure 4.51a indicates coating of SiO_2 core with a rich shell of TiO_2 layer. Minor traces of Fe and S are distributed throughout. Figure 4.51b clearly demonstrates regions of ~100 nm SiO_2 rich layer at surface of bulk aggregate that includes Ti, Fe and S species. A dense TiO_2 rich coating region is also observed that also contains Si, Fe and S. Elemental maps of all Ti series catalysts therefore confirms core shell nature of SiO_2 rich region coated with TiO_2 and containing Fe and S elements.

Table 4.21 - Averaged TEM-EDX Results for Ti Series

Element	Averaged wt%		
	0.1M-TiFeSi	0.55M-TiFesi	1.0M-TiFeSi
O	41.5 (± 0.50)	39.3 (± 2.72)	45.7 (± 4.82)
Si	0.90 (± 0.18)	1.11 (± 0.42)	4.70 (± 3.47)
S	0.39 (± 0.23)	1.41 (± 0.16)	0.53 (± 0.40)
Ti	54.5 (± 0.79)	56.4 (± 3.80)	46.2 (± 0.48)
Fe	2.79 (± 0.35)	1.81 (± 1.34)	2.82 (± 0.18)

4.8 Dispersion Properties

4.8.1 Dynamic Light Scattering

DLS analysis was performed at 30 °C temperature in methanol using Malvern Zetasizer nano to simulate how catalyst would be dispersed prior to addition of cooking oil in a biodiesel production process. Results for Ti series and Zn series are given in Figure 4.52 and Figure 4.53 respectively, where raw experimental measurements are shown as bar plots and an assumed Gaussian distribution is overlayed. Values of PDI and Z-average from cumulant analysis were found to contain significant errors due to large > 1 μm aggregates that formed towards bottom of dip cell during analysis, indicating that settling out and aggregation was occurring. Therefore, reported results are from regularization approach with %PDI calculated from monodisperse peak within 0-500 nm interval. All results confirm presence of a singular monodisperse peak within analysis region between 100-450 nm which agrees with SEM and TEM imaging discussed in Chapter 4.6. Key distribution parameters including intensity based D_{10}, D_{50}, D_{100} values and %PDI are summarised in Table 4.22. For all materials %PDI < 20% confirmed singular monodisperse peak. For Ti series shown in Figure 4.52, post acid treatment appeared to increase aggregation behaviour of microclusters when suspended in methanol. Average aggregate size increased from 207 nm for TiFeSi support to 349 nm broad size distribution for 0.1M-TiFeSi. Further increase in chlorosulfonic acid concentration only led to increase to 241 nm and 290 nm for 0.55M-TiFeSi and 1.0M-TiFeSi respectively. A potential explanation for this trend could be due to highest loading of sulfur content found in 0.55M-TiFeSi stabilising the dispersion via surface acidic sites. Interestingly, for Zn series the opposite trend appears to occur, with post acid treated catalysts all less aggregated when dispersed in methanol as compared to ZnFeSi support. Average aggregate size decreased from 347 nm for ZnFeSi support to 182 nm, 222 nm and 231 nm for increasing chlorosulfonic acid concentrations of 0.1 M, 0.55 M and 1.0 M. This difference in aggregation behaviour may be explained by variation in surface chemistry brought on by acid treatment, especially considering Zn series was notably more hydrated than Ti series and surface hydration has been suggested to influence aggregation effects [618]. Comparisons between Ti and Zn series size distribution are shown in Figure 4.54 and indicate 100-450 nm bulk microclusters would be present during biodiesel production. This highlights the importance of initial ultrasonication and continued agitation to avoid further aggregation and enable desirable accessibility to surface nanostructures.

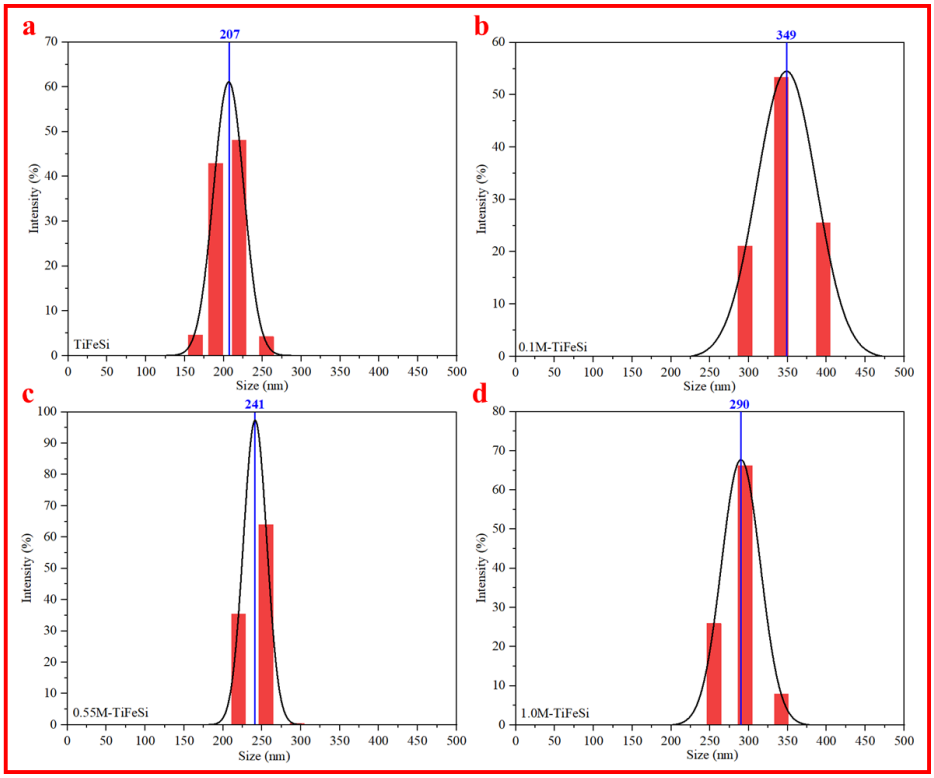

Figure 4.52 - DLS Intensity Size Distributions for Ti Series

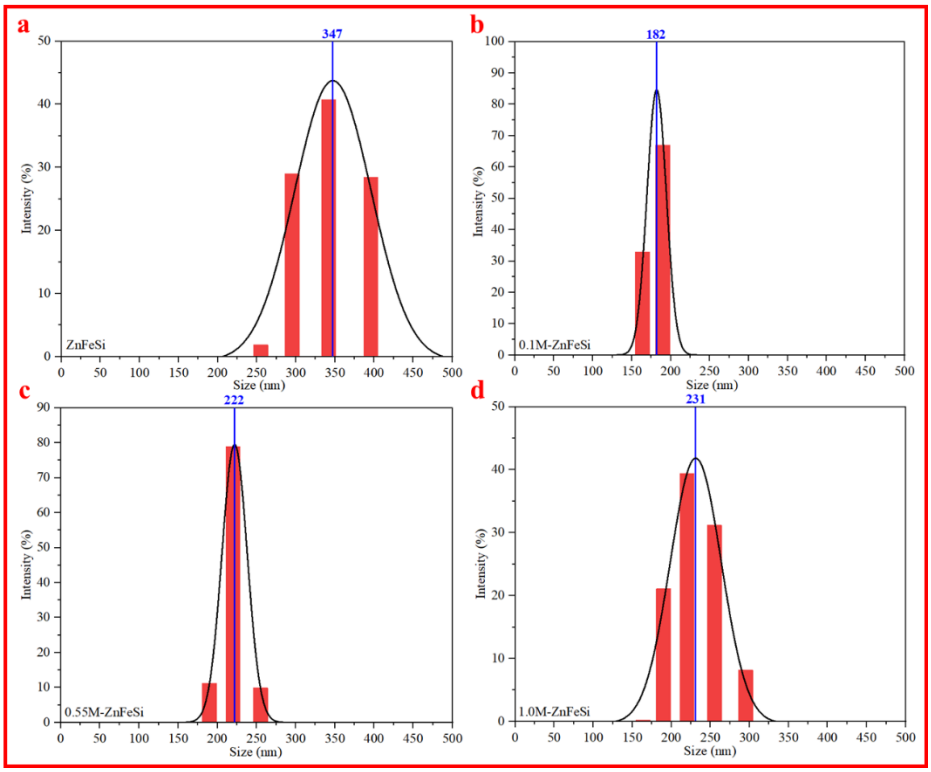

Figure 4.53 - DLS Intensity Size Distributions for Zn Series

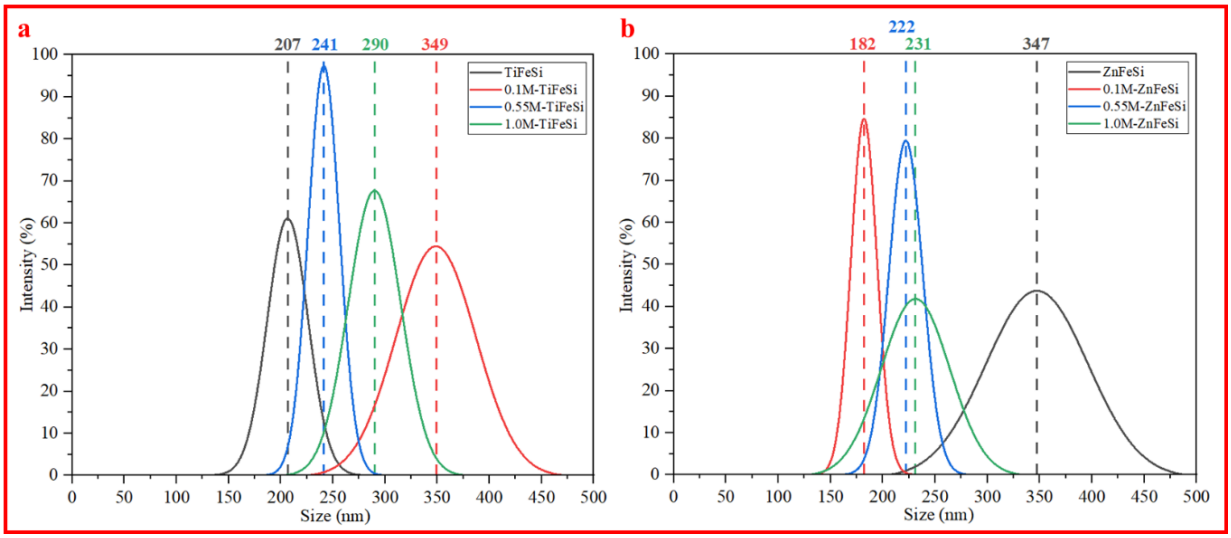

Figure 4.54 - Comparison between Ti (a) and Zn (b) Series DLS Size Distributions

Table 4.22 - Summary of DLS Results for Ti and Zn Series

Sample	$D_{i,10}$ (nm)	$D_{i,50}$ (nm)	$D_{i,90}$ (nm)	Span	FWHM (nm)	σ (nm)	%PDI
TiFeSi	182	207	232	0.242	46.1	19.6	9.45
0.1M-TiFeSi	302	349	397	0.272	90.3	38.3	11.0
0.55M-TiFeSi	222	241	261	0.162	35.3	15.0	6.22
1.0M-TiFeSi	258	290	321	0.217	59.1	25.1	8.65
ZnFeSi	290	347	407	0.337	115	49.0	14.1
0.1M-ZnFeSi	166	182	198	0.176	29.3	12.4	6.83
0.55M-ZnFeSi	201	222	243	0.189	38.1	16.2	7.29
1.0M-ZnFeSi	190	231	270	0.346	77.2	32.8	14.2

4.8.2 Zetapotential

To further understand the aggregation effects that may occur over the course of biodiesel production reaction, zetapotential measurements were carried out using Malvern Zetasizer nano with catalyst suspended in methanol phase. Effect of reaction temperature on dispersion stability was explored by measuring zetapotential at 30 °C, 45 °C and 60 °C setpoints used during later DoE analysis. Results are summarised in Figure 4.55 for Ti series and Zn series respectively.

For Ti series shown in Figure 4.55a only slight influence of temperature on zetapotential was observed, therefore similar aggregation rate should be expected regardless of reaction temperature. Enhancement of average zetapotential of -16.6 mV for TiFeSi support to -31.9 mV and -30.4 mV for 0.1M-TiFeSi and 1.0M-TiFeSi respectively indicates that post acid functionalisation, treated catalysts become more stable and would hence be less prone to aggregate over course of biodiesel reaction. Interestingly, for 0.55M-TiFeSi a change in sign was observed with average zetapotential of +26.3 mV, also an enhancement in stability compared to TiFeSi support. While zetapotential does not directly equal surface charge, the change in sign suggests greater presence of H^+ species compared to OH^- and hence improved Brønsted acidic nature, in agreement with pyridine-TPD studies in Chapter 4.5.2.

For Zn series shown in Figure 4.55b a more significant influence of temperature on zetapotential was observed, which could be explained by considering the surface chemistry of bound hydroxyls interacting with liquid methanol phase. At higher temperature, less OH^- groups due to increased acidity of methanol solvent could lead to lowering of surface charge and hence reduction in long term dispersion stability. Acid treatment led to increase in zetapotential from average of -24.5 mV for ZnFeSi support to -6.8 mV and -8.8 mV for 0.1M-ZnFeSi and 0.55M-ZnFesi respectively. Protonation of OH^- species into bound water groups and loading of more Brønsted acidic sites would increase positive charge on surface and explain increased zetapotential measurement. Interestingly for 1.0M-ZnFeSi zetapotential lowered to -29.4 mV, this may be from overabundance of negatively charged oxygen introduced via surface sulfate groups, loss of Zn cations from acidic digestion or increased formation of surface methoxide anions leading to increased negative charge. Very low absolute value of zetapotential for 0.1M-ZnFeSi and 0.55M-ZnFeSi suggests high instability and aggregation rate would be high.

Overall, all synthesised catalysts had absolute zetapotential values <40 mV and so displayed, at best, only moderate stability. Therefore, without continued agitation eventual aggregation and settling out of catalyst material from methanol phase would likely occur over the course of several hours of biodiesel production leading to loss of reaction rate and catalyst activity. Exact measured values of electrophoretic mobility and subsequent computed zetapotential results are summarised in Table 4.23 for all analysed samples.

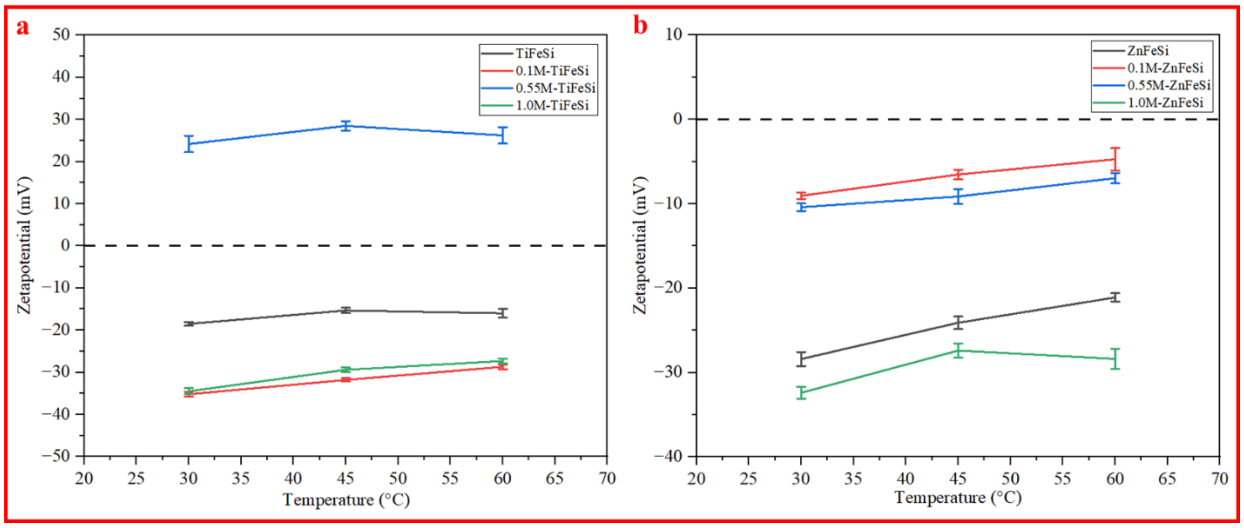

Figure 4.55 - Zetapotential with 30-60 °C for Ti Series (a) and Zn Series (b)

Table 4.23 - Summary of Zetapotential Analysis

Sample	Temperature (°C)	Electrophoretic Mobility (µmcm/Vs)	Zetapotential (mV)
TiFeSi	30, 45, 60	-1.05, -1.05, -1.30	-18.5, -15.3, -16.0
0.1M-TiFeSi	30, 45, 60	-2.01, -2.18, -2.33	-35.2, -31.8, -28.7
0.55M-TiFeSi	30, 45, 60	1.38, 1.96, 2.13	24.2, 28.5, 26.2
1.0M-TiFeSi	30, 45, 60	-1.97, -2.02, -2.23	-34.5, -29.4, -27.3
ZnFeSi	30, 45, 60	-1.62, -1.65, -1.72	-28.4, -24.1, -21.1
0.1M-ZnFeSi	30, 45, 60	-0.52, -0.45, -0.38	-9.05, -6.53, -4.72
0.55M-ZnFeSi	30, 45, 60	-0.59, -0.63, -0.57	-10.4, -9.13, -6.97
1.0M-ZnFeSi	30, 45, 60	-1.85, -1.89, -2.31	-32.4, -27.4, -28.4

4.9 Summary

In this Chapter the six synthesised novel nanocatalysts were characterized through a variety of techniques to determine physical properties achieved, whether Ti or Zn series was more desirable and how chlorosulfonic acid concentration affects observed properties. It is clear that Ti series shows more desirable properties as compared to Zn series and should hence be expected to have superior catalytic performance overall. In particular, 0.55M-TiFeSi has a superior balance of crystallinity, thermal stability, surface chemistry, morphology, elemental composition and dispersion behaviour indicating this nanocatalyst may be most active for biodiesel production. A short summary of the main findings in each subsection now follows.

Visual observations in Chapter 4.2 showed that upon loading of Fe species onto 100 nm SiO_2 a rust red, non-magnetic powder was produced likely due to Fe-Si or α-Fe_2O_3 formation. Lack of magnetic separability is indicative of hematite being too weakly magnetic when loaded onto 100nm nanoparticle support. Loading of Ti and Zn species led to formation of off-white TiFeSi and light beige ZnFeSi supports. Post acid treatment, a noticeable change in colour occurred, with increased darkening in colour as chlorosulfonic acid concentration was raised possibly due to more oxygen vacancies created upon sulfate loading alongside presence of toluene/carbon impurities. All bulk powders exhibited high degree of aggregation during dry storage.

Crystallinity results in Chapter 4.3 indicated that after first synthesis step, amorphous hydrated SiO_2 was converted into semicrystalline Fe-SiO_2 with underlying hematite structure. This was followed by production of anatase TiFeSi and hexagonal wurtzite ZnFeSi in the second synthesis step via XRD analysis. Post acid functionalisation led to a retained sulfated TiFeSi anatase crystallinity at slightly larger average crystallite size compared to non-functionalised support. For sulfated ZnO however, significant new peaks at larger d-spacing were detected and are attributed to hydrated $Zn(OH)_2$ or sulfated ZnO crystal phases. SAED analysis of all sulfated Ti nanocatalysts also confirmed a predominantly polycrystalline anatase TiO_2 formation, with minor regions of amorphous nature and single crystals also observed.

Thermal stability work performed in Chapter 4.4 indicated that Ti series was substantially more thermally stable as compared to Zn series. Detection of new mass loss peaks post acid treatment indicated presence of sulfate groups that thermally decomposed into SO_x upon heating. Increased degradation temperature of sulfate species at greater chlorosulfonic acid concentration in both Ti and Zn series of nanocatalysts suggested enhancement of acid strength to form medium and strong acid sites. Large exothermic behaviour in sulfated Zn series suggests recrystallisation of hydrated $Zn(OH)_2$ phase and may indicate higher calcination temperature is needed post functionalisation.

Surface chemistry analysis in Chapter 4.5 confirmed via ATR-FTIR the successful loading of sulfate S-O and S=O groups post acidic treatment in both Ti and Zn series, with a likely bridged bidentate structure. However, evidence of sulfate groups in FeSi and ZnFeSi support was also noted indicating sulfate species were not fully removed post washing steps. Evidence of bound water and surface hydroxyls was also observed that contribute towards Brønsted acidity. Characterisation of the nature of surface acidic sites via pyridine TPD confirmed an increasing acid strength was achieved with increasing chlorosulfonic acid concentration. While FeSi support had both Lewis and Brønsted acidity, TiFeSi and ZnFeSi support had only Lewis acidity. Upon acidic treatment however, all sulfated Ti catalysts exhibited Brønsted acidity only. It is likely that with no significant Lewis acidic sites present in Ti series of nanocatalysts, and only medium to strong Brønsted acidic sites, esterification reaction would be preferred over transesterification. For Zn series a surprising increase in acid strength was observed upon heating, which could be explained by conversion of hydrated water in Brønsted acidic hydroxyl groups, indicating further drying and recalcination of Zn sulfated nanocatalysts may be required than current method used. NMR analysis also detected presence of surface hydrate and hydroxyls. Post acid treatment a decrease in basic OH groups and increase in H_2O was seen in Ti series suggesting protonation. Surface chemistry was also explored via XPS analysis and indicated that 0.55M-TiFeSi had greatest ratio of S:Ti out of the Ti series. Overall Zn series showed greater ratios of sulfur to metal cation indicating greater sulfate loading was achieved in Zn series. Presence of Fe was not detected at surface except for in FeSi support, suggesting that Fe was only present within core structures and exposed Fe may have leached during synthesis. While Si was not detected in Ti or Zn support materials, post acidic treatment slight evidence of SiO_2 was observed in all Ti nanocatalysts and for 0.1M-ZnFeSi, this may be due to core exposure or evidence of inhomogeneous coating around SiO_2 core. Evidence of sulfate and hydroxyl groups at surface was observed for all nanocatalysts.

Chapter 4.6 investigated obtained structural and morphological information. BET isotherms indicated the presence of ink-bottle pores for all nanomaterials except starting SiO_2 while porosity for all materials was seen to be mesoporous. Decrease in surface area and pore size from SiO_2 to FeSi confirmed loading of Fe successfully into mesopores of 100 nm SiO_2 and further decrease in pore size was noted upon synthesis of TiFeSi and ZnFeSi supports. Significant order of magnitude difference in specific surface area was observed between TiFeSi and ZnFeSi, indicating that while loading of TiO_2 onto FeSi support had successfully improved surface area, Zn series had unsuccessfully formed around FeSi support and hence hindered active site accessibility. This is likely due to synthesis conditions and a modified future synthesis procedure is recommended with different Zn precursor salt, solvent, precipitation conditions or drying and calcination treatment. Investigation of microporosity via t-plot analysis indicated that SiO_2, FeSi and 1.0M-TiFeSi all exhibited microporosity. Large deviation in surface area between BJH method and BET method was attributed to non-cylindrical pore shape and existence of micropores. In 1.0M-TiFeSi the increased microporosity may be due to high chlorosulfonic acid strength leaching. Surprisingly little surface area and pore size variation was observed within Ti series, possibly due to relatively low level of sulfur loaded onto surface. Therefore, deviation in reaction behaviour between Ti nanocatalysts is unlikely to be due to structural changes. SEM imaging indicates a spherical aggregation morphology of Ti series, whereas for Zn series the aggregation morphology was more "nugget" shaped. Differences in microscale aggregation behaviour may be attributed to issues with irregular coprecipitation of Zn layer around FeSi, alongside difficulties noted during the washing, drying and functionalisation steps in ZnFeSi synthesis. High degree of aggregation was observed at the microscale with 100-450 nm aggregate clusters, however evidence of sub 50 nm nanoparticles were observed coating the microstructure surface in a core-shell like configuration. The ink-bottle pores detected may therefore be due to void space between surface nanostructures. TEM imaging of Ti series confirms a core-shell nature with uncoated ~100 nm SiO_2 surrounded by thin <100 nm coatings of Fe and Ti oxide nanoparticle species. High aggregation was observed with 100-450 nm clusters and significant inhomogeneity was noted throughout samples with both coated and uncoated SiO_2 observed. Nanostructure appeared similar in both SEM and TEM images regardless of chlorosulfonic acid treatment concentration.

Composition analysis in Chapter 4.7 all confirmed that 0.55M-TiFeSi nanocatalyst had greatest loading of sulfur species amongst the Ti series synthesised. CHONS analysis indicated that while sulfur loading increased with chlorosulfonic acid concentration in Zn series, a maximum was achieved with 0.55-TiFeSi possibly since further acid concentration led to acidic digestion or self-dimerization instead of sulfur loading. Zn nanocatalysts displayed considerable carbon impurities suggesting that vacuum drying and calcination was insufficient to remove toluene impurity, possibly due to reduced surface area of Zn nanocatalysts or formation of more viscous sol post functionalisation as compared to Ti series. Sulfur was detected in FeSi and ZnFeSi support indicating not all sulfate had been removed from precursor solution during washing. Non thermal composition methods were also employed to detect inorganic species. SEM-EDX agreed with CHONS results and greatest loading of sulfur was found in 0.55M-TiFeSi for Ti series and in 1.0M-ZnFeSi for Zn species. While Si and Fe was detected within localised clusters and distributed inhomogeneously throughout nanocatalyst support samples, elemental composition was significantly lower than that of Ti and Zn catalytically active layer. Evidence of small quantities of Fe and Si was still detected post acidic treatment. Future resynthesis may need to optimise quantities of support dispersed in each step to achieve greater inclusion of Si and Fe. TEM-EDX analysis of Ti series agreed that highest S loading was achieved in 0.55M-TiFeSi with evidence of SiO_2 rich cores containing Fe that were coated in a layer of dense Ti outer shell layer for all Ti nanocatalysts. Elemental maps highlighted both regions of uncoated SiO_2 and core-shell structures.

Finally, Chapter 4.8 explored dispersion properties of the synthesised nanocatalysts in methanol solution similar to how nanocatalyst would be initially dispersed during biodiesel reactions. Ti series showed an increase in aggregation behaviour post acidic treatment with largest aggregate size observed for 0.1M-TiFeSi. Increased charge of surface Brønsted acids in 0.55M-TiFeSi may have led to most stable and hence smallest increase in aggregate size as compared to TiFeSi support. However, for Zn series, post acid treatment led to significant reduction in aggregation behaviour. This may be due to hydrated $Zn(OH)_2$ stabilising the dispersion in polar methanol. All aggregation was seen to be monodisperse. Further zetapotential measurements showed that 0.55M-TiFeSi displayed positive charge unlike all other Ti series potentially due to greatest Brønsted acidity. Little change in aggregation behaviour was seen at increased temperature for Ti series, however Zn series was more prone to aggregate at higher temperature. At best only moderate stability was achieved in methanol hence all nanocatalysts would tend to aggregate over time.

A summary of key findings for Ti and Zn nanocatalysts is presented in Table 4.24 and Table 4.25 below. Since only limited quantity of 1.0M-ZnFeSi was obtained due to significant leaching of support, a full range of characterisation was not able to be performed and thus only some results are presented. Characterisation results suggest Ti series, and in particular 0.55M-TiFeSi, will be superior in catalytic activity. This prediction is further explored in subsequent Chapters 5 and 6.

Table 4.24 - Summary of Main Characterisation Results of Ti Series

Property	TiFeSi	0.1M-TiFeSi	0.55M-TiFeSi	1.0M-TiFeSi
Average Crystallite Size (nm)	9.95	11.2	10.4	11.0
Total Mass Loss (wt%)	3.14	10.0	13.8	10.4
Decomposition Temperature (°C)	-	461	470	461, 633
Weak/Strong Acid Sites (mmol/g)	0.33 / 0.33	2.08 / 0.81	2.7 / 1.29	0.67 / 0.66
Strong Acidity Ratio (T_{350}/T_{150})	0.99	0.39	0.48	0.98
Major Acidity Type (B/L)	Lewis	Brønsted	Brønsted	Brønsted
NMR Basic OH/H_2O Ratio	1.27	0.46	0.11	0.12
XPS S:Ti Surface Ratio	-	0.54	1.41	0.31
XPS O:S/O:Ti Ratio	- / 2.93	15.2 / 8.28	19.2 / 27.0	19.1 / 5.92
BET/BJH Surface Area (m^2/g)	81.3 / 74.7	72.1 / 69.6	75.8 / 68.2	72.6 / 39.8
Pore Volume (cm^3/g)	0.0905	0.0945	0.0959	0.0532
Average Pore Diameter (nm)	3.64	3.64	3.62	3.64
SEM Surface Structure Size (nm)	-	33	40	28
CHONS Sulfur wt%	0.20	2.32	3.88	1.80
SEM-EDX Sulfur wt%	0.13	1.92	4.86	0.95
TEM-EDX Sulfur wt%	-	0.39	1.41	0.53
SEM-EDX Ti/Fe/Si wt%	45.9/0.18/0.14	49.6/0.81/0.05	40.8/0.91/0.09	51.3/0.61/0.12
TEM-EDX Ti/Fe/Si wt%	-	54.5/2.79/0.90	56.4/1.81/1.11	46.2/2.82/4.70
DLS D_{90} Aggregates (nm)	232	397	261	321
Zetapotential (mV) at 60 °C	-16.0	-28.7	26.2	-27.3

Table 4.25 - Summary of Main Characterisation Results of Zn Series

Property	ZnFeSi	0.1M-ZnFeSi	0.55M-ZnFeSi	1.0M-ZnFeSi
Average Crystallite Size (nm)	20.1	16.7	24.7	-
Total Mass Loss (wt%)	18.9	68.7	58.3	53.9
Decomposition Temperature (°C)	-	469, 561	464, 515, 569	470, 549, 584
NMR Basic OH/H_2O Ratio	2	2.7	1.5	-
XPS S:Zn Surface Ratio	0.64	3.34	3	-
XPS O:S/O:Zn Ratio	8.81 / 5.63	6.21 / 20.7	3.25 / 9.73	-
BET/BJH Surface Area (m^2/g)	7.81 / 10.4	12.6 / 22.8	6.07 / 13.9	-
Pore Volume (cm^3/g)	0.0321	0.0506	0.0179	-
Average Pore Diameter (nm)	4.06	4.06	3.63	-
SEM Surface Structure Size (nm)	-	32	34	38
CHONS Sulfur wt%	7.56	13.16	13.21	16.05
CHONS Carbon wt%	0.15	21.89	29.07	3.46
SEM-EDX Sulfur wt%	4.70	12.2	13.7	14.8
SEM-EDX Zn/Fe/Si wt%	27.1/14.4/6.44	18.9/0.70/0.10	14.5/1.05/0.03	25.2/3.75/0.15
DLS D_{90} Aggregates (nm)	407	198	243	270
Zetapotential (mV) at 60 °C	-21.1	-4.72	-6.97	-28.4

Chapter 5.

Chapter 5. Reaction Performance in Model One-Step Esterification

5.1 Introduction

From the extensive characterisation results of Chapter 4 it was predicted that Ti series is more likely to be a superior nanocatalyst for biodiesel production than Zn series. In order to test this prediction, a model one-step esterification pathway was developed for each of the novel nanocatalysts. This chapter focuses on the application of design of experiments methodology to determine the effectiveness of each nanocatalyst in lowering FFA loading of used cooking oils. Chapter 5.2 begins by comparing different methods of detecting FAME yield via FTIR, NMR and GC-MS analysis. Relative advantages and disadvantages of each method for this project are discussed to justify use of GC-MS as quantitative method of measuring reaction performance. In Chapter 5.3 initial batch trials are performed using a previously reported optimum condition suggested in literature. Results indicate that while each nanocatalyst is unable to perform transesterification, an initial esterification treatment step using the acidic nanocatalysts followed by KOH base transesterification enhances the reactivity of KOH. To investigate if this is due to conversion of FFA in an initial esterification reaction, the rest of Chapter 5.4 focuses on development of a one-step model esterification study. Oleic acid was selected as a model FFA commonly found in used cooking oils. To ensure sufficient experimental data was collected from the limited amount of nanocatalyst available, Chapter 5.4.1 recalls a design of experiments 20 run screening experiment discussed prior in Chapter 3.4. Factors under investigation were restricted to reaction temperature, reaction time, catalyst loading wt% and methanol to oil molar ratio, with screening of the resultant model utilised to indicate most influential factors. Initial control reactions performed in Chapter 5.4.2 indicates that through only thermal effects a maximum methyl oleate yield of ~10% is attainable. Chapter 5.4.3 demonstrates that non functionalised TiFeSi and ZnFeSi support is unable to achieve significant methyl oleate yield beyond control results. Each of the Ti series and Zn series of novel nanocatalysts is then explored throughout Chapter 5.4.4 and Chapter 5.4.5, respectively. Key findings are summarised in Chapter 5.5 and indicate 0.1M-TiFeSi and 0.55M-TiFeSi are the best nanocatalysts in esterification step. Reaction temperature and reaction time are consistently the most significant factors, however catalyst loading and methanol to oil ratio are also influential. Development of a two-step pathway, further optimisation, kinetic and thermodynamic modelling is subsequently addressed in Chapter 6.

5.2 Comparison of FAME Detection Methods

In order to determine catalyst effectiveness for converting used cooking oils into biodiesel, the quantity of FAME (or methyl oleate) obtained post reaction had to be quantitatively measured to calculate reaction yields. For this work yield determination was explored using FTIR, ^{1}H-NMR and GC-MS. UCO post filtering and drying was analysed alongside a methyl nonadecanoate internal standard (C_{19} IS) and treated UCO reacted with KOH for 2.5 hours at 60 °C. Results are provided in Figure 5.1 for ATR-FTIR (a), ^{1}H-NMR (b) and GC-MS (c) techniques respectively.

For FTIR results in in Figure 5.1a, peak regions at ~1750 cm^{-1} and ~1160 cm^{-1} corresponding to C=O and C-H methyl ester bonds were attempted to be used to quantify FAME concentration as reported in prior studies [509]. Other peaks corresponded to hexane solvent or would be present in both glycerides and esters and therefore could not be used for yield determination. External calibration curves with C_{19} IS led to strong degree of fit as discussed in Chapter 3.5.2. Unfortunately, no noticeable difference between feedstock UCO, internal standard FAME or treated UCO spectra could be detected within these analysis regions. To confirm this issue was not due to poor bulk sensitivity of ATR-FTIR technique, a different flowcell FTIR setup in transmission mode was also used. Flowcell method demanded excessive sample mass per analysis run to be suitable for this work. Moreover, no discernible difference in spectral peaks could be observed. Therefore, FTIR methods were not selected to determine FAME yield post reaction.

Proton NMR result in Figure 5.1b confirms that a new methyl ester proton group can be observed at 3.66 ppm for both C_{19} IS and treated UCO. Comparing to signal at 2.30 ppm corresponding to glyceride only protons, a percentage yield of FAME could be computed as reported in previous studies [510, 511] and discussed in Chapter 3.5.2. All other observed peaks are reported to be from aliphatic protons on the carbon chain and not unique to either glyceride or methyl ester hence unusable for FAME determination. Unfortunately, use of NMR facilities had several practical disadvantages for this work including requirement of deuterated solvents such as $CDCl_3$ and only being able to analyse limited number of samples each day. Additionally, NMR is reported to have lower limits of detection compared to chromatographic methods and for small sample masses a high sensitivity was especially important. Therefore, in this work NMR was used to qualitatively confirm that methyl ester group had been produced post reaction and hence catalytic activity was indeed occurring, however GC-MS method was preferred for the quantitative analysis.

Figure 5.1c shows that for both UCO feedstock and C_{19} IS no notable peaks other than at 18.5 minutes could be detected. An m/z value of 312 confirms this peak to be methyl nonadecanoate. Therefore, without conversion of glyceride compounds into methyl esters, no other peak responses in the chromatogram can be observed. This makes GC-MS an especially powerful analysis method for confirming and quantifying the extent of catalytic activity. Post treatment of UCO with KOH, new peaks can be observed at 15.8 minutes (m/z: 294) and 15.9 minutes (m/z: 296) corresponding to methyl linoleate C18:2 and methyl oleate C18:1 respectively. Other minor peaks at 13.8 minutes (m/z: 270) and 16.3 minutes (m/z: 298) are from methyl palmitate C16:0 and methyl stearate C18:0 respectively. By using known quantity of internal standard to convert peak area into concentrations, FAME yield can be accurately determined as discussed in past studies [145] and Chapter 3.5.2. Since GC-MS facilities could provide a highly sensitive method of detecting FAME content even with small sample mass available for analysis, alongside the potential to run up to ~100 samples per analysis batch, GC-MS method was deemed most applicable for this work. Presence of new peaks at expected retention times and with known m/z values provided qualitative confirmation that UCO had been successfully converted into FAME. This was further supported with NMR analysis to detect new methyl ester group at 3.66 ppm. Then comparison with known quantity of C_{19} IS loaded into each biodiesel sample was used to quantitatively calculate FAME yield. A summary of these key comparisons is included in Table 5.1 below.

Table 5.1 - Comparison of FAME Detection Methods

Method	Advantages	Disadvantages	Use in this work
ATR-FTIR	Rapid analysis Small sample mass	Cannot distinguish UCO/FAME Low sensitivity	Not Used
Flowcell-FTIR	Rapid analysis Improved sensitivity	Cannot distinguish UCO/FAME Large sample mass	Not Used
1H-NMR	Rapid analysis FAME peak is unique Peak ratios give FAME%	Limited throughput per day Less sensitive than GC-MS $CDCl_3$ solvent required	Qualitative FAME Analysis
GC-MS	High throughput per day FAME peaks are unique High sensitivity Small sample mass	C_{19} internal standard required Long run time per sample Regular column washing runs	Qualitative and Quantitative FAME Analysis

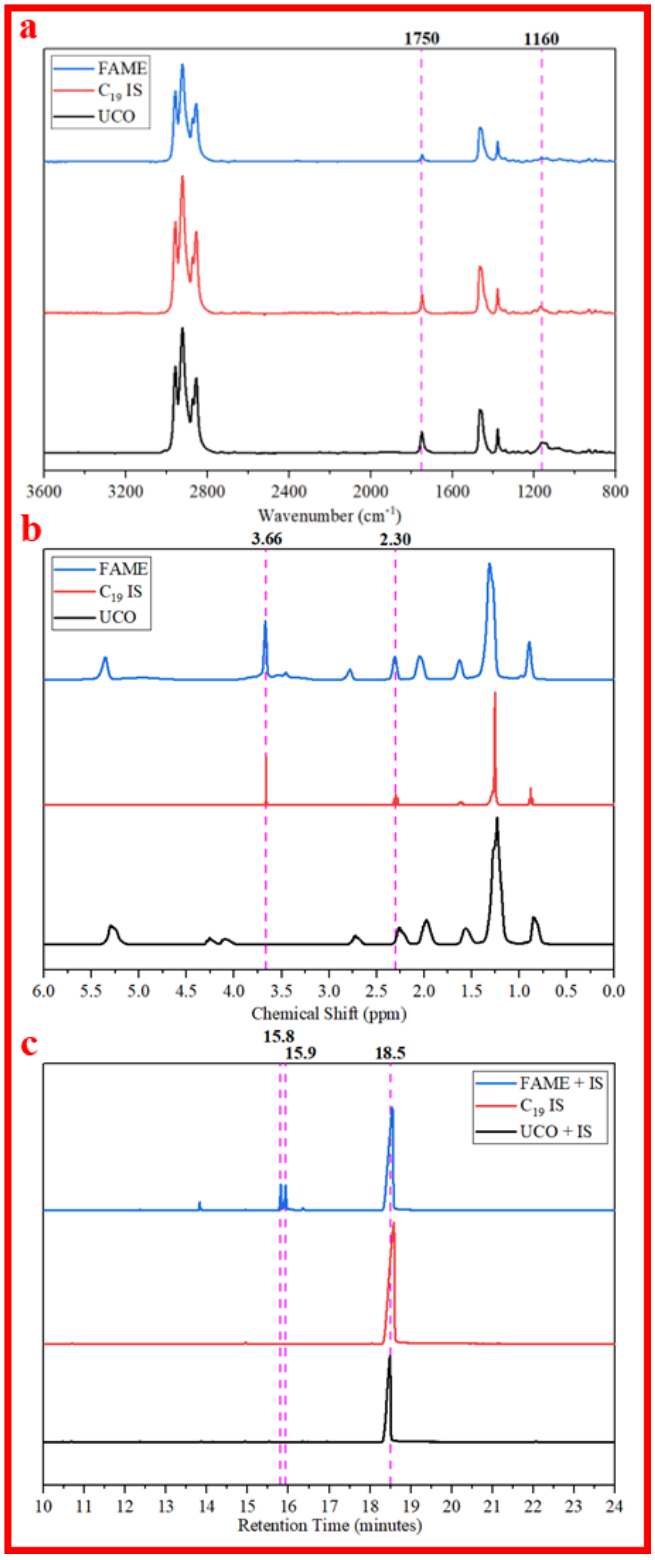

Figure 5.1 - Comparison of FAME Detection via FTIR (a), 1H-NMR (b) and GC-MS (c)

5.3 Initial Batch Trials

To determine if synthesised nanocatalysts were able to achieve high FAME yield through simultaneous one step transesterification and esterification reaction, initial batch trials were performed using method discussed prior in Chapter 3.5.1 with fresh UCO feedstock. Ti series of nanocatalysts were tested initially over Zn series due to more desirable characterisation results as discussed throughout Chapter 4. Previously reported optimum reaction conditions by Gardy et al. [145] for similar sulfated core shell nanocatalysts were adapted and taken as 2.5 hours reaction time, 3 wt% catalyst loading and 10:1 methanol to oil ratio. Reaction temperature was set at 60 °C since suggested value of 90 °C required an unavailable pressurised reactor vessel. FAME yield was verified by GC-MS method.

Unfortunately, very low FAME yields of 2.13%, 0.85% and 1.30% were obtained for 0.1M-TiFeSi, 0.55M-TiFeSi and 1.0M-TiFeSi respectively under these reaction conditions. Non-functionalised TiFeSi and ZnFeSi support were also tested and achieved only 2.49% and 2.81% yield respectively. Meanwhile, a control reaction without catalyst addition was able to achieve a similar 2.23% FAME yield. Under these reaction conditions explored, the catalytic activity of TiFeSi nanocatalysts in one step simultaneous transesterification/esterification of fresh UCO were therefore found to be no better than purely thermal effect alone within ± 5% experimental error. Failure to achieve any notable transesterification activity may be due to lack of Lewis acidity as reported in Chapter 4.5.2, since Brønsted acidic sites preferentially enable esterification route. Later work in Chapter 6.3.2 determined that fresh UCO only contained 3.7% FFA content, meaning that if TiFeSi nanocatalysts were only esterification active at reasonable reaction conditions, it would be expected to see poor yields in a feedstock mainly comprised of glycerides that require transesterification route to form FAME. From these results it may also be concluded that the initial conditions explored were suboptimal. Perhaps through significant increase in reaction time or temperature an improved yield may have been eventually achieved in one step reaction. However, for an acidic nanocatalyst to be industrially relevant, the main focus should be on lowering FFA content via esterification under reasonable reaction conditions. By cleaning up FFA impurities, a significantly more kinetically favourable base catalyst could hence be utilised in subsequent transesterification step. This is more industrially useful than reporting high FAME yield in one step with the major caveat that excessive reaction temperature or duration is required.

Since the optimum reaction conditions for KOH transesterification were not known, one step reaction under same conditions and reaction setup were also explored using fresh UCO and compared with a fresh vegetable oil feed. FAME yield with vegetable oil was found to be 63.8% which decreased to 46.3% when fresh UCO was used as feedstock. Clearly it can also be concluded that these initial reaction conditions were suboptimal for KOH catalyst, however the expected drop in FAME yield was observed likely due to presence of FFA impurities in the fresh UCO hindering transesterification. It was predicted that if the Ti series of nanocatalysts were only esterification active under reasonable reaction conditions, then by pre-treating the fresh UCO before using KOH an increase in yield beyond 46.3% may be achievable by reduction of the FFA content. If this were the case, then the synthesised nanocatalysts should be explored in a two-step reaction scheme.

Fresh UCO was subsequently treated with Ti series of nanocatalysts at same reaction conditions of 2.5 hours, 60 °C, 3 wt% and 10:1 methanol to oil ratio in order to test this prediction. Following the initial esterification step, KOH reaction was then performed under same conditions. The initial FAME yield of KOH with fresh UCO of 46.3% in one step route was seen to increase to 58.2%, 56.0% and 67.1% for 0.1 M, 0.55 M and 1.0M-TiFeSi respectively. This result conclusively suggested that TiFeSi series was indeed able to improve KOH transesterification performance likely via esterification of FFA content. Figure 5.2 provides a brief summary of these initial batch trial results. Due to experimental error and the suboptimal conditions utilised, it was too early to determine with reasonable confidence which Ti nanocatalyst was most effective at esterifying FFA impurities. The rest of this chapter therefore focuses on esterification studies using oleic acid as a model FFA under a range of reaction conditions to determine most active nanocatalyst.

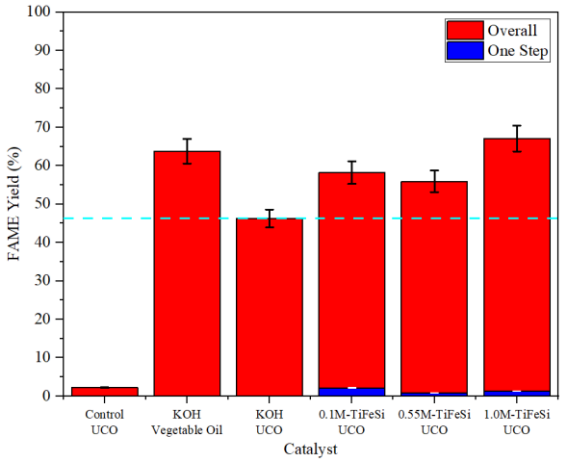

Figure 5.2 - Initial Batch Trials (2.5 hr, 60 °C, 3 wt%, 10:1)

5.4 One-Step Model Esterification Study

5.4.1 Design of Experiments Approach

Oleic acid was selected as a model FFA feedstock to explore which synthesised catalyst demonstrated superior esterification performance and could best remove UCO acidic impurities. Table 5.2 has been reproduced from Chapter 3.4.2 illustrating the 10-run batch esterification screening experiment design. Runs are labelled A-J with one additional replicate per treatment run.

Table 5.2 - Custom 10 Run DoE Esterification Study

Run	Time (hr)	Temperature (°C)	Catalyst Loading (wt%)	Alcohol : Oil Ratio	Randomised Run Order
A1, A2	1	30	3	4	2, 12
B1, B2	5	60	1	4	1, 16
C1, C2	1	60	5	16	10, 13
D1, D2	1	45	1	10	6, 18
E1, E2	5	45	3	16	4, 17
F1, F2	5	30	5	10	9, 19
G1, G2	9	60	3	10	7, 14
H1, H2	9	45	5	4	3, 20
I1, I2	9	30	1	16	8, 15
J1, J2	5	45	3	10	5, 11

5.4.2 Control Reactions

Reactions were performed as detailed in Table 5.2 except with absence of catalytic material to explore the level of esterification that occurs through heating effects alone. Maximum average methyl oleate yield of 9.86% was achieved in reaction run B after 5 hours of reaction at 60 °C and 4:1 methanol to oleic acid ratio. Results for all runs are summarised in Table 5.3 and indicates that while slight esterification of oleic acid to methyl oleate does take place upon mixing with methanol and heating, the conversion is very inefficient and unfavourable without use of a catalyst.

Table 5.3 - Methyl Oleate Yields for Control Esterification Trials

Run	Methyl Oleate Yield (%)		Average Yield (%)
	Reaction 1	Reaction 2	
A	0.29	0.73	0.51
B	8.14	11.6	9.86
C	1.05	1.40	1.22
D	0.10	0.14	0.12
E	1.65	4.29	2.97
F	0.37	0.55	0.46
G	6.40	8.02	7.21
H	2.59	4.63	3.61
I	2.59	4.54	3.56
J	1.45	2.22	1.84

Table 5.4 - Effect Screening for Control Esterification Trials

Effect	Scaled Estimate	Log Worth	P Value (%)	Bayes Posterior Probability (%)	t Ratio	f Ratio	Comment
Time	2.09	2.95	0.11	61.0	4.15	17.3	**Significant**
Temperature	2.29	3.27	0.05	70.8	4.56	20.8	**Significant**
A:O Ratio	-1.04	1.22	5.97	8.45	-2.06	4.25	Insignificant
Time^2	-1.56	1.11	7.74	7.10	-1.92	3.68	Insignificant
Temperature^2	1.73	1.28	5.30	9.18	2.13	4.53	Insignificant
A:O Ratio^2	1.19	0.77	16.8	4.45	1.46	2.13	Insignificant

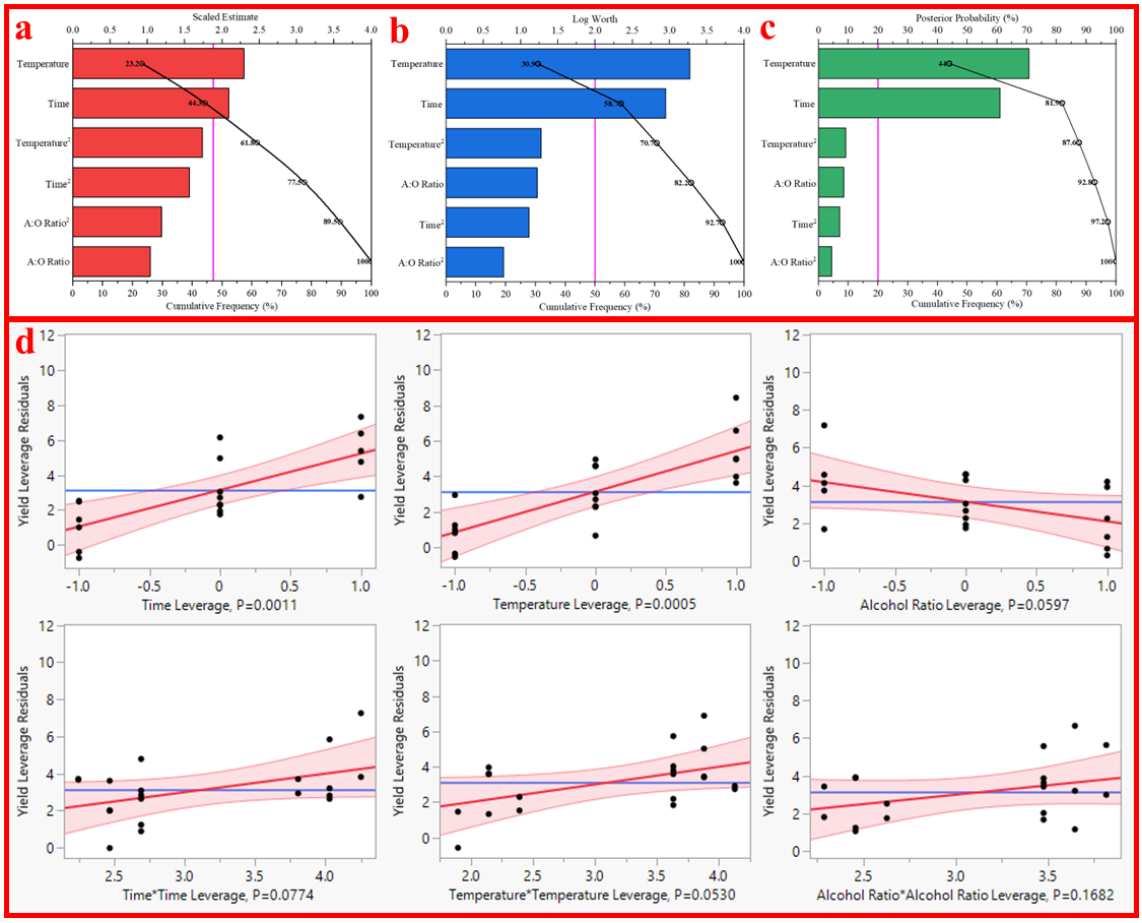

Figure 5.3 – Effect Screening Plots for Control Esterification Trials

Effect screening on the obtained experimental results was performed as discussed previously in Chapter 3.5.4 and results are summarised in Table 5.4, with scaled estimate model coefficients (a), p-value log-worths (b), Bayesian analysis (c) and effect leveraging plots (d) given in Figure 5.3a-d respectively. Unsurprisingly both reaction temperature and reaction time were seen to significantly influence yield as would be expected from a kinetically limited reaction. Negative scaled estimate coefficient of -1.04 for A:O ratio term suggests that further dilution of oil feedstock with excess methanol impeded kinetics by lowering overall oleic acid concentration, whereas negative value of -1.56 for Time^2 suggests that increasing reaction time beyond maxima point hinders oleic acid conversion due to reversibility of esterification reaction. From these results it is clear that while reaction temperature and reaction time do have a strong influence on methyl oleate yield, without suitable catalyst present only a very low 9.86% maximum yield was obtained. To test if catalytic activity was indeed due to chlorosulfonic acid functionalisation, both TiFeSi and ZnFeSi supports were subsequently tested under identical DoE model.

5.4.3 Catalyst Supports

5.4.3.1 TiFeSi Support

Results of oleic acid esterification trials with TiFeSi support are given in Table 5.5 and effect screening from obtained results are summarised in Table 5.6 and Figure 5.4a-d. Maximum average methyl oleate yield of 8.06% was achieved in reaction run B with conditions of 5 hours, 60 °C, 1 wt% TiFeSi material and 4:1 ratio methanol to oleic acid. Since maximum average yield was similar to control reactions it can be concluded that non-functionalised TiFeSi provided no observable catalytic improvement in the esterification reaction. In fact, the scaled estimate for catalyst loading linear effect of -0.9 suggests that yield was reduced with increasing TiFeSi loading. While this might be due to suspended solid increasing the viscosity of oleic acid phase and hence hindering reactant mass transfer at liquid-liquid interface, it was noted as a minor significant effect as compared to reaction temperature, time and ratio of alcohol to oleic acid.

From these results it was evident that achieving oleic acid esterification beyond ~10% methyl oleate yield would be unexplainable by thermal effects or catalytic activity of TiFeSi support material alone, hence for all Ti series a significant improvement in yield beyond ~10% would confirm catalytic enhancement due to chlorosulfonic acid functionalisation.

Table 5.5 - Methyl Oleate Yields for TiFeSi Support Esterification Trials

Run	Methyl Oleate Yield (%)		Average Yield (%)
	Reaction 1	Reaction 2	
A	0.35	0.69	0.52
B	7.94	8.18	8.06
C	0.64	0.97	0.80
D	0.10	0.11	0.11
E	1.58	1.67	1.62
F	0.38	1.04	0.71
G	5.65	6.61	6.13
H	2.88	2.63	2.76
I	1.39	1.58	1.49
J	1.18	1.76	1.47

Table 5.6 - Effect Screening for TiFeSi Support Esterification Trials

Effect	Scaled Estimate	Log Worth	P Value (%)	Bayes Posterior Probability (%)	t Ratio	f Ratio	Comment
Time	1.49	6.57	<0.01	100	11.1	122	**Significant**
Temperature	2.05	8.00	<0.01	100	15.2	231	**Significant**
Catalyst Loading	-0.90	4.44	<0.01	99.6	-6.65	44.2	**Significant**
Alcohol Ratio	-1.24	5.76	<0.01	99.9	-9.17	84.2	**Significant**
Time^2	-1.30	4.00	0.01	95.5	-5.92	35.1	**Significant**
Temperature^2	1.65	4.92	<0.01	99.8	7.50	56.2	**Significant**
Catalyst Loading^2	-0.24	0.54	29.1	3.43	-1.11	1.23	Insignificant
Alcohol Ratio^2	0.42	1.09	8.23	12.7	1.91	3.66	Insignificant

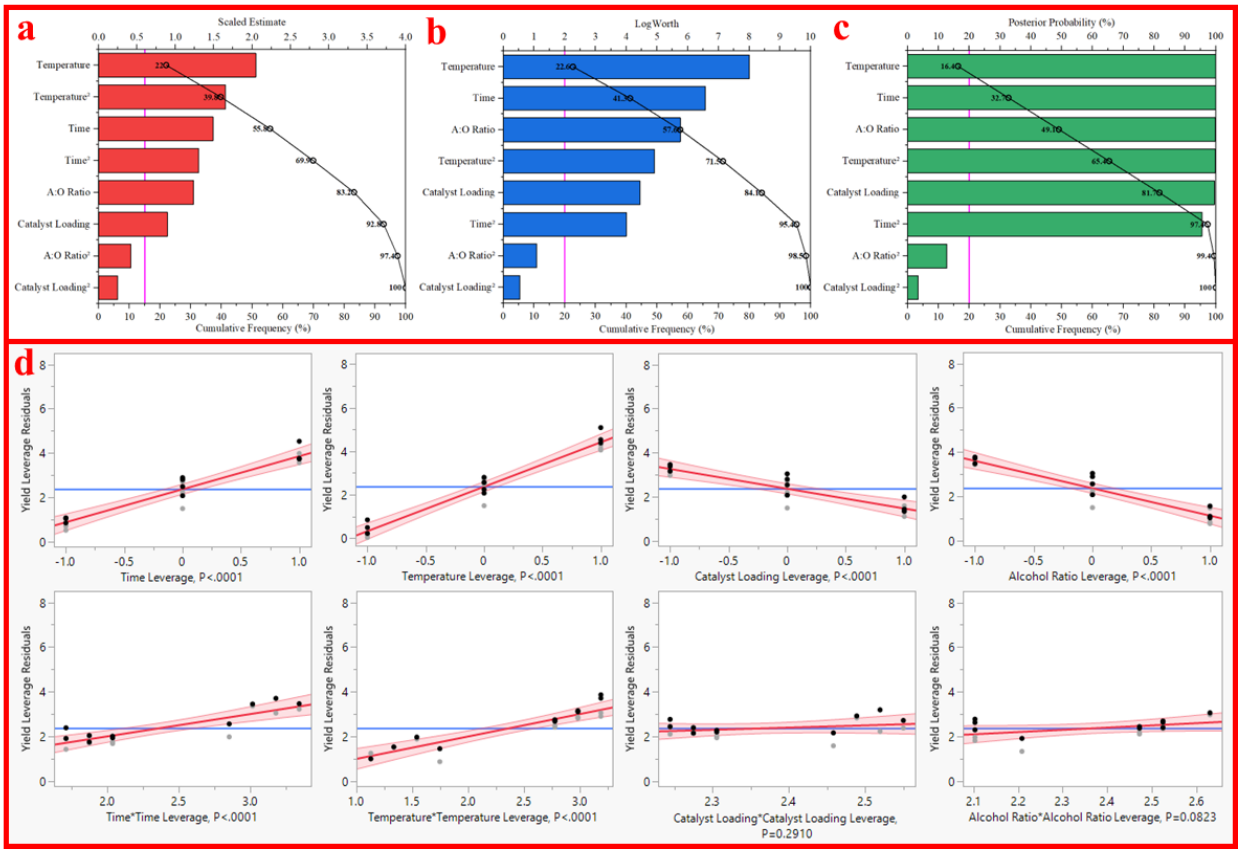

Figure 5.4 – Effect Screening Plots for TiFeSi Support Esterification Trials

5.4.3.2 ZnFeSi Support

Results of oleic acid esterification trials with ZnFeSi support are given in Table 5.7, additionally effect screening from obtained results are summarised in Table 5.8 and Figure 5.5a-d. A maximum average yield of 11.2% methyl oleate was obtained in run G after 9 hours of reaction at 60 °C, 3 wt% ZnFeSi loading and 10:1 ratio of methanol to oleic acid. This result is only slightly above 9.86% obtained in control study and could therefore be explained by experimental and statistical variation error estimated to be up to ± 5%. Scaled estimate of -0.92 for linear catalyst loading effect and -1.60 for quadratic effect agrees with previous findings in TiFeSi trials, where addition of further support material increasingly hinders methyl oleate formation, likely due to greater viscosity of liquid phases impeding mass transfer. All effects were considered to be significant although reaction time and temperature were again most influential as could be expected from a kinetically limited reaction.

While ZnFeSi performed marginally better than thermal control or TiFeSi, considering that esterification performance is still incredibly poor given the 9 hours of reaction time at 60 °C, ZnFeSi can be considered non-catalytic. Therefore, similar to Ti series if any notable methyl oleate yield >10% is observed in Zn series esterification trials, it is likely a direct consequence of chlorosulfonic acid treatment step.

Table 5.7 - Methyl Oleate Yields for ZnFeSi Support Esterification Trials

Run	Methyl Oleate Yield (%)		Average Yield (%)
	Reaction 1	Reaction 2	
A	0.92	1.14	1.03
B	6.55	6.11	6.33
C	1.75	1.81	1.78
D	0.07	0.13	0.10
E	1.55	1.57	1.56
F	0.60	0.56	0.58
G	11.0	11.4	11.2
H	3.22	4.04	3.63
I	5.38	4.77	5.07
J	1.88	2.58	2.23

Table 5.8 - Effect Screening for ZnFeSi Support Esterification Trials

Effect	Scaled Estimate	Log Worth	P Value (%)	Bayes Posterior Probability (%)	t Ratio	f Ratio	Comment
Time	2.83	11.0	<0.01	100	29.1	849	**Significant**
Temperature	2.10	9.64	<0.01	100	21.6	468	**Significant**
Catalyst Loading	-0.92	5.89	<0.01	98.0	-9.46	89.5	**Significant**
Alcohol Ratio	-0.43	2.99	<0.01	54.3	-4.42	19.5	**Significant**
Time^2	1.06	4.46	<0.01	93.3	6.67	44.5	**Significant**
Temperature^2	2.65	8.43	<0.01	99.8	16.7	279	**Significant**
Catalyst Loading^2	-1.60	6.16	0.10	98.8	-10.1	101	**Significant**
Alcohol Ratio^2	-0.64	2.72	0.19	45.0	-4.06	16.4	**Significant**

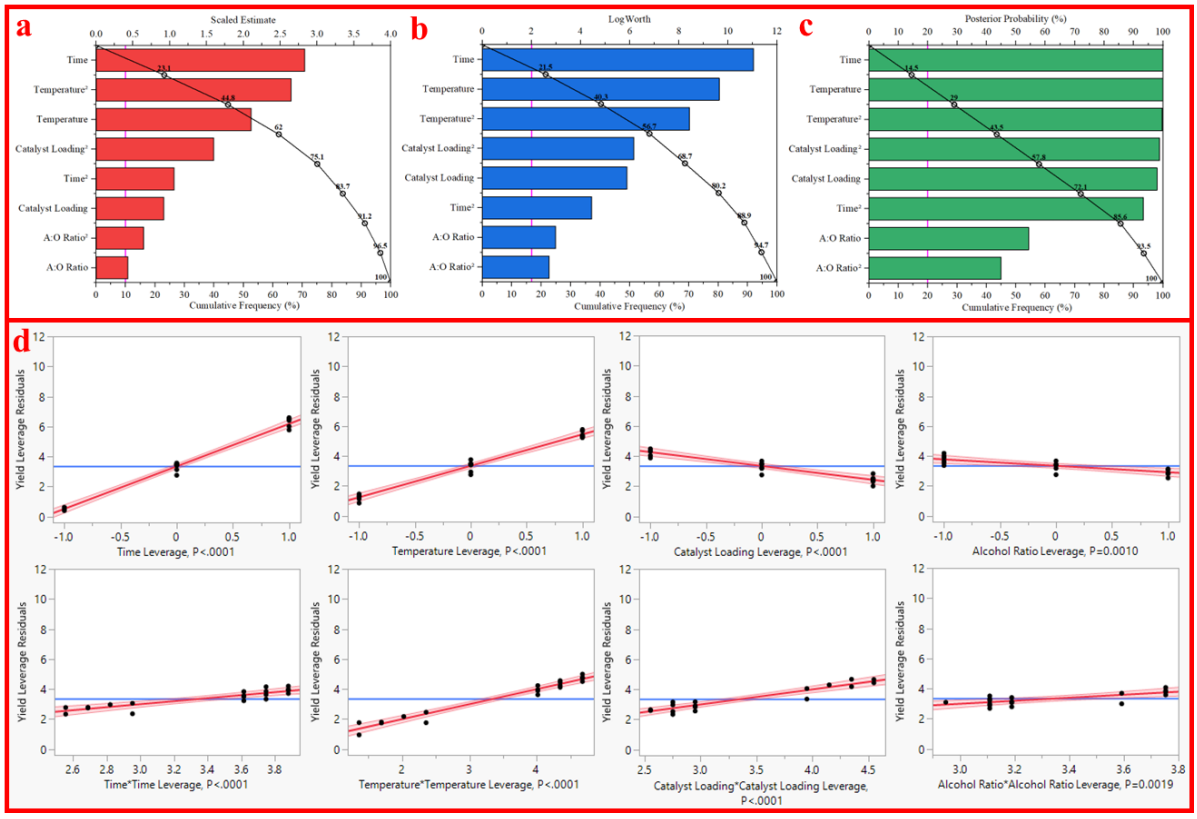

Figure 5.5 – Effect Screening Plots for ZnFeSi Support Esterification Trials

5.4.4 Ti Series Functionalised Catalysts

5.4.4.1 0.1M-TiFeSi

Reaction results for 0.1M-TiFeSi functionalised catalyst reacting with oleic acid are provided in Table 5.9 with effect screening results summarised in Table 5.10 and Figure 5.6. Greatest average methyl oleate yield of 82.3% was achieved in reaction run G with 9 hours of reaction at 60 °C, 3 wt% catalyst loading and 10:1 ratio of methanol to oleic acid. This is a substantial order of magnitude increase in methyl oleate yield compared to only 8.06% for unfunctionalised TiFeSi support. Hence it can certainly be said that acidic treatment was successfully able to introduce catalytically active sites onto nanomaterial surface. Such sites are likely Brønsted acidic in nature as indicated in Chapter 4.5.2 and from these results would be highly suitable for converting FFA impurities such as oleic acid commonly found in waste cooking oil. From effect screening results it is interesting to note that while catalyst loading is an insignificant linear term, the quadratic term is highly influential and substantially reduces yield upon modification as noted by scaled estimate of -24.5. This suggests highly nonlinear behaviour where even slight deviation away from maxima point in mass of 0.1M-TiFeSi loaded will significantly impact the yield achieved, further confirming that presence of this nanocatalyst is highly influential on reaction performance. While methyl oleate yield of 82.3% shows strong catalytic activity, it was hoped that a yield >90% could be achieved to be commercially viable. Subsequent optimisation is discussed further in Chapter 6.

Table 5.9 - Methyl Oleate Yields for 0.1M-TiFeSi Catalyst Esterification Trials

Run	Methyl Oleate Yield (%)		Average Yield (%)
	Reaction 1	Reaction 2	
A	1.68	1.39	1.54
B	17.3	14.3	15.8
C	33.7	30.1	31.9
D	0.26	0.27	0.26
E	38.0	32.5	35.3
F	9.19	7.24	8.22
G	81.9	82.7	82.3
H	7.65	5.27	6.46
I	17.7	20.7	19.2
J	28.5	25.9	27.2

Table 5.10 - Effect Screening for 0.1M-TiFeSi Catalyst Esterification Trials

Effect	Scaled Estimate	Log Worth	P Value (%)	Bayes Posterior Probability (%)	t Ratio	f Ratio	Comment
Time	12.4	7.11	<0.01	100	12.5	156	**Significant**
Temperature	16.8	8.51	<0.01	100	17.0	288	**Significant**
Catalyst Loading	1.89	1.08	8.39	9.66	1.90	3.61	Insignificant
Alcohol Ratio	10.4	6.35	<0.01	100	10.5	111	**Significant**
Time^2	5.44	2.20	0.64	4.49	3.36	11.3	Insignificant
Temperature^2	14.1	5.53	<0.01	98.3	8.70	75.7	**Significant**
Catalyst Loading^2	-24.5	7.98	<0.01	100	-15.1	228	**Significant**
Alcohol Ratio^2	-10.3	4.28	<0.01	99.2	-6.37	40.6	**Significant**

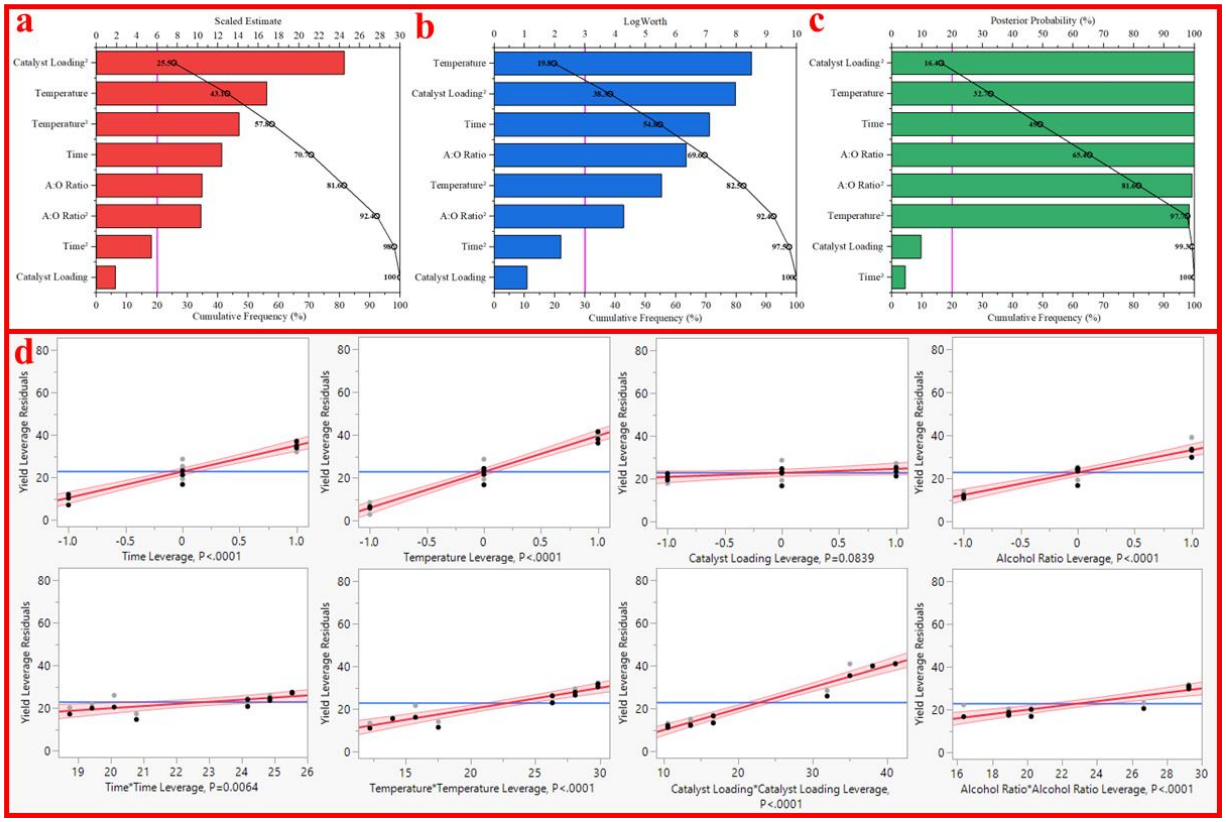

Figure 5.6 – Effect Screening Plots for 0.1M-TiFeSi Catalyst Esterification Trials

5.4.4.2 0.55M-TiFeSi

Methyl oleate batch esterification yields for 0.55M-TiFeSi are given in Table 5.11 with effect screening results provided in Table 5.12 and Figure 5.7. An impressive 88.4% maximum average yield was achieved in reaction run G using 3 wt% catalyst loading, 10:1 ratio of methanol to oleic acid and 9 hours of reaction at 60 °C. This represents an improvement of ~6% compared to 0.1M-TiFeSi under similar conditions and is slightly above the maximum ± 5% variation that could be expected from experimental errors and statistical noise. This improvement may be due to enhancement of surface acidity noted throughout Chapter 4.5.2. Similarly to 0.1M-TiFeSi the quadratic effect of catalyst loading is highly significant with scaled estimate of -22.1, however for 0.55M-TiFeSi the linear effect is slightly significant albeit least significant as compared to all other terms studied. Negative value suggests again that yield is highly sensitive to mass of 0.55M-TiFeSi loaded and slight shifts away from maxima value will dramatically lower yield, confirming the strong effect the nanocatalyst has on improving esterification performance. A methyl oleate yield of 88.4% is close to >90% desired for commercial application and further optimisation is explored later in Chapter 6.2, alongside further analysis of 0.1M-TiFeSi and 0.55M-TiFeSi results to confirm if 0.55M-TiFeSi truly is catalytically superior beyond ± 5% maximum error threshold.

Table 5.11 - Methyl Oleate Yields for 0.55M-TiFeSi Catalyst Esterification Trials

Run	Methyl Oleate Yield (%)		Average Yield (%)
	Reaction 1	Reaction 2	
A	2.59	2.37	2.48
B	74.5	69.9	72.2
C	66.0	61.9	64.0
D	0.26	0.28	0.27
E	71.7	66.8	69.3
F	8.25	8.59	8.42
G	88.7	88.1	88.4
H	11.3	14.7	13.0
I	35.1	38.2	36.6
J	51.1	52.4	51.7

Table 5.12 - Effect Screening for 0.55M-TiFeSi Catalyst Esterification Trials

Effect	Scaled Estimate	Log Worth	P Value (%)	Bayes Posterior Probability (%)	t Ratio	f Ratio	Comment
Time	11.9	7.81	<0.01	99.9	14.6	213	**Significant**
Temperature	29.5	12.1	<0.01	100	36.2	1310	**Significant**
Catalyst Loading	-3.95	3.29	0.05	73.4	-4.84	23.5	**Significant**
Alcohol Ratio	13.7	8.46	<0.01	99.9	16.8	282	**Significant**
Time^2	-17.0	7.20	<0.01	99.8	-12.7	162	**Significant**
Temperature^2	16.7	7.14	<0.01	99.7	12.6	158	**Significant**
Catalyst Loading^2	-22.1	8.41	<0.01	99.9	-16.6	275	**Significant**
Alcohol Ratio^2	9.44	4.69	<0.01	96.3	7.09	50.3	**Significant**

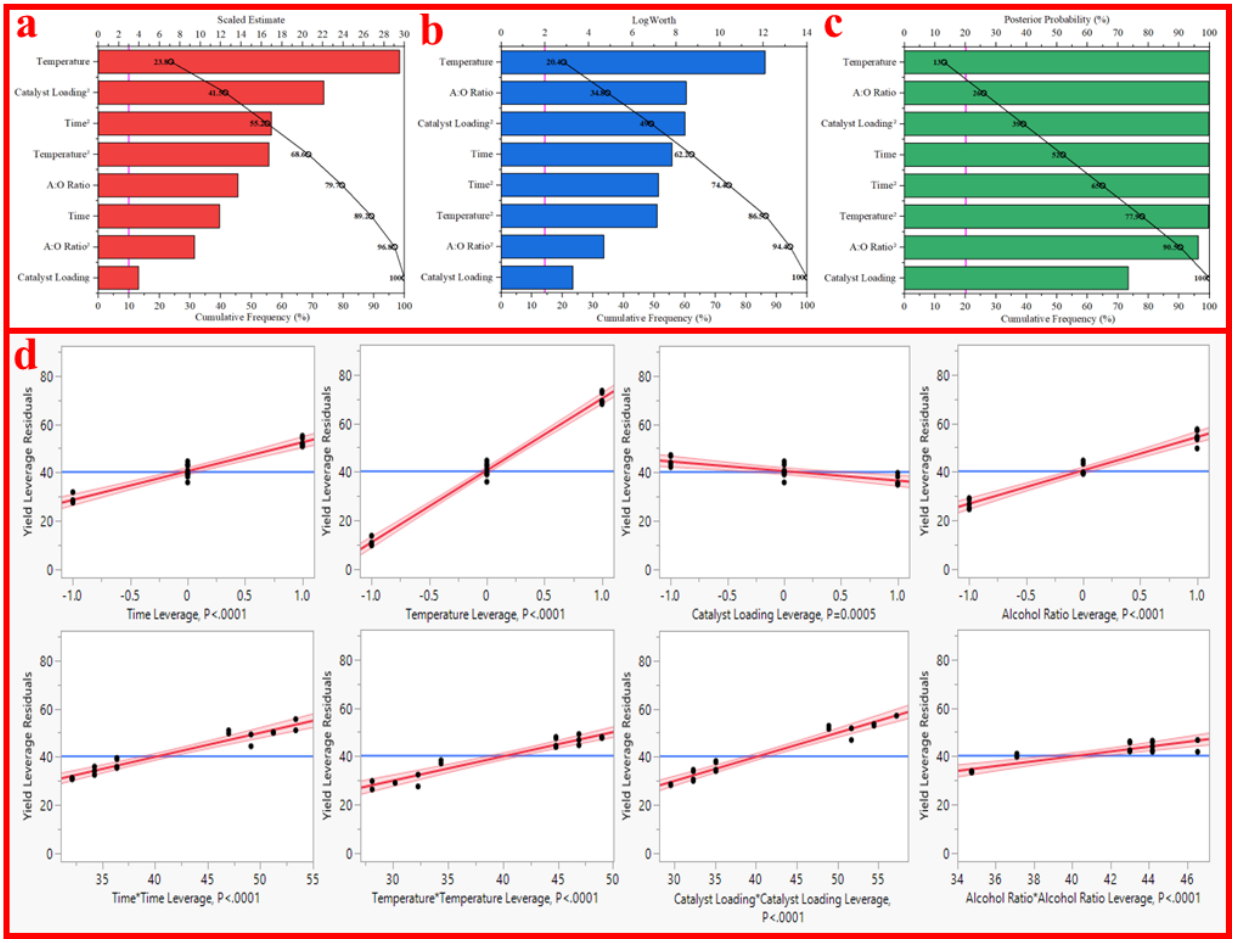

Figure 5.7 – Effect Screening Plots for 0.55M-TiFeSi Catalyst Esterification Trials

5.4.4.3 1.0M-TiFeSi

Reaction results for 1.0M-TiFeSi are given in Table 5.13 and effect screening summarised in Table 5.14 and Figure 5.8. Low catalytic performance was observed with only 10.8% maximum average methyl oleate yield observed in reaction run G with 9 hours of reaction at 60 °C, 3 wt% catalyst loading and 10:1 ratio of methanol to oleic acid. This result is only slightly greater than control and TiFeSi results at 9.86% and 8.06% respectively and falls within experimental error. The significant lack of catalytic activity for 1.0M-TiFeSi is likely due to low sulfate site loading achieved as discussed previously in Chapter 4.5.2 and indicates that while acidic strength and thermal stability may have been improved at higher chlorosulfonic acid concentration, low overall acid site density impedes reaction kinetics and leads to poor FFA esterification. While the linear effect of catalyst loading is seen to be statistically significant and hence may explain slight improvement in yield above thermal effects, both reaction temperature and reaction time are more influential. Alcohol to methyl oleate ratio was found to be insignificant, likely due to weak catalytic performance having more influence on low yields achieved. Very poor catalytic activity of the 1.0M-TiFeSi functionalised catalyst and TiFeSi non-functionalised support demonstrated that extreme values of chlorosulfonic acid concentration led to suboptimal catalyst performance that failed to reduce FFA impurities. Of the Ti series catalysts studied, only 0.1M-TiFeSi and 0.55M-TiFeSi demonstrated desirable esterification performance.

Table 5.13 - Methyl Oleate Yields for 1.0M-TiFeSi Catalyst Esterification Trials

Run	Methyl Oleate Yield (%)		Average Yield (%)
	Reaction 1	Reaction 2	
A	0.53	1.04	0.79
B	8.81	7.67	8.24
C	7.43	7.97	7.70
D	0.04	0.06	0.05
E	3.59	3.24	3.41
F	2.87	4.10	3.49
G	10.5	11.1	10.8
H	4.24	5.02	4.63
I	2.69	3.07	2.88
J	3.54	3.87	3.70

Table 5.14 - Effect Screening for 1.0M-TiFeSi Catalyst Esterification Trials

Effect	Scaled Estimate	Log Worth	P Value (%)	Bayes Posterior Probability (%)	t Ratio	f Ratio	Comment
Time	1.63	6.98	<0.01	100	12.1	147	**Significant**
Temperature	3.27	10.2	<0.01	100	24.3	590	**Significant**
Catalyst Loading	0.77	3.90	0.01	97.5	5.76	33.2	**Significant**
Alcohol Ratio	0.06	0.17	68.2	2.59	0.42	0.18	Insignificant
Time^2	-0.60	1.72	1.92	3.71	-2.74	7.52	Insignificant
Temperature^2	2.92	7.40	<0.01	100	13.3	177	**Significant**
Catalyst Loading^2	-0.53	1.47	3.38	21.0	-2.42	5.87	Insignificant
Alcohol Ratio^2	-0.20	0.42	38.3	3.21	-0.91	0.83	Insignificant

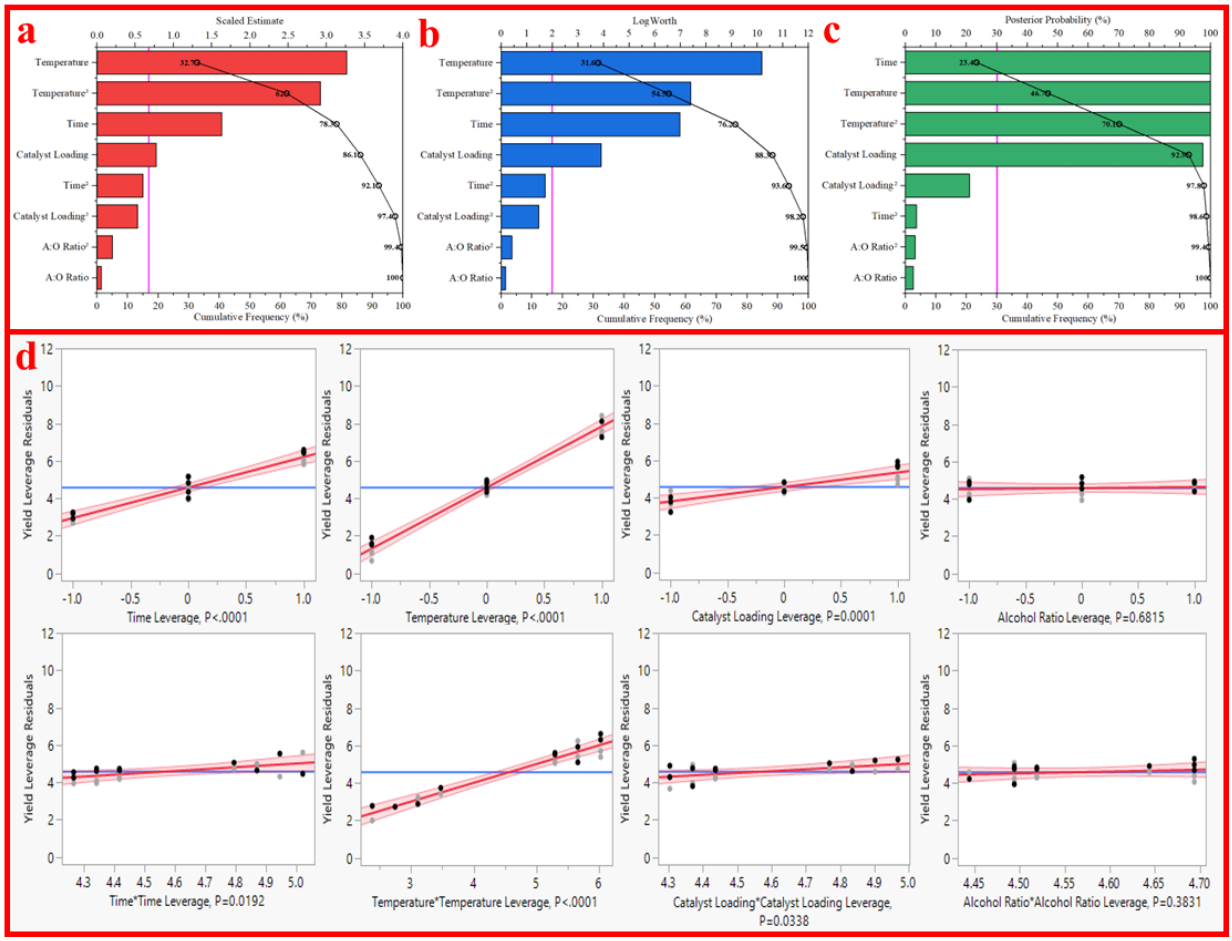

Figure 5.8 – Effect Screening Plots for 1.0M-TiFeSi Catalyst Esterification Trials

5.4.5 Zn Series Functionalised Catalysts

5.4.5.1 0.1M-ZnFeSi

Methyl oleate yields for batch trials with 0.1M-ZnFeSi are given in Table 5.15 and effect screening results summarised in Table 5.16 and Figure 5.9. Highest average methyl oleate yield of 22.2% was obtained in reaction run G at conditions of 3 wt% catalyst loading, 10:1 ratio of methanol to oleic acid and 9 hours of reaction at 60 °C. This represents a doubling in yield achieved as compared to pre-functionalised ZnFeSi support that only achieved 11.2% maximum average yield. Hence treatment with chlorosulfonic acid did lead to improvement in catalytic activity. Reaction time and temperature were seen to be very influential as expected of kinetically limited reaction. Quadratic effect of catalyst loading was significant while linear effect was insignificant indicating high degree of nonlinearity in yield response to nanocatalyst loading. A scaled estimate of -6.13 indicated strong decrease in yield upon modification of catalyst amount beyond maxima point. Despite 0.1M-ZnFeSi achieving a significant increase in methyl oleate yield compared to ZnFeSi support, catalytic activity was disappointing considering the extensive 9 hours reaction time at 60 °C. Especially in comparison to 0.1M-TiFeSi which achieved maximum average value of 82.3% yield. This could be due to order of magnitude difference in specific surface area between Ti and Zn series of catalysts leading to poor site accessibility and reduced esterification performance.

Table 5.15 - Methyl Oleate Yields for 0.1M-ZnFeSi Catalyst Esterification Trials

Run	Methyl Oleate Yield (%)		Average Yield (%)
	Reaction 1	Reaction 2	
A	0.45	0.99	0.72
B	13.0	13.7	13.3
C	7.66	9.35	8.51
D	0.17	0.24	0.21
E	14.6	11.5	13.1
F	1.09	1.56	1.33
G	22.3	22.1	22.2
H	4.94	3.90	4.42
I	6.91	4.66	5.79
J	10.1	10.5	10.3

Table 5.16 - Effect Screening for 0.1M-ZnFeSi Catalyst Esterification Trials

Effect	Scaled Estimate	Log Worth	P Value (%)	Bayes Posterior Probability (%)	t Ratio	f Ratio	Comment
Time	3.83	7.13	<0.01	99.9	12.5	157	**Significant**
Temperature	6.04	9.22	<0.01	100	19.8	391	**Significant**
Catalyst Loading	-0.85	1.75	1.79	26.2	-2.78	7.72	Insignificant
Alcohol Ratio	1.48	3.28	0.05	74.1	4.83	23.3	**Significant**
Time^2	-2.01	2.71	<0.01	79.5	-4.03	16.3	**Significant**
Temperature^2	3.01	4.08	<0.01	66.6	6.05	36.5	**Significant**
Catalyst Loading^2	-6.13	7.05	<0.01	99.9	-12.3	151	**Significant**
Alcohol Ratio^2	-0.01	0.01	97.8	2.44	-0.03	<0.01	Insignificant

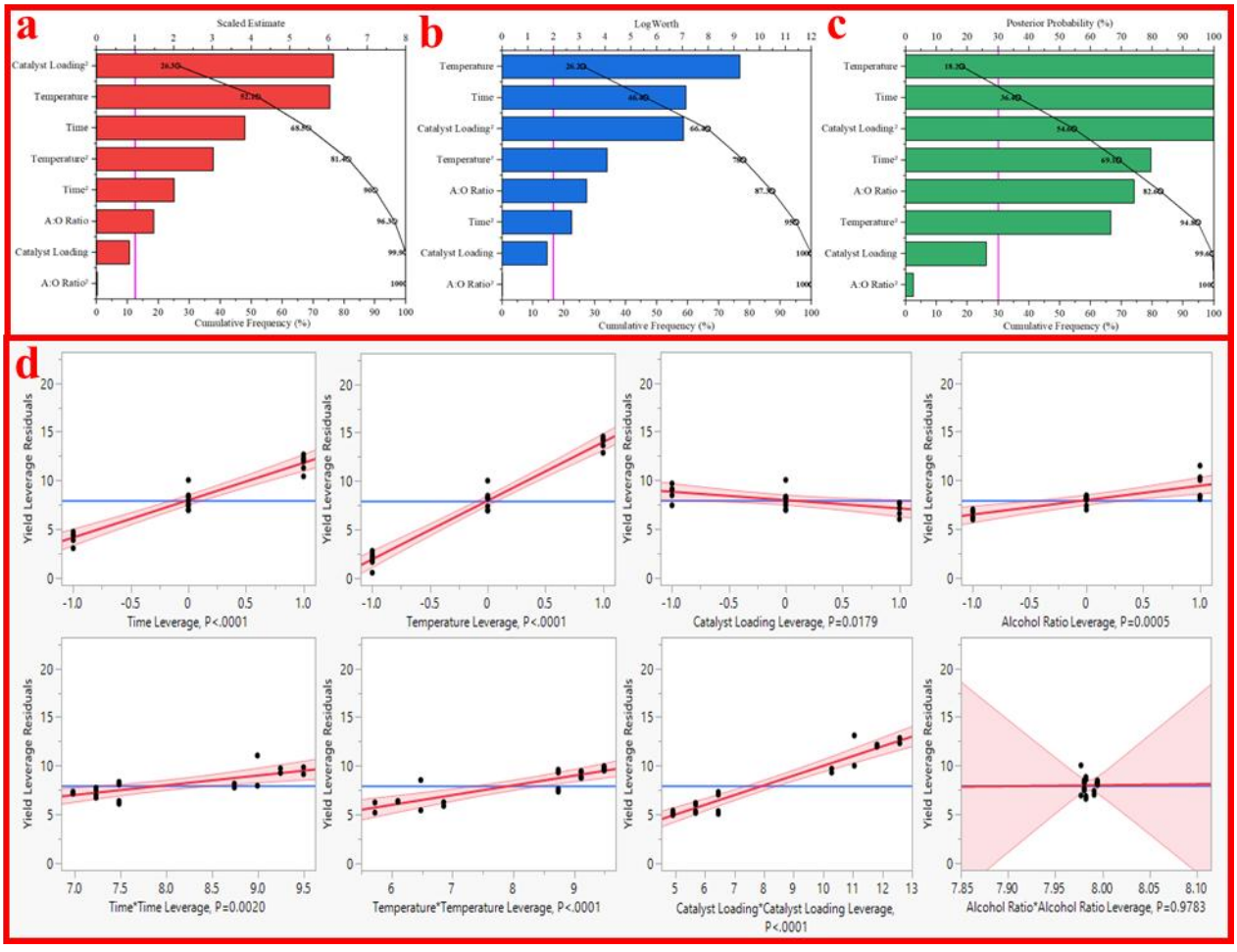

Figure 5.9 – Effect Screening Plots for 0.1M-ZnFeSi Catalyst Esterification Trials

5.4.5.2 0.55M-ZnFeSi

Reaction results for 0.55M-ZnFeSi and oleic acid batch esterification trials are provided in Table 5.17 and a summary of effect screening results given in Table 5.18 and Figure 5.10. Maximum average methyl oleate yield of 25.4% was obtained in reaction run G under conditions of 9 hours reaction at 60 °C, 3 wt% catalyst loading and 10:1 ratio of methanol to oleic acid. This represents a slight increase in catalytic activity as compared to 0.1M-ZnFeSi which achieved 22.2% yield under same conditions. While similar improvement in catalytic activity was also observed in Ti series when increasing chlorosulfonic acid concentration from 0.1M to 0.55M, increase in yield was ~6% for Ti series compared to ~3% improvement achieved for 0.55M-ZnFeSi. Since this is within maximum ± 5% variation from experimental and statistical errors, it is unclear if extra acid treatment led to a significant improvement in reactivity. It should be noted that characterisation results throughout Chapter 4 indicated 0.55M-ZnFeSi had fewer desirable properties compared to 0.1M-ZnFeSi such as higher carbon impurities and increased loss of material during synthesis step. It is therefore questionable if small improvement of ~3% yield is worth such disadvantages. Only the linear effect of catalyst loading is insignificant for 0.55M-ZnFeSi, however the quadratic term is highly dominant with a scaled estimate of -8.20 confirming changes to catalyst loading had nonlinear influence on yield achieved. Unfortunately, esterification performance of only ~20% methyl oleate yield after 9 hours at 60 °C suggests 0.55M-ZnFeSi has low catalytic activity.

Table 5.17 - Methyl Oleate Yields for 0.55M-ZnFeSi Catalyst Esterification Trials

Run	Methyl Oleate Yield (%)		Average Yield (%)
	Reaction 1	Reaction 2	
A	2.80	3.43	3.11
B	13.1	12.0	12.5
C	14.5	13.8	14.2
D	0.14	0.12	0.13
E	19.7	20.6	20.1
F	2.20	3.58	2.89
G	24.8	26.0	25.4
H	4.86	5.72	5.29
I	11.9	11.0	11.4
J	13.4	12.0	12.7

Table 5.18 - Effect Screening for 0.55M-ZnFeSi Catalyst Esterification Trials

Effect	Scaled Estimate	Log Worth	P Value (%)	Bayes Posterior Probability (%)	t Ratio	f Ratio	Comment
Time	4.12	8.55	<0.01	100	17.1	292	**Significant**
Temperature	5.77	10.1	<0.01	100	23.9	573	**Significant**
Catalyst Loading	-0.30	0.62	24.0	3.73	-1.24	1.55	Insignificant
Alcohol Ratio	4.13	8.55	<0.01	100	17.1	293	**Significant**
Time^2	-1.66	2.84	0.14	86.3	-4.22	17.8	**Significant**
Temperature^2	3.35	5.44	<0.01	91.2	8.50	72.2	**Significant**
Catalyst Loading^2	-8.20	9.46	<0.01	100	-20.8	433	**Significant**
Alcohol Ratio^2	1.92	3.31	0.05	77.5	4.88	23.8	**Significant**

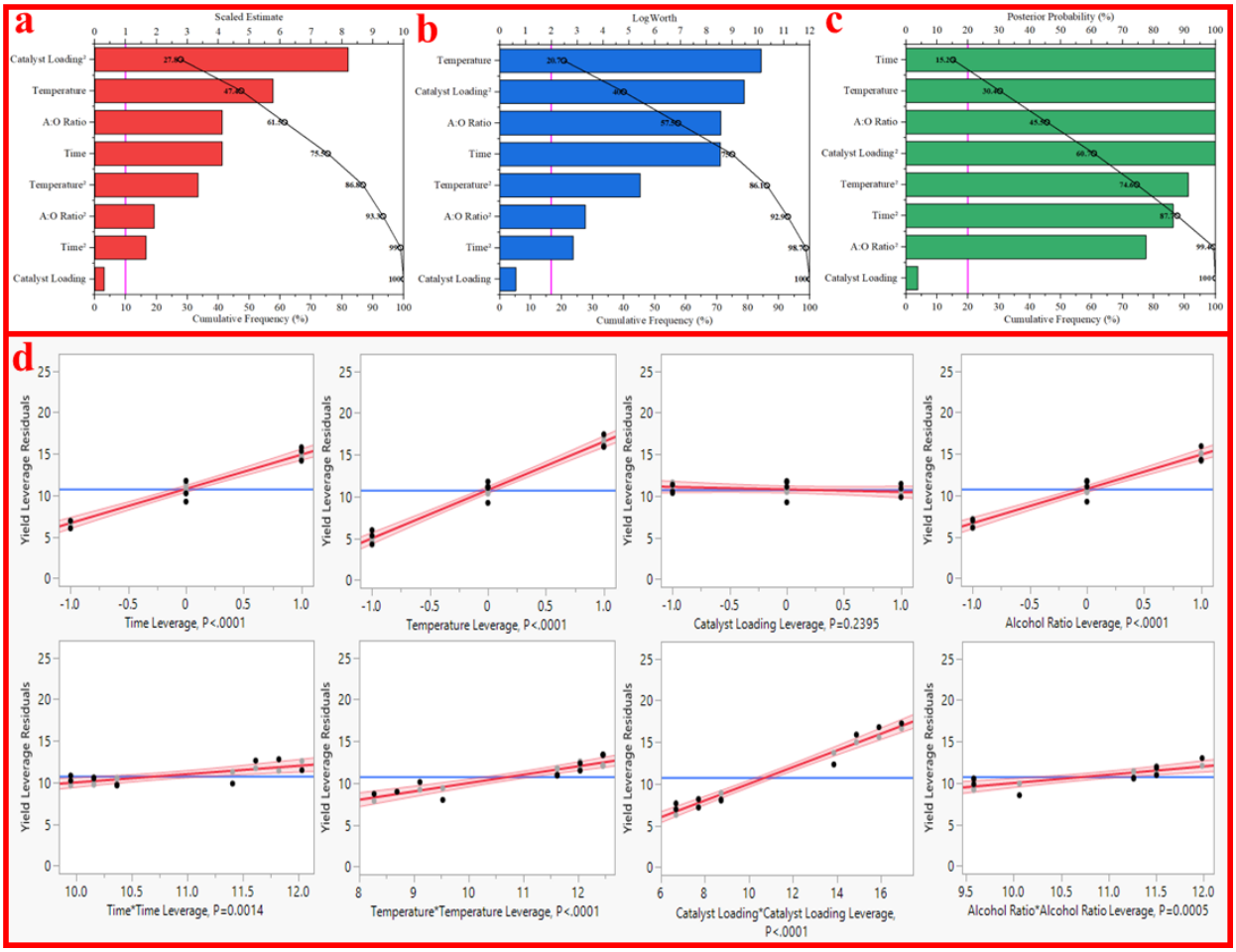

Figure 5.10 – Effect Screening Plots for 0.55M-ZnFeSi Catalyst Esterification Trials

5.4.5.3 1.0M-ZnFeSi

Methyl oleate batch esterification yields for 1.0M-ZnFeSi are given in Table 5.19 and effect screening results summarised in Table 5.20 and Figure 5.11. Maximum average yield of only 6.98% was obtained in reaction run G at conditions of 9 hours reaction at 60 °C, 3 wt% catalyst loading and 10:1 ratio of methanol to oleic acid. Since this reaction performance was within ~3% of control reaction at 9.86% methyl oleate yield, no significant catalytic activity was observed for 1.0M-ZnFeSi material beyond thermal effects. Linear effect of catalyst loading had scaled estimate of -0.82, similarly quadratic effect also had negative scaled estimate of -1.41. This suggests that higher amounts of suspended solid may have increased the viscosity of oleic acid phase, hindering reactant mass transfer at liquid-liquid interface as discussed prior with TiFeSi and ZnFeSi results.

Failure of 1.0M-ZnFeSi to demonstrate catalytic activity of FFA esterification is a similar finding to batch trial results for 1.0M-TiFeSi. While increasing chlorosulfonic acid loading may improve acid site strength and thermal stability, it is vital this does not come at the expense of sufficient catalytically active sulfate sites on surface. High concentrations of chlorosulfonic acid favoured acidic digestion of support material over functionalisation and the resulting 1.0M series of nanocatalysts have negligible reactivity as a result. Overall, the Zn series of nanocatalysts displayed inferior esterification performance to Ti series under same reaction conditions, likely due to more desirable chemical, structural and morphological properties as predicted in Chapter 4.

Table 5.19 - Methyl Oleate Yields for 1.0M-ZnFeSi Catalyst Esterification Trials

Run	Methyl Oleate Yield (%)		Average Yield (%)
	Reaction 1	Reaction 2	
A	0.29	0.47	0.38
B	5.62	6.88	6.25
C	1.69	1.85	1.77
D	0.10	0.64	0.37
E	4.83	4.69	4.76
F	1.18	1.34	1.26
G	6.94	7.02	6.98
H	1.31	1.37	1.34
I	2.07	3.23	2.65
J	2.12	2.79	2.46

Table 5.20 - Effect Screening for 1.0M-ZnFeSi Catalyst Esterification Trials

Effect	Scaled Estimate	Log Worth	P Value (%)	Bayes Posterior Probability (%)	t Ratio	f Ratio	Comment
Time	1.41	4.30	<0.01	80.0	6.41	41.1	**Significant**
Temperature	1.79	5.25	<0.01	91.8	8.13	66.1	**Significant**
Catalyst Loading	-0.82	2.47	0.34	44.4	-3.72	13.8	**Significant**
Alcohol Ratio	0.20	0.42	37.8	3.22	0.92	0.84	Insignificant
Time^2	-1.49	2.79	0.16	50.4	-4.15	17.2	**Significant**
Temperature^2	1.41	2.63	0.23	42.2	3.93	15.5	**Significant**
Catalyst Loading^2	-1.41	2.64	0.23	46.4	-3.94	15.5	**Significant**
Alcohol Ratio^2	0.34	0.44	36.2	3.29	0.95	0.90	Insignificant

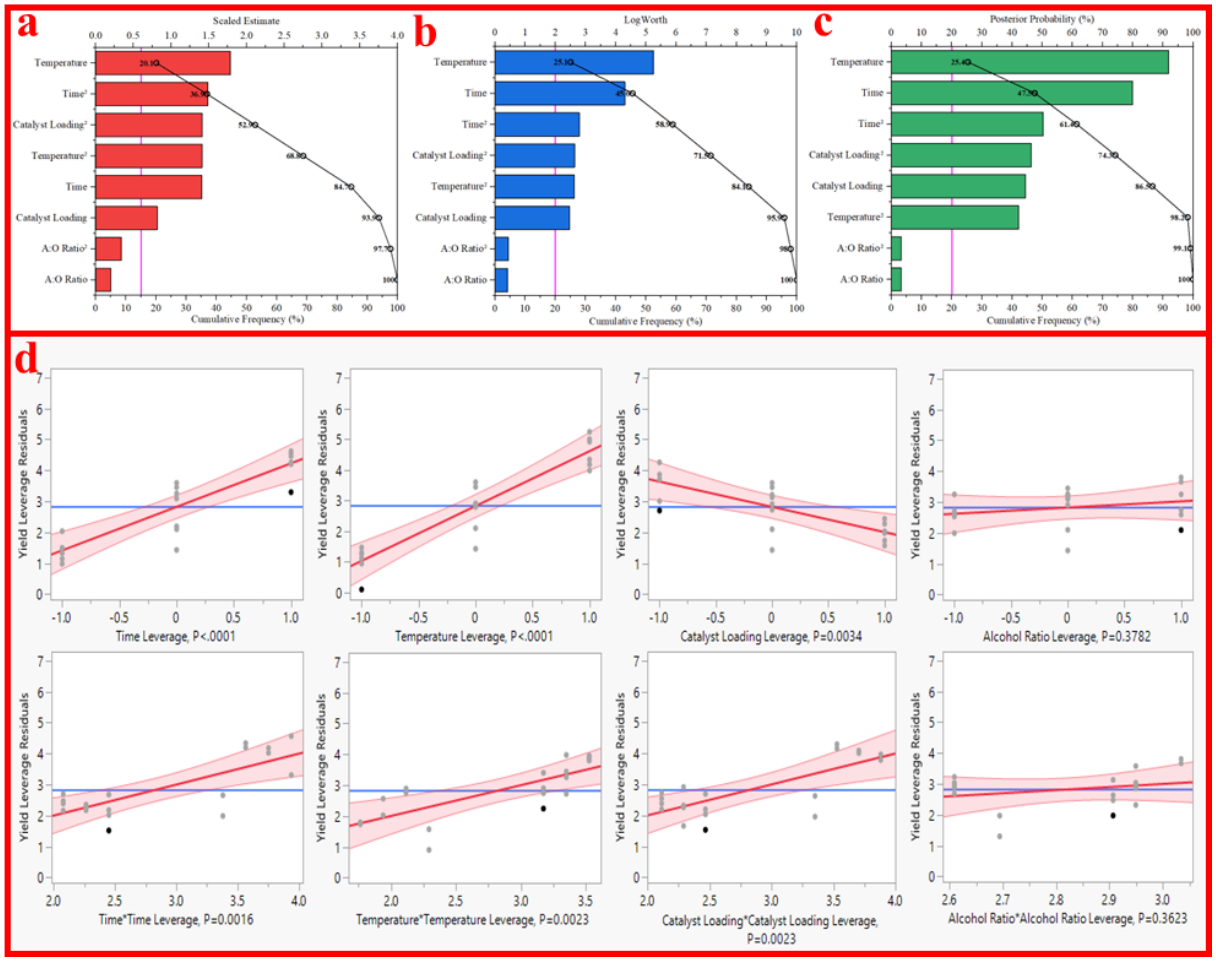

Figure 5.11 – Effect Screening Plots for 1.0M-ZnFeSi Catalyst Esterification Trials

5.5 Summary

Maximum methyl oleate yield achieved by each nanomaterial throughout this chapter is summarised in Table 5.21 and colour coded based on relative degree of reactivity. The average yield in each batch trial performed is also summarised graphically in Figure 5.12. It is clear that 0.1M-TiFeSi and 0.55M-TiFeSi are both highly suitable candidates for further optimisation studies and testing with UCO feedstock in a two-step pathway, being the only two nanocatalysts able to achieve >80% yield. Due to similar yields obtained between 0.1 M and 0.55 M TiFeSi nanocatalysts however, further optimisation studies are required to determine which nanocatalyst is truly superior. This work is continued in Chapter 6. The initial hypothesis proposed at the end of Chapter 4 predicted that Ti series should be more catalytically active than Zn series due to more desirable properties such as crystallinity, surface acidity, thermal stability, reduced carbon contamination, specific surface area and porosity. Results from Chapter 5 certainly confirm this to be the case, highlighting the importance of synthesising a nanocatalyst with suitable properties to maximise reaction performance. Without chlorosulfonic acid functionalisation, there is no significant difference in methyl oleate production between support materials and thermal control. At excessive concentration of chlorosulfonic acid, such as 1.0M-TiFeSi and 1.0M-ZnFeSi, there is again no significant difference between catalyst and thermal control. Future work is recommended where a greater range of nanocatalysts are synthesised to determine the exact point acid concentration goes from enhancing catalytic activity to impeding reaction performance.

Table 5.21 - Summary of Maximum Average Methyl Oleate Yield Achieved

Catalyst Tested	Maximum Yield (%)	Comment
Control	9.86	Thermal Effect Only
TiFeSi	8.06	No Notable Improvement
ZnFeSi	11.2	No Notable Improvement
0.1M-TiFeSi	**82.3**	**Strong Catalytic Activity**
0.55M-TiFeSi	**88.4**	**Strong Catalytic Activity**
1.0M-TiFeSi	10.8	No Notable Improvement
0.1M-ZnFeSi	22.2	Weak Catalytic Activity
0.55M-ZnFeSi	25.4	Weak Catalytic Activity
1.0M-ZnFeSi	6.98	No Notable Improvement

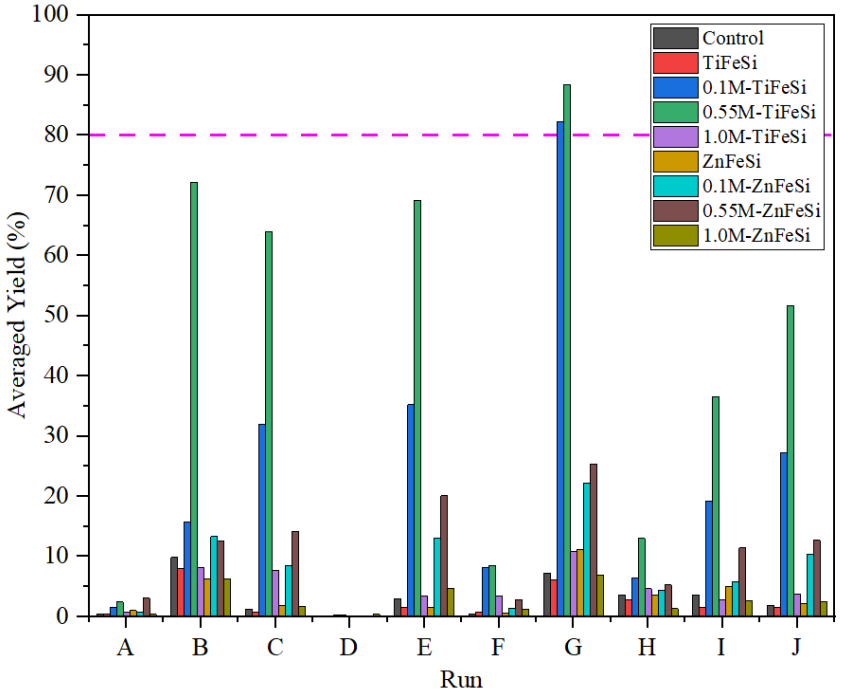

Figure 5.12 – Summary of Oleic Acid Batch Esterification Trials

Scaled estimate model coefficients for each nanocatalyst investigated throughout this chapter have been summarised in Table 5.22. Factors determined to be statistically insignificant are marked in red and italicised.

Table 5.22 - Summary of Esterification Model Coefficients and Significant Effects

Model Parameter	Control	TiFeSi	ZnFeSi	0.1M-TiFeSi	0.55M-TiFeSi	1.0M-TiFeSi	0.1M-ZnFeSi	0.55M-ZnFeSi	1.0M-ZnFeSi
Intercept	2.32	2.05	2.47	32.0	48.4	3.62	11.1	13.5	3.51
Time	2.09	1.49	2.83	12.4	11.9	1.63	3.83	4.12	1.41
Temperature	2.29	2.05	2.10	16.8	29.5	3.27	6.04	5.77	1.79
Catalyst Loading	-	-0.90	-0.92	*1.89*	-3.95	0.77	*-0.85*	*-0.30*	-0.82
Alcohol Ratio	*-1.04*	-1.24	-0.43	10.4	13.7	*0.06*	1.48	4.13	*0.20*
Time^2	*-1.56*	-1.30	1.06	*5.44*	-17.0	*-0.60*	-2.01	-1.66	-1.49
Temperature^2	*1.73*	1.65	2.65	14.1	16.7	2.92	3.01	3.35	1.41
Catalyst Loading^2	-	*-0.24*	-1.60	-24.5	-22.1	*-0.53*	-6.13	-8.20	-1.41
Alcohol Ratio^2	*1.19*	*0.42*	-0.64	-10.3	9.44	*-0.20*	*-0.01*	1.92	*0.34*

Reaction time and temperature were found to always have a significant linear effect. Reaction time tended to exhibit significant concave nonlinearity (maxima), suggesting that excessive reaction duration eventually favours the reverse reaction. Conversely, temperature exhibited significant convex nonlinearity (minima) suggesting that higher temperatures always favoured the esterification process. These results indicate a kinetically limited endothermic reversible process, where yield can be maximised by reacting at greatest temperature possible and halting the reaction before methyl oleate backreacts into oleic acid. Kinetic and thermodynamic modelling in Chapter 6.2.2 will further investigate this prediction.

Catalyst loading was always found to display a maximum point as indicated by negative quadratic coefficient. If too little nanocatalyst is added then mass transfer of reactants to surface active sites may become impeded, however if excess nanocatalyst is added the resulting viscosity increase of the oil-methanol phase could also contribute to mass transfer impediment. In every nanomaterial tested, either the linear effect or nonlinear quadratic effect of catalyst loading was found to be significant. Therefore, the quantity of nanocatalyst loaded into each reaction remains an important factor to optimise alongside determining optimal reaction duration at 60 °C.

Increased alcohol to oil ratio tended to enhance yield for catalytically active nanomaterials. Since esterification is a reversible reaction, increasing the concentration of reacting methanol favours the forward reaction and increases methyl oleate yield. For 0.1M-TiFeSi, a significant maxima point was observed indicating that excess methanol eventually becomes counterproductive by lowering methyl oleate concentration and hindering reaction kinetics. For 0.55M-TiFeSi and 0.55M-ZnFeSi a significant minima point was noted at 4:1 methanol to oleic acid ratio where insufficient methanol is present to favour forward reaction pathway. Increasing methanol loading not only eventually hinders reaction kinetics, but requires a larger reactor, increased heating duty and eventual separation of the extra unreacted methanol that was added. Therefore, the alcohol to oil ratio remains an important factor to optimise.

In summary, 0.1M-TiFeSi and 0.55M-TiFeSi were found to be most desirable of the novel nanocatalysts studied for lowering FFA content in impure oil feedstocks. Reaction time, temperature, catalyst loading and alcohol to oil ratio were all found to be significant factors, contributing linearly and/or nonlinearly to yield achieved. Further work will now explore increasing methyl oleate yield beyond 90% and testing real UCO feedstocks in a two-step reaction.

Chapter 6.

Chapter 6. Reaction Modelling and Two-Step Pathway Development

6.1 Introduction

Results from Chapter 5 indicated that further optimisation of reaction conditions is required in order to achieve methyl oleate yields >90% in the oleic acid model esterification pathway. In this Chapter, the obtained DOE models are utilised to predict and experimentally validate maximum reduction of FFA content achievable by the most effective nanocatalyst. Realistic industrial feedstocks are then explored in a two-step batch biodiesel synthesis reaction, where the optimal sulfated nanocatalyst performs initial FFA esterification followed by an optimised KOH transesterification step. Results are compared with one step KOH transesterification to confirm sulfated nanocatalysts enhance base catalysis by lowering FFA loading. Finally, recyclability challenges that must be addressed before industrial viability of these synthesised nanomaterials are discussed.

Chapter 6.2 explores the optimisation of the DOE models developed throughout Chapter 5 to predict optimum factor setpoints and maximum methyl oleate yield achievable. Since the models were primarily designed for screening, results are validated experimentally to determine which nanocatalyst has superior esterification activity. Application of the obtained model is then used to understand thermodynamic and kinetic characteristics of the esterification pathway, testing the prediction in Chapter 5 that reaction is reversible and endothermic in nature. In Chapter 6.3 a fresh sample of UCO from a local restaurant is compared to a degraded sample of UCO kept in laboratory ambient storage for extended duration. Both feedstocks are characterised to explore how FFA impurity concentration changes over time, alongside confirming unsuitability for base transesterification without prior pretreatment. Two-step biodiesel production pathway is developed and optimised in Chapter 6.4, starting with locating optimum reaction conditions of KOH with pure vegetable oil. Effect of FFA loading on transesterification step is validated before confirmation that sulfated nanocatalyst pretreatment step leads to an improvement in biodiesel yield. Finally, the challenge of recyclability is investigated to understand cause of deactivation over repeated uses. Chapter 7 will subsequently conclude main findings of the research and suggest opportunities for future research work.

6.2 Esterification Reaction Modelling

6.2.1 Model Validation

6.2.1.1 Response Surface Optimisation

Results from Chapter 5 indicated that 0.1M-TiFeSi and 0.55MTiFeSi were the two most active catalysts for oleic acid esterification in the initial screening trials. Unfortunately, it was unclear which catalyst of the two was superior beyond experimental error. To explore esterification performance in greater detail, nonlinear optimisation was performed on the obtained DoE regression models to produce response surface profiles and search for theoretical maximum yield that could be achieved. Response surface plots for Ti series and Zn series of catalysts are given in Figure 6.1a-c and Figure 6.2a-c respectively. Predicted optimum point and maximum expected yield is summarised in Table 6.1. Quadratic model alone led to overprediction above 100% yield for 0.55M-TiFeSi (~120%) hence logistic fitting was employed to restrict response between limits of 0% and 100%. Logistic fitting was also used in 0.55M-ZnFeSi as optimum of 31.2% was suspected to be too low in quadratic model. Extra degree of freedom available was used to reduce lack of fit errors or model the most significant temperature-time interaction effect, which only improved prediction accuracy for case of 0.1M-ZnFeSi. Results suggest that 0.55M-TiFeSi catalyst is superior with theoretical maximum methyl oleate yield of 99.3% after 6.75 hours at 60 °C with 3.19 wt% catalyst loading and 16:1 ratio of methanol to oleic acid.

Table 6.1 - Predicted Optimum Setpoint from Custom DoE Designs

Catalyst	Time (hr)	Temperature (°C)	Catalyst Loading (wt%)	Alcohol : Oil Ratio	Predicted Yield (%)
0.1M-TiFeSi	9.00	60.0	3.08	13.0	83.4
0.55M-TiFeSi	6.75	60.0	3.19	16.0	99.3
1.0M-TiFeSi	9.00	60.0	4.46	10.9	11.1
0.1M-ZnFeSi	9.00	60.0	2.82	16.0	25.0
0.55M-ZnFeSi	7.09	60.0	3.28	16.0	76.5
1.0M-ZnFeSi	6.89	60.0	2.42	16.0	7.70

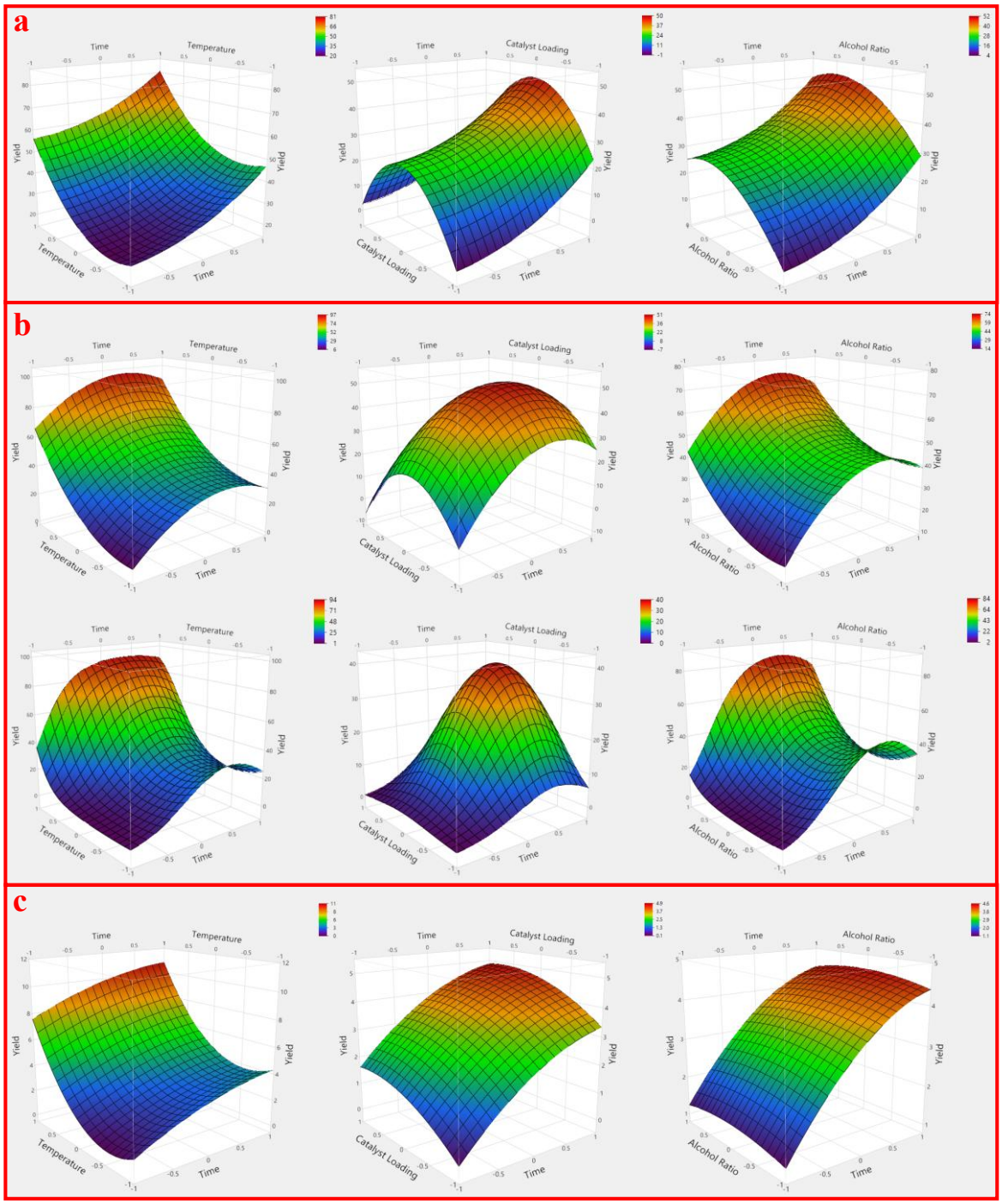

Figure 6.1 - Response Surface Plots for 0.1M-TiFeSi (a),
0.55M-TiFeSi Quadratic (Top) and Logistic (Bottom) models (b), 1.0M-TiFeSi (c)

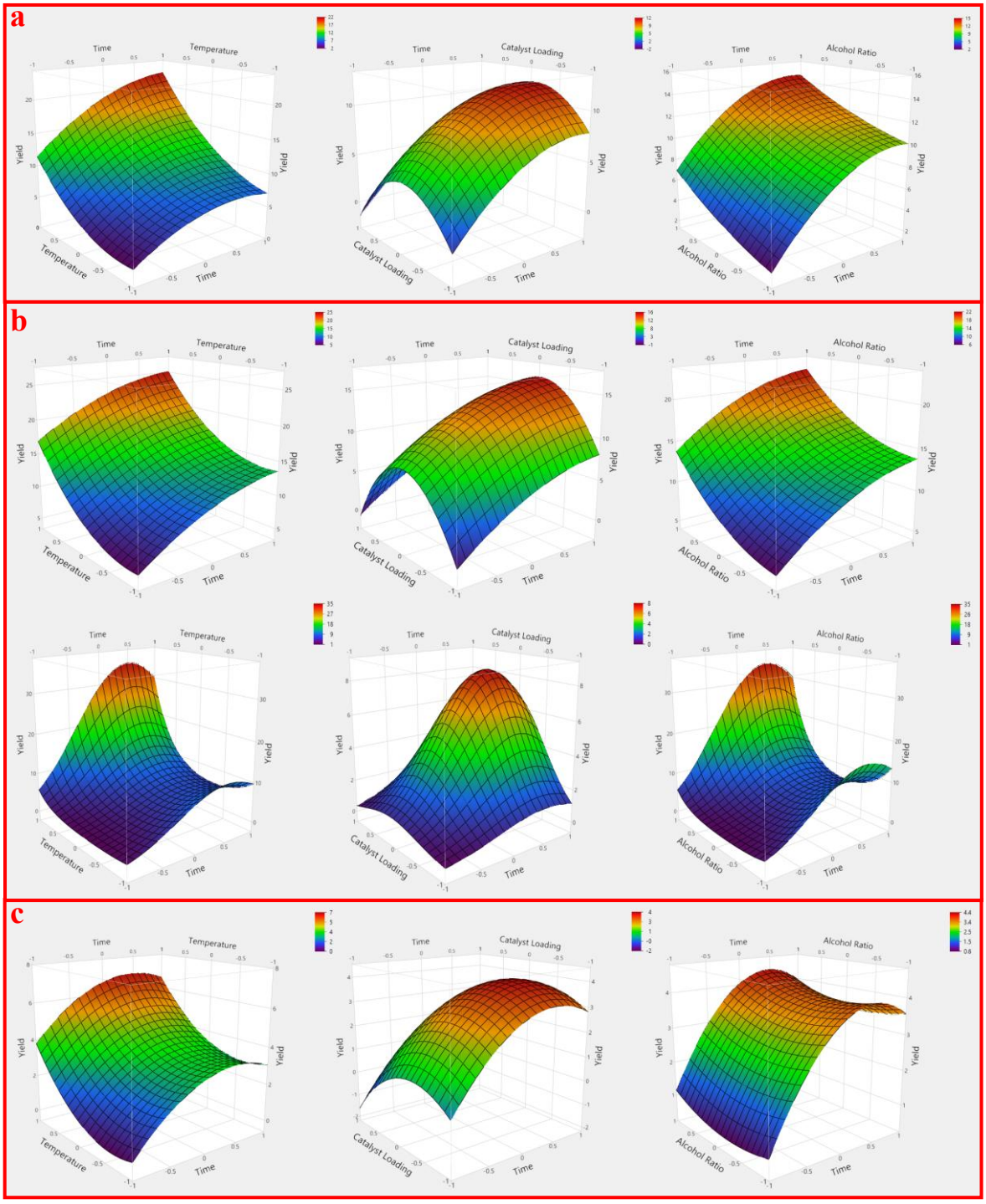

Figure 6.2 - Response Surface Plots for 0.1M-ZnFeSi (a),
0.55M-ZnFeSi Quadratic (Top) and Logistic (Bottom) models (b), 1.0M-ZnFeSi (c)

6.2.1.2 Model Fit

To quantify the main source of error in optimum point estimations, analysis of variance (ANOVA) was performed using JMP with results summarised in Table 6.2. For all catalysts the model error accounted for statistically more significant variance than pure random error with p value <0.01% in all cases, even under logistic model transformation or modelling of extra terms in 0.55M-TiFeSi, 0.1M-ZnFeSi and 0.55M-ZnFeSi. Results of ANOVA confirms all models could detect response variation to statistical significance and main cause of error between prediction and actual value was due to model fitting. Plots of actual yield vs predicted yield are included in Figure 6.3 for Ti series (a-d) and Zn series (e-h) respectively. Quadratic models display high degree of fitting within 95% confidence bounds. Logistic transformation for 0.55M-TiFeSi (Figure 6.3c) and 0.55M-ZnFeSi (Figure 6.3g) display greater prediction errors, especially around central yield values where inflection point in a logistic function would be expected. Increased prediction error is likely due to model biasing from only modelling nonlinearity via quadratic terms. However, logistic fit does account for the plateau nature of yield response at 100% and leads to more realistic optimum point estimation. For instance, ~100% yield is predicted as compared to ~120% for 0.55M-TiFeSi catalyst. For 0.55M-ZnFeSi, a yield significantly above ~30% is estimated which accounts for an expected improvement in reactivity as compared to 0.1M-ZnFeSi catalyst. Studentised residual plots for each model are provided in Figure 6.4 and confirm no outliers were observed beyond 95% confidence interval. Experimental verification was subsequently used to confirm model fit.

Table 6.2 - Analysis of Variance for Custom DoE Esterification Models

Catalyst	Sum of Squares			Mean Square		f Ratio
	Model	Error	Corrected Total	Model	Error	
0.1M-TiFeSi	10507	130	10637	1313	11.8	111
0.55M-TiFeSi	106	2.77	109	13.2	0.252	52.5
1.0M-TiFeSi	206	2.39	208	25.7	0.217	119
0.1M-ZnFeSi	875	9.9	885	109	1.12	98.1
0.55M-ZnFeSi	45.2	2.33	47.5	5.65	0.212	26.6
1.0M-ZnFeSi	96.9	6.37	103	12.1	0.579	20.9

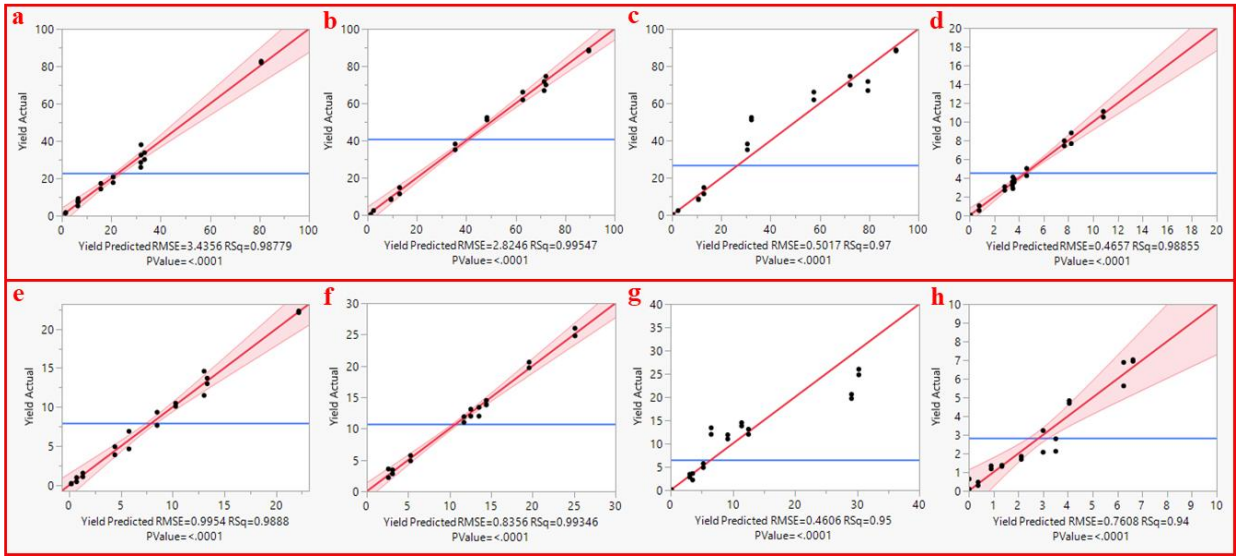

Figure 6.3 - Actual by Predicted Plots for 0.1M-TiFeSi (a), 0.55M-TiFeSi (b, c), 1.0M-TiFeSi (d) and 0.1M-ZnFeSi (e), 0.55M-ZnFeSi (f, g), 1.0M-ZnFeSi (h)

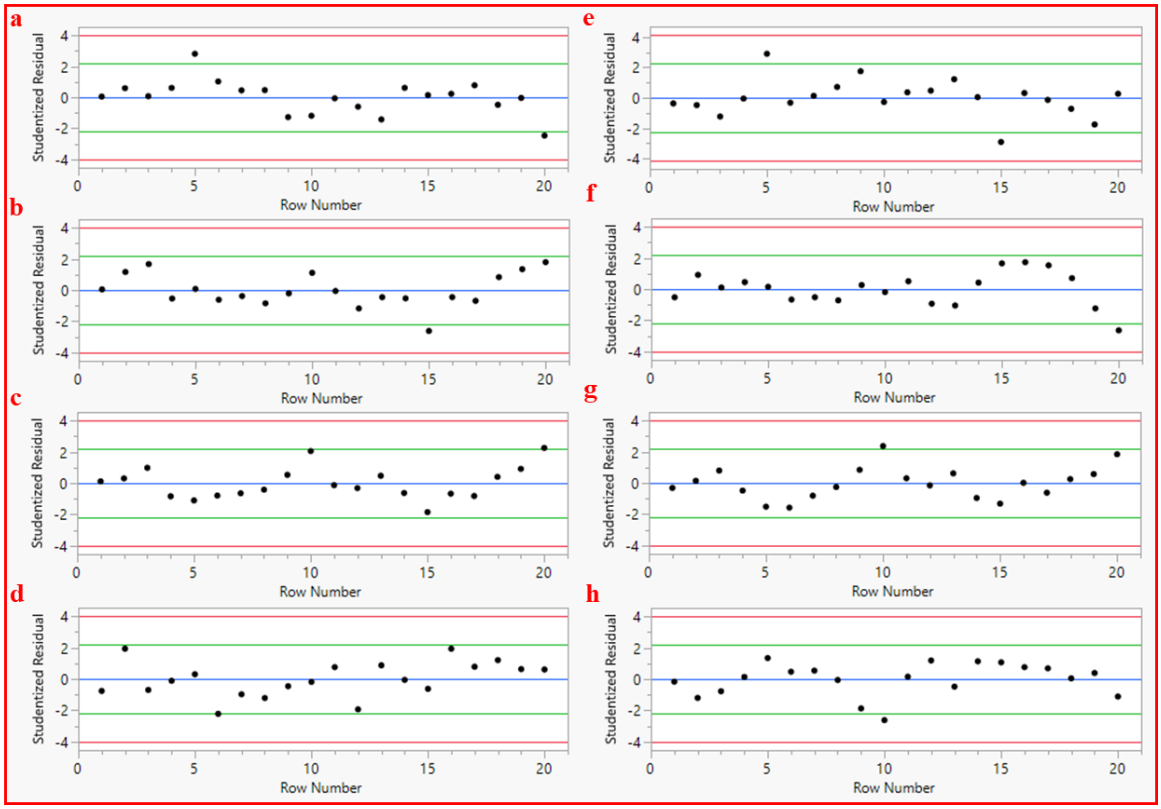

Figure 6.4 - Studentised Residual Plots for 0.1M-TiFeSi (a), 0.55M-TiFeSi (b, c), 1.0M-TiFeSi (d) and 0.1M-ZnFeSi (e), 0.55M-ZnFeSi (f, g), 1.0M-ZnFeSi (h)

6.2.1.3 Experimental Confirmation

Two runs at predicted optimum point as given in Table 6.1 were performed for each catalyst except 1.0M-ZnFeSi due to lack of sufficient material. Average yield observed and comparison to model predictions are summarised in Table 6.3. Results confirmed that 0.55M-TiFeSi was superior nanocatalyst with complete conversion of oleic acid into methyl oleate after 6.75 hours at 60 °C with 3.19 wt% catalyst loading and 16:1 ratio of methanol to oleic acid. While 0.1M-TiFeSi catalyst still displayed high catalytic activity, performance was slightly worse than predicted with an extra 0.96% absolute error beyond ± 5% expected maximum error likely due to model fitting. Even under optimised conditions 1.0M-TiFeSi catalyst showed no improvement over non catalytic heating control trial. For both Zn catalysts tested an improvement in experimentally obtained yield as compared to maximum value predicted by quadratic model was observed. In the case of 0.1M-ZnFeSi a prediction of 23.4% was increased to 25.0% by including temperature-time interaction effect. Actual yield of 31.4% was achieved which represents an extra 1.41% absolute error beyond ± 5% expected maximum error, again likely due to poor model fit. For 0.55M-ZnFeSi a quadratic model optimal yield of 31.2% was deemed far too low (-25.2% absolute error) whilst logistic fit optimum of 76.5% deemed too high. Reaction at predicted optimum settings post logistic fit gave 56.4% observed yield, suggesting that 0.55M-ZnFeSi is potentially more active than 0.1M-ZnFeSi but highlighting high degree of model error (+20.1%). This is likely due to lack of interaction term modelling, limited number of runs possible to perform and undesirable characterisation results for 0.55M-ZnFeSi discussed in Chapter 4. Results suggest 0.55M-TiFeSi is the superior nanocatalyst.

Table 6.3 - Experimental Validation of Model Optimum Point Estimation

Catalyst	Predicted Yield (%)	Confidence Interval (95%)	Actual Yield (%)	Absolute Error (%)
0.1M-TiFeSi	83.4	78.4 - 88.4	77.4	+5.96
0.55M-TiFeSi	**99.3**	**98.5 - 99.7**	**~100**	**-3.37**
1.0M-TiFeSi	11.1	10.4 - 11.8	15.2	-4.12
0.1M-ZnFeSi	25.0	22.3 - 27.7	31.4	-6.41
0.55M-ZnFeSi	76.5	62.6 - 86.4	56.4	+20.1

6.2.2 Kinetic and Thermodynamic Modelling

Obtained custom DoE model identified 0.55M-TiFeSi as the superior nanocatalyst and successfully located optimum reaction point with a theoretical yield within experimental error of observed result. This nanocatalyst model was therefore selected as most suitable for further kinetic and thermodynamic modelling to gain greater understanding of how FFA interacts with 0.55M-TiFeSi. Simulated runs were performed in JMP using quadratic model at low reaction temperatures and enabling logistic fitting at higher reaction temperatures. Predicted methyl oleate yield profiles with time for reaction temperatures at 30 °C, 45 °C and 60 °C is shown below in Figure 6.5a. Region of greatest reaction rate is indicated for each isotherm and was used to estimate reaction order and rate constant as described in Chapter 3.5.4. Linearised plots are given in Figure 6.5b-d and results are summarised in Table 6.4. Reaction is found to be first order with respect to FFA concentration which should be expected due to excess 16:1 methanol to FFA loading.

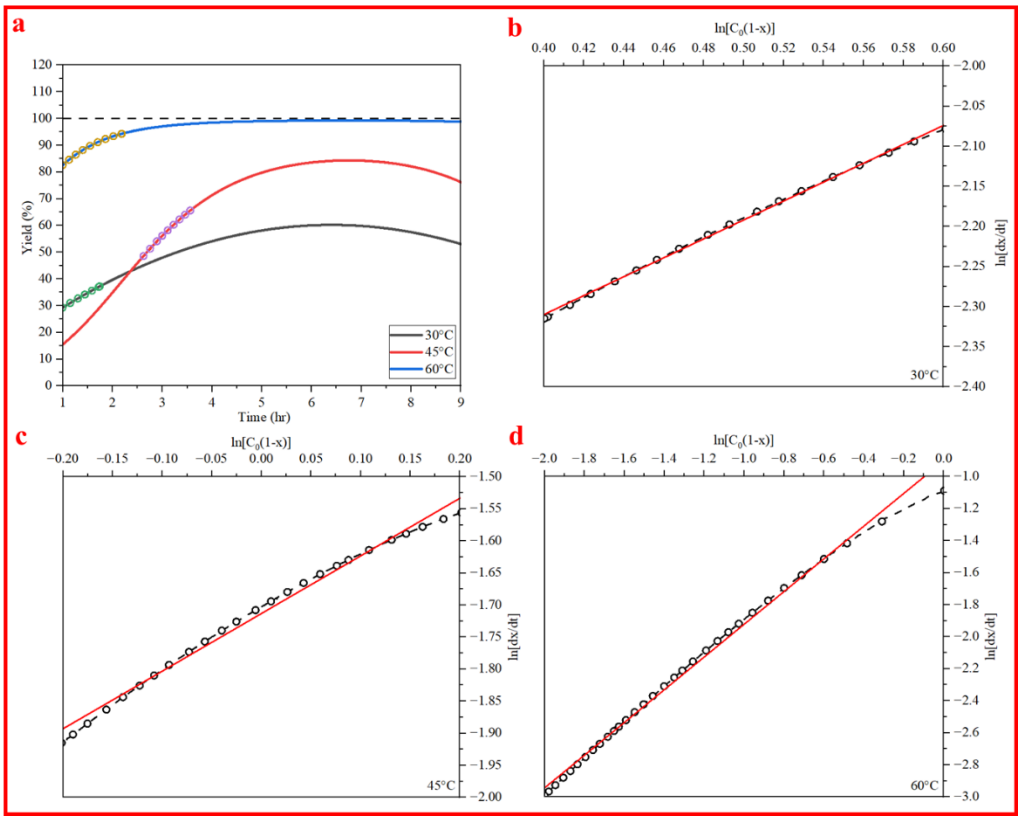

Figure 6.5 - Predicted Methyl Oleate Yield vs. Time (a),
Rate Equation Fitting at 30 °C, 45 °C and 60 °C (b-d)

Table 6.4 - Kinetic Parameters of 0.55M-TiFeSi via Log Linear Fitting

Temperature (°C)	Order (Gradient)	ln[$K_{average}$] (Intercept)	Linear Fit R^2	$K_{average}$ (hr^{-1})	K_{max} (hr^{-1})
30	1.18	-2.78	0.999	0.062	0.069
45	0.90	-1.71	0.991	0.180	0.183
60	1.02	-0.90	0.996	0.406	0.411

Average rate constant was determined from intercept of linearised plots, whereas maximum instantaneous reaction rate was used to determine maximum value of rate constant. Trend of rate constant with temperature facilitated calculation of activation energy via Arrhenius equation, while thermodynamic parameters were obtained via Eyring-Polanyi equation as detailed in Chapter 3.5.4. Arrhenius and Eyring-Polanyi plots for 0.55M-TiFeSi are given in Figure 6.6 with results summarised in Table 6.5. Both plots showed high degree of fitting with R^2 of 0.997.

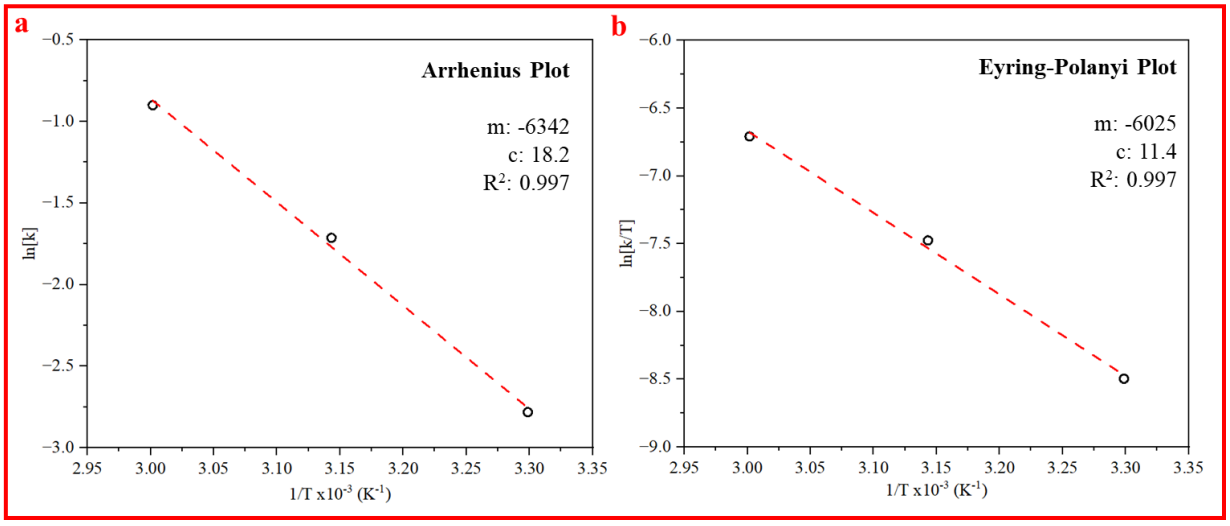

Figure 6.6 - Arrhenius (a) and Eyring-Polanyi (b) plots for 0.55M-TiFeSi

Table 6.5 - Thermodynamic and Kinetic Parameters for 0.55M-TiFeSi at 60 °C

Parameter	Value	Unit
$K_{average}$	0.406	hr^{-1}
A	7.76×10^7	hr^{-1}
E_a	52.7	kJ/mol
TON	29.8	-
TOF	4.42	hr^{-1}
$\Delta H^{\ddagger}$	50.1	kJ/mol
$\Delta S^{\ddagger}$	-0.54	kJ/mol·K
$\Delta G^{\ddagger}$ at 60 °C	231	kJ/mol

An activation energy of 52.7 kJ/mol for esterification of oleic acid in methanol with 0.55M-TiFeSi nanocatalyst is within 30-80 kJ/mol range typically reported in literature, as summarised in Table 2.18 in Chapter 2.5.1, indicating no unexpected impediment to catalysing reaction. Turnover number at optimum conditions was determined to be 29.8 with a turnover frequency of 4.42 hr^{-1} at moderate reaction temperature of 60 °C. While this is below typical range of TOF for general industrial use, results are in similar range to other catalysts for biodiesel production [619, 620]. Activation enthalpy change of +50.1 kJ/mol confirms oleic acid esterification with 0.55M-TiFeSi nanocatalyst is endothermic in nature. Predicted activation energy is slightly greater than activation enthalpy change, however both confirm an initial energy barrier in forming the transition intermediate on catalyst surface. Slight decrease in entropy of -0.54 kJ/mol·K is observed as predicted from increased order of methyl oleate transition intermediate as compared to free oleic acid and methanol molecules. Overall Gibbs energy change of +231 kJ/mol indicates a highly non-spontaneous reaction due to both decreasing entropy and endothermic nature of transition methyl oleate formation. Results strongly reconfirmed the need for maximum temperature setpoint of 60 °C as both kinetically as well as thermodynamically most favourable reaction condition.

6.3 Feedstock Degradation Study

Prior to performing two-step batch biodiesel production trials of real UCO feedstocks with optimum 0.55M-TiFeSi catalyst, it was important to quantify the extent of degradation such food oils may exhibit after frying and during storage. A previous container of UCO used in prior work by Gardy et al. [145] dated May 2018 was available for use in this project, alongside recently disposed UCO that was collected in November 2022 from same source restaurant. These feedstocks are denoted as "fresh UCO" (November 2022) and "degraded UCO" (May 2018) respectively. Ideally, a degradation study would sample at periodic time intervals from the same UCO batch, observing how key property changes occur as a function of storage time. Since fresh and degraded UCO samples may differ due to batch variability or use different vegetable sources with dissimilar glyceride profiles, direct comparison between feedstocks is difficult. However, after several years of ambient storage it might be expected that significant deterioration in feedstock quality had occurred, leading to noticeable impact on biodiesel yield achievable. Therefore, both UCO samples were characterised and explored for two step biodiesel production. Store bought vegetable oil was also used as reference to confirm FFA impurities led to loss of one step KOH reaction performance.

6.3.1 Visual Properties

Figure 6.7 shows the notable difference in colour between fresh unused vegetable oil and post frying oil, likely caused by hydrolysis, oxidation, and polymerization degradation pathways [621, 622]. From the increased darkening of degraded UCO as compared to fresh UCO, it is clear that degradation continues (albeit likely at a slower rate) even when stored under ambient conditions. From just visual observation it was predicted that degraded oil had increased FFA% as glycerides continued to undergo hydrolysis converting into FFA and darkening coloration [623].

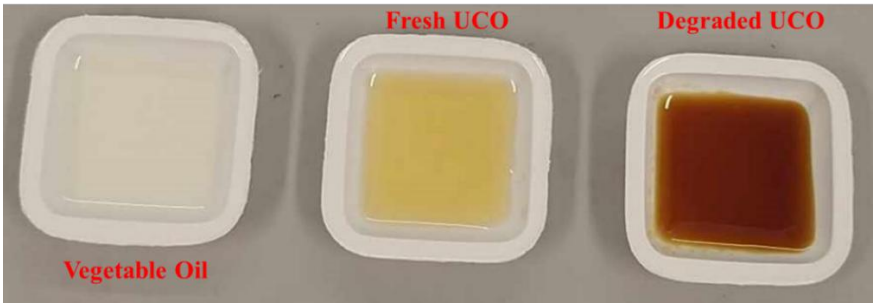

Figure 6.7 – Visual Comparison between Feedstock Oils

6.3.2 Titrations

Results of titrations are summarised in Table 6.6 for both fresh and degraded UCO samples. Saponification value increased from 180 mgKOH/g for fresh UCO to 200 mgKOH/g for degraded oil which may be explained by increasing FFA content over time as previously observed in literature [624, 625]. This was also noted with increase in Acid Value from 7.3 mgKOH/g for fresh UCO to 12 mgKOH/g for degraded UCO. Overall FFA% increased 3.7% to 5.9% between fresh and degraded UCO, with both samples being above the recommended <2% FFA limit for efficient conversion to biodiesel with base catalysed route [626]. This increase in FFA content and hence glycerol formation was also confirmed by variation in average molecular weight from 980 $g \cdot mol^{-1}$ to 880 $g \cdot mol^{-1}$ between fresh and degraded UCO feedstocks and these values of molecular weight were subsequently used in determining catalyst loading wt% and alcohol to oil molar ratios in Chapter 6.4. Dispersion of 100 µL UCO into 5 mL deionised water gave pH values of 6.52 and 5.61 for fresh and degraded UCO respectively, confirming the increasingly acidic nature of degraded UCO. A reference sample of vegetable oil had no notable change in pH value compared to deionised water, indicative of no FFA impurity. Specific gravity of fresh UCO was found to be 0.959 and slightly below unity as expected for food oil, a decrease to 0.908 for degraded UCO agreed with lower molecular weight as dense glycerides hydrolysed into FFA and glycerol impurities.

Table 6.6 - Summary of Titration Analysis of Fresh and Degraded UCO

Property	Unit	Fresh UCO	Degraded UCO
Saponification Value (SV)	mgKOH/g	180 ± 5.6	200 ± 5.5
Acid Value (AV)	mgKOH/g	7.3 ± 1.2	12 ± 1.1
Molecular Weight	$g \cdot mol^{-1}$	980 ± 39	880 ± 31
FFA%	% (Oleic)	3.7 ± 0.6	5.9 ± 0.6
Acidity (pH)	-	6.52 ± 0.05	5.61 ± 0.05
Specific Gravity	-	0.959 ± 0.001	0.908 ± 0.001

6.3.3 Thermal Analysis

While it may have been expected that level of water impurity should increase over extended storage of degraded UCO under ambient conditions, no observable difference between fresh and degraded feedstocks upon heating was seen in TGA analysis below 200 °C. A maximum mass loss of ~4% from ambient to 200 °C for both fresh and degraded UCO could be attributed to loss of adsorbed gases, volatiles and residual moisture. To more thoroughly quantify if moisture content increased over several years of storage, it is recommended to perform Karl-Fischer titration, unfortunately reagents for this test were unavailable during this project timeline.

Additional thermal analysis was performed using Stanhope-Seta Flashpoint analyser. It was expected that flashpoint should decrease as bulkier glyceride structures degraded over time leading to more volatile FFA present in the degraded UCO. Tests were performed in triplicate and average flashpoint for fresh and degraded UCO was found to be 184 °C and 172 °C respectively. This agrees with initial hypothesis and suggests degradation of glycerides into FFA likely occurred.

6.3.4 Chromatographic and Spectroscopic Analysis

GPC was performed on vegetable oil, fresh and degraded UCO to determine if average molecular weight was reduced in degraded sample as suggested from titration results. Although no suitable internal standard was available to correlate retention times to molecular weight, a qualitative analysis was still possible to perform, and these results are shown in Figure 6.8. Major peak for vegetable oil and fresh UCO had retention times of 8.77 min and 8.75 min respectively, whereas major peak for degraded UCO had retention time of 9.19 min. Increased retention time observed in degraded UCO confirms presence of molecules of smaller size and lower molecular weight as compared to fresh UCO and suggests degradation of larger glycerides into smaller FFA molecules. Fresh UCO however had similar average molecular size to unused vegetable oil, with minor peak at 8.10 min likely due to polymerisation reactions that occurred during frying. Even these minor polymerised molecules likely degraded during storage with shift of minor peak in degraded UCO up to 8.49 min. Detectable amounts of smaller volatile molecules as noted in other work [627] were seen in fresh UCO at retention time of 9.94 min. Lack of such signal in degraded UCO may be due to either continued degradation or evaporation of similar volatile species during storage. Results of GPC agree with titration and thermal analysis results.

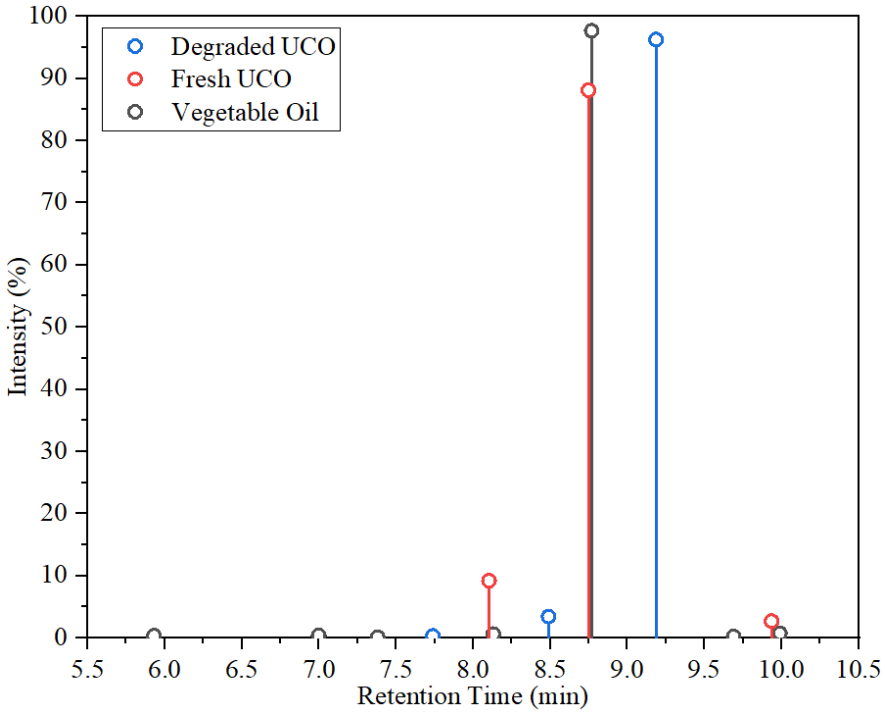

Figure 6.8 – GPC Chromatogram for Vegetable Oil, Fresh UCO and Degraded UCO Feedstocks

GCMS analysis was then subsequently performed to determine nature of chemical species present in vegetable oil, fresh and degraded UCO. GCMS spectra for Vegetable Oil and fresh UCO displayed no peaks other than C19 methyl nonadecanoate standard, whereas spectrum for degraded oil as shown in Figure 6.9 indicates presence of FAME components likely to be C18:0 methyl palmitate (16.9 min, 270.5 $g \cdot mol^{-1}$), C18:2 methyl linoleate (19.3 min, 294.5 $g \cdot mol^{-1}$) and C18:1 methyl oleate (19.5 min, 296.5 $g \cdot mol^{-1}$). Estimated FAME yield was calculated to be 4.06% and likely caused by degradation pathways that produced alcoholic species which facilitated slight thermal esterification during storage. To confirm that esterification of FFA to methyl ester compounds had indeed occurred, NMR spectroscopy was also performed with results given in Figure 6.10 for Oleic acid, C19 internal standard, vegetable oil, fresh and degraded UCO feedstock. Sharp singlet peak at 3.66 ppm in C19 internal standard spectrum corresponding to methyl ester proton was seen to only be present in degraded UCO feedstock at a value of 3.60 ppm. All other peaks observed corresponded to protons on aliphatic carbon chains of either glyceride or FFA structures. This agrees with GCMS results that methyl ester could only be detected in degraded UCO sample and confirms slight esterification had taken place in storage.

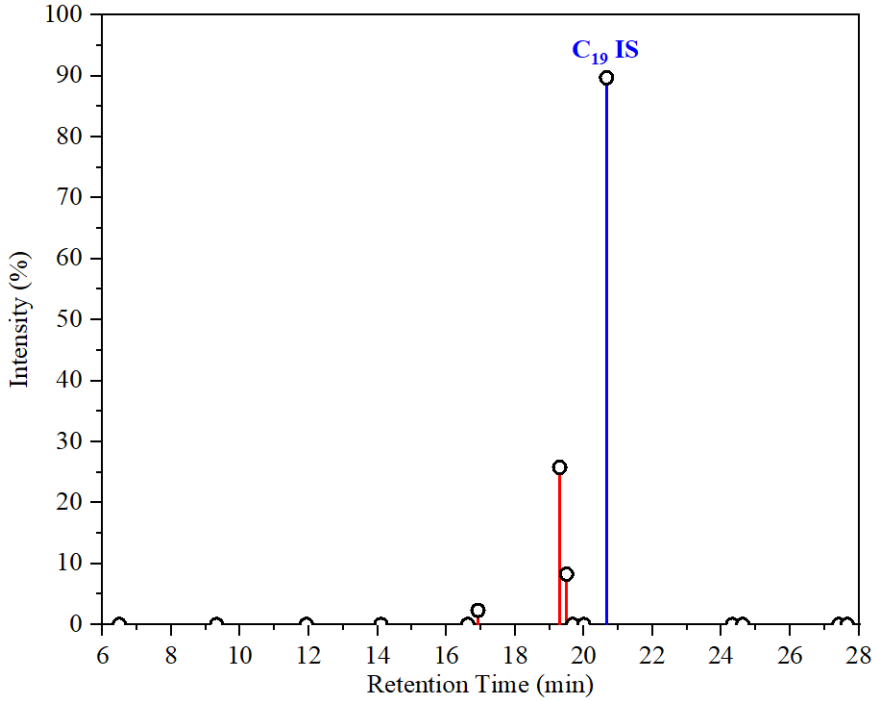

Figure 6.9 – GCMS Chromatogram of Degraded UCO with C19 Internal Standard

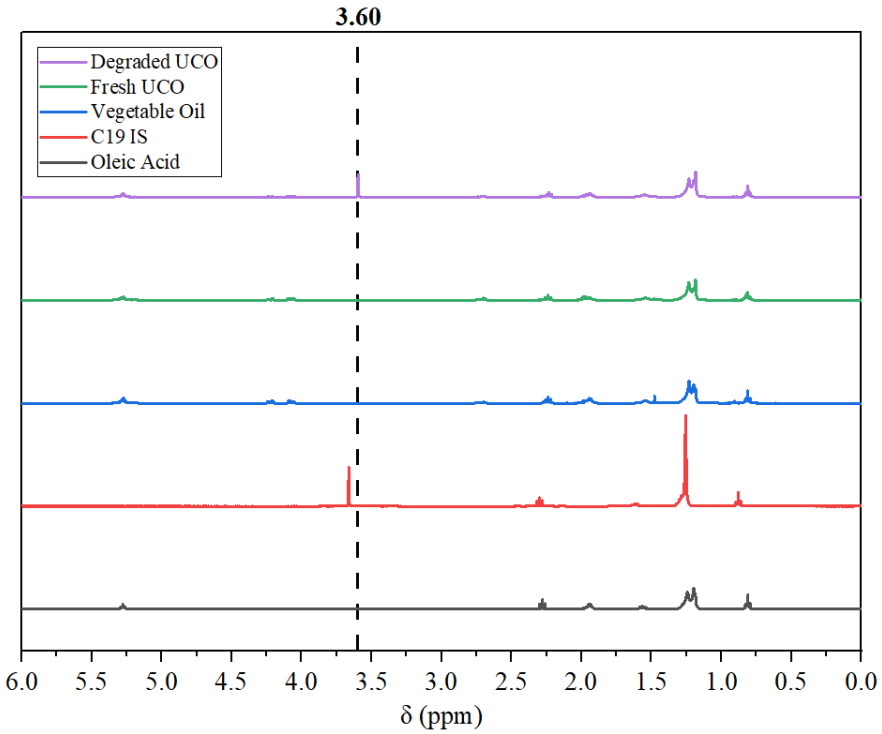

Figure 6.10 – NMR Spectra for Model and Real Feedstocks

Since GC-MS spectrum of vegetable oil and fresh UCO had no observable peaks except C19 IS, a derivatisation reaction was performed using 3 wt% KOH at 60 °C for 1 hour and 10:1 methanol to oil ratio to convert glycerides into detectable FAME content. Results are summarised in Table 6.7 along with average molecular weight assuming FAME composition is an accurate representation of actual triglyceride composition. For all feedstocks the average carbon chain length is around 18 with composition predominantly a mixture of C18:1 methyl oleate and C18:2 methyl linoleate fatty esters. For degraded oil sample, average molecular weight determined by titration agrees closely with value obtained via GC-MS, however for fresh oil GC-MS predicts a lower value of 881 g/mol. GPC result indicates presence of polymerised high molecular weight impurity found in fresh UCO sample and upcoming rheology measurements in Chapter 6.3.5 confirms fresh UCO is most viscous sample suggesting higher molecular weight, also in agreement with higher specific gravity measurement. Since it is likely that bulky impurities were too non-volatile to be detected via the applied GC-MS method, a value of 980 g/mol was chosen for calculating fresh UCO reaction conditions in agreement with titration, GPC and rheology results.

Table 6.7 - Glyceride Composition Determined by GC-MS and KOH Derivatization

FAME	Structure	MW (g/mol)	RT (min)	Composition (wt%)		
				Vegetable Oil	Fresh UCO	Degraded UCO
Methyl Tetradecanoate	C14:0	242.4	11.7	0.04	0.09	0.47
Methyl Palmitate	C16:0	270.5	13.8	3.95	9.22	12.0
Methyl Palmitoleate	C16:1	268.4	13.5	0.19	0.09	0.56
Methyl Stearate	C18:0	298.5	16.3	1.74	2.79	4.10
Methyl Oleate	C18:1	296.5	16.0	76.6	41.5	60.6
Methyl Linoleate	C18:2	294.5	15.8	15.9	45.0	21.2
Methyl Linolenate	C18:3	292.5	16.1	0.91	0.44	0.62
Methyl Arachidate	C20:0	326.6	20.9	0.44	0.29	0.33
Methyl Behenate	C22:0	354.6	27.0	0.20	0.26	0.20
Other Components				0.03	0.32	< 0.01
Average MW (g/mol)				886	881	878

6.3.5 Rheology

While performing visual inspection of fresh and degraded UCO it was readily apparent that a change in viscosity had occurred during storage, since degraded UCO presented notably less flow resistance when transferring via pipette. A change in viscosity could lead to differences in reaction performance, both by enabling more effective mass transfer during reaction and influencing catalyst recovery post reaction. Agitation speed could not be accurately controlled during small scale batch trials and was hence kept at constant 500 rpm setting throughout this work. No notable settling out of nanocatalyst material was observed during reactions and no formation of liquid-liquid layer between methanol and oil was seen, therefore impact of viscosity-limited mass transfer was estimated to be less significant than studied factors of reaction time, temperature, catalyst loading and alcohol to oil ratio. Nevertheless, it was deemed desirable to analytically quantify the extent of viscosity change that occurred during storage.

Rheological studies of vegetable oil, fresh and degraded UCO was performed using RheoPlus MCR301 setup at batch trial reaction temperatures of 30 °C, 45 °C and 60 °C. Results are provided in Table 6.8 and confirms observation that degraded UCO had reduced viscosity after extended time in ambient storage. This could be explained by breakdown of bulky glyceride structures into smaller FFA molecules as discussed in prior titration and GPC results. Viscosity increased slightly from unused cooking oil to fresh UCO which is likely due to slight polymerisation reactions that occurred during frying. These bulkier molecules were noted in GPC results previously. For all feedstocks a reduction in viscosity was observed with increasing temperature as should be expected, therefore reaction at higher temperatures should be expected to enhance both kinetics and mass transfer within oil phase.

Table 6.8 - Dynamic Viscosity of Feedstock Oils

Temperature (°C)	Dynamic Viscosity (mPa·s)		
	Vegetable Oil	Fresh UCO	Degraded UCO
30	45.9	58.2	18.3
45	27.7	33.8	11.8
60	18.1	21.5	8.2

Flow curves for vegetable oil, fresh and degraded UCO are plotted in Figure 6.11a-c and display typical linear profile as expected from Newtonian fluids. Gradient of the plots represent the constant values of viscosity as provided in Table 6.8 with notable influence of temperature. Viscometry results hence agree with GPC and titration findings of less bulky species present in degraded UCO leading to lower average molecular weight and reduction in viscosity.

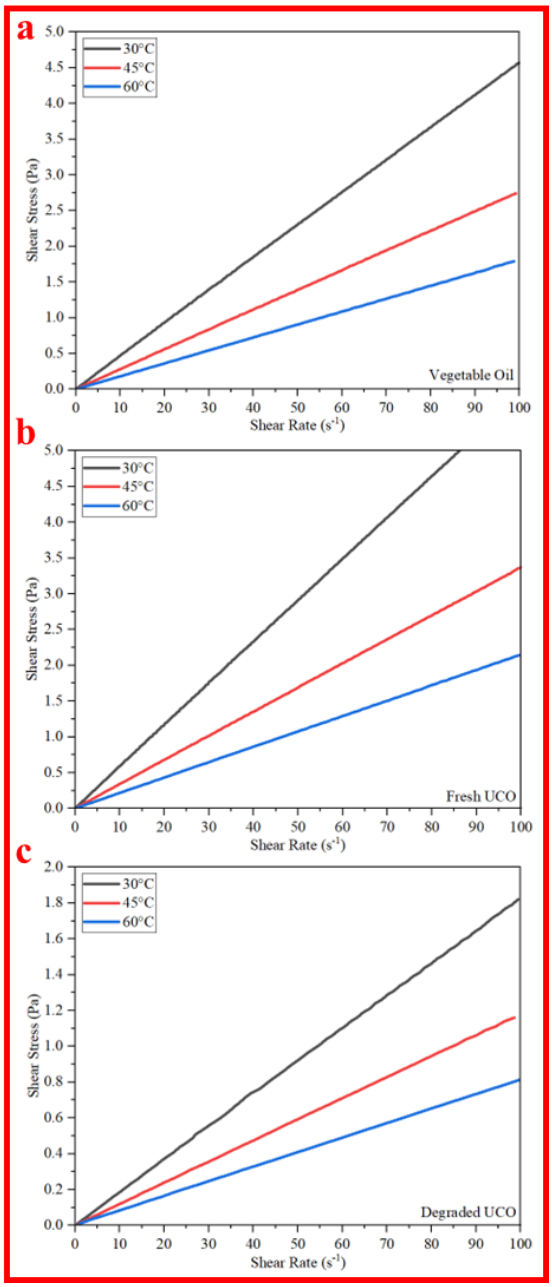

Figure 6.11 - Flow Curves for Vegetable Oil (a), Fresh (b) and Degraded (c) UCO

6.4 Two-Step Batch Trials

6.4.1 Design of Experiments Approach

In order to determine performance of 0.55M-TiFeSi catalyst in two-step batch biodiesel production using real UCO feedstocks, it was first necessary to optimise the second reaction step performed with KOH catalyst. Due to time and material constraints on how many experimental trials could be ran and with desire to identify most dominant factors, the same 10 run DoE screening design as used in Chapter 5.4 was utilised and is reproduced in Table 6.9 for reference. Instead of oleic acid as model feedstock for esterification pathway, now pure vegetable oil was used as model feedstock for transesterification pathway using KOH as catalyst.

Table 6.9 - Custom 10 Run DoE Transesterification Study

Run	Time (hr)	Temperature (°C)	Catalyst Loading (wt%)	Alcohol : Oil Ratio	Randomised Run Order
A1, A2	1	30	3	4	2, 12
B1, B2	5	60	1	4	1, 16
C1, C2	1	60	5	16	10, 13
D1, D2	1	45	1	10	6, 18
E1, E2	5	45	3	16	4, 17
F1, F2	5	30	5	10	9, 19
G1, G2	9	60	3	10	7, 14
H1, H2	9	45	5	4	3, 20
I1, I2	9	30	1	16	8, 15
J1, J2	5	45	3	10	5, 11

6.4.2 Optimisation of Transesterification Step

6.4.2.1 Effect Screening

Results of model batch transesterification trials with KOH catalyst and vegetable oil is shown in Table 6.10 with approximately ~100% yield achieved in reactions A, D and F. Effect screening results are provided in Table 6.11 and Figure 6.12 and suggest reaction temperature, catalyst loading and non-linear effects of alcohol to oil ratio are the most significant model parameters. Reaction time is surprisingly not observed to be significant unlike in all esterification trials, this is potentially due to very high reaction rate of a homogeneous base catalyst such as KOH. Reaction temperature was found to be inversely proportional to yield. This indicates that transesterification was not kinetically hindered by low 30 °C reaction temperature, but instead saponification and other unwanted side reactions may become more dominating at increased temperature leading to loss of yield. Excess addition of KOH lead to worsening yield which agrees with literature studies on KOH [628] where catalyst loads ~1 wt% or lower have been found most optimal. This could be due to increased favourability for saponification or increased viscosity of reactants with greater catalyst loading. Initial trial results with vegetable oil feedstock suggested a ~100% FAME yield was certainly achievable with current experimental setup and KOH catalyst. Nonlinear optimisation of the obtained model and model validation was subsequently performed to determine best factor setpoints for the transesterification step.

Table 6.10 - FAME Yields for KOH Model Transesterification Trials

Run	FAME Yield (%)		Average Yield (%)
	Reaction 1	Reaction 2	
A	**~100**	**~100**	**~100**
B	85.2	81.5	83.3
C	60.2	58.5	59.3
D	**~100**	**~100**	**~100**
E	80.9	80.2	80.5
F	**~100**	**~100**	**~100**
G	83.5	88.2	85.9
H	63.3	62.4	62.8
I	84.6	83.6	84.1
J	86.6	86.1	86.4

Table 6.11 – Effect Screening for KOH Model Transesterification Trials

Effect	Scaled Estimate	Log Worth	P Value (%)	Bayes Posterior Probability (%)	t Ratio	f Ratio	Comment
Time	-4.39	2.13	0.75	15.3	-3.27	10.7	Insignificant
Temperature	-9.23	4.57	<0.01	73.4	-6.87	47.2	**Significant**
Catalyst Loading	-7.54	3.80	0.02	57.1	-5.61	31.5	**Significant**
Alcohol Ratio	-3.68	1.72	1.92	9.25	-2.74	7.52	Insignificant
Time^2	-3.48	0.85	14.1	8.17	-1.59	2.52	Insignificant
Temperature^2	6.77	1.98	1.04	4.40	3.08	9.52	Insignificant
Catalyst Loading^2	-4.73	1.27	5.39	11.9	-2.16	4.66	Insignificant
Alcohol Ratio^2	-14.4	4.39	<0.01	70.0	-6.57	43.1	**Significant**

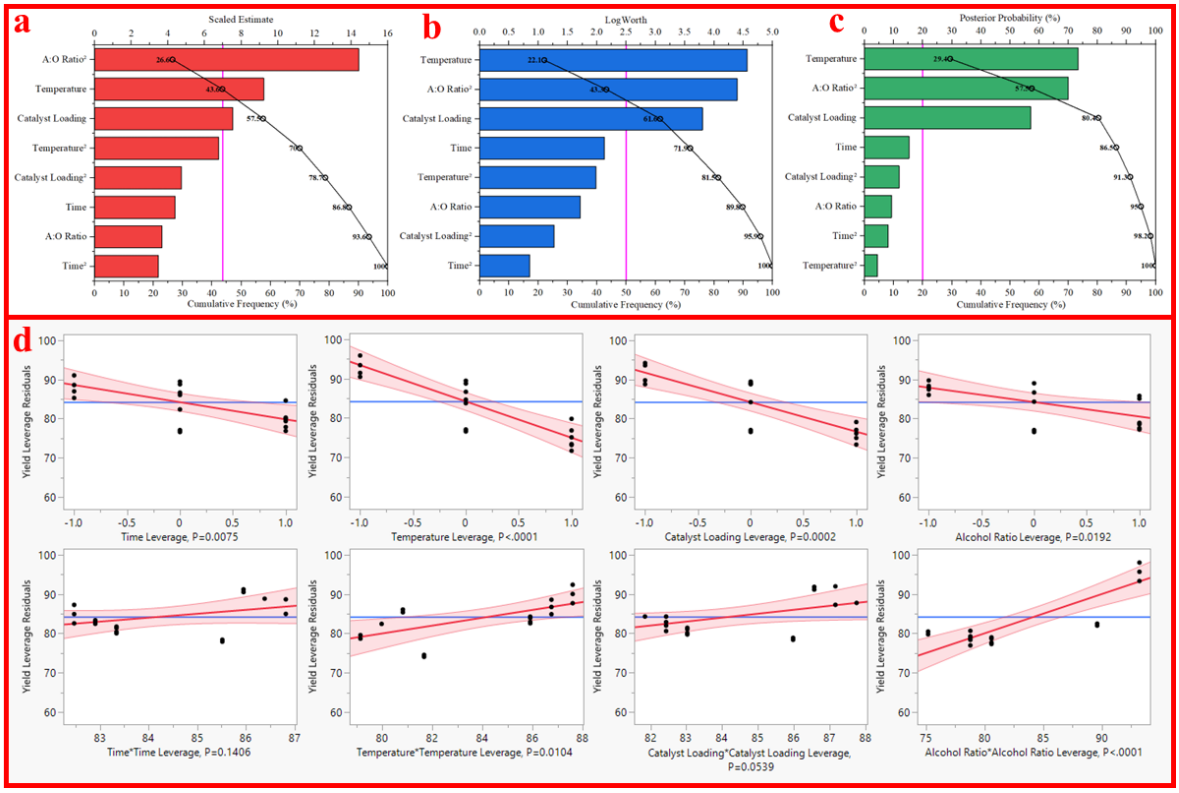

Figure 6.12 – Effect Screening Plots for KOH Model Transesterification Trials

6.4.2.2 Model Optimisation

Analysis of Variance testing was performed on the obtained quadratic model and post-logistic fitting model with results presented in Table 6.12. A confirmed high degree of statistical significance ($p < 0.01\%$) was observed in both optimisation models, with error predominantly due to lack of fit over random noise. Lack of fitting errors can be seen in Figure 6.13 for quadratic (a) and logistic (b) models via actual by predicted plots and is likely due to significant interaction effects that were unable to be modelled due to restrictions on number of runs performable within research timeframe and material constraints. Fortunately, no outliers beyond 95% confidence interval were observed from studentised residuals plots hence provided that modelling error fell within approximate ±5% experimental error a reasonable optimum setpoint could be predicted using data from all 20 batch transesterification reactions.

Table 6.12 - Analysis of Variance for KOH and Vegetable Oil Custom DOE Models

Model	Sum of Squares			Mean Square		f Ratio
	Model (DF: 8)	Error (DF: 11)	Corrected Total (DF: 19)	Model	Error	
Quadratic	3451	238	3689	431	21.7	19.9
Logistic	122	13.3	136	15.3	1.21	12.6

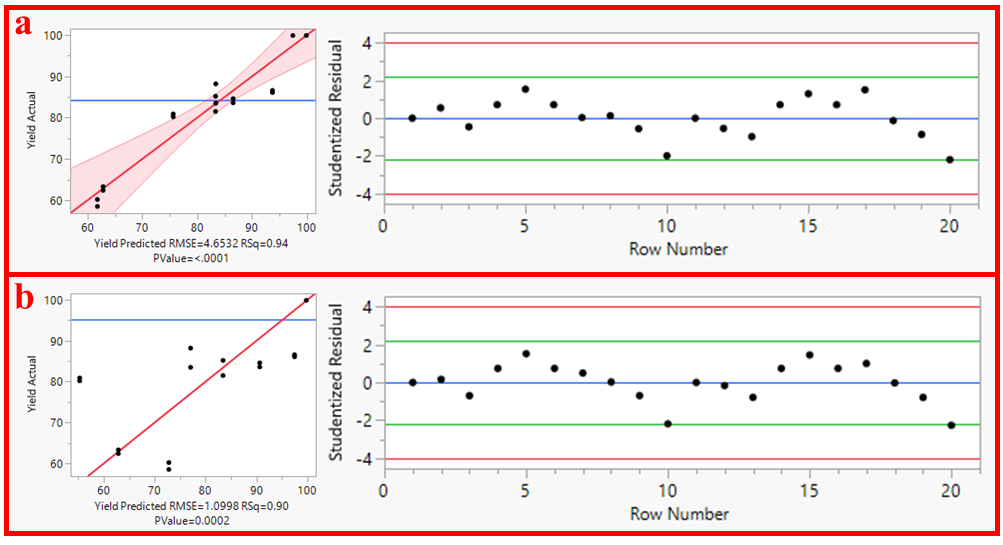

Figure 6.13 - Actual by Predicted and Studentised Residual Plots for KOH and Vegetable Oil

Response surface profile plots of KOH and vegetable oil transesterification for quadratic (a) and logistic (b) fitted models are provided in Figure 6.14 and suggest that optimum setpoint occurs for a minimum value of reaction time, reaction temperature and catalyst loading while alcohol to oil ratio should be slightly below centre of design space. Optimum settings and predicted yields are summarised in Table 6.13. For quadratic model a maximum yield of 114% was observed suggesting lack of fit at maximum yield values whereas logistic fitting gives slightly lower bounds for all factor settings. Since quadratic model only predicted a difference in yield of ~0.6% between the two different setpoints, reaction conditions of 1 hour at 30 °C, 1 wt% catalyst loading and ~9:1 ratio of methanol to vegetable oil loading were selected for transesterification step. Two experimental validation reactions gave average yield of 95.3% confirming model predicted optimum was within experimental error. Impact of FFA loading on yield was next to be explored.

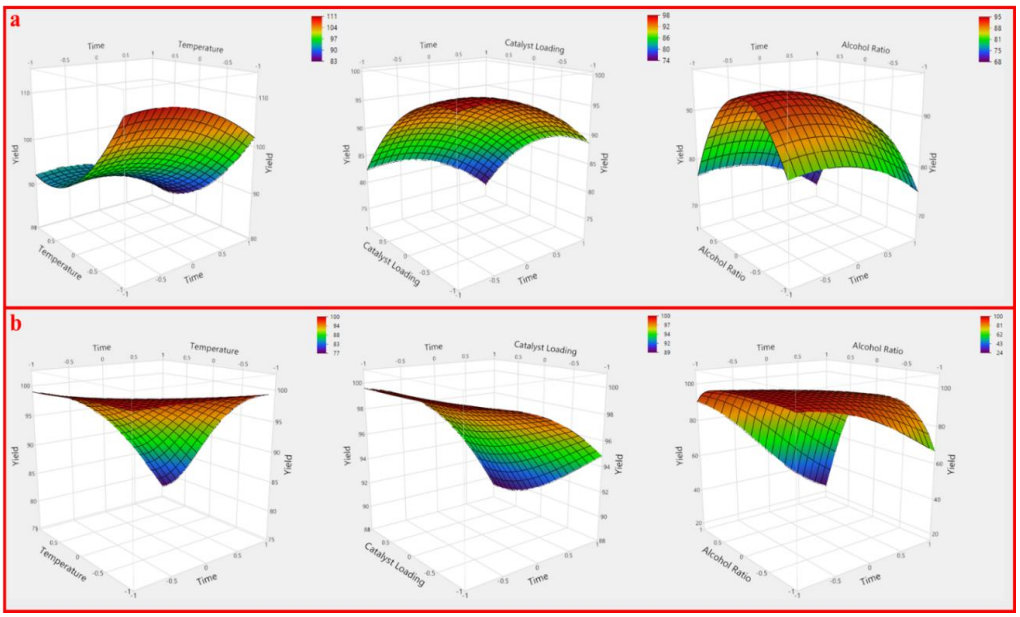

Figure 6.14 - Response Surface Plots for KOH and Vegetable Oil
with Quadratic (a) and Logistic (b) Fitting Models

Table 6.13 - Optimum Factor Settings for KOH and Vegetable Oil Transesterification

Model	Time (hr)	Temperature (°C)	Catalyst Loading (wt%)	Alcohol : Oil Ratio	Predicted Yield (%)
Quadratic	2.48	30.0	1.41	9.23	~100
Logistic	1.00	30.0	1.00	8.89	~100

6.4.3 Impact of FFA Loading

In order to explore how FFA% impacts transesterification step, vegetable oil was spiked with 75% oleic acid feedstock used in esterification trials. Resultant contaminated oil was treated with KOH under optimum reaction condition discussed prior in Chapter 6.4.2.2 and results of these trials are presented in Table 6.14. Only minor loss of yield was observed up to 2% FFA with obtained yield slightly below experimental error range. Sudden complete loss of reactivity was observed upon FFA% greater than 3% with visible saponification observed as depicted in Figure 6.15 by a white soapy gel that formed upon addition of completely dissolved methanolic KOH solution. This agrees with literature on the necessity to keep FFA% < 2% to prevent base deactivation [626].

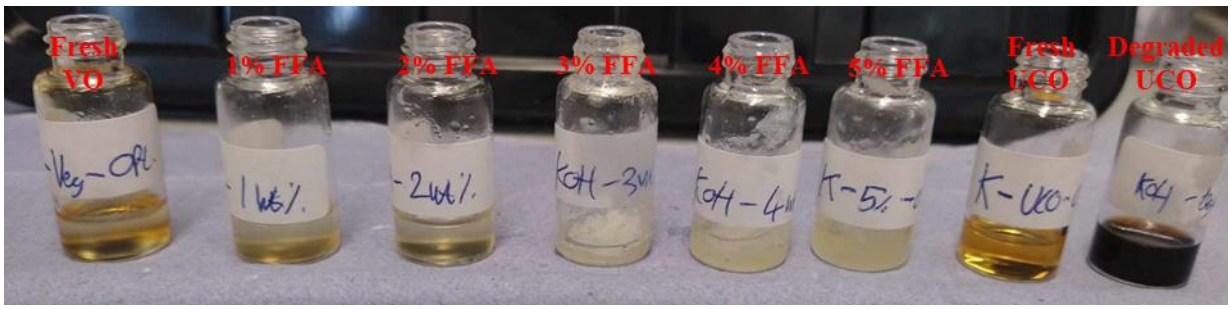

Figure 6.15 - Visual Effects of FFA% on Transesterification Step

Interestingly, upon testing with fresh UCO (~3.7% FFA) and degraded UCO (~5.9% FFA) an average yield of 57.8% and 47.8% was observed despite both feedstocks being above 2% FFA limit. This indicates that unlike model contaminated vegetable oil where reaction dramatically ceases, for a real feedstock transesterification is hindered but not completely prevented by saponification. As illustrated qualitatively in Figure 6.16, FAME yield is more likely to decrease exponentially as FFA% increases, with a logistic fit from observed results providing a more accurate model as compared to a dramatic step-change. It was hence clear that to explore a two-step reaction pathway a used cooking oil sample would be required over model vegetable oil feedstock spiked with oleic acid impurity. Both fresh and degraded UCO samples characterised previously in Chapter 6.3 were therefore utilised in a two-step reaction scheme whereby 0.55M-TiFeSi would lower the FFA% via esterification prior to KOH transesterification.

Table 6.14 - Effect of FFA% on One Step KOH Transesterification

Sample	FAME Yield (%)		Average Yield (%)
	Reaction 1	Reaction 2	
Fresh Vegetable Oil (VO)	**93.9**	**96.8**	**95.3**
1 wt% FFA VO	~100	89.0	96.1
2 wt% FFA VO	96.4	83.6	90.0
3 wt% FFA VO	0.45	0.43	0.44
Fresh UCO (~3.7 wt% FFA)	**58.0**	**57.7**	**57.8**
4 wt% FFA VO	0.56	0.59	0.58
5 wt% FFA VO	1.14	1.33	1.24
Degraded UCO (~5.9 wt% FFA)	**47.3**	**48.2**	**47.8**
10 wt% FFA VO	0.89	1.30	1.10
15 wt% FFA VO	0.72	1.24	0.98
20 wt% FFA VO	0.67	1.15	0.91
Oleic Acid (75 wt% FFA)	0.51	0.34	0.42

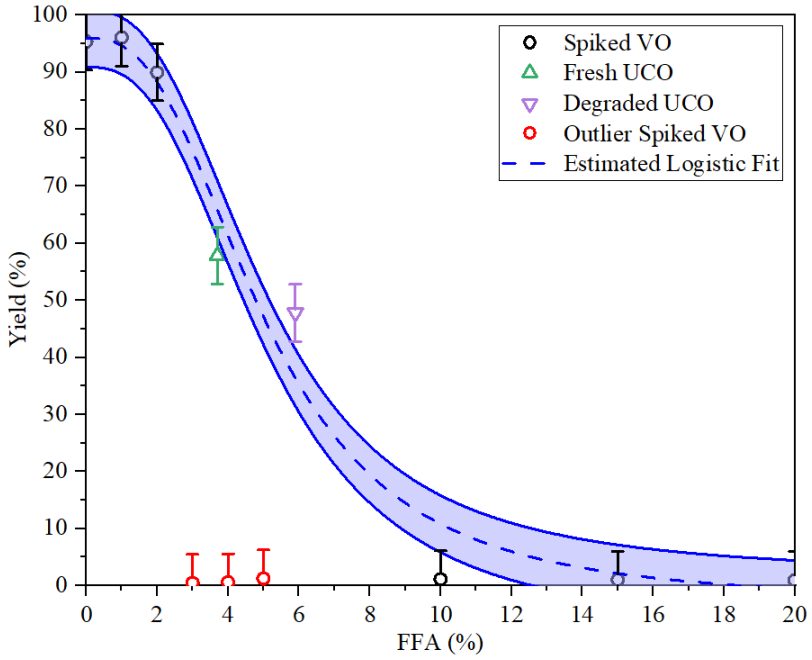

Figure 6.16 - Effect of FFA% on KOH Transesterification Performance

6.4.4 Two Step Pathway with Real Feedstock

Two step reaction was performed using 0.55M-TiFeSi for esterification step (6.75 hr, 60 °C, 3.19 wt%, 16:1) followed by KOH for transesterification step (1 hr, 30 °C, 1 wt%, 9:1) at optimum reaction conditions obtained as previously discussed. As described earlier in Chapter 3.5.1, after each reaction the stopper and cap were removed before rapid flash heating at 75 °C to remove all methanol and halt further reaction or potential back-reaction during storage. Post first reaction step, the reaction vial was left to stand overnight at ambient conditions to gravitationally separate solid nanocatalyst and glycerol layers at bottom and methyl ester layer towards the top. Top layer was isolated into a new 5 mL vial for yield determination via GC-MS and for use in the second transesterification reaction step respectively. Post second reaction step, similar overnight gravitational separation was performed at ambient conditions to separate bottom glycerol layer from upper methyl ester layer. Top layer was again isolated into a new vial, washed with deionised water until washings were unable to detect KOH via phenolphthalein indicator, and dried at 100 °C overnight prior to yield determination via GC-MS. Recovery and recycling of used nanocatalyst is discussed further in Chapter 6.4.5. Results for fresh and degraded UCO feedstock are presented in **Error! Reference source not found.** with comparison between one-step KOH route and two-step approach.

Table 6.15 - Two Step Pathway via 0.55M-TiFeSi Esterification and KOH Transesterification

Feedstock	Treatment	Esterification Step FAME yield (%)	Transesterification Step FAME yield (%)
Fresh Vegetable Oil (0% FFA)	KOH Only	-	95.3
Fresh UCO (~3.7 wt% FFA)	KOH Only	-	57.8
	0.55M-TiFeSi, KOH	1.90	73.6
Degraded UCO (~5.9 wt% FFA)	KOH Only	-	47.8
	0.55M-TiFeSi, KOH	50.8	78.4

For fresh UCO feedstock an enhancement in FAME yield of +15.8% was achieved in the two-step route, while for degraded UCO feedstock an increase of +30.6% FAME yield was obtained in the two-step route. These results strongly confirm that 0.55M-TiFeSi is successfully reducing FFA% loading in esterification step and facilitating superior KOH performance in subsequent transesterification step. More surprisingly, FAME yield measured after the initial esterification step showed that 0.55M-TiFeSi was successfully able to perform simultaneous transesterification-esterification with the degraded UCO sample. This may be due to increased breaking down of bulky triglycerides into smaller di/monoglycerides that occurs during FFA production, which 0.55M-TiFeSi can successfully catalyse despite Brønsted Acid dominated surface that favours esterification over transesterification mechanism. Alternatively, sufficiently enhanced mass transfer in less viscous degraded UCO may have contributed to improved reaction performance in initial esterification step with 0.55M-TiFeSi nanocatalyst.

While these results are reassuring, it is clear more work is required to optimise the two-step approach to increase FAME yield up towards the 95.3% achievable using KOH and vegetable oil which is currently performed at industrial scales. It may be that optimum factor setpoint found for transesterification step is suitable for vegetable oil model feedstock but not for UCO, since reduction of FFA% alone does not make UCO chemically identical to pure vegetable oil. Leftover 0.55M-TiFeSi catalyst and glycerol from esterification step may also have not been effectively removed from top layer during overnight gravitational separation, meaning improvements to the washing and separation methodology between each reaction stage could lead to improved yield.

6.4.5 Recyclability

6.4.5.1 Acid Catalyst Recycling

While the initial results after a single run appeared promising and future studies may be able to optimise yield further, it is important to develop efficient nanocatalysts that can be employed for multiple cycles to achieve industrial viability. Spent 0.55M-TiFeSi was recovered via centrifuge and washed in equal parts deionised water and n-heptane prior to vacuum oven drying overnight at 120 °C and then reweighed for use in further esterification steps with fresh and degraded UCO feedstock. Results for four reaction cycles with fresh (a) and degraded (b) UCO are illustrated in Figure 6.17 where run 0 represents the baseline performance in one-step KOH treatment. For fresh UCO, FAME yield was enhanced in the initial two-step reaction (run 1) however for subsequent runs no further improvement was noticed beyond experimental error from one-step KOH treatment. For degraded UCO, similarly after the first initial two-step reaction no further improvement in yield could be observed. Interestingly, 0.55M-TiFeSi was still successfully able to achieve similar esterification step yields throughout runs 1-4 however this did not enhance KOH transesterification performance in subsequent step. This could be due to sufficiently enhanced mass transfer in less viscous degraded UCO, or 0.55M-TiFeSi facilitating conversion of smaller mono/diglycerides or other impurities that KOH could also effectively convert into FAME products but not lowering the acidic impurities such as FFA which remain unreacted and hinder KOH in the second reaction step. No further reaction runs could be performed due to negligible recovery after run 4. FTIR analysis was performed to explore deactivation effects.

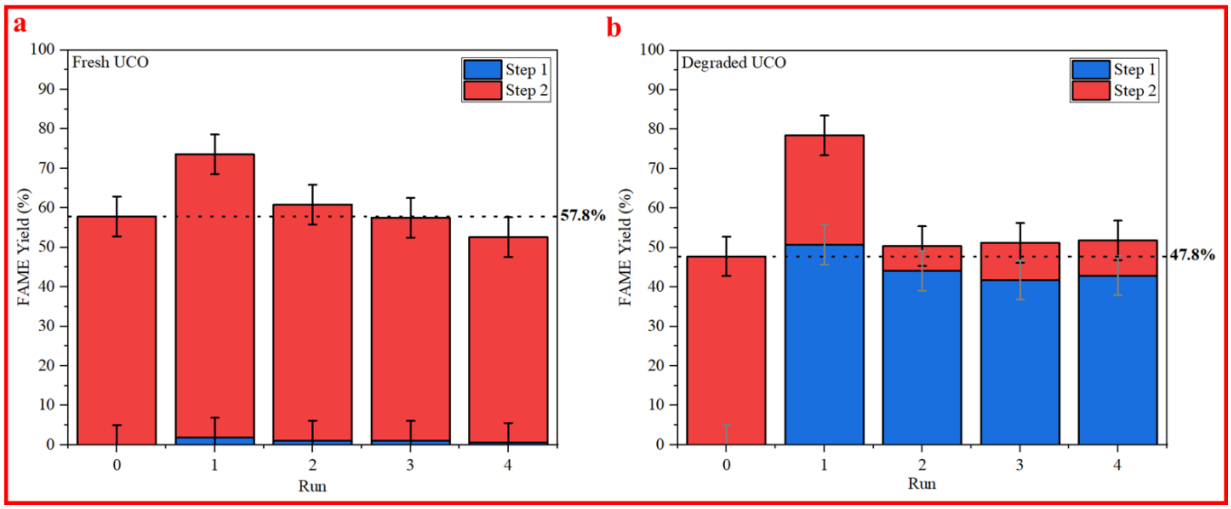

Figure 6.17 - Recyclability Studies for 0.55M-TiFeSi in Two Step Reactions

6.4.5.2 Deactivation Study

ATR-FTIR was employed to investigate changes to 0.55M-TiFeSi catalyst surface that may explain loss of activity. No new peaks could be observed in spectrum indicating that washing and drying step without recalcination was successfully able to remove oil and glyceride impurities that have been reported in literature to cause deactivation. As illustrated in Figure 6.18 however, significant loss of S-O (990 cm^{-1}, 1038 cm^{-1}) and S=O (1125 cm^{-1}, 1190 cm^{-1}) functional groups occurs on nanocatalyst surface after one reaction with both fresh and degraded UCO feedstocks. Complete loss of surface hydroxyl groups (2650-3650 cm^{-1}) and corresponding reduction in bound water (1630 cm^{-1}) was also noted. Loss of reaction performance is hence likely due to leaching of Brønsted acid sites responsible for esterification of FFA. Other studies on sulfated TiO_2 surfaces, summarised prior in Table 2.4, have reported multiple reaction cycles being achievable before acidic site loss led to loss of reactivity, utilising similar washing and drying steps as performed in this work. Further optimisation of chlorosulfonic acid functionalisation conditions, such as exploring concentrations between 0.55-1.0 M or using different functionalisation temperature or treatment durations, may lead to enhancement of sulfur loading and hence surface Brønsted acid site density and strength. Recyclability could therefore be increased by improving stability of Brønsted sites, or ensuring sufficient sites remain post initial reaction to facilitate further reactions. Future work should focus on improving surface acid stability, increasing acid site density or explore the possibility of a catalyst reacidification step to produce a truly recyclable nanocatalyst.

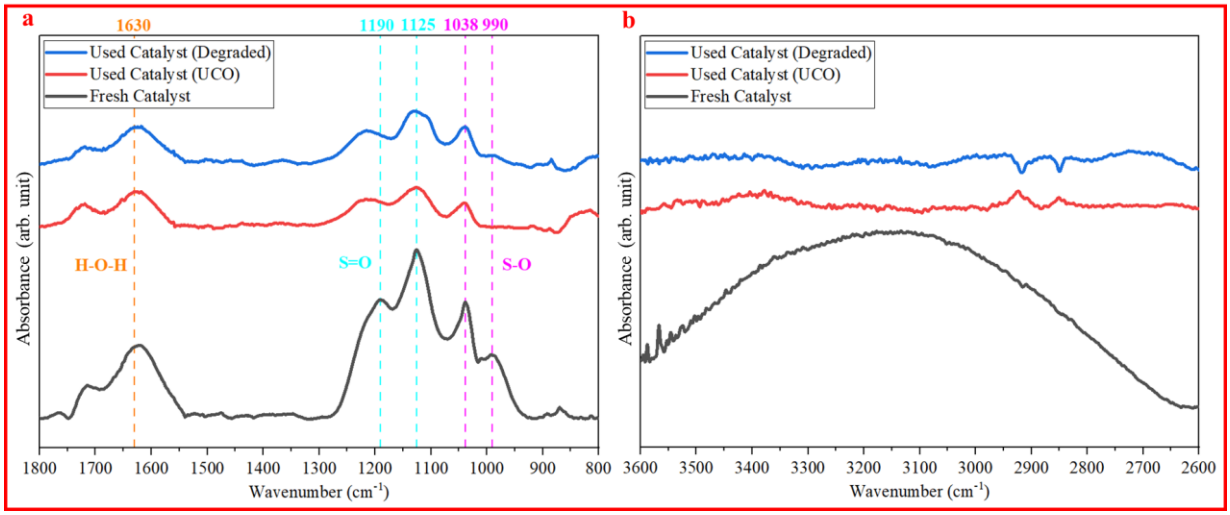

Figure 6.18 - ATR-FTIR Spectra of Fresh and Used 0.55M-TiFeSi

6.5 Summary

The focus of this Chapter has been to model and optimise the FFA esterification pathway of most optimal nanocatalyst for use in a two-step reaction pathway with real UCO feedstocks. Use of the custom screening DoE model developed and applied in Chapter 5 was found to detect impact of most significant factors on yield response to a statistically significant level via ANOVA analysis. Error was mainly due to model fit and not random noise, with no outlier datapoints identified. Developing a new optimisation model to include interaction effects, increase number of runs and maximise goodness of fit would be preferable but was out of scope of this research work. However, even with the more limited screening model obtained, the optimum reaction conditions were experimentally validated within reasonable ~5% level of error for Ti series of catalysts. Response surface diagrams enabled visualisation of methyl oleate yield throughout the design space.

For 0.1M-TiFeSi a predicted optimum of 83.4% yield at reaction conditions of 9 hours at 60 °C, 3.08 wt% catalyst loading and 13:1 methanol to oleic acid ratio was found to achieve 77.4% methyl oleate yield experimentally. For 0.55M-TiFeSi a predicted optimum of 99.3% yield at 60 °C reaction for 6.75 hours, 3.19 wt% catalyst loading and 16:1 methanol to oleic acid ratio achieved approximately 100% methyl oleate yield. Results at the end of Chapter 5 suggested that either 0.1M-TiFeSi or 0.55M-TiFeSi would be most optimal in FFA esterification and in this Chapter, it was decided that 0.55M-TiFeSi is the most superior nanocatalyst that was synthesised. This is likely due to many desirable properties of the 0.55M-TiFeSi nanocatalyst as observed throughout Chapter 4 that led to enhanced reactivity. Kinetic and thermodynamic modelling indicated that the esterification reaction of oleic acid, one of the most common FFA observed in cooking oils, with the 0.55M-TiFeSi nanocatalyst was endothermic in nature and non-spontaneous. Rate constant of 0.406 hr^{-1} at 60 °C, activation energy of 52.7 kJ/mol and TOF of 4.42 hr^{-1} was observed. Same reaction conditions as found optimal during oleic acid esterification were taken forwards into the first step treatment of real UCO feedstocks.

Two UCO feedstocks, a fresh sample obtained in November 2022 and a degraded sample stored under ambient laboratory conditions since May 2018 were available for use and were characterised to observe if degraded sample was of significantly lower quality as predicted. While exact comparison between UCO samples is challenging since one is not a direct aged version of the other, the degraded sample was noticeably of lower quality.

Evidence of increased FFA up to 5.9% and increased acidity with AV of 12, alongside evidence of FAME trace components, reduced viscosity and much darker colour indicated that oxidation, thermal esterification, hydrolysis and microbial degradation may have occurred. A sample of fresh vegetable oil was tested with KOH and optimised using custom DoE design. Again, ANOVA confirmed statistically significant effect of factors on yield response with reaction temperature, catalyst loading and nonlinearity of alcohol to oil ratio most influential. Model errors dominated random noise, and no outliers were observed in experimental runs. A maximum theoretical 100% FAME yield after 1 hour at 30 °C, 1 wt% catalyst loading and ~9:1 methanol to vegetable oil ratio was validated by 95.3% experimental result.

Influence of FFA% on KOH transesterification was experimentally confirmed to completely halt reaction after 2% oleic acid was loaded into pure vegetable oil. Interestingly, fresh UCO (3.7% FFA) and degraded UCO (5.9% FFA) samples could achieve 57.8% and 47.8% FAME yield under one step KOH transesterification indicating that while reaction performance as compared to pure vegetable oil had been hindered, it was not a sudden loss of all catalytic activity like with the spiked vegetable oil trials. Hence real feedstocks are more suitable for modelling two step reaction. Using 0.55M-TiFeSi at optimum reaction conditions found in oleic acid model (60 °C, 6.75 hours, 3.19 wt%, 16:1) as a first esterification treatment step was able to enhance KOH transesterification performance in the second transesterification step (30 °C, 1 hour, 1 wt%, 9:1). For fresh UCO an increase in FAME yield from 57.8% to 73.6% was achieved, whereas for degraded UCO an increase from 47.8% to 78.4% was achieved. Two major conclusions can be drawn from these results. Firstly, it is clear that 0.55M-TiFeSi was better able to esterify the more degraded UCO feedstock with higher FFA content. And secondly, the inability to obtain 100% FAME yield suggests the results of individual optimised reaction conditions of first and second step with model oleic acid and vegetable oil did not translate to the case of using real feedstocks. Due to different chemical nature of a UCO as compared to chemically ideal oleic acid FFA and unused vegetable oil, reaction conditions may require further reaction time, different catalyst quantities and further loading of alcohol to oil ratio to achieve superior yield.

Repeated recycles were performed and unfortunately after first successful reaction cycle, there was no observable benefit to the KOH transesterification step from performing esterification step with 0.55M-TiFeSi in fresh UCO. In degraded UCO, 0.55M-TiFeSi in first step was able to achieve similar FAME yield as use of KOH alone for multiple runs, possibly due to improved mass transfer via reduced viscosity of degraded UCO, or high degree of free glycerides and FFA that were relatively facile to catalyse into FAME, however no enhancement beyond 47.8% could be achieved. Investigation as to the cause of deactivation by ATR-FTIR confirmed that even without recalcination and only use of washing and drying step, no presence of organic impurity peak could be seen. Therefore, loss of activity by organic deposition was ruled out. Instead, reduction in sulfate S-O and S=O peaks and loss of acidic hydroxyls had occurred. While no recycling study of oleic acid esterification was performed due to preference of using remaining 0.55M-TiFeSi to study application in real UCO feedstocks, it is likely similar issues with reusability may occur from loss of sulfate sites that enhanced Brønsted acidity. Suggested future work to improve recyclability includes exploring reacidification with chlorosulfonic acid to restore sulfate sites, adjustments to functionalisation conditions or use of alternate intermediate layer to increase sulfate site stability, or adjustments to the reaction conditions in two-step route to improve initial first step performance closer to 100% FAME yield. A brief overview of the research journey is now summarised. Evidence of successful synthesis of 0.55M-TiFeSi nanocatalyst was confirmed, with Chapter 4 predicting desirable physical and chemical properties led to enhanced esterification performance. While lack of medium-strong Lewis sites likely made transesterification unfeasible at reasonable reaction conditions, initial model reaction tests in Chapter 5 highlighted 0.1M-TiFeSi and 0.55M-TiFeSi as promising candidates for further study due to strong esterification activity. In this Chapter, complete conversion of oleic acid into methyl oleate was achieved under optimised conditions and 0.55M-TiFeSi identified as the most superior nanocatalyst synthesised in this work for treating FFA impurities. For a single reaction cycle, notable improvement over one step KOH transesterification was achieved by using a two-step route where 0.55M-TiFeSi lowers FFA impurities in fresh and degraded UCO. The more impure degraded feedstock was converted with even greater success than fresh UCO sample. However, recyclability and optimisation of the two step pathway remains a challenge. Chapter 7 concludes all research work presented, answers the six research questions posed and demonstrates knowledge contributions, provides context of results to wider literature, confirms originality and suggests areas of future research opportunities.

Chapter 7.

Chapter 7. Conclusions and Future Opportunities

7.1 Introduction

This Chapter provides a broad overview of the major findings from Chapters 4, 5 and 6 and addresses the research questions posed at the beginning in Chapter 1. Alongside providing answers to the key questions under investigation, evidence of originality to previous literature is highlighted and findings are evaluated within the wider literature context. Finally, recommendations for how future research can build on these results is provided, alongside challenges that remain to be addressed and new opportunities for exploration.

7.2 Research Outcomes

7.2.1 Research Questions

7.2.1.1 Research Question One

"Can novel core-shell nanocatalyst designs be successfully synthesised based on the proposed synthesis route outlined in Chapter 3.2?"

Results from Chapter 4 confirm that six core-shell nanocatalysts have been obtained based on a principle of coating a layer of commercial 100 nm SiO_2 nanoparticles with a layer of Fe, followed by a catalytically active layer of TiO_2 or ZnO respectively. Treatment of chlorosulfonic acid at varying concentrations was confirmed to load sulfate species onto surface and led to enhancement of Brønsted acidity. While the Ti series of nanocatalysts showed desirable physical properties and the synthesis route can certainly be considered successful, the Zn series was considerably less optimal. Recommendations of improvements to the ZnFeSi synthesis route for future work is discussed later in Chapter 7.3.

7.2.1.2 Research Question Two

"What structural, morphological and chemical properties do the novel nanocatalysts possess when Ti or Zn oxide is used for catalytically active layer?"

Chapter 4 reports an extensive range of characterisation results for both Ti and Zn series of nanocatalysts and major results are summarised in Table 4.24 and Table 4.25 respectively. For both Ti and Zn series a highly aggregated core shell structure is achieved with 100-450 nm microscale aggregates that are decorated with <100 nm nanoparticle on the surface. Morphology of Ti series is spherical while more elongated "nugget" shaped for Zn series. Porosity is mesoporous in nature with 3-4 nm sized ink bottle pore shape and specific surface areas of 72-82 m^2/g for Ti nanocatalysts compared to 6-13 m^2/g for Zn nanocatalysts. Ti nanocatalysts are also significantly more thermally stable as compared to Zn series. Crystalline phases of anatase TiO_2 and hexagonal wurtzite ZnO was observed pre acid functionalisation. Post acidification the Ti series crystallinity remained similar, however new crystalline phases of hydrated $Zn(OH)_2$ or sulfated ZnO were observed.

In regard to chemical properties, evidence of S-O and S=O surface species are confirmed for all nanocatalysts with bridged bidentate sulfate structure. Surface hydroxyls and bound water is confirmed via FTIR and NMR techniques. Brønsted acidity was found to dominate post acidic treatment and results from Chapter 5 confirm these Brønsted sites determine catalytic activity, since esterification reaction is enhanced while transesterification performance is very poor. Evidence of Si, Fe, Ti/Zn and S species are all confirmed via various composition analysis methods although Si and Fe composition is much lower than outer Ti/Zn layer. Elemental distribution was inhomogeneous in nature with regions of uncoated Si and regions of rich Ti/Zn phases. Surface Si was occasionally noted in XPS indicating uncoated or exposed core region while no surface Fe was detected likely since surface Fe would leach during acid treatment. Zn series displays high degree of carbon contamination likely due to issues of drying and calcination of a thick viscous sol of low specific surface area. Overall, the Ti series of nanocatalysts displayed much more desirable structural, morphological, and chemical properties.

7.2.1.3 Research Question Three

"How does chlorosulfonic acid concentration during functionalisation step influence the properties of the novel nanocatalysts?"

Surprisingly, there was little deviation in specific surface area, pore size or pore volumes upon changing chlorosulfonic acid concentration. This is likely due to relatively small deviation in sulfur quantity loaded onto the surface ultimately not having a significant effect on pore filling, although for 1.0M-TiFeSi some microporosity was observed potentially due to acid digestion creating new microstructures or enhancing surface nanoparticle aggregation. No change in crystallinity was seen in Ti series, however for all Zn functionalised nanocatalysts new crystalline phases of $Zn(OH)_2$ and possible sulfated ZnO was observed. Variation in zetapotential was observed through changing the acid concentration, especially in 0.55M-TiFeSi where considerable Brønsted acidic sites may explain the positive charge observed. The effect of chlorosulfonic acid concentration on acid strength and surface chemistry was considerable. For both Ti and Zn series an increase in chlorosulfonic acid concentration led to increasing Brønsted acid strength and site stability found via pyridine TPD and TGA. However, increased treatment concentration did not always lead to higher sulfur surface composition or acid site loading density. In Zn series the greatest sulfur loading was seen to be in 1.0M-ZnFeSi as may be expected, however for Ti series the greatest sulfur loading was seen in 0.55M-TiFeSi as determined via CHONS, XPS and STEM-EDX analysis. For Ti series the sulfur loading in 0.1M-TiFeSi was greater than in 1.0M-TiFeSi on average. Acid site density for Ti series naturally followed the same trend, with increased level of sulfur loading enhancing both weak and strong acid site density. To explain this surprising difference in trends between Zn and Ti series, it was noted during ZnFeSi support analysis that sulfate species remained from Zn precursor salt, and chlorosulfonic acid reacted more readily with ZnFeSi as noted from significant digestion that occurred, both of which could have favoured increased sulfate loading with acid concentration. In TiFeSi functionalisation however, the support was both considerably more chemically resilient and less contaminated with residual sulfate, hence concentrated chlorosulfonic acid may have preferentially reacted with solvent or self-dimerised rather than loading surface sulfate groups, explaining the surprisingly low sulfur content in 1.0M-TiFeSi. Further studies should focus on better understanding the acid functionalisation step to inform future optimisation. It was noted in Chapter 5 and 6 that 0.55M-TiFeSi was most active for esterification of FFA likely due to an ideal balance between acid site density, strength and stability.

7.2.1.4 Research Question Four

"Can the novel nanocatalysts successfully convert high FFA% waste feedstocks such as UCO into biodiesel through transesterification and/or esterification pathways?"

Under the reaction conditions explored, it was not possible to observe a transesterification pathway using synthesised nanocatalysts. This may be due to lack of sufficient Lewis acidity that favours transesterification or kinetic unfavorability at industrially relevant conditions utilised in this work. Therefore, a two-step reaction pathway was selected to evaluate if synthesised nanocatalysts could reduce FFA% and enhance base transesterification in second step. Use of a custom screening DoE model and oleic acid as model feedstock revealed that both 0.1M-TiFeSi and 0.55M-TiFeSi were able to achieve >80% methyl oleate yield under run G (9 hr, 60 °C, 3 wt%, 10:1). Meanwhile, 0.1M-ZnFeSi and 0.55M-ZnFeSi were only able to achieve 20-25% methyl oleate yields. For 1.0M-TiFeSi, 1.0M-ZnFeSi and the unfunctionalised supports, no significant difference was noted from the thermal control test. Results from Chapter 5 indicated that 0.1M-TiFeSi and 0.55M-TiFeSi could effectively reduce FFA% via esterification. Screening results indicated that reaction time, temperature, catalyst loading and alcohol to oil ratio were all significant in contributing to methyl oleate yield in a linear and/or nonlinear fashion, hence further optimisation of the two successful Ti nanocatalysts was explored.

7.2.1.5 Research Question Five

"Which novel nanocatalyst is most optimal for biodiesel production from impure feedstocks within the range of explored reaction conditions?"

Results from Chapter 5 indicated that both 0.1M-TiFeSi and 0.55M-TiFeSi could achieve desirable reduction in FFA% under model oleic acid feedstock. Further optimisation work in Chapter 6 using the developed DoE models predicted maximum methyl oleate yields of 83.4% (9 hr, 60 °C, 3.08 wt%, 13:1) for 0.1M-TiFeSi and 99.3% (6.75 hr, 60 °C, 3.19 wt%, 16:1) for 0.55M-TiFeSi respectively. Experimental validation achieved methyl oleate yields of 77.4% and ~100% therefore 0.55M-TiFeSi had greatest catalytic activity in esterification step. This is likely due to most optimal sulfur loading and surface chemistry achieved, balancing high acid site loading density with presence of both medium and strong acidic sites. Kinetic modelling from DoE results suggested a rate constant of 0.406 hr^{-1} at 60 °C, activation energy of 52.7 kJ/mol and TOF of 4.42 hr^{-1} with reaction pathway both endothermic and non-spontaneous.

7.2.1.6 Research Question Six

"Can the optimal novel nanocatalyst lead to an enhancement in FAME yield in a two-step pathway as compared to one step base transesterification over multiple reaction cycles?"

Optimisation of KOH transesterification in fresh vegetable oil through custom DoE model led to an achieved FAME yield of 95.3% after 1hr of reaction at 30 °C, 1 wt% KOH loading and 9:1 methanol to oil ratio. When feedstock was changed to fresh UCO (~3.7 wt% FFA) and degraded UCO (~5.9 wt% FFA), only 57.8% and 47.8% FAME yield could be achieved under similar reaction conditions in the one step transesterification route. In the two-step reaction pathway, an increase in biodiesel yield to 73.6% and 78.4% for fresh and degraded UCO feedstocks was achieved, clearly confirming that 0.55M-TiFeSi pretreatment led to enhancement in FAME yield. Nanocatalyst was likely able to reduce FFA impurity levels and protect base catalyst performance. However, two-step process with UCO was still below 95.3% yield achieved using one-step vegetable oil route. It is likely that optimum transesterification conditions obtained in vegetable oil model are not directly translatable to UCO feedstock, since conversion of FFA impurities alone does not make UCO chemically identical to pure vegetable oil. Therefore, an overall optimisation of the two-step route process conditions is recommended in future work. Deactivation occurred after first reaction cycle and so no improvement in two-step route could be achieved in further recycles with fresh UCO. Interestingly for degraded UCO, the initial esterification step with 0.55M-TiFeSi achieved similar FAME yield to one-step KOH treatment for multiple runs. This may be due to improved mass transfer via reduced viscosity of degraded UCO, or high degree of free glycerides and FFA in degraded UCO that could be readily converted by either 0.55M-TiFeSi or KOH. Nevertheless, no enhancement beyond 47.8% yield was achieved after first cycle. Leaching of sulfate species was confirmed via ATR-FTIR and therefore spent nanocatalyst lacked sufficient Brønsted acid sites to continue esterification of FFA impurities. To improve recyclability, future work should continue to optimise functionalisation conditions to achieve increased acid site density, strength and stability. Alternatively, use of new intermediate layers may help to enhance site stability and prevent leaching, or reacidification could be attempted in between reaction steps to try and regenerate lost activity.

7.2.2 Research Originality

As identified in Chapter 2.5.2 this work builds upon research opportunities identified by thorough reviewing of literature. While a variety of sulfated metal oxides, mixed metal oxides and supported metal oxide acid nanocatalyst designs have been explored, to date no study has proposed a design in which SiO_2 nanoparticles are coated with an intermediate layer of Fe oxide, then further surrounded with an outer layer of TiO_2 or ZnO prior to being made catalytically active by chlorosulfonic acid treatment. Since a wide range of potential nanocatalyst designs remain to be studied it is likely that this is a research area of continuing novelty. Optimisation of the functionalisation conditions remains limited and poorly understood in literature, with many different functionalisation agents and treatment conditions having significant impact on obtained surface chemistry. Past studies as discussed in Chapter 2.5.2.2 highlight that an optimum level of chlorosulfonic acid concentration likely exists. Results in this work agree and explore through a wide variety of characterisation techniques the influence that treatment concentration has on obtained thermal, chemical, morphological and structural properties, prior to trialling in esterification reactions. More work is recommended to further develop understanding of how functionalisation step can be optimised to maximise esterification performance and recyclability. Unlike other literature summarised throughout Chapter 2.3 where only model FFA feedstocks were tested, both a model esterification pathway was tested as well as exploring the transferability of such results to genuine UCO feedstocks of differing quality. Reaction conditions were kept within an industrially relevant range, unlike other studies where high transesterification performance is reported with an important caveat of excessive reaction time and temperature. It is vital that industrial usability is strongly kept in mind when developing new nanocatalysts, therefore this work considered the lesser explored two-step approach and focused on optimising the esterification step via custom DoE modelling, for which solid acid nanocatalysts are best suited. While recyclability was found to be unobtainable, the cause of deactivation was identified to guide how synthesis route might be optimised in future to improve reusability. Obtained DoE model was also used to predict kinetic and thermodynamic parameters which are often left unreported and are important to consider for future upscaling work in continuous reaction systems. A comparison of obtained results within the wider research context is now presented in upcoming subchapter.

7.2.3 Wider Research Context

In Table 7.1 the best performing 0.55M-TiFeSi nanocatalyst is compared with other literature studies of solid acid nanocatalysts in model esterification reactions. Reactivity and obtained properties are comparable to other literature indicating 0.55M-TiFeSi can effectively convert FFA completely into methyl ester similar to other reported acid nanocatalysts. While recyclability with oleic acid was not explored due to primary focus on testing reaction performance in realistic UCO feedstocks, it is likely that sulfate site leaching could remain an issue hence future work should continue to optimise functionalisation step to balance desirable acidity, activity and stability.

Table 7.1 - Literature Comparison of 0.55M-TiFeSi Esterification Performance in Model FFA

Catalyst	Feedstock	A:O Ratio	Catalyst Loading (wt%)	Time (min)	T (°C)	Yield Y Conversion C	Recycles (runs)	Particle Size (nm)	Pore Size (nm)	Surface Area (m^2/g)	Acidity (mmol/g)	Ref.
0.55M-TiFeSi	**Oleic acid**	**16:1**	**3.19**	**405**	**60**	**~100% Y**	**-**	**~260**	**3.62**	**75.8**	**1.29-2.7**	**This Work**
TiO_2/SO_4^{2-}	Acetic acid	1.2 butanol	1.8g	150	120	92.2-52.1% Y	4	8-10	12.9	121	0.79	[196]
$SO_4^{2-}/ZrO_2–B_2O_3–Fe_3O_4$	Acetic acid	-	-	240	100	98.2 – 96.7% Y	5	-	-	-	-	[212]
$SO_4^{2-}/TiO_2/SiO_2$	Acetic acid	-	-	-	120	91.4% C	-	-	-	550	-	[218]
PC-SO_3H	Acetic acid	10:1	10	600	75	94 – 80% C	3	0.2-0.4 $x10^5$	17	140	1.58	[243]
KIT-6/C-SO_3H	Maleic anhydride	6:1	0.2g	1800	-	~60% Y	4	-	11	590	3.0	[223]
FCHC-SO_3H	Oleic acid	15:1	4	180	80	96.7-84.3% Y	5	144	6.4	41.4	1.20	[191]
$TiO_2/SO_4^{2-}/(NH_4)_2SO_4$	Oleic acid	10:1	2	180	80	82.2% C	-	-	4.2	178	1.1	[195]
Sulphated ZrO_2	Oleic acid	10:1	10	240	150	81.3% Y	-	-	5.9	65.8	0.414	[208]
SO_4^{2-}/La_2O_3/HZSM-5	Oleic acid	5:1	10	420	100	~100% C	1	17-150 $x10^3$	5.2-120	217	-	[225]
SO_3H-Graphene Oxide (GO)	Oleic acid	0.1 mol/g	5	240	100	97.6-74% C	3	-	3.8	437	-	[239]
Al^{3+}/ SO_4^{2-}/MWCNT	Oleic acid	12:1	0.9	420	65	95-81.1% C	8	W: ~25	-	-	-	[245]
ZrO_2-TiO_2-SO_3H	Palmitic acid	20:1	5	240	100	93.1-85.1% Y	5	L/W: 4000/100	-	32.5	1.9	[121]
SBA-15-SO_3H	Palmitic acid	30:1	0.05g	360	60	50% Y	-	-	3.9	938	0.22	[220]
SBA-15-SO_3H	Palmitic acid	30:1	0.05g	360	60	33.5% C	-	-	13.8	531	0.19	[222]

Modelled kinetic parameters of 0.55M-TiFeSi in the esterification reaction are compared with previously reported results in literature as summarised in Table 7.2 and it can be seen that predicted activation energy lies within 30-80 kJ/mol range [374] expected for biodiesel production and reasonably close to other values found for sulfated metal oxide nanocatalysts. While obtained nanocatalyst acid sites are less efficient than SBA-15-SO_3H with reduced TON/TOF at similar reaction temperature, likely due to significantly higher specific surface area of zeolitic materials, it should be noted that SBA-15-SO_3H only achieved ~50% FAME yield as compared to approximately complete conversion of oleic acid into methyl oleate achieved with 0.55M-TiFeSi. Reactivity of 0.55M-TiFeSi is similar to FCHC-SO_3H sulfated metal oxide core-shell nanocatalyst, with less favourable rate constant and activation energy likely due to improved mass transfer of smaller 144 nm particle size as compared to ~260 nm bulk aggregate of 0.55M-TiFeSi in methanol. It is noted that most literature fails to adequately report kinetic data making comparison to other synthesised nanocatalysts challenging. Future studies are strongly encouraged to report TOF and Arrhenius plots wherever possible. To improve reaction kinetics at 60 °C reaction temperature, modification of the synthesis route to use smaller starting SiO_2 nanoparticles may enhance mass transfer effects but at a cost of impeding separability post reaction without simultaneous development of a truly magnetically active layer. Alternatively, further optimisation of functionalisation conditions to increase acid site density, strength and site stability would improve esterification efficiency and recycling potential.

Table 7.2 - Comparison of Esterification Kinetics Reported in Literature

Catalyst	Feedstock	Temperature (°C)	TOF (min^{-1})	Activation Energy (kJ/mol)	Rate Constant (min^{-1})	Order	Reference
0.55M-TiFeSi	**Oleic acid**	**60**	**0.0737**	**53**	**0.00677**	**1**	**This Work**
KIT-6/C-SO_3H	Maleic anhydride	-	0.57	-	-	-	[223]
SO_4^{2-}/La_2O_3/HZSM-5	Oleic acid	100	-	44	-	1	[225]
SO_3H-GO	Oleic acid	100	-	13	0.921	1	[239]
FCHC-SO_3H	Oleic acid	80	-	38	0.0173	1	[191]
SBA-15-SO_3H	Palmitic acid	60	0.13 - 0.58	-	-	-	[220]
SBA-15-SO_3H	Palmitic acid	60	0.20 - 2.00	-	-	-	[222]

Since transesterification activity could not be readily observed in 0.55M-TiFeSi either due to lack of strong Lewis acidity or less severe reaction conditions utilised in this work, two step performance was explored as an alternative to use of pressurised reaction conditions. Comparison of FAME yield from UCO with other studies exploring acidic nanocatalysts is given in Table 7.3. While the achieved yield is lower than other studies, reaction temperature was able to be decreased significantly compared to past work by utilising high reactivity of base catalysis in second step. It should be noted that optimised reaction conditions used in transesterification step were based on KOH trials with vegetable oil. By further optimisation of overall two step reaction route with real UCO feedstocks it is feasible that yield could be increased closer towards 80-90% in future work. Recyclability also needs to be improved as discussed prior. Work by Gardy et al. [145] achieved impressive recyclability and reactivity with SO_4^{2-}/Fe-Al-TiO_2 that might be due to significantly lower particle size improving mass transfer effects or use of intermediate Al oxide layer that contributed stability and Lewis acidity, although reaction temperature of 90 °C would still necessitate use of increased pressure conditions.

Table 7.3 - Literature Comparison of 0.55M-TiFeSi and KOH Performance in UCO Feedstock

Catalyst	A:O Ratio	Catalyst Loading (wt%)	Time (min)	T (°C)	Yield Y Conversion C	Reusability (runs)	Particle Size (nm)	Pore Size (nm)	Surface Area (m^2/g)	Acidity (mmol/g)	Ref.
1st: 0.55M-TiFeSi 2nd: KOH	**16:1 9:1**	**3.19**	**405 60**	**60 30**	**73.6% Y Fresh**	**1**	**~260**	**3.62**	**75.8**	**1.29-2.7**	**This Work**
1st: 0.55M-TiFeSi 2nd: KOH	**16:1 9:1**	**3.19**	**405 60**	**60 30**	**78.4% Y Degraded**	**1**	**~260**	**3.62**	**75.8**	**1.29-2.7**	**This Work**
SO_4^{2-}/TiO_2-SiO_2	20:1	10	180	120	77% C	1	-	2.85	457	-	[224]
Fe_2O_3-MnO- SO_4^{2-}/ZrO_2	20:1	3	240	180	~96.5% Y	6	11.5-21	-	1.39 x10^{-6}	4.32 A 1.52 B	[214]
SO_4^{2-}/Zr-SBA-15	40:1	3	180	160	98.5 - 80% C	6	-	3.27-5.47	271	-	[227]
$Ti(SO_4)O$	9:1	1.5	180	75	97.1 - 94.12% Y	8	25	22.7	44.5	-	[198]
$TiO_2/PrSO_3H$	15:1	4.5	540	60	98.3 - 94.16% Y	4	8.2 - 42	24.6	38.6	-	[199]
SO_4^{2-}/Fe-Al-TiO_2	10:1	3	150	90	96->90% Y	10	<50	11.1	51	1.18	[145, 248]
SO_4^{2-}/Mg-Al-Fe_3O_4	9:1	4	300	95	~98.5% Y	5	25-165	6.5	123	2.35	[146]

Comparison of the two-step biodiesel production route via 0.55M-TiFeSi and KOH with other literature that explored a two-step approach is provided in Table 7.4. Achieved yield is similar to other studies in which a solid acid catalyst was utilised. Reaction temperature can be kept below boiling point of methanol by use of such production route, removing the need for pressurised reaction vessels while still keeping reaction duration within reasonable residence time for future continuous reactor scaleup. It is recommended that more researchers exploring solid acid biodiesel catalysis focus on a two-step route to keep reaction conditions industrially desirable.

Table 7.4 - Literature Comparison to Previous Two-Step Biodiesel Studies

Catalyst	A:O Ratio	Catalyst Loading (wt%)	Time (min)	T (°C)	Yield Y Conversion C	Reusability (runs)	Particle Size (nm)	Pore Size (nm)	Surface Area (m^2/g)	Acidity (mmol/g)	Ref.
1st: 0.55M-TiFeSi 2nd: KOH	**16:1 9:1**	**3.19 1**	**405 60**	**60 30**	**73.6% Y Fresh**	**1**	**~260**	**3.62**	**75.8**	**1.29-2.7**	**This Work**
1st: 0.55M-TiFeSi 2nd: KOH	**16:1 9:1**	**3.19 1**	**405 60**	**60 30**	**78.4% Y Degraded**	**1**	**~260**	**3.62**	**75.8**	**1.29-2.7**	**This Work**
1st: $Fe_2(SO_4)_3$ 2nd: CaO	7:1 -	0.4 -	180 180	60 60	81.3% Y UCO	-	-	-	-	-	[64]
1st: 12-TPA/Nb_2O_5 2nd: ZnO/Na-Y zeolite	14:1 24:1	1.65 20	300 360	65 65	80% Y UCO	6	-	-	- 500	1.6-2.3 0.71-1.09	[48]
1st: H_2SO_4 2nd: NaOH	12:1 9:1	1.35 0.62	30 25	60 (340W)	~99% Y Beef Tallow	-	-	-	-	-	[66]
1st: H_2SO_4 2nd: CaO	6:1 9:1	6.5mL 3	120 15	78	97.4% Y Shea butter oil	-	-	5.30-9.18 $x10^3$	-	-	[67]

7.3 Future Opportunities

While six novel nanocatalysts were able to be successfully obtained in this work, after analysis of experimental results it is clear that many opportunities remain to improve upon the current design. Modification of the synthesis route and functionalisation step may lead to more active and recyclable TiFeSi and ZnFeSi nanocatalysts. Introduction of different chemical species within intermediate layer to produce new core-shell designs may also be worth exploring. Finally, the two-step approach should continue to be optimised with real UCO feedstocks to demonstrate a pure biodiesel product can be repeatedly produced at low reaction temperature and reasonable reaction time with an aim towards a continuous reaction scheme at increased benchtop scale.

7.3.1 Adjustments to Synthesis Route

During synthesis of FeSi and ZnFeSi it was noted that washing step was unable to completely remove sulfate precursors. Future synthesis is recommended to use non-sulfate Zn and Fe salts that could lead to purer FeSi and ZnFeSi support material. It may be that large presence of aqueous sulfate species during ZnO layer coprecipitation led to an order of magnitude reduction in specific surface area as compared to TiFeSi support, therefore repeating ZnFeSi synthesis with non-sulfate precursor might dramatically enhance surface area. Should this fail to make a difference, other sub-optimal synthesis conditions may have led to underwhelming surface area in ZnFeSi support such as: solvents used, solution temperature, agitation rate, pH endpoint, rate of NH_3OH addition or the amount of rest time given for ripening and ageing to occur. Additionally, different parameters during the drying and calcination step post synthesis may be required, especially after chlorosulfonic acid treatment of ZnFeSi where significant hydration and notable level of carbon impurity was noted. Due to excessive digestion that occurred during functionalisation of 1.0M-ZnFeSi and subsequent low mass recovery achieved, it is likely that functionalisation conditions may need to be milder for less chemically resilient ZnFeSi support as compared to those used for TiFeSi. This could mean a lowering of acid concentration, lower temperature, shorter functionalisation time or use of a different functionalisation agent entirely. Optimisation of functionalisation conditions is also recommended for Ti series to obtain a superior balance of acid site density, acidic strength and stability of sulfate surface groups. Other improvements that could be made to synthesis route includes adjusting the ratios of how much Si, Fe and Ti/Zn precursors are added in each step in order to achieve a range of Si, Fe and Ti/Zn elemental compositions. While evidence of Si and Fe was certainly detected in final functionalised nanocatalysts, the predominant phase present was the acid functionalised outer catalytically active layer. Use of smaller 50 nm SiO_2 commercially available nanoparticles may lead to improved mass transfer and enhanced esterification kinetics. It is unclear if lack of magnetic separability in FeSi was due to 100 nm SiO_2 core being too large for weakly magnetic hematite, or if hematite layer failed to achieve superparamagnetism due to excessive thickness. For TiFeSi and ZnFeSi a low composition of Fe, increased aggregation and even larger particle size likely further hindered magnetic separability. Should use of smaller SiO_2 and thin hematite layer continue to show poor magnetism, use of Fe(II) salt is strongly recommended in coprecipitation step alongside Fe(III) however this would require performing future synthesis steps under inert N_2 atmosphere.

7.3.2 Introduction of New Chemical Species

Alongside use of Fe(II) salt to aim for a more strongly magnetic magnetite or maghemite crystallinity, other adjustments to intermediate layer may be beneficial to increase transesterification performance or further enhance sulfate stability for repeated recycling. The impressive SO_4^{2-}/Fe-Al-TiO_2 core-shell design by Gardy et al. [145] was able to achieve 10 reuses and showed strong reactivity in simultaneous transesterification-esterification, albeit at higher 90 °C reaction temperature. Al and Fe oxide layers may have aided sulfate stability, and as reported in other work [629, 630] may have led to enhancement in Lewis acidity. Alternatively, inclusion of other metal oxides to improve acidity or use of base to produce bifunctional surface chemistry could lead to other novel core-shell designs yet to be reported.

7.3.3 Optimisation of Two Step Reaction Scheme

Under more extreme reaction temperature, extensive reaction times, or higher methanol loading, the transesterification pathway may be possible for sulfated TiFeSi nanocatalyst. To test for this, pure triglyceride such as triolein could be used in a design of experiments approach under much wider reaction conditions similar to method used in Chapter 5. However, extensive work in literature continues to develop superior base nanocatalysts for transesterification step for which acidic pretreatment remains crucial. It is therefore recommended instead to continue developing the two-step reaction scheme. The DoE approach should be expanded to fully model all linear, nonlinear and interaction terms with optimisation of reaction conditions determined with UCO feedstock instead of model FFA and vegetable oil. Implementation of suggested improvements to TiFeSi design and synthesis route may enable a consistently achievable >90% FAME yield over repeated reuses under a completely optimised two-step batch reaction scheme. Succeeding in this research goal, it would next be recommended to increase the quantity of nanocatalyst produced to begin scale up from 5 mL glass vial batch reactions towards bench scale continuous reaction vessels. Increasing the quantity of nanocatalyst produced could provide an opportunity to investigate reproducibility and batch variability of the synthesis route. Modelling a bench scale continuous reactor could enable real time disturbance modelling of feedstock purity, demonstration of a continuous magnetic separation unit and offline reacidification step. The future of acid nanocatalysis for biodiesel production looks set to remain an exciting research area. It is hoped that global collaboration continues to build a brighter, cleaner and greener tomorrow.

References

References

1. Filonchyk, M., Peterson, M.P., Zhang, L., Hurynovich, V. and He, Y. Greenhouse gases emissions and global climate change: Examining the influence of CO2, CH4, and N2O. *Science of The Total Environment.* [Online]. 2024, **935**, p.173359. Available from: https://doi.org/10.1016/j.scitotenv.2024.173359
2. Althor, G., Watson, J.E.M. and Fuller, R.A. Global mismatch between greenhouse gas emissions and the burden of climate change. *Scientific Reports.* [Online]. 2016, **6**(1), p.20281. Available from: https://doi.org/10.1038/srep20281
3. Lamb, W.F., Wiedmann, T., Pongratz, J., Andrew, R., Crippa, M., Olivier, J.G.J., Wiedenhofer, D., Mattioli, G., Khourdajie, A.A., House, J., Pachauri, S., Figueroa, M., Saheb, Y., Slade, R., Hubacek, K., Sun, L., Ribeiro, S.K., Khennas, S., de la Rue du Can, S., Chapungu, L., Davis, S.J., Bashmakov, I., Dai, H., Dhakal, S., Tan, X., Geng, Y., Gu, B. and Minx, J. A review of trends and drivers of greenhouse gas emissions by sector from 1990 to 2018. *Environmental Research Letters.* [Online]. 2021, **16**(7), p.073005. Available from: https://doi.org/10.1088/1748-9326/abee4e
4. Chen, R. and Kong, Y. A comprehensive review of greenhouse gas based on subject categories. *Science of The Total Environment.* [Online]. 2023, **866**, p.161314. Available from: https://doi.org/10.1016/j.scitotenv.2022.161314
5. Yaman, C. A Review on the Process of Greenhouse Gas Inventory Preparation and Proposed Mitigation Measures for Reducing Carbon Footprint. *Gases.* [Online]. 2024, **4**(1), pp.18-40. Available from: https://doi.org/10.3390/gases4010002
6. Manabe, S. Role of greenhouse gas in climate change**. *Tellus A: Dynamic Meteorology and Oceanography.* [Online]. 2019, **71**(1), p.1620078. Available from: https://doi.org/10.1080/16000870.2019.1620078
7. Butler, C.D. Climate Change, Health and Existential Risks to Civilization: A Comprehensive Review (1989–2013). *Int J Environ Res Public Health.* [Online]. 2018, **15**(10). Available from: https://doi.org/10.3390/ijerph15102266
8. Bolan, S., Padhye, L.P., Jasemizad, T., Govarthanan, M., Karmegam, N., Wijesekara, H., Amarasiri, D., Hou, D., Zhou, P., Biswal, B.K., Balasubramanian, R., Wang, H., Siddique, K.H.M., Rinklebe, J., Kirkham, M.B. and Bolan, N. Impacts of climate change on the fate of contaminants through extreme weather events. *Science of The Total Environment.* [Online]. 2024, **909**, p.168388. Available from: https://doi.org/10.1016/j.scitotenv.2023.168388
9. Magnan, A.K., Pörtner, H.-O., Duvat, V.K.E., Garschagen, M., Guinder, V.A., Zommers, Z., Hoegh-Guldberg, O. and Gattuso, J.-P. Estimating the global risk of anthropogenic climate change. *Nature Climate Change.* [Online]. 2021, **11**(10), pp.879-885. Available from: https://doi.org/10.1038/s41558-021-01156-w
10. COP21. *Paris Agreement.* Paris: United Nations, 2015.
11. Leiter, T. Nationally determined contributions (NDCs) as a governance instrument – accounting for politics, negotiation progress, and related mechanisms under the Paris Agreement. *Environmental Politics.* [Online]. 2024, **33**(3), pp.552-557. Available from: https://doi.org/10.1080/09644016.2023.2252312
12. *Final UK greenhouse gas emissions national statistics: 1990 to 2022.* 2024.
13. IEA. Greenhouse Gas Emissions from Energy Data Explorer. [Online]. 2024. Available from: https://www.iea.org/data-and-statistics/data-tools/greenhouse-gas-emissions-from-energy-data-explorer
14. Aryanpur, V. and Rogan, F. Decarbonising road freight transport: The role of zero-emission trucks and intangible costs. *Scientific Reports.* [Online]. 2024, **14**(1), p.2113. Available from: https://doi.org/10.1038/s41598-024-52682-4
15. Alanazi, F. Electric Vehicles: Benefits, Challenges, and Potential Solutions for Widespread Adaptation. *Applied Sciences.* [Online]. 2023, **13**(10). Available from: https://doi.org/10.3390/app13106016
16. Pamidimukkala, A., Kermanshachi, S., Rosenberger, J.M. and Hladik, G. Barriers and motivators to the adoption of electric vehicles: A global review. *Green Energy and Intelligent Transportation.* [Online]. 2024, **3**(2), p.100153. Available from: https://doi.org/10.1016/j.geits.2024.100153
17. Guzek, M., Jackowski, J., Jurecki, R.S., Szumska, E.M., Zdanowicz, P. and Żmuda, M. Electric Vehicles—An Overview of Current Issues—Part 2—Infrastructure and Road Safety. *Energies.* [Online]. 2024, **17**(2). Available from: https://doi.org/10.3390/en17020495
18. Mali, B., Shrestha, A., Chapagain, A., Bishwokarma, R., Kumar, P. and Gonzalez-Longatt, F. Challenges in the penetration of electric vehicles in developing countries with a focus on Nepal. *Renewable Energy Focus.* [Online]. 2022, **40**, pp.1-12. Available from: https://doi.org/10.1016/j.ref.2021.11.003
19. Ibrahim, H.A., Ayomoh, M.K., Bansal, R.C., Gitau, M.N., Yadavalli, V.S.S. and Naidoo, R. Sustainability of power generation for developing economies: A systematic review of power sources mix. *Energy Strategy Reviews.* [Online]. 2023, **47**, p.101085. Available from: https://doi.org/10.1016/j.esr.2023.101085
20. Falcone, P.M. Sustainable Energy Policies in Developing Countries: A Review of Challenges and Opportunities. *Energies.* [Online]. 2023, **16**(18). Available from: https://doi.org/10.3390/en16186682
21. Nduhuura, P., Garschagen, M. and Zerga, A. Impacts of Electricity Outages in Urban Households in Developing Countries: A Case of Accra, Ghana. *Energies.* [Online]. 2021, **14**(12). Available from: https://doi.org/10.3390/en14123676
22. Pathak, P.K., Yadav, A.K. and Padmanaban, S. Transition toward emission-free energy systems by 2050: Potential role of hydrogen. *International Journal of Hydrogen Energy.* [Online]. 2023, **48**(26), pp.9921-9927. Available from: https://doi.org/10.1016/j.ijhydene.2022.12.058
23. IEA. *Global EV Outlook 2024.* Paris: IEA, 2024.
24. IEA. Global EV Data Explorer. [Online]. 2024. Available from: https://www.iea.org/data-and-statistics/data-tools/global-ev-data-explorer
25. IEA. *Road transport.* Paris: IEA, 2023.
26. Songstad, D.D., Lakshmanan, P., Chen, J., Gibbons, W., Hughes, S. and Nelson, R. Historical Perspective of Biofuels: Learning from the Past to Rediscover the Future. *In Vitro Cellular & Developmental Biology. Plant.* [Online]. 2009, **45**(3), pp.189-192. [Accessed 2025/03/13/]. Available from: http://www.jstor.org/stable/20541026
27. Jeswani, H.K., Chilvers, A. and Azapagic, A. Environmental sustainability of biofuels: a review. *Proc Math Phys Eng Sci.* [Online]. 2020, **476**(2243), p.20200351. Available from: https://doi.org/10.1098/rspa.2020.0351
28. Sivakumar, G., Vail, D.R., Xu, J., Burner, D.M., Lay, J.O., Ge, X. and Weathers, P.J. Bioethanol and biodiesel: Alternative liquid fuels for future generations. *Engineering in Life Sciences.* [Online]. 2010, **10**(1), pp.8-18. [Accessed 2025/03/13]. Available from: https://doi.org/10.1002/elsc.200900061

29. Guo, M., Song, W. and Buhain, J. Bioenergy and biofuels: History, status, and perspective. *Renewable and Sustainable Energy Reviews.* [Online]. 2015, **42**, pp.712-725. Available from: https://doi.org/10.1016/j.rser.2014.10.013
30. Vasudevan, P.T. and Briggs, M. Biodiesel production—current state of the art and challenges. *Journal of Industrial Microbiology and Biotechnology.* [Online]. 2008, **35**(5), pp.421-421. [Accessed 3/13/2025]. Available from: https://doi.org/10.1007/s10295-008-0312-2
31. Verma, P. and Sharma, M.P. Comparative analysis of effect of methanol and ethanol on Karanja biodiesel production and its optimisation. *Fuel.* [Online]. 2016, **180**, pp.164-174. Available from: https://doi.org/10.1016/j.fuel.2016.04.035
32. Farobie, O. and Matsumura, Y. A comparative study of biodiesel production using methanol, ethanol, and tert-butyl methyl ether (MTBE) under supercritical conditions. *Bioresource Technology.* [Online]. 2015, **191**, pp.306-311. Available from: https://doi.org/10.1016/j.biortech.2015.04.102
33. Sethin, A., Oo, Y.M., Thawornprasert, J. and Somnuk, K. Effects of Blended Diesel–Biodiesel Fuel on Emissions of a Common Rail Direct Injection Diesel Engine with Different Exhaust Gas Recirculation Rates. *ACS Omega.* [Online]. 2024, **9**(19), pp.20906-20918. Available from: https://doi.org/10.1021/acsomega.3c10125
34. BSI. *BS EN 14214.* 2021.
35. Lowe, B., Gardy, J. and Hassanpour, A. The Role of Sulfated Materials for Biodiesel Production from Cheap Raw Materials. *Catalysts.* [Online]. 2022, **12**(2). Available from: https://doi.org/10.3390/catal12020223
36. IEA. Global biofuel demand in transport in the Net Zero Scenario, 2016-2030. [Online]. 2023. Available from: https://www.iea.org/data-and-statistics/charts/global-biofuel-demand-in-transport-in-the-net-zero-scenario-2016-2030-2
37. Gui, M.M., Lee, K.T. and Bhatia, S. Feasibility of edible oil vs. non-edible oil vs. waste edible oil as biodiesel feedstock. *Energy.* [Online]. 2008, **33**(11), pp.1646-1653. Available from: https://doi.org/10.1016/j.energy.2008.06.002
38. Kemp, W.H. *Biodiesel: basics and beyond: a comprehensive guide to production and use for the home and farm.* Tamworth, Ont.: Aztext Press, 2006.
39. Mohammadshirazi, A., Akram, A., Rafiee, S. and Bagheri Kalhor, E. Energy and cost analyses of biodiesel production from waste cooking oil. *Renewable and Sustainable Energy Reviews.* [Online]. 2014, **33**, pp.44-49. Available from: https://doi.org/10.1016/j.rser.2014.01.067
40. Monika, Banga, S. and Pathak, V.V. Biodiesel production from waste cooking oil: A comprehensive review on the application of heterogenous catalysts. *Energy Nexus.* [Online]. 2023, **10**, p.100209. Available from: https://doi.org/10.1016/j.nexus.2023.100209
41. Degfie, T.A., Mamo, T.T. and Mekonnen, Y.S. Optimized Biodiesel Production from Waste Cooking Oil (WCO) using Calcium Oxide (CaO) Nano-catalyst. *Scientific Reports.* [Online]. 2019, **9**(1), p.18982. Available from: https://doi.org/10.1038/s41598-019-55403-4
42. Sahani, S., Roy, T. and Sharma, Y.C. Smart waste management of waste cooking oil for large scale high quality biodiesel production using Sr-Ti mixed metal oxide as solid catalyst: Optimization and E-metrics studies. *Waste Management.* [Online]. 2020, **108**, pp.189-201. Available from: https://doi.org/10.1016/j.wasman.2020.04.036
43. Cavelius, P., Engelhart-Straub, S., Mehlmer, N., Lercher, J., Awad, D. and Brück, T. The potential of biofuels from first to fourth generation. *PLoS Biol.* [Online]. 2023, **21**(3), p.e3002063. Available from: https://doi.org/10.1371/journal.pbio.3002063
44. IEA. Total biofuel production by feedstock, main case, 2021-2027. [Online]. 2022. Available from: https://www.iea.org/data-and-statistics/charts/total-biofuel-production-by-feedstock-main-case-2021-2027
45. Yusup, S. and Khan, M.A. Base catalyzed transesterification of acid treated vegetable oil blend for biodiesel production. *Biomass and Bioenergy.* [Online]. 2010, **34**(10), pp.1500-1504. Available from: https://doi.org/10.1016/j.biombioe.2010.04.027
46. Miyuranga, K.A.V., Arachchige, U.S.P.R., Marso, T.M.M. and Samarakoon, G. Biodiesel Production through the Transesterification of Waste Cooking Oil over Typical Heterogeneous Base or Acid Catalysts. *Catalysts.* [Online]. 2023, **13**(3). Available from: https://doi.org/10.3390/catal13030546
47. Jitputti, J., Kitiyanan, B., Rangsunvigit, P., Bunyakiat, K., Attanatho, L. and Jenvanitpanjakul, P. Transesterification of crude palm kernel oil and crude coconut oil by different solid catalysts. *Chemical Engineering Journal.* [Online]. 2006, **116**(1), pp.61-66. Available from: https://doi.org/10.1016/j.cej.2005.09.025
48. Srilatha, K., Prabhavathi Devi, B.L.A., Lingaiah, N., Prasad, R.B.N. and Sai Prasad, P.S. Biodiesel production from used cooking oil by two-step heterogeneous catalyzed process. *Bioresource Technology.* [Online]. 2012, **119**, pp.306-311. Available from: https://doi.org/10.1016/j.biortech.2012.04.098
49. Isahak, W.N.R.W. and Al-Amiery, A. Catalysts driving efficiency and innovation in thermal reactions: A comprehensive review. *Green Technologies and Sustainability.* [Online]. 2024, **2**(2), p.100078. Available from: https://doi.org/10.1016/j.grets.2024.100078
50. Kamalzare, M. 10 - Recovery and reusability of catalysts in various organic reactions. In: Maleki, A. ed. *Heterogeneous Micro and Nanoscale Composites for the Catalysis of Organic Reactions*. Elsevier, 2022, pp.149-165.
51. Kibar, M.E., Hilal, L., Çapa, B.T., Bahçıvanlar, B. and Abdeljelil, B.B. Assessment of Homogeneous and Heterogeneous Catalysts in Transesterification Reaction: A Mini Review. *ChemBioEng Reviews.* [Online]. 2023, **10**(4), pp.412-422. [Accessed 2025/03/25]. Available from: https://doi.org/10.1002/cben.202200021
52. Ahmed, M., Ahmad, K.A., Vo, D.-V.N., Yusuf, M., Haq, A., Abdullah, A., Aslam, M., Patle, D.S., Ahmad, Z., Ahmad, E. and Athar, M. Recent trends in sustainable biodiesel production using heterogeneous nanocatalysts: Function of supports, promoters, synthesis techniques, reaction mechanism, and kinetics and thermodynamic studies. *Energy Conversion and Management.* [Online]. 2023, **280**, p.116821. Available from: https://doi.org/10.1016/j.enconman.2023.116821
53. Sheehan, J., Camobreco, V., Duffield, J., Graboski, M. and Shapouri, H. *An Overview of Biodiesel and Petroleum Diesel Life Cycles.* National Renewable Energy Lab. (NREL), Golden, CO (United States), 1998.
54. Alsultan, A.G., Asikin Mijan, N., Mansir, N., Razali, S.Z., Yunus, R. and Taufiq-Yap, Y.H. Combustion and Emission Performance of CO/NO(x)/SO(x) for Green Diesel Blends in a Swirl Burner. *ACS Omega.* [Online]. 2021, **6**(1), pp.408-415. Available from: https://doi.org/10.1021/acsomega.0c04800
55. Hoekman, S.K. and Robbins, C. Review of the effects of biodiesel on NOx emissions. *Fuel Processing Technology.* [Online]. 2012, **96**, pp.237-249. Available from: https://doi.org/10.1016/j.fuproc.2011.12.036
56. Wahyudi, Wardana, I.N.G., Widodo, A. and Wijayanti, W. Improving Vegetable Oil Properties by Transforming Fatty Acid Chain Length in Jatropha Oil and Coconut Oil Blends. *Energies.* [Online]. 2018, **11**(2). Available from: https://doi.org/10.3390/en11020394
57. Lichtenstein, A.H. Lipids (fats and oils). In: Caballero, B. ed. *Encyclopedia of Human Nutrition (Fourth Edition)*. Oxford: Academic Press, 2023, pp.291-300.

58. Wilson, K. and Lee, A.F. Rational design of heterogeneous catalysts for biodiesel synthesis. *Catalysis Science & Technology.* [Online]. 2012, **2**(5), pp.884-897. Available from: https://doi.org/10.1039/C2CY20038D
59. Alaba, P.A., Sani, Y.M. and Ashri Wan Daud, W.M. ChemInform Abstract: Efficient Biodiesel Production via Solid Superacid Catalysis: A Critical Review on Recent Breakthrough. *ChemInform.* [Online]. 2016, **47**(42). [Accessed 2025/03/14]. Available from: https://doi.org/10.1002/chin.201642271
60. Cancela, A., Maceiras, R., Urrejola, S. and Sanchez, A. Microwave-Assisted Transesterification of Macroalgae. *Energies.* [Online]. 2012, **5**(4), pp.862-871. Available from: https://doi.org/10.3390/en5040862
61. Kalsum, U., Kusuma Heri, S., Roesyadi, A. and Mahfud, M. Production Biodiesel via In-situ Transesterification from Chlorella sp. using Microwave with Base Catalyst. *Korean Chemical Engineering Research.* [Online]. 2018, **56**(5), pp.773-778. Available from: https://doi.org/10.9713/KCER.2018.56.5.773
62. Larimi, A., Harvey, A.P., Phan, A.N., Beshtar, M., Wilson, K. and Lee, A.F. Aspects of Reaction Engineering for Biodiesel Production. *Catalysts.* [Online]. 2024, **14**(10). Available from: https://doi.org/10.3390/catal14100701
63. Chanakaewsomboon, I., Phoungthong, K., Palamanit, A., Seechamnanturakit, V. and Cheng, C.K. Biodiesel produced using potassium methoxide homogeneous alkaline catalyst: effects of various factors on soap formation. *Biomass Conversion and Biorefinery.* [Online]. 2023, **13**(10), pp.9237-9247. Available from: https://doi.org/10.1007/s13399-021-01787-1
64. Omar, W.N.N.W., Nordin, N., Mohamed, M. and Amin, N.A.S. A Two-Step Biodiesel Production from Waste Cooking Oil: Optimization of Pre-Treatment Step. *Journal of Applied Sciences.* [Online]. 2009, **9**(17), pp.3098-3103. Available from: https://doi.org/10.3923/jas.2009.3098.3103
65. Srilatha, K., Lingaiah, N., Devi, B.L.A.P., Prasad, R.B.N., Venkateswar, S. and Prasad, P.S.S. Esterification of free fatty acids for biodiesel production over heteropoly tungstate supported on niobia catalysts. *Applied Catalysis A: General.* [Online]. 2009, **365**(1), pp.28-33. Available from: https://doi.org/10.1016/j.apcata.2009.05.025
66. Suwannapa, P. and Tippayawong, N. Optimization of Two-Step Biodiesel Production from Beef Tallow with Microwave Heating. *Chemical Engineering Communications.* [Online]. 2017, **204**(5), pp.618-624. Available from: https://doi.org/10.1080/00986445.2017.1294585
67. Ogunsola, A.D., Durowoju, M.O., Alade, A.O., Jekayinfa, S.O. and Ogunkunle, O. Modeling and optimization of two-step shea butter oil biodiesel synthesis using snail shells as heterogeneous base catalysts. *Energy Advances.* [Online]. 2022, **1**(2), pp.113-128. Available from: https://doi.org/10.1039/D1YA00042J
68. Yang, Z., Wei, Y., Wei, J. and Yang, Z. Chiral superstructures of inorganic nanorods by macroscopic mechanical grinding. *Nature Communications.* [Online]. 2022, **13**(1), p.5844. Available from: https://doi.org/10.1038/s41467-022-33638-6
69. Shivakumar, N., Ramesh, T., K., S.P., Pugazhenthi, A. and Manikandan, S.P. Novel Method of Nanoparticle Synthesis using Surface Grinding. *International Journal of Innovative Technology and Exploring Engineering.* [Online]. 2020, **9**(5), pp.1643-1646. Available from: https://doi.org/10.35940/ijitee.E3044.039520
70. Joy, J., Krishnamoorthy, A., Tanna, A., Kamathe, V., Nagar, R. and Srinivasan, S. Recent Developments on the Synthesis of Nanocomposite Materials via Ball Milling Approach for Energy Storage Applications. *Applied Sciences.* [Online]. 2022, **12**(18). Available from: https://doi.org/10.3390/app12189312
71. Saepurahman and Hashaikeh, R. Insight into ball milling for size reduction and nanoparticles production of H-Y zeolite. *Materials Chemistry and Physics.* [Online]. 2018, **220**, pp.322-330. Available from: https://doi.org/10.1016/j.matchemphys.2018.08.080
72. Leybo, D., Firestein, K.L., Evdokimenko, N.D., Ryzhova, A.A., Baidyshev, V.S., Chepkasov, I.V., Popov, Z.I., Kustov, A.L., Konopatsky, A.S., Golberg, D.V. and Shtansky, D.V. Ball-Milled Processed, Selective Fe/h-BN Nanocatalysts for CO2 Hydrogenation. *ACS Applied Nano Materials.* [Online]. 2022, **5**(11), pp.16475-16488. Available from: https://doi.org/10.1021/acsanm.2c03540
73. Wu, Z., Li, X., Jiang, P., Feng, G., Cao, L.-a., Wang, X.-M., Tan, R. and Feng, E. Mechanical milling promotes the preparation of catalyst lanthanum dodecyl sulfate and green solvent-free grinding for synthesis of N-heterocyclic derivatives. *Applied Catalysis A: General.* [Online]. 2024, **684**, p.119893. Available from: https://doi.org/10.1016/j.apcata.2024.119893
74. Xu, Q., Sheng, X., Li, N., Zhang, J., Shi, H., Niu, M., Ping, Q. and Li, N. Ball-Milling: A Productive, Economical, and Widely Applicable Method for Condensation of Biomass-Derived Aldehydes and Ketones at Mild Temperatures. *ACS Sustainable Chemistry & Engineering.* [Online]. 2021, **9**(24), pp.8232-8237. Available from: https://doi.org/10.1021/acssuschemeng.1c02270
75. Tanner, A., Baranek, M., Eastlack, T., Butts, B., Beazley, M. and Hampton, M. Biodiesel Production Directly from Rapeseeds. *Water.* [Online]. 2023, **15**(14). Available from: https://doi.org/10.3390/w15142595
76. Yang, N., Sheng, X., Ti, L., Jia, H., Ping, Q. and Li, N. Ball-milling transesterification process on biodiesel production: RSM optimization, life cycle assessment and market dynamics analysis. *Energy.* [Online]. 2023, **283**(C). Available from: https://doi.org/10.1016/j.energy.2023.129
77. Campbell, E., Brown, A., Nguyen, H.T.M., He, K., Batmunkh, M. and Zhong, Y.L. Recent Advances in Selective Chemical Etching of Nanomaterials for High-Performance Electrodes in Electrocatalysis and Energy Storage. *Small.* [Online]. 2025, **21**(8), p.2409552. [Accessed 2025/03/14]. Available from: https://doi.org/10.1002/smll.202409552
78. Shrestha, N.K., Patil, S.A., Han, J., Cho, S., Inamdar, A.I., Kim, H. and Im, H. Chemical etching induced microporous nickel backbones decorated with metallic Fe@hydroxide nanocatalysts: an efficient and sustainable OER anode toward industrial alkaline water-splitting. *Journal of Materials Chemistry A.* [Online]. 2022, **10**(16), pp.8989-9000. Available from: https://doi.org/10.1039/D1TA10103J
79. Nur'aini, A. and Oh, I. Deep Etching of Silicon Based on Metal-Assisted Chemical Etching. *ACS Omega.* [Online]. 2022, **7**(19), pp.16665-16669. Available from: https://doi.org/10.1021/acsomega.2c01113
80. Grau-Carbonell, A., Sadighikia, S., Welling, T.A.J., van Dijk-Moes, R.J.A., Kotni, R., Bransen, M., van Blaaderen, A. and van Huis, M.A. In Situ Study of the Wet Chemical Etching of SiO2 and Nanoparticle@SiO2 Core–Shell Nanospheres. *ACS Applied Nano Materials.* [Online]. 2021, **4**(2), pp.1136-1148. Available from: https://doi.org/10.1021/acsanm.0c02771
81. Nwatu, D., Kip, D. and Hasse, K. Femtosecond laser assisted selective etching of microchannels in lithium niobate. *Optics Express.* [Online]. 2023, **31**(23), pp.37618-37629. Available from: https://doi.org/10.1364/OE.500439
82. Long, Y., Wang, S., Wang, Y., Deng, F. and Ding, T. Light-Directed Growth/Etching of Gold Nanoparticles via Plasmonic Hot Carriers. *The Journal of Physical Chemistry C.* [Online]. 2020, **124**(35), pp.19212-19218. Available from: https://doi.org/10.1021/acs.jpcc.0c04672

83. Mansouri, G. and Mansouri, M. Synthesis and Characterization of Co-Mn Nanocatalyst Prepared by Thermal Decomposition for Fischer-Tropsch Reaction. *Iranian Journal of Chemistry and Chemical Engineering.* [Online]. 2018, **37**, pp.1-9.
84. Salavati-Niasari, M., Davar, F. and Mazaheri, M. Synthesis of Mn3O4 nanoparticles by thermal decomposition of a [bis(salicylidiminato)manganese(II)] complex. *Polyhedron.* [Online]. 2008, **27**(17), pp.3467-3471. Available from: https://doi.org/10.1016/j.poly.2008.04.015
85. Betancourt-Galindo, R., Reyes-Rodriguez, P.Y., Puente-Urbina, B.A., Avila-Orta, C.A., Rodríguez-Fernández, O.S., Cadenas-Pliego, G., Lira-Saldivar, R.H. and García-Cerda, L.A. Synthesis of Copper Nanoparticles by Thermal Decomposition and Their Antimicrobial Properties. *Journal of Nanomaterials.* [Online]. 2014, **2014**(1), p.980545. [Accessed 2025/03/14]. Available from: https://doi.org/10.1155/2014/980545
86. Palacios-Hernández, T., Hirata-Flores, G.A., Contreras-López, O.E., Mendoza-Sánchez, M.E., Valeriano-Arreola, I., González-Vergara, E. and Méndez-Rojas, M.A. Synthesis of Cu and Co metal oxide nanoparticles from thermal decomposition of tartrate complexes. *Inorganica Chimica Acta.* [Online]. 2012, **392**, pp.277-282. Available from: https://doi.org/10.1016/j.ica.2012.03.039
87. Innocenzi, P., Malfatti, L., Marmiroli, B. and Falcaro, P. Hard X-rays and soft-matter: processing of sol–gel films from a top down route. *Journal of Sol-Gel Science and Technology.* [Online]. 2014, **70**(2), pp.236-244. Available from: https://doi.org/10.1007/s10971-013-3227-y
88. Roy, A., Elzaki, A., Tirth, V., Kajoak, S., Osman, H., Algahtani, A., Islam, S., Faizo, N.L., Khandaker, M.U., Islam, M.N., Emran, T.B. and Bilal, M. Biological Synthesis of Nanocatalysts and Their Applications. *Catalysts.* [Online]. 2021, **11**(12). Available from: https://doi.org/10.3390/catal11121494
89. Roohi, Fatima, Z., Zaheer, M.R. and Kuddus, M. Nano-catalyst Production Using Nano-biotechnology. In: Kharissova, O.V., Torres-Martínez, L.M. and Kharisov, B.I. eds. *Handbook of Nanomaterials and Nanocomposites for Energy and Environmental Applications*. Cham: Springer International Publishing, 2021, pp.2541-2557.
90. Dhaka, A., Chand Mali, S., Sharma, S. and Trivedi, R. A review on biological synthesis of silver nanoparticles and their potential applications. *Results in Chemistry.* [Online]. 2023, **6**, p.101108. Available from: https://doi.org/10.1016/j.rechem.2023.101108
91. Wen, W. and Wu, J.-M. Nanomaterials via solution combustion synthesis: a step nearer to controllability. *RSC Advances.* [Online]. 2014, **4**(101), pp.58090-58100. Available from: https://doi.org/10.1039/C4RA10145F
92. Varma, A., Mukasyan, A.S., Rogachev, A.S. and Manukyan, K.V. Solution Combustion Synthesis of Nanoscale Materials. *Chemical Reviews.* [Online]. 2016, **116**(23), pp.14493-14586. Available from: https://doi.org/10.1021/acs.chemrev.6b00279
93. Akhtar, M.T., Ahmad, M., Shaheen, A., Zafar, M., Ullah, R., Asma, M., Sultana, S., Munir, M., Rashid, N., Malik, K., Saeed, M. and Waseem, A. Comparative Study of Liquid Biodiesel From Sterculia foetida (Bottle Tree) Using CuO-CeO2 and Fe2O3 Nano Catalysts. *Frontiers in Energy Research.* [Online]. 2019, **7**. Available from: https://doi.org/10.3389/fenrg.2019.00004
94. Li, Y., Zhang, X.-D., Sun, L., Zhang, J. and Xu, H.-P. Fatty acid methyl ester synthesis catalyzed by solid superacid catalyst SO42-/ZrO2–TiO2/La3+. *Applied Energy.* [Online]. 2010, **87**(1), pp.156-159. Available from: https://doi.org/10.1016/j.apenergy.2009.06.030
95. Reyna-Villanueva, L.R., M. Dias, J., Medellín-Castillo, N.A., Ocampo-Pérez, R., Martínez-Rosales, J.M., Peñaflor-Galindo, T. and Alvarez Fuentes, G. Biodiesel production using layered double hidroxides and derived mixed oxides: The role of the synthesis conditions and the catalysts properties on biodiesel conversion. *Fuel.* [Online]. 2019, **251**, pp.285-292. Available from: https://doi.org/10.1016/j.fuel.2019.03.128
96. Macala, G.S., Robertson, A.W., Johnson, C.L., Day, Z.B., Lewis, R.S., White, M.G., Iretskii, A.V. and Ford, P.C. Transesterification Catalysts from Iron Doped Hydrotalcite-like Precursors: Solid Bases for Biodiesel Production. *Catalysis Letters.* [Online]. 2008, **122**(3), pp.205-209. Available from: https://doi.org/10.1007/s10562-008-9480-y
97. Primadi, T.R., Fajaroh, F., Santoso, A., Nazriati and Ciptawati, E. Synthesis of CaO@CoFe2O4 Nanoparticles and its Application as a Catalyst for Biodiesel Production from Used Cooking Oil. *Key Engineering Materials.* [Online]. 2020, **851**, pp.184-193. Available from: https://doi.org/10.4028/www.scientific.net/KEM.851.184
98. Chen, X.-R., Ju, Y.-H. and Mou, C.-Y. Direct Synthesis of Mesoporous Sulfated Silica-Zirconia Catalysts with High Catalytic Activity for Biodiesel via Esterification. *The Journal of Physical Chemistry C.* [Online]. 2007, **111**(50), pp.18731-18737. Available from: https://doi.org/10.1021/jp0749221
99. Tadros, T. Ostwald Ripening. In: Tadros, T. ed. *Encyclopedia of Colloid and Interface Science*. Berlin, Heidelberg: Springer Berlin Heidelberg, 2013, pp.820-820.
100. Andhare, D.D., Jadhav, S.A., Khedkar, M.V., Somvanshi, S.B., More, S.D. and Jadhav, K.M. Structural and Chemical Properties of ZnFe2O4 Nanoparticles Synthesised by Chemical Co-Precipitation Technique. *Journal of Physics: Conference Series.* [Online]. 2020, **1644**(1), p.012014. Available from: https://doi.org/10.1088/1742-6596/1644/1/012014
101. Sonia, L.C., Victory, M. and Phanjoubam, S. A Comparative Study of the Properties of Zinc Ferrite Nanoparticles Synthesized by Different Techniques for Nanofluid Preparation. *Integrated Ferroelectrics.* [Online]. 2020, **204**(1), pp.100-111. Available from: https://doi.org/10.1080/10584587.2019.1674978
102. Bagherzadeh, S.B. and Haghighi, M. Plasma-enhanced comparative hydrothermal and coprecipitation preparation of CuO/ZnO/Al2O3 nanocatalyst used in hydrogen production via methanol steam reforming. *Energy Conversion and Management.* [Online]. 2017, **142**, pp.452-465. Available from: https://doi.org/10.1016/j.enconman.2017.03.069
103. Rajaeiyan, A. and Bagheri-Mohagheghi, M.M. Comparison of sol-gel and co-precipitation methods on the structural properties and phase transformation of γ and α-Al2O3 nanoparticles. *Advances in Manufacturing.* [Online]. 2013, **1**(2), pp.176-182. Available from: https://doi.org/10.1007/s40436-013-0018-1
104. Bader, N., Benkhayal, A. and Zimmermann, B. Co-precipitation as a sample preparation technique for trace element analysis: An overview. *International Journal of Chemical Sciences.* [Online]. 2014, **12**, pp.519-525.
105. Hui, B.H. and Salimi, M.N. Production of Iron Oxide Nanoparticles by Co-Precipitation method with Optimization Studies of Processing Temperature, pH and Stirring Rate. *IOP Conference Series: Materials Science and Engineering.* [Online]. 2020, **743**(1), p.012036. Available from: https://doi.org/10.1088/1757-899X/743/1/012036
106. Spiridigliozzi, L., Dell'Agli, G., Biesuz, M., Sglavo, V.M. and Pansini, M. Effect of the Precipitating Agent on the Synthesis and Sintering Behavior of 20 mol% Sm-Doped Ceria. *Advances in Materials Science and Engineering.* [Online]. 2016, **2016**(1), p.6096123. [Accessed 2025/03/14]. Available from: https://doi.org/10.1155/2016/6096123

107. Lamdab, U., Wetchakun, K., Kangwansupamonkon, W. and Wetchakun, N. Effect of a pH-controlled co-precipitation process on rhodamine B adsorption of MnFe2O4 nanoparticles. *RSC Advances.* [Online]. 2018, **8**(12), pp.6709-6718. Available from: https://doi.org/10.1039/C7RA13570J
108. Peternele, W.S., Monge Fuentes, V., Fascineli, M.L., Rodrigues da Silva, J., Silva, R.C., Lucci, C.M. and Bentes de Azevedo, R. Experimental Investigation of the Coprecipitation Method: An Approach to Obtain Magnetite and Maghemite Nanoparticles with Improved Properties. *Journal of Nanomaterials.* [Online]. 2014, **2014**(1), p.682985. [Accessed 2025/03/14]. Available from: https://doi.org/10.1155/2014/682985
109. Zhang, Z., Wang, Z., He, S., Wang, C., Jin, M. and Yin, Y. Redox reaction induced Ostwald ripening for size- and shape-focusing of palladium nanocrystals. *Chemical Science.* [Online]. 2015, **6**(9), pp.5197-5203. Available from: https://doi.org/10.1039/c5sc01787d
110. Wang, D., Belharouak, I., Koenig, G.M., Zhou, G. and Amine, K. Growth mechanism of Ni0.3Mn0.7CO3 precursor for high capacity Li-ion battery cathodes. *Journal of Materials Chemistry.* [Online]. 2011, **21**(25), pp.9290-9295. Available from: https://doi.org/10.1039/C1JM11077B
111. Xing, X., Dai, S., Li, W., Li, X., Shao, Z. and Shao, H. A facile surfactant-assisted co-precipitation route preparation of LiNi0.5Mn1.5O4 cathode material. *Ionics.* [Online]. 2023, **29**(11), pp.4509-4517. Available from: https://doi.org/10.1007/s11581-023-05184-8
112. Darr, J.A., Zhang, J., Makwana, N.M. and Weng, X. Continuous Hydrothermal Synthesis of Inorganic Nanoparticles: Applications and Future Directions. *Chemical Reviews.* [Online]. 2017, **117**(17), pp.11125-11238. Available from: https://doi.org/10.1021/acs.chemrev.6b00417
113. Guo, Y., Wang, Z., Shao, H. and Jiang, X. Hydrothermal synthesis of highly fluorescent carbon nanoparticles from sodium citrate and their use for the detection of mercury ions. *Carbon.* [Online]. 2013, **52**, pp.583-589. Available from: https://doi.org/10.1016/j.carbon.2012.10.028
114. Wang, L., Li, S., Zhu, B. and Wang, Y. Nickel nanocatalysts prepared via continuous supercritical hydrothermal synthesis for supercritical water gasification. *Fuel.* [Online]. 2024, **368**, p.131637. Available from: https://doi.org/10.1016/j.fuel.2024.131637
115. Gan, Y.X., Jayatissa, A.H., Yu, Z., Chen, X. and Li, M. Hydrothermal Synthesis of Nanomaterials. *Journal of Nanomaterials.* [Online]. 2020, **2020**(1), p.8917013. [Accessed 2025/03/15]. Available from: https://doi.org/10.1155/2020/8917013
116. Geldasa, F., Kebede, M., Shura, M.W. and Hone, F. Experimental and computational study of metal oxide nanoparticles for the photocatalytic degradation of organic pollutants: a review. *RSC Advances.* [Online]. 2023, **13**, pp.18404-18442. Available from: https://doi.org/10.1039/D3RA01505J
117. Munnik, P., de Jongh, P.E. and de Jong, K.P. Recent Developments in the Synthesis of Supported Catalysts. *Chemical Reviews.* [Online]. 2015, **115**(14), pp.6687-6718. Available from: https://doi.org/10.1021/cr500486u
118. Wang, N., Sun, Q., Zhang, T., Mayoral, A., Li, L., Zhou, X., Xu, J., Zhang, P. and Yu, J. Impregnating Subnanometer Metallic Nanocatalysts into Self-Pillared Zeolite Nanosheets. *Journal of the American Chemical Society.* [Online]. 2021, **143**(18), pp.6905-6914. Available from: https://doi.org/10.1021/jacs.1c00578
119. Hassani Rad, S.J., Haghighi, M., Alizadeh Eslami, A., Rahmani, F. and Rahemi, N. Sol–gel vs. impregnation preparation of MgO and CeO2 doped Ni/Al2O3 nanocatalysts used in dry reforming of methane: Effect of process conditions, synthesis method and support composition. *International Journal of Hydrogen Energy.* [Online]. 2016, **41**(11), pp.5335-5350. Available from: https://doi.org/10.1016/j.ijhydene.2016.02.002
120. Xie, J.-F., Li, H.-T., Gao, Q., Wang, H. and Gong, Y.-S. A convenient and efficient precursor transformation route to well-dispersed, stable, and highly accessible supported Au nanocatalysts with excellent catalytic hydrogenation performances. *RSC Advances.* [Online]. 2018, **8**(69), pp.39384-39393. Available from: https://doi.org/10.1039/c8ra08379g
121. Fan, M., Si, Z., Sun, W. and Zhang, P. Sulfonated ZrO2-TiO2 nanorods as efficient solid acid catalysts for heterogeneous esterification of palmitic acid. *Fuel.* [Online]. 2019, **252**, pp.254-261. Available from: https://doi.org/10.1016/j.fuel.2019.04.121
122. Dahdah, E., Estephane, J., Haydar, R., Youssef, Y., El Khoury, B., Gennequin, C., Aboukaïs, A., Abi-Aad, E. and Aouad, S. Biodiesel production from refined sunflower oil over Ca–Mg–Al catalysts: Effect of the composition and the thermal treatment. *Renewable Energy.* [Online]. 2020, **146**, pp.1242-1248. Available from: https://doi.org/10.1016/j.renene.2019.06.171
123. Bálsamo, N., Mendieta, S., Heredia, A. and Crivello, M. Nanoclays as dispersing precursors of La and Ce oxide catalysts to produce high-valued derivatives of biodiesel by-product. *Molecular Catalysis.* [Online]. 2020, **481**, p.110290. Available from: https://doi.org/10.1016/j.mcat.2019.01.010
124. Parapat, R.Y., Schwarze, M., Ibrahim, A., Tasbihi, M. and Schomäcker, R. Efficient preparation of nanocatalysts. Case study: green synthesis of supported Pt nanoparticles by using microemulsions and mangosteen peel extract. *RSC Advances.* [Online]. 2022, **12**(53), pp.34346-34358. Available from: https://doi.org/10.1039/d2ra04134k
125. Akbari, M., Mirzaei, A.A. and Arsalanfar, M. Microemulsion based synthesis of promoted Fe–Co/MgO nanocatalyst: Influence of calcination atmosphere on the physicochemical properties, activity and light olefins selectivity for hydrogenation of carbon monoxide. *Materials Chemistry and Physics.* [Online]. 2020, **249**, p.123003. Available from: https://doi.org/10.1016/j.matchemphys.2020.123003
126. López-Quintela, M.A., Rivas, J., Blanco, M.C. and Tojo, C. Synthesis of Nanoparticles in Microemulsions. In: Liz-Marzán, L.M. and Kamat, P.V. eds. *Nanoscale Materials*. Boston, MA: Springer US, 2003, pp.135-155.
127. Ganguli, A.K., Ahmad, T., Vaidya, S. and Ahmed, J. Microemulsion route to the synthesis of nanoparticles. [Online]. 2008, **80**(11), pp.2451-2477. [Accessed 2025-03-15]. Available from: https://doi.org/10.1351/pac200880112451
128. Yahyazadehfar, M., Ahmadi, S.A., Sheikhhosseini, E. and Ghazanfari, D. High-yielding strategy for microwave-assisted synthesis of Cr2O3 nanocatalyst. *Journal of Materials Science: Materials in Electronics.* [Online]. 2020, **31**(14), pp.11618-11623. Available from: https://doi.org/10.1007/s10854-020-03710-2
129. Kato, K., Vaucher, S., Hoffmann, P., Xin, Y. and Shirai, T. A novel single-mode microwave assisted synthesis of metal oxide as visible-light photocatalyst. *Materials Letters.* [Online]. 2019, **235**, pp.125-128. Available from: https://doi.org/10.1016/j.matlet.2018.09.132
130. Gutiérrez-Wing, C., Esparza, R., Vargas-Hernández, C., Fernández García, M.E. and José-Yacamán, M. Microwave-assisted synthesis of gold nanoparticles self-assembled into self-supported superstructures. *Nanoscale.* [Online]. 2012, **4**(7), pp.2281-2287. Available from: https://doi.org/10.1039/c2nr12053d

131. Li, A.Y., Kaushik, M., Li, C.-J. and Moores, A. Microwave-Assisted Synthesis of Magnetic Carboxymethyl Cellulose-Embedded Ag–Fe3O4 Nanocatalysts for Selective Carbonyl Hydrogenation. *ACS Sustainable Chemistry & Engineering.* [Online]. 2016, **4**(3), pp.965-973. Available from: https://doi.org/10.1021/acssuschemeng.5b01048
132. Yadav, N., Yadav, G. and Ahmaruzzaman, M. Microwave-assisted biodiesel production using –SO3H functionalized heterogeneous catalyst derived from a lignin-rich biomass. *Scientific Reports.* [Online]. 2023, **13**(1), p.9074. Available from: https://doi.org/10.1038/s41598-023-36380-1
133. Mahmood, S. and Al Yaqoobi, A.M. Microwave assisted production of biodiesel using CaO nano-catalyst produced from mango fallen leaves extract. *Journal of Ecological Engineering.* [Online]. 2024, **26**(1), pp.248-259. Available from: https://doi.org/10.12911/22998993/195650
134. Bokov, D., Turki Jalil, A., Chupradit, S., Suksatan, W., Javed Ansari, M., Shewael, I.H., Valiev, G.H. and Kianfar, E. Nanomaterial by Sol-Gel Method: Synthesis and Application. *Advances in Materials Science and Engineering.* [Online]. 2021, **2021**(1), p.5102014. [Accessed 2025/03/15]. Available from: https://doi.org/10.1155/2021/5102014
135. Baraket, L. and Ghorbel, A. Control preparation of aluminium chromium mixed oxides by Sol-Gel process. In: Delmon, B., Jacobs, P.A., Maggi, R., Martens, J.A., Grange, P. and Poncelet, G. eds. *Studies in Surface Science and Catalysis*. Elsevier, 1998, pp.657-667.
136. Valenzuela, M.A., Bosch, P., Aguilar-Rios, G., Montoya, A. and Schifter, I. Comparison between sol-gel, coprecipitation and wet mixing synthesis of ZnAl2O4. *Journal of Sol-Gel Science and Technology.* [Online]. 1997, **8**(1), pp.107-110. Available from: https://doi.org/10.1007/BF02436826
137. Calafat, A., Avilán, L. and Aldana, J. The influence of preparation conditions on the surface area and phase formation of MoO3/ZrO2 catalysts. *Applied Catalysis A: General.* [Online]. 2000, **201**(2), pp.215-223. Available from: https://doi.org/10.1016/S0926-860X(00)00441-5
138. Veith, M., Haas, M. and Huch, V. Single Source Precursor Approach for the Sol−Gel Synthesis of Nanocrystalline ZnFe2O4 and Zinc−Iron Oxide Composites. *Chemistry of Materials.* [Online]. 2005, **17**(1), pp.95-101. Available from: https://doi.org/10.1021/cm0401802
139. Kurian, M. and Nair, D.S. Effect of preparation conditions on Nickel Zinc Ferrite nanoparticles: A comparison between sol–gel auto combustion and co-precipitation methods. *Journal of Saudi Chemical Society.* [Online]. 2016, **20**, pp.S517-S522. Available from: https://doi.org/10.1016/j.jscs.2013.03.003
140. Sri Rajeswary, S. and Kannan, C. A novel template for the AlPO4-Tridymite fabrication and its high catalytic activity on biodiesel synthesis at room temperature. *Fuel.* [Online]. 2025, **379**, p.132946. Available from: https://doi.org/10.1016/j.fuel.2024.132946
141. C. Hulteen, J. and Martin, C.R. A general template-based method for the preparation of nanomaterials. *Journal of Materials Chemistry.* [Online]. 1997, **7**(7), pp.1075-1087. Available from: https://doi.org/10.1039/A700027H
142. Ebadinezhad, B., Haghighi, M. and Zeinalzadeh, H. Carbon-templated meso-design of nanostructured CeAPSO-34 for biodiesel production from free fatty acid and waste oil. *Renewable Energy.* [Online]. 2022, **195**, pp.716-733. Available from: https://doi.org/10.1016/j.renene.2022.05.159
143. Ghaedi, H. and Zhao, M. Review on Template Removal Techniques for Synthesis of Mesoporous Silica Materials. *Energy & Fuels.* [Online]. 2022, **36**(5), pp.2424-2446. Available from: https://doi.org/10.1021/acs.energyfuels.1c04435
144. Borah, M.J., Devi, A., Borah, R. and Deka, D. Synthesis and application of Co doped ZnO as heterogeneous nanocatalyst for biodiesel production from non-edible oil. *Renewable Energy.* [Online]. 2019, **133**, pp.512-519. Available from: https://doi.org/10.1016/j.renene.2018.10.069
145. Gardy, J., Osatiashtiani, A., Céspedes, O., Hassanpour, A., Lai, X., Lee, A.F., Wilson, K. and Rehan, M. A magnetically separable SO4/Fe-Al-TiO2 solid acid catalyst for biodiesel production from waste cooking oil. *Applied Catalysis B: Environmental.* [Online]. 2018, **234**, pp.268-278. Available from: https://doi.org/10.1016/j.apcatb.2018.04.046
146. Gardy, J., Nourafkan, E., Osatiashtiani, A., Lee, A.F., Wilson, K., Hassanpour, A. and Lai, X. A core-shell SO4/Mg-Al-Fe3O4 catalyst for biodiesel production. *Applied Catalysis B: Environmental.* [Online]. 2019, **259**, p.118093. Available from: https://doi.org/10.1016/j.apcatb.2019.118093
147. Roy, P.K., Datta, S., Nandi, S. and Al Basir, F. Effect of mass transfer kinetics for maximum production of biodiesel from Jatropha Curcas oil: A mathematical approach. *Fuel.* [Online]. 2014, **134**, pp.39-44. Available from: https://doi.org/10.1016/j.fuel.2014.05.021
148. Badday, A.S., Abdullah, A.Z., Lee, K.T. and Khayoon, M.S. Intensification of biodiesel production via ultrasonic-assisted process: A critical review on fundamentals and recent development. *Renewable and Sustainable Energy Reviews.* [Online]. 2012, **16**(7), pp.4574-4587. Available from: https://doi.org/10.1016/j.rser.2012.04.057
149. Nguyen, V.T., Pham, N.H. and Papavassiliou, D.V. Prediction of the aggregation rate of nanoparticles in porous media in the diffusion-controlled regime. *Scientific Reports.* [Online]. 2024, **14**(1), p.1916. Available from: https://doi.org/10.1038/s41598-023-50643-x
150. Bagheri, S., Muhd Julkapli, N. and Bee Abd Hamid, S. Titanium Dioxide as a Catalyst Support in Heterogeneous Catalysis. *The Scientific World Journal.* [Online]. 2014, **2014**, p.727496. Available from: https://doi.org/10.1155/2014/727496
151. Crabbe, E., Nolasco-Hipolito, C., Kobayashi, G., Sonomoto, K. and Ishizaki, A. Biodiesel production from crude palm oil and evaluation of butanol extraction and fuel properties. *Process Biochemistry.* [Online]. 2001, **37**(1), pp.65-71. Available from: https://doi.org/10.1016/S0032-9592(01)00178-9
152. Al-Widyan, M.I. and Al-Shyoukh, A.O. Experimental evaluation of the transesterification of waste palm oil into biodiesel. *Bioresource Technology.* [Online]. 2002, **85**(3), pp.253-256. Available from: https://doi.org/10.1016/S0960-8524(02)00135-9
153. Farag, H.A., El-Maghraby, A. and Taha, N.A. Optimization of factors affecting esterification of mixed oil with high percentage of free fatty acid. *Fuel Processing Technology.* [Online]. 2011, **92**(3), pp.507-510. Available from: https://doi.org/10.1016/j.fuproc.2010.11.004
154. Lotero, E., Liu, Y., Lopez, D.E., Suwannakarn, K., Bruce, D.A. and Goodwin, J.G. Synthesis of Biodiesel via Acid Catalysis. *Industrial & Engineering Chemistry Research.* [Online]. 2005, **44**(14), pp.5353-5363. Available from: https://doi.org/10.1021/ie049157g
155. Liu, K.-S. Preparation of fatty acid methyl esters for gas-chromatographic analysis of lipids in biological materials. *Journal of the American Oil Chemists' Society.* [Online]. 1994, **71**(11), pp.1179-1187. Available from: https://doi.org/10.1007/BF02540534
156. Samios, D., Pedrotti, F., Nicolau, A., Reiznautt, Q.B., Martini, D.D. and Dalcin, F.M. A Transesterification Double Step Process — TDSP for biodiesel preparation from fatty acids triglycerides. *Fuel Processing Technology.* [Online]. 2009, **90**(4), pp.599-605. Available from: https://doi.org/10.1016/j.fuproc.2008.12.011

157. Soriano, N.U., Venditti, R. and Argyropoulos, D.S. Biodiesel synthesis via homogeneous Lewis acid-catalyzed transesterification. *Fuel.* [Online]. 2009, **88**(3), pp.560-565. Available from: https://doi.org/10.1016/j.fuel.2008.10.013
158. Otera, J. Transesterification. *Chem. Rev.* [Online]. 1993, **93**, pp.1449-1470. Available from: https://doi.org/10.1021/cr00020a004,
159. Guan, G., Kusakabe, K., Sakurai, N. and Moriyama, K. Transesterification of vegetable oil to biodiesel fuel using acid catalysts in the presence of dimethyl ether. *Fuel.* [Online]. 2009, **88**(1), pp.81-86. Available from: https://doi.org/10.1016/j.fuel.2008.07.021
160. Miao, X., Li, R. and Yao, H. Effective acid-catalyzed transesterification for biodiesel production. *Energy Conversion and Management.* [Online]. 2009, **50**(10), pp.2680-2684. Available from: https://doi.org/10.1016/j.enconman.2009.06.021
161. Math, M.C., Kumar, S.P. and Chetty, S.V. Technologies for biodiesel production from used cooking oil — A review. *Energy for Sustainable Development.* [Online]. 2010, **14**(4), pp.339-345. Available from: https://doi.org/10.1016/j.esd.2010.08.001
162. Nigatu Gebremariam, S. and Mario Marchetti, J. Biodiesel production technologies: review. *AIMS Energy.* [Online]. 2017, **5**(3), pp.425-457. Available from: https://doi.org/10.3934/energy.2017.3.425
163. Metre, A.V. and Nath, K. Super phosphoric acid catalyzed esterification of Palm Fatty Acid Distillate for biodiesel production: physicochemical parameters and kinetics. *Polish Journal of Chemical Technology.* [Online]. 2015, **17**(1), pp.88-96. Available from: https://doi.org/10.1515/pjct-2015-0013
164. Su, C.-H. Recoverable and reusable hydrochloric acid used as a homogeneous catalyst for biodiesel production. *Applied Energy.* [Online]. 2013, **104**, pp.503-509. Available from: https://doi.org/10.1016/j.apenergy.2012.11.026
165. Suranani, S., Maralla, Y., Gaikwad, S.M. and Sonawane, S.H. Process intensification using corning® advanced-flow™ reactor for continuous flow synthesis of biodiesel from fresh oil and used cooking oil. *Chemical Engineering and Processing - Process Intensification.* [Online]. 2018, **126**, pp.62-73. Available from: https://doi.org/10.1016/j.cep.2018.02.013
166. Cao, F., Chen, Y., Zhai, F., Li, J., Wang, J., Wang, X., Wang, S. and Zhu, W. Biodiesel production from high acid value waste frying oil catalyzed by superacid heteropolyacid. *Biotechnology and Bioengineering.* [Online]. 2008, **101**(1), pp.93-100. [Accessed 2021-06-07t16:19:42]. Available from: https://doi.org/10.1002/bit.21879
167. Sulaiman, S. Overview Of Catalysts In Biodiesel Production. *Journal of Engineering and Applied Sciences.* [Online]. 2016, **11**.
168. Eze, V.C., Harvey, A.P. and Phan, A.N. Determination of the kinetics of biodiesel saponification in alcoholic hydroxide solutions. *Fuel.* [Online]. 2015, **140**, pp.724-730. Available from: https://doi.org/10.1016/j.fuel.2014.10.001
169. Namwong, S. and Punsuvon, V. Biodiesel Production from Used Vegetable Oil Using Ethanol and Sodium Methoxide Catalyst. *Key Engineering Materials.* [Online]. 2017, **723**, pp.551-555. Available from: https://doi.org/10.4028/www.scientific.net/KEM.723.551
170. Zhang, Y. and Zhang, L. Biodiesel Production from Beef Fat with the Assistance of CH3ONa. *Energy Sources, Part A: Recovery, Utilization, and Environmental Effects.* [Online]. 2015, **37**(10), pp.1110-1113. Available from: https://doi.org/10.1080/15567036.2011.601788
171. Thangaraj, B., Solomon, P.R., Muniyandi, B., Ranganathan, S. and Lin, L. Catalysis in biodiesel production—a review. *Clean Energy.* [Online]. 2019, **3**(1), pp.2-23. [Accessed 2/4/2021]. Available from: https://doi.org/10.1093/ce/zky020
172. Gardy, J., Rehan, M., Hassanpour, A., Lai, X. and Nizami, A.-S. Advances in nano-catalysts based biodiesel production from non-food feedstocks. *Journal of Environmental Management.* [Online]. 2019, **249**, p.109316. Available from: https://doi.org/10.1016/j.jenvman.2019.109316
173. Saydut, A., Kafadar, A.B., Aydin, F., Erdogan, S., Kaya, C. and Hamamci, C. Effect of homogeneous alkaline catalyst type on biodiesel production from soybean [Glycine max (L.) Merrill] oil. *Indian Journal of Biotechnology.* [Online]. 2016, **15**, pp.596-600.
174. Schuchardt, U., Sercheli, R. and Vargas, R.M. Transesterification of vegetable oils: A review. *Journal of the Brazilian Chemical Society.* [Online]. 1998, **9**(3), pp.199-210. Available from: https://doi.org/10.1590/s0103-50531998000300002
175. Meher, L.C., Sagar, D.V. and Naik, S.N. Technical aspects of biodiesel production by transesterification-a review. *Renew Sust Energ Rev.* [Online]. 2004, (3), pp.1-21. Available from: https://doi.org/10.1016/j.rser.2004.09.002
176. Felizardo, P., Neiva Correia, M.J., Raposo, I., Mendes, J.F., Berkemeier, R. and Bordado, J.M. Production of biodiesel from waste frying oils. *Waste Management.* [Online]. 2006, **26**(5), pp.487-494. Available from: https://doi.org/10.1016/j.wasman.2005.02.025
177. Encinar, J.M., González, J.F., Martínez, G., Sánchez, N. and González, C.G. Synthesis and characterization of biodiesel obtained from castor oil transesterification. *RE&PQJ.* [Online]. 2024, **9**(1), pp.1078-1083. Available from: https://doi.org/10.24084/repqj09.549
178. Chung, K.-H., Kim, J. and Lee, K.-Y. Biodiesel production by transesterification of duck tallow with methanol on alkali catalysts. *Biomass and Bioenergy.* [Online]. 2009, **33**(1), pp.155-158. Available from: https://doi.org/10.1016/j.biombioe.2008.04.014
179. Ojolo, S.J., Adelaja, A., Ogbonnaya, M. and Ogunsina, B. Study of an effective technique for the production of biodiesel from jatropha oil. *Journal of Emerging Trends in Engineering and Applied Sciences.* [Online]. 2011, **2**, pp.79-86.
180. Abdurrahman, A. Optimization of Potassium Carbonate-based DES as Catalyst in the Production of Biodiesel via Transesterification. *Journal of the Nigerian Society of Physical Sciences.* [Online]. 2023, **5**(1), p.1048. [Accessed %2025/%03/%15]. Available from: https://doi.org/10.46481/jnsps.2023.1048
181. Meher, L.C., Dharmagadda, V.S.S. and Naik, S.N. Optimization of alkali-catalyzed transesterification of Pongamia pinnata oil for production of biodiesel. *Bioresource Technology.* [Online]. 2006, **97**(12), pp.1392-1397. Available from: https://doi.org/10.1016/j.biortech.2005.07.003
182. Ouanji, F., Kacimi, M., Ziyad, M., Puleo, F. and Liotta, L.F. Production of biodiesel at small-scale (10 L) for local power generation. *International Journal of Hydrogen Energy.* [Online]. 2017, **42**(13), pp.8914-8921. Available from: https://doi.org/10.1016/j.ijhydene.2016.06.182
183. Fadhil, A.B. and Ali, L.H. Alkaline-catalyzed transesterification of Silurus triostegus Heckel fish oil: Optimization of transesterification parameters. *Renewable Energy.* [Online]. 2013, **60**, pp.481-488. Available from: https://doi.org/10.1016/j.renene.2013.04.018
184. Hossain, A. and Boyce, A.N. Biodiesel production from waste sunflower cooking oil as an environmental recycling process and renewable energy. *Bulgarian Journal of Agricultural Science.* [Online]. 2009, **15**, pp.313-318.
185. Miyuranga, K.A.V., Balasuriya, B.M.C.M., Arachchige, U.S.P.R., Jayasinghe, R.A. and Weerasekara, N.A. Comparison of Performance of Various Homogeneous Alkali Catalysts in Transesterification of Waste Cooking Oil. *Asian Journal of Chemistry.* [Online]. 2022, **34**(12), pp.3157-3161. Available from: https://doi.org/10.14233/ajchem.2022.23849
186. Uzun, B.B., Kılıç, M., Özbay, N., Pütün, A.E. and Pütün, E. Biodiesel production from waste frying oils: Optimization of reaction parameters and determination of fuel properties. *Energy.* [Online]. 2012, **44**(1), pp.347-351. Available from: https://doi.org/10.1016/j.energy.2012.06.024

187. Momma, K. and Izumi, F. VESTA 3 for three-dimensional visualization of crystal, volumetric and morphology data. *Journal of Applied Crystallography.* [Online]. 2011, **44**(6), pp.1272-1276. Available from: https://doi.org/10.1107/S0021889811038970
188. Cornell, R.M. and Schwertmann, U. *The iron oxides: structure, properties, reactions, occurrences and uses.* Hoboken, NJ, USA: John Wiley & Sons, 2003.
189. Huber, D.L. Synthesis, Properties, and Applications of Iron Nanoparticles. *Small.* [Online]. 2005, **1**(5), pp.482-501. [Accessed 2022/01/24]. Available from: https://doi.org/10.1002/smll.200500006
190. Ali, A., Zafar, H., Zia, M., Ul Haq, I., Phull, A.R., Ali, J.S. and Hussain, A. Synthesis, characterization, applications, and challenges of iron oxide nanoparticles. *Nanotechnology, Science and Applications.* [Online]. 2016, **Volume 9**, pp.49-67. Available from: https://doi.org/10.2147/nsa.s99986
191. Wang, A., Li, H., Pan, H., Zhang, H., Xu, F., Yu, Z. and Yang, S. Efficient and green production of biodiesel catalyzed by recyclable biomass-derived magnetic acids. *Fuel Processing Technology.* [Online]. 2018, **181**, pp.259-267. Available from: https://doi.org/10.1016/j.fuproc.2018.10.003
192. Ibrahim, N.A., Rashid, U., Taufiq-Yap, Y.H., Yaw, T.C.S. and Ismail, I. Synthesis of carbonaceous solid acid magnetic catalyst from empty fruit bunch for esterification of palm fatty acid distillate (PFAD). *Energy Conversion and Management.* [Online]. 2019, **195**, pp.480-491. Available from: https://doi.org/10.1016/j.enconman.2019.05.022
193. Scirè, S., Fiorenza, R., Bellardita, M. and Palmisano, L. 21 - Catalytic applications of TiO2. In: Parrino, F. and Palmisano, L. eds. *Titanium Dioxide (Tio₂) and Its Applications*. Amsterdam, The Netherlands: Elsevier, 2021, pp.637-679.
194. Carlucci, C., Degennaro, L. and Luisi, R. Titanium Dioxide as a Catalyst in Biodiesel Production. *Catalysts.* [Online]. 2019, **9**(1). Available from: https://doi.org/10.3390/catal9010075
195. Ropero-Vega, J.L., Aldana-Pérez, A., Gómez, R. and Niño-Gómez, M.E. Sulfated titania [TiO2/SO42−]: A very active solid acid catalyst for the esterification of free fatty acids with ethanol. *Applied Catalysis A: General.* [Online]. 2010, **379**(1), pp.24-29. Available from: https://doi.org/10.1016/j.apcata.2010.02.020
196. Zhao, H., Jiang, P., Dong, Y., Huang, M. and Liu, B. A high-surface-area mesoporous sulfated nano-titania solid superacid catalyst with exposed (101) facets for esterification: facile preparation and catalytic performance. *New Journal of Chemistry.* [Online]. 2014, **38**(9), pp.4541-4548. Available from: https://doi.org/10.1039/c4nj00494a
197. Anuradha, S., Raj, K.J.A., Vijayaraghavan, V.R. and Viswanathan, B. Sulphated Fe2O3-TiO2 catalysed transesterification of soybean oil to biodiesel. *Indian Journal of Chemistry - Section A Inorganic, Physical, Theoretical and Analytical Chemistry.* [Online]. 2014, **53**(12), pp.1493-1499. Available from: https://doi.org/http://nopr.niscair.res.in/handle/123456789/30041
198. Gardy, J., Hassanpour, A., Lai, X. and Ahmed, M.H. Synthesis of Ti(SO4)O solid acid nano-catalyst and its application for biodiesel production from used cooking oil. *Applied Catalysis A: General.* [Online]. 2016, **527**, pp.81-95. Available from: https://doi.org/10.1016/j.apcata.2016.08.031
199. Gardy, J., Hassanpour, A., Lai, X., Ahmed, M.H. and Rehan, M. Biodiesel production from used cooking oil using a novel surface functionalised TiO2 nano-catalyst. *Applied Catalysis B: Environmental.* [Online]. 2017, **207**, pp.297-310. Available from: https://doi.org/10.1016/j.apcatb.2017.01.080
200. Kumar, P., Kumar, R. and Singh, R. Transition Metals Doped ZnO Nanoparticles for 3D Printing: A State of the Art Review and Prospective Applications. In: *Reference Module in Materials Science and Materials Engineering*. Amsterdam, The Netherlands: Elsevier, 2020.
201. Borysiewicz, M.A. ZnO as a Functional Material, a Review. *Crystals.* [Online]. 2019, **9**(10). Available from: https://doi.org/10.3390/cryst9100505
202. Sokolov, P.S., Baranov, A.N., Dobrokhotov, Z.V. and Solozhenko, V.L. Synthesis and thermal stability of cubic ZnO in the salt nanocomposites. *Russian Chemical Bulletin.* [Online]. 2010, **59**(2), pp.325-328. Available from: https://doi.org/10.1007/s11172-010-0082-7
203. Karmee, S.K. and Chadha, A. Preparation of biodiesel from crude oil of Pongamia pinnata. *Bioresource Technology.* [Online]. 2005, **96**(13), pp.1425-1429. Available from: https://doi.org/10.1016/j.biortech.2004.12.011
204. Istadi, I., Anggoro, D.D., Buchori, L., Rahmawati, D.A. and Intaningrum, D. Active Acid Catalyst of Sulphated Zinc Oxide for Transesterification of Soybean Oil with Methanol to Biodiesel. *Procedia Environmental Sciences.* [Online]. 2015, **23**, pp.385-393. Available from: https://doi.org/10.1016/j.proenv.2015.01.055
205. Soltani, S., Rashid, U., Al-Resayes, S.I. and Nehdi, I.A. Sulfonated mesoporous ZnO catalyst for methyl esters production. *Journal of Cleaner Production.* [Online]. 2017, **144**, pp.482-491. Available from: https://doi.org/10.1016/j.jclepro.2016.12.128
206. Keiteb, A.S., Saion, E., Zakaria, A. and Soltani, N. Structural and Optical Properties of Zirconia Nanoparticles by Thermal Treatment Synthesis. *Journal of Nanomaterials.* [Online]. 2016, **2016**, p.1913609. Available from: https://doi.org/10.1155/2016/1913609
207. Sun, Y., Ma, S., Du, Y., Yuan, L., Wang, S., Yang, J., Deng, F. and Xiao, F.-S. Solvent-Free Preparation of Nanosized Sulfated Zirconia with Brønsted Acidic Sites from a Simple Calcination. *The Journal of Physical Chemistry B.* [Online]. 2005, **109**(7), pp.2567-2572. Available from: https://doi.org/10.1021/jp046335a
208. Raia, R.Z., da Silva, L.S., Marcucci, S.M.P. and Arroyo, P.A. Biodiesel production from Jatropha curcas L. oil by simultaneous esterification and transesterification using sulphated zirconia. *Catalysis Today.* [Online]. 2017, **289**, pp.105-114. Available from: https://doi.org/10.1016/j.cattod.2016.09.013
209. Jung, K.T. and Bell, A.T. The effects of synthesis and pretreatment conditions on the bulk structure and surface properties of zirconia. *Journal of Molecular Catalysis A: Chemical.* [Online]. 2000, **163**(1), pp.27-42. Available from: https://doi.org/10.1016/S1381-1169(00)00397-6
210. Garcia, C.M., Teixeira, S., Marciniuk, L.L. and Schuchardt, U. Transesterification of soybean oil catalyzed by sulfated zirconia. *Bioresource Technology.* [Online]. 2008, **99**(14), pp.6608-6613. Available from: https://doi.org/10.1016/j.biortech.2007.09.092
211. Muthu, H., Sathyaselvabala, V., Varathachary, T.K., Kirupha Selvaraj, D., Nandagopal, J. and Subramanian, S. Synthesis of biodiesel from Neem oil using sulfated zirconia via tranesterification. *Brazilian Journal of Chemical Engineering.* [Online]. 2010, **27**(4), pp.601-608. Available from: https://doi.org/10.1590/s0104-66322010000400012
212. Guan, D., Fan, M., Wang, J., Zhang, Y., Liu, Q. and Jing, X. Synthesis and properties of magnetic solid superacid: SO42−/ZrO2–B2O3–Fe3O4. *Materials Chemistry and Physics.* [Online]. 2010, **122**(1), pp.278-283. Available from: https://doi.org/10.1016/j.matchemphys.2010.02.049

213. Yee, K.F., Lee, K.T., Ceccato, R. and Abdullah, A.Z. Production of biodiesel from Jatropha curcas L. oil catalyzed by SO42-/ZrO2 catalyst: Effect of interaction between process variables. *Bioresource Technology.* [Online]. 2011, **102**(5), pp.4285-4289. Available from: https://doi.org/10.1016/j.biortech.2010.12.048
214. Alhassan, F.H., Rashid, U. and Taufiq-Yap, Y.H. Synthesis of waste cooking oil-based biodiesel via effectual recyclable bi-functional Fe2O3MnOSO42−/ZrO2 nanoparticle solid catalyst. *Fuel.* [Online]. 2015, **142**, pp.38-45. Available from: https://doi.org/10.1016/j.fuel.2014.10.038
215. Marczewski, M., Jakubiak, A., Marczewska, H., Frydrych, A., Gontarz, M. and Śnieguła, A. Acidity of sulfated oxides: Al2O3, TiO2 and SiO2. Application of test reactions. *Physical Chemistry Chemical Physics.* [Online]. 2004, **6**(9), pp.2513-2522. Available from: https://doi.org/10.1039/B400625A
216. Narayan, R., Nayak, U.Y., Raichur, A.M. and Garg, S. Mesoporous Silica Nanoparticles: A Comprehensive Review on Synthesis and Recent Advances. *Pharmaceutics.* [Online]. 2018, **10**(3), p.118. Available from: https://doi.org/10.3390/pharmaceutics10030118
217. López, D.E., Goodwin, J.G., Bruce, D.A. and Furuta, S. Esterification and transesterification using modified-zirconia catalysts. *Applied Catalysis A: General.* [Online]. 2008, **339**(1), pp.76-83. Available from: https://doi.org/10.1016/j.apcata.2008.01.009
218. Yang, H., Lu, R. and Wang, L. Study of preparation and properties on solid superacid sulfated titania–silica nanomaterials. *Materials Letters.* [Online]. 2003, **57**(5), pp.1190-1196. Available from: https://doi.org/10.1016/S0167-577X(02)00954-0
219. Mbaraka, I.K., McGuire, K.J. and Shanks, B.H. Acidic Mesoporous Silica for the Catalytic Conversion of Fatty Acids in Beef Tallow. *Industrial & Engineering Chemistry Research.* [Online]. 2006, **45**(9), pp.3022-3028. Available from: https://doi.org/10.1021/ie0601089
220. Dhainaut, J., Dacquin, J.-P., Lee, A.F. and Wilson, K. Hierarchical macroporous–mesoporous SBA-15 sulfonic acidcatalysts for biodiesel synthesis. *Green Chem.* [Online]. 2010, **12**(2), pp.296-303. Available from: https://doi.org/10.1039/b919341c
221. Melero, J.A., Bautista, L.F., Morales, G., Iglesias, J. and Sánchez-Vázquez, R. Biodiesel production from crude palm oil using sulfonic acid-modified mesostructured catalysts. *Chemical Engineering Journal.* [Online]. 2010, **161**(3), pp.323-331. Available from: https://doi.org/10.1016/j.cej.2009.12.037
222. Dacquin, J.P., Lee, A.F., Pirez, C. and Wilson, K. Pore-expanded SBA-15 sulfonic acid silicas for biodiesel synthesis. *Chem. Commun.* [Online]. 2012, **48**(2), pp.212-214. Available from: https://doi.org/10.1039/c1cc14563k
223. Valle-Vigón, P., Sevilla, M. and Fuertes, A.B. Sulfonated mesoporous silica–carbon composites and their use as solid acid catalysts. *Applied Surface Science.* [Online]. 2012, **261**, pp.574-583. Available from: https://doi.org/10.1016/j.apsusc.2012.08.059
224. Shao, G.N., Sheikh, R., Hilonga, A., Lee, J.E., Park, Y.-H. and Kim, H.T. Biodiesel production by sulfated mesoporous titania–silica catalysts synthesized by the sol–gel process from less expensive precursors. *Chemical Engineering Journal.* [Online]. 2013, **215-216**, pp.600-607. Available from: https://doi.org/10.1016/j.cej.2012.11.059
225. Vieira, S.S., Magriotis, Z.M., Santos, N.A., Saczk, A.A., Hori, C.E. and Arroyo, P.A. Biodiesel production by free fatty acid esterification using Lanthanum (La3+) and HZSM-5 based catalysts. *Bioresour Technol.* [Online]. 2013, **133**, pp.248-255. Available from: https://doi.org/10.1016/j.biortech.2013.01.107
226. Wang, H., Covarrubias, J., Prock, H., Wu, X., Wang, D. and Bossmann, S.H. Acid-Functionalized Magnetic Nanoparticle as Heterogeneous Catalysts for Biodiesel Synthesis. *The Journal of Physical Chemistry C.* [Online]. 2015, **119**(46), pp.26020-26028. Available from: https://doi.org/10.1021/acs.jpcc.5b08743
227. Yi, Q., Zhang, J., Zhang, X., Feng, J. and Li, W. Synthesis of SO42−/Zr-SBA-15 catalyst for the transesterification of waste cooking oil as a bio-flotation agent in coal flotation. *Fuel.* [Online]. 2015, **143**, pp.390-398. Available from: https://doi.org/10.1016/j.fuel.2014.11.065
228. Isaacs, M.A., Parlett, C.M.A., Robinson, N., Durndell, L.J., Manayil, J.C., Beaumont, S.K., Jiang, S., Hondow, N.S., Lamb, A.C., Jampaiah, D., Johns, M.L., Wilson, K. and Lee, A.F. A spatially orthogonal hierarchically porous acid–base catalyst for cascade and antagonistic reactions. *Nature Catalysis.* [Online]. 2020, **3**(11), pp.921-931. Available from: https://doi.org/10.1038/s41929-020-00526-5
229. Timofeeva, M.N. Acid catalysis by heteropoly acids. *Applied Catalysis A: General.* [Online]. 2003, **256**(1), pp.19-35. Available from: https://doi.org/10.1016/S0926-860X(03)00386-7
230. Okuhara, T., Mizuno, N. and Misono, M. Catalytic Chemistry of Heteropoly Compounds. In: Eley, D.D., Haag, W.O. and Gates, B. eds. *Advances in Catalysis*. Academic Press, 1996, pp.113-252.
231. Pesaresi, L., Brown, D.R., Lee, A.F., Montero, J.M., Williams, H. and Wilson, K. Cs-doped H4SiW12O40 catalysts for biodiesel applications. *Applied Catalysis A: General.* [Online]. 2009, **360**(1), pp.50-58. Available from: https://doi.org/10.1016/j.apcata.2009.03.003
232. Narasimharao, K., Brown, D.R., Lee, A.F., Newman, A.D., Siril, P.F., Tavener, S.J. and Wilson, K. Structure–activity relations in Cs-doped heteropolyacid catalysts for biodiesel production. *Journal of Catalysis.* [Online]. 2007, **248**(2), pp.226-234. Available from: https://doi.org/10.1016/j.jcat.2007.02.016
233. Da Silva, M.J., Vilanculo, C.B., Teixeira, M.G. and Julio, A.A. Catalysis of vegetable oil transesterification by Sn(II)-exchanged Keggin heteropolyacids: bifunctional solid acid catalysts. *Reaction Kinetics, Mechanisms and Catalysis.* [Online]. 2017, **122**(2), pp.1011-1030. Available from: https://doi.org/10.1007/s11144-017-1258-z
234. Zhang, D., Zhang, X., Li, Y., Wang, S., Wang, X. and Jiang, Z. Incorporation of Ce(3+) ions into dodecatungstophosphoric acid for the production of biodiesel from waste cooking oil. *Mater Sci Eng C Mater Biol Appl.* [Online]. 2018, **92**, pp.922-931. Available from: https://doi.org/10.1016/j.msec.2018.07.047
235. Al-Shammari, B., A. Alsulami, Q. and Narasimharao, K. Lanthanum Exchanged Keggin Structured Heteropoly Compounds for Biodiesel Production. *Catalysts.* [Online]. 2019, **9**(12). Available from: https://doi.org/10.3390/catal9120979
236. Jeon, Y., Chi, W.S., Hwang, J., Kim, D.H., Kim, J.H. and Shul, Y.-G. Core-shell nanostructured heteropoly acid-functionalized metal-organic frameworks: Bifunctional heterogeneous catalyst for efficient biodiesel production. *Applied Catalysis B: Environmental.* [Online]. 2019, **242**, pp.51-59. Available from: https://doi.org/10.1016/j.apcatb.2018.09.071
237. Kulkarni, M.G., Gopinath, R., Meher, L.C. and Dalai, A.K. Solid acid catalyzed biodiesel production by simultaneous esterification and transesterification. *Green Chemistry.* [Online]. 2006, **8**(12), pp.1056-1062. Available from: https://doi.org/10.1039/b605713f
238. Malani, R.S., Choudhury, H.A. and Moholkar, V.S. Chapter 13 - Waste biorefinery based on waste carbon sources: case study of biodiesel production using carbon based catalysts and mixed feedstocks of nonedible and waste oils. In: Bhaskar, T., Pandey, A., Rene, E.R. and Tsang, D.C.W. eds. *Waste Biorefinery*. Amsterdam, The Netherlands: Elsevier, 2020, pp.337-378.

239. Mahto, T.K., Jain, R., Chandra, S., Roy, D., Mahto, V. and Sahu, S.K. Single step synthesis of sulfonic group bearing graphene oxide: A promising carbo-nano material for biodiesel production. *Journal of Environmental Chemical Engineering.* [Online]. 2016, **4**(3), pp.2933-2940. Available from: https://doi.org/10.1016/j.jece.2016.06.006
240. Gohain, M., Laskar, K., Paul, A.K., Daimary, N., Maharana, M., Goswami, I.K., Hazarika, A., Bora, U. and Deka, D. Carica papaya stem: A source of versatile heterogeneous catalyst for biodiesel production and C–C bond formation. *Renewable Energy.* [Online]. 2020, **147**, pp.541-555. Available from: https://doi.org/10.1016/j.renene.2019.09.016
241. Poonjarernsilp, C., Sano, N. and Tamon, H. Hydrothermally sulfonated single-walled carbon nanohorns for use as solid catalysts in biodiesel production by esterification of palmitic acid. *Applied Catalysis B: Environmental.* [Online]. 2014, **147**, pp.726-732. Available from: https://doi.org/10.1016/j.apcatb.2013.10.006
242. Stellwagen, D.R., van der Klis, F., van Es, D.S., de Jong, K.P. and Bitter, J.H. Functionalized Carbon Nanofibers as Solid-Acid Catalysts for Transesterification. *ChemSusChem.* [Online]. 2013, **6**(9), pp.1668-1672. [Accessed 2021/08/22]. Available from: https://doi.org/10.1002/cssc.201300372
243. Tamborini, L.H., Casco, M.E., Militello, M.P., Silvestre-Albero, J., Barbero, C.A. and Acevedo, D.F. Sulfonated porous carbon catalysts for biodiesel production: Clear effect of the carbon particle size on the catalyst synthesis and properties. *Fuel Processing Technology.* [Online]. 2016, **149**, pp.209-217. Available from: https://doi.org/10.1016/j.fuproc.2016.04.006
244. Guan, Q., Li, Y., Chen, Y., Shi, Y., Gu, J., Li, B., Miao, R., Chen, Q. and Ning, P. Sulfonated multi-walled carbon nanotubes for biodiesel production through triglycerides transesterification. *RSC Advances.* [Online]. 2017, **7**(12), pp.7250-7258. Available from: https://doi.org/10.1039/c6ra28067f
245. Shu, Q., Tang, G., Liu, F., Zou, W., He, J., Zhang, C. and Zou, L. Study on the preparation, characterization of a novel solid Lewis acid Al3+-SO42−/MWCNTs catalyst and its catalytic performance for the synthesis of biodiesel via esterification reaction of oleic acid and methanol. *Fuel.* [Online]. 2017, **209**, pp.290-298. Available from: https://doi.org/10.1016/j.fuel.2017.07.113
246. Nongbe, M.C., Ekou, T., Ekou, L., Yao, K.B., Le Grognec, E. and Felpin, F.-X. Biodiesel production from palm oil using sulfonated graphene catalyst. *Renewable Energy.* [Online]. 2017, **106**, pp.135-141. Available from: https://doi.org/10.1016/j.renene.2017.01.024
247. Tafesh, A. and Basheer, S. Pretreatment Methods in Biodiesel Production Processes. In: Fang, Z. ed. *Pretreatment Techniques for Biofuels and Biorefineries*. Berlin, Heidelberg: Springer Berlin Heidelberg, 2013, pp.417-434.
248. Gardy, J. *Biodiesel production from used cooking oil using novel solid acid catalysts*. PhD thesis, University of Leeds, 2017.
249. Tadic, M., Panjan, M., Damnjanovic, V. and Milosevic, I. Magnetic properties of hematite (α-Fe2O3) nanoparticles prepared by hydrothermal synthesis method. *Applied Surface Science.* [Online]. 2014, **320**, pp.183-187. Available from: https://doi.org/10.1016/j.apsusc.2014.08.193
250. Meijer, J.M. and Rossi, L. Preparation, properties, and applications of magnetic hematite microparticles. *Soft Matter.* [Online]. 2021, **17**(9), pp.2354-2368. Available from: https://doi.org/10.1039/d0sm01977a
251. Rezki, B., Essamlali, Y., Amadine, O., Sair, S., Aadil, M. and Zahouily, M. Microwave-driven oleic acid esterification over chlorosulfonic acid-treated hydroxyapatite: synergism for intensified biodiesel production. *RSC Advances.* [Online]. 2024, **14**(45), pp.33019-33033. Available from: https://doi.org/10.1039/d4ra05862c
252. Banerjee, S., Sahani, S. and Chandra Sharma, Y. Process dynamic investigations and emission analyses of biodiesel produced using Sr–Ce mixed metal oxide heterogeneous catalyst. *Journal of Environmental Management.* [Online]. 2019, **248**, article no: 109218 [no pagination]. Available from: https://doi.org/10.1016/j.jenvman.2019.06.119
253. Sulaiman, N.F., Lee, S.L., Toemen, S. and Bakar, W.A.W.A. Physicochemical characteristics of Cu/Zn/γ-Al2O3 catalyst and its mechanistic study in transesterification for biodiesel production. *Renewable Energy.* [Online]. 2020, **156**, pp.142-157. Available from: https://doi.org/10.1016/j.renene.2020.04.021
254. Sulaiman, N.F., Wan Abu Bakar, W.A., Toemen, S., Kamal, N.M. and Nadarajan, R. In depth investigation of bi-functional, Cu/Zn/γ-Al2O3 catalyst in biodiesel production from low-grade cooking oil: Optimization using response surface methodology. *Renewable Energy.* [Online]. 2019, **135**, pp.408-416. Available from: https://doi.org/10.1016/j.renene.2018.11.111
255. Malani, R.S., Shinde, V., Ayachit, S., Goyal, A. and Moholkar, V.S. Ultrasound–assisted biodiesel production using heterogeneous base catalyst and mixed non–edible oils. *Ultrasonics Sonochemistry.* [Online]. 2019, **52**, pp.232-243. Available from: https://doi.org/10.1016/j.ultsonch.2018.11.021
256. Jamil, F., Al-Riyami, M., Al-Haj, L., Al-Muhtaseb, A.H., Myint, M.T.Z., Baawain, M. and Al-Abri, M. Waste Balanites aegyptiaca seed oil as a potential source for biodiesel production in the presence of a novel mixed metallic oxide catalyst. *International Journal of Energy Research.* [Online]. 2020, **45**(12), pp.17189-17202. Available from: https://doi.org/10.1002/er.5609
257. Boz, N., Degirmenbasi, N. and Kalyon, D.M. Conversion of biomass to fuel: Transesterification of vegetable oil to biodiesel using KF loaded nano-γ-Al2O3 as catalyst. *Applied Catalysis B: Environmental.* [Online]. 2009, **89**(3), pp.590-596. Available from: https://doi.org/10.1016/j.apcatb.2009.01.026
258. Dionicio-Navarrete, M., Dinorah Arrieta-Gonzalez, C., Quinto-Hernandez, A., Casales-Diaz, M., Zuñiga-Diaz, J., Porcayo-Calderon, J. and Martinez-Gomez, L. Synthesis of NdAlO3 nanoparticles and evaluation of the catalytic capacity for biodiesel synthesis. *Nanomaterials.* [Online]. 2019, **9**(11), article no: 1545 [no pagination]. Available from: https://doi.org/10.3390/nano9111545
259. Nayebzadeh, H., Saghatoleslami, N., Haghighi, M. and Tabasizadeh, M. Catalytic Activity of KOH–CaO–Al2O3 Nanocomposites in Biodiesel Production: Impact of Preparation Method. *International Journal of Self-Propagating High-Temperature Synthesis.* [Online]. 2019, **28**(1), pp.18-27. Available from: https://doi.org/10.3103/s1061386219010102
260. Jeon, H., Kim, D.J., Kim, S.J. and Kim, J.H. Synthesis of mesoporous MgO catalyst templated by a PDMS–PEO comb-like copolymer for biodiesel production. *Fuel Processing Technology.* [Online]. 2013, **116**, pp.325-331. Available from: https://doi.org/10.1016/j.fuproc.2013.07.013
261. Albuquerque, M.C.G., Azevedo, D.C.S., Cavalcante, C.L., Santamaría-González, J., Mérida-Robles, J.M., Moreno-Tost, R., Rodríguez-Castellón, E., Jiménez-López, A. and Maireles-Torres, P. Transesterification of ethyl butyrate with methanol using MgO/CaO catalysts. *Journal of Molecular Catalysis A: Chemical.* [Online]. 2009, **300**(1), pp.19-24. Available from: https://doi.org/10.1016/j.molcata.2008.10.033
262. Rasouli, H. and Esmaeili, H. Characterization of MgO nanocatalyst to produce biodiesel from goat fat using transesterification process. *3 Biotech.* [Online]. 2019, **9**(11), article no: 429 [no pagination]. Available from: https://doi.org/10.1007/s13205-019-1963-6
263. Kaur, M. and Ali, A. Lithium ion impregnated calcium oxide as nano catalyst for the biodiesel production from karanja and jatropha oils. *Renewable Energy.* [Online]. 2011, **36**(11), pp.2866-2871. Available from: https://doi.org/10.1016/j.renene.2011.04.014

264. Wang, A., Li, H., Zhang, H., Pan, H. and Yang, S. Efficient Catalytic Production of Biodiesel with Acid-Base Bifunctional Rod-Like Ca-B Oxides by the Sol-Gel Approach. *Materials.* [Online]. 2018, **12**(1), p.83. Available from: https://doi.org/10.3390/ma12010083
265. Çakırca, E.E., N Tekin, G., İlgen, O. and N Akın, A. Catalytic activity of CaO-based catalyst in transesterification of microalgae oil with methanol. *Energy & Environment.* [Online]. 2018, **30**(1), pp.176-187. [Accessed 2020/11/27]. Available from: https://doi.org/10.1177/0958305x18787317
266. Ngamcharussrivichai, C., Totarat, P. and Bunyakiat, K. Ca and Zn mixed oxide as a heterogeneous base catalyst for transesterification of palm kernel oil. *Applied Catalysis A: General.* [Online]. 2008, **341**(1), pp.77-85. Available from: https://doi.org/10.1016/j.apcata.2008.02.020
267. Ali Bashah, N.A., Luin, A., Jalaluddin, I.A., Shahhaizad, I.A., Ismail, N.F. and Wan Kamis, W.Z. Characteristics of chromium based mixed oxide catalyst in biodiesel production. In: *Journal of Physics: Conference Series*, 2019.
268. Jamil, F., Al-Muhtaseb, A.a., Myint, M.T.Z., Al-Hinai, M., Al-Haj, L., Baawain, M., Al-Abri, M., Kumar, G. and Atabani, A.E. Biodiesel production by valorizing waste Phoenix dactylifera L. Kernel oil in the presence of synthesized heterogeneous metallic oxide catalyst (Mn@MgO-ZrO2). *Energy Conversion and Management.* [Online]. 2018, **155**, pp.128-137. Available from: https://doi.org/10.1016/j.enconman.2017.10.064
269. Kawashima, A., Matsubara, K. and Honda, K. Development of heterogeneous base catalysts for biodiesel production. *Bioresource Technology.* [Online]. 2008, **99**(9), pp.3439-3443. Available from: https://doi.org/10.1016/j.biortech.2007.08.009
270. Sierra-Cantor, J.F., Parra-Santiago, J.J. and Guerrero-Fajardo, C.A. Leaching and reusing analysis of calcium–zinc mixed oxides as heterogeneous catalysts in the biodiesel production from refined palm oil. *International Journal of Environmental Science and Technology.* [Online]. 2019, **16**(2), pp.643-654. Available from: https://doi.org/10.1007/s13762-018-1710-2
271. Kim, H.-J., Kang, B.-S., Kim, M.-J., Park, Y.M., Kim, D.-K., Lee, J.-S. and Lee, K.-Y. Transesterification of vegetable oil to biodiesel using heterogeneous base catalyst. *Catalysis Today.* [Online]. 2004, **93-95**, pp.315-320. Available from: https://doi.org/10.1016/j.cattod.2004.06.007
272. Tantirungrotechai, J., Chotmongkolsap, P. and Pohmakotr, M. Synthesis, characterization, and activity in transesterification of mesoporous Mg–Al mixed-metal oxides. *Microporous and Mesoporous Materials.* [Online]. 2010, **128**(1), pp.41-47. Available from: https://doi.org/10.1016/j.micromeso.2009.08.001
273. Taufiq-Yap, Y.H., Lee, H.V., Yunus, R. and Juan, J.C. Transesterification of non-edible Jatropha curcas oil to biodiesel using binary Ca–Mg mixed oxide catalyst: Effect of stoichiometric composition. *Chemical Engineering Journal.* [Online]. 2011, **178**, pp.342-347. Available from: https://doi.org/10.1016/j.cej.2011.10.019
274. Mguni, L.L., Meijboom, R. and Jalama, K. Biodiesel Production over nanoMgO Supported on Titania. *International Journal of Materials and Metallurgical Engineering.* [Online]. 2012, **6**, pp.380 - 384. Available from: https://doi.org/10.5281/zenodo.1080404
275. Rashtizadeh, E., Farzaneh, F. and Talebpour, Z. Synthesis and characterization of Sr3Al2O6 nanocomposite as catalyst for biodiesel production. *Bioresource Technology.* [Online]. 2014, **154**, pp.32-37. Available from: https://doi.org/10.1016/j.biortech.2013.12.014
276. Pasupulety, N., Rempel, G.L. and Ng, F.T.T. Studies on Mg-Zn mixed oxide catalyst for biodiesel production. *Applied Catalysis A: General.* [Online]. 2015, **489**, pp.77-85. Available from: https://doi.org/10.1016/j.apcata.2014.10.015
277. Navas, M.B., Ruggera, J.F., Lick, I.D. and Casella, M.L. A sustainable process for biodiesel production using Zn/Mg oxidic species as active, selective and reusable heterogeneous catalysts. *Bioresources and Bioprocessing.* [Online]. 2020, **7**(1), article no: 4 [no pagination]. Available from: https://doi.org/10.1186/s40643-019-0291-3
278. Singh, R., Kumar, A. and Chandra Sharma, Y. Biodiesel Production from Microalgal Oil Using Barium-Calcium-Zinc Mixed Oxide Base Catalyst: Optimization and Kinetic Studies. *Energy and Fuels.* [Online]. 2019, **33**(2), pp.1175-1184. Available from: https://doi.org/10.1021/acs.energyfuels.8b03461
279. Alonso, D.M., Mariscal, R., Granados, M.L. and Maireles-Torres, P. Biodiesel preparation using Li/CaO catalysts: Activation process and homogeneous contribution. *Catalysis Today.* [Online]. 2009, **143**(1), pp.167-171. Available from: https://doi.org/10.1016/j.cattod.2008.09.021
280. Marinković, D.M., Avramović, J.M., Stanković, M.V., Stamenković, O.S., Jovanović, D.M. and Veljković, V.B. Synthesis and characterization of spherically-shaped CaO/γ-Al2O3 catalyst and its application in biodiesel production. *Energy Conversion and Management.* [Online]. 2017, **144**, pp.399-413. Available from: https://doi.org/10.1016/j.enconman.2017.04.079
281. Rahmani Vahid, B. and Haghighi, M. Biodiesel production from sunflower oil over MgO/MgAl2O4 nanocatalyst: Effect of fuel type on catalyst nanostructure and performance. *Energy Conversion and Management.* [Online]. 2017, **134**, pp.290-300. Available from: https://doi.org/10.1016/j.enconman.2016.12.048
282. Verziu, M., Cojocaru, B., Hu, J., Richards, R., Ciuculescu, C., Filip, P. and Parvulescu, V.I. Sunflower and rapeseed oil transesterification to biodiesel over different nanocrystalline MgO catalysts. *Green Chemistry.* [Online]. 2008, **10**(4), pp.373-381. Available from: https://doi.org/10.1039/b712102d
283. Feyzi, M. and Shahbazi, E. Catalytic performance and characterization of Cs–Ca/SiO2–TiO2 nanocatalysts for biodiesel production. *Journal of Molecular Catalysis A: Chemical.* [Online]. 2015, **404-405**, pp.131-138. Available from: https://doi.org/10.1016/j.molcata.2015.04.018
284. Dai, Y.M., Li, Y.Y., Lin, J.H., Kao, I.H., Lin, Y.J. and Chen, C.C. Applications of M2ZrO2 (M = Li, Na, K) composite as a catalyst for biodiesel production. *Fuel.* [Online]. 2021, **286**, article no: 119392 [no pagination]. Available from: https://doi.org/10.1016/j.fuel.2020.119392
285. Wen, Z., Yu, X., Tu, S.-T., Yan, J. and Dahlquist, E. Biodiesel production from waste cooking oil catalyzed by TiO2–MgO mixed oxides. *Bioresource Technology.* [Online]. 2010, **101**(24), pp.9570-9576. Available from: https://doi.org/10.1016/j.biortech.2010.07.066
286. Papargyriou, D., Broumidis, E., de Vere-Tucker, M., Gavrielides, S., Hilditch, P., Irvine, J.T.S. and Bonaccorso, A.D. Investigation of solid base catalysts for biodiesel production from fish oil. *Renewable Energy.* [Online]. 2019, **139**, pp.661-669. Available from: https://doi.org/10.1016/j.renene.2019.02.124
287. Singha Roy, A., Kesavan Pillai, S. and Ray, S.S. Layered Double Hydroxides for Sustainable Agriculture and Environment: An Overview. *ACS Omega.* [Online]. 2022, **7**(24), pp.20428-20440. Available from: https://doi.org/10.1021/acsomega.2c01405
288. Xu, M. and Wei, M. Layered Double Hydroxide-Based Catalysts: Recent Advances in Preparation, Structure, and Applications. *Advanced Functional Materials.* [Online]. 2018, **28**(47), p.1802943. [Accessed 2025/03/15]. Available from: https://doi.org/10.1002/adfm.201802943

289. Gabriel, R., Carvalho, S.H.V.d., Duarte, J.L.d.S., Oliveira, L.M.T.M., Giannakoudakis, D.A., Triantafyllidis, K.S., Soletti, J.I. and Meili, L. Mixed metal oxides derived from layered double hydroxide as catalysts for biodiesel production. *Applied Catalysis A: General.* [Online]. 2022, **630**, p.118470. Available from: https://doi.org/10.1016/j.apcata.2021.118470
290. Altalhi, A.A., Mohamed, E.A. and Negm, N.A. Recent advances in layered double hydroxide (LDH)-based materials: fabrication, modification strategies, characterization, promising environmental catalytic applications, and prospective aspects. *Energy Advances.* [Online]. 2024, **3**(9), pp.2136-2151. Available from: https://doi.org/10.1039/D4YA00272E
291. Liu, Y., Lotero, E., Goodwin, J.G. and Mo, X. Transesterification of poultry fat with methanol using Mg–Al hydrotalcite derived catalysts. *Applied Catalysis A: General.* [Online]. 2007, **331**, pp.138-148. Available from: https://doi.org/10.1016/j.apcata.2007.07.038
292. Zeng, H.-y., Feng, Z., Deng, X. and Li, Y.-q. Activation of Mg–Al hydrotalcite catalysts for transesterification of rape oil. *Fuel.* [Online]. 2008, **87**(13), pp.3071-3076. Available from: https://doi.org/10.1016/j.fuel.2008.04.001
293. Nur Fazira Edlina, I., Nazrizawati, A.T., Erma Hafiza, I.A.Z. and Noraini, H. MgAl mixed oxide derived alkali-free hydrotalcite for transesterification of waste cooking oil to biodiesel. *ASM Science Journal.* [Online]. 2020, **13**, article no: 416 [no pagination]. Available from: https://doi.org/10.32802/asmscj.2020.416
294. Gutiérrez-Ortega, N., Ramos-Ramírez, E., Serafín-Muñoz, A., Zamorategui-Molina, A. and Monjaraz-Vallejo, J. Use of Co/Fe-Mixed oxides as heterogeneous catalysts in obtaining biodiesel. *Catalysts.* [Online]. 2019, **9**(5), article no: 403 [no pagination]. Available from: https://doi.org/10.3390/catal9050403
295. Hájek, M., Vávra, A. and Mück, J. Butanol as a co-solvent for transesterification of rapeseed oil by methanol under homogeneous and heterogeneous catalyst. *Fuel.* [Online]. 2020, **277**, article no: 118239 [no pagination]. Available from: https://doi.org/10.1016/j.fuel.2020.118239
296. Li, E., Xu, Z.P. and Rudolph, V. MgCoAl–LDH derived heterogeneous catalysts for the ethanol transesterification of canola oil to biodiesel. *Applied Catalysis B: Environmental.* [Online]. 2009, **88**(1), pp.42-49. Available from: https://doi.org/10.1016/j.apcatb.2008.09.022
297. Trakarnpruk, W. and Porntangjitlikit, S. Palm oil biodiesel synthesized with potassium loaded calcined hydrotalcite and effect of biodiesel blend on elastomer properties. *Renewable Energy.* [Online]. 2008, **33**(7), pp.1558-1563. Available from: https://doi.org/10.1016/j.renene.2007.08.003
298. Shumaker, J.L., Crofcheck, C., Tackett, S.A., Santillan-Jimenez, E., Morgan, T., Ji, Y., Crocker, M. and Toops, T.J. Biodiesel synthesis using calcined layered double hydroxide catalysts. *Applied Catalysis B: Environmental.* [Online]. 2008, **82**(1), pp.120-130. Available from: https://doi.org/10.1016/j.apcatb.2008.01.010
299. Rosset, M. and Perez-Lopez, O.W. FTIR spectroscopy analysis for monitoring biodiesel production by heterogeneous catalyst. *Vibrational Spectroscopy.* [Online]. 2019, **105**, article no: 102990 [no pagination]. Available from: https://doi.org/10.1016/j.vibspec.2019.102990
300. Lima-Corrêa, R.A.B., Castro, C.S., Damasceno, A.S. and Assaf, J.M. The enhanced activity of base metal modified MgAl mixed oxides from sol-gel hydrotalcite for ethylic transesterification. *Renewable Energy.* [Online]. 2020, **146**, pp.1984-1990. Available from: https://doi.org/10.1016/j.renene.2019.08.047
301. Sedaghat-Hoor, S. and Anbia, M. ZnO impregnated MgAl(O) catalyst with improved properties for biodiesel production: The influence of synthesis method on stability and reusability. *Particulate Science and Technology.* [Online]. 2019, **37**(7), pp.893-899. Available from: https://doi.org/10.1080/02726351.2018.1461153
302. Xie, W. and Zhao, L. Heterogeneous CaO–MoO3–SBA-15 catalysts for biodiesel production from soybean oil. *Energy Conversion and Management.* [Online]. 2014, **79**, pp.34-42. Available from: https://doi.org/10.1016/j.enconman.2013.11.041
303. Malhotra, R. and Ali, A. Lithium-doped ceria supported SBA−15 as mesoporous solid reusable and heterogeneous catalyst for biodiesel production via simultaneous esterification and transesterification of waste cottonseed oil. *Renewable Energy.* [Online]. 2018, **119**, pp.32-44. Available from: https://doi.org/10.1016/j.renene.2017.12.001
304. Malhotra, R. and Ali, A. 5-Na/ZnO doped mesoporous silica as reusable solid catalyst for biodiesel production via transesterification of virgin cottonseed oil. *Renewable Energy.* [Online]. 2019, **133**, pp.606-619. Available from: https://doi.org/10.1016/j.renene.2018.10.055
305. Liu, H., Su, L., Shao, Y. and Zou, L. Biodiesel production catalyzed by cinder supported CaO/KF particle catalyst. *Fuel.* [Online]. 2012, **97**, pp.651-657. Available from: https://doi.org/10.1016/j.fuel.2012.02.002
306. Prabu, M., Manikandan, M., Kandasamy, P., Kalaivani, P.R., Rajendiran, N. and Raja, T. Synthesis of Biodiesel using the Mg/Al/Zn Hydrotalcite/SBA-15 Nanocomposite Catalyst. *ACS Omega.* [Online]. 2019, **4**(2), pp.3500-3507. Available from: https://doi.org/10.1021/acsomega.8b02547
307. Xie, W. and Fan, M. Biodiesel production by transesterification using tetraalkylammonium hydroxides immobilized onto SBA-15 as a solid catalyst. *Chemical Engineering Journal.* [Online]. 2014, **239**, pp.60-67. Available from: https://doi.org/10.1016/j.cej.2013.11.009
308. Russbueldt, B.M.E. and Hoelderich, W.F. New sulfonic acid ion-exchange resins for the preesterification of different oils and fats with high content of free fatty acids. *Applied Catalysis A: General.* [Online]. 2009, **362**(1), pp.47-57. Available from: https://doi.org/10.1016/j.apcata.2009.04.019
309. Roslan, N.A., Abdullah, N. and Abidin, S.Z. The synthesis of sulphonated hypercrosslinked exchange resin for free fatty acid esterification. *Comptes Rendus Chimie.* [Online]. 2019, **22**(11), pp.761-770. Available from: https://doi.org/10.1016/j.crci.2019.08.004
310. Oliveira, E., Costa, L., Thomaz, D., Costa, M. and Maria, L. Transesterification of Soybean Oil to Biodiesel by Anionic and Cationic Ion Exchange Resins. *Revista Virtual de Química.* [Online]. 2015, **7**, pp.2314-2333. Available from: https://doi.org/10.5935/1984-6835.20150138
311. Shibasaki-Kitakawa, N., Honda, H., Kuribayashi, H., Toda, T., Fukumura, T. and Yonemoto, T. Biodiesel production using anionic ion-exchange resin as heterogeneous catalyst. *Bioresource Technology.* [Online]. 2007, **98**(2), pp.416-421. Available from: https://doi.org/10.1016/j.biortech.2005.12.010
312. Keneni, Y.G., Hvoslef-Eide, A.K. and Marchetti, J.M. Optimization of the production of biofuel form Jatropha oil using a recyclable anion-exchange resin. *Fuel.* [Online]. 2020, **278**, p.118253. Available from: https://doi.org/10.1016/j.fuel.2020.118253

313. Kouzu, M., Nakagaito, A. and Hidaka, J.-s. Pre-esterification of FFA in plant oil transesterified into biodiesel with the help of solid acid catalysis of sulfonated cation-exchange resin. *Applied Catalysis A: General.* [Online]. 2011, **405**(1), pp.36-44. Available from: https://doi.org/10.1016/j.apcata.2011.07.026
314. Son, S.M., Kimura, H. and Kusakabe, K. Esterification of oleic acid in a three-phase, fixed-bed reactor packed with a cation exchange resin catalyst. *Bioresource Technology.* [Online]. 2011, **102**(2), pp.2130-2132. Available from: https://doi.org/10.1016/j.biortech.2010.08.089
315. Feng, Y., He, B., Cao, Y., Li, J., Liu, M., Yan, F. and Liang, X. Biodiesel production using cation-exchange resin as heterogeneous catalyst. *Bioresource Technology.* [Online]. 2010, **101**(5), pp.1518-1521. Available from: https://doi.org/10.1016/j.biortech.2009.07.084
316. Li, J., Fu, Y.-J., Qu, X.-J., Wang, W., Luo, M., Zhao, C.-J. and Zu, Y.-G. Biodiesel production from yellow horn (Xanthoceras sorbifolia Bunge.) seed oil using ion exchange resin as heterogeneous catalyst. *Bioresource Technology.* [Online]. 2012, **108**, pp.112-118. Available from: https://doi.org/10.1016/j.biortech.2011.12.129
317. Lei, Z., Chen, B., Koo, Y.-M. and MacFarlane, D.R. Introduction: Ionic Liquids. *Chemical Reviews.* [Online]. 2017, **117**(10), pp.6633-6635. Available from: https://doi.org/10.1021/acs.chemrev.7b00246
318. Mehnert, C.P., Mozeleski, E.J. and Cook, R.A. Supported ionic liquid catalysis investigated for hydrogenation reactions. *Chemical Communications.* [Online]. 2002, (24), pp.3010-3011. Available from: https://doi.org/10.1039/B210214E
319. Zhang, Y. and Sun, S. A review on biodiesel production using basic ionic liquids as catalysts. *Industrial Crops and Products.* [Online]. 2023, **202**, p.117099. Available from: https://doi.org/10.1016/j.indcrop.2023.117099
320. Zhang, Q., Hu, Y., Li, S., Zhang, M., Wang, Y., Wang, Z., Peng, Y., Wang, M., Li, X. and Pan, H. Recent advances in supported acid/base ionic liquids as catalysts for biodiesel production. *Front Chem.* [Online]. 2022, **10**, p.999607. Available from: https://doi.org/10.3389/fchem.2022.999607
321. Troter, D.Z., Todorović, Z.B., Đokić-Stojanović, D.R., Stamenković, O.S. and Veljković, V.B. Application of ionic liquids and deep eutectic solvents in biodiesel production: A review. *Renewable and Sustainable Energy Reviews.* [Online]. 2016, **61**, pp.473-500. Available from: https://doi.org/10.1016/j.rser.2016.04.011
322. Sun, J., Yang, J., Li, S. and Xu, X. Basic ionic liquid immobilized oxides as heterogeneous catalyst for biodiesel synthesis from waste cooking oil. *Catalysis Communications.* [Online]. 2016, **83**, pp.35-38. Available from: https://doi.org/10.1016/j.catcom.2016.05.002
323. Han, M., Li, Y., Gu, Z., Shi, H., Chen, C., Wang, Q., Wan, H. and Guan, G. Immobilization of thiol-functionalized ionic liquids onto the surface of MIL-101(Cr) frameworks by SCr coordination bond for biodiesel production. *Colloids and Surfaces A: Physicochemical and Engineering Aspects.* [Online]. 2018, **553**, pp.593-600. Available from: https://doi.org/10.1016/j.colsurfa.2018.05.085
324. Ye, C., Qi, Z., Cai, D. and Qiu, T. Design and Synthesis of Ionic Liquid Supported Hierarchically Porous Zr Metal–Organic Framework as a Novel Brønsted–Lewis Acidic Catalyst in Biodiesel Synthesis. *Industrial & Engineering Chemistry Research.* [Online]. 2019, **58**(3), pp.1123-1132. Available from: https://doi.org/10.1021/acs.iecr.8b04107
325. Li, M., Chen, J., Huang, Y., Li, M., Lin, X. and Qiu, T. Reusable and efficient heterogeneous catalysts for biodiesel production from free fatty acids and oils: Self-solidifying hybrid ionic liquids. *Energy.* [Online]. 2020, **211**, p.118631. Available from: https://doi.org/10.1016/j.energy.2020.118631
326. Liang, X. and Yang, J. Synthesis of a novel multi –SO3H functionalized ionic liquid and its catalytic activities for biodiesel synthesis. *Green Chemistry.* [Online]. 2010, **12**(2), pp.201-204. Available from: https://doi.org/10.1039/b922966n
327. Fan, M., Liu, H. and Zhang, P. Ionic liquid on the acidic organic-inorganic hybrid mesoporous material with good acid-water resistance for biodiesel production. *Fuel.* [Online]. 2018, **215**, pp.541-550. Available from: https://doi.org/10.1016/j.fuel.2017.11.085
328. Hosseini, S., Moradi, G.R. and Bahrami, K. Synthesis of a novel stabilized basic ionic liquid through immobilization on boehmite nanoparticles: A robust nanocatalyst for biodiesel production from soybean oil. *Renewable Energy.* [Online]. 2019, **138**, pp.70-78. Available from: https://doi.org/10.1016/j.renene.2019.01.037
329. Ribeiro, B.D., de Castro, A.M., Coelho, M.A. and Freire, D.M. Production and use of lipases in bioenergy: a review from the feedstocks to biodiesel production. *Enzyme Res.* [Online]. 2011, **2011**, p.615803. Available from: https://doi.org/10.4061/2011/615803
330. Ortiz, C., Ferreira, M.L., Barbosa, O., dos Santos, J.C.S., Rodrigues, R.C., Berenguer-Murcia, Á., Briand, L.E. and Fernandez-Lafuente, R. Novozym 435: the "perfect" lipase immobilized biocatalyst? *Catalysis Science & Technology.* [Online]. 2019, **9**(10), pp.2380-2420. Available from: https://doi.org/10.1039/C9CY00415G
331. Ergan, F., Trani, M. and André, G. Solvent free triglyceride synthesis using lipozymeTM IM-20. *Biotechnology Letters.* [Online]. 1988, **10**(9), pp.629-634. Available from: https://doi.org/10.1007/BF01024714
332. Winayanuwattikun, P., Kaewpiboon, C., Piriyakananon, K., Chulalaksananukul, W., Yongvanich, T. and Svasti, J. Immobilized lipase from potential lipolytic microbes for catalyzing biodiesel production using palm oil as feedstock. *African Journal of Biotechnology.* [Online]. 2011, **10**. Available from: https://doi.org/10.5897/ajb10.1802
333. Ferrero, G.O., Faba, E.M.S. and Eimer, G.A. Biodiesel production from alternative raw materials using a heterogeneous low ordered biosilicified enzyme as biocatalyst. *Biotechnol Biofuels.* [Online]. 2021, **14**(1), p.67. Available from: https://doi.org/10.1186/s13068-021-01917-x
334. Shamel, M.M., Hasan, M. and Ramachandran, K.B. Operational Stability of Lipase Enzyme: Effect of Temperature and Shear. *Developments in Chemical Engineering and Mineral Processing.* [Online]. 2005, **13**(5-6), pp.599-604. [Accessed 2025/03/15]. Available from: https://doi.org/10.1002/apj.5500130509
335. Lotti, M., Pleiss, J., Valero, F. and Ferrer, P. Effects of methanol on lipases: Molecular, kinetic and process issues in the production of biodiesel. *Biotechnology Journal.* [Online]. 2015, **10**(1), pp.22-30. [Accessed 2025/03/15]. Available from: https://doi.org/10.1002/biot.201400158
336. Macías-Alonso, M., Hernández-Soto, R., Carrera-Rodríguez, M., Salazar-Hernández, C., Mendoza-Miranda, J.M., Villegas-Alcaraz, J.F. and Marrero, J.G. Obtention of biodiesel through an enzymatic two-step process. Study of its performance and characteristic emissions. *RSC Advances.* [Online]. 2022, **12**(36), pp.23747-23753. Available from: https://doi.org/10.1039/d2ra03578b
337. Nehdi, I.A., Sbihi, H.M., Blidi, L.E., Rashid, U., Tan, C.P. and Al-Resayes, S.I. Biodiesel Production from Citrillus colocynthis Oil Using Enzymatic Based Catalytic Reaction and Characterization Studies. *Protein Pept Lett.* [Online]. 2018, **25**(2), pp.164-170. Available from: https://doi.org/10.2174/0929866524666170223150839

338. De, B.K., Bhattacharyya, D.K. and Bandhu, C. Enzymatic synthesis of fatty alcohol esters by alcoholysis. *Journal of the American Oil Chemists' Society.* [Online]. 1999, **76**(4), pp.451-453. [Accessed 2021/06/13]. Available from: https://doi.org/10.1007/s11746-999-0023-5
339. Jeong, G.T. and Park, D.H. Lipase-catalyzed transesterification of rapeseed oil for biodiesel production with tert-butanol. *Appl Biochem Biotechnol.* [Online]. 2008, **148**(1-3), pp.131-139. Available from: https://doi.org/10.1007/s12010-007-8050-x
340. Shimada, Y., Watanabe, Y., Sugihara, A. and Tominaga, Y. Enzymatic alcoholysis for biodiesel fuel production and application of the reaction to oil processing. *Journal of Molecular Catalysis B: Enzymatic.* [Online]. 2002, **17**(3), pp.133-142. Available from: https://doi.org/10.1016/S1381-1177(02)00020-6
341. Kusdiana, D. and Saka, S. Methyl esterification of free fatty acids of rapeseed oil astreated in supercritical methanol. *Journal of Chemical Engineering of Japan.* [Online]. 2001, **34**(3), pp.383-387. Available from: https://doi.org/10.1252/jcej.34.383
342. Kusdiana, D. and Saka, S. Two-step preparation for catalyst-free biodiesel fuel production: Hydrolysis and methyl esterification. *Applied Biochemistry and Biotechnology - Part A Enzyme Engineering and Biotechnology.* [Online]. 2004, **115**(1-3), pp.781-791. Available from: https://doi.org/10.1385/abab:115:1-3:0781
343. Kusdiana, D. and Saka, S. Effects of water on biodiesel fuel production by supercritical methanol treatment. *Bioresource Technology.* [Online]. 2004, **91**(3), pp.289-295. Available from: https://doi.org/10.1016/S0960-8524(03)00201-3
344. Warabi, Y., Kusdiana, D. and Saka, S. Biodiesel fuel from vegetable oil by various supercritical alcohols. *Applied Biochemistry and Biotechnology - Part A Enzyme Engineering and Biotechnology.* [Online]. 2004, **115**(1-3), pp.793-801. Available from: https://doi.org/10.1007/978-1-59259-837-3_64
345. Warabi, Y., Kusdiana, D. and Saka, S. Reactivity of triglycerides and fatty acids of rapeseed oil in supercritical alcohols. *Bioresource Technology.* [Online]. 2004, **91**(3), pp.283-287. Available from: https://doi.org/10.1016/S0960-8524(03)00202-5
346. Abedini Najafabadi, H., Vossoughi, M. and Pazuki, G. The role of co-solvents in improving the direct transesterification of wet microalgal biomass under supercritical condition. *Bioresource Technology.* [Online]. 2015, **193**, pp.90-96. Available from: https://doi.org/10.1016/j.biortech.2015.06.045
347. Jomtib, N., Prommuak, C., Goto, M., Sasaki, M. and Shotipruk, A. Effect of Co-Solvents on Transesterification of Refined Palm Oil in Supercritical Methanol. *Engineering Journal.* [Online]. 2011, **15**(3), pp.49-58. Available from: https://doi.org/10.4186/ej.2011.15.3.49
348. Zeng, D., Yang, L. and Fang, T. Process optimization, kinetic and thermodynamic studies on biodiesel production by supercritical methanol transesterification with CH3ONa catalyst. *Fuel.* [Online]. 2017, **203**, pp.739-748. Available from: https://doi.org/10.1016/j.fuel.2017.05.019
349. Geuens, J., Kremsner, J.M., Nebel, B.A., Schober, S., Dommisse, R.A., Mittelbach, M., Tavernier, S., Kappe, C.O. and Maes, B.U.W. Microwave-Assisted Catalyst-Free Transesterification of Triglycerides with 1-Butanol under Supercritical Conditions. *Energy & Fuels.* [Online]. 2008, **22**(1), pp.643-645. Available from: https://doi.org/10.1021/ef700617q
350. Geuens, J., Sergeyev, S., Maes, B.U.W. and Tavernier, S.M.F. Influence of the Free Fatty Acids, Water, Temperature, and Reaction Time on the Catalyst-Free Microwave-Assisted Transesterification of Triglycerides with 1-Butanol. *Energy & Fuels.* [Online]. 2013, **27**(5), pp.2637-2642. Available from: https://doi.org/10.1021/ef400069x
351. Melo-Júnior, C.A.R., Albuquerque, C.E.R., Fortuny, M., Dariva, C., Egues, S., Santos, A.F. and Ramos, A.L.D. Use of Microwave Irradiation in the Noncatalytic Esterification of C18 Fatty Acids. *Energy & Fuels.* [Online]. 2009, **23**(1), pp.580-585. Available from: https://doi.org/10.1021/ef800766x
352. Patil, P.D., Reddy, H., Muppaneni, T., Ponnusamy, S., Cooke, P., Schuab, T. and Deng, S. Microwave-mediated non-catalytic transesterification of algal biomass under supercritical ethanol conditions. *The Journal of Supercritical Fluids.* [Online]. 2013, **79**, pp.67-72. Available from: https://doi.org/10.1016/j.supflu.2012.11.023
353. Patil, P.D., Reddy, H., Muppaneni, T., Schaub, T., Holguin, F.O., Cooke, P., Lammers, P., Nirmalakhandan, N., Li, Y., Lu, X. and Deng, S. In situ ethyl ester production from wet algal biomass under microwave-mediated supercritical ethanol conditions. *Bioresource Technology.* [Online]. 2013, **139**, pp.308-315. Available from: https://doi.org/10.1016/j.biortech.2013.04.045
354. El Sherbiny, S.A., Refaat, A.A. and El Sheltawy, S.T. Production of biodiesel using the microwave technique. *Journal of Advanced Research.* [Online]. 2010, **1**(4), pp.309-314. Available from: https://doi.org/10.1016/j.jare.2010.07.003
355. Joelianingsih, Nabetani, H., Sagara, Y., Tambunan, A.H. and Abdullah, K. A continuous-flow bubble column reactor for biodiesel production by non-catalytic transesterification. *Fuel.* [Online]. 2012, **96**, pp.595-599. Available from: https://doi.org/10.1016/j.fuel.2012.01.020
356. Zimmerman, W.B. and Kokoo, R. Esterification for biodiesel production with a phantom catalyst: Bubble mediated reactive distillation. *Applied Energy.* [Online]. 2018, **221**, pp.28-40. Available from: https://doi.org/10.1016/j.apenergy.2018.03.147
357. Boocock, D.G.B., Konar, S.K., Mao, V. and Sidi, H. Fast one-phase oil-rich processes for the preparation of vegetable oil methyl esters. *Biomass and Bioenergy.* [Online]. 1996, **11**(1), pp.43-50. Available from: https://doi.org/10.1016/0961-9534(95)00111-5
358. Demirbas, A. Progress and recent trends in biodiesel fuels. *Energy Conversion and Management.* [Online]. 2009, **50**(1), pp.14-34. Available from: https://doi.org/10.1016/j.enconman.2008.09.001
359. Van Gerpen, J., Shanks, B., Pruszko, R., Clements, D. and Knothe, G. *Biodiesel Production Technology: August 2002--January 2004.* United States, 2004.
360. Gunawan, F., Kurniawan, A., Gunawan, I., Ju, Y.-H., Ayucitra, A., Soetaredjo, F.E. and Ismadji, S. Synthesis of biodiesel from vegetable oils wastewater sludge by in-situ subcritical methanol transesterification: Process evaluation and optimization. *Biomass and Bioenergy.* [Online]. 2014, **69**, pp.28-38. Available from: https://doi.org/10.1016/j.biombioe.2014.07.005
361. Felix, C., Ubando, A., Madrazo, C., Gue, I.H., Sutanto, S., Tran-Nguyen, P.L., Go, A.W., Ju, Y.-H., Culaba, A., Chang, J.-S. and Chen, W.-H. Non-catalytic in-situ (trans) esterification of lipids in wet microalgae Chlorella vulgaris under subcritical conditions for the synthesis of fatty acid methyl esters. *Applied Energy.* [Online]. 2019, **248**, pp.526-537. Available from: https://doi.org/10.1016/j.apenergy.2019.04.149
362. Ju, Y.-H., Huynh, L.H., Tsigie, Y.A. and Ho, Q.-P. Synthesis of biodiesel in subcritical water and methanol. *Fuel.* [Online]. 2013, **105**, pp.266-271. Available from: https://doi.org/10.1016/j.fuel.2012.05.061
363. Ren, X., Wei, C., Yan, Q., Shan, X., Wu, M., Zhao, X. and Song, Y. Optimization of a novel lipid extraction process from microalgae. *Sci Rep.* [Online]. 2021, **11**(1), p.20221. Available from: https://doi.org/10.1038/s41598-021-99356-z

364. Tien Thanh, N., Mostapha, M., Lam, M.K., Ishak, S., Kanna Dasan, Y., Lim, J.W., Tan, I.S., Lau, S.Y., Chin, B.L.F. and Hadibarata, T. Fundamental understanding of in-situ transesterification of microalgae biomass to biodiesel: A critical review. *Energy Conversion and Management.* [Online]. 2022, **270**, p.116212. Available from: https://doi.org/10.1016/j.enconman.2022.116212
365. Sankumgon, A., Assawadithalerd, M., Phasukarratchai, N., Chollacoop, N. and Tongcumpou, C. Properties and performance of microemulsion fuel: blending of jatropha oil, diesel, and ethanol- surfactant. *Renewable Energy Focus.* [Online]. 2018, **24**, pp.28-32. Available from: https://doi.org/10.1016/j.ref.2017.12.001
366. Parvizsedghy, R., Sadrameli, S.M. and Towfighi Darian, J. Upgraded Biofuel Diesel Production by Thermal Cracking of Castor Biodiesel. *Energy & Fuels.* [Online]. 2016, **30**(1), pp.326-333. Available from: https://doi.org/10.1021/acs.energyfuels.5b01879
367. Su, G., Ong, H.C., Mofijur, M., Mahlia, T.M.I. and Ok, Y.S. Pyrolysis of waste oils for the production of biofuels: A critical review. *Journal of Hazardous Materials.* [Online]. 2022, **424**, p.127396. Available from: https://doi.org/10.1016/j.jhazmat.2021.127396
368. Govindaraju, R., Chen, S.-S., Wang, L.-P., Chang, H.-M. and Pasawan, M. Significance of Membrane Applications for High-Quality Biodiesel and Byproduct (Glycerol) in Biofuel Industries—Review. *Current Pollution Reports.* [Online]. 2021, **7**(2), pp.128-145. Available from: https://doi.org/10.1007/s40726-021-00182-8
369. Ramachandran, K., Suganya, T., Nagendra Gandhi, N. and Renganathan, S. Recent developments for biodiesel production by ultrasonic assist transesterification using different heterogeneous catalyst: A review. *Renewable and Sustainable Energy Reviews.* [Online]. 2013, **22**, pp.410-418. Available from: https://doi.org/10.1016/j.rser.2013.01.057
370. Widiastuti, N., Silitonga, R.S., Dharma, H.N.C., Jaafar, J., Widyanto, A.R. and Purwanto, M. Decreasing free fatty acid of crude palm oil with polyvinylidene fluoride hollow fiber membranes using a combination of chitosan and glutaraldehyde. *RSC Advances.* [Online]. 2022, **12**(35), pp.22662-22670. Available from: https://doi.org/10.1039/d2ra04005k
371. Ningaraju, C., Murali, A., Priya, S., Mohan, S. and Geetha Balakrishna, R. Non-catalytic Processes for Biodiesel Production. In: Balakrishna, R.G., Mohan, S. and Zaki Sharara, T. eds. *Developments in Biodiesel: Feedstock, Production, and Properties*. Royal Society of Chemistry, 2024, p.0.
372. ASTM. *D6751 - 20a.* West Conshohocken, PA, USA: ASTM International, 2020.
373. Gregório, J., Ferrera, B., Fuscaldo, R. and Souza, R. Proposal of a Standard Unit for Turnover Frequencies: Hz. *Journal of the Brazilian Chemical Society.* [Online]. 2014, **25**, pp.2137-2139. Available from: https://doi.org/10.5935/0103-5053.20140219
374. Reyero, I., Arzamendi, G., Zabala, S. and Gandía, L.M. Kinetics of the NaOH-catalyzed transesterification of sunflower oil with ethanol to produce biodiesel. *Fuel Processing Technology.* [Online]. 2015, **129**, pp.147-155. Available from: https://doi.org/10.1016/j.fuproc.2014.09.008
375. Mahin, J. and Torrente-Murciano, L. Continuous synthesis of monodisperse iron@iron oxide core@shell nanoparticles. *Chemical Engineering Journal.* [Online]. 2020, **396**, p.125299. Available from: https://doi.org/10.1016/j.cej.2020.125299
376. Zhang, Y., Wong, W.-T. and Yung, K.-F. Biodiesel production via esterification of oleic acid catalyzed by chlorosulfonic acid modified zirconia. *Applied Energy.* [Online]. 2014, **116**, pp.191-198. Available from: https://doi.org/10.1016/j.apenergy.2013.11.044
377. Noda, L., Almeida, R., Probst, L. and Gonçalves, N. Characterization of sulfated TiO2 prepared by the sol–gel method and its catalytic activity in the n-hexane isomerization reaction. *Journal of Molecular Catalysis A: Chemical.* [Online]. 2005, **225**, pp.39–46. Available from: https://doi.org/10.1016/j.molcata.2004.08.025
378. Niju, S., Raj, F.R., Anushya, C. and Balajii, M. Optimization of acid catalyzed esterification and mixed metal oxide catalyzed transesterification for biodiesel production from Moringa oleifera oil. *Green Processing and Synthesis.* [Online]. 2019, **8**(1), pp.756-775. Available from: https://doi.org/10.1515/gps-2019-0045
379. Friedrich, W., Knipping, P. and von Laue, M. *Interferenz-Erscheinungen bei Röntgenstrahlen.* Verlag der Kgl. Bayer. Akad. der Wiss., 1912.
380. Thomas, J.M. The birth of X-ray crystallography. *Nature.* [Online]. 2012, **491**(7423), pp.186-187. Available from: https://doi.org/10.1038/491186a
381. Bragg, W.H. and Bragg, W.L. The reflection of X-rays by crystals. *Proceedings of the Royal Society of London. Series A, Containing Papers of a Mathematical and Physical Character.* [Online]. 1913, **88**(605), pp.428-438. Available from: https://doi.org/10.1098/rspa.1913.0040
382. *The Nobel Prize in Physics 1915.* [Online]. 2025. [Accessed]. Available from: https://www.nobelprize.org/prizes/physics/1915/summary/
383. Shabir, Q., Pokale, A., Loni, A., Johnson, D.R., Canham, L.T., Fenollosa, R., Tymczenko, M., Rodríguez, I., Meseguer, F., Cros, A. and Cantarero, A. Medically Biodegradable Hydrogenated Amorphous Silicon Microspheres. *Silicon.* [Online]. 2011, **3**(4), pp.173-176. Available from: https://doi.org/10.1007/s12633-011-9097-4
384. Doebelin, N. and Kleeberg, R. Profex: a graphical user interface for the Rietveld refinement program BGMN. *Journal of Applied Crystallography.* [Online]. 2015, **48**(5), pp.1573-1580. Available from: https://doi.org/10.1107/s1600576715014685
385. Langford, J.I. and Wilson, A.J.C. Scherrer after sixty years: A survey and some new results in the determination of crystallite size. *Journal of Applied Crystallography.* [Online]. 1978, **11**(2), pp.102-113. [Accessed 2025/03/16]. Available from: https://doi.org/10.1107/S0021889878012844
386. Toro, R.G., Diab, M., de Caro, T., Al-Shemy, M., Adel, A. and Caschera, D. Study of the Effect of Titanium Dioxide Hydrosol on the Photocatalytic and Mechanical Properties of Paper Sheets. *Materials.* [Online]. 2020, **13**(6). Available from: https://doi.org/10.3390/ma13061326
387. Lima, F.M., Martins, F.M., Maia Júnior, P.H.F., Almeida, A.F.L. and Freire, F.N.A. Nanostructured titanium dioxide average size from alternative analysis of Scherrer's Equation. *Matéria (Rio de Janeiro).* [Online]. 2018, **23**(1). Available from: https://doi.org/10.1590/s1517-707620170001.0301
388. *STARe Excellence Thermal Analysis Software.* [Online]. [Accessed]. Available from: https://www.mt.com/gb/en/home/products/Laboratory_Analytics_Browse/TA_Family_Browse/TA_software_browse.html
389. Barr, E.S. The infrared pioneers—I. Sir William Herschel. *Infrared Physics.* [Online]. 1961, **1**(1), pp.1-IN6. Available from: https://doi.org/10.1016/0020-0891(61)90037-9
390. Tsai, S.R. and Hamblin, M.R. Biological effects and medical applications of infrared radiation. *J Photochem Photobiol B.* [Online]. 2017, **170**, pp.197-207. Available from: https://doi.org/10.1016/j.jphotobiol.2017.04.014
391. El-Azazy, M. Introductory Chapter: Infrared Spectroscopy - A Synopsis of the Fundamentals and Applications. In: El-Azazy, M. ed. *Infrared Spectroscopy - Principles, Advances, and Applications*. Rijeka: IntechOpen, 2018.

392. Koç, M. and Karabudak, E. History of spectroscopy and modern micromachined disposable Si ATR-IR spectroscopy. *Applied Spectroscopy Reviews.* [Online]. 2018, **53**(5), pp.420-438. Available from: https://doi.org/10.1080/05704928.2017.1366341
393. Coblentz, W.W. *Investigations of infra-red spectra*. Washington, D.C., :: Carnegie institution of Washington. 1905.
394. Cooley, J.W. and Tukey, J.W. An Algorithm for the Machine Calculation of Complex Fourier Series. *Papers on Digital Signal Processing.* [Online]. The MIT Press, 1969. Available from: https://doi.org/10.7551/mitpress/5222.003.0014
395. Haynes, W.M. CRC Handbook of Chemistry and Physics. [Online]. 2014. Available from: https://doi.org/10.1201/b17118
396. Binetin, S. and Devillers, J. QSAR for organic chemical sorption in soils and sediments. *Chemosphere.* [Online]. 1994, **28**(6), pp.1171-1188. Available from: https://doi.org/10.1016/0045-6535(94)90335-2
397. Perrin, D.D. *Dissociation Constants of Organic Bases in Aqueous Solution: Hauptbd.* Butterworths, 1965.
398. Perrin, C.L. and Fabian, M.A. Multicomponent NMR titration for simultaneous measurement of relative pKaS. *Anal Chem.* [Online]. 1996, **68**(13), pp.2127-2134. Available from: https://doi.org/10.1021/ac960117z
399. Micromeritics. Characterization of Acid Sites Using Temperature-Programmed Desorption. *Application Note 134.* [Online]. 2003. Available from: https://www.micromeritics.com.cn/downloads/Appnotes/ApplicationNote-134.pdf
400. Liu, D., Yuan, P., Liu, H., Cai, J., Tan, D., He, H., Zhu, J. and Chen, T. Quantitative characterization of the solid acidity of montmorillonite using combined FTIR and TPD based on the NH3 adsorption system. *Applied Clay Science.* [Online]. 2013, **80-81**, pp.407-412. Available from: https://doi.org/10.1016/j.clay.2013.07.006
401. Micromeritics. *Characterizing Acid Sites of H+ ß (SiO2/Al2O3:75/1).* [Online]. 2024. [Accessed]. Available from: https://www.azom.com/article.aspx?ArticleID=13548
402. Zaki, M.I., Hasan, M.A., Al-Sagheer, F.A. and Pasupulety, L. In situ FTIR spectra of pyridine adsorbed on SiO2–Al2O3, TiO2, ZrO2 and CeO2: general considerations for the identification of acid sites on surfaces of finely divided metal oxides. *Colloids and Surfaces A: Physicochemical and Engineering Aspects.* [Online]. 2001, **190**(3), pp.261-274. Available from: https://doi.org/10.1016/S0927-7757(01)00690-2
403. Śliwa, M., Samson, K., Ruggiero–Mikołajczyk, M., Żelazny, A. and Grabowski, R. Influence of Montmorillonite K10 Modification with Tungstophosphoric Acid on Hybrid Catalyst Activity in Direct Dimethyl Ether Synthesis from Syngas. *Catalysis Letters.* [Online]. 2014, **144**(11), pp.1884-1893. Available from: https://doi.org/10.1007/s10562-014-1359-5
404. Specac. *Specac Technical Note TN21-02: ATR Penetration Depth.* [Online]. [Accessed]. Available from: https://specac.com/wp-content/uploads/2022/03/TN21-02-ATR-Penetration-Depth.pdf
405. Kaneko, K. Determination of pore size and pore size distribution: 1. Adsorbents and catalysts. *Journal of membrane science.* [Online]. 1994, **96**(1-2), pp.59-89.
406. Sarna-Boś, K., Skic, K., Sobieszczański, J., Boguta, P. and Chałas, R. Contemporary Approach to the Porosity of Dental Materials and Methods of Its Measurement. *International Journal of Molecular Sciences.* [Online]. 2021, **22**(16). Available from: https://doi.org/10.3390/ijms22168903
407. Zdravkov, B., Čermák, J., Šefara, M. and Janků, J. Pore classification in the characterization of porous materials: A perspective. *Open Chemistry.* [Online]. 2007, **5**(2), pp.385-395. Available from: https://doi.org/10.2478/s11532-007-0017-9
408. Rouquerol, J., Avnir, D., Fairbridge, C.W., Everett, D.H., Haynes, J.M., Pernicone, N., Ramsay, J.D.F., Sing, K.S.W. and Unger, K.K. Recommendations for the characterization of porous solids (Technical Report). [Online]. 1994, **66**(8), pp.1739-1758. [Accessed 2025-03-16]. Available from: https://doi.org/10.1351/pac199466081739
409. Wang, X., Peng, Y., Wang, J. and Zeng, Q. Pore Structure Damages in Cement-Based Materials by Mercury Intrusion: A Non-Destructive Assessment by X-Ray Computed Tomography. *Materials (Basel).* [Online]. 2019, **12**(14). Available from: https://doi.org/10.3390/ma12142220
410. Rouquerol, J., Baron, G., Denoyel, R., Giesche, H., Groen, J., Klobes, P., Levitz, P., Neimark, A.V., Rigby, S., Skudas, R., Sing, K., Thommes, M. and Unger, K. Liquid intrusion and alternative methods for the characterization of macroporous materials (IUPAC Technical Report). [Online]. 2011, **84**(1), pp.107-136. [Accessed 2025-03-16]. Available from: https://doi.org/10.1351/PAC-REP-10-11-19
411. Langmuir, I. *Irving Langmuir – Nobel Lecture.* [Online]. 1932. [Accessed]. Available from: https://www.nobelprize.org/prizes/chemistry/1932/langmuir/lecture/
412. Kalam, S., Abu-Khamsin, S.A., Kamal, M.S. and Patil, S. Surfactant Adsorption Isotherms: A Review. *ACS Omega.* [Online]. 2021, **6**(48), pp.32342-32348. Available from: https://doi.org/10.1021/acsomega.1c04661
413. Brunauer, S., Emmett, P.H. and Teller, E. Adsorption of Gases in Multimolecular Layers. *Journal of the American Chemical Society.* [Online]. 1938, **60**(2), pp.309-319. Available from: https://doi.org/10.1021/ja01269a023
414. Thommes, M., Kaneko, K., Neimark, A.V., Olivier, J.P., Rodriguez-Reinoso, F., Rouquerol, J. and Sing, K.S.W. Physisorption of gases, with special reference to the evaluation of surface area and pore size distribution (IUPAC Technical Report). [Online]. 2015, **87**(9-10), pp.1051-1069. [Accessed 2025-03-16]. Available from: https://doi.org/10.1515/pac-2014-1117
415. Ambroz, F., Macdonald, T.J., Martis, V. and Parkin, I.P. Evaluation of the BET Theory for the Characterization of Meso and Microporous MOFs. *Small Methods.* [Online]. 2018, **2**(11), p.1800173. [Accessed 2025/03/16]. Available from: https://doi.org/10.1002/smtd.201800173
416. Sinha, P., Datar, A., Jeong, C., Deng, X., Chung, Y.G. and Lin, L.-C. Surface Area Determination of Porous Materials Using the Brunauer–Emmett–Teller (BET) Method: Limitations and Improvements. *The Journal of Physical Chemistry C.* [Online]. 2019, **123**(33), pp.20195-20209. Available from: https://doi.org/10.1021/acs.jpcc.9b02116
417. Rouquerol, J., Llewellyn, P. and Rouquerol, F. Is the bet equation applicable to microporous adsorbents? In: Llewellyn, P.L., Rodriquez-Reinoso, F., Rouqerol, J. and Seaton, N. eds. *Studies in Surface Science and Catalysis*. Elsevier, 2007, pp.49-56.
418. Shimizu, S. and Matubayasi, N. Surface Area Estimation: Replacing the Brunauer-Emmett-Teller Model with the Statistical Thermodynamic Fluctuation Theory. *Langmuir.* [Online]. 2022, **38**(26), pp.7989-8002. Available from: https://doi.org/10.1021/acs.langmuir.2c00753
419. Sing, K.S.W. Reporting physisorption data for gas/solid systems with special reference to the determination of surface area and porosity (Recommendations 1984). [Online]. 1985, **57**(4), pp.603-619. [Accessed 2025-03-16]. Available from: https://doi.org/10.1351/pac198557040603
420. Kuila, U. and Prasad, M. Application of nitrogen gas-adsorption technique for characterization of pore structure of mudrocks. *The Leading Edge.* [Online]. 2013, **32**(12), pp.1478-1485.

421. Harkins, W.D. and Jura, G. Surfaces of Solids. XIII. A Vapor Adsorption Method for the Determination of the Area of a Solid without the Assumption of a Molecular Area, and the Areas Occupied by Nitrogen and Other Molecules on the Surface of a Solid. *Journal of the American Chemical Society.* [Online]. 1944, **66**(8), pp.1366-1373. Available from: https://doi.org/10.1021/ja01236a048
422. Barrett, E.P., Joyner, L.G. and Halenda, P.P. The Determination of Pore Volume and Area Distributions in Porous Substances. I. Computations from Nitrogen Isotherms. *Journal of the American Chemical Society.* [Online]. 1951, **73**(1), pp.373-380. Available from: https://doi.org/10.1021/ja01145a126
423. Siminiceanu, I., Lazau, I., Ecsedi, Z., Lupa, L. and Burciag, C. Textural Characterization of a New Iron-Based Ammonia Synthesis Catalyst. [Online]. 2008.
424. Choma, J., Jaroniec, M. and Kloske, M. Improved pore-size analysis of carbonaceous adsorbents. *Adsorption Science & Technology.* [Online]. 2002, **20**(3), pp.307-315.
425. Medina, B. and Alvarado, V. Use of Gas Adsorption and Inversion Methods for Shale Pore Structure Characterization. *Energies.* [Online]. 2021, **14**, p.2880. Available from: https://doi.org/10.3390/en14102880
426. Nguyen, C. and Do, D.D. The Dubinin–Radushkevich equation and the underlying microscopic adsorption description. *Carbon.* [Online]. 2001, **39**(9), pp.1327-1336. Available from: https://doi.org/10.1016/S0008-6223(00)00265-7
427. Horváth, G. and Kawazoe, K. Method for the calculation of effective pore size distribution in molecular sieve carbon. *Journal of Chemical Engineering of Japan.* [Online]. 1983, **16**(6), pp.470-475. Available from: https://doi.org/10.1252/jcej.16.470
428. Cheng, L.S. and Ralph T, Y. Improved Horvath—Kawazoe equations including spherical pore models for calculating micropore size distribution. *Chemical Engineering Science.* [Online]. 1994, **49**(16), pp.2599-2609. Available from: https://doi.org/10.1016/0009-2509(94)E0054-T
429. Saito, A. and Foley, H.C. Curvature and parametric sensitivity in models for adsorption in micropores. *AIChE Journal.* [Online]. 1991, **37**(3), pp.429-436. [Accessed 2025/03/16]. Available from: https://doi.org/10.1002/aic.690370312
430. Huang, B., Bartholomew, C.H. and Woodfield, B.F. Improved calculations of pore size distribution for relatively large, irregular slit-shaped mesopore structure. *Microporous and Mesoporous Materials.* [Online]. 2014, **184**, pp.112-121. Available from: https://doi.org/10.1016/j.micromeso.2013.10.008
431. Miyata, T., Endo, A., Ohmori, T., Akiya, T. and Nakaiwa, M. Evaluation of pore size distribution in boundary region of micropore and mesopore using gas adsorption method. *Journal of Colloid and Interface Science.* [Online]. 2003, **262**(1), pp.116-125. Available from: https://doi.org/10.1016/S0021-9797(02)00254-0
432. Fu, S., Fang, Q., Li, A., Li, Z., Han, J., Dang, X. and Han, W. Accurate characterization of full pore size distribution of tight sandstones by low-temperature nitrogen gas adsorption and high-pressure mercury intrusion combination method. *Energy Science & Engineering.* [Online]. 2021, **9**(1), pp.80-100. [Accessed 2025/03/16]. Available from: https://doi.org/10.1002/ese3.817
433. Ball, C.S. The Early History of the Compound Microscope. *Bios.* [Online]. 1966, **37**(2), pp.51-60. [Accessed 2025/03/16/]. Available from: http://www.jstor.org/stable/4606667
434. Mondal, H., Mondal, S., Saha, K. and Roul, B. Development of a Low-cost Smartphone-connected Digital Microscope. *J Microsc Ultrastruct.* [Online]. 2020, **8**(2), pp.51-54. Available from: https://doi.org/10.4103/jmau.Jmau_35_19
435. Wollman, A.J., Nudd, R., Hedlund, E.G. and Leake, M.C. From Animaculum to single molecules: 300 years of the light microscope. *Open Biol.* [Online]. 2015, **5**(4), p.150019. Available from: https://doi.org/10.1098/rsob.150019
436. Smolyaninov, II. Optical microscopy beyond the diffraction limit. *Hfsp j.* [Online]. 2008, **2**(3), pp.129-131. Available from: https://doi.org/10.2976/1.2912559
437. Abbe, E. Beiträge zur Theorie des Mikroskops und der mikroskopischen Wahrnehmung. *Archiv für Mikroskopische Anatomie.* [Online]. 1873, **9**(1), pp.413-468. Available from: https://doi.org/10.1007/BF02956173
438. Abbe, H. The Relation of Aperture and Power in the Microscope (continued). *Journal of the Royal Microscopical Society.* [Online]. 1882, **2**(4), pp.460-473. [Accessed 2025/03/16]. Available from: https://doi.org/10.1111/j.1365-2818.1882.tb04805.x
439. de Broglie, L. *Recherches sur la théorie des Quanta*. thesis, Migration - université en cours d'affectation, 1924.
440. Davisson, C. and Germer, L.H. Diffraction of Electrons by a Crystal of Nickel. *Physical Review.* [Online]. 1927, **30**(6), pp.705-740. Available from: https://doi.org/10.1103/PhysRev.30.705
441. Busch, H. Über die Wirkungsweise der Konzentrierungsspule bei der Braunschen Röhre. *Archiv für Elektrotechnik.* [Online]. 1927, **18**(6), pp.583-594. Available from: https://doi.org/10.1007/BF01656203
442. Knoll, M. and Ruska, E. Das Elektronenmikroskop. *Zeitschrift für Physik.* [Online]. 1932, **78**(5), pp.318-339. Available from: https://doi.org/10.1007/BF01342199
443. Herrero, Y.R., Camas, K.L. and Ullah, A. Chapter 4 - Characterization of biobased materials. In: Ahmed, S. and Annu eds. *Advanced Applications of Biobased Materials*. Elsevier, 2023, pp.111-143.
444. Dusevich, V.M., Purk, J.H. and Eick, J.D. Choosing the Right Accelerating Voltage for SEM (An Introduction for Beginners). *Microscopy Today.* [Online]. 2010, **18**(1), pp.48-52. [Accessed 3/16/2025]. Available from: https://doi.org/10.1017/S1551929510991190
445. Nellist, P.D. and Pennycook, S.J. The principles and interpretation of annular dark-field Z-contrast imaging. In: Hawkes, P.W. ed. *Advances in Imaging and Electron Physics*. Elsevier, 2000, pp.147-203.
446. Barkla, C.G. and Sadler, C.A. XXXVII. Secondary x-rays and the atomic weight of nickel. *The London, Edinburgh, and Dublin Philosophical Magazine and Journal of Science.* [Online]. 1907, **14**(81), pp.408-422. Available from: https://doi.org/10.1080/14786440709463697
447. *The Nobel Prize in Physics 1917.* [Online]. 2025. [Accessed]. Available from: https://www.nobelprize.org/prizes/physics/1917/summary/
448. Moseley, H.G.J. XCIII. The high-frequency spectra of the elements. *Philosophical Magazine Series 1.* [Online]. 1913, **26**, pp.1024-1034.
449. Hardouin Duparc, O. Pierre Auger – Lise Meitner: Comparative contributions to the Auger effect. [Online]. 2009, **100**(9), pp.1162-1166. [Accessed 2025-03-16]. Available from: https://doi.org/10.3139/146.110163
450. Siegbahn, M. Relations between the K and L Series of the High-Frequency Spectra. *Nature.* [Online]. 1916, **96**(2416), pp.676-676. Available from: https://doi.org/10.1038/096676b0
451. Hertz, H. Ueber einen Einfluss des ultravioletten Lichtes auf die electrische Entladung. *Annalen der Physik.* [Online]. 1887, **267**(8), pp.983-1000. Available from: https://doi.org/10.1002/andp.18872670827

452. Lenard, P. Ueber die lichtelektrische Wirkung. *Annalen der Physik.* [Online]. 1902, **313**(5), pp.149-198. [Accessed 2025/03/16]. Available from: https://doi.org/10.1002/andp.19023130510
453. Beck, A. and Havas, P. *The Collected Papers of Albert Einstein, Volume 2: The Swiss Years: Writings, 1900-1909 (English translation supplement).* Princeton University Press, 1989.
454. *The Nobel Prize in Physics 1921.* [Online]. 2025. [Accessed]. Available from: https://www.nobelprize.org/prizes/physics/1921/summary/
455. Levenberg, K. A method for the solution of certain non-linear problems in least squares. *Quarterly of Applied Mathematics.* [Online]. 1944, **2**(2), pp.164-168. Available from: https://doi.org/10.1090/qam/10666
456. Marquardt, D.W. An Algorithm for Least-Squares Estimation of Nonlinear Parameters. *Journal of the Society for Industrial and Applied Mathematics.* [Online]. 1963, **11**(2), pp.431-441. [Accessed 2025/03/16]. Available from: https://doi.org/10.1137/0111030
457. Rabi, I.I., Zacharias, J.R., Millman, S. and Kusch, P. A New Method of Measuring Nuclear Magnetic Moment. *Physical Review.* [Online]. 1938, **53**(4), pp.318-318. Available from: https://doi.org/10.1103/PhysRev.53.318
458. *The Nobel Prize in Physics 1944.* [Online]. 2025. [Accessed]. Available from: https://www.nobelprize.org/prizes/physics/1944/summary/
459. Purcell, E.M., Torrey, H.C. and Pound, R.V. Resonance Absorption by Nuclear Magnetic Moments in a Solid. *Physical Review.* [Online]. 1946, **69**(1-2), pp.37-38. Available from: https://doi.org/10.1103/PhysRev.69.37
460. Bloch, F., Hansen, W.W. and Packard, M. Nuclear Induction. *Physical Review.* [Online]. 1946, **69**(3-4), pp.127-127. Available from: https://doi.org/10.1103/PhysRev.69.127
461. Yadav, L.D.S. 13C NMR Spectroscopy. In: Yadav, L.D.S. ed. *Organic Spectroscopy*. Dordrecht: Springer Netherlands, 2005, pp.195-223.
462. Stokes, G.G. On the theories of the internal friction of fluids in motion, and of the equilibrium and motion of elastic solids. [Online]. 2007.
463. Einstein, A. Über einen die Erzeugung und Verwandlung des Lichtes betreffenden heuristischen Gesichtspunkt. *Annalen der Physik.* [Online]. 1905, **322**(6), pp.132-148. [Accessed 2025/03/16]. Available from: https://doi.org/10.1002/andp.19053220607
464. Einstein, A. Zur Theorie der Brownschen Bewegung. *Annalen der Physik.* [Online]. 1906, **324**(2), pp.371-381. [Accessed 2025/03/16]. Available from: https://doi.org/10.1002/andp.19063240208
465. Brown, R. XXVII. A brief account of microscopical observations made in the months of June, July and August 1827, on the particles contained in the pollen of plants; and on the general existence of active molecules in organic and inorganic bodies. *The philosophical magazine.* [Online]. 1828, **4**(21), pp.161-173.
466. Sutherland, W. LXXV. A dynamical theory of diffusion for non-electrolytes and the molecular mass of albumin. *The London, Edinburgh, and Dublin Philosophical Magazine and Journal of Science.* [Online]. 1905, **9**(54), pp.781-785. Available from: https://doi.org/10.1080/14786440509463331
467. Tyndall, J. IV. On the blue colour of the sky, the polarization of skylight, and on the polarization of light by cloudy matter generally. *Proceedings of the Royal Society of London.* [Online]. 1869, **17**(0), pp.223-233. Available from: https://doi.org/10.1098/rspl.1868.0033
468. Strutt, J.W. LVIII. On the scattering of light by small particles. *The London, Edinburgh, and Dublin Philosophical Magazine and Journal of Science.* [Online]. 1871, **41**(275), pp.447-454.
469. Rayleigh, L. On the light from the sky, its polarization and colour. *Phil Mag.* [Online]. 1871, **41**, p.274.
470. Mie, G. Beiträge zur Optik trüber Medien, speziell kolloidaler Metallösungen. *Annalen der Physik.* [Online]. 1908, **330**(3), pp.377-445. [Accessed 2025/03/16]. Available from: https://doi.org/10.1002/andp.19083300302
471. Pecora, R. Doppler Shifts in Light Scattering from Pure Liquids and Polymer Solutions. *The Journal of Chemical Physics.* [Online]. 1964, **40**(6), pp.1604-1614. [Accessed 3/17/2025]. Available from: https://doi.org/10.1063/1.1725368
472. Debye, P. Zerstreuung von Röntgenstrahlen. *Annalen der Physik.* [Online]. 1915, **351**(6), pp.809-823. [Accessed 2025/03/16]. Available from: https://doi.org/10.1002/andp.19153510606
473. Siegert, A. *On the fluctuations in signals returned by many independently moving scatterers.* Radiation Laboratory, Massachusetts Institute of Technology, 1943.
474. Stetefeld, J., McKenna, S.A. and Patel, T.R. Dynamic light scattering: a practical guide and applications in biomedical sciences. *Biophys Rev.* [Online]. 2016, **8**(4), pp.409-427. Available from: https://doi.org/10.1007/s12551-016-0218-6
475. Parker, E.T. and Lollar, P. Measurement of the Translational Diffusion Coefficient and Hydrodynamic Radius of Proteins by Dynamic Light Scattering. *Bio Protoc.* [Online]. 2021, **11**(20), p.e4195. Available from: https://doi.org/10.21769/BioProtoc.4195
476. Ragheb, R. and Nobbmann, U. Multiple scattering effects on intercept, size, polydispersity index, and intensity for parallel (VV) and perpendicular (VH) polarization detection in photon correlation spectroscopy. *Scientific Reports.* [Online]. 2020, **10**(1), p.21768. Available from: https://doi.org/10.1038/s41598-020-78872-4
477. Danaei, M., Dehghankhold, M., Ataei, S., Hasanzadeh Davarani, F., Javanmard, R., Dokhani, A., Khorasani, S. and Mozafari, M.R. Impact of Particle Size and Polydispersity Index on the Clinical Applications of Lipidic Nanocarrier Systems. *Pharmaceutics.* [Online]. 2018, **10**(2). Available from: https://doi.org/10.3390/pharmaceutics10020057
478. Malvern. *Application of Dynamic Light Scattering (DLS) to Protein Therapeutic Formulations: Principles, Measurements and Analysis - 3. DLS Deconvolution Algorithms.* [Online]. 2014. [Accessed]. Available from: https://www.malvernpanalytical.com/en/learn/knowledge-center/whitepapers/wp140207applicdlsprotein3
479. Chowdhury, M.A., Uddin, M.M.K., Shuvho, M.B.A., Rana, M. and Hossain, N. A novel temperature dependent method for borophene synthesis. *Applied Surface Science Advances.* [Online]. 2022, **11**, p.100308. Available from: https://doi.org/10.1016/j.apsadv.2022.100308
480. Németh, Z., Csóka, I., Semnani Jazani, R., Sipos, B., Haspel, H., Kozma, G., Kónya, Z. and Dobó, D.G. Quality by Design-Driven Zeta Potential Optimisation Study of Liposomes with Charge Imparting Membrane Additives. *Pharmaceutics.* [Online]. 2022, **14**(9). Available from: https://doi.org/10.3390/pharmaceutics14091798
481. Moitzi, C. and Petrillo, B. *Faster, more sensitive zeta-potential measurements with cmPALS and the Litesizer 500, Anton paar application report d51.* a021 technical report, 2016.
482. Bellmann, C., Caspari, A., Moitzi, C., Babick, F., Schäffler, M., Luxbacher, T., Stintz, M. and Fradler, C. *Dynamic and Electrophoretic Light Scattering: Guidelines for Particle Size Analysis and Zeta Potential Determination.* Anton Paar GmbH, 2019.

483. Luxbacher, T. and Anton Paar Gmb, H. *The Zeta potential for solid surface analysis : a practical guide to streaming potential measurement.* 1st ed. Austria: Anton Paar GmbH, 2014.
484. Kaszuba, M., Corbett, J., Watson, F.M. and Jones, A. High-concentration zeta potential measurements using light-scattering techniques. *Philos Trans A Math Phys Eng Sci.* [Online]. 2010, **368**(1927), pp.4439-4451. Available from: https://doi.org/10.1098/rsta.2010.0175
485. Prakash, S. and Yeom, J. Chapter 2 - Fundamentals for Microscale and Nanoscale Flows. In: Prakash, S. and Yeom, J. eds. *Nanofluidics and Microfluidics*. William Andrew Publishing, 2014, pp.9-38.
486. Danaei, M., Kalantari, M., Raji, M., Samareh Fekri, H., Saber, R., Asnani, G.P., Mortazavi, S.M., Mozafari, M.R., Rasti, B. and Taheriazam, A. Probing nanoliposomes using single particle analytical techniques: effect of excipients, solvents, phase transition and zeta potential. *Heliyon.* [Online]. 2018, **4**(12), p.e01088. Available from: https://doi.org/10.1016/j.heliyon.2018.e01088
487. Fairhurst, D. *An Overview of the Zeta Potential - Part 2: Measurement.* [Online]. 2013. [Accessed]. Available from: https://www.americanpharmaceuticalreview.com/Featured-Articles/134634-An-Overview-of-the-Zeta-Potential-Part-2-Measurement/
488. Polaczyk, A.L., Amburgey, J.E., Alansari, A., Poler, J.C., Propato, M. and Hill, V.R. Calculation and uncertainty of zeta potentials of microorganisms in a 1:1 electrolyte with a conductivity similar to surface water. *Colloids and Surfaces A: Physicochemical and Engineering Aspects.* [Online]. 2020, **586**, p.124097. Available from: https://doi.org/10.1016/j.colsurfa.2019.124097
489. Kaasalainen, M., Aseyev, V., von Haartman, E., Karaman, D.Ş., Mäkilä, E., Tenhu, H., Rosenholm, J. and Salonen, J. Size, Stability, and Porosity of Mesoporous Nanoparticles Characterized with Light Scattering. *Nanoscale Research Letters.* [Online]. 2017, **12**(1), p.74. Available from: https://doi.org/10.1186/s11671-017-1853-y
490. Reichardt, C. and Welton, T. *Solvents and solvent effects in organic chemistry.* John Wiley & Sons, 2011.
491. Bogdanov, M.G., Svinyarov, I., Kunkel, H., Steinle, C., Arkhipova, M., Kantlehner, W. and Maas, G. Empirical Polarity Parameters for Hexaalkylguanidinium-based Room-temperature Ionic Liquids. [Online]. 2010, **65**(7), pp.791-797. [Accessed 2025-03-17]. Available from: https://doi.org/10.1515/znb-2010-0704
492. Reichardt, C. Polarity of ionic liquids determined empirically by means of solvatochromic pyridinium N-phenolate betaine dyes. *Green Chemistry.* [Online]. 2005, **7**(5), pp.339-351. Available from: https://doi.org/10.1039/B500106B
493. Lowry, G.V., Hill, R.J., Harper, S., Rawle, A.F., Hendren, C.O., Klaessig, F., Nobbmann, U., Sayre, P. and Rumble, J. Guidance to improve the scientific value of zeta-potential measurements in nanoEHS. *Environmental Science: Nano.* [Online]. 2016, **3**(5), pp.953-965. Available from: https://doi.org/10.1039/C6EN00136J
494. Bowden, G.D., Pichler, B.J. and Maurer, A. A Design of Experiments (DoE) Approach Accelerates the Optimization of Copper-Mediated (18)F-Fluorination Reactions of Arylstannanes. *Sci Rep.* [Online]. 2019, **9**(1), p.11370. Available from: https://doi.org/10.1038/s41598-019-47846-6
495. Cao, B., Adutwum, L.A., Oliynyk, A.O., Luber, E.J., Olsen, B.C., Mar, A. and Buriak, J.M. How To Optimize Materials and Devices via Design of Experiments and Machine Learning: Demonstration Using Organic Photovoltaics. *ACS Nano.* [Online]. 2018, **12**(8), pp.7434-7444. Available from: https://doi.org/10.1021/acsnano.8b04726
496. Dejaegher, B. and Vander Heyden, Y. Experimental designs and their recent advances in set-up, data interpretation, and analytical applications. *Journal of Pharmaceutical and Biomedical Analysis.* [Online]. 2011, **56**(2), pp.141-158. Available from: https://doi.org/10.1016/j.jpba.2011.04.023
497. Weissman, S.A. and Anderson, N.G. Design of Experiments (DoE) and Process Optimization. A Review of Recent Publications. *Organic Process Research & Development.* [Online]. 2015, **19**(11), pp.1605-1633. Available from: https://doi.org/10.1021/op500169m
498. Box, J.F. RA Fisher and the design of experiments, 1922–1926. *The American Statistician.* [Online]. 1980, **34**(1), pp.1-7.
499. Fisher, R.A. The arrangement of field experiments. *Journal of the Ministry of Agriculture.* [Online]. 1926, **33**, pp.503-515. Available from: https://doi.org/10.23637/rothamsted.8v61q
500. Fisher, R.A. *The design of experiments.* Oxford, England: Oliver & Boyd, 1935.
501. Plackett, R.L. and Burman, J.P. THE DESIGN OF OPTIMUM MULTIFACTORIAL EXPERIMENTS. *Biometrika.* [Online]. 1946, **33**(4), pp.305-325. [Accessed 3/17/2025]. Available from: https://doi.org/10.1093/biomet/33.4.305
502. Box, G.E. and Behnken, D.W. Some new three level designs for the study of quantitative variables. *Technometrics.* [Online]. 1960, **2**(4), pp.455-475.
503. Tsui, K.-L. AN OVERVIEW OF TAGUCHI METHOD AND NEWLY DEVELOPED STATISTICAL METHODS FOR ROBUST DESIGN. *IIE Transactions.* [Online]. 1992, **24**(5), pp.44-57. Available from: https://doi.org/10.1080/07408179208964244
504. Jones, B. and Nachtsheim, C.J. A Class of Three-Level Designs for Definitive Screening in the Presence of Second-Order Effects. *Journal of Quality Technology.* [Online]. 2011, **43**(1), pp.1-15. Available from: https://doi.org/10.1080/00224065.2011.11917841
505. JMP. *JMP Statistical Discovery LLC.* [Online]. 2025. [Accessed]. Available from: https://www.jmp.com/en/home
506. Draper, N.R. Center Points in Second-Order Response Surface Designs. *Technometrics.* [Online]. 1982, **24**(2), pp.127-133. [Accessed 2025/03/16/]. Available from: https://doi.org/10.2307/1268490
507. Borkowski, J.J. Spherical Prediction-Variance Properties of Central Composite and Box-Behnken Designs. *Technometrics.* [Online]. 1995, **37**(4), pp.399-410. [Accessed 2025/03/16/]. Available from: https://doi.org/10.2307/1269732
508. Yuan, T., Akochi-Koble, E., Pinchuk, D. and van de Voort, F.R. FTIR on-line monitoring of biodiesel transesterification. *Int. J. Renew. Energy Biofuels.* [Online]. 2014, **2014**, pp.1-13.
509. Torres, A., Fuentes, B., Rodríguez, K.E., Brito, A. and Díaz, L. Analysis of the Content of Fatty Acid Methyl Esters in Biodiesel by Fourier-Transform Infrared Spectroscopy: Method and Comparison with Gas Chromatography. *Journal of the American Oil Chemists' Society.* [Online]. 2020, **97**(6), pp.651-661. [Accessed 2025/03/16]. Available from: https://doi.org/10.1002/aocs.12350
510. Moawia, R.M., Nasef, M.M., Mohamed, N.H., Ripin, A. and Farag, H. Production of biodiesel from cottonseed oil over aminated flax fibres catalyst: Kinetic and thermodynamic behaviour and biodiesel properties. *Advances in Chemical Engineering and Science.* [Online]. 2019, **9**(4), pp.281-298.
511. Borges, M.E., Díaz, L., Gavín, J. and Brito, A. Estimation of the content of fatty acid methyl esters (FAME) in biodiesel samples from dynamic viscosity measurements. *Fuel Processing Technology.* [Online]. 2011, **92**(3), pp.597-599. Available from: https://doi.org/10.1016/j.fuproc.2010.11.016
512. Dodds, E.D., McCoy, M.R., Rea, L.D. and Kennish, J.M. Gas chromatographic quantification of fatty acid methyl esters: flame ionization detection vs. electron impact mass spectrometry. *Lipids.* [Online]. 2005, **40**(4), pp.419-428. Available from: https://doi.org/10.1007/s11745-006-1399-8

513. Monteiro, M.R., Ambrozin, A.R.P., Lião, L.M. and Ferreira, A.G. Critical review on analytical methods for biodiesel characterization. *Talanta.* [Online]. 2008, **77**(2), pp.593-605. Available from: https://doi.org/10.1016/j.talanta.2008.07.001
514. ASTM. *Standard Test Method for Determination of the Saponification Value of Fats and Oils.* West Conshohocken, PA, USA: ASTM International, 1995.
515. ASTM. *Standard Test Method for Acid and Base Number by Color-Indicator Titration.* West Conshohocken, PA, USA: ASTM International, 2016.
516. Tat, M.E. and Van Gerpen, J.H. The specific gravity of biodiesel and its blends with diesel fuel. *Journal of the American Oil Chemists' Society.* [Online]. 2000, **77**(2), pp.115-119. [Accessed 2025/03/16]. Available from: https://doi.org/10.1007/s11746-000-0019-3
517. BSI. *BS EN 14103:2020.* BSI, 2020.
518. BSI. *BS EN 14105:2020.* BSI, 2020.
519. Di Pietro, M.E., Mannu, A. and Mele, A. NMR Determination of Free Fatty Acids in Vegetable Oils. *Processes.* [Online]. 2020, **8**(4). Available from: https://doi.org/10.3390/pr8040410
520. Ivanova, M., Hanganu, A., Dumitriu, R., Tociu, M., Ivanov, G., Stavarache, C., Popescu, L., Ghendov-Mosanu, A., Sturza, R., Deleanu, C. and Chira, N.-A. Saponification Value of Fats and Oils as Determined from 1H-NMR Data: The Case of Dairy Fats. *Foods.* [Online]. 2022, **11**(10). Available from: https://doi.org/10.3390/foods11101466
521. Doudin, K.I. Quantitative and qualitative analysis of biodiesel by NMR spectroscopic methods. *Fuel.* [Online]. 2021, **284**, p.119114. Available from: https://doi.org/10.1016/j.fuel.2020.119114
522. Igwe, I.O. The effects of temperature on the viscosity of vegetable oils in solution. *Industrial Crops and Products.* [Online]. 2004, **19**(2), pp.185-190. Available from: https://doi.org/10.1016/j.indcrop.2003.09.006
523. Box, G.E.P. and Meyer, R.D. An Analysis for Unreplicated Fractional Factorials. *Technometrics.* [Online]. 1986, **28**(1), pp.11-18. [Accessed 2025/03/16/]. Available from: https://doi.org/10.2307/1269599
524. Hazrat, M.A., Rasul, M.G., Khan, M.M.K., Ashwath, N., Silitonga, A.S., Fattah, I.M.R. and Mahlia, T.M.I. Kinetic Modelling of Esterification and Transesterification Processes for Biodiesel Production Utilising Waste-Based Resource. *Catalysts.* [Online]. 2022, **12**(11). Available from: https://doi.org/10.3390/catal12111472
525. van Schendel, R.K.A., Yang, W., Uslamin, E.A. and Pidko, E.A. Utilizing Design of Experiments Approach to Assess Kinetic Parameters for a Mn Homogeneous Hydrogenation Catalyst. *ChemCatChem.* [Online]. 2021, **13**(23), pp.4886-4896. [Accessed 2025/03/16]. Available from: https://doi.org/10.1002/cctc.202101140
526. Hone, C.A., Boyd, A., O'Kearney-Mcmullan, A., Bourne, R.A. and Muller, F.L. Definitive screening designs for multistep kinetic models in flow. *Reaction Chemistry & Engineering.* [Online]. 2019, **4**(9), pp.1565-1570. Available from: https://doi.org/10.1039/c9re00180h
527. El Saey, H.S., Abo El Naga, A.O., El Saied, M., Shaban, S.A., Abdel-Gawad, S.A. and Salih, S.A. Kinetic and thermodynamic studies on the esterification of oleic acid with methanol over sulfonated biochar catalyst derived from waste tea dregs. *Biomass and Bioenergy.* [Online]. 2023, **176**, p.106892. Available from: https://doi.org/10.1016/j.biombioe.2023.106892
528. Jiang, W., Lai, K.-L., Hu, H., Zeng, X.-B., Lan, F., Liu, K.-X., Wu, Y. and Gu, Z.-W. The effect of [Fe3+]/[Fe2+] molar ratio and iron salts concentration on the properties of superparamagnetic iron oxide nanoparticles in the water/ethanol/toluene system. *Journal of Nanoparticle Research.* [Online]. 2011, **13**(10), pp.5135-5145. Available from: https://doi.org/10.1007/s11051-011-0495-8
529. Kang, X., Yu, J., Li, Y., Gao, P. and Han, Y. A comparison between the magnetic reduction behavior of hematite in H2 and CO atmospheres. *International Journal of Hydrogen Energy.* [Online]. 2025, **111**, pp.449-461. Available from: https://doi.org/10.1016/j.ijhydene.2025.02.233
530. Bi, X., Du, G., Kalam, A., Sun, D., Yu, Y., Su, Q., Xu, B. and Al-Sehemi, A.G. Tuning oxygen vacancy content in TiO2 nanoparticles to enhance the photocatalytic performance. *Chemical Engineering Science.* [Online]. 2021, **234**, p.116440. Available from: https://doi.org/10.1016/j.ces.2021.116440
531. Xue, X., Chen, H., Xiong, Y., Chen, R., Jiang, M., Fu, G., Xi, Z., Zhang, X.L., Ma, J., Fang, W. and Jin, Z. Near-Infrared-Responsive Photo-Driven Nitrogen Fixation Enabled by Oxygen Vacancies and Sulfur Doping in Black TiO2–xSy Nanoplatelets. *ACS Applied Materials & Interfaces.* [Online]. 2021, **13**(4), pp.4975-4983. Available from: https://doi.org/10.1021/acsami.0c17947
532. Roberts, A.P., Zhao, X., Hu, P., Abrajevitch, A., Chen, Y.-H., Harrison, R.J., Heslop, D., Jiang, Z., Li, J., Liu, Q., Muxworthy, A.R., Oda, H., O'Neill, H.S.C., Pillans, B.J. and Sato, T. Magnetic Domain State and Anisotropy in Hematite (α-Fe2O3) From First-Order Reversal Curve Diagrams. *Journal of Geophysical Research: Solid Earth.* [Online]. 2021, **126**(12), p.e2021JB023027. [Accessed 2025/03/22]. Available from: https://doi.org/10.1029/2021JB023027
533. Ghani, N., Saeed, M.A. and Hashim, I.H. Thermoluminescence (TL) response of silica nanoparticles subjected to 50 Gy gamma irradiation. *Malays J Fundam Appl Sci.* [Online]. 2017, **13**(3), pp.178-180.
534. Munasir, M., Hidayat, N., Kusumawati, D.H., Putri, N.P., Taufiq, A. and Sunaryono, S. Amorphous-SiO2 nanoparticles for water treatment materials. *AIP Conference Proceedings.* [Online]. 2020, **2251**(1), p.040030. [Accessed 3/21/2025]. Available from: https://doi.org/10.1063/5.0015673
535. Liang, Y., Ouyang, J., Wang, H., Wang, W., Chui, P. and Sun, K. Synthesis and characterization of core–shell structured SiO2@YVO4:Yb3+,Er3+ microspheres. *Applied Surface Science.* [Online]. 2012, **258**(8), pp.3689-3694. Available from: https://doi.org/10.1016/j.apsusc.2011.12.006
536. Biswas, R.K., Khan, P., Mukherjee, S., Mukhopadhyay, A.K., Ghosh, J. and Muraleedharan, K. Study of short range structure of amorphous Silica from PDF using Ag radiation in laboratory XRD system, RAMAN and NEXAFS. *Journal of Non-Crystalline Solids.* [Online]. 2018, **488**, pp.1-9. Available from: https://doi.org/10.1016/j.jnoncrysol.2018.02.037
537. Hariyanto, B., Wardani, D.A.P., Kurniawati, N., Har, N.P., Darmawan, N. and Irzaman. X-Ray Peak Profile Analysis of Silica by Williamson–Hall and Size-Strain Plot Methods. *Journal of Physics: Conference Series.* [Online]. 2021, **2019**(1), p.012106. Available from: https://doi.org/10.1088/1742-6596/2019/1/012106
538. Calik, A., Erenoglu, R., Erenoglu, O., Ulugergerli, E. and Arslan, N. *Imaging of Spectral Properties of Opal Mineral using Sensor Data, Yenice District, North-Western Turkey.* 2017.
539. Elzea, J.M., Odom, I.E. and Miles, W.J. Distinguishing well ordered opal-CT and opal-C from high temperature cristobalite by x-ray diffraction. *Analytica Chimica Acta.* [Online]. 1994, **286**(1), pp.107-116. Available from: https://doi.org/10.1016/0003-2670(94)80182-7

540. Scheres Firak, D., Rocha Ribeiro, R., de Liz, M.V. and Peralta-Zamora, P. Investigations on iron leaching from oxides and its relevance for radical generation during Fenton-like catalysis. *Environmental Earth Sciences.* [Online]. 2018, **77**(4), p.117. Available from: https://doi.org/10.1007/s12665-018-7274-0
541. Darabian, L.M., Gonçalves, G.R., Schettino, M.A., Passamani, E.C. and Freitas, J.C.C. Synthesis of nanostructured iron oxides and study of the thermal crystallization process using DSC and in situ XRD experiments. *Materials Chemistry and Physics.* [Online]. 2022, **285**, p.126065. Available from: https://doi.org/10.1016/j.matchemphys.2022.126065
542. Wahab, R., Khan, F. and Al-Khedhairy, A.A. Hematite iron oxide nanoparticles: apoptosis of myoblast cancer cells and their arithmetical assessment. *RSC Advances.* [Online]. 2018, **8**(44), pp.24750-24759. Available from: https://doi.org/10.1039/c8ra02613k
543. Chernavskiy, P.A., Novakova, A.A., Pankina, G.V., Pankratov, D.A., Panfilov, S.I. and Petrovskaya, G.A. Synthesis and Characterization of Hematite, Magnetite and Maghemite Supported on Silica Gel. *Magnetochemistry.* [Online]. 2023, **9**(11). Available from: https://doi.org/10.3390/magnetochemistry9110228
544. Nistor, S.V., Ghica, D., Stefan, M., Vlaicu, I., Barascu, J.N. and Bartha, C. Magnetic defects in crystalline Zn(OH)2 and nanocrystalline ZnO resulting from its thermal decomposition. *Journal of Alloys and Compounds.* [Online]. 2013, **548**, pp.222-227. Available from: https://doi.org/10.1016/j.jallcom.2012.09.016
545. Jia, W., Dang, S., Liu, H., Zhang, Z., Yu, C., Liu, X. and Xu, B. Evidence of the formation mechanism of ZnO in aqueous solution. *Materials Letters.* [Online]. 2012, **82**, pp.99-101. Available from: https://doi.org/10.1016/j.matlet.2012.05.013
546. Elumalai, N., Gowdhaman, A., Masilamani, S., Harish, S., Navaneethan, M., Rajabathar, J.R., Al-Lohedan, H., Selvaraj, M., Ramesh, R. and Ramu, P. Zn-MOF-derived γ-Zn(OH)2/Zn(OH)2.0.5H2O/Zn(OH)2/activated charcoal-based electrode material for supercapacitor applications. *Journal of Materials Science: Materials in Electronics.* [Online]. 2023, **34**(32), p.2164. Available from: https://doi.org/10.1007/s10854-023-11591-4
547. Saha, J. and Podder, J. Crystallization Of Zinc Sulphate Single Crystals And Its Structural, Thermal And Optical Characterization. *Journal of Bangladesh Academy of Sciences.* [Online]. 2011, **35**(2), pp.203-210. Available from: https://doi.org/10.3329/jbas.v35i2.9426
548. Rosdiana, E., Prasetya, N. and Gunawan, G. Synthesis and Characterization of TiO2-Chitosan Beads and Its Application as A Degradation Agent of Methylene Blue. *Trends in Sciences.* [Online]. 2023, **20**, p.6670. Available from: https://doi.org/10.48048/tis.2023.6670
549. Bagabas, A., Alshammari, A., Aboud, M. and Kosslick, H. Room-temperature synthesis of zinc oxide nanoparticles in different media and their application in cyanide photodegradation. *Nanoscale Research Letters.* [Online]. 2013, **8**, p.516. Available from: https://doi.org/10.1186/1556-276X-8-516
550. Jamdagni, P., Rana, J.S., Khatri, P. and Nehra, K. Comparative account of antifungal activity of green and chemically synthesized zinc oxide nanoparticles in combination with agricultural fungicides. [Online]. 2018.
551. De Boer, C.B., Mullender, T.A.T. and Dekkers, M.J. Low-temperature behaviour of haematite: susceptibility and magnetization increase on cycling through the Morin transition. *Geophysical Journal International.* [Online]. 2001, **146**(1), pp.201-216. [Accessed 3/21/2025]. Available from: https://doi.org/10.1046/j.0956-540x.2001.01443.x
552. Reddy, J.A., Lakshya, A.K., Raj, R., Kumar, L. and Chowdhury, A. Characterizing Curie and Néel Point Phase Transitions via Thermal Techniques. *physica status solidi (b).* [Online]. 2023, **260**(9), p.2300008. [Accessed 2025/03/21]. Available from: https://doi.org/10.1002/pssb.202300008
553. Kurban, G.V.T., Rego, A.S.C., Mello, N.M., Brocchi, E.A., Navarro, R.C.S. and Souza, R.F.M. Thermodynamics and Kinetic Modeling of the ZnSO4·H2O Thermal Decomposition in the Presence of a Pd/Al2O3 Catalyst. *Energies.* [Online]. 2022, **15**(2). Available from: https://doi.org/10.3390/en15020548
554. Krikorian, O.H. and Shell, P.K. The utilization of ZnSO4 decomposition in thermochemical hydrogen cycles. *International Journal of Hydrogen Energy.* [Online]. 1982, **7**(6), pp.463-469. Available from: https://doi.org/10.1016/0360-3199(82)90102-1
555. Liao, H., Xu, H., Zhang, X., Dai, W. and Zhang, Z. Stable bidentate coordination sulfated TiO2 for highly durable photocatalytic degradation of gaseous acetone. *Applied Catalysis A: General.* [Online]. 2023, **657**, p.119158. Available from: https://doi.org/10.1016/j.apcata.2023.119158
556. Otis, G., Ejgenberg, M. and Mastai, Y. Solvent-Free Mechanochemical Synthesis of ZnO Nanoparticles by High-Energy Ball Milling of ε-Zn(OH)(2) Crystals. *Nanomaterials (Basel).* [Online]. 2021, **11**(1). Available from: https://doi.org/10.3390/nano11010238
557. Moezzi, A., Cortie, M.B. and McDonagh, A.M. Zinc hydroxide sulphate and its transformation to crystalline zinc oxide. *Dalton Transactions.* [Online]. 2013, **42**(40), pp.14432-14437. Available from: https://doi.org/10.1039/C3DT51638E
558. Barzinjy, A.A. and Azeez, H.H. Green synthesis and characterization of zinc oxide nanoparticles using Eucalyptus globulus Labill. leaf extract and zinc nitrate hexahydrate salt. *SN Applied Sciences.* [Online]. 2020, **2**(5), p.991. Available from: https://doi.org/10.1007/s42452-020-2813-1
559. Sharbatdaran, M. and Janbazi, M. Effect of temperature on the structure, catalyst and magnetic properties of un-doped zinc oxide nanoparticles: experimental and DFT calculation. *RSC Advances.* [Online]. 2024, **14**(42), pp.31153-31164. Available from: https://doi.org/10.1039/d4ra04252b
560. Oh, T. and Choi, C.K. Comparison between SiOC Thin Film by plasma enhance chemical vapor deposition and SiO2 Thin Film by Fourier Transform Infrared Spectroscopy. *Journal of the Korean Physical Society.* [Online]. 2010, **56**(4), pp.1150-1155. Available from: https://doi.org/10.3938/jkps.56.1150
561. Shen, X., Wang, Q., Liu, Y., Xue, W., Ma, L., Feng, S., Wan, M., Wang, F. and Mao, C. Manganese Phosphate Self-assembled Nanoparticle Surface and Its application for Superoxide Anion Detection. *Scientific Reports.* [Online]. 2016, **6**(1), p.28989. Available from: https://doi.org/10.1038/srep28989
562. Sobhanardakani, S., Jafari, A., Zandipak, R. and Meidanchi, A. Removal of heavy metal (Hg(II) and Cr(VI)) ions from aqueous solutions using Fe2O3@SiO2 thin films as a novel adsorbent. *Process Safety and Environmental Protection.* [Online]. 2018, **120**, pp.348-357. Available from: https://doi.org/10.1016/j.psep.2018.10.002
563. Shao, H., Zhou, Y., Qi, J., Hu, P. and He, J. Characterization of Fe3O4/γ-Fe2O3@ SiO2 Core-Shell Structure Composite Magnetic Fluid by Microemulsion Method. *Journal of Superconductivity and Novel Magnetism.* [Online]. 2019, **32**(2), pp.247-252. Available from: https://doi.org/10.1007/s10948-018-4910-6
564. Kaur, K., Jain, P., Sobti, A. and Toor, A.P. Sulfated metal oxides: eco-friendly green catalysts for esterification of nonanoic acid with methanol. *Green Processing and Synthesis.* [Online]. 2016, **5**(1), pp.93-100. Available from: https://doi.org/10.1515/gps-2015-0087

565. Eggleston, C.M., Hug, S., Stumm, W., Sulzberger, B. and Dos Santos Afonso, M. Surface Complexation of Sulfate by Hematite Surfaces: FTIR and STM Observations. *Geochimica et Cosmochimica Acta.* [Online]. 1998, **62**(4), pp.585-593. Available from: https://doi.org/10.1016/S0016-7037(97)00372-4
566. Lefèvre, G. In situ Fourier-transform infrared spectroscopy studies of inorganic ions adsorption on metal oxides and hydroxides. *Advances in Colloid and Interface Science.* [Online]. 2004, **107**(2), pp.109-123. Available from: https://doi.org/10.1016/j.cis.2003.11.002
567. Khalaf, H.A., Mansour, S.E. and El-Madani, E.A. The influence of sulfate contents on the surface properties of sulfate-modified tin(IV) oxide catalysts. *Journal of the Association of Arab Universities for Basic and Applied Sciences.* [Online]. 2011, **10**(1), pp.15-20. Available from: https://doi.org/10.1016/j.jaubas.2011.06.003
568. Marlowe, J., Acharya, S., Zuber, A. and Tsilomelekis, G. Characterization of Sulfated SnO2-ZrO2 Catalysts and Their Catalytic Performance on the Tert-Butylation of Phenol. *Catalysts.* [Online]. 2020, **10**(7). Available from: https://doi.org/10.3390/catal10070726
569. Mekhemer, G.A.H., Khalaf, H.A., Mansour, S.A.A. and Nohman, A.K.H. Sulfated Alumina Catalysts: Consequences of Sulfate Content and Source. *Monatshefte für Chemie / Chemical Monthly.* [Online]. 2005, **136**(12), pp.2007-2016. Available from: https://doi.org/10.1007/s00706-005-0374-z
570. Hemmann, F., Jaeger, C. and Kemnitz, E. Comparison of acidic site quantification methods for a series of nanoscopic aluminum hydroxide fluorides. *RSC Adv.* [Online]. 2014, **4**(100), pp.56900-56909. Available from: https://doi.org/10.1039/c4ra09477h
571. Hartmeyer, G., Marichal, C., Lebeau, B., Rigolet, S., Caullet, P. and Hernandez, J. Speciation of Silanol Groups in Precipitated Silica Nanoparticles by 1H MAS NMR Spectroscopy. *The Journal of Physical Chemistry C.* [Online]. 2007, **111**(26), pp.9066-9071. Available from: https://doi.org/10.1021/jp071490l
572. Xiao, S.-T., Wu, S.-M., Dong, Y., Liu, J.-W., Wang, L.-Y., Wu, L., Zhang, Y.-X., Tian, G., Janiak, C., Shalom, M., Wang, Y.-T., Li, Y.-Z., Jia, R.-K., Bahnemann, D.W. and Yang, X.-Y. Rich surface hydroxyl design for nanostructured TiO2 and its hole-trapping effect. *Chemical Engineering Journal.* [Online]. 2020, **400**, p.125909. Available from: https://doi.org/10.1016/j.cej.2020.125909
573. Gottlieb, H.E., Kotlyar, V. and Nudelman, A. NMR Chemical Shifts of Common Laboratory Solvents as Trace Impurities. *The Journal of Organic Chemistry.* [Online]. 1997, **62**(21), pp.7512-7515. Available from: https://doi.org/10.1021/jo971176v
574. Aramendía, M.a.A., Borau, V., Jiménez, C., Marinas, J.M., Ruiz, J.R. and Urbano, F.J. XRD and 1H MAS NMR spectroscopic study of mixed oxides obtained by calcination of layered-double hydroxides. *Materials Letters.* [Online]. 2000, **46**(6), pp.309-314. Available from: https://doi.org/10.1016/S0167-577X(00)00193-2
575. Rivlin, M., Eliav, U. and Navon, G. NMR studies of proton exchange kinetics in aqueous formaldehyde solutions. *Journal of Magnetic Resonance.* [Online]. 2014, **242**, pp.107-112. Available from: https://doi.org/10.1016/j.jmr.2014.02.021
576. Liepinsh, E., Otting, G. and Wüthrich, K. NMR spectroscopy of hydroxyl protons in aqueous solutions of peptides and proteins. *Journal of Biomolecular NMR.* [Online]. 1992, **2**(5), pp.447-465. Available from: https://doi.org/10.1007/BF02192808
577. Shelyapina, M.G., Nefedov, D.Y., Antonenko, A.O., Valkovskiy, G.A., Yocupicio-Gaxiola, R.I. and Petranovskii, V. Nanoconfined Water in Pillared Zeolites Probed by (1)H Nuclear Magnetic Resonance. *Int J Mol Sci.* [Online]. 2023, **24**(21). Available from: https://doi.org/10.3390/ijms242115898
578. Dalai, A.K., Sethuraman, R., Katikaneni, S.P.R. and Idem, R.O. Synthesis and Characterization of Sulfated Titania Solid Acid Catalysts. *Industrial & Engineering Chemistry Research.* [Online]. 1998, **37**(10), pp.3869-3878. Available from: https://doi.org/10.1021/ie980091x
579. Mogilevsky, G., Karwacki, C.J., Peterson, G.W. and Wagner, G.W. Surface hydroxyl concentration on Zr(OH)4 quantified by 1H MAS NMR. *Chemical Physics Letters.* [Online]. 2011, **511**(4), pp.384-388. Available from: https://doi.org/10.1016/j.cplett.2011.06.072
580. Chen, J., Hope, M.A., Lin, Z., Wang, M., Liu, T., Halat, D.M., Wen, Y., Chen, T., Ke, X., Magusin, P.C.M.M., Ding, W., Xia, X., Wu, X.-P., Gong, X.-Q., Grey, C.P. and Peng, L. Interactions of Oxide Surfaces with Water Revealed with Solid-State NMR Spectroscopy. *Journal of the American Chemical Society.* [Online]. 2020, **142**(25), pp.11173-11182. Available from: https://doi.org/10.1021/jacs.0c03760
581. Koller, H. and Weiß, M. Solid State NMR of Porous Materials. In: Chan, J.C.C. ed. *Solid State NMR*. Berlin, Heidelberg: Springer Berlin Heidelberg, 2012, pp.189-227.
582. Krishna, D.N.G. and Philip, J. Review on surface-characterization applications of X-ray photoelectron spectroscopy (XPS): Recent developments and challenges. *Applied Surface Science Advances.* [Online]. 2022, **12**, p.100332. Available from: https://doi.org/10.1016/j.apsadv.2022.100332
583. Davydov, V., Rakhmanina, a., Kireev, a., Alieva, b., Zhironkina, b., Strelkova, O., Dianova, b., Samani, b., Mireles, K., Yahia, L.H., Uzbekov, R. and Khabashesku, V. Solid state synthesis of carbon-encapsulated iron carbide nanoparticles and their interaction with living cells. *Journal of Materials Chemistry.* [Online]. 2014. Available from: https://doi.org/10.1039/C3TB21599G
584. Hou, F., Gorthy, R., Mardon, I., Tang, D. and Goode, C. Low voltage environmentally friendly plasma electrolytic oxidation process for titanium alloys. *Scientific Reports.* [Online]. 2022, **12**, p.6037. Available from: https://doi.org/10.1038/s41598-022-09693-w
585. Glaria, A., Soulé, S., Hallali, N., Ojo, W.-S., Mirjolet, M., Fuks, G., Cornejo, A., Allouche, J., Dupin, J.C., Martinez, H., Carrey, J., Chaudret, B., Delpech, F., Lachaize, S. and Nayral, C. Silica coated iron nanoparticles: synthesis, interface control, magnetic and hyperthermia properties. *RSC Advances.* [Online]. 2018, **8**(56), pp.32146-32156. [Accessed 2024-08-02T20:38:52]. Available from: https://doi.org/10.1039/c8ra06075d
586. Herrmann-Geppert, I., Kramm, U., Radnik, J., Fiechter, S. and Bogdanoff, P. Influence of Sulfur on the Pyrolysis of CoTMPP as Electrocatalyst for the Oxygen Reduction Reaction. *Journal of The Electrochemical Society.* [Online]. 2009, **156**. Available from: https://doi.org/10.1149/1.3185852
587. Chagas, P., Silva, A., Passamani, E., Ardisson, J., Oliveira, L., Fabris, J. and Paniago, R. δ-FeOOH: A superparamagnetic material for controlled heat release under AC magnetic field. *Journal of Nanoparticle Research.* [Online]. 2013, **15**, p.1. Available from: https://doi.org/10.1007/s11051-013-1544-2
588. Ma, H.-P., Yang, J.-H., Yang, J.-G., Zhu, L.-Y., Huang, W., Yuan, G.-J., Feng, J.-J., Jen, T.-C. and Lu, H.-L. Systematic Study of the SiOx Film with Different Stoichiometry by Plasma-Enhanced Atomic Layer Deposition and Its Application in SiOx/SiO2 Super-Lattice. *Nanomaterials.* [Online]. 2019, **9**(1). Available from: https://doi.org/10.3390/nano9010055

589. Lin, Y.-J. and Su, T.-H. SiO2 substrate passivation effects on the temperature-dependent electrical properties of MoS2 prepared by the chemical vapor deposition method. *Journal of Materials Science: Materials in Electronics.* [Online]. 2017, **28**, pp.10106-10111. Available from: https://doi.org/10.1007/s10854-017-6772-2
590. Nocun, M. and Kwaśny, S. Preparation and characterization of V2O5 doped SiO2-TiO2 thin films. *Open Engineering.* [Online]. 2011, **2**, pp.123-128. Available from: https://doi.org/10.2478/s13531-011-0041-6
591. Ferreira-Neto, E., Ullah, S., Martinez, V., Yabarrena, J., Batista Simões, M., Perissinotto, A., Wender, H., De Vicente, F., Noeske, P.L., Ribeiro, S. and Rodrigues Filho, U. Thermally stable SiO 2 @TiO 2 core@shell nanoparticles for application in photocatalytic self-cleaning ceramic tiles. *Materials Advances.* [Online]. 2021, **2**. Available from: https://doi.org/10.1039/D0MA00785D
592. Adyani, S.M. and Ghorbani, m. A comparative study of physicochemical and photocatalytic properties of visible light responsive Fe, Gd and P single and tri-doped TiO 2 nanomaterials. *Journal of Rare Earths.* [Online]. 2017. Available from: https://doi.org/10.1016/j.jre.2017.06.012
593. Lei, T., Yiming, X., Wang, X., Miao, S., Xiong, J. and Yan, C. TiO2 Feather Duster as Effective Polysulfides Restrictor for Enhanced Electrochemical Kinetics in Lithium–Sulfur Batteries. *Small.* [Online]. 2017, **13**. Available from: https://doi.org/10.1002/smll.201701013
594. Beamson, G. and Briggs, D. High resolution XPS of organic polymers. *The Scienta ESCA 300 Database.* [Online]. 1992.
595. Khung, Y., Ngalim, S., Scaccabarozzi, A. and Narducci, D. Formation of stable Si–O–C submonolayers on hydrogen-terminated silicon(111) under low-temperature conditions. *Beilstein journal of nanotechnology.* [Online]. 2015, **6**, pp.19-26. Available from: https://doi.org/10.3762/bjnano.6.3
596. Abdel-Fattah, E., Elsayed, I. and Fahmy, T. Substrate temperature and laser fluence effects on properties of ZnO thin films deposited by pulsed laser deposition. *Journal of Materials Science: Materials in Electronics.* [Online]. 2018, **29**. Available from: https://doi.org/10.1007/s10854-018-0124-8
597. Chen, X.Q., Wu, S.-B., Cao, R. and Tao, J. Preparation and Characterization of Nanosized Hematite Colloids Using Green Vitriol as Ferrum Source. *Journal of Nanomaterials.* [Online]. 2014, **2014**, p.8. Available from: https://doi.org/10.1155/2014/749562
598. Smart, R., Amarantidis, J., Skinner, W., Prestidge, C., Vanier, L. and Grano, S. Surface Analytical Studies of Oxidation and Collector Adsorption in Sulfide Mineral Flotation. In, 2008, pp.3-62.
599. Morgan, D.J. X-Ray Photoelectron Spectroscopy (XPS) : An Introduction. In, 2012.
600. Xu, Y., Kai, H., Xiang, J. and Wang, X. On the Dependence of Band Alignment of SiO_2/Si Stack on SiO_2 Thickness: Extrinsic Or Intrinsic? *IEEE Access.* [Online]. 2020, **PP**, pp.1-1. Available from: https://doi.org/10.1109/ACCESS.2020.3020072
601. Kaur, A., Chahal, P. and Hogan, T. Selective Fabrication of SiC/Si Diodes by Excimer Laser Under Ambient Conditions. *IEEE Electron Device Letters.* [Online]. 2016, **37**, pp.1-1. Available from: https://doi.org/10.1109/LED.2015.2508479
602. Xu, B., Duan, X., Zhou, T., Hao, J., Qin, H., Zhao, Y., Ye, W. and Cao, J. Optically Active Oxygen Defects in Titanium Dioxide Doped with Inorganic Acid Ions. *Nanomaterials.* [Online]. 2024, **14**(12). Available from: https://doi.org/10.3390/nano14121020
603. Saka, A., Jule, L.T., Badassa, B., Gudata, L., Nagaprasad, N., Shanmugam, R., Dwarampudi, L.P., Seenivasan, V. and Ramaswamy, K. Biosynthesis of TiO2 nano particles by using Rosemary (Rosmarinus officinalis) leaf extracts and its application for crystal dye degradation under sunlight. *BMC Chemistry.* [Online]. 2024, **18**(1), p.123. Available from: https://doi.org/10.1186/s13065-024-01229-9
604. Galmiz, O., Stupavska, M., Wulff, H., Kersten, H., Brablec, A. and Cernak, M. Deposition of Zn-containing films using atmospheric pressure plasma jet. *Open Chemistry.* [Online]. 2015, **13**(1). [Accessed 2024-08-07T17:26:19]. Available from: https://doi.org/10.1515/chem-2015-0020
605. Ishak, S., Mandal, S., Lee, H.-S. and Singh, J.K. Microencapsulation of stearic acid with SiO2 shell as phase change material for potential energy storage. *Scientific Reports.* [Online]. 2020, **10**(1), p.15023. Available from: https://doi.org/10.1038/s41598-020-71940-9
606. Stando, G., Han, S., Kumanek, B., Łukowiec, D. and Janas, D. Tuning wettability and electrical conductivity of single-walled carbon nanotubes by the modified Hummers method. *Scientific Reports.* [Online]. 2022, **12**(1), p.4358. Available from: https://doi.org/10.1038/s41598-022-08343-5
607. de Morais, A., Alves, J., Lima, A., Lira-Cantu, M. and Nogueira, A. Enhanced photovoltaic performance of inverted hybrid bulk-heterojunction solar cells using TiO 2 /reduced graphene oxide films as electron transport layers. *Journal of Photonics for Energy.* [Online]. 2015, **5**, p.057408. Available from: https://doi.org/10.1117/1.JPE.5.057408
608. Rabee, A.I.M., Mekhemer, G.A.H., Osatiashtiani, A., Isaacs, M.A., Lee, A.F., Wilson, K. and Zaki, M.I. Acidity-Reactivity Relationships in Catalytic Esterification over Ammonium Sulfate-Derived Sulfated Zirconia. *Catalysts.* [Online]. 2017, **7**(7). Available from: https://doi.org/10.3390/catal7070204
609. Morishige, K. Revisiting the Nature of Adsorption and Desorption Branches: Temperature Dependence of Adsorption Hysteresis in Ordered Mesoporous Silica. *ACS Omega.* [Online]. 2021, **6**(24), pp.15964-15974. Available from: https://doi.org/10.1021/acsomega.1c01643
610. AntonPaar. *BET surface area analyzer: Nova.* [Online]. 2025. [Accessed]. Available from: https://www.anton-paar.com/corp-en/products/details/nova/
611. Allanas, E., Rahman, A., Arlin, E. and Prasetyanto, E.A. Study Surface Area and Pore Size Distribution on Synthetic Zeolite X using BET, BJH and DFT Methods. *Journal of Physics: Conference Series.* [Online]. 2021, **2019**(1), p.012094. Available from: https://doi.org/10.1088/1742-6596/2019/1/012094
612. Fernando, I., Qian, T. and Zhou, Y. Long term impact of surfactants & polymers on the colloidal stability, aggregation and dissolution of silver nanoparticles. *Environmental Research.* [Online]. 2019, **179**, p.108781. Available from: https://doi.org/10.1016/j.envres.2019.108781
613. Chen, Y., Zhang, Z., Wu, Y., Wu, Y., Wang, J., Liu, M. and Chen, L. Surfactant-Free Method to Prevent Gold Nanoparticle Aggregation and Its Surface-Enhanced Raman Scattering Applications. *Langmuir.* [Online]. 2024, **40**(41), pp.21832-21841. Available from: https://doi.org/10.1021/acs.langmuir.4c03096
614. Johnson, L., Gray, D.M., Niezabitowska, E. and McDonald, T.O. Multi-stimuli-responsive aggregation of nanoparticles driven by the manipulation of colloidal stability. *Nanoscale.* [Online]. 2021, **13**(17), pp.7879-7896. Available from: https://doi.org/10.1039/d1nr01190a

615. Liao, J., Qing, S., Zhang, X., Huang, X. and Wang, X. Factors that influence the aggregation structure of nanoparticles in nanofluids: A molecular dynamics simulation. *Journal of Molecular Liquids.* [Online]. 2022, **368**, p.120716. Available from: https://doi.org/10.1016/j.molliq.2022.120716
616. Mohapatra, P., Shaw, S., Mendivelso-Perez, D., Bobbitt, J.M., Silva, T.F., Naab, F., Yuan, B., Tian, X., Smith, E.A. and Cademartiri, L. Calcination does not remove all carbon from colloidal nanocrystal assemblies. *Nature Communications.* [Online]. 2017, **8**(1), p.2038. Available from: https://doi.org/10.1038/s41467-017-02267-9
617. Cahill, J.T., Ruppert, J.N., Wallis, B., Liu, Y. and Graeve, O.A. Development of mesoporosity in scandia-stabilized zirconia: particle size, solvent, and calcination effects. *Langmuir.* [Online]. 2014, **30**(19), pp.5585-5591. Available from: https://doi.org/10.1021/la4049743
618. Sun, H., Jiao, R., An, G., Xu, H. and Wang, D. Influence of particle size on the aggregation behavior of nanoparticles: Role of structural hydration layer. *Journal of Environmental Sciences.* [Online]. 2021, **103**, pp.33-42. Available from: https://doi.org/10.1016/j.jes.2020.10.007
619. Sani, Y.M., Daud, W.M.A.W. and Abdul Aziz, A.R. Activity of solid acid catalysts for biodiesel production: A critical review. *Applied Catalysis A: General.* [Online]. 2014, **470**, pp.140-161. Available from: https://doi.org/10.1016/j.apcata.2013.10.052
620. Saetiao, P., Kongrit, N., Cheng, C.K., Jitjamnong, J., Direksilp, C. and Khantikulanon, N. Catalytic conversion of palm oil into sustainable biodiesel using rice straw ash supported-calcium oxide as a heterogeneous catalyst: Process simulation and techno-economic analysis. *Case Studies in Chemical and Environmental Engineering.* [Online]. 2023, **8**, p.100432. Available from: https://doi.org/10.1016/j.cscee.2023.100432
621. Choe, E. and Min, D.B. Chemistry of Deep-Fat Frying Oils. *Journal of Food Science.* [Online]. 2007, **72**(5), pp.R77-R86. [Accessed 2025/03/21]. Available from: https://doi.org/10.1111/j.1750-3841.2007.00352.x
622. Yılmaz, B., Şahin, T.Ö. and Ağagündüz, D. Oxidative Changes in Ten Vegetable Oils Caused by the Deep-Frying Process of Potato. *Journal of Food Biochemistry.* [Online]. 2023, **2023**(1), p.6598528. [Accessed 2025/03/21]. Available from: https://doi.org/10.1155/2023/6598528
623. Xu, X.-Q. A chromametric method for the rapid assessment of deep frying oil quality. *Journal of the Science of Food and Agriculture.* [Online]. 2003, **83**(13), pp.1293-1296. [Accessed 2025/03/21]. Available from: https://doi.org/10.1002/jsfa.1535
624. Gbadamosi Waheed, A., Raji Ahmed, K. and Oyegoke Jamal, A. Comparative Analysis of the Effects of Domestic Frying and Storage on Some Selected Oil Samples from Local and Commercial Sources. *Earthline Journal of Chemical Sciences.* [Online]. 2019, **3**(1). [Accessed 2025/03/22]. Available from: https://doi.org/10.34198/ejcs.3120.1734
625. Ndiaye, E.M., Faye, P.G., Sow, A., Niane, K., Ndiaye, S., Baldé, S., Cisse, O.I.K., Ayessou, N.C. and Cisse, M. Impact of storage conditions on the physicochemical characteristics of baobab (Adansonia digitata L.) seed oil. *Food and Nutrition Sciences.* [Online]. 2022, **13**(4), pp.373-386.
626. Anisah, P.M., Suwandi and Agustian, E. Effect of transesterification on the result of waste cooking oil conversion to biodiesel. *Journal of Physics: Conference Series.* [Online]. 2019, **1170**(1), p.012067. Available from: https://doi.org/10.1088/1742-6596/1170/1/012067
627. Takeoka, G., Perrino, C. and Buttery, R. Volatile Constituents of Used Frying Oils. *Journal of Agricultural and Food Chemistry.* [Online]. 1996, **44**(3), pp.654-660. Available from: https://doi.org/10.1021/jf950430m
628. Hoque, M.E. and Gee, L.P. Biodiesel from plant resources—sustainable solution to ever increasing fuel oil demands. *Journal of sustainable bioenergy systems.* [Online]. 2013, **3**(3), pp.163-170.
629. Alqurashi, G.K., Al-Shehri, A. and Narasimharao, K. Effect of TiO2 morphology on the benzyl alcohol oxidation activity of Fe2O3–TiO2 nanomaterials. *RSC Advances.* [Online]. 2016, **6**(75), pp.71076-71091. Available from: https://doi.org/10.1039/C6RA13958B
630. Camposeco, R., Castillo, S., Mejía-Centeno, I., Navarrete, J. and Nava, N. Boosted surface acidity in TiO2 and Al2O3-TiO2 nanotubes as catalytic supports. *Applied Surface Science.* [Online]. 2015, **356**, pp.115-123. Available from: https://doi.org/10.1016/j.apsusc.2015.08.026